

molecules

Dendrimers

A Themed Issue in Honor
of Professor Donald A.
Tomalia on the Occasion
of His 80th Birthday

Edited by
Ashok Kakkar

Printed Edition of the Special Issue Published in *Molecules*

Dendrimers

Dendrimers

**A Themed Issue in Honor of Professor
Donald A. Tomalia on the Occasion of
His 80th Birthday**

Special Issue Editor

Ashok Kakkar

MDPI • Basel • Beijing • Wuhan • Barcelona • Belgrade



Special Issue Editor
Ashok Kakkar
McGill University
Canada

Editorial Office
MDPI
St. Alban-Anlage 66
4052 Basel, Switzerland

This is a reprint of articles from the Special Issue published online in the open access journal *Molecules* (ISSN 1420-3049) from 2017 to 2018 (available at: https://www.mdpi.com/journal/molecules/special_issues/dendrimer_tomalia)

For citation purposes, cite each article independently as indicated on the article page online and as indicated below:

LastName, A.A.; LastName, B.B.; LastName, C.C. Article Title. <i>Journal Name</i> Year , Article Number, Page Range.

ISBN 978-3-03897-378-2 (Pbk)

ISBN 978-3-03897-379-9 (PDF)

© 2018 by the authors. Articles in this book are Open Access and distributed under the Creative Commons Attribution (CC BY) license, which allows users to download, copy and build upon published articles, as long as the author and publisher are properly credited, which ensures maximum dissemination and a wider impact of our publications.

The book as a whole is distributed by MDPI under the terms and conditions of the Creative Commons license CC BY-NC-ND.

Contents

About the Special Issue Editor	vii
Preface to "Dendrimers"	ix
Donald A. Tomalia A Serendipitous Journey Leading to My Love of Dendritic Patterns and Chemistry Reprinted from: <i>Molecules</i> 2018 , <i>23</i> , 824, doi:10.3390/molecules23040824	1
Anne-Marie Caminade and Jean-Pierre Majoral Which Dendrimer to Attain the Desired Properties? Focus on Phosphorhydrazone Dendrimers Reprinted from: <i>Molecules</i> 2018 , <i>23</i> , 622, doi:10.3390/molecules23030622	3
In-Yup Jeon, Hyuk-Jun Noh and Jong-Beom Baek Hyperbranched Macromolecules: From Synthesis to Applications Reprinted from: <i>Molecules</i> 2018 , <i>23</i> , 657, doi:10.3390/molecules23030657	15
Didier Astruc, Christophe Deraedt, Rodrigue Djeda, Catia Ornelas, Xiang Liu, Amalia Rapakousiou, Jaime Ruiz, Yanlan Wang and Qi Wang <i>Dentromers</i> , a Family of Super Dendrimers with Specific Properties and Applications Reprinted from: <i>Molecules</i> 2018 , <i>23</i> , 966, doi:10.3390/molecules23040966	36
Burcu Sumer Bolu, Rana Sanyal and Amitav Sanyal Drug Delivery Systems from Self-Assembly of Dendron-Polymer Conjugates Reprinted from: <i>Molecules</i> 2018 , <i>23</i> , 1570, doi:10.3390/molecules23071570	51
Elizabeth Ladd, Amir Sheikhi, Na Li, Theo G.M. van de Ven and Ashok Kakkar Design and Synthesis of Dendrimers with Facile Surface Group Functionalization, and an Evaluation of Their Bactericidal Efficacy Reprinted from: <i>Molecules</i> 2017 , <i>22</i> , 868, doi:10.3390/molecules22060868	77
Takane Imaoka, Noriko Bukeo and Kimihisa Yamamoto Epitaxially Grown Ultra-Flat Self-Assembling Monolayers with Dendrimers Reprinted from: <i>Molecules</i> 2018 , <i>23</i> , 485, doi:10.3390/molecules23020485	95
Matteo Savastano, Carla Bazzicalupi, Claudia Giorgi, Paola Gratteri and Antonio Bianchi Cation, Anion and Ion-Pair Complexes with a G-3 Poly(ethylene imine) Dendrimer in Aqueous Solution Reprinted from: <i>Molecules</i> 2017 , <i>22</i> , 816, doi:10.3390/molecules22050816	102
Marisol Gouveia, João Figueira, Manuel G. Jardim, Rita Castro, Helena Tomás, Kari Rissanen and João Rodrigues Poly(alkylidenimine) Dendrimers Functionalized with the Organometallic Moiety [Ru(η^5 -C ₅ H ₅)(PPh ₃) ₂] ⁺ as Promising Drugs Against <i>Cisplatin</i> -Resistant Cancer Cells and Human Mesenchymal Stem Cells Reprinted from: <i>Molecules</i> 2018 , <i>23</i> , 1471, doi:10.3390/molecules23061471	114
Yossef Alnasser, Siva P. Kambhampati, Elizabeth Nance, Labchan Rajbhandari, Shiva Shrestha, Arun Venkatesan, Rangaramanujam M. Kannan and Sujatha Kannan Preferential and Increased Uptake of Hydroxyl-Terminated PAMAM Dendrimers by Activated Microglia in Rabbit Brain Mixed Glial Culture Reprinted from: <i>Molecules</i> 2018 , <i>23</i> , 1025, doi:10.3390/molecules23051025	131

Noemi Molina, Angela Martin-Serrano, Tahia D. Fernandez, Amene Tesfaye, Francisco Najera, María J. Torres, Cristobalina Mayorga, Yolanda Vida, María I. Montañez and Ezequiel Perez-Inestrosa	
Dendrimeric Antigens for Drug Allergy Diagnosis: A New Approach for Basophil Activation Tests	
Reprinted from: <i>Molecules</i> 2018 , <i>23</i> , 997, doi:10.3390/molecules23050997	145
Lisa Christadore, Mark W. Grinstaff and Scott E. Schaus	
Fluorescent Dendritic Micro-Hydrogels: Synthesis, Analysis and Use in Single-Cell Detection	
Reprinted from: <i>Molecules</i> 2018 , <i>23</i> , 936, doi:10.3390/molecules23040936	157
Feng Gao, Ivan Djordjevic, Oleksandr Pokholenko, Haobo Zhang, Junying Zhang and Terry W.J. Steele	
On-Demand Bioadhesive Dendrimers with Reduced Cytotoxicity	
Reprinted from: <i>Molecules</i> 2018 , <i>23</i> , 796, doi:10.3390/molecules23040796	167
Abhay Singh Chauhan	
Dendrimers for Drug Delivery	
Reprinted from: <i>Molecules</i> 2018 , <i>23</i> , 938, doi:10.3390/molecules23040938	180
Mohiuddin Quadir, Susanne Fehse, Gerhard Multhaup and Rainer Haag	
Hyperbranched Polyglycerol Derivatives as Prospective Copper Nanotransporter Candidates	
Reprinted from: <i>Molecules</i> 2018 , <i>23</i> , 1281, doi:10.3390/molecules23061281	189
Celia Sehad, Tze Chieh Shiao, Lamyaa M. Sallam, Abdelkrim Azzouz and René Roy	
Effect of Dendrimer Generation and Aglyconic Linkers on the Binding Properties of Mannosylated Dendrimers Prepared by a Combined Convergent and Onion Peel Approach	
Reprinted from: <i>Molecules</i> 2018 , <i>23</i> , 1890, doi:10.3390/molecules23081890	216
Patrik Stenström, Dario Manzanares, Yuning Zhang, Valentin Ceña and Michael Malkoch	
Evaluation of Amino-Functional Polyester Dendrimers Based on Bis-MPA as Nonviral Vectors for siRNA Delivery	
Reprinted from: <i>Molecules</i> 2018 , <i>23</i> , 2028, doi:10.3390/molecules23082028	237
Renan Vinicius de Araújo, Soraya da Silva Santos, Elizabeth Igne Ferreira and Jeanine Giarolla	
New Advances in General Biomedical Applications of PAMAM Dendrimers	
Reprinted from: <i>Molecules</i> 2018 , <i>23</i> , 2849, doi:10.3390/molecules23112849	252

About the Special Issue Editor

Ashok Kakkar is a Professor in the Department of Chemistry at McGill University in Montreal, Quebec, Canada. He obtained his PhD from University of Waterloo (Canada, Professor Todd B Marder), followed by post-doctoral studies at University of Cambridge (UK, Professor the Lord Lewis) and Northwestern University (USA, Professor Tobin Marks). His research interests include developing methodologies to complex nanostructures for applications in a variety of areas including drug delivery and diagnostics. His work is very well recognized and his group has published extensively in this area including editing a book "Miktoarm Star Polymers: From Basics of Branched Structure to Synthesis, Self-Assembly and Applications," RSC 2017.

Preface to “Dendrimers”

Dendrimers constitute well-defined hyperbranched and monodispersed macromolecules, the overall composition of which can be articulated through variations of the core, backbone and surface. Through detailed and elegant studies, these intriguing macromolecules are now firmly recognized as a class of polymers. Polyamidoamine dendrimers, which have been widely investigated especially for biomedical applications, were developed by Dr. Donald A Tomalia soon after the first report of dendrimers appeared in 1978. Through synthetic elaboration and detailed evaluation of the potential in areas including nanomedicine, the dendrimer field has seen explosive growth in the past 40 years. The trend is expected to continue, with increased efforts in the commercialization of nanotechnology in medicine.

Celebrating the outstanding contributions to the dendrimer space by Dr. Donald A Tomalia on his 80th birthday in 2018, this monograph is specially designed to guide the reader through detailed reviews written by experts in the field, on different aspects of dendrimers and dendritic architectures, to recent research on several aspects of these macromolecules. Chapter 1 is a brief overview by Dr. Tomalia of his thoughts on the current state of affairs in this area. Chapters 2–5 are review articles on dendrimers and related architectures to provide an understanding of their structure and properties. Chapter 6 describes simple and versatile synthetic methodologies for dendrimers with bactericidal effects. Chapters 7 and 8 explore self-assembled systems from dendrimers, and Chapters 9–18 describe biomedical applications of dendrimers.

This book is an essential read for all scientists just beginning their careers in nanoscience, as well as firmly established ones. It captures the essence of dendrimers, and provides an impetus to continue to explore these intriguing macromolecules.

Ashok Kakkar
Special Issue Editor

Editorial

A Serendipitous Journey Leading to My Love of Dendritic Patterns and Chemistry

Donald A. Tomalia ^{1,2,3}

¹ Department of Chemistry, University of Pennsylvania, Philadelphia, PA 19104, USA

² Department of Physics, Virginia Commonwealth University, Richmond, VA 23284, USA

³ National Dendrimer & Nanotechnology Center, NanoSynthons LLC, 1200 N. Fancher Avenue, Mt. Pleasant, MI 48858, USA; donald.tomalia@gmail.com; Tel.: +1-989-317-3737

Academic Editor: Derek J. McPhee

Received: 30 March 2018; Accepted: 2 April 2018; Published: 4 April 2018

As the oldest of four Midwestern boys who were offsprings of an accountant and a housewife, each with less than a formal high school degree, we were blessed to have such parents. They provided invaluable nurturing, guidance, and wisdom. Their parental nurturing was no surprise; it was a standard legacy taught by my grandparents as immigrants from Czechoslovakia in the early 1900s. However, their extraordinary wisdom and guidance could not be so easily rationalized, especially based on their meager academic pedigrees.

More specifically, my father regularly shared with me his deep interest as well as the importance of understanding natural patterns (i.e., periodicities); whether it was dealing with the weather, best fishing dates, or seashell morphologies. That unarguably influenced my keen interest in trees, dendritic patterns, and architectures which indeed emerged later in my chemistry adventure. He frequently told me that a clear understanding of fundamental patterns always rewarded the beholder with a leveraged comprehension of some hidden order within any area of chaos. That lesson became abundantly clear to me later as I pondered the power of Mendeleev's Periodic Tables, the possibility of similar periodic order in well-defined nanoscale structures, the purpose of tree branching, and the pervasive presence of dendritic patterns throughout nature.

In the case of my mother, it was the more personal understanding of her oldest son's personality that truly remained with me, even eight decades later. This is readily summed up in the following advice she shared with me at a very early age: "Son, your robust curiosity leads you into many fascinating areas; however, my biggest worry is that you will become hopelessly bored and disappointed when you feel you have all the answers." In paraphrased form, she frequently reminded me that my true lifetime challenge for happiness and fulfillment would be: "To pick a career that presented an endless list of questions/mysteries that could never be totally answered and with goals that I may never completely attain".

In my youth, I never quite appreciated her wisdom. However, my nearly six decades in chemistry have truly delivered on that challenge. I have yet to exhaust my long list of chemical mysteries and questions to be answered, which has left me too busy to be bored. For many individuals, such a career would actually be a curse; however, for me, it has turned out to be an amazing blessing.

Needless to say, I must add to this blessing my very supportive family, a long list of unselfish mentors (i.e., Prof. H. Blecker, University of Michigan; Prof. H. Heine, Bucknell University; Prof. H. Hart, Michigan State University; Prof. N.J. Turro, Columbia University; Prof. W.A. Goddard, Cal. Tech., plus countless others), as well as many loyal friends and invaluable colleagues, all of whom have enriched my life.

Now you may begin to understand, even after eight decades, how this serendipitous journey has truly led to my relentless love of chemistry, and is still going strong.



© 2018 by the author. Licensee MDPI, Basel, Switzerland. This article is an open access article distributed under the terms and conditions of the Creative Commons Attribution (CC BY) license (<http://creativecommons.org/licenses/by/4.0/>).

Review

Which Dendrimer to Attain the Desired Properties? Focus on Phosphorhydrazone Dendrimers[†]

Anne-Marie Caminade^{1,2,*} and Jean-Pierre Majoral^{1,2}

¹ CNRS, LCC (Laboratoire de Chimie de Coordination), 205 route de Narbonne, BP 44099, F-31077 Toulouse CEDEX 4, France; jean-pierre.majoral@lcc-toulouse.fr

² LCC-CNRS, Université de Toulouse, CNRS, F-31077 Toulouse CEDEX 4, France

* Correspondence: anne-marie.caminade@lcc-toulouse.fr; Tel.: +33-561-333-100

[†] Dedicated to Prof. Donald Tomalia on the occasion of his 80th birthday.

Received: 12 February 2018; Accepted: 7 March 2018; Published: 9 March 2018

Abstract: Among the six Critical Nanoscale Design Parameters (CNDPs) proposed by Prof. Donald A. Tomalia, this review illustrates the influence of the sixth one, which concerns the elemental composition, on the properties of dendrimers. After a large introduction that summarizes different types of dendrimers that have been compared with PolyAMidoAMine (PAMAM) dendrimers, this review will focus on the properties of positively and negatively charged phosphorhydrazone (PPH) dendrimers, especially in the field of biology, compared with other types of dendrimers, in particular PAMAM dendrimers, as well as polypropyleneimine (PPI), carbosilane, and p-Lysine dendrimers.

Keywords: dendrimers; chemical composition; biological properties; phosphorhydrazone

1. Introduction

Prof. Donald A. Tomalia created the word “dendrimer” from two Greek words δέντρο (dendro), which translates to “tree”, and μέρος (meros), which translates to “part,” and synthesized the famous PAMAM (PolyAMidoAMine) dendrimers [1–3]. In addition to this pioneering work, he has recently proposed a new concept for unifying and defining nanoscience, which he has called “CNDPs,” which stands for Critical Nanoscale Design Parameters [4,5]. This concept can be applied to both hard (metal-based) nanoparticles and to soft (organic) nanoparticles. It is particularly well adapted to the definition and properties of dendrimers, which are soft nano-objects, synthesized step by step to finely tune their properties [6,7]. Six parameters have been defined in the CNDP concept; they concern the (i) size; (ii) shape; (iii) surface chemistry; (iv) flexibility/rigidity; (v) architecture; and (vi) elemental composition of nano-objects. In this review, we will particularly emphasize the sixth parameter, concerning the elemental composition of dendrimers, with particular attention on the differences this criterion induces on properties, despite identical terminal functions.

A non-exhaustive search in the literature reveals that comparison experiments have been carried out in most cases with PAMAM dendrimers compared to other types of dendrimers, such as PPI (polypropyleneimine) [8–10], triazine [11,12], aliphatic ester [13,14], and carbosilane [15,16] dendrimers. The structure of the third generation of these dendrimers is shown in Figure 1. We will consider only publications in which comparative experiments have been done under conditions that are exactly the same and have been reported in an experimental publication, and not publications in which the comparison has been done with references to literature. Comparisons between PAMAM and PPI have been the most widely studied and in different areas. Differences in the fluorescence of the dye phenol blue encapsulated within the dendrimers demonstrated as expected that the interior of PPI dendrimers is slightly less polar than that of PAMAM dendrimers, both having amino terminal functions [17]. The comparison has also been carried out for catalysis. Different generations of both families of dendrimers have been used for the synthesis of gold nanoparticles (about 2 nm diameter in all cases)

by a wet chemical NaBH_4 method. The nanoparticles were then used for catalyzing the reduction of 4-nitrophenol. For Generations 2 and 3, it was shown that the rate constant with nanoparticles entrapped inside PAMAM dendrimers is higher than with PPI dendrimers, but no marked difference was observed for higher generations [18]. Generations 1–5 of PAMAM and PPI (called DAB in this study) dendrimers have been functionalized by promesogenic units derived from salicylaldehyde. All these dendrimers exhibit liquid crystalline properties. The only differences between both series are a higher thermal stability and a wider mesophase temperature range in the PAMAM series, as a consequence of an increased rigidity, due to hydrogen bonds between the amido groups [19].

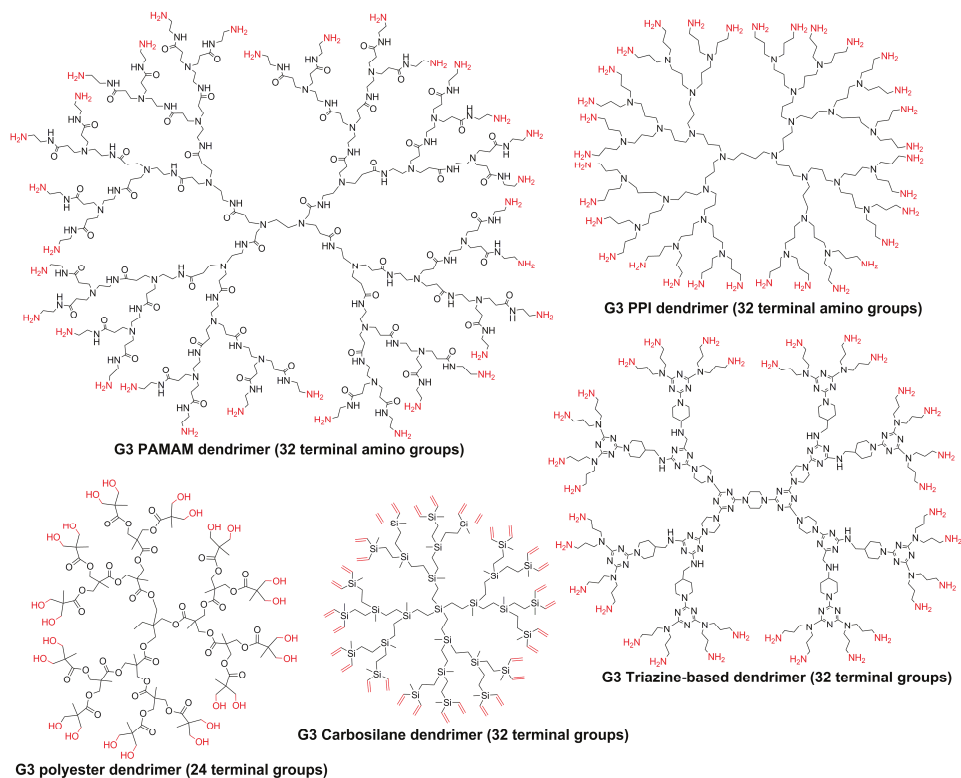


Figure 1. Chemical structure of different types of third-generation dendrimers.

However, the largest number of comparisons between PAMAM and PPI dendrimers concerns their biological properties. Their toxicity has been tested toward the B16F10 cancerous cell line and *in vivo* in mice bearing this tumor. It has been shown that both families of dendrimers behaved essentially similarly, depending on the type of their terminal functions, and not on their internal structure [20]. Other toxicity assays have been carried out with Chinese hamster ovary and human ovarian carcinoma (SKOV3) cells. It has been shown that the two Generation 4 dendrimers with amino terminal functions are very harmful toward both types of cells [21]. MRI (magnetic resonance imaging) contrast agents based on gadolinium complexes have been grafted on the surface of Generation 4 PAMAM and PPI dendrimers, and these compounds were injected to mice. It was shown that the PPI dendrimer (DAB), compared with the PAMAM dendrimer, accumulated more significantly in the liver than in the blood [22]. Hyperpolarized xenon, generally protected in a cage of type cryptophane-A, is another MRI agent. These cages were entrapped most efficiently inside PAMAM dendrimers than

inside PPI dendrimers (11 cages versus 4 for the fifth generations) [23]. Different types of molecules of biological interest have been entrapped also inside both families of dendrimers. This comprises the encapsulation of Vitamins C, B-3, and B-6 [24], phenylbutazone (an anti-inflammatory agent) for which PAMAM dendrimers have a higher loading ability than PPI dendrimers [25], and bortezomib (a proteasome inhibitor), which was by far more efficiently solubilized in water by PPI dendrimers than by PAMAM dendrimers [26].

A few other types of dendrimers have been compared to PAMAM dendrimers. For instance, the catalytic efficiency of carbosilane dendrimers bearing SCS-pincer palladium complexes as terminal functions has been compared to that of PAMAM dendrimers bearing the same type of terminal functions. The PAMAM dendrimers were found to be superior, by showing a higher reaction rate and a higher linear/branched ratio, in the cross coupling reaction between vinyl epoxide and styrylboronic acid. In the auto-tandem catalysis of cinnamyl chloride, hexamethylditin, and 4-nitrobenzaldehyde, only small differences were observed in the efficiency of both families of dendrimers [27]. The effect of PAMAM dendrimers and of triazine dendrimers of comparable size and number of terminal functions, both families being capped with primary amines, was tested toward platelet aggregation, in human platelet-rich plasma. It was shown that triazine dendrimers provoked platelet aggregation less aggressively than PAMAM dendrimers did [28]. The cytotoxicity of a series of aliphatic polyester dendrimers and PAMAM dendrimers, both having alcohol terminal functions, was evaluated toward human cervical cancer (HeLa), acute monocytic leukemia cells (THP.1), and primary human monocyte-derived macrophages. The aliphatic polyester dendrimers were found to be less toxic than the PAMAM dendrimers, and more easily cleavable [29].

To conclude this introductory overview, it seems that the internal structure is of relative importance for the properties of dendrimers. However, in this review, in which phosphorhydrazone dendrimers are compared with other types of dendrimers (including PAMAM and carbosilane dendrimers), we will show that the internal structure of dendrimers may be of crucial importance, in particular when considering the biological properties.

2. Phosphorhydrazone Dendrimers Compared to Other Types of Dendrimers

Two different families of phosphorus-containing dendrimers have been compared with other types of dendrimers: those having positive charges (ammoniums) as terminal functions, and those having negative charges (phosphonates) as terminal functions. They will be presented in this order. In all cases, the comparison is focused on the biological properties [30,31], as these dendrimers are soluble in water [32].

2.1. Positively Charged Phosphorus Dendrimers

Several generations of phosphorhydrazone (PPH) dendrimers having tertiary amines as terminal functions, subsequently protonated (the third generation is shown in Figure 2), have been compared essentially with PAMAM dendrimers, and occasionally with carbosilane dendrimers, having primary amines/ammoniums as terminal functions. These positively charged phosphorus dendrimers have been shown to be efficient transfection agents [33], and they display a high anti-prion activity *in vivo*, against the scrapie form of several strains of prions [34].

In the following sections, we will compare positively charged PPH dendrimers with other types of cationic dendrimers, concerning their interference with clinical chemistry tests, their efficiency as carriers, and their efficiency against neurodegenerative diseases.

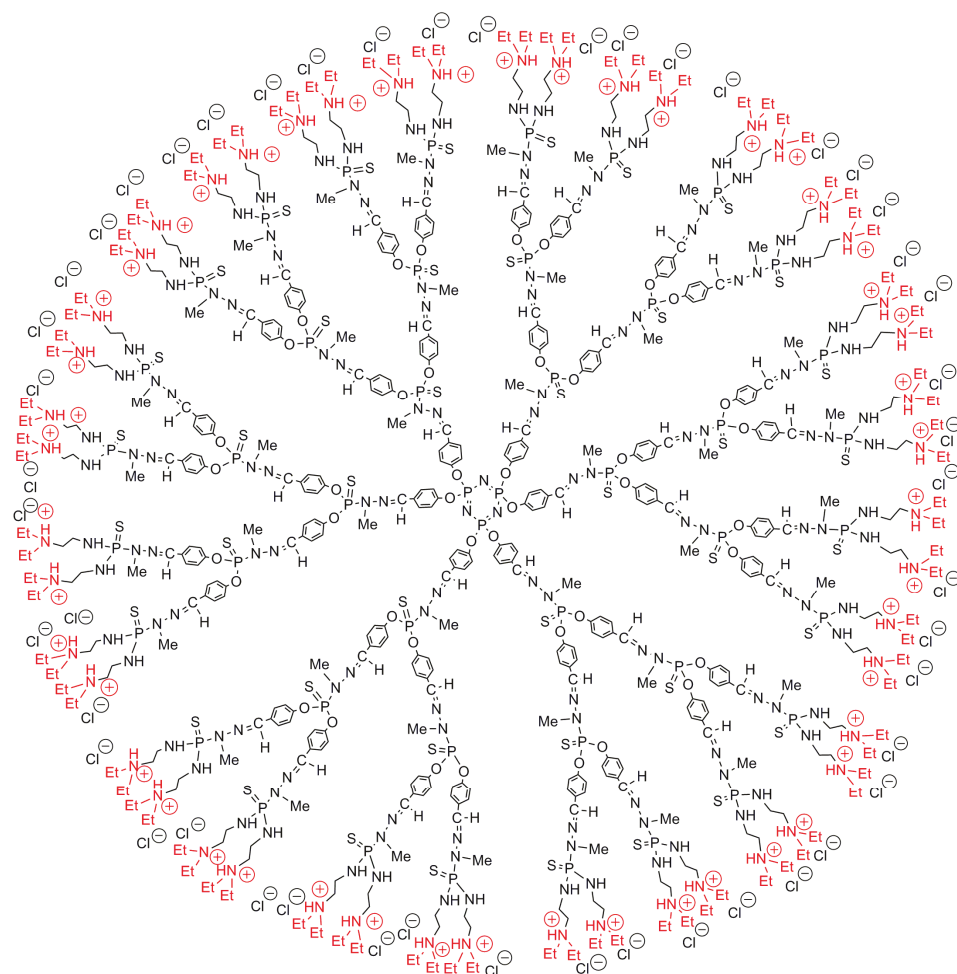


Figure 2. Water-soluble third-generation phosphorus dendrimer with 48 tertiary ammonium terminal functions.

2.1.1. Comparative Interference with Clinical Chemistry Tests

Classical clinical chemistry tests (analysis of blood biochemical parameters) are widely used for assessing the toxicity of compounds. However, it is important to determine if the presence of nanoparticles in general and of dendrimers in particular can interfere or not with these tests. The tests were carried out with positively charged dendrimers of type phosphorhydrazone (Generation 4, 96 tertiary ammonium groups), PAMAM (Generation 4, 64 primary ammonium groups), and carboxilane (Generation 3, 24 quaternary ammonium groups) in standardized human serum, in the absence of cells. It was shown that these dendrimers interfere with the clinical chemistry tests, inducing changes in enzymes activity, and interactions with the test reagents (but not with a protein). These changes can be wrongly interpreted as the appearance of dysfunctions of the liver or buds, so this type of preliminary evaluation is necessary before any animal tests [35].

2.1.2. Comparative Efficiency as Carriers

As already indicated, the transport and delivery properties of positively charged phosphorhydrazone dendrimers have been discovered very early, with the transport of the luciferase plasmid through the membrane of mammalian cells and its delivery inside the nucleus [33]. Changing the nature of the ammonium terminal functions did not improve the transfection efficiency [36]. Positively charged PAMAM and PPH dendrimers, both of Generation 4, were tentatively used to carry the plasmid, inducing an increased GDNF expression (the Glial cell line-Derived Neurotrophic Factor) into Schwann cells, isolated from sciatic nerves. The phosphorhydrazone dendrimers were found to be less effective than the PAMAM dendrimers for the transfection of these Schwann cells, but both were by far less effective than HIV-based lentiviruses. The transgenic Schwann cells were then used to regenerate transected peripheral nerves in rats [37]. PAMAM, PPH, and carbosilane dendrimers were used to complex different anticancer siRNA (small interfering RNA). Then, heparin was added to determine if the siRNA could be released from the dendrimer and if its structure was maintained. These dendrimers are effective for protecting siRNAs from RNase A activity, but treatment with heparin induced the release of siRNA only from the complexes obtained with PAMAM or carbosilane dendrimers, whereas the complexes formed with the phosphorhydrazone dendrimers were not destroyed by heparin [38]. These experiments were carried out in the perspective of the gene therapy of cancers, so these complexes were transfected in HeLa and HL-60 cancerous cell lines. The most effective carriers of siRNA among the three types of dendrimers tested were the PPH dendrimers [39].

2.1.3. Comparative Efficiency against Neurodegenerative Diseases

The very first example in this field, using phosphorhydrazone dendrimers, concerned their interaction with the scrapie form of prions (PrP^{Sc}), which is responsible for several types of spongiform encephalopathies, such as Creutzfeldt–Jakob disease and mad cow disease. The Generation 4 of positively charged phosphorhydrazone dendrimers was able to eliminate the PrP^{Sc} from infected cells, and was even found efficient *in vivo*, for mice infected with brain cells from terminally ill mice [34]. A sequel of this work concerned the interaction of dendrimers with the PrP 106–126 peptide, which is suspected to be involved in the formation of amyloid fibrils in these encephalopathies, as well as the A β 1–28 peptide for Alzheimer’s disease. The interaction of three types of positively charged dendrimers (phosphorhydrazone Generation 4, PAMAM Generations 5 and 6, and PPI Generation 3) with both types of peptides was assessed, using EPR analyzes with a spin probe. It was shown that the interactions of the dendrimers with PrP 106–126 are weaker than with A β 1–28. The PAMAM dendrimers seem to be better peptide-aggregation scavengers than the other dendrimers [40].

The interaction of the same three families of dendrimers with heparin, which is involved in the process of fibril formation in the prion diseases, was also measured. All these dendrimers interact with heparin, mainly by electrostatic interactions. These interactions are indirectly responsible for the inhibition or enhancement of fibril formation, depending on the concentration. At high concentrations, the dendrimers directly impede fibril formation, whereas at low concentrations, they sequester the heparin, preventing it from inducing fibril formation. The dye Thioflavin T-3516 (ThT), which is generally used for detecting amyloid structures, as it fluoresces only in their presence, was used for detecting the interaction of the phosphorhydrazone dendrimers with heparin. Although ThT did not fluoresce in the presence of the dendrimers alone, or heparin alone, a fluorescence was detected for the complex between heparin and the phosphorhydrazone dendrimers. Only these phosphorus dendrimers behaved this way, as no fluorescence was detected for the complexes formed with PAMAM or PPI dendrimers [41].

Rotenone is a pesticide, which is also a damaging agent, increasing the amount of reactive oxygen species (ROS) in neurons, α -synuclein aggregation, and the activation of microglia, and which is associated with an increased risk of Parkinson’s disease. In view of the above-mentioned properties of dendrimers on brain diseases, in particular for preventing aggregation and the formation of fibrils,

it seemed important to investigate if positively charged dendrimers can prevent the damages caused by rotenone on mouse mHippoE-18 cells *in vitro*. The dendrimers tested here were PAMAM dendrimers, PPH dendrimers, and small viologen-phosphorus dendrimers [42,43]. These dendrimers increased cell viability, decreased ROS production, and preserved the mitochondrial function [44].

2.2. Negatively Charged Phosphorus Dendrimers

Negatively charged dendrimers are classically obtained by grafting carboxylic acids as terminal functions, from which sodium salts are easily obtained. This was done in particular with phosphorhydrazone dendrimers [45,46]. However, the negatively charged phosphorus dendrimer possessing the most important biological properties up to now has not carboxylates but azabisphosphonate salts as terminal functions. The structure of the first generation is shown in Figure 3, called “ABP,” which stands for AzaBisPhosphonate. In a first experiment, it was shown that this dendrimer is able to induce *in vitro* the activation of human monocytes, which are a pivotal cell population of innate immunity in the blood [47]. It was shown later that this activation of monocytes occurs through an anti-inflammatory pathway [48]. Among a series of PPH dendrimers having different types of negatively charged terminal functions and of different generations (0 to 2), it was shown that the first generation shown in Figure 3 was the most active [49]. Tailoring the number of terminal functions from 2 to 30 for first-generation PPH dendrimers, by playing with the reactivity of the cyclotriphosphazene, demonstrated that compounds decorated with 8–12 azabisphosphonate terminal functions are the most efficient [50].

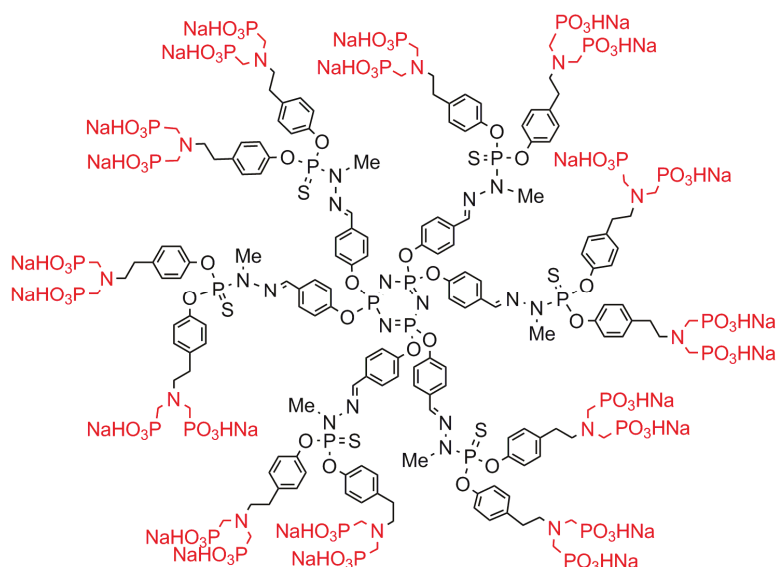


Figure 3. First-generation phosphorhydrazone dendrimer with azabisphosphonate terminal functions (ABP).

In a second experiment, it was shown that the same dendrimer ABP is able to multiply by several hundreds the number of natural killer (NK) cells, which are pivotal for innate immunity, implicated in the early immune response against infections and playing a crucial role in anticancer immunity. As the proliferation of NK cells was extremely tedious to achieve before our work, it was important to verify if the NK cells obtained thanks to this dendrimer were fully functional. Their ability to kill the same cancer cell lines with the same efficiency as uncultured NK cells was successfully assessed with respect

to 15 cell lines (leukemia and carcinoma). Importantly, no aggressiveness of the NK cells generated with this dendrimer toward lymphocytes coming from the same blood donor was observed, demonstrating the safety of this compound [49]. It was shown later on that a multistep cross-talk between monocytes and NK cells is necessary before the proliferation of NK cells [51].

In a third experiment, the anti-inflammatory properties of this dendrimer ABP were tested *in vivo* against chronic inflammatory diseases such as multiple sclerosis (MS) in mice. MS is a chronic inflammatory disease of the central nervous system, thought to be due to an inflammatory attack by autoreactive T cells, which amplify an inflammatory cascade, inducing myelin sheath, resulting in impaired nerve conduction. In a mouse model of MS, in which an experimental autoimmune encephalomyelitis (EAE) has been induced, the dendrimer ABP prevents the development of EAE, and inhibits the progression of established disease. One important mechanism of action of the dendrimer ABP in this case is that it skews the cytokine production by splenocytes from an inflammatory pattern to an anti-inflammatory one [52].

In continuing the study of the structure/activity relationship, the same terminal functions were grafted to the surface of a series of dendrimers. These functions were first grafted to the surface of a first-generation PPI dendrimer, and both dendrimers were tested against another chronic inflammatory disease, rheumatoid arthritis (RA). RA is an autoimmune inflammatory disease, which is characterized by inflammation of the synovial membrane, cartilage degradation, and bone erosion, leading to major handicaps. The ABP dendrimer was found to be very efficient in mice suffering from an RA-like inflammatory disease, whereas the PPI dendrimer had no activity. The dendrimers were given weekly, either intravenously or orally. For mice treated with the dendrimer ABP, normal synovial membranes, reduced levels of inflammatory cytokines, and the absence of both cartilage destruction and bone erosion were observed. Dendrimer ABP increases the level of anti-inflammatory cytokines and has anti-osteoclastic properties. On the contrary, for mice that received the PPI dendrimer decorated with the same azabiphosphonate terminal functions, no difference was observed compared to untreated mice [53].

This work displayed for the first time a drastic difference between the biological activity of two dendrimers having the same terminal functions, but a different internal structure. This idea was then developed to test a larger number of dendrimer families. As the activation of monocytes is the first step for all biological properties of the dendrimer ABP, this was considered as the suitable test to determine the properties of these dendrimers (Figure 4). Dendrimers of type thiophosphate and carbosilane were functionalized with exactly the same function as with ABP. Dendrimers with amine terminal functions (PPI, PAMAM, and p-Lysine) were functionalized by peptide couplings, affording a linker different from the one used for ABP. Thus, the same linker was used also on the surface of a first-generation phosphorhydrazone dendrimer. The dendrimers containing heteroatoms (P or Si) in their structure, even those having a structure very different from that of ABP (thiophosphate and carbosilane), are efficient for the activation of monocytes, even if ABP is still the most efficient. On the contrary, all the "organic" dendrimers (PPI, PAMAM, and p-Lysine) have absolutely no efficiency for the activation of monocytes. In order to try to understand this surprising result, all-atom molecular dynamics simulations were carried out for all of these families of dendrimers. It was shown that all of the compounds that are active have all of their terminal functions gathered in a single side of the dendrimers, which look like cauliflowers and afford a localized high density of functions. On the contrary, the dendrimers that are non-active have a rather spherical structure, and the terminal functions are distributed all over the surface, affording a low local density of functions. This study was the largest given the number of different families that were assayed in identical conditions [54].

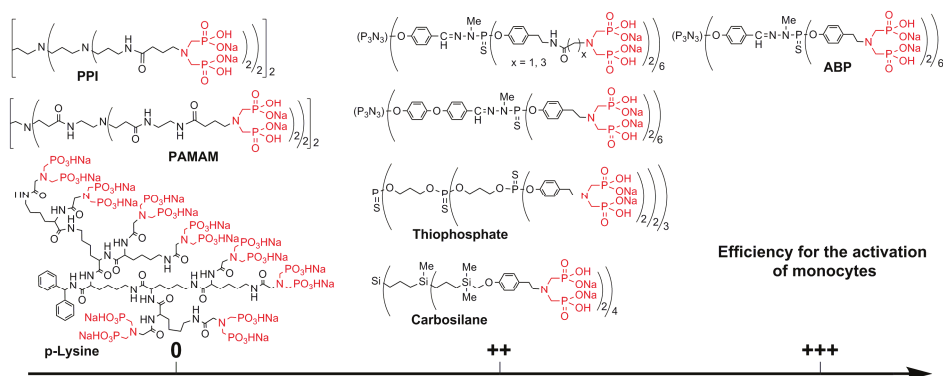


Figure 4. Efficiency of the activation of monocytes, depending on the internal structure of the dendrimers (0: no activation; ++: good activation; +++: the highest activation).

3. Conclusions

In view of all these results, how can our initial question of which dendrimer attains the most desirable properties be answered? Concerning positively charged dendrimers, in particular their transfection efficiency when using plasmids, the PAMAM dendrimers are generally more efficient than the phosphorhydrazone dendrimers. However, when considering the delivery of siRNA, the phosphorhydrazone dendrimers seem more efficient than the PAMAM dendrimers. For other properties, in particular concerning brain diseases, PAMAM, PPI, and PPH dendrimers have almost the same properties, with either PAMAM or PPH being slightly better depending on the precise type of experiment. The situation is very different concerning negatively charged dendrimers. Indeed, with strictly identical terminal functions, the dendrimers containing heteroatoms (P or Si) in their structure have anti-inflammatory properties, whereas the “organic” dendrimers do not. Table 1 summarizes the types of dendrimers and their types and numbers of terminal functions, which have been compared to PPH dendrimers.

Table 1. Types of dendrimers, with the nature and number of their terminal functions, used for comparison in different biological experiments. The most efficient compound for each experiment is highlighted in red.

PPH	PAMAM	PPI	PCSi	P-Lys	Experiment	Ref.
-NEt ₂ H) ₉₆	-NH ₃) ₆₄		-NMe ₃) ₂₄		Clinical tests	[35]
-NEt ₂ H) ₉₆	-NH₃)₆₄				Transfection	[37]
-NEt₂H)₄₈ / -NEt₂H)₉₆	-NH ₃) ₃₂ / -NH ₃) ₆₄		-NMe ₃) ₈		Protection SiRNA ¹	[38]
-NEt₂H)₄₈ / -NEt₂H)₉₆	-NH ₃) ₃₂ / -NH ₃) ₆₄		-NMe ₃) ₈		Carrier of Si RNA	[39]
-NEt ₂ H) ₉₆	-NH₃)₆₄ / -NH₃)₁₂₈	-NH ₃) ₁₆			Peptide aggregation scavenger	[40]
-NEt₂H)₉₆	-NH ₃) ₆₄ / -NH ₃) ₁₂₈	-NH ₃) ₁₆			Interaction with heparin	[41]
-NEt ₂ H) ₄₈ / -NEt ₂ H) ₉₆	-NH₃)₃₂ / -NH₃)₆₄				Decrease ROS ² levels	[44]
(PO₃HNa)₂)₁₂		(PO ₃ HNa) ₂) ₈			Against RA ³	[53]
(PO₃HNa)₂)₁₂ ⁴	(PO ₃ HNa) ₂) ₈	(PO ₃ HNa) ₂) ₈	(PO ₃ HNa) ₂) ₈	(PO ₃ HNa) ₂) ₈	Activation of monocytes	[54]

¹ Small interfering RNA. ² Reactive Oxygen Species. ³ Rheumatoid Arthritis. ⁴ Same efficiency with PPH (PO₃HNa)₂)₈ [50].

Thus, the real conclusion of this review is that the sixth parameter of the CNDPs, concerning the elemental composition of nano-compounds, especially dendrimers, has to be taken into account when dealing with properties, especially biological properties. Definitively, the internal structure of dendrimers is not an “innocent” scaffold.

Acknowledgments: We thank the CNRS (Centre National de la Recherche Scientifique) and the COST action CM1302 (SIPs) for financial support.

Author Contributions: A.-M.C. designed and wrote the paper, with support from J.-P.M.

Conflicts of Interest: The authors declare no conflict of interest.

References

1. Tomalia, D.A.; Baker, H.; Dewald, J.; Hall, M.; Kallos, G.; Martin, S.; Roeck, J.; Ryder, J.; Smith, P. A new class of polymers—Starburst-dendritic macromolecules. *Polym. J.* **1985**, *17*, 117–132. [[CrossRef](#)]
2. Tomalia, D.A.; Baker, H.; Dewald, J.; Hall, M.; Kallos, G.; Martin, S.; Roeck, J.; Ryder, J.; Smith, P. Dendritic macromolecules. Synthesis of starburst dendrimers. *Macromolecules* **1986**, *19*, 2466–2468. [[CrossRef](#)]
3. Tomalia, D.A.; Naylor, A.M.; Goddard, W.A. Starburst dendrimers—Molecular-level control of size, shape, surface-chemistry, topology, and flexibility from atoms to macroscopic matter. *Angew. Chem. Int. Ed.* **1990**, *29*, 138–175. [[CrossRef](#)]
4. Tomalia, D.A. In quest of a systematic framework for unifying and defining nanoscience. *J. Nanopart. Res.* **2009**, *11*, 1251–1310. [[CrossRef](#)] [[PubMed](#)]
5. Tomalia, D.A.; Khanna, S.N. A Systematic Framework and Nanoperiodic Concept for Unifying Nanoscience: Hard/Soft Nanoelements, Superatoms, Meta-Atoms, New Emerging Properties, Periodic Property Patterns, and Predictive Mendeleev-like Nanoperiodic Tables. *Chem. Rev.* **2016**, *116*, 2705–2774. [[CrossRef](#)] [[PubMed](#)]
6. Tomalia, D.A. Dendrons/dendrimers: Quantized, nano-element like building blocks for soft-soft and soft-hard nano-compound synthesis. *Soft Matter* **2010**, *6*, 456–474. [[CrossRef](#)]
7. Tomalia, D.A. Dendritic effects: Dependency of dendritic nano-periodic property patterns on critical nanoscale design parameters (CNDPs). *New J. Chem.* **2012**, *36*, 264–281. [[CrossRef](#)]
8. Buhleier, E.; Wehner, F.; Vögtle, F. “Cascade-” and “Nonskid-chain-like” syntheses of molecular cavity topologies. *Synthesis* **1978**, *78*, 155–158. [[CrossRef](#)]
9. Worner, C.; Mulhaupt, R. Polynitrile-Functional and Polyamine-Functional Poly(Trimethylene Imine) Dendrimers. *Angew. Chem. Int. Ed.* **1993**, *32*, 1306–1308. [[CrossRef](#)]
10. De Brabander van den Berg, E.M.M.; Meijer, E.W. Poly(propylene imine) dendrimers—Large-scale synthesis by heterogeneously catalyzed hydrogenations. *Angew. Chem. Int. Ed.* **1993**, *32*, 1308–1311. [[CrossRef](#)]
11. Takagi, K.; Hattori, T.; Kunisada, H.; Yuki, Y. Triazine dendrimers by divergent and convergent methods. *J. Polym. Sci. Part A-Polym. Chem.* **2000**, *38*, 4385–4395. [[CrossRef](#)]
12. Zhang, W.; Simanek, E.E. Dendrimers based on melamine. Divergent and orthogonal, convergent syntheses of a G3 dendrimer. *Org. Lett.* **2000**, *2*, 843–845. [[CrossRef](#)] [[PubMed](#)]
13. Ihre, H.; Hult, A.; Soderlind, E. Synthesis, characterization, and H-1 NMR self-diffusion studies of dendritic aliphatic polyesters based on 2,2-bis(hydroxymethyl)propionic acid and 1,1,1-tris(hydroxyphenyl)ethane. *J. Am. Chem. Soc.* **1996**, *118*, 6388–6395. [[CrossRef](#)]
14. Ihre, H.; Hult, A.; Frechet, J.M.J.; Gitsov, I. Double-stage convergent approach for the synthesis of functionalized dendritic aliphatic polyesters based on 2,2-bis(hydroxymethyl)propionic acid. *Macromolecules* **1998**, *31*, 4061–4068. [[CrossRef](#)]
15. Zhou, L.L.; Hadjichristidis, N.; Toporowski, P.M.; Roovers, J. Synthesis and properties of regular star polybutadienes with 32 arms. *Rubber Chem. Technol.* **1992**, *65*, 303–314. [[CrossRef](#)]
16. Zhou, L.L.; Roovers, J. Synthesis of novel carbosilane dendritic macromolecules. *Macromolecules* **1993**, *26*, 963–968. [[CrossRef](#)]
17. Richter-Egger, D.L.; Tesfai, A.; Tucker, S.A. Spectroscopic investigations of poly(propyleneimine)dendrimers using the solvatochromic probe phenol blue and comparisons to poly(Amidoamine) dendrimers. *Anal. Chem.* **2001**, *73*, 5743–5751. [[CrossRef](#)] [[PubMed](#)]

18. Esumi, K.; Miyamoto, K.; Yoshimura, T. Comparison of PAMAM-Au and PPI-Au nanocomposites and their catalytic activity for reduction of 4-nitrophenol. *J. Colloid Interface Sci.* **2002**, *254*, 402–405. [[CrossRef](#)] [[PubMed](#)]
19. Donnio, B.; Barbera, J.; Gimenez, R.; Guillon, D.; Marcos, M.; Serrano, J.L. Controlled molecular conformation and morphology in poly(amidoamine) (PAMAM) and poly(propyleneimine) (DAB) dendrimers. *Macromolecules* **2002**, *35*, 370–381. [[CrossRef](#)]
20. Malik, N.; Wiwattanapatapee, R.; Klopsch, R.; Lorenz, K.; Frey, H.; Weener, J.W.; Meijer, E.W.; Paulus, W.; Duncan, R. Dendrimers: Relationship between structure and biocompatibility in vitro, and preliminary studies on the biodistribution of I-125-labelled polyamidoamine dendrimers in vivo. *J. Control. Release* **2000**, *65*, 133–148. [[CrossRef](#)]
21. Janaszewska, A.; Maczynska, K.; Matuszko, G.; Appelhans, D.; Voit, B.; Klajnert, B.; Bryszewska, M. Cytotoxicity of PAMAM, PPI and maltose modified PPI dendrimers in Chinese hamster ovary (CHO) and human ovarian carcinoma (SKOV3) cells. *New J. Chem.* **2012**, *36*, 428–437. [[CrossRef](#)]
22. Kobayashi, H.; Kawamoto, S.; Saga, T.; Sato, N.; Hiraga, A.; Ishimori, T.; Akita, Y.; Mamede, M.H.; Konishi, J.; Togashi, K. Novel liver macromolecular MR contrast agent with a polypropyleneimine diaminobutyl dendrimer core: Comparison to the vascular MR contrast agent with the polyamidoamine dendrimer core. *Magn. Reson. Med.* **2001**, *46*, 795–802. [[CrossRef](#)] [[PubMed](#)]
23. Mynar, J.L.; Lowery, T.J.; Wemmer, D.E.; Pines, A.; Frechet, J.M.J. Xenon biosensor amplification via dendrimer-cage supramolecular constructs. *J. Am. Chem. Soc.* **2006**, *128*, 6334–6335. [[CrossRef](#)] [[PubMed](#)]
24. Boisselier, E.; Liang, L.Y.; Dalko-Csiba, M.; Ruiz, J.; Astruc, D. Interactions and Encapsulation of Vitamins C, B-3, and B-6 with Dendrimers in Water. *Chem.-Eur. J.* **2010**, *16*, 6056–6068. [[CrossRef](#)] [[PubMed](#)]
25. Shao, N.M.; Su, Y.Z.; Hu, J.J.; Zhang, J.H.; Zhang, H.F.; Cheng, Y.Y. Comparison of generation 3 polyamidoamine dendrimer and generation 4 polypropyleneimine dendrimer on drug loading, complex structure, release behavior, and cytotoxicity. *Int. J. Nanomed.* **2011**, *6*, 3361–3372. [[CrossRef](#)]
26. Chaudhary, S.; Gothwal, A.; Khan, I.; Srivastava, S.; Malik, R.; Gupta, U. Polypropyleneimine and polyamidoamine dendrimer mediated enhanced solubilization of bortezomib: Comparison and evaluation of mechanistic aspects by thermodynamics and molecular simulations. *Mater. Sci. Eng. C-Mater. Biol. Appl.* **2017**, *72*, 611–619. [[CrossRef](#)] [[PubMed](#)]
27. Pijnenburg, N.J.M.; Lutz, M.; Siegler, M.A.; Spek, A.; van Koten, G.; Gebbink, R. The role of the dendritic support in the catalytic performance of peripheral pincer Pd-complexes. *New J. Chem.* **2011**, *35*, 2356–2365. [[CrossRef](#)]
28. Enciso, A.E.; Neun, B.; Rodriguez, J.; Ranjan, A.P.; Dobrovolskaia, M.A.; Simanek, E.E. Nanoparticle Effects on Human Platelets in Vitro: A Comparison between PAMAM and Triazine Dendrimers. *Molecules* **2016**, *21*, 428. [[CrossRef](#)] [[PubMed](#)]
29. Feliu, N.; Walter, M.V.; Montanez, M.I.; Kunzmann, A.; Hult, A.; Nystrom, A.; Malkoch, M.; Fadeel, B. Stability and biocompatibility of a library of polyester dendrimers in comparison to polyamidoamine dendrimers. *Biomaterials* **2012**, *33*, 1970–1981. [[CrossRef](#)] [[PubMed](#)]
30. Caminade, A.M.; Turrin, C.O.; Majoral, J.P. Biological properties of phosphorus dendrimers. *New J. Chem.* **2010**, *34*, 1512–1524. [[CrossRef](#)]
31. Caminade, A.M. Phosphorus dendrimers for nanomedicine. *Chem. Commun.* **2017**, *53*, 9830–9838. [[CrossRef](#)] [[PubMed](#)]
32. Caminade, A.M.; Hameau, A.; Majoral, J.P. Multicharged and/or Water-Soluble Fluorescent Dendrimers: Properties and Uses. *Chem.-Eur. J.* **2009**, *15*, 9270–9285. [[CrossRef](#)] [[PubMed](#)]
33. Loup, C.; Zanta, M.A.; Caminade, A.M.; Majoral, J.P.; Meunier, B. Preparation of water-soluble cationic phosphorus-containing dendrimers as DNA transfecting agents. *Chem.-Eur. J.* **1999**, *5*, 3644–3650. [[CrossRef](#)]
34. Solassol, J.; Crozet, C.; Perrier, V.; Leclaire, J.; Beranger, F.; Caminade, A.M.; Meunier, B.; Dormont, D.; Majoral, J.P.; Lehmann, S. Cationic phosphorus-containing dendrimers reduce prion replication both in cell culture and in mice infected with scrapie. *J. Gen. Virol.* **2004**, *85*, 1791–1799. [[CrossRef](#)] [[PubMed](#)]

35. Shcharbin, D.; Shcharbina, N.; Milowska, K.; de la Mata, F.J.; Munoz-Fernandez, M.A.; Mignani, S.; Gomez-Ramirez, R.; Majoral, J.P.; Bryszewska, M. Interference of cationic polymeric nanoparticles with clinical chemistry tests—Clinical relevance. *Int. J. Pharm.* **2014**, *473*, 599–606. [[CrossRef](#)] [[PubMed](#)]
36. Padie, C.; Maszewska, M.; Majchrzak, K.; Nawrot, B.; Caminade, A.M.; Majoral, J.P. Polycationic phosphorus dendrimers: Synthesis, characterization, study of cytotoxicity, complexation of DNA, and transfection experiments. *New J. Chem.* **2009**, *33*, 318–326. [[CrossRef](#)]
37. Shakhbazau, A.; Mohanty, C.; Shcharbin, D.; Bryszewska, M.; Caminade, A.M.; Majoral, J.P.; Alant, J.; Midha, R. Doxycycline-regulated GDNF expression promotes axonal regeneration and functional recovery in transected peripheral nerve. *J. Control. Release* **2013**, *172*, 841–851. [[CrossRef](#)] [[PubMed](#)]
38. Ionov, M.; Lazniewska, J.; Dzmitruk, V.; Halets, I.; Loznikova, S.; Novopashina, D.; Apartsin, E.; Krasheninina, O.; Venyaminova, A.; Milowska, K.; et al. Anticancer siRNA cocktails as a novel tool to treat cancer cells. Part (A). Mechanisms of interaction. *Int. J. Pharm.* **2015**, *485*, 261–269. [[CrossRef](#)] [[PubMed](#)]
39. Dzmitruk, V.; Szulc, A.; Shcharbin, D.; Janaszewska, A.; Shcharbina, N.; Lazniewska, J.; Novopashina, D.; Buyanova, M.; Ionov, M.; Klajnert-Maculewicz, B.; et al. Anticancer siRNA cocktails as a novel tool to treat cancer cells. Part (B). Efficiency of pharmacological action. *Int. J. Pharm.* **2015**, *485*, 288–294. [[CrossRef](#)] [[PubMed](#)]
40. Klajnert, B.; Cangiotti, M.; Calici, S.; Majoral, J.P.; Caminade, A.M.; Cladera, J.; Bryszewska, M.; Ottaviani, M.F. EPR study of the interactions between dendrimers and peptides involved in Alzheimer’s and prion diseases. *Macromol. Biosci.* **2007**, *7*, 1065–1074. [[CrossRef](#)] [[PubMed](#)]
41. Klajnert, B.; Cangiotti, M.; Calici, S.; Ionov, M.; Majoral, J.P.; Caminade, A.M.; Cladera, J.; Bryszewska, M.; Ottaviani, M.F. Interactions between dendrimers and heparin and their implications for the anti-prion activity of dendrimers. *New J. Chem.* **2009**, *33*, 1087–1093. [[CrossRef](#)]
42. Katir, N.; Majoral, J.P.; El Kadib, A.; Caminade, A.M.; Bousmina, M. Molecular and Macromolecular Engineering with Viologens as Building Blocks. Rational Design of Phosphorus-Viologen Dendritic Structures. *Eur. J. Org. Chem.* **2012**, *2012*, 269–273. [[CrossRef](#)]
43. Ciepluch, K.; Katir, N.; El Kadib, A.; Felczak, A.; Zawadzka, K.; Weber, M.; Klajnert, B.; Lisowska, K.; Caminade, A.M.; Bousmina, M.; et al. Biological Properties of New Viologen-Phosphorus Dendrimers. *Mol. Pharm.* **2012**, *9*, 448–457. [[CrossRef](#)] [[PubMed](#)]
44. Milowska, K.; Szwed, A.; Zablocka, M.; Caminade, A.M.; Majoral, J.P.; Mignani, S.; Gabryelak, T.; Bryszewska, M. In vitro PAMAM, phosphorus and viologen-phosphorus dendrimers prevent rotenone-induced cell damage. *Int. J. Pharm.* **2014**, *474*, 42–49. [[CrossRef](#)] [[PubMed](#)]
45. Boggiano, M.K.; Soler-Illia, G.J.A.A.; Rozes, L.; Sanchez, C.; Turrin, C.O.; Caminade, A.M.; Majoral, J.P. New mesostructured hybrid materials made from assemblies of dendrimers and titanium (IV) oxo-organo clusters. *Angew. Chem. Int. Ed.* **2000**, *39*, 4249–4254. [[CrossRef](#)]
46. Kim, D.H.; Karan, P.; Göring, P.; Leclaire, J.; Caminade, A.M.; Majoral, J.P.; Gösele, U.; Steinhart, M.; Knoll, W. Formation of dendrimer nanotubes by layer-by-layer deposition. *Small* **2005**, *1*, 99–102. [[CrossRef](#)] [[PubMed](#)]
47. Poupot, M.; Griffe, L.; Marchand, P.; Maraval, A.; Rolland, O.; Martinet, L.; L’Faquhi-Olive, F.E.; Turrin, C.O.; Caminade, A.M.; Fournie, J.J.; et al. Design of phosphorylated dendritic architectures to promote human monocyte activation. *FASEB J.* **2006**, *20*, 2339–2351. [[CrossRef](#)] [[PubMed](#)]
48. Fruchon, S.; Poupot, M.; Martinet, L.; Turrin, C.O.; Majoral, J.P.; Fournie, J.J.; Caminade, A.M.; Poupot, R. Anti-inflammatory and immunosuppressive activation of human monocytes by a bioactive dendrimer. *J. Leukoc. Biol.* **2009**, *85*, 553–562. [[CrossRef](#)] [[PubMed](#)]
49. Griffe, L.; Poupot, M.; Marchand, P.; Maraval, A.; Turrin, C.O.; Rolland, O.; Metivier, P.; Bacquet, G.; Fournie, J.J.; Caminade, A.M.; et al. Multiplication of human natural killer cells by nanosized phosphonate-capped dendrimers. *Angew. Chem. Int. Ed.* **2007**, *46*, 2523–2526. [[CrossRef](#)] [[PubMed](#)]
50. Rolland, O.; Griffe, L.; Poupot, M.; Maraval, A.; Ouali, A.; Coppel, Y.; Fournie, J.J.; Bacquet, G.; Turrin, C.O.; Caminade, A.M.; et al. Tailored control and optimisation of the number of phosphonic acid termini on phosphorus-containing dendrimers for the ex-vivo activation of human monocytes. *Chem.-Eur. J.* **2008**, *14*, 4836–4850. [[CrossRef](#)] [[PubMed](#)]

51. Hayder, M.; Varilh, M.; Turrin, C.O.; Saoudi, A.; Caminade, A.M.; Poupot, R.; Liblau, R.S. Phosphorus-Based Dendrimer ABP Treats Neuroinflammation by Promoting IL-10-Producing CD4(+) T Cells. *Biomacromolecules* **2015**, *16*, 3425–3433. [[CrossRef](#)] [[PubMed](#)]
52. Hayder, M.; Poupot, M.; Baron, M.; Nigon, D.; Turrin, C.O.; Caminade, A.M.; Majoral, J.P.; Eisenberg, R.A.; Fournie, J.J.; Cantagrel, A.; et al. A Phosphorus-Based Dendrimer Targets Inflammation and Osteoclastogenesis in Experimental Arthritis. *Sci. Transl. Med.* **2011**, *3*, 81. [[CrossRef](#)] [[PubMed](#)]
53. Poupot, M.; Turrin, C.O.; Caminade, A.M.; Fournie, J.J.; Attal, M.; Poupot, R.; Fruchon, S. Poly(phosphorhydrazone) dendrimers: Yin and yang of monocyte activation for human NK cell amplification applied to immunotherapy against multiple myeloma. *Nanomed.-Nanotechnol. Biol. Med.* **2016**, *12*, 2321–2330. [[CrossRef](#)] [[PubMed](#)]
54. Caminade, A.M.; Fruchon, S.; Turrin, C.O.; Poupot, M.; Ouali, A.; Maraval, A.; Garzoni, M.; Maly, M.; Furer, V.; Kovalenko, V.; et al. The key role of the scaffold on the efficiency of dendrimer nanodrugs. *Nat. Commun.* **2015**, *6*, 7722. [[CrossRef](#)] [[PubMed](#)]



© 2018 by the authors. Licensee MDPI, Basel, Switzerland. This article is an open access article distributed under the terms and conditions of the Creative Commons Attribution (CC BY) license (<http://creativecommons.org/licenses/by/4.0/>).

Review

Hyperbranched Macromolecules: From Synthesis to Applications

In-Yup Jeon ^{1,*}, Hyuk-Jun Noh ² and Jong-Beom Baek ^{2,*}

¹ Department of Chemical Engineering, Wonkwang University, 460, Iksandae-ro, Iksan, Jeonbuk 54538, Korea

² School of Energy and Chemical Engineering/Center for Dimension-Controllable Organic Frameworks, Ulsan National Institute of Science and Technology (UNIST), 50, UNIST, Ulsan 44919, Korea; hyukjun93@unist.ac.kr

* Correspondence: iyjeon79@wku.ac.kr (I.-Y.J.); jbaek@unist.ac.kr (J.-B.B.);
Tel.: +82-63-850-7277 (I.-Y.J.); +82-52-217-2510 (J.-B.B.)

Received: 11 February 2018; Accepted: 10 March 2018; Published: 14 March 2018

Abstract: Hyperbranched macromolecules (HMs, also called hyperbranched polymers) are highly branched three-dimensional (3D) structures in which all bonds converge to a focal point or core, and which have a multiplicity of reactive chain-ends. This review summarizes major types of synthetic strategies exploited to produce HMs, including the step-growth polycondensation, the self-condensing vinyl polymerization and ring opening polymerization. Compared to linear analogues, the globular and dendritic architectures of HMs endow new characteristics, such as abundant functional groups, intramolecular cavities, low viscosity, and high solubility. After discussing the general concepts, synthesis, and properties, various applications of HMs are also covered. HMs continue being materials for topical interest, and thus this review offers both concise summary for those new to the topic and for those with more experience in the field of HMs.

Keywords: hyperbranched macromolecules; polymerization; photoelectric materials; stabilizers; bio-applications; carbon nanomaterial

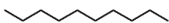
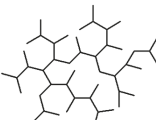
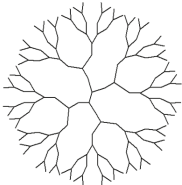
1. Introduction

Dendritic macromolecules have unique architectures quite unlike their linear, branched, and crosslinked analogues. Dendritic macromolecules are classified as dendrons, dendrimers, or hyperbranched macromolecules (HMs, also called hyperbranched polymers), all of which are composed of successive branching units. Dendritic macromolecules have attracted considerable attention during recent decades, because of their unusual properties, such as low viscosity, high solubility, and high functionality (Table 1). These properties stem from their globular and spherical molecular architectures.

A dendrimer consists of two types of structural units: uniform terminal units on the globular surface and dendritic units inside. Thus, dendrimers have well-defined molecular weights with unique symmetric structures. The main drawback for practical applications of dendrimers is the tedious stepwise synthesis required, along with time-consuming purification at each step. Consequently, more efficient methods for production of dendritic macromolecules should involve less tedious synthesis procedures. This is possible by forming hyperbranched macromolecules (HMs). While dendrimers have well defined structure and molecular weight, HMs consist of a mixture of linear and branched units inside with multifunctional groups on their periphery. They still possess a highly branched architecture with a three-dimensional globular shape. The structural difference between dendrimers and HMs is ascribed to the difference in their formation mechanism; thus, it can be further related to their different synthetic approaches used for them. In the case of HMs, their termini are located on the periphery, which is similar to dendrimers. However, the structure of the former is irregular, because linear and branched units are randomly distributed within

the macromolecular framework (or polymer backbone). In brief, HMs have more irregular structures with polydispersity of molecular weight than do dendrimers, which have perfect structures with monodispersity of molecular weight [1–6]. Nevertheless, HMs have demonstrated several characteristics similar to those of dendrimers, including multifunctionality on their periphery, low solution (melt) viscosity, and better solubility [4]. This section focuses on the synthesis, properties, and the applications of HMs developed during the last decades.

Table 1. Comparison of hyperbranched macromolecules with linear polymers and dendrimers. Reproduced from [7] with permission from the Royal Society of Chemistry.

	Linear	Hyperbranched	Dendrimer
Structure			
Topology	1D, linear	3D, irregular	3D, regular
Synthesis	One-step, facile	One-step, relatively facile	Multi-step, laborious
Purification	Precipitation	Precipitation or classification	Chromatography
Scaling-up	Already, easy	Already, easy	Difficult
MW ¹	Discrepant	Discrepant	Identical
PDI ²	>1.1	>1.1	1.0 (<1.05)
DB ³	0	0.4–0.6	1.0
Entanglement	Strong	Weak	Very weak or none
Viscosity	High	Low	Very low
Solubility	Low	High	High
Functional group	At two ends	At linear and terminal units	On periphery (terminal units)
Reactivity	Low	High	High
Strength	High	Low	Very low

¹ Molecular weight; ² Polydispersity index; ³ Degree of branching.

2. Synthesis of HMs

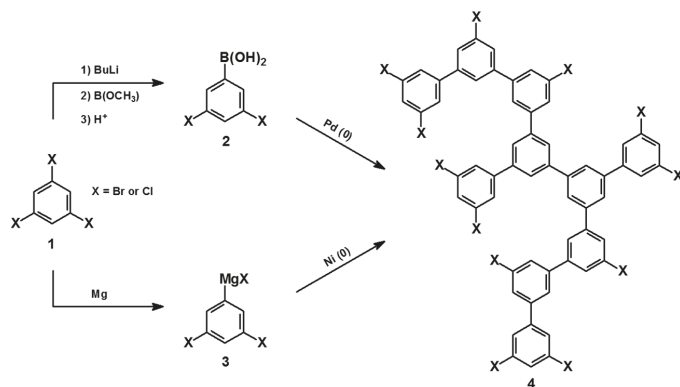
There are three main approaches to the synthesis of HMs: (i) step-growth polycondensation of AB_x ($x \geq 2$) or A₂ + B₃ monomers, (ii) self-condensing vinyl polymerization, and (iii) ring-opening polymerization [8].

2.1. Step-Growth Polycondensation

This strategy involves the polymerization of AB_x ($x \geq 2$) monomers via one-step polycondensation [9–15]. The primary advantage of this approach is that normal step-growth polymerization characteristics are obeyed. However, the main drawbacks include gelation, which often occurs during the polymerization. A monomer with functionality of three or more can form HMs and can fast reach gel point forming a cross-linked network structure even at low fractional conversion. The conversion, at which a tree-like topology turns into a network structure, is known as a gel point. The step-polymerization can be simply quenched the reaction prior to reach the gel point. Still, the purification is required to exclude minor cross-linked structures, and thus to afford pure desired HMs.

Another drawback is that the AB_x monomers employed have to be synthesized prior to polymerization and this is a distinct disadvantage for commercial applications. However, the step-growth polycondensation process offers diverse synthesis of HMs using a variety of available monomers, which provides the potential for preparation of a wide spectrum of functionalities.

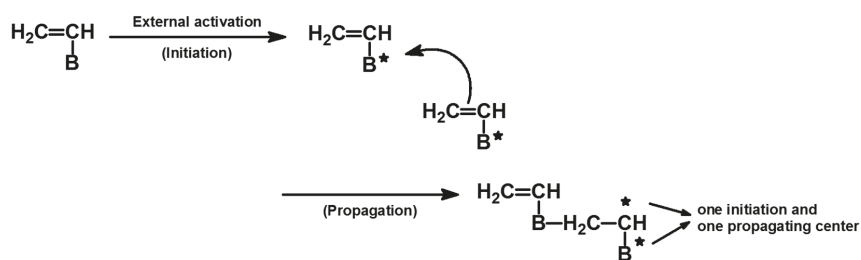
AB₂-type monomers are often used as building blocks, due probably to their easy synthesis (Scheme 1), while the other AB_x (x ≥ 3) monomers have been reported for use in the preparation of hyperbranched polyesters [15,16] and polysiloxanes [17]. For example, 5-acetoxyisophthalic acid was used as the AB₂ monomer in melt polymerization to prepare hyperbranched aromatic polyesters that were insoluble in organic solvents. This was due to intermolecular dehydration, which occurred between the carboxylic acid groups during melt polymerization. However, hydrolysis of the crude product produced a soluble hyperbranched polyester with a large number of carboxylic acid groups [18]. Aromatic-aliphatic hyperbranched polyethers were also prepared by forming benzyl ether linkages in the presence of K₂CO₃ and crown ether (18-crown-6) in acetone [19].



Scheme 1. Synthesis of HMs via step-growth polycondensation. Reproduced from [9–11] with permission from the American Chemical Society.

2.2. Self-Condensing Vinyl Polymerization

Self-condensing vinyl polymerization was defined by Fréchet et al. [20]. This process involves the use of monomers that feature one vinyl group and one initiating moiety (AB* monomers) to generate HMs (Scheme 2). The activated species can be a radical, cation, or even a carbanion.

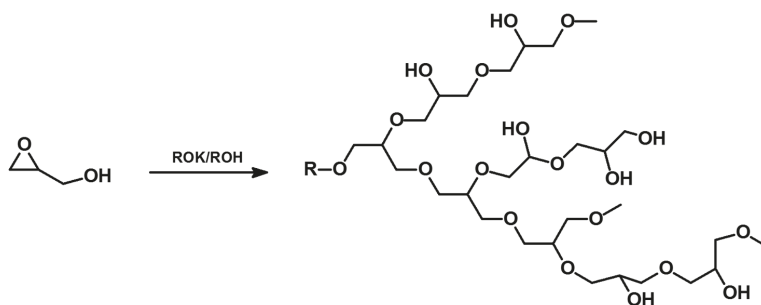


Scheme 2. Synthesis of HMs via self-condensing vinyl polymerization. Reproduced from [21] with permission from the Springer Nature.

After the initiating moiety is activated, it is reacted with a vinyl group to form a covalent bond and a new active site on the α -carbon atom of the double bond. The number of activation sites increases in proportion with the propagation reaction in self-condensing vinyl polymerization, whereas two functional groups are always consumed during polymerization. Therefore, in this process, living/controlled polymerization systems are preferred in order to avoid crosslinking reactions (i.e., gelation) caused by dimerization or chain-transfer reactions.

2.3. Ring-Opening Polymerization

The third approach is called ring-opening polymerization (Scheme 3). Although the monomer itself does not contain branching points, these are generated through the propagation reaction, similar to that in the self-condensing vinyl polymerization (Scheme 2). Therefore, the monomer can be considered a latent AB_x monomer. Polymerization is driven by addition of a proper initiator to the corresponding monomer. As an example, anionic ring-opening polymerization of glycidol was used to prepare hyperbranched aliphatic polyether that contained one epoxide and one hydroxy group, representing a latent AB_2 monomer [22].



Scheme 3. Synthesis of HMs via ring-opening polymerization. Reproduced from [21] with permission from the Springer Nature.

2.4. Alternative Routes for HMs

In addition to the three main routes discussed to prepare HMs, there are a few notable variants that merit discussion. As a consequence of the infrequent commercial availability of AB_2 monomers, other researchers have begun to focus on polycondensation of A_2 and B_3 monomers (the $A_2 + B_3$ route). Generally, the success of this approach is dependent upon many factors, including the ratio of functionalities, solvent and reagent purity, and the reaction time and temperature (conversion). This type of approach is obviously difficult to control and the resultant HMs often have high molecular masses upon gelation [23–25].

Other approaches led to polymers with topologies similar to that of comb or star shaped polymer architectures. The issue of polymerization control has proven to be paramount. In the case of the ‘graft onto’ approach, although steric and dilution effects limit the size of the polymers, they possess a high degree of branching. In the case of the ‘graft from’ approach, a high degree of control over the polymer architecture were obtained. A ‘graft onto’ polymerization was reported in 1991 [26]. Using the polyoxazoline approach, comb-burst poly(ethylenimine)-poly 2-ethyl-2-oxazoline copolymers, and poly(ethylenimine) homopolymers were produced. In contrast, the ‘graft from’ approach described, was used to form branched copolymers utilizing ‘living’ free radical polymerization in 1997 [27]. This approach was utilized to afford a wide variety of complex architectures in relatively few steps from commercially available monomers.

3. Properties of HMs

The physical properties of HMs are of key importance for their implementation in industrial applications. The viscosity of HMs, in both solution and molten states, has been found to be considerably lower than for their linear analogues [8,28]. Low-viscosity is one of the most interesting features of HMs, along with very good solubility in various solvents.

3.1. Solubility

The high solubility of HMs induced by a branched backbone is one important way that they differ from the linear polymers. Kim and Webster reported that hyperbranched polyphenylenes [11] had much better solubility in various solvents than did linear polyphenylenes. The solubility and solution behavior of HMs differ from those of linear ones. It is well known that the solution viscosity of dendritic macromolecules is lower than that of conventional linear polymers [18,29,30]. Such low viscosity indicates that dendritic macromolecules are less entangled due to their unique spherical shape. The relationship between intrinsic viscosity and molecular weight (MW) is shown in Figure 1. Dendrimers display a bell-shaped relationship, resulting from their well-defined globular structures. On the other hand, the intrinsic viscosity of HMs increases with MW, and the slopes of their plots are much lower than those of linear polymers. Moreover, the size exclusion chromatography (SEC) measurements indicated that the retention volume for HMs tended to be greater than that of linear polymers, when compared with the same MWs. The results suggested more compact conformation of HMs than of linear polymers in a solution.

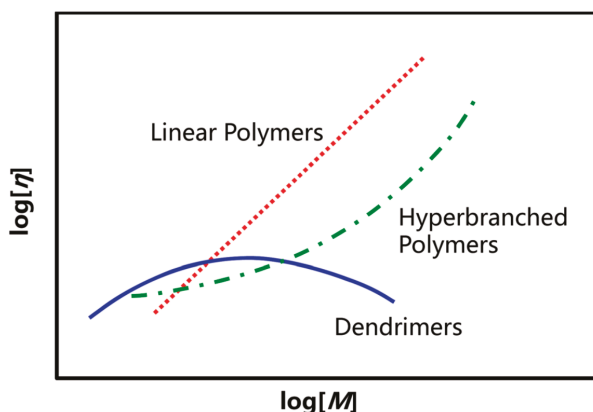


Figure 1. Relationship between log MW and log $[\eta]$ for linear, dendrimer, and hyperbranched molecules. Reproduced from [31] with permission from the Royal Society of Chemistry.

3.2. Thermal Properties

HMs are mostly amorphous materials, though some exceptional examples have been reported. For example, HMs have been modified to induce liquid crystallinity [32,33] or crystallinity [34]. The lower glass transition temperature (T_g) of HMs than of linear polymers is another important feature. The glass transition behavior is related to the relatively large segmental motions within the polymeric frameworks, and the role of the end groups can be disregarded above a certain MW of a linear polymer. However, in the case of HMs, the segmental motions are strongly affected by the branching points, which induce large free volume, as well as the presence of abundant end groups. Therefore, the glass transition for HMs is strongly affected by the translational movement of the entire molecule instead of segmental movements [11,35]. Moreover, the chemical nature of HMs has a decisive effect on T_g . For example, an aliphatic polyester generally has a much lower T_g value than an aromatic polyester having the same MW [35].

3.3. Mechanical Properties

Mechanical properties (e.g., initial modulus, tensile strength, compressive modulus) reflect the highly branched, compact structures of these relatively new polymer architectures [36,37]. The less or non-entangled state of HMs imposes rather poor mechanical integrity, sometimes resulting in

brittleness. These features of HMs have limited their use in thermoplastics, in which mechanical strength is of importance. However, HMs can be used as additives for modification of viscosity to enhance the processability of thermoplastics.

4. Structure of HMs

4.1. Degree of Branching (DB)

A perfectly branched dendrimer is composed of two types of structural units: terminal units on the globular surface and dendritic units inside. On the other hand, HMs possess three types of structural units as illustrated in Figure 2: dendritic unit (D = fully incorporated with AB_x monomer), terminal units (T = two unreacted B groups), and linear units (L = one unreacted B group). The linear segments are generally described as defects. Fréchet et al. [38] defined the term 'degree of branching' (DB) as:

$$DB = (D + T)/(D + L + T) \quad (1)$$

where D, T, and L are the number of dendritic, terminal, and linear units, respectively. DB is one of the important characteristics that indicate the branching structure of HMs. Frey and colleagues [39] reported a modified definition of DB based on the growth directions as:

$$DB = 2D/(2D + L) = (D + T - N)/(D + L + T - N) \quad (2)$$

where N is the number of molecules. The two Equations give almost the same DBs for HMs with high MWs. This is because the N in Frey's equation is negligible in such cases.

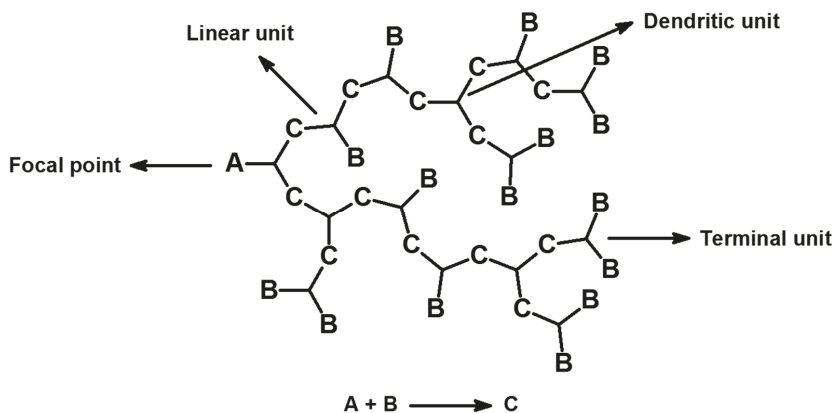


Figure 2. Different segment types in HMs.

The DB of HMs can be measured via direct and indirect methods. The direct methods include NMR measurements and degradation of the polymer units. The model compounds need to be characterized by ^{13}C -nuclear magnetic resonance (NMR). On the basis of ^{13}C -NMR spectra, different peaks from the different branching units of HMs can be assigned. DB can also be calculated from integrals of the corresponding peaks [38]. In addition, an indirect method based on degradation of the hyperbranched backbone was introduced by Kambouris and Hawker [40]. The chain ends are chemically modified and then the hyperbranched skeleton is fully degraded by hydrolysis. The degradation products are identified using capillary chromatography. To use this technique successfully, there are two prerequisites. First, the chain ends must remain intact during the degradation, and second, conversion to elementary subunits must be complete [40].

DB can be altered or tuned to some extent [41–46] via four major methods: (i) copolymerization of AB_2 and AB monomers with different feed ratios [13]; (ii) changing the polymerization conditions such as temperature, the ratio of monomer to catalyst and solvent [47–50], and the monomer pressure [51,52]; (iii) host-guest inclusion of AB_2 or a multifunctional monomer [53]; and (iv) combinations of these three. Moreover, five methods have been tried to increase DB: (i) increasing the reactivity of the B' group (residual functional group on the linear unit) [54], (ii) addition of core molecules [55], (iii) polycondensation of dendrons [56], (iv) post-modification of the formed HMs to convert the linear units to dendritic ones [57], and (v) using a special catalyst [58].

4.2. Molecular Weight

Molecular weight (MW) and the polydispersity index (PDI) are significant parameters for determining the characteristics of HMs. Based on statistical and kinetic methods for HMs prepared by the polycondensation of AB_x ($x \geq 2$) monomers, DP and PDI depend on conversion of the monomers [59,60]. Obviously, PDI increases with increasing conversion. Nevertheless, in some experiments, PDI could be narrowed by utilizing specific techniques, including: (i) slow addition of monomers [61–65], (ii) copolymerization with core molecules [55,63–67], and (iii) separation by dialysis or precipitation [68].

5. Potential Applications of HMs

Generally, in comparison with linear analogues, HMs display many peculiar features, such as large number of reactive end-groups, few chain entanglements, and little or no crystallization (amorphous). The new properties allow them to provide new features such as large free volume, tailor-made properties, enhanced solubility, and low viscosity. To tune their properties, it gives rise to diverse HMs with desirable functional groups (e.g., $-\text{COOH}$, $-\text{OH}$, $-\text{NH}_2$, $\text{O}=\text{C}-\text{NH}_2$, etc.) and topologies such as segmented or sequential units. Benefiting from tunable nature and correspondingly new properties, the produced HMs have been widely applied in various new fields, including photoelectronics, nanotechnology, biomedicine, composites, coatings, adhesives, and modifiers (Figure 3).

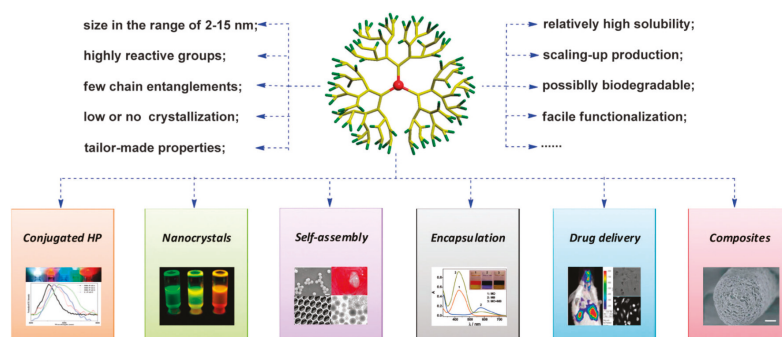


Figure 3. Relationship between the structure and properties of HMs and their major applications. Reproduced from [7] with permission from the Royal Society of Chemistry.

5.1. Photoelectric Materials

When compared with linear polymers, conjugated HMs (CHMs) have better solubility and processability. Moreover, their highly branched and globular frameworks can prevent aggregation and reduce interunit reactions. Driven by the requirement for unusual properties, much effort has been devoted to the design and synthesis of CHMs.

With donor- π -acceptor chromophores, non-linear optical (NLO) materials play a significant role in latent electro-optic applications [69]. For high performance NLO materials, one of the daunting problems is how to eliminate intermolecular dipole-dipole interactions. Such defects can be efficiently restrained by building chromophores in the main-chain [70,71], side-chain [72,73], and periphery [74] of HMs.

To prevent undesired dipole-dipole interactions, direct polycondensation through an $A_2 + B_4$ route using Suzuki coupling reaction has been applied for the synthesis of soluble HMs (two hyperbranched NLO polymers HP1 and HP2) with isolated chromophores [70]. HP1 and HP2 from $A_4 + B_2$ (boronic ester) monomers, containing nitro-based chromophore and sulfonyl-based chromophore, were also prepared via click reaction. According to second harmonic generation measurements, the d_{33} coefficients were 40.0 and 73.6 pm V^{-1} with Φ values of 0.11 and 0.13. Peripheral chromophore-modified HMs can also reduce the dipole-dipole interactions. Although the content of such a chromophore is lower (~20–23 wt %) than that of their linear polymers, the d_{33} coefficients are similar (up to 65 pm V^{-1}). The result can be attributed to their unique molecular architectures [75].

Among the diverse CHMs, polyfluorines (PFs) are very important candidates for blue light emitting diodes (LEDs) due to their desirable luminous intensity [76–83]. To reduce detrimental green emission and/or inherent ketonic defects, the incorporation of triazole, truxene, oxadiazole, or carbazole building units into hyperbranched polyfluorines (HPFs) has been used to improve their electron transport capabilities. A series of novel HPFs were prepared using Suzuki cross-coupling [78]. The resultant products were soluble in common organic solvents (i.e., $CHCl_3$, CH_2Cl_2 , and toluene) and displayed good thermal stability. Either in film or in chloroform solution, they exhibited absorption maxima at 349–378 nm (Figure 4). For an LED using HPF as the emitting layer, the blue emission was up to 212 cd m^{-2} at about 19 V.

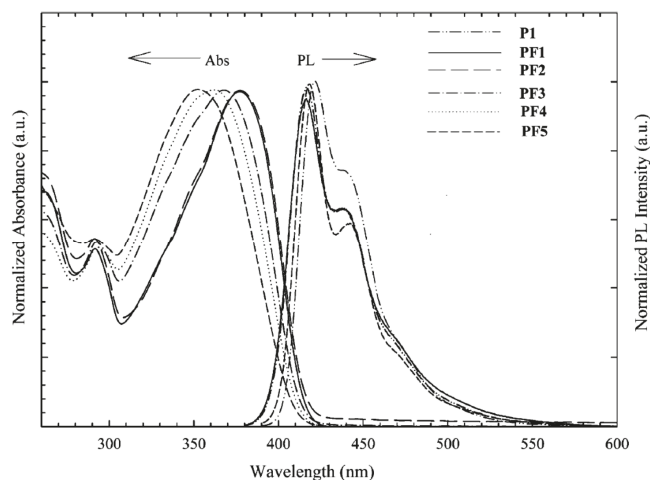


Figure 4. Photoluminescence and absorption spectra of HPFs in $CHCl_3$. Reproduced from [78] with permission from the American Chemical Society.

5.2. Stabilizers for Nanocrystals

Nanocrystals (NCs or nanoparticles) include insulator, semiconductor, and metal crystals that show unique size-dependent physical or chemical properties [84,85]. Spontaneous aggregation of NC particles leads to degradation of performance. Therefore, to minimize the problem, HMs are often used as stabilizers in the preparation of NCs due to their special characteristics, such as their specific three-dimensional structure, good solubility, and lots of intramolecular hollow space (free-volume).

The influence of the HM structure on the synthesis of NCs is mainly shown in the following three aspects: (i) their unique 3D structure can provide sufficient hindrance, and thus can efficiently suppress the aggregation tendency of NCs, (ii) the presence of many cavities in the HM templates confines the free diffusion of NC precursors, and hence are useful for controlling the size of NC particles, and (iii) the terminal groups of HMs provide enough functional flexibility to facilitate the synthesis and dimensional control of NC particles.

Three methods have been reported for the synthesis of NCs: (i) HMs first (HMs use as stabilizers to directly prepare NCs); (ii) ligand exchange (NCs-coated surfactants or linear polymers as ligands are exchanged into an appropriate HMs); and (iii) NCs first (the grafting or in-situ growth of HMs occurs on the surface of NCs) (Figure 5).

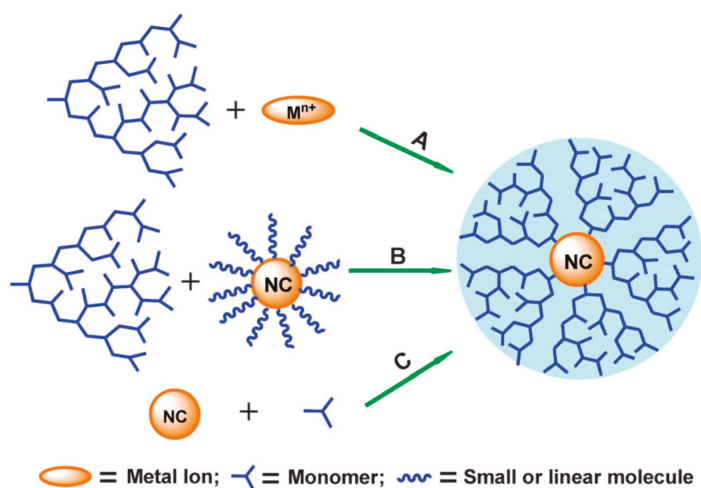


Figure 5. HMs as stabilizer for nanocrystals (NCs): (A) HMs first, (B) ligand exchange, and (C) NCs first. Reproduced from [7] with permission from the Royal Society of Chemistry.

To date, six major kinds of HMs have been employed to prepare NCs. As shown in Figure 6, the acronyms of these HMs are hyperbranched polyamidoamines (HPAMAM) [86,87], hyperbranched poly(ethylene imine) (HPEI) [88–90], hyperbranched polyglycerol (HPG) [91–93], hyperbranched polyester (HPE) [94,95], hyperbranched poly(acryl amide) (HPAM) [96–98] and hyperbranched poly(ether polyols) (HPEO) [99]. Using these HMs as stabilizers, various semiconducting and metallic-conducting NCs have been prepared for diverse applications.

Most quantum dots (QDs) are synthesized using the ‘HMs first’ approach [88–90,100–104]. Hydroxyl-ended HPG ($M_n > 20000 \text{ g mol}^{-1}$) was directly used as the stabilizer to prepare QDs that included ZnS, Ag_2S , PbS, CuS, and CdS [92]. Due to the role of HPG, various QDs displayed good solubility in water and DMF, and also showed low toxicity with good biocompatibility. Excluding unmodified HPGs, thioether-functionalized HPGs could be employed to prepare CdS and CdSe QDs [93]. Interestingly, the sizes of the resultant QDs depended on the molecular weights of the modified HPGs. In addition, the ligand-exchange strategy showed its superiority with regard to the size control of the NCs, because NC particles can be pre-formed. HPEI exchanged with hydrophobic surfactants of CdSe@ZnS QDs, can form very stable colloids in chloroform [105]. Compared with the aforementioned approaches, surface chemical grafting onto QDs is a more reliable way to stabilize NCs. Coating QDs with a protective shell can effectively avoid fluorescence quenching or the release of toxic metal ions [106–109].

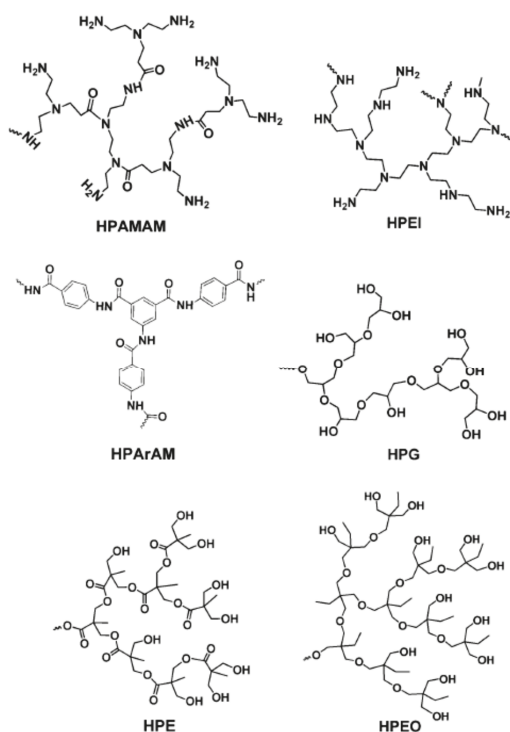


Figure 6. Schematic structures of classic HMs (and their acronyms) used as stabilizers to prepare NCs.

Incidentally, multifarious factors, such as DB, the reaction temperature, and the concentration of metal ions, contribute to the particle size of NCs [110–112]. Other than monometallic (Au, Ag, Pt, Pd, and Ru) NCs, bimetallic (Au/Pt, Au/Pd, and Au/Ru) NCs [98] and smart HM-stabilized NCs [113] (thermo- or pH-responsive ones) have also easily been achieved using a similar strategy.

5.3. Bio-Applications

Similar to the amphiphilic linear block copolymers, amphiphilic HMs can be self-assembled into various supramolecular structures in solution or through interfacial self-assembly. Supramolecular structures have potential applications in biomedical areas, because of their biocompatibility and adjustable molecular architectures. Hyperbranched polyethers, polyesters, polyphosphates, and polysaccharides could be candidates for biomedical uses in areas including cytomimetic chemistry, drug delivery, gene transfection, antimicrobial material, and bio-imaging fields [114–116].

Compared with small molecular liposomes, the HM vesicles (HMsVs) formed, display lower membrane fluidity and higher stability. HMsVs can induce multivalent interactions among vesicles, like a biomembrane does. Moreover, the size of HMsVs is very close to that of a cell, allowing direct observation through optical or fluorescent microscopy. Zhou and Yan revealed that membrane fusions were initiated even by small perturbations or by changing the osmotic pressure [117,118].

Apart from cytomimetic chemistry, supramolecular aggregates formed by HM self-assembly have been utilized to load drugs. Compared with naked drugs, HM-drug complexes can improve solubility and prolong service time. At the same time, they can easily penetrate cell membranes and selectively accumulate, as well as be retained, at tumor sites [119].

Cationic HMs (e.g., hyperbranched polyethylenimine, HPEI) mixed with electronegative DNA can form HM-DNA polyplexes for gene transfection. Compared with viral vectors, HMs displayed various advantages such as higher safety, weaker immune responses, more facile synthesis, and easier operation [120–126].

HMs have also been widely used as antibacterial/antifouling materials. Due to their good biocompatibility and chemical stability, HPGs are promising antifouling materials that can be employed to prevent the attachment of proteins [127].

In the bio-imaging field, HM-probe-conjugates with good water solubility and available functional groups are good solutions to problems associated with low quantum yield and poor specificity. Zhu and Yan grafted fluorescein isothiocyanate on peripheral hyperbranched polysulfonamine (HPSA) through the reaction of isothiocyanate and a primary amino group [128,129]. With low cytotoxicity and good serum compatibility, the HPSA-probe conjugate can be used for bio-imaging or for tracking cells [125].

Star-like HMs (HCP-N-PEG and HCP-O-PEG) have an hyperbranched conjugated polymer (HCP) core and linear polyethylene glycol (PEG) arms. They showed superior fluorescein response sensitivity compared to that of small fluorophores, and could be used as drug carriers for tumor therapy (Figure 7) [130].

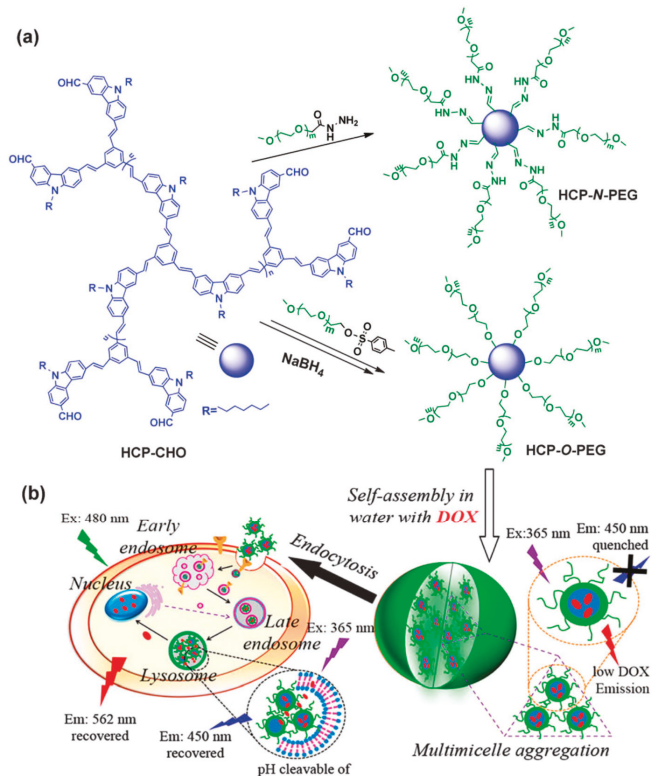


Figure 7. (a) Synthesis of HCP-N-PEG and HCP-O-PEG conjugated copolymers; (b) Self-assembly of conjugated copolymers and their endocytosis in tumor cells. Reproduced from [130] with permission from the American Chemical Society.

5.4. Carbon Nanomaterial/HM Nanocomposites

Because of their highly branched architecture, HMs have less intermolecular entanglement, which leads to good solubility, low viscosity, and unusual rheological properties. Their unique 3-D architecture offers enough steric hindrance to avoid aggregation of the nanoparticles. Therefore, HPs are good dispersants and surface modifiers for carbon nanomaterials, such as carbon nanotubes (CNTs) and graphene (or graphene nanoplatelets).

When dendritic sulfonated hyperbranched poly-(ether-ketone) (SHPEK) was grafted onto the surfaces of multiwall carbon nanotubes (MWCNT or MWNT), the resultant nanocomposites (e.g., SHPEK-g-MWCNT) were easily dispersible in water (zeta potential of -57.8 mV; see Figure 8). SHPEK-g-MWCNT film showed sheet resistance as low as $63 \Omega/\text{sq}$ and high electrocatalytic activity for the oxygen reduction reaction (ORR), without heteroatom doping onto the MWCNT framework [131].

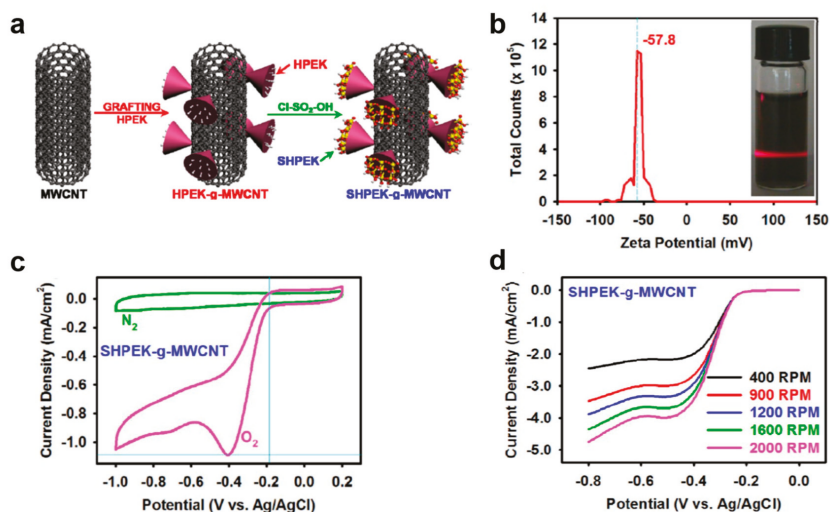


Figure 8. (a) Schematic demonstrations for SHPEK-g-MWCNT. (b) Zeta-potential curve of SHPEK-g-MWCNT (Inset: a photograph of the solution with hand-held laser shining). (c) Cyclic voltammograms in nitrogen- and oxygen-saturated 0.1 M aqueous KOH solution for SHPEK-g-MWCNT. (d) RDE voltammograms in oxygen-saturated 0.1 M aq. KOH solution with a scan rate of 0.01 V/s at different rotation rates. Reproduced from [131] with permission from the American Chemical Society.

Carbon nanomaterial/HM nanocomposites exhibited enhanced performance due to their favorable synergistic effects [132,133]. HMs exhibit low intrinsic viscosity, thus endowing the nanocomposites with good processability. There are two major methods for preparing nanocomposites or hybrids: (i) direct mixing of HMs with carbon nanomaterials and (ii) in situ polymerization of HMs in the presence of carbon nanomaterials. If HMs and carbon nanomaterials are linked by covalent bonds, the phase separation issue at the interface can be efficiently eliminated and the overall performance is greatly enhanced.

In the case of HPPS-g-MWCNT prepared from grafting of hyperbranched poly(phenyl sulfide) (HPPS) onto the surface of MWCNT, the dispersibility and melt-processability of the nanocomposite were significantly enhanced. Thus, the nanocomposite specimens could be easily compression-molded. Without chemical doping, the surface conductivities of as-prepared HPPS-g-MWNT film were in the semi-metallic transport region (3.56 S cm^{-1}) [134].

Graphene has attracted increasing attention and been subjected to rapid development because of its unique atom-thick 2-D structure and excellent properties. It has a wide range of promising potential applications [135,136]. Exfoliation of graphite to produce graphene could be achieved very simply

by a wedge effect using HMs. In situ ‘direct’ grafting of HMs to the edges of pristine graphite could exfoliate graphitic layers to form graphene (Figure 9). Due to the 3-D molecular architectures of HMs, the solubility of HM grafted graphene is profoundly improved compared with grafting of its linear analogue. This result is because HM provides numerous polar peripheral groups that not only act as macromolecular wedges, but also exhibit chemical affinity for solvents [137].

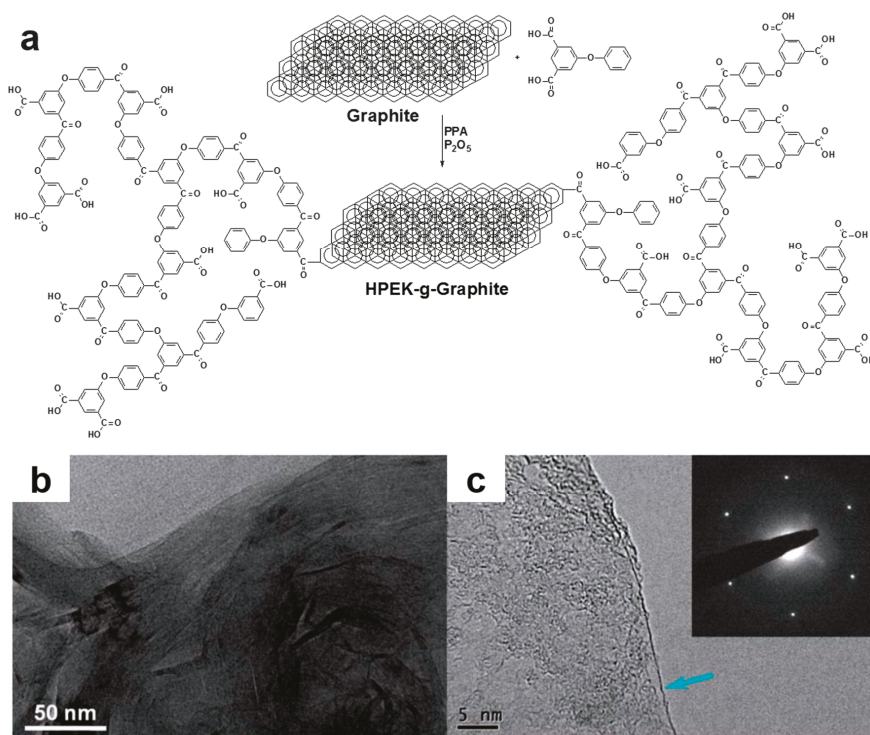


Figure 9. (a) ‘Direct’ Friedel-Crafts acylation reaction between graphite and HPEK in PPA/P₂O₅ medium. TEM images: (b) HPEK-g-graphite; (c) ‘Edge-on’ view (Inset: a selected area electron diffraction (SAED) pattern obtained from the basal area). Reproduced from [137] with permission from the Royal Society of Chemistry.

Graphene oxide (GO) possesses many available functional groups (e.g., hydroxyl and epoxide groups) on its basal area and along edges [138], which allow further chemical modification. Furthermore, these functional groups endow GO sheets with strong hydrophilicity, which makes GO fully dispersible in water or polar solvents (such as DMF and NMP) [139]. Through a liquid crystal self-templating methodology, next-generation continuous nacre-mimics with extreme strength and toughness have been achieved [140,141]. Hierarchically assembled fibers exhibited the highest tensile strength (652 MPa) and excellent ductility, with a toughness of 18 MJ m⁻³. The outstanding mechanical performance of GO-HPG fibers is ascribed to their hierarchically assembled structure and uniform alignment of GO sheets (Figure 10).

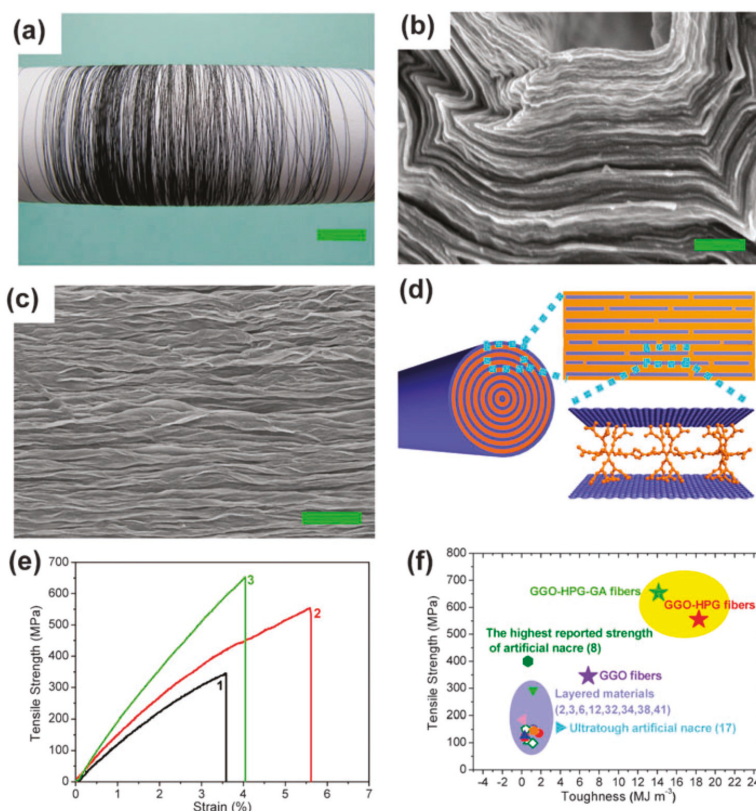


Figure 10. (a) Image of a 30 m long GO-HPG gel fiber (scale bar = 10 mm). (b,c) SEM images of a cross-section of a GO-HPG gel fiber ((b,c), scale bars of 250 nm and 3.0 mm, respectively); (d) Wet-spinning assembly of complex LCs into nacre-mimetic fibers with hierarchical structures; (e) Typical stress-strain curves: (1) GO only; (2) GO-HPG; (3) GO-HPG-GA; (f) The strain rate is 10% per minute. Reproduced from [140] with permission from Nature.

6. Conclusions and Outlook

The major developments of synthetic strategies, the relationship between structures and properties, and many of the applications for HMs have been summarized in this paper. It is noteworthy that the development of applications for HMs is still in its infancy and further research is required to maximize their full potential. Moreover, because this is still an area of emerging research, some problems need to be solved, many knowledge gaps should be filled, and key limitations should be overcome. These include such as DB control, introduction of hetero-atoms, synthesis of HMs with 2D structure, development of sequence-controlled HMs, and biocompatibility.

Acknowledgments: This research was supported by the Creative Research Initiative (CRI, 2014R1A2069102), BK21 Plus (10Z20130011057), Science Research Center (SRC, 2016R1A5A1009405), and Technology Development Program to Solve Climate Change (2016M1A2A2940910, 2016M1A2A2940912) programs through the National Research Foundation (NRF) of Korea.

Conflicts of Interest: The authors declare no conflict of interest.

References

- Jiang, W.; Zhou, Y.; Yan, D. Hyperbranched polymer vesicles: From self-assembly, characterization, mechanisms, and properties to applications. *Chem. Soc. Rev.* **2015**, *12*, 3874–3889. [[CrossRef](#)] [[PubMed](#)]
- Carminade, A.-M.; Yan, D.; Smith, D.K. Dendrimers and hyperbranched polymers. *Chem. Soc. Rev.* **2015**, *44*, 3870–3873. [[CrossRef](#)] [[PubMed](#)]
- Sun, H.-J.; Zhang, S.; Percec, V.F. From structure to function via complex supramolecular dendrimer systems. *Chem. Soc. Rev.* **2015**, *12*, 3900–3923. [[CrossRef](#)] [[PubMed](#)]
- Wu, W.; Tang, R.; Li, Q.; Li, Z. Functional hyperbranched polymers with advanced optical, electrical and magnetic properties. *Chem. Soc. Rev.* **2015**, *12*, 3997–4022. [[CrossRef](#)] [[PubMed](#)]
- Voit, B.I.; Lederer, A. Hyperbranched and Highly Branched Polymer Architectures—Synthetic Strategies and Major Characterization Aspects. *Chem. Rev.* **2009**, *109*, 5924–5973. [[CrossRef](#)] [[PubMed](#)]
- Carlmark, A.; Hawker, C.; Hult, A.; Malkoch, M. New methodologies in the construction of dendritic materials. *Chem. Soc. Rev.* **2009**, *38*, 352–362. [[CrossRef](#)] [[PubMed](#)]
- Zheng, Y.; Li, S.; Weng, Z.; Gao, C. Hyperbranched polymers: Advances from synthesis to applications. *Chem. Soc. Rev.* **2015**, *44*, 4091–4130. [[CrossRef](#)] [[PubMed](#)]
- Jikei, M.; Kakimoto, M.-A. Hyperbranched polymers: A promising new class of materials. *Prog. Polym. Sci.* **2001**, *26*, 1233–1285. [[CrossRef](#)]
- Cook, A.B.; Barbey, R.; Burns, J.A.; Perrier, S. Hyperbranched Polymers with High Degrees of Branching and Low Dispersity Values: Pushing the Limits of Thiol–Yne Chemistry. *Macromolecules* **2016**, *49*, 1296–1304. [[CrossRef](#)]
- Sun, J.; Aly, K.I.; Kuckling, D. A novel one-pot process for the preparation of linear and hyperbranched polycarbonates of various diols and triols using dimethyl carbonate. *RSC Adv.* **2017**, *7*, 12550–12560. [[CrossRef](#)]
- Kim, Y.H.; Webster, O.W. Hyperbranched polyphenylenes. *Macromolecules* **1992**, *25*, 5561–5572. [[CrossRef](#)]
- Aydogan, C.; Yilmaz, G.; Yagci, Y.; Morgenroth, F. Synthesis of Hyperbranched Polymers by Photoinduced Metal-Free ATRP. *Macromolecules* **2017**, *50*, 9115–9120. [[CrossRef](#)]
- Khalyavina, A.; Schallauskay, F.; Komber, H.; Samman, M.A.; Radke, W.; Lederer, A. Aromatic–Aliphatic Polyesters with Tailored Degree of Branching Based on AB/AB₂ and ABB*/AB₂ Monomers. *Macromolecules* **2010**, *43*, 3268–3276. [[CrossRef](#)]
- Xue, Z.; Finke, A.D.; Moore, J.S. Synthesis of Hyperbranched Poly(m-phenylene)s via Suzuki Polycondensation of a Branched AB₂ Monomer. *Macromolecules* **2010**, *43*, 9277–9282. [[CrossRef](#)]
- Yamaguchi, N.; Wang, J.-S.; Hewitt, J.M.; Lenhart, W.C.; Mourey, T.H. Acid chloride-functionalized hyperbranched polyester for facile and quantitative chain-end modification: One-pot synthesis and structure characterization. *J. Polym. Sci. Part A Polym. Chem.* **2002**, *40*, 2855–2867. [[CrossRef](#)]
- Mahdavi, H.; Shahalizade, T. Preparation, characterization and performance study of cellulose acetate membranes modified by aliphatic hyperbranched polyester. *J. Membr. Sci.* **2015**, *473*, 256–266. [[CrossRef](#)]
- Niu, S.; Yan, H.; Chen, Z.; Li, S.; Xu, P.; Zhi, X. Unanticipated bright blue fluorescence produced from novel hyperbranched polysiloxanes carrying unconjugated carbon–carbon double bonds and hydroxyl groups. *Polym. Chem.* **2016**, *7*, 3747–3755. [[CrossRef](#)]
- Ye, L.; Letchford, K.; Heller, M.; Liggins, R.; Guan, D.; Kizhakkedathu, J.N.; Brooks, D.E.; Jackson, J.K.; Burt, H.M. Synthesis and Characterization of Carboxylic Acid Conjugated, Hydrophobically Derivatized, Hyperbranched Polyglycerols as Nanoparticulate Drug Carriers for Cisplatin. *Biomacromolecules* **2011**, *12*, 145–155. [[CrossRef](#)] [[PubMed](#)]
- Perala, S.K.; Ramakrishnan, S. Effect of Spacer Stiffness on the Properties of Hyperbranched Polymers. *Macromolecules* **2017**, *50*, 8536–8543. [[CrossRef](#)]
- Fréchet, J.M.J.; Henmi, M.; Gitsov, I.; Aoshima, S.; Leduc, M.R.; Grubbs, R.B. Self-Condensing Vinyl Polymerization: An Approach to Dendritic Materials. *Science* **1995**, *269*, 1080–1083. [[CrossRef](#)] [[PubMed](#)]
- Higashihara, T.; Segawa, Y.; Sinananwanich, W.; Ueda, M. Synthesis of hyperbranched polymers with controlled degree of branching. *Polym. J.* **2011**, *44*, 14–29. [[CrossRef](#)]
- Satoh, Y.; Miyachi, K.; Matsuno, H.; Isono, T.; Tajima, K.; Kakuchi, T.; Satoh, T. Synthesis of Well-Defined Amphiphilic Star-Block and Miktoarm Star Copolyethers via t-Bu-P4-Catalyzed Ring-Opening Polymerization of Glycidyl Ethers. *Macromolecules* **2016**, *49*, 499–509. [[CrossRef](#)]

23. Rannard, S.; Davis, N.; McFarland, H. Synthesis of dendritic polyamides using novel selective chemistry. *Polym. Int.* **2000**, *49*, 1002–1006. [[CrossRef](#)]
24. Choi, J.-Y.; Oh, S.-J.; Lee, H.-J.; Wang, D.H.; Tan, L.-S.; Baek, J.-B. In-Situ Grafting of Hyperbranched Poly(ether ketone)s onto Multiwalled Carbon Nanotubes via the A₃ + B₂ Approach. *Macromolecules* **2007**, *40*, 4474–4480. [[CrossRef](#)]
25. Masukawa, S.; Kikkawa, T.; Fujimori, A.; Oishi, Y.; Shibasaki, Y. Synthesis of a A2B3-type Hyperbranched Copolymers Based on a 3-Armed Unimolecular 4-N-Methylbenzamide Pentamer and Poly(propylene oxide). *Chem. Lett.* **2015**, *44*, 536–538. [[CrossRef](#)]
26. Tomalia, D.A.; Hedstrand, D.M.; Ferritto, M.S. Comb-burst dendrimer topology: New macromolecular architecture derived from dendritic grafting. *Macromolecules* **1991**, *24*, 1435–1438. [[CrossRef](#)]
27. Nguyen, C.; Hawker, C.J.; Miller, R.D.; Huang, E.; Hedrick, J.L.; Gauderon, R.; Hilborn, J.G. Hyperbranched Polyesters as Nanoporosity Templating Agents for Organosilicates. *Macromolecules* **2000**, *33*, 4281–4284. [[CrossRef](#)]
28. Zhou, Y.; Huang, W.; Liu, J.; Zhu, X.; Yan, D. Self-Assembly of Hyperbranched Polymers and Its Biomedical Applications. *Adv. Mater.* **2010**, *22*, 4567–4590. [[CrossRef](#)] [[PubMed](#)]
29. Mourey, T.H.; Turner, S.R.; Rubinstein, M.; Frechet, J.M.J.; Hawker, C.J.; Wooley, K.L. Unique behavior of dendritic macromolecules: Intrinsic viscosity of polyether dendrimers. *Macromolecules* **1992**, *25*, 2401–2406. [[CrossRef](#)]
30. Ohta, Y.; Sakurai, K.; Matsuda, J.; Yokozawa, T. Chain-growth condensation polymerization of 5-aminoisophthalic acid triethylene glycol ester to afford well-defined, water-soluble, thermoresponsive hyperbranched polyamides. *Polymer* **2016**, *101*, 305–310. [[CrossRef](#)]
31. Chen, H.; Kong, J. Hyperbranched polymers from A₂ + B₃ strategy: Recent advances in description and control of fine topology. *Polym. Chem.* **2016**, *7*, 3643–3663. [[CrossRef](#)]
32. Zigmund, J.S.; Pavia-Sanders, A.; Russell, J.D.; Wooley, K.L.; Percec, V. Dynamic Anti-Icing Coatings: Complex, Amphiphilic Hyperbranched Fluoropolymer Poly(ethylene glycol) Cross-Linked Networks with an Integrated Liquid Crystalline Comonomer. *Chem. Mater.* **2016**, *28*, 5471–5479. [[CrossRef](#)]
33. Zigmund, J.S.; Letteri, R.A.; Wooley, K.L.; Percec, V. Amphiphilic Cross-Linked Liquid Crystalline Fluoropolymer-Poly(ethylene glycol) Coatings for Application in Challenging Conditions: Comparative Study between Different Liquid Crystalline Comonomers and Polymer Architectures. *ACS Appl. Energy Mater.* **2016**, *8*, 33386–33393. [[CrossRef](#)] [[PubMed](#)]
34. Wang, G.-W.; Chen, B.; Zhuang, L.-H.; Yun, K.; Guo, J.-R.; Wang, Y.; Xu, B. Dyeing performances of ramie fabrics modified with an amino-terminated aliphatic hyperbranched polymer. *Cellulose* **2015**, *22*, 1401–1404. [[CrossRef](#)]
35. Kim, Y.H.; Beckerbauer, R. Role of End Groups on the Glass Transition of Hyperbranched Polyphenylene and Triphenylbenzene Derivatives. *Macromolecules* **1994**, *27*, 1968–1971. [[CrossRef](#)]
36. Wu, C.; Huang, X.; Wang, G.; Wu, X.; Yang, K.; Li, S.; Jiang, P. Hyperbranched-polymer functionalization of graphene sheets for enhanced mechanical and dielectric properties of polyurethane composites. *J. Mater. Chem.* **2012**, *14*, 7010–7019. [[CrossRef](#)]
37. Lei, X.; Chen, Y.; Qiao, M.; Tian, L.; Zhang, Q.; Romagnoli, B. Hyperbranched polysiloxane (HBPSi)-based polyimide films with ultralow dielectric permittivity, desirable mechanical and thermal properties. *J. Mater. Chem. C* **2016**, *11*, 2134–2146. [[CrossRef](#)]
38. Gadwal, I.; Binder, S.; Stuparu, M.C.; Khan, A. Dual-Reactive Hyperbranched Polymer Synthesis through Proton Transfer Polymerization of Thiol and Epoxide Groups. *Macromolecules* **2014**, *47*, 5070–5080. [[CrossRef](#)]
39. Hölter, D.; Burgath, A.; Frey, H. Degree of branching in hyperbranched polymers. *Acta Polym.* **1997**, *48*, 30–35. [[CrossRef](#)]
40. Kambouris, P.; Hawker, C.J. A versatile new method for structure determination in hyperbranched macromolecules. *J. Chem. Soc. Perkin Trans. 1* **1993**, *22*, 2717–2721. [[CrossRef](#)]
41. Zhu, X.; Zhou, Y.; Yan, D. Influence of branching architecture on polymer properties. *J. Polym. Sci. Part B Polym. Phys.* **2011**, *49*, 1277–1286. [[CrossRef](#)]
42. Spears, B.R.; Waksal, J.; mcQuade, C.; Lanier, L.; Harth, E. Controlled branching of polyglycidol and formation of protein–glycidol bioconjugates via a graft-from approach with “PEG-like” arms. *Chem. Commun.* **2013**, *49*, 2394–2396. [[CrossRef](#)] [[PubMed](#)]

43. Unal, S.; Lin, Q.; Mourey, T.H.; Long, T.E. Tailoring the Degree of Branching: Preparation of Poly(ether ester)s via Copolymerization of Poly(ethylene glycol) Oligomers (A2) and 1,3,5-Benzenetricarbonyl Trichloride (B3). *Macromolecules* **2005**, *38*, 3246–3254. [[CrossRef](#)]
44. Unal, S.; Oguz, C.; Yilgor, E.; Gallivan, M.; Long, T.E.; Yilgor, I. Understanding the structure development in hyperbranched polymers prepared by oligomeric A2 + B3 approach: Comparison of experimental results and simulations. *Polymer* **2005**, *46*, 4533–4543. [[CrossRef](#)]
45. Schubert, C.; Schömer, M.; Steube, M.; Decker, S.; Friedrich, C.; Frey, H. Systematic Variation of the Degree of Branching (DB) of Polyglycerol via Oxyanionic Copolymerization of Glycidol with a Protected Glycidyl Ether and Its Impact on Rheological Properties. *Macromol. Chem. Phys.* **2018**, *219*, 1700376. [[CrossRef](#)]
46. Segawa, Y.; Higashihara, T.; Ueda, M. Synthesis of hyperbranched polymers with controlled structure. *Polym. Chem.* **2013**, *4*, 1746–1759. [[CrossRef](#)]
47. Mai, Y.; Zhou, Y.; Yan, D.; Lu, H. Effect of Reaction Temperature on Degree of Branching in Cationic Polymerization of 3-Ethyl-3-(hydroxymethyl)oxetane. *Macromolecules* **2003**, *36*, 9667–9669. [[CrossRef](#)]
48. Popeney, C.S.; Lukowiak, M.C.; Böttcher, C.; Schade, B.; Welker, P.; Mangoldt, D.; Gunkel, G.; Guan, Z.; Haag, R. Tandem Coordination, Ring-Opening, Hyperbranched Polymerization for the Synthesis of Water-Soluble Core-Shell Unimolecular Transporters. *ACS Macro Lett.* **2012**, *1*, 564–567. [[CrossRef](#)]
49. Shi, Y.; Graff, R.W.; Cao, X.; Wang, X.; Gao, H. Chain-Growth Click Polymerization of AB₂ Monomers for the Formation of Hyperbranched Polymers with Low Polydispersities in a One-Pot Process. *Angew. Chem. Int. Ed.* **2015**, *54*, 7631–7635. [[CrossRef](#)] [[PubMed](#)]
50. Segawa, Y.; Higashihara, T.; Ueda, M. Hyperbranched Polymers with Controlled Degree of Branching from 0 to 100%. *J. Am. Chem. Soc.* **2010**, *132*, 11000–11001. [[CrossRef](#)] [[PubMed](#)]
51. Guan, Z. Recent Progress of Catalytic Polymerization for Controlling Polymer Topology. *Chem. Asian J.* **2010**, *5*, 1058–1070. [[CrossRef](#)] [[PubMed](#)]
52. Guan, Z. Chain Walking: A New Strategy to Control Polymer Topology. *Science* **1999**, *283*, 2059–2062. [[CrossRef](#)] [[PubMed](#)]
53. Chen, L.; Zhu, X.; Yan, D.; Chen, Y.; Chen, Q.; Yao, Y. Controlling Polymer Architecture through Host-Guest Interactions. *Angew. Chem. Int. Ed.* **2006**, *45*, 87–90. [[CrossRef](#)] [[PubMed](#)]
54. Liu, N.; Vignolle, J.; Vincent, J.-M.; Robert, F.; Landais, Y.; Cramail, H.; Taton, D. One-Pot Synthesis and PEGylation of Hyperbranched Polyacetals with a Degree of Branching of 100%. *Macromolecules* **2014**, *47*, 1532–1542. [[CrossRef](#)]
55. Radke, W.; Litvinenko, G.; Müller, A.H.E. Effect of Core-Forming Molecules on Molecular Weight Distribution and Degree of Branching in the Synthesis of Hyperbranched Polymers. *Macromolecules* **1998**, *31*, 239–248. [[CrossRef](#)]
56. Ishida, Y.; Sun, A.C.F.; Jikei, M.; Kakimoto, M.-A. Synthesis of Hyperbranched Aromatic Polyamides Starting from Dendrons as AB_x Monomers: Effect of Monomer Multiplicity on the Degree of Branching. *Macromolecules* **2000**, *33*, 2832–2838. [[CrossRef](#)]
57. Lach, C.; Frey, H. Enhancing the Degree of Branching of Hyperbranched Polymers by Postsynthetic Modification. *Macromolecules* **1998**, *31*, 2381–2383. [[CrossRef](#)]
58. Huang, W.; Su, L.; Bo, Z. Hyperbranched Polymers with a Degree of Branching of 100% Prepared by Catalyst Transfer Suzuki-Miyaura Polycondensation. *J. Am. Chem. Soc.* **2009**, *131*, 10348–10349. [[CrossRef](#)] [[PubMed](#)]
59. Zhou, Z.; Yan, D. Kinetic analysis for polycondensation of AB (g) type monomers. *Chem. J. Chin. Univ. Chin.* **1999**, *20*, 1978–1981.
60. Cao, X.; Shi, Y.; Wang, X.; Graff, R.W.; Gao, H. Design a Highly Reactive Trifunctional Core Molecule To Obtain Hyperbranched Polymers with over a Million Molecular Weight in One-Pot Click Polymerization. *Macromolecules* **2016**, *49*, 760–766. [[CrossRef](#)]
61. Cheng, K.-C.; Chuang, T.-H.; Chang, J.-S.; Guo, W.; Su, W.-F. Effect of Feed Rate on Structure of Hyperbranched Polymers Formed by Self-Condensing Vinyl Polymerization in Semibatch Reactor. *Macromolecules* **2005**, *38*, 8252–8257. [[CrossRef](#)]
62. Cheng, K.-C. Effect of feed rate on structure of hyperbranched polymers formed by stepwise addition of AB₂ monomers into multifunctional cores. *Polymer* **2003**, *44*, 1259–1266. [[CrossRef](#)]
63. Möck, A.; Burgath, A.; Hanselmann, R.; Frey, H. Synthesis of Hyperbranched Aromatic Homo- and Copolyesters via the Slow Monomer Addition Method. *Macromolecules* **2001**, *34*, 7692–7698. [[CrossRef](#)]

64. Zhou, Z.; Jia, Z.; Yan, D. Effect of slow monomer addition on molecular parameters of hyperbranched polymers synthesized in the presence of multifunctional core molecules. *Sci. China Chem.* **2010**, *53*, 891–897. [[CrossRef](#)]
65. Cheng, K.-C.; Lai, W.-J. Effect of feed rate of end-capping molecules on structure of hyperbranched polymers formed from monomers A2 and B4 in semibatch process. *Eur. Polym. J.* **2017**, *89*, 339–348. [[CrossRef](#)]
66. Tobita, H. Markovian Approach to Self-Condensing Vinyl Polymerization: Distributions of Molecular Weights, Degrees of Branching, and Molecular Dimensions. *Macromol. Theory Simul.* **2014**, *24*, 117–132. [[CrossRef](#)]
67. Litvinenko, G.I.; Müller, A.H.E. Molecular Weight Averages and Degree of Branching in Self-Condensing Vinyl Copolymerization in the Presence of Multifunctional Initiators. *Macromolecules* **2002**, *35*, 4577–4583. [[CrossRef](#)]
68. Gao, C.; Yan, D.; Frey, H. Promising Dendritic Materials: An Introduction to Hyperbranched Polymers. In *Hyperbranched Polymers: Synthesis, Properties, and Applications*; John Wiley & Sons, Inc.: Hoboken, NJ, USA, 2011; pp. 1–26.
69. Li, Z.; Li, Q.; Qin, J. Some new design strategies for second-order nonlinear optical polymers and dendrimers. *Polym. Chem.* **2011**, *2*, 2723–2740. [[CrossRef](#)]
70. Wu, W.; Huang, L.; Xiao, L.; Huang, Q.; Tang, R.; Ye, C.; Qin, J.; Li, Z. New second-order nonlinear optical (NLO) hyperbranched polymers containing isolation chromophore moieties derived from one-pot “A2 + B4” approach via Suzuki coupling reaction. *RSC Adv.* **2012**, *2*, 6520–6526. [[CrossRef](#)]
71. Zhu, Z.; Li, Z.A.; Tan, Y.; Li, Z.; Li, Q.; Zeng, Q.; Ye, C.; Qin, J. New hyperbranched polymers containing second-order nonlinear optical chromophores: Synthesis and nonlinear optical characterization. *Polymer* **2006**, *47*, 7881–7888. [[CrossRef](#)]
72. Bai, Y.; Song, N.; Gao, J.P.; Sun, X.; Wang, X.; Yu, G.; Wang, Z.Y. A New Approach to Highly Electrooptically Active Materials Using Cross-Linkable, Hyperbranched Chromophore-Containing Oligomers as a Macromolecular Dopant. *J. Am. Chem. Soc.* **2005**, *127*, 2060–2061. [[CrossRef](#)] [[PubMed](#)]
73. Li, Z.; Qin, A.; Lam, J.W.Y.; Dong, Y.; Dong, Y.; Ye, C.; Williams, I.D.; Tang, B.Z. Facile Synthesis, Large Optical Nonlinearity, and Excellent Thermal Stability of Hyperbranched Poly(aryleneethynylene)s Containing Azobenzene Chromophores. *Macromolecules* **2006**, *39*, 1436–1442. [[CrossRef](#)]
74. Scarpaci, A.; Blart, E.; Montebault, V.R.; Fontaine, L.; Rodriguez, V.; Odobel, F. Synthesis and Nonlinear Optical Properties of a Peripherally Functionalized Hyperbranched Polymer by DR1 Chromophores. *ACS Appl. Mater. Interfaces* **2009**, *1*, 1799–1806. [[CrossRef](#)] [[PubMed](#)]
75. Scarpaci, A.; Blart, E.; Montebault, V.; Fontaine, L.; Rodriguez, V.; Odobel, F. A new crosslinkable system based on thermal Huisgen reaction to enhance the stability of electro-optic polymers. *Chem. Commun.* **2009**, *14*, 1825–1827. [[CrossRef](#)] [[PubMed](#)]
76. Li, J.; Bo, Z. “AB₂ + AB” Approach to Hyperbranched Polymers Used as Polymer Blue Light Emitting Materials. *Macromolecules* **2004**, *37*, 2013–2015. [[CrossRef](#)]
77. Xin, Y.; Wen, G.-A.; Zeng, W.-J.; Zhao, L.; Zhu, X.-R.; Fan, Q.-L.; Feng, J.-C.; Wang, L.-H.; Peng, B.; Cao, Y.; et al. Hyperbranched Oxadiazole-Containing Polyfluorenes: Toward Stable Blue Light PLEDs. *Macromolecules* **2005**, *38*, 6755–6758. [[CrossRef](#)]
78. Tsai, L.-R.; Chen, Y. Novel Hyperbranched Polyfluorenes Containing Electron-Transporting Aromatic Triazole as Branch Unit. *Macromolecules* **2007**, *40*, 2984–2992. [[CrossRef](#)]
79. Cao, X.-Y.; Zhou, X.-H.; Zi, H.; Pei, J. Novel Blue-Light-Emitting Truxene-Containing Hyperbranched and Zigzag Type Copolymers: Synthesis, Optical Properties, and Investigation of Thermal Spectral Stability. *Macromolecules* **2004**, *37*, 8874–8882. [[CrossRef](#)]
80. Wu, Y.; Hao, X.; Wu, J.; Jin, J.; Ba, X. Pure Blue-Light-Emitting Materials: Hyperbranched Ladder-Type Poly(p-phenylene)s Containing Truxene Units. *Macromolecules* **2010**, *43*, 731–738. [[CrossRef](#)]
81. Wu, G.; Yang, Y.; He, C.; Chen, X.; Li, Y. A new triphenylamine-based hyperbranched polyfluorene with oxadiazole units on its side chains. *Eur. Polym. J.* **2008**, *44*, 4047–4053. [[CrossRef](#)]
82. Li, Z.A.; Ye, S.; Liu, Y.; Yu, G.; Wu, W.; Qin, J.; Li, Z. New Hyperbranched Conjugated Polymers Containing Hexaphenylbenzene and Oxadiazole Units: Convenient Synthesis and Efficient Deep Blue Emitters for PLEDs Application. *J. Phys. Chem. B* **2010**, *114*, 9101–9108. [[CrossRef](#)] [[PubMed](#)]

83. Liu, J.; Yu, L.; Zhong, C.; He, R.; Yang, W.; Wu, H.; Cao, Y. Highly efficient green-emitting electrophosphorescent hyperbranched polymers using a bipolar carbazole-3,6-diyl-co-2,8-octyldibenzothiophene-5,5-dioxide-3,7-diyl unit as the branch. *RSC Adv.* **2012**, *2*, 689–696. [[CrossRef](#)]
84. Hu, X.; Zhou, L.; Gao, C. Hyperbranched polymers meet colloid nanocrystals: A promising avenue to multifunctional, robust nanohybrids. *Colloid Polym. Sci.* **2011**, *289*, 1299–1320. [[CrossRef](#)]
85. Zhu, Q.; Qiu, F.; Zhu, B.; Zhu, X. Hyperbranched polymers for bioimaging. *RSC Adv.* **2013**, *3*, 2071–2083. [[CrossRef](#)]
86. Pérignon, N.; Marty, J.-D.; Mingotaud, A.-F.; Dumont, M.; Rico-Lattes, I.; Mingotaud, C. Hyperbranched Polymers Analogous to PAMAM Dendrimers for the Formation and Stabilization of Gold Nanoparticles. *Macromolecules* **2007**, *40*, 3034–3041. [[CrossRef](#)]
87. Saliba, S.; Valverde Serrano, C.; Keilitz, J.; Kahn, M.L.; Mingotaud, C.; Haag, R.; Marty, J.-D. Hyperbranched Polymers for the Formation and Stabilization of ZnO Nanoparticles. *Chem. Mater.* **2010**, *22*, 6301–6309. [[CrossRef](#)]
88. Tuchbreiter, L.; Mecking, S. Hydroformylation with Dendritic-Polymer-Stabilized Rhodium Colloids as Catalyst Precursors. *Macromol. Chem. Phys.* **2007**, *208*, 1688–1693. [[CrossRef](#)]
89. Gladitz, M.; Reinemann, S.; Radosch, H.-J. Preparation of Silver Nanoparticle Dispersions via a Dendritic-Polymer Template Approach and their Use for Antibacterial Surface Treatment. *Macromol. Mater. Eng.* **2009**, *294*, 178–189. [[CrossRef](#)]
90. Krämer, M.; Pérignon, N.; Haag, R.; Marty, J.-D.; Thomann, R.; Lauth-de Viguerie, N.; Mingotaud, C. Water-Soluble Dendritic Architectures with Carbohydrate Shells for the Templatation and Stabilization of Catalytically Active Metal Nanoparticles. *Macromolecules* **2005**, *38*, 8308–8315. [[CrossRef](#)]
91. Shen, Z.; Duan, H.; Frey, H. Water-Soluble Fluorescent Ag Nanoclusters Obtained from Multiarm Star Poly(acrylic acid) as “Molecular Hydrogel” Templates. *Adv. Mater.* **2007**, *19*, 349–352. [[CrossRef](#)]
92. Zhou, L.; Gao, C.; Hu, X.; Xu, W. General Avenue to Multifunctional Aqueous Nanocrystals Stabilized by Hyperbranched Polyglycerol. *Chem. Mater.* **2011**, *23*, 1461–1470. [[CrossRef](#)]
93. Wan, D.; Fu, Q.; Huang, J. Synthesis of a thioether modified hyperbranched polyglycerol and its template effect on fabrication of CdS and CdSe nanoparticles. *J. Appl. Polym. Sci.* **2006**, *102*, 3679–3684. [[CrossRef](#)]
94. Wei, X.; Zhu, B.; Xu, Y. Preparation and stability of copper particles formed using the template of hyperbranched poly(amine-ester). *Colloid Polym. Sci.* **2005**, *284*, 102–107. [[CrossRef](#)]
95. Zhao, Y.; Zou, J.; Shi, W. Synthesis and characterization of PbS/modified hyperbranched polyester nanocomposite hollow spheres at room temperature. *Mater. Lett.* **2005**, *59*, 686–689. [[CrossRef](#)]
96. Monticelli, O.; Russo, S.; Campagna, R.; Voit, B. Preparation and characterisation of blends based on polyamide 6 and hyperbranched aramids as palladium nanoparticle supports. *Polymer* **2005**, *46*, 3597–3606. [[CrossRef](#)]
97. Kakati, N.; Mahapatra, S.S.; Karak, N. Silver Nanoparticles in Polyacrylamide and Hyperbranched Polyamine Matrix. *J. Macromol. Sci. Part A Pure Appl. Chem.* **2008**, *45*, 658–663. [[CrossRef](#)]
98. Mahapatra, S.S.; Karak, N. Silver nanoparticle in hyperbranched polyamine: Synthesis, characterization and antibacterial activity. *Mater. Chem. Phys.* **2008**, *112*, 1114–1119. [[CrossRef](#)]
99. Richter, T.V.; Schüler, F.; Thomann, R.; Mülhaupt, R.; Ludwigs, S. Nanocomposites of Size-Tunable ZnO-Nanoparticles and Amphiphilic Hyperbranched Polymers. *Macromol. Rapid Commun.* **2009**, *30*, 579–583. [[CrossRef](#)] [[PubMed](#)]
100. Sun, Y.; Liu, Y.; Guizhe, Z.; Zhang, Q. Effects of hyperbranched poly(amido-amine)s structures on synthesis of Ag particles. *J. Appl. Polym. Sci.* **2007**, *107*, 9–13. [[CrossRef](#)]
101. Drozd, M.; Pietrzak, M.; Parzuchowski, P.; Mazurkiewicz-Pawlicka, M.; Malinowka, E. Peroxidase-like activity of gold nanoparticles stabilized by hyperbranched polyglycidol derivatives over a wide pH range. *Nanotechnology* **2015**, *16*, 495101. [[CrossRef](#)] [[PubMed](#)]
102. Zhu, L.; Shi, Y.; Tu, C.; Wang, R.; Pang, Y.; Qiu, F.; Zhu, X.; Yan, D.; He, L.; Jin, C.; et al. Construction and Application of a pH-Sensitive Nanoreactor via a Double-Hydrophilic Multiarm Hyperbranched Polymer. *Langmuir* **2010**, *26*, 8875–8881. [[CrossRef](#)] [[PubMed](#)]
103. Keilitz, J.; Radoski, M.R.; Marty, J.-D.; Haag, R.; Gauffre, F.; Mingotaud, C. Dendritic Polymers with a Core–Multishell Architecture: A Versatile Tool for the Stabilization of Nanoparticles. *Chem. Mater.* **2008**, *20*, 2423–2425. [[CrossRef](#)]

104. Moisan, S.; Martinez, V.; Weisbecker, P.; Cansell, F.; Mecking, S.; Aymonier, C. General Approach for the Synthesis of Organic–Inorganic Hybrid Nanoparticles Mediated by Supercritical CO₂. *J. Am. Chem. Soc.* **2007**, *129*, 10602–10606. [[CrossRef](#)] [[PubMed](#)]
105. Chen, Y.; Frey, H.; Thomann, R.; Stiriba, S.-E. Optically active amphiphilic hyperbranched polyglycerols as templates for palladium nanoparticles. *Inorg. Chim. Acta* **2006**, *359*, 1837–1844. [[CrossRef](#)]
106. Zhou, L.; Gao, C.; Hu, X.; Xu, W. One-Pot Large-Scale Synthesis of Robust Ultrafine Silica-Hybridized CdTe Quantum Dots. *ACS Appl. Mater. Interfaces* **2010**, *2*, 1211–1219. [[CrossRef](#)] [[PubMed](#)]
107. Zhou, L.; Gao, C.; Xu, W. Magnetic Dendritic Materials for Highly Efficient Adsorption of Dyes and Drugs. *ACS Appl. Mater. Interfaces* **2010**, *2*, 1483–1491. [[CrossRef](#)] [[PubMed](#)]
108. Zhou, L.; Gao, C.; Xu, W.; Wang, X.; Xu, Y. Enhanced Biocompatibility and Biostability of CdTe Quantum Dots by Facile Surface-Initiated Dendritic Polymerization. *Biomacromolecules* **2009**, *10*, 1865–1874. [[CrossRef](#)] [[PubMed](#)]
109. Shi, Y.; Du, J.; Zhou, L.; Li, X.; Zhou, Y.; Li, L.; Zang, X.; Zhang, X.; Pan, F.; Zhang, H.; et al. Size-controlled preparation of magnetic iron oxidenanocrystals within hyperbranched polymers and their magnetofection in vitro. *J. Mater. Chem.* **2012**, *22*, 355–360. [[CrossRef](#)]
110. Yu, B.; Jiang, X.; Yin, J. Responsive hybrid nanosheets of hyperbranched poly(ether amine) as a 2D-platform for metal nanoparticles. *Chem. Commun.* **2013**, *49*, 603–605. [[CrossRef](#)] [[PubMed](#)]
111. Zhou, Y.; Yan, D. Supramolecular self-assembly of amphiphilic hyperbranched polymers at all scales and dimensions: Progress, characteristics and perspectives. *Chem. Commun.* **2009**, *10*, 1172–1188. [[CrossRef](#)] [[PubMed](#)]
112. Dey, P.; Blakey, I.; Thurecht, K.J.; Fredericks, P.M. Self-Assembled Hyperbranched Polymer–Gold Nanoparticle Hybrids: Understanding the Effect of Polymer Coverage on Assembly Size and SERS Performance. *Langmuir* **2013**, *29*, 525–533. [[CrossRef](#)] [[PubMed](#)]
113. Shen, Y.; Kuang, M.; Shen, Z.; Nieberle, J.; Duan, H.; Frey, H. Gold Nanoparticles Coated with a Thermosensitive Hyperbranched Polyelectrolyte: Towards Smart Temperature and pH Nanosensors. *Angew. Chem. Int. Ed.* **2008**, *47*, 2227–2230. [[CrossRef](#)] [[PubMed](#)]
114. Jin, H.; Huang, W.; Zhu, X.; Zhou, Y.; Yan, D. Biocompatible or biodegradable hyperbranched polymers: From self-assembly to cytomimetic applications. *Chem. Soc. Rev.* **2012**, *41*, 5986–5997. [[CrossRef](#)] [[PubMed](#)]
115. Wang, D.; Chen, H.; Su, Y.; Qiu, F.; Zhu, L.; Huan, X.; Zhu, B.; Yan, D.; Guo, F.; Zhu, X. Supramolecular amphiphilic multiarm hyperbranched copolymer: Synthesis, self-assembly and drug delivery applications. *Polym. Chem.* **2013**, *4*, 85–94. [[CrossRef](#)]
116. Hartlieb, M.; Floyd, T.; Cook, A.B.; Sanchez-Cano, C.; Catrouillet, S.; Burns, J.A.; Perrier, S. Well-defined hyperstar copolymers based on a thiol–yne hyperbranched core and a poly(2-oxazoline) shell for biomedical applications. *Polym. Chem.* **2017**, *13*, 2014–2054. [[CrossRef](#)]
117. Zhou, Y.; Yan, D. Real-Time Membrane Fusion of Giant Polymer Vesicles. *J. Am. Chem. Soc.* **2005**, *127*, 10468–10469. [[CrossRef](#)] [[PubMed](#)]
118. Zhou, Y.; Yan, D. Real-Time Membrane Fission of Giant Polymer Vesicles. *Angew. Chem. Int. Ed.* **2005**, *44*, 3223–3226. [[CrossRef](#)] [[PubMed](#)]
119. Gregory, A.; Stenzel, M.H. Complex polymer architectures via RAFT polymerization: From fundamental process to extending the scope using click chemistry and nature’s building blocks. *Prog. Polym. Sci.* **2012**, *37*, 38–105. [[CrossRef](#)]
120. Wang, X.; He, Y.; Wu, J.; Gao, C.; Xu, Y. Synthesis and Evaluation of Phenylalanine-Modified Hyperbranched Poly(amido amine)s as Promising Gene Carriers. *Biomacromolecules* **2010**, *11*, 245–251. [[CrossRef](#)] [[PubMed](#)]
121. Ren, Y.; Jiang, X.; Pan, D.; Mao, H.-Q. Charge Density and Molecular Weight of Polyphosphoramidate Gene Carrier Are Key Parameters Influencing Its DNA Compaction Ability and Transfection Efficiency. *Biomacromolecules* **2010**, *11*, 3432–3439. [[CrossRef](#)] [[PubMed](#)]
122. Newland, B.; Tai, H.; Zheng, Y.; Velasco, D.; Di Luca, A.; Howdle, S.M.; Alexander, C.; Wang, W.; Pandit, A. A highly effective gene delivery vector—Hyperbranched poly(2-(dimethylamino)ethyl methacrylate) from in situ deactivation enhanced ATRP. *Chem. Commun.* **2010**, *46*, 4698–4700. [[CrossRef](#)] [[PubMed](#)]
123. Chen, M.; Wu, J.; Zhou, L.; Jin, C.; Tu, C.; Zhu, B.; Wu, F.; Zhu, Q.; Zhu, X.; Yan, D. Hyperbranched glycoconjugated polymer from natural small molecule kanamycin as a safe and efficient gene vector. *Polym. Chem.* **2011**, *2*, 2674–2682. [[CrossRef](#)]

124. Tu, C.; Li, N.; Zhu, L.; Zhou, L.; Su, Y.; Li, P.; Zhu, X. Cationic long-chain hyperbranched poly(ethylene glycol)s with low charge density for gene delivery. *Polym. Chem.* **2013**, *4*, 393–401. [[CrossRef](#)]
125. Yu, S.; Chen, J.; Dong, R.; Su, Y.; Ji, B.; Zhou, Y.; Zhu, X.; Yan, D. Enhanced gene transfection efficiency of PDMAEMA by incorporating hydrophobic hyperbranched polymer cores: Effect of degree of branching. *Polym. Chem.* **2012**, *3*, 3324–3329. [[CrossRef](#)]
126. Wang, G.; Yin, H.; Yin Ng, J.C.; Cai, L.; Li, J.; Tang, B.Z.; Liu, B. Polyethyleneimine-grafted hyperbranched conjugated polyelectrolytes: Synthesis and imaging of gene delivery. *Polym. Chem.* **2013**, *4*, 5297–5304. [[CrossRef](#)]
127. Siegers, C.; Biesalski, M.; Haag, R. Self-Assembled Monolayers of Dendritic Polyglycerol Derivatives on Gold That Resist the Adsorption of Proteins. *Chem. Eur. J.* **2004**, *10*, 2831–2838. [[CrossRef](#)] [[PubMed](#)]
128. Chen, S.; Tan, Z.; Li, N.; Wang, R.; He, L.; Shi, Y.; Jiang, L.; Li, P.; Zhu, X. Highly Efficient Intracellular Drug Delivery with a Negatively Charged Hyperbranched Polysulfonamide. *Macromol. Biosci.* **2011**, *11*, 828–838. [[CrossRef](#)] [[PubMed](#)]
129. Qiu, W.; Xu, J.; Li, X.; Zhong, L.; Li, J.; Li, J.; Nan, F. Design and Synthesis of Matrix Metalloprotease Photoaffinity Trimodular Probes. *Chin. J. Chem.* **2009**, *27*, 825–833. [[CrossRef](#)]
130. Qiu, F.; Wang, D.; Zhu, Q.; Zhu, L.; Tong, G.; Lu, Y.; Yan, D.; Zhu, X. Real-Time Monitoring of Anticancer Drug Release with Highly Fluorescent Star-Conjugated Copolymer as a Drug Carrier. *Biomacromolecules* **2014**, *15*, 1355–1364. [[CrossRef](#)] [[PubMed](#)]
131. Sohn, G.-J.; Choi, H.-J.; Jeon, I.-Y.; Chang, D.W.; Dai, L.; Baek, J.-B. Water-Dispersible, Sulfonated Hyperbranched Poly(ether-ketone) Grafted Multiwalled Carbon Nanotubes as Oxygen Reduction Catalysts. *ACS Nano* **2012**, *6*, 6345–6355. [[CrossRef](#)] [[PubMed](#)]
132. Caruso, F. Nanoengineering of Particle Surfaces. *Adv. Mater.* **2001**, *13*, 11–22. [[CrossRef](#)]
133. Hood, M.; Mari, M.; Muñoz-Espí, R. Synthetic Strategies in the Preparation of Polymer/Inorganic Hybrid Nanoparticles. *Materials* **2014**, *7*, 4057–4087. [[CrossRef](#)] [[PubMed](#)]
134. Jeon, I.-Y.; Lee, H.-J.; Choi, Y.S.; Tan, L.-S.; Baek, J.-B. Semimetallic Transport in Nanocomposites Derived from Grafting of Linear and Hyperbranched Poly(phenylene sulfide)s onto the Surface of Functionalized Multi-Walled Carbon Nanotubes. *Macromolecules* **2008**, *41*, 7423–7432. [[CrossRef](#)]
135. Novoselov, K.S. Electric Field Effect in Atomically Thin Carbon Films. *Science* **2004**, *306*, 666–669. [[CrossRef](#)] [[PubMed](#)]
136. Roldán, R.; Chirolli, L.; Prada, E.; Silva-Guillén, J.A.; San-Jose, P.; Guinea, F. Theory of 2D crystals: Graphene and beyond. *Chem. Soc. Rev.* **2017**, *15*, 4387–4399. [[CrossRef](#)] [[PubMed](#)]
137. Jeon, I.-Y.; Choi, H.-J.; Bae, S.-Y.; Chang, D.W.; Baek, J.-B. Wedging graphite into graphene and graphene-like platelets by dendritic macromolecules. *J. Mater. Chem.* **2011**, *21*, 7820–7826. [[CrossRef](#)]
138. Zhu, Y.; Murali, S.; Cai, W.; Li, X.; Suk, J.W.; Potts, J.R.; Ruoff, R.S. Graphene and Graphene Oxide: Synthesis, Properties, and Applications. *Adv. Mater.* **2010**, *22*, 3906–3924. [[CrossRef](#)] [[PubMed](#)]
139. Hirata, M.; Gotou, T.; Ohba, M. Thin-film particles of graphite oxide. Preliminary studies for internal micro fabrication of single particle and carbonaceous electronic circuits. *Carbon* **2005**, *43*, 503–510. [[CrossRef](#)]
140. Hu, X.; Xu, Z.; Liu, Z.; Gao, C. Liquid crystal self-templating approach to ultrastrong and tough biomimic composites. *Sci. Rep.* **2013**, *3*, 2374. [[CrossRef](#)] [[PubMed](#)]
141. Xu, Z.; Gao, C. Graphene in Macroscopic Order: Liquid Crystals and Wet-Spun Fibers. *Acc. Chem. Res.* **2014**, *47*, 1267–1276. [[CrossRef](#)] [[PubMed](#)]



© 2018 by the authors. Licensee MDPI, Basel, Switzerland. This article is an open access article distributed under the terms and conditions of the Creative Commons Attribution (CC BY) license (<http://creativecommons.org/licenses/by/4.0/>).

Review

Dentromers, a Family of Super Dendrimers with Specific Properties and Applications

Didier Astruc^{1,*}, Christophe Deraedt¹, Rodrigue Djeda^{1,2}, Catia Ornelas^{1,3}, Xiang Liu^{1,4}, Amalia Rapakousiou^{1,5}, Jaime Ruiz¹, Yanlan Wang^{1,6} and Qi Wang¹

¹ ISM, UMR 5255, University of Bordeaux, 33405 Talence CEDEX, France; c.deraedt@yahoo.fr (C.D.); rodrigue.djeda@gmail.com (R.D.); catiaornelas@catiaornelaslab.com (C.O.); xiang.liu@ctgu.edu.cn (X.L.); amalia.rapakousiou@imdea.org (A.R.); jaime.ruiz-aranzaes@u-bordeaux.fr (J.R.); wangyanlan419@hotmail.com (Y.W.); youling1993@126.com (Q.W.)

² Université Jean Lorougnon Guédé, BP 150 Daloa, Ivory Coast

³ Institute of Chemistry, University of Campinas-Unicamp, 13083-861 Campinas, SP, Brazil

⁴ College of Materials and Chemical Engineering, China Three Gorges University, Yichang 443002, China

⁵ Chemistry of Low-Dimensional Materials, IMDEA Nanoscience Institute, Calle Faraday, 9, 28049 Madrid, Spain

⁶ Department of Chemistry and Chemical Engineering, Liaocheng University, 1, Hunan Road, Liaocheng 252059, China

* Correspondence: didier.astruc@u-bordeaux.fr; Tel.: +33-540-006-271

Academic Editor: Ashok Kakkar

Received: 22 March 2018; Accepted: 18 April 2018; Published: 20 April 2018

Abstract: *Dentromers* (from *dentro*, δέντρο: tree in Greek), and *meros* (μερος, in greek: part) are introduced as a family of dendrimers constructed according to successive divergent 1 → 3 branching. The smaller *dentromers* have 27 terminal branches. With alcohol termini they were originally named arborols by Newkome, who pioneered 1 → 3 constructions of dendrimers and dendrons. Giant *dentromers* have been constructed and decorated in particular with ferrocene and other redox active groups. The synthesis, specific properties, and applications are examined in this mini review article dedicated to Don Tomalia, with an emphasis on dense peripheral packing favoring the functions of encapsulation, redox sensing, and micellar template for catalysis in water and aqueous solvents.

Keywords: dendrimer; dendron; *dentromer*; sensor; catalysis; redox; ferrocene; template; micelle

1. Introduction

Besides the seminal articles on dendrimers by Tomalia [1], Newkome [2], and Denkewalter [3] in the early 1980s, the beauty and enormous potential of dendrimers were revealed to the scientific community by the superb prospective review article published by Don Tomalia in *Angewandte Chemie* in the late 1980s [4]. Tomalia was the one who astutely coined the term dendrimer [4]. He also produced by far the most popular family of dendrimers, the polyamidoamine dendrimers known to all chemists as PAMAM dendrimers [4,5], with great potential in biomedical applications [6–9]. These dendrimers, like most of the other dendrimer families, were synthesized according to a double-branching construction called 1 → 2 branching, whereby each group is branched to two other groups, and so on, i.e., doubling the number of peripheral groups from one generation to the next [10–38].

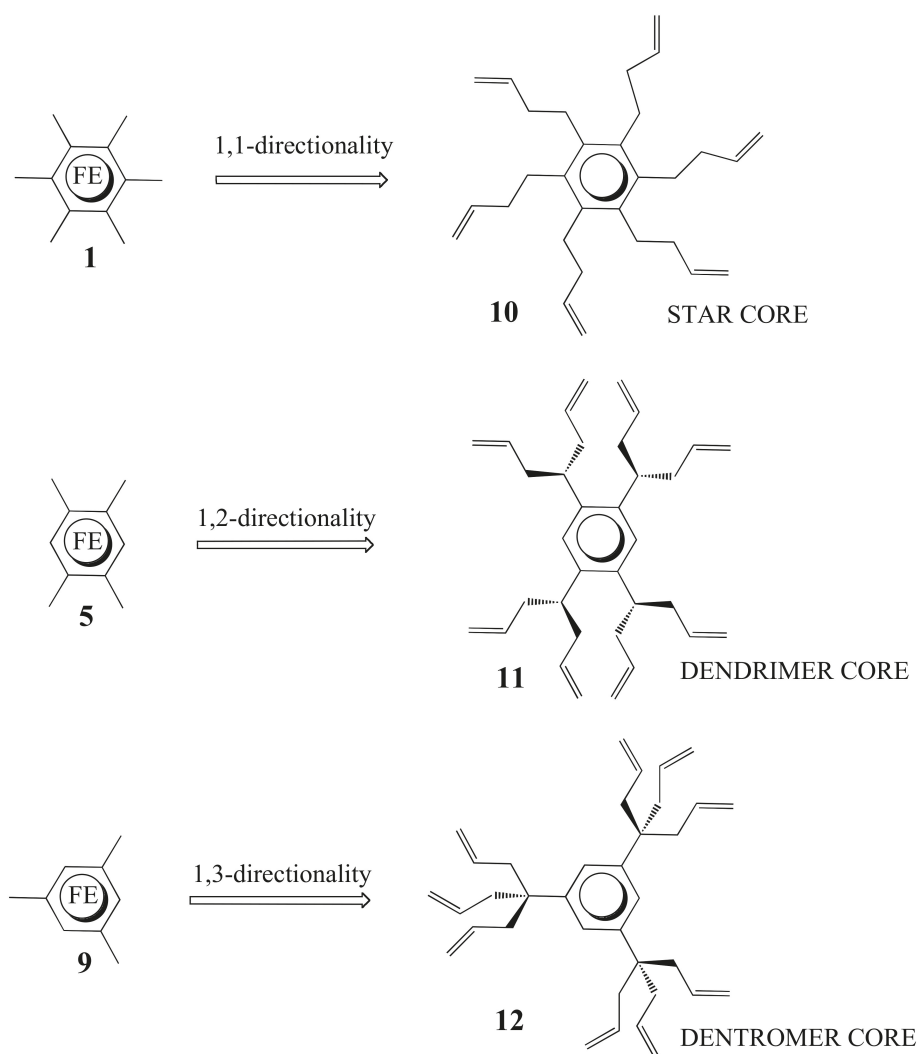
In the present mini-review, we wish to highlight another dendrimer family, synthesized upon *triple branching*, therefore leading to a much larger number of tethers than double branching for the same generation number. We call this family “*dentromers*” from *dentro* (δέντρο, in Greek: tree) and *meros* (μερος, in Greek: part, etymologically “made of several parts,” like in *polymers*). The triple-branching dendrimer construction [39] is much less frequent than the double-branching one [40–43]. It was

pioneered by Newkome in his seminal article on unimolecular micelles called arborols in 1985 [2]. The topology of triple branching is found with linkers such as a trisubstituted carbon connected to a substrate, a 1,3,5-trisubstituted arene, or gallic acid with the 3,4,5 arene hydroxy substituents and derivatives.

The first method of triple branching was extensively used by Newkome to synthesize useful dendrons [44]. For instance, derivatives of tris(hydroxymethyl)methane were shown to react cleanly with acrylonitrile to yield a tris-nitrile or with chloroacetic acid in methanol to yield tris(esters) [45,46], and nitromethane was also a starting point reacting with acrylic esters to yield tris(ester) derivatives [46,47]. Another strategy consisted of the connection of a pre-synthesized trifunctional dendron, was achieved by Newkome's group upon the reaction of a bromo-terminated dendrimer core with a dendron bearing a focal point terminated by an ethynyl group [46,48]. Interestingly, this pre-prepared dendron grafting strategy was even applied to PAMAM dendrimers to form molecular micelles [49] and to perform calixarene core functionalization [50]. Miller and Neenan initiated an arene-cored triple-branching construction with 1,3,5-triiodobenzene when they reported their seminal convergent dendrimer construction in 1990 [11] (as Hawker and Fréchet [10]), but the convergent strategy further involved arene desymmetrization with only double branching. Finally, another family of useful dendrons is Percec dendrons derived from gallic acid, leading to the assembly of a variety of soft materials with various shapes [51].

2. Organoiron Arene Activation

Our *dendrimer* construction and other branched molecule constructions were initiated by powerful temporary organoiron activation of mono- or polymethyl arenes. The principles of activation of simple and commercial arenes for branching out are detailed as follows. The η^5 -cyclopentadienyl (Cp) iron group is indeed an excellent, simple, cheap, and non-toxic (contrary to metal carbonyls) arene activator in both the 18-electron cationic sandwich complexes $[\text{CpFe}^{\text{II}}(\eta^6\text{-arene})][\text{PF}_6]$ [52,53] and in the 19-electron neutral isostructural analogues $[\text{CpFe}^{\text{I}}(\eta^6\text{-arene})]$ [54–56]. These cationic complexes are easily synthesized on a large scale by reactions of the arenes with ferrocene [57]. In 1979, a series of six iterated sequences consisting of deprotonation/nucleophilic substitution reactions allowed us to transform the hexamethylbenzene ligand in the cationic complex $[\text{CpFe}^{\text{II}}(\eta^6\text{-C}_6\text{Me}_6)][\text{PF}_6]$, **1**, into hexaethylbenzene in the complex $[\text{CpFe}^{\text{II}}(\eta^6\text{-C}_6\text{Et}_6)][\text{PF}_6]$, **2**. The reactions were conducted under ambient conditions either stepwise [54] or as a one-pot reaction [58]. This was the beginning of an iteration strategy to synthesize arene-centered star molecules, including functional ones according to a $1 \rightarrow 1$ directionality [59]. Upon reaction of complex **1** with *t*-BuOK and allyl bromide, it was possible to selectively synthesize from complex **1** the hexabutanyl benzene complex $[\text{CpFe}^{\text{II}}(\eta^6\text{-C}_6(\text{CH}_2\text{CH}_2\text{CH}=\text{CH}_2)_6)][\text{PF}_6]$, **3** (see the arene ligand structure of **3** in scheme 1) in one day or, much more slowly, the dodecaallyl dendritic molecule $[\text{CpFe}^{\text{II}}\{\eta^6\text{-C}_6[\text{CH}(\text{CH}_2\text{CH}=\text{CH}_2)_2]_6\}][\text{PF}_6]$, **4** upon reaction in three weeks. This later reaction corresponds to a $1 \rightarrow 2$ directionality [60]. This double branching with allyl groups was much more easily obtained by utilizing the same reaction starting from the 1,2,4,5-tetramethylbenzene (durene) complex $[\text{CpFe}^{\text{II}}(\eta^6\text{-1,2,4,5-C}_6\text{H}_2\text{Me}_4)][\text{PF}_6]$, **5** [60] or from the other 18-electron complex $[\text{CpCo}^{\text{III}}(\eta^5\text{-C}_5\text{Me}_5)][\text{PF}_6]$, **6** [61], providing the dendrimer cores $[\text{CpFe}^{\text{II}}(\eta^6\text{-1,2,4,5-C}_6\text{H}_2(\text{CH}(\text{CH}_2\text{CH}=\text{CH}_2)_2)_4)][\text{PF}_6]$, **7** (see the arene ligand structure of **7** in scheme 1) and $[\text{CpCo}^{\text{III}}(\eta^5\text{-C}_5[\text{CH}(\text{CH}_2\text{CH}=\text{CH}_2)_2]_5)][\text{PF}_6]$, **8** respectively. This reactivity trend shows that the branching facilities in the polymethylbenzene complexes $[\text{CpFe}^{\text{II}}(\eta^6\text{-C}_6\text{H}_n\text{Me}_{6-n})][\text{PF}_6]$ at a given methyl arene substituent strongly depends on the number of methyl group neighbors of this methyl group (Scheme 1).

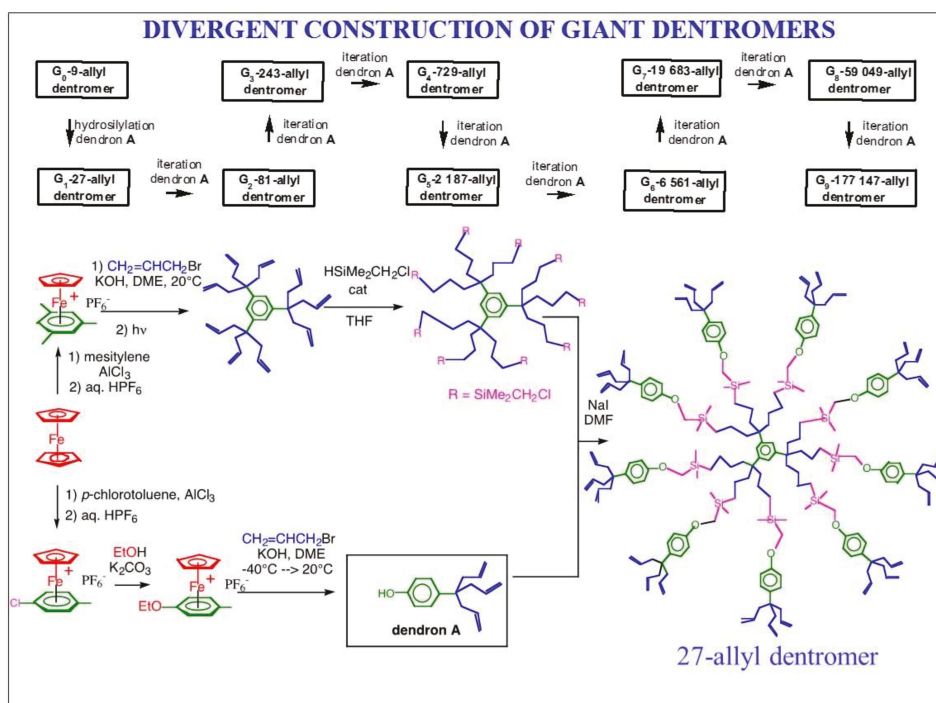


Scheme 1. Various directionalities quantitatively obtained upon perallylation of cationic polymethylbenzene iron sandwich complexes upon reaction with KOH and allylbromide in THF under ambient conditions followed by visible-light photodecomplexation. Complex **1** = $[\text{CpFe}^{\text{II}}(\eta^6\text{-C}_6\text{Me}_6)] [\text{PF}_6]$; in the scheme, $\text{FE} = (\eta^5\text{-C}_5\text{H}_5\text{Fe}^{\text{II}})^+$ with the PF_6^- counter anion.

This rule was establishing from the beginning with methyl iodide and was completed with the mesitylene ligand of the complex $[\text{CpFe}^{\text{II}}(\eta^6\text{-1,3,5-C}_6\text{H}_3\text{Me}_3)] [\text{PF}_6]$, **9** in which the methyl substituents have no neighbors [58]. In this latter case, no steric inhibition prevents the one-pot replacement of the three H atoms of each methyl groups by 3 methyl or allyl groups upon a series of nine iterative deprotonation/methylation or allylation sequences. In this case, the reactions correspond to 1 \rightarrow 3 directionality. The bursting one-pot nona-allylation of the mesitylene complex is especially interesting because it is virtually quantitative and quickly provides a nonafunctional dendritic (*dentromeric*) core **9** [62]. In addition, the arene ligand is readily displaced by mesitylene upon visible photolysis to regenerate the starting complex **9**. Altogether, after photochemical decomplexation using visible

light, the star core **10**, the dendrimer core **11** and the *dentromeric* core **12** are readily accessible upon temporary complexation of the precursor hexamethylbenzene, durene, and mesitylene, respectively.

Another challenge was the extension of these multiple iteration sequences to the synthesis of a dendron. This was achieved starting from the *p*-chlorotoluene complex [CpFe^{II}(η^6 -*p*-C₆H₄Me(Cl))] [PF₆], **13**. The large-scale reaction of this complex **13** with K₂CO₃ in ethanol at 50 °C provided the 4-ethoxytoluene complex [CpFe^{II}(η^6 -*p*-C₆H₄Me(OEt))] [PF₆] that reacted with *t*-BuOK + allyl bromide to directly yield, in a one-pot reaction, the iron-free dendron *p*-HOC₆H₄C(CH₂CH=CH₂)₃, **A**, in 40% yield [63], as shown in the bottom of Scheme 2. In this eight-step one-pot reaction, *t*-BuOK plays three roles: base to deprotonate the benzylic methyl groups (three times), nucleophilic cleavage of the O-C bond (assisted by CpFe⁺ activation) and finally electron-transfer reagent to transfer an electron to the iron sandwich cation, yielding the highly unstable 19-electron species [64]. Subsequent ferrocenylation upon hydrosilylation with FcSi(H)Me₂ (Fc, ferrocenyl = η^5 -C₅H₅Fe η^5 -C₅H₄) readily afforded a triferrocenyl dendron *p*-HOC₆H₄C(CH₂CH₂-CH₂Si(Me)₂Fc)₃ that was convenient (with a phenol group at the focal point) for ferrocenyl-terminated *dentromer* constructions [65].



Scheme 2. Construction of giant *dentromers* starting from ferrocene.

3. *Dentromer* Construction

A remarkable advantage of *dentromers* over dendrimers of the same generation is the larger number of terminal groups produced. For instance, starting from a nonbranched core (0th generation, see Scheme 2), *dentromers* reach a theoretical number of 729 terminal in only four generations, whereas 1 → 2 branching from the same core reaches only 48 terminal groups in four generations (see Figure 1 for the 3rd generation 243-allyl *dentromer*).

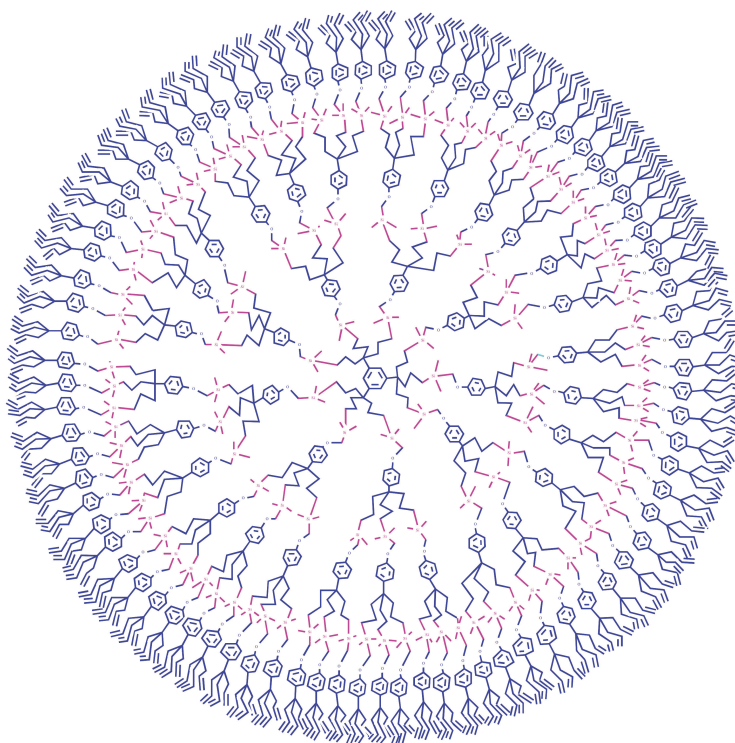


Figure 1. Planar representation of the 243-allyl dendrimer (Scheme 2, 3rd generation).

This nonaallylated core **12** was easily functionalized in many ways. For instance its hydroboration followed by oxidation by H_2O_2 yields a nano-ol and hydrosilylation inter alia with $\text{HSiMe}_2(\text{CH}_2\text{SiCl})$ leads to an air-robust nona-chloromethyl-terminated dendritic core in which nucleophilic substitution by NaI , NaN_3 , or sodium phenolate yields nona-iodo, nona-azido, and nonaaryloxy-terminated dendrimers, respectively, that are suitable for further Williamson or “click” reactions. At this point the introduction of additional $1 \rightarrow 3$ directional dendrons by appropriate coupling with the core provided clean divergent construction of *dendromers* whereby the terminal branch number is multiplied by 3 from a generation to the next one. For instance, the reaction of the nona-chloromethyl-terminated dendritic core with the phenoltriallylmethyl dendron **A** in the presence of sodium iodide by Williamson reaction leads to the next generation of polyallyl dendrimer with 27 allyl groups [66]. Iterative dendron branching up to the 9th generation led to a *dendromer* with a theoretical number of 177,147 branches, although the divergent construction inherently results in defects that are more numerous as the generation number increases. Nevertheless, the ^1H , ^{13}C , and ^{29}Si NMR spectra, HRTEM and AFM in particular, allowed us to progressively follow the *dendromer* construction, indicating that in generation 9 the actual branch number is on the order of 10^5 [66].

Another powerful method consisted of applying copper-catalyzed azide alkyne cycloaddition (CuAAC), i.e., “click” chemistry [67–69]. For instance, a reaction of the nona-azido core with the phenol dendron functionalized at the focal point with a propargyl group provides suitable 1,2,3-triazole-linked *dendromers* [70].

Thus the trifunctional dendrons may be used either to proceed from one generation to the next or to decorate *dendromers* in the same time as multiplying their number of terminal branches. Examples have been provided with dendrons that are trifunctionalized with various organometallics such as redox-active ones [71–74] or water-solubilizing ones [75]. In this later series, the Percec dendron [42,43],

initially based on gallic acid, is particularly useful because the terminal hydroxyl groups are easily alkylated with triethylene glycol (TEG) bromide for water solubility.

4. The Applications of *Dentromers*

Starting from the nano-allylated core obtained by CpFe-induced nona-allylation of mesitylene, only one generation is needed to reach a 27-functional *dentromer* that is used as a sensor, template, and micelle, in particular for catalysis applications [76].

Construction of ferrocenyl-terminated dendrimers (Figure 2) was achieved until the 7th generation containing a theoretical number of 19,683 ferrocenyl groups. Actually electrochemical and spectroscopic monitoring led to an estimation of approximately 15,000 terminal groups. AFM showed the steady increase of the height of the *dentromer* layer upon increasing generation numbers. The images of the 5th and 6th generations showed regularly distributed spots [72].

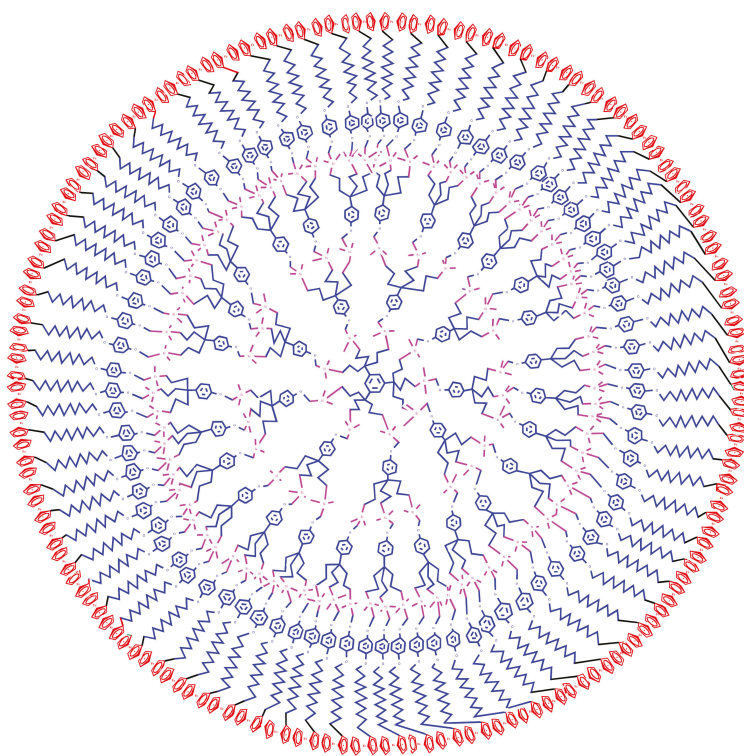


Figure 2. Planar representation of an 81-ferrocenyl *dentromer* (2nd generation).

Cyclic voltammograms consisted of a single wave from the 0th to the 7th generation without significant irreversibility or slow electron transfer, indicating faster rotation of the *dentromer* and/or electron hopping from redox site to redox site. Oxidation of the 5th generation ferrocene *dentromer* led to a reversible size increase of nearly 50% by AFM of the *dentromer* upon oxidation, meaning that these nanosystems breathe like molecular machines upon redox cycling. The apparent equivalence of all the peripheral redox sites in cyclic voltammetry has a very important consequence for redox recognition and sensing.

Indeed, redox sensing is a useful property of *dentromers* terminated by redox-active groups such as ferrocene [77], biferrocene [74], CpFe(η^6 -arene) [77], $[(\eta^5\text{-C}_5\text{Me}_5)\text{Fe}(\text{dppe})]$ [78], cobalticinium [79],

or $\text{Fe}_4\text{Cp}_4(\text{CO})_4$ clusters [80]. Besides the ion pairing and supramolecular hydrogen bonding properties, the parameter that boosts the redox recognition of substrates is the dendritic effect involving encapsulation of substrates inside the dendrimer periphery. This crucial dendritic effect is optimized in *dentromers* because they ensure a denser packing of terminal groups with $1 \rightarrow 3$ branching than in looser $1 \rightarrow 2$ branching. This phenomenon appears particularly marked in amidoferrocenes [81,82] and click ferrocenyl dendrimers, which sense both oxo-anions such as ATP^{2-} (a DNA fragment) [83] and transition-metal cations [70,74]. The combined use of gold nanoparticles (NPs) and dendrons organized with $1 \rightarrow 3$ connectivity such as nanosilylferrocene dendrons with a thiol terminal group allows us to construct large ferrocenyl *dentromers* in which the weak interaction between the silicon atom bonded to ferrocene and the anionic phosphate group of ATP^{2-} also provides a good means of ATP^{2-} redox sensing (Figure 3).

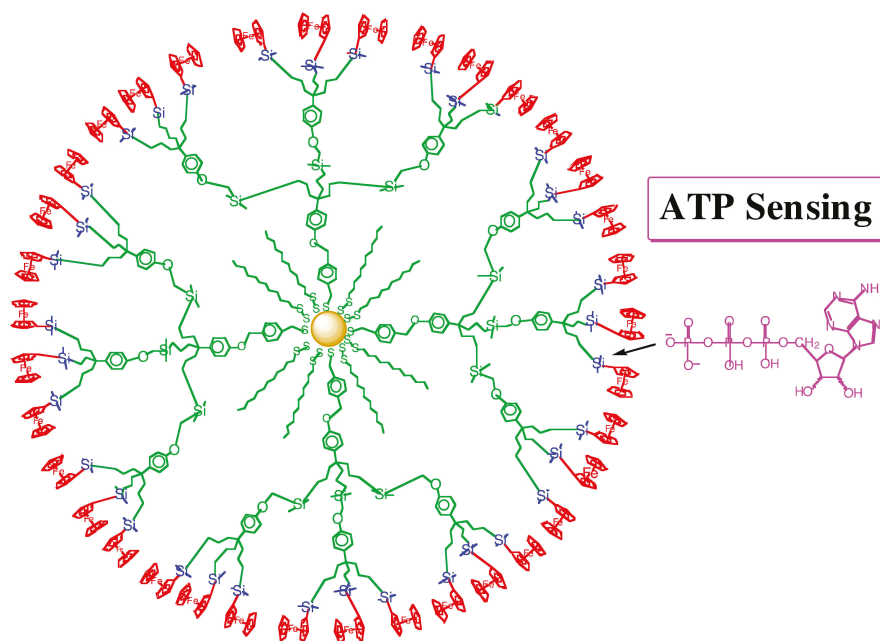


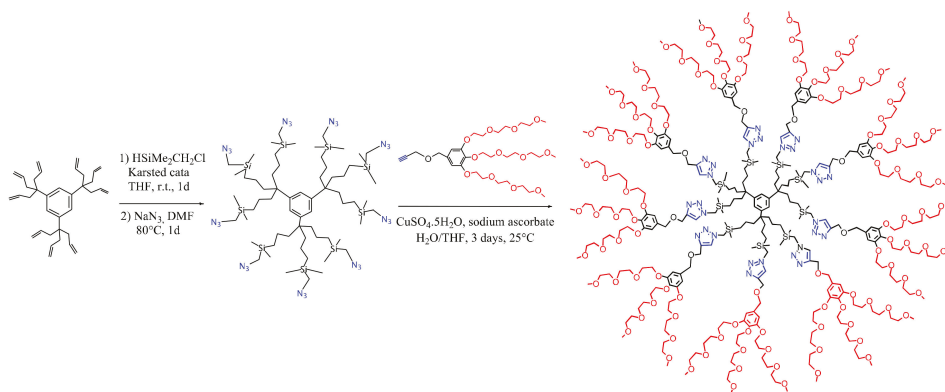
Figure 3. Redox ATP^{2-} sensing using a large gold NP-cored silylferrocenyl-terminated *dentromer*. The cyclic voltammetry wave of the silylferrocenyl groups interacting with ATP^{2-} is significantly shifted, allowing titration. Modified electrodes with this *dentromer* allow repetitive titrations.

Another area in which *dentromers* have an additional advantage compared with dendrimers is that of support and template in catalysis. PAMAM dendrimers have already been shown to be efficient templates for catalysis of olefin hydrogenation and cross carbon–carbon coupling reactions by dendrimer-encapsulated NPs [84,85]. “Click” *dentromers* are advantageous alternatives, however.

The first catalytic applications of “click” *dentromer*-encapsulated NPs were conducted for olefin hydrogenation and the Suzuki–Miyaura reaction [70]. These *dentromers* are terminated by triazolylferrocenes, and cyclic-voltammetry-monitored titration indicated that they coordinate, for instance, with one triazole group per Pd^{II} . Reduction of Pd^{II} to Pd^0 atoms led to Pd NP formation. The sizes of these NPs, determined by transmission electron microscopy, showed that for the 27- and 81-*dentromers* they contained a number of atoms corresponding to the same number of previously coordinated Pd^{II} cations. These numbers are 36 atoms ($27 + 9$) for the 27-*dentromer* and 117 atoms ($81 + 27 + 9$) for the 81-*dentromers*. The theoretical sizes were 1.0 and 1.6 nm for the 27- and 81-*dentromers* respectively, and the observed sizes were 1.1 ± 0.2 nm

and 1.6 ± 0.3 nm, respectively, showing that the agglomerated atoms were retained inside the *dentromers* in *dentromer*-encapsulated NPs. This information was useful to understand the catalytic reaction mechanisms. Whereas, for hydrogenation, the observed TOFs were as expected, the NP size was smaller, as already known for polymer-stabilized NPs [86]; in Suzuki–Miyaura reactions, the TOF was hardly dependent on the dendrimer generation, reaching values of 5×10^5 . This observation led to the suggestion that a leaching mechanism was in operation. In this mechanism catalysis is probably ensured by the leaching of single atoms or small clusters containing a few atoms subsequent to aryl halide oxidative addition onto the NP surface. These active atoms are supposedly more easily caught by the mother NP as the NP catalyst is higher, which would explain the “homeopathic” catalysis [70,87]. This behavior is related to that observed by de Vries’ group for a Heck reaction conducted at 150 °C [88], but, interestingly, the Suzuki–Miyaura reactions analyzed here, unlike the Heck reactions, were carried out under ambient conditions.

The small water-soluble *dentromer* containing nine Percec-type dendrons with a propargyl group at the focal point connected to the nonaazido dendritic core by CuAAC click reaction (Scheme 3) turned out to be remarkably productive and recyclable in several types of catalysis conducted in water or aqueous solvents, including olefin metathesis catalyzed by commercial Ru-benzylidene catalysts, the click reaction catalyzed by Cu^{I} -tren catalyst, and several NP-catalyzed reactions [89]. Reactions were compared using either this 27-*dentromer* or the higher-generation 81-*dentromer* terminated by the same Percec dendron, and they did not result in significant dendritic effects, i.e., the TOFs did not improve upon using the 81-*dentromer* template compared to the lower-generation *dentromer*.



Scheme 3. Synthesis of the standard water-soluble *dentromer* terminated by Percec-type dendrons serving as micellar template for a variety of reactions catalyzed by transition-metal complexes or NPs in water or aqueous solvents.

For instance, the use of the 27-*dentromer* allows us to decrease the amount of CuSO_4 catalyst to ppm amounts followed by reduction to Cu^{I} by Na ascorbate and to apply this catalyst to the synthesis of triazole molecules of biomedical interest. In other examples, the same 27-*dentromer* served as a template to catalyze the CuAAC or carbon–carbon coupling reactions using ppms of Cu or Pd NP catalyst, respectively [90]. The presence of intra-*dentromer* ligands was essential in dendrimer-encapsulation NP catalysis, as demonstrated by the sizes of Au NPs obtained in 81-*dentromers* with or without inter-*dentromer* triazole ligands.

With intra-*dentromer* triazoles, the size of Au NPs formed by the addition of HAuCl_4 followed by reduction using NaBH_4 was approximately as expected from the number of triazole groups showing intra-*dentromer* formation, whereas without triazole groups the Au NP size obtained was much larger, indicating AuNP formation outside the dendrimer [73]. Using HRTEM and HAAD STEM, it was possible to precisely locate Au NP [91] and Ag NPs [92] in nanosnakes or at the inner periphery of

dentromers. As illustrated in Figure 1, NPs can accommodate dendrons upon binding to the core, which can also provide very efficient catalysts [93].

Finally, the zeroth (Scheme 3) and first-generation *dentromers* (Figure 4) terminated by water-solubilizing TEG-Percec dendrons are among the best supports for catalyzing hydrogen production from ammonia-borane hydrolysis under ambient conditions, showing the potential of new applications of *dentromers* in the field of energy [94].

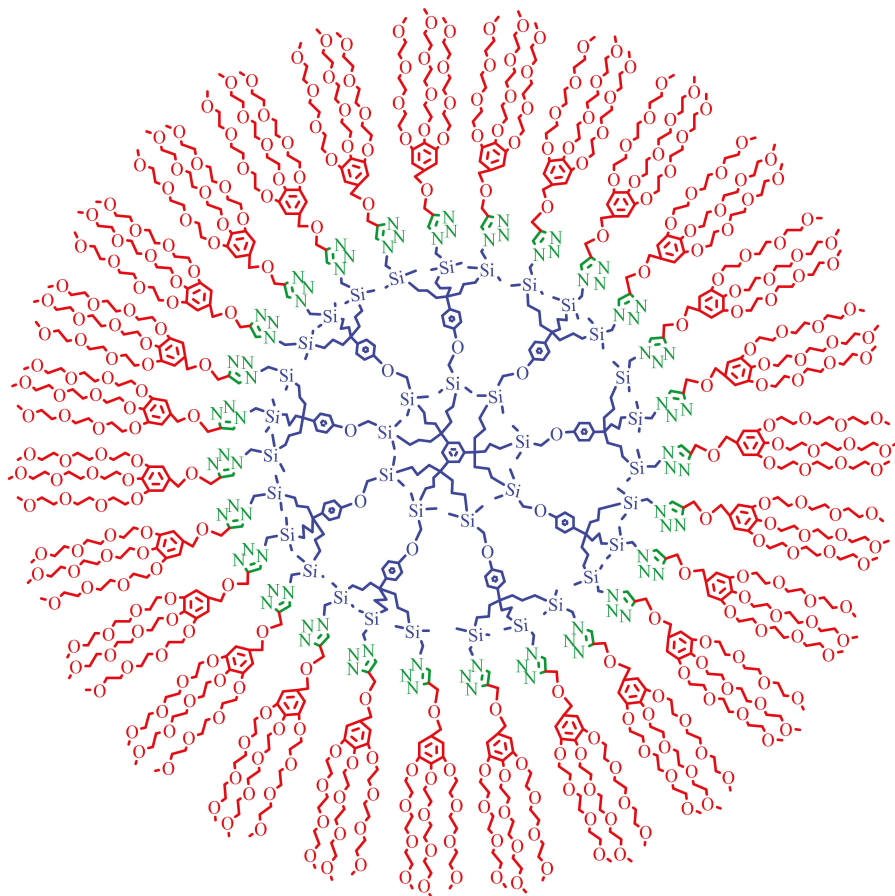


Figure 4. Planar representation of a 81-TEG *dentromer* (1st generation).

Dentromers have so far scarcely been applied to the biomedical field unlike the other dendrimers [6–9,32–38,95]. Nevertheless, gold nanoparticle-centered silylferrocenyl-terminated *dentromers* have been shown to electrochemically recognize the ATP anion, a DNA fragment [81]. In this case, *dentromers* present a significant advantage over other dendrimers, because a close dendrimer–substrate interaction is favored by triple branching, as shown by a positive dendritic effect (i.e., the fact that the increase in the generation number results in better recognition [77], unlike in catalysis [94]). *Dentromers* have also been shown to encapsulate various substrates [96–100], including vitamin C and other vitamins [96,97], dopamine, and acetylcholine [98,99]. It has not been demonstrated that gold-nanoparticle-cored *dentromers* would necessarily present an advantage

over other dendrimers in drug delivery, however. For instance, water-soluble TEG-terminated gold nanoparticles were shown by 600 MHz ^1H NMR in D_2O to encapsulate nine molecules of docetaxel (Figure 5). This taxane, known in its classic formulation as taxoter, is one of the most powerful and efficient anti-cancer drugs; thus, this nanodevice was designed for in vitro drug delivery [101,102].

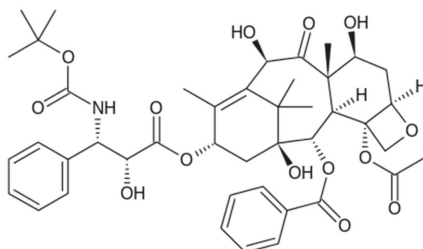


Figure 5. Molecular structure of the strong anti-cancer drug docetaxel.

5. Concluding Remarks

The original organoiron chemistry of arene activation and multiple functionalization was used in the late 1970s to propose a set of reactions leading to stars and dendritic cores. The principle of iterations has since then been the key to dendritic, dendronic, and *dentromeric* constructions. Around the turn of the century, new dendrons and giant *dentromers*, a family of dendrimers with 1 → 3 branching, were constructed based on these principles. Specific applications include the fast synthesis of *dentromers* with a large number of peripheral groups, such as ferrocene and other organometallics, leading, for instance, to molecular batteries and redox sensors. This redox behavior parallels that of the polyelectronic reduction of fullerenes [103,104], but with an electrostatic effect that is almost nil in dendrimers and *dentromers* terminated with redox groups. The fast access to small *dentromers* terminated with Percec-type dendrons also allowed many applications as micellar templates for catalysis in water or aqueous solvents. The shortcomings of *dentromers* are not apparent, although biomedical applications remain rare (vide supra); such applications might be of great interest [95].

In conclusion, the ideas and works presented in this mini-review could be developed in part thanks to the concept of dendrimers developed by Tomalia in his seminal 1990 review.

Acknowledgments: Invaluable collaborations and discussions with Jean-René Hamon and Jean-Yves Saillard (Rennes), Lionel Salmon (LCC, Toulouse), Marie-Christine Onuta (UMBC, MD, USA), Fengyu Fu, Sylvain Gatard, Haibin Gu, Na Li, Feng Lu, Dong Wang, Changlong Wang (Bordeaux), Pengxiang Zhao (Chengdu), and Sergio Moya and his group (biomaGUNE, San Sebastian, Spain). Financial support from the University of Bordeaux, the Centre National de la Recherche Scientifique, the Agence Nationale pour la Recherche (D.A.), the Ministère de l'Enseignement Supérieur et de la Recherche (PhD grant to C.D.), the Institut Universitaire de France (D.A.), the Chinese Scholarship Council (PhD grants to X.L., Q.W., and Y.W.), and L'Oréal (D.A.) are gratefully acknowledged.

Conflicts of Interest: The authors declare no conflict of interest.

References

1. Tomalia, D.A.; Baker, H.; Dewald, J.; Hall, M.; Kallos, G.; Martin, S.; Roeck, J.; Ryder, J.; Smith, P. A New Class of Polymers: Starburst-Dendritic Macromolecules. *Polym. J.* **1985**, *17*, 117–132. [\[CrossRef\]](#)
2. Newkome, G.R.; Yao, Z.; Baker, G.R.; Gupta, V.K. Micelles. Part 1. Cascade molecules: A new approach to micelles. A [27]-arborol. *J. Org. Chem.* **1985**, *50*, 2003–2004. [\[CrossRef\]](#)
3. Denkwalter, R.G.; Kolc, J.F.; Lukasavage, W.J. Macromolecular Highly Branched Homogeneous Compounds. U.S. Patent 4,410,688, 18 October 1983.
4. Tomalia, D.A.; Naylor, A.M.; Goddard, W.A. Starburst Dendrimers: Molecular-Level Control of Size, Shape, Surface Chemistry, Topology, and Flexibility from Atoms to Macroscopic Matter. *Angew. Chem. Int. Ed.* **1990**, *29*, 138–175. [\[CrossRef\]](#)

5. Tomalia, D.A. Birth of a New Macromolecular Architecture: Dendrimers as Quantized Building Blocks for Nanoscale Synthetic Polymer Chemistry. *Prog. Polym. Sci.* **2005**, *30*, 294–324. [[CrossRef](#)]
6. Wiener, E.C.; Brechbiel, M.W.; Brothers, H.; Magin, R.L.; Gansow, O.A.; Tomalia, D.A.; Lautebur, P.C. Dendrimer-based metal chelates: A new class of magnetic resonance imaging contrast agents. *Magn. Reson. Med.* **1994**, *31*, 1–8. [[CrossRef](#)] [[PubMed](#)]
7. Esfand, R.; Tomalia, D.A. Poly(amidoamine) (PAMAM) dendrimers: From biomimicry to drug delivery and biomedical applications. *Drug. Discov. Today* **2001**, 427–436.
8. Lee, C.C.; MacKay, J.A.; Fréchet, J.M.J.; Szoka, F.C. Designing dendrimers for biological applications. *Nat. Biotechnol.* **2005**, *23*, 1517–1526. [[CrossRef](#)] [[PubMed](#)]
9. Kannan, R.M.; Nance, E.; Kannan, S.; Tomalia, D.A. Emerging concepts in dendrimer-based nanomedicine: From design principles to clinical applications. *J. Intern. Med.* **2014**, *276*, 579–617. [[CrossRef](#)] [[PubMed](#)]
10. Hawker, C.J.; Fréchet, J.M.J. Preparation of polymers with controlled molecular architecture. A new convergent approach to dendritic macromolecules. *J. Am. Chem. Soc.* **1990**, *112*, 7638–7639. [[CrossRef](#)]
11. Miller, T.M.; Neenan, T.X. Convergent synthesis of monodisperse dendrimers based upon 1,3,5-trisubstituted benzenes. *Chem. Mater.* **1990**, *2*, 346–349. [[CrossRef](#)]
12. Yamamoto, K.; Higuchi, M.; Shiki, S.; Tsuruta, M.; Chiba, H. Stepwise radial complexation of imine groups in phenylazomethine dendrimers. *Nature* **2002**, *415*, 509–511. [[CrossRef](#)] [[PubMed](#)]
13. Serroni, S.; Denti, G.; Campagna, S.; Balzani, V. Arborols Based on Luminescent and Redox-Active Transition Metal Complexes. *Angew. Chem. Int. Ed.* **1992**, *31*, 1493–1495.
14. Van der Made, A.W.; van Leeuwen, P.W.N.M. Silane Dendrimers. *J. Chem. Soc. Chem. Commun.* **1992**, 1400–1401. [[CrossRef](#)]
15. Nagasaki, T.; Ukon, M.; Arimori, S.; Shinkai, S. Crowned arborols. *J. Chem. Soc. Chem. Commun.* **1992**, *8*, 608–609. [[CrossRef](#)]
16. De Brabander-van den Berg, E.M.M.; Meijer, E.W. Poly(propylene imine) Dendrimers: Large-Scale Synthesis by Heterogeneously Catalyzed Hydrogenations. *Angew. Chem., Int. Ed. Engl.* **1993**, *105*, 1370–1372. [[CrossRef](#)]
17. Moors, R.; Vögtle, F. Dendrimeric Polyamines. *Chem. Ber.* **1993**, *126*, 2133–2135. [[CrossRef](#)]
18. Seyferth, D.; Son, D.Y.; Rheingold, A.L.; Ostrander, R.L. Synthesis of an organosilicon dendrimer containing 324 Si-H bonds. *Organometallics* **1994**, *13*, 2682–2690. [[CrossRef](#)]
19. Bryce, M.R.; Devonport, W.; Moore, A.J. Dendritic macromolecules incorporating tetrafulvalene units. *Angew. Chem. Int. Ed.* **1994**, *33*, 1761–1763. [[CrossRef](#)]
20. Launay, N.; Caminade, A.-M.; Lahana, R.; Majoral, J.-P. A General Synthetic Strategy for Neutral Phosphorus-Containing Dendrimers. *Angew. Chem. Int. Ed.* **1994**, *33*, 1589–1592. [[CrossRef](#)]
21. Launay, N.; Caminade, A.-M.; Majoral, J.-P. Synthesis and reactivity of unusual phosphorous dendrimers. A useful divergent growth approach up to the seventh generation. *J. Am. Chem. Soc.* **1995**, *117*, 3282–3283. [[CrossRef](#)]
22. Sourmies, F.; Crasnier, F.; Graffeuil, M.; Faucher, J.-P.; Labarre, M.-C.; Labarre, J.-F. Spherical Cyclophosphazene Dendrimers to the Fifth Generation. *Angew. Chem. Int. Ed.* **1995**, *34*, 578–581. [[CrossRef](#)]
23. Casado, C.M.; Cuadrado, I.; Moran, M.; Alonso, B.; Lobete, F.; Losada, J. Synthesis of the first redox-active organometallic polymers containing cyclosiloxanes as frameworks. *Organometallics* **1995**, *14*, 2618–2620. [[CrossRef](#)]
24. Casado, C.M.; Cuadrado, I.; Moran, M.; Alonso, B.; Garcia, B.; Gonzales, B.; Losada, J. Redox-active ferrocenyl dendrimers and polymers in solution and immobilized on electrode surfaces. *J. Coord. Chem. Rev.* **1998**, *185*, 53–79.
25. Balzani, V.; Campagna, S.; Denti, G.; Juris, A.; Serroni, S.; Venturi, M. Designing dendrimers based on transition-metal complexes. Light harvesting properties and predetermined redox patterns. *Acc. Chem. Res.* **1998**, *31*, 26–34. [[CrossRef](#)]
26. Armaroli, N.; Boudon, C.; Felder, D.; Gisselbrecht, D.; Gross, J.-P.; Marconi, M.; Nicoud, G.; Nierengarten, J.-F.; Vicinelli, V. A copper (I) bis-phenanthroline complex buried in fullerene-functionalized dendritic black boxes. *Angew. Chem. Int. Ed. Engl.* **1999**, *38*, 3730–3733. [[CrossRef](#)]
27. Newkome, G.R.; He, E.; Moorefield, C.N. Suprasupermolecules with novel properties: Metallodendrimers. *Chem. Rev.* **1999**, *99*, 1689–1746. [[CrossRef](#)] [[PubMed](#)]

28. Caminade, A.-M.; Majoral, J.-P. Dendrimers containin heteroatoms (Si, P, B, Ge or Bi). *Chem. Rev.* **1999**, *99*, 845–880.
29. Bosman, A.W.; Janssen, H.M.; Meijer, E.W. About dendrimers: Structure, physical properties and applications. *Chem. Rev.* **1999**, *99*, 1665–1688. [[CrossRef](#)] [[PubMed](#)]
30. Nierengarten, J.F. Fullerodendrimers: A new class of compounds for supramolecular chemistry and material science applications. *Chem. Eur. J.* **2000**, *6*, 3667–3670. [[CrossRef](#)]
31. Grayson, S.M.; Fréchet, J.M.J. Convergent dendrons and dendrimers: From synthesis to applications. *Chem. Rev.* **2001**, *101*, 3819–3867. [[CrossRef](#)] [[PubMed](#)]
32. Newkome, G.R.; Moorefield, C.N.; Vögtle, F. *Dendrimers and Dendrons: Concepts, Syntheses, Applications*; Wiley-vch: Weinheim, Germany, 2001.
33. Tomalia, D.A.; Fréchet, J.M.J. (Eds.) *Dendrimers and Other Dendritic Polymers*; Wiley: Amsterdam, The Netherlands, 2001.
34. Newkome, G.R.; Shreiner, C.D. Poly(amidoamine), polypropylenimine, and related dendrimers and dendrons possessing different 1 → 2 branching motifs: An overview of the divergent procedures. *Polymer* **2008**, *49*, 1–173. [[CrossRef](#)]
35. Astruc, D.; Boisselier, E.; Ornelas, C. Dendrimers Designed for Functions: From Physical, Photophysical and Supramolecular Properties to Applications in Sensing, Catalysis, Molecular Electronics, Photonics and Nanomedicine. *Chem. Rev.* **2010**, *110*, 1857–1959. [[CrossRef](#)] [[PubMed](#)]
36. Caminade, A.-M.; Turrin, C.-O.; Laurent, R.; Ouali, A.; Delavaux-Nicot, B. *Dendrimers Towards Catalytic, Material and Biomedical Uses*; John Wiley & Sons: Chichester, UK, 2011.
37. Tomalia, D.A.; Christensen, J.B.; Boas, U. *Dendrimers, Dendrons and Dendritic Polymers*; Cambridge University Press: Cambridge, UK, 2012.
38. Campagna, S.; Ceroni, P.; Puntoriero, F. (Eds.) *Designing Dendrimers*; Wiley: Hoboken, NJ, USA, 2012.
39. Newkome, G.R.; Shreiner, C. Dendrimers derived from 1 → 3 branching motifs. *Chem. Rev.* **2010**, *110*, 6338–6442. [[CrossRef](#)] [[PubMed](#)]
40. Rengan, K.; Engel, R. Ammonium cascade molecules. *J. Chem. Soc. Chem. Commun.* **1992**, 757–758. [[CrossRef](#)]
41. Denliker, P.J.; Diederich, F.; Gross, M.; Knobler, C.B.; Louati, A.; Sanford, E.M. Dendritic Porphyrins: Modulating Redox Potentials of Electroactive Chromophores with Pendant Multifunctionality. *Angew. Chem. Int. Ed.* **1994**, *33*, 1739.
42. Percec, V.; Mitchell, C.M.; Cho, W.D.; Uchida, S.; Glodde, M.; Goran, U.; Zeng, X.; Liu, Y.; Balagurusamy, V.S.K.; Heiney, P.A. Designing Libraries of First Generation AB₃ and AB₂ Self-Assembling Dendrons via the Primary Structure Generated from Combinations of (AB)_y-AB₃ and (AB)-AB₂ Building Blocks. *J. Am. Chem. Soc.* **2004**, *126*, 6078–6094. [[CrossRef](#)] [[PubMed](#)]
43. Rosen, B.M.; Wilson, C.J.; Wilson, D.A.; Percec, V. Dendron-Mediated Self-Assembly, Disassembly, and Self-Organization of Complex Systems. *Chem. Rev.* **2009**, *109*, 6275–6540. [[CrossRef](#)] [[PubMed](#)]
44. Newkome, G.R. Suprasupermolecular chemistry: The chemistry within the dendrimer. *Pure Appl. Chem.* **1998**, *70*, 2337–2343. [[CrossRef](#)]
45. Newkome, G.R.; Yao, Z.-Q.; Baker, G.R.; Gupta, V.K.; Russo, P.S.; Saunders, M.J. Chemistry of micelles series. Part 2. Cascade molecules. Synthesis and characterization of a benzene[9]3-arborol. *J. Am. Chem. Soc.* **1986**, *108*, 849–850. [[CrossRef](#)]
46. Newkome, G.R.; Moorefield, C.N.; Baker, G.R. Building Blocks for Dendritic Macromolecules. *Aldrichim. Acta* **1992**, *25*, 31–38.
47. Newkome, G.R.; Moorefield, C.N.; Theriot, K.J. A convenient synthesis of bis-homotris: 4-amino-4-[1-(3-hydroxypropyl)]-1,7-heptanediol and 1-azoniaprpellane. *J. Org. Chem.* **1988**, *53*, 5552–5554. [[CrossRef](#)]
48. Moorefield, C.N.; Newkome, G.R. A Review of Dendritic Macromolecules. In *Advances in Dendritic Molecules*; Newkome, G.R., Ed.; JAI: Greenwich, UK, 1994; Volume 1, pp. 1–67.
49. Twyman, L.J.; Beezer, A.E.; Esfand, R.; Hardy, M.J.; Mitchell, J.C. The Synthesis of Water-Soluble Dendrimers and their Application as Possible Drug Delivery Systems. *Tetrahedron Lett.* **1999**, 1743–1746. [[CrossRef](#)]
50. Newkome, G.R.; Hu, Y.; Saunders, M.J.; Fronzsek, S.R. Silvanols: Water-Soluble Calixarenes. *Tetrahedron Lett.* **1991**, *32*, 1133. [[CrossRef](#)]
51. Rudick, J.G.; Percec, V. Induced Helical Backbone Conformations of Self-Organizable Dendronized Polymers. *Acc. Chem. Res.* **2008**, *41*, 1641–1652. [[CrossRef](#)] [[PubMed](#)]

52. Abd-El-Aziz, A.S.; Bernardin, S. Synthesis and reactivity of arenes coordinated to cyclopentadienyliron cations. *Coord. Chem. Rev.* **2000**, *203*, 219–267. [[CrossRef](#)]
53. Catheline, D.; Astruc, D. The Use of Ferrocene in Organometallic Synthesis: A two Step Preparation of Cyclopentadienyliron Acetonitrile and Phosphine Cations via Photolysis of Cyclopentadienyliron Tricarbonyl or Arene Cations. *J. Organomet. Chem.* **1984**, *272*, 417–426. [[CrossRef](#)]
54. Astruc, D.; Hamon, J.-R.; Althoff, G.; Román, E.; Batail, P.; Michaud, P.; Mariot, J.-P.; Varret, F.; Cozak, D. Design, Stabilization and Efficiency of Organometallic “Electron Reservoirs”. 19-Electron Sandwiches $\eta^5\text{-C}_5\text{R}_5\text{Fe(I)} \eta^6\text{-C}_6\text{R}_6$, a Key Class Active in Redox Catalysis. *J. Am. Chem. Soc.* **1979**, *101*, 5445–5447. [[CrossRef](#)]
55. Astruc, D.; Roman, E.; Hamon, J.-R.; Batail, P. Novel Reactions of Dioxygen in Organometallic Chemistry. Hydrogen Atom Abstraction versus Dimerization of the 19-Electron Complexes $\eta^6\text{-Cyclopentadienyl Iron(I)} \eta^6\text{-Arene}$. *J. Am. Chem. Soc.* **1979**, *101*, 2240–2242. [[CrossRef](#)]
56. Moinet, C.; Roman, E.; Astruc, D. Electrochemical Reduction of Cations $\eta^5\text{-Cyclopentadienyl Fe}^+ \eta^6\text{-Arene}$ in Basic Media. Study of the Behavior of the Radicals Formed “in Situ”. *J. Electroanal. Chem.* **1981**, *121*, 241–253. [[CrossRef](#)]
57. Astruc, D. Why is Ferrocene so Exceptional. *Eur. J. Inorg. Chem.* **2017**, 6–29. [[CrossRef](#)]
58. Hamon, J.-R.; Saillard, J.-Y.; Le Beuze, A.; McGlinchey, M.; Astruc, D. Multiple Formation and Cleavage of C-C Bonds in $\text{CpFe}^+(\text{Arene})$ Sandwichs and the Unusual C_6Et_6 Geometry in the X-Ray Crystal Structure of $\text{CpFe}^+(\eta^6\text{-C}_6\text{Et}_6)\text{PF}_6^-$. *J. Am. Chem. Soc.* **1982**, *104*, 7549–7555. [[CrossRef](#)]
59. Moulines, F.; Astruc, D. Tentacled Iron Sandwichs. *Angew. Chem. Int. Ed. Engl.* **1988**, *27*, 1347–1349. [[CrossRef](#)]
60. Moulines, F.; Gloaguen, B.; Astruc, D. One-Pot Multifunctionalization of Polymethyl Hydrocarbon π -Ligands. Maximum Space Occupancy by Double Branching and Formation of Arborols. *Angew. Chem. Int. Ed. Engl.* **1992**, *28*, 458–460. [[CrossRef](#)]
61. Gloaguen, B.; Astruc, D. Chiral Pentaisopropyl- and Pentaisopentyl Complexes: One-Pot Synthesis by Formation of Ten Carbon-Carbon Bonds from Pentamethylcobalticinium. *J. Am. Chem. Soc.* **1990**, *112*, 4607–4609. [[CrossRef](#)]
62. Moulines, F.; Djakovitch, L.; Boese, R.; Gloaguen, B.; Thiel, W.; Fillaut, J.-L.; Delville, M.-H.; Astruc, D. Organometallic Molecular Trees as Multi-Electron and Proton Reservoirs: CpFe^+ Induced Nona-Allylation of Mesitylene and Phase-Transfer Catalyzed Synthesis of a Redox Active Nona-Iron Complex. *Angew. Chem., Int. Ed. Engl.* **1993**, *32*, 1075–1077. [[CrossRef](#)]
63. Sartor, V.; Djakovitch, L.; Fillaut, J.-L.; Moulines, F.; Neveu, F.; Marvaud, V.; Guittard, J.; Blais, F.; Neveu, J.-C.; Astruc, D. Organoiron Routes to a New Dendron for Fast Dendritic Syntheses Using Divergent and Convergent Methods. *J. Am. Chem. Soc.* **1999**, *121*, 2929–2930. [[CrossRef](#)]
64. Ruiz, J.; Lacoste, M.; Astruc, D. Arene Exchange by P Donors in the 19-Electron Complexes $\text{Fe}^I\text{Cp}(\text{Arene})$: Kinetics, Mechanism and Salt Effects; Characterization and Reactivity of the New 17-Electron and 19-Electron Radicals $\text{Fe}^I\text{Cp}(\text{PR}_3)_n$ ($n = 2$ and 3). *J. Am. Chem. Soc.* **1990**, *112*, 5471–5483. [[CrossRef](#)]
65. Nlate, S.; Ruiz, J.; Blais, J.-C.; Astruc, D. Ferrocenylsilylation of Dendrons: A Fast Convergent Route to Redox-Stable Ferrocene Dendrimers. *Chem. Commun.* **2000**, *5*, 417–418. [[CrossRef](#)]
66. Ruiz, J.; Lafuente, G.; Marcen, S.; Ornelas, C.; Lazare, S.; Cloutet, E.; Blais, J.-C.; Astruc, D. Construction of Giant Dendrimers Using a Tripodal Buiding Block. *J. Am. Chem. Soc.* **2003**, *125*, 7250–7257. [[CrossRef](#)] [[PubMed](#)]
67. Kob, H.C.; Finn, M.G.; Sharpless, K.B. Click Chemistry: Diverse Chemical Functions from a Few Good Reactions. *Angew. Chem., Int. Ed.* **2001**, *40*, 2004–2021.
68. Binder, W.H.; Sachsenhofer, R. Click Chemistry in Polymer and Materials Science. *Macromol. Commun.* **2007**, *28*, 15–54. [[CrossRef](#)]
69. Franc, G.; Kakkar, A.K. Click methodologies: Efficient, simple and greener routes to design dendrimers. *Chem. Soc. Rev.* **2010**, *39*, 1536–1544. [[CrossRef](#)] [[PubMed](#)]
70. Ornelas, C.; Ruiz, J.; Cloutet, E.; Astruc, D. Click Assembly of 1,2,3-Triazole-Linked Dendrimers Including Ferrocenyl Dendrimers that Sense Both Oxo-anions and Metal Cations. *Angew. Chem. Int. Ed.* **2007**, *46*, 872–877. [[CrossRef](#)] [[PubMed](#)]

71. Diallo, A.K.; Ornelas, C.; Salmon, L.; Ruiz, J.; Astruc, D. Homeopathic Catalytic Activity and Atom-Leaching Mechanism in the Miyaura-Suzuki Reactions under Ambient Conditions Using Precise “Click” Dendrimer-Stabilized Pd Nanoparticles. *Angew. Chem. Int. Ed. Engl.* **2007**, *46*, 8644–8648. [[CrossRef](#)] [[PubMed](#)]
72. Ornelas, C.; Ruiz, J.; Belin, C.; Astruc, D. Giant Dendritic Molecular Electrochrome Batteries with Ferrocenyl and Pentamethylferrocenyl Termini. *J. Am. Chem. Soc.* **2009**, *131*, 590–601. [[CrossRef](#)] [[PubMed](#)]
73. Wang, Y.; Salmon, L.; Ruiz, J.; Astruc, D. Metallo dendrimers in Three Oxidation States with Electronically Interacting Metals and Stabilization of Size-Selected Gold Nanoparticles. *Nat. Commun.* **2014**, *5*, 3489. [[CrossRef](#)] [[PubMed](#)]
74. Djeda, R.; Rapakousiou, A.; Liang, L.; Guidolin, N.; Ruiz, J.; Astruc, D. Click Syntheses of Large 1,2,3-Triazolyl Biferrocenyl Dendrimers and Selective Roles of the Inner and Outer Ferrocenyl Groups in the Redox Recognition of the ATP²⁻ Anion and Pd^{II} Cation. *Angew. Chem. Int. Ed.* **2010**, *49*, 8152–8156. [[CrossRef](#)] [[PubMed](#)]
75. Boisselier, E.; Diallo, A.K.; Salmon, L.; Ornelas, C.; Ruiz, J.; Astruc, D. Encapsulation and Stabilization of Gold Nanoparticles with “Click” Polyethyleneglycol Dendrimers. *J. Am. Chem. Soc.* **2010**, *132*, 2729–2742. [[CrossRef](#)] [[PubMed](#)]
76. Astruc, D.; Liang, L.; Rapakousiou, A.; Ruiz, J. Click Dendrimers and Triazole-Related Aspects: Catalysts, Mechanism, Synthesis, and Functions. A Bridge between Dendritic Architectures and Nanomaterials. *Acc. Chem. Res.* **2012**, *45*, 630–640. [[CrossRef](#)] [[PubMed](#)]
77. Valério, C.; Fillaut, J.-L.; Ruiz, J.; Guittard, J.; Blais, J.-C.; Astruc, D. The Dendritic Effect in Molecular Recognition: Ferrocene Dendrimers and their Use as Supramolecular Redox Sensors for the Recognition of Small Inorganic Anions. *J. Am. Chem. Soc.* **1997**, *119*, 2588–2589. [[CrossRef](#)]
78. Valério, C.; Alonso, E.; Ruiz, J.; Blais, J.-C.; Astruc, D. A Polycationic Metallo dendrimer with 24 Organoiron Termini which Senses Chloride and Bromide Anions. *Angew. Chem. Int. Ed. Engl.* **1999**, *38*, 1747–1751. [[CrossRef](#)]
79. Astruc, D.; Ornelas, C.; Ruiz, J. Metallocenyl Dendrimers and their Applications in Molecular Electronics, Sensing and Catalysis. *Acc. Chem. Res.* **2008**, *41*, 841–856. [[CrossRef](#)] [[PubMed](#)]
80. Ruiz, J.; Belin, C.; Astruc, D. Assembly of Dendrimers with Redox-Active Clusters [CpFe(μ_3 -CO)]₄ at the Periphery and Application to Oxo-anion and Adenosyne-5'-Triphosphate (ATP) Sensing. *Angew. Chem. Int. Ed.* **2006**, *45*, 132–136.
81. Daniel, M.-C.; Ruiz, J.; Nlate, S.; Blais, J.-C.; Astruc, D. Nanoscopic Assemblies Between Supramolecular Redox Active Metallo dendrons and Gold Nanoparticles: Syntheses, Characterization and Selective Recognition of H₂PO₄⁻, HSO₄⁻ and Adenosine-5'-Triphosphate (ATP²⁻) Anions. *J. Am. Chem. Soc.* **2003**, *125*, 2617–2628. [[CrossRef](#)] [[PubMed](#)]
82. Daniel, M.-C.; Ruiz, J.; Astruc, D. Supramolecular H-bonded Assemblies of Redox-Active Metallo dendrimers and Positive and Unusual Dendritic Effects on the Recognition of H₂PO₄⁻. *J. Am. Chem. Soc.* **2003**, *125*, 1150–1151. [[CrossRef](#)] [[PubMed](#)]
83. Stryer, L. *Biochemistry*, 2nd ed.; Freeman: New York, NY, USA, 1981; p. 240.
84. Crooks, R.M.; Zhao, M.; Sun, L.; Chechik, V.; Yeung, L.K. Dendrimer-Encapsulated Metal Nanoparticles: Synthesis, Characterization, and Application to Catalysis. *Acc. Chem. Res.* **2001**, *34*, 181–190. [[CrossRef](#)] [[PubMed](#)]
85. Scott, R.W.J.; Wilson, O.M.; Crooks, R.M. Synthesis, Characterization, and Applications of Dendrimer-Encapsulated Nanoparticles. *J. Phys. Chem. B* **2005**, *109*, 692–704. [[CrossRef](#)] [[PubMed](#)]
86. Toshima, N.; Yonezawa, T. Bimetallic nanoparticles—novel materials for chemical and physical applications. *New J. Chem.* **1998**, *22*, 1179–1201. [[CrossRef](#)]
87. Deraedt, C.; Astruc, D. “Homeopathic” Palladium Nanoparticle Catalysis of Cross Carbon–Carbon Coupling Reactions. *Acc. Chem. Res.* **2014**, *47*, 494–503. [[CrossRef](#)] [[PubMed](#)]
88. De Vries, J.G. A unifying mechanism for all high-temperature Heck reactions. The role of palladium colloids and anionic species. *Dalton Trans.* **2006**, 421–429. [[CrossRef](#)] [[PubMed](#)]
89. Diallo, A.K.; Boisselier, E.; Liang, L.; Ruiz, J.; Astruc, D. Dendrimer-induced Molecular Catalysis in Water: The Example of Olefin Metathesis. *Chem. Eur. J.* **2010**, *16*, 11832–11835. [[CrossRef](#)] [[PubMed](#)]
90. Deraedt, C.; Pinaud, N.; Astruc, D. A Recyclable Catalytic Dendrimer Nanoreactor for Part-Per-Million Cu(I) Catalysis of “click” Reactions in Water. *J. Am. Chem. Soc.* **2014**, *136*, 12092–12098. [[CrossRef](#)] [[PubMed](#)]

91. Rapakousiou, A.; Deraedt, C.; Gu, H.; Salmon, L.; Belin, C.; Ruiz, J.; Astruc, D. Mixed-Valent Intertwined Polymer Units Containing Biferrocenium Chloride Side Chains Form Nanosnakes that Encapsulate Gold Nanoparticles. *J. Am. Chem. Soc.* **2014**, *136*, 13995–13998. [[CrossRef](#)] [[PubMed](#)]
92. Liu, X.; Gregurec, D.; Irigoyen, J.; Martinez, A.; Moya, S.; Ciganda, R.; Hermange, P.; Ruiz, J.; Astruc, D. Precise Localization of Metal Nanoparticles in Dendrimer Nanosnakes or Inner Periphery and Consequences in Catalysis. *Nat. Commun.* **2016**, *7*, 13152. [[CrossRef](#)] [[PubMed](#)]
93. Wang, C.; Ciganda, R.; Salmon, L.; Gregurec, D.; Irigoyen, J.; Moya, S.; Ruiz, J.; Astruc, D. Highly efficient transition metal nanoparticle catalysts in aqueous solutions. *Angew. Chem. Int. Ed.* **2016**, *55*, 3091–3095. [[CrossRef](#)] [[PubMed](#)]
94. Astruc, D.; Wang, Q.; Fu, F.; Escobar, A.; Moya, S.; Ruiz, J. “Click” dendrimer-stabilized nanocatalysts for hydrogen release upon ammonia-borane hydrolysis. *ChemCatChem* **2018**, *0*. [[CrossRef](#)]
95. Ornelas, C. Brief Timelapse on dendrimer Chemistry: Advances, limitations and Expectations. *Macromol. Chem. Phys.* **2016**, *217*, 149–174. [[CrossRef](#)]
96. Boisselier, E.; Ruiz, J.; Astruc, D. Encapsulation de la vitamine C dans des dendrimères solubles dans l’eau. French Patent 101305FR, 22 January 2008.
97. Zhao, P.; Ruiz, J.; Astruc, D. Encapsulation of water-soluble vitamins in hydrophobic media. *Chem. Lett.* **2012**, *41*, 1107–1109. [[CrossRef](#)]
98. Ornelas, C.; Boisselier, E.; Martinez, V.; Pianet, I.; Ruiz, J.; Astruc, D. New Water-soluble Polymeric Dendrimers and Binding of Acetylcholin in Water by Mean of Supramolecular Interactions. *Chem. Commun.* **2007**, 5093–5095. [[CrossRef](#)] [[PubMed](#)]
99. Boisselier, E.; Ornelas, C.; Pianet, I.; Ruiz, J.; Astruc, D. Four Generations of Water Soluble Dendrimers with 9 to 243 Benzoate Tethers: Synthesis and Dendritic Effects on Their Ion Paring with Acetylcholine, Benzyltriethylammonium and Dopamine in Water. *Chem. Eur. J.* **2008**, *14*, 5577–5587. [[CrossRef](#)] [[PubMed](#)]
100. Diallo, A.K.; Boisselier, E.; Ruiz, J.; Astruc, D. Nouveau Procédé de métathèse d’oléfines ou d’énynes. French Patent 08/05548FR, 8 October 2008.
101. François, A.; Laroche, A.; Pinaud, N.; Salmon, L.; Ruiz, J.; Robert, J.; Astruc, D. Encapsulation of docetaxel into PEGylated gold nanoparticles for vectorization to cancer cells and in vitro results. *ChemMedChem* **2011**, *6*, 2003–2008. [[CrossRef](#)] [[PubMed](#)]
102. Zhao, P.; Astruc, D. Docetaxel nanotechnology in anti-cancer therapy. *ChemMedChem* **2012**, *7*, 952–972. [[CrossRef](#)] [[PubMed](#)]
103. Bossard, C.; Rigaut, S.; Astruc, D.; Delville, M.-H.; Félix, G.; Février-Bouvier, A.; Amiell, J.; Flandrois, S.; Delhaès, P. One-, Two- and Three-Electron Reduction of C₆₀ Using the Electron-Reservoir Complex [Fe^ICp(C₆Me₆)]. *J. Chem. Soc. Chem. Commun.* **1993**, *3*, 333–334. [[CrossRef](#)]
104. Zhou, F.M.; Jehoulet, C.; Bard, A.J. Reduction and electrochemistry of fullerene C₆₀ in liquid ammonia. *J. Am. Chem. Soc.* **1992**, *114*, 11004. [[CrossRef](#)]



© 2018 by the authors. Licensee MDPI, Basel, Switzerland. This article is an open access article distributed under the terms and conditions of the Creative Commons Attribution (CC BY) license (<http://creativecommons.org/licenses/by/4.0/>).

Review

Drug Delivery Systems from Self-Assembly of Dendron-Polymer Conjugates [†]

Burcu Sumer Bolu ¹, Rana Sanyal ^{1,2,*} and Amitav Sanyal ^{1,2,*}

¹ Department of Chemistry, Bogazici University, Bebek, 34342 Istanbul, Turkey; burcusumer@gmail.com

² Center for Life Sciences and Technologies, Bogazici University, 34342 Istanbul, Turkey

* Correspondence: rana.sanyal@boun.edu.tr (R.S.); amitav.sanyal@boun.edu.tr (A.S.);
Tel.: +90-212-359-4793 (R.S.); +90-212-359-7613 (A.S.)

[†] Dedicated to Prof. Donald A. Tomalia on occasion of his 80th birthday.

Academic Editor: Ashok Kakkur

Received: 18 May 2018; Accepted: 21 June 2018; Published: 28 June 2018

Abstract: This review highlights the utilization of dendron-polymer conjugates as building blocks for the fabrication of nanosized drug delivery vehicles. The examples given provide an overview of the evolution of these delivery platforms, from simple micellar containers to smart stimuli- responsive drug delivery systems through their design at the macromolecular level. Variations in chemical composition and connectivity of the dendritic and polymeric segments provide a variety of self-assembled micellar nanostructures that embody desirable attributes of viable drug delivery systems.

Keywords: dendrimer; dendron; conjugates; nanotherapeutics; drug delivery; polymers

1. Introduction

1.1. Nanosized Polymeric Materials as Drug Delivery Vehicles

Recent decades have witnessed an increasing trend in the application of polymeric nanomaterials for cancer therapy [1–3]. Widespread employment of polymer-based nanomaterials such as micellar aggregates and polymeric nanoparticles (NPs) in various application areas such as smart drug delivery systems, disease diagnosis and medical nanodevices has drawn attention to their vast potential [4–6]. A volume of studies in the area of polymer-based drug delivery systems has established that in most cases combining a drug to such a nanosized construct increases the efficacy of the drug. Moreover, when the drug is simply encapsulated or covalently attached as a prodrug, this happens without changing the molecular structure and the reaction of the target cells with the drug [7]. During the distribution phase, these nanoscale particles protect the drug from plasma components such as enzymes and thus preserve its stability. Since many drug molecules are quite hydrophobic, their association with hydrophilic nanocarriers increase their solubility and thus minimizes the need for additional solubilizing excipients, which can cause undesirable side effects [8,9]. Due to increased size of the carrier compared to the drug molecule, the plasma elimination half-life, tumor accumulation and renal clearance rate of the drug can be enhanced. Consequently, the therapeutic index of various chemotherapy agents which are currently in the clinic can be improved, in particular, by reducing their overall toxicity or by enhancing their efficacy [10]. Additionally, incorporation of specific targeting moieties to these nanosized aggregates facilitates delivery of the cargoes such as drugs, nucleic acids, imaging agents to specific cells or particular organelles [11–13]. Employing NPs to generate novel vaccines in order to improve their immunogenic response is another important area, with distinguished examples such as nicotine nanovaccines prepared from lipid-polymeric hybrid NPs displaying great potential for overcoming nicotine addiction through an innovative immunotherapeutic approach [14–17].

Although the overall picture appears quite simplistic, there are several challenges in using micellar constructs as delivery platforms [18]. When NPs are introduced or enter into biological milieus like blood stream, interstitial fluid or extracellular matrix (ECM), the coronas of particles come in close contact with biomacromolecules and adsorb them as in the case of opsonization in plasma [19]. The resulting coating around NP periphery might alter the final efficiency of drug delivery system (DDS) by changing its size, stability and surface charge [20]. As a result, numerous biological variables determining the final efficacy of the DDS such as biodistribution, toxicity, tumor extravasation and cellular internalization profiles of NPs can be distinctively different than conjectured.

Nanotherapeutic agents with an average size in the range of 10 to 200 nm can escape filtration through the kidneys, with a renal clearance cut off value around 5 nm. As a result, these NPs can stay in the blood stream circulating for prolonged periods of time. In this extra time frame, NPs have increased probability to extravasate to the tumor tissue leading to improved drug accumulation profiles [21]. The ultimate toxicity and efficacy of the delivered cargo is notably changed where the biological fate of drugs integrated to DDSs displays distinguished variances regarding pharmacokinetic (PK) properties and biodistribution of parent drugs.

Nanotherapeutics can enhance a drug's efficacy profile during three phases; initially by interaction with the reticuloendothelial system (RES) agents while in systemic circulation; secondly during extravasation from the blood vessel towards tumor environment and finally upon uptake by target cells and release of the delivered agents. RES is a system composed of macrophages widespread in multiple organs and sites, such as lymph nodes, adipose tissue, and bone marrow, but the most essential ones are those located in the spleen and liver, since they have the greatest potential to alter the clearance profiles of NPs. The NP-corona complex formed after introduction to serum may induce recognition by macrophages and removal of these particles via phagocytic routes, as macrophages can detect the NPs coated by these serum proteins [22,23]. Thus, any aspect affecting the opsonization state of the NPs regulates the extent of interaction of the NPs with the RES components, which is the key element for gaining the preferred circulatory time and clearance rates. Surface modification of nanostructures using poly(ethylene glycol) (PEG) segments has been evaluated as an approach to address this barrier [23,24]. The PEGylation level at particle corona, the size, the composition, the surface charge and the shape of NPs are some of the features determining RES interactions. Such criterions which determine the interaction of the nanosized DDS with the biological environment and thus effecting the ultimate fate of these carriers must be kept in mind while designing a nanoparticle based carrier.

1.2. Dendritic Architecture-Based Drug Delivery Vehicles

The concept of three-dimensional branched polymers like dendrimers, possessing an alternative macromolecular structure compared to linear polymers was first proposed by Flory in the early 1950s [25]. However, the initial examples of this class of cascade polymeric structure was iteratively synthesized first by Vögtle and coworkers in 1978 [26], shortly followed by synthesis of lysine dendrimers in the work of Denkewalter and coworkers in 1979 [27]. Thereafter, the poly(amidoamine) dendrimers (PAMAM) were introduced through the work of Tomalia and Dewald, patented and published at 1983 and 1985, respectively [28,29]. Additionally, Newkome and coworkers in 1985 reported the monocascade sphere (arborol) type dendrimers with expendable interior cavities and modifiable surface groups indicating their potential use as micellar delivery agents [30].

Initially termed as cascade molecules or star polymers, dendrimers or dendrons are polymers with well-defined structures due to their step-by-step preparation composed of AB_n type monomers (n usually 2 or 3) rather than the standard AB monomers which result in linear polymers. They are synthesized in an iterative manner, thereby allowing an excellent unimolecular molecular weight distribution as well as providing control over desired core and/or peripheral functionalization [31–33]. In addition, their branched structure offer several modifiable peripheral groups and bulky internal capacities that allow host-guest chemistry [34]. Unimolecular micelles made from dendritic domains

show improved properties as low polydispersity and does not have dissociation problems due to critical micelle concentration as observed for their linear polymeric counterpart [35].

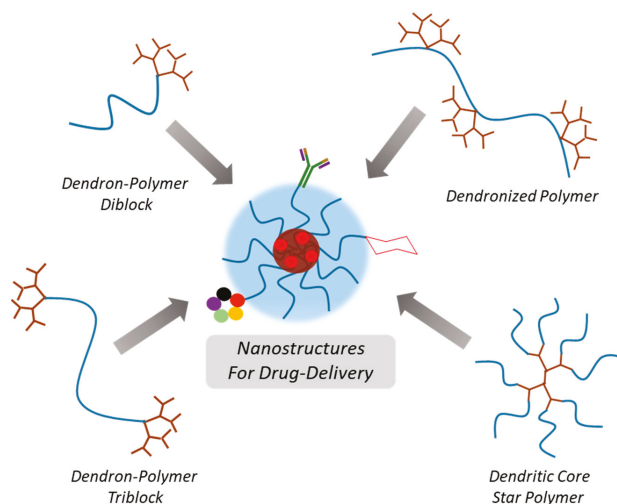
Newkome and co-workers highlighted the concept of unimolecular micelles as a stable delivery system with a hydrophobic core and hydrophilic surface [30,36]. The capacity of dendrimers to act as carriers for therapeutic cargo is enhanced by their elevated internal void volumes and it is further affected by the nature of the backbone which leads to solubilization or complex formation with its cargo through multiple intermolecular forces, such as hydrogen bonding, π - π stacking, ion-dipole interactions, or by electrostatic interactions between its surface groups and the delivered molecules [37,38]. So far, several studies have also shown that direct conjugation strategy of drugs to the dendrimer surface is feasible for increasing drug loading capacities on these type of delivery systems [39].

One of the most widely investigated dendrimer family is the PAMAM dendrimer one, which can have either amine groups or carboxylic esters as termini, depending on the growth step. Hydroxyl terminal groups can also be introduced at their periphery. The presence of reactive surface functional groups enables conjugation of drugs or targeting moieties. In addition, improved encapsulation efficiency of hydrophobic cargos is possible due to noncovalent interactions with the internal tertiary amines or through altering the core of dendrimers by incorporating hydrophobic linkers. However, the poor biodegradability profile and limited biocompatibility of PAMAM dendrimers is a major factor restraining their employment for broader biological applications. Poly (propyleneimine) (PPI)-based dendrimers are another important dendrimer family group containing amine groups at the periphery which can be altered to more biocompatible terminal groups at the dendrimer surface [40,41].

Fréchet and coworkers proposed an ether-based dendritic backbone with similar molecular structure to PEG, which provides biocompatibility to resulting dendrimers [42]. Other types of dendrimers as benzyl ether and melamine-based were also used in combination with PEG modifications to generate soluble delivery systems [43]. Another class of dendritic materials that has received a lot of attention over the past decade are the polyester dendrimers based on 2,2-bis(hydroxymethyl)propionic acid (bis-MPA) [44]. The polyester-based dendrimers composed of bis-MPA monomer units and their conjugates with PEG provide not only biocompatibility and water solubility but also biodegradability to the DDS [45]. Following the introduction of biodegradable polyester-based dendrimers, numerous monomeric building blocks such as glycerol, succinic acid, phenylalanine and lactic acid have been utilized in dendrimer backbones to achieve the generation of bio-dendrimers eligible for tissue engineering [46].

In contrast to the PAMAM dendrimers with peripheral amines leading to dose-, generation- and exposure time-dependent toxicity, dendrimers with polyester backbones display outstanding biocompatibility [47]. For this reason, it has been demonstrated that dendron-polymer conjugates containing these dendritic elements are favorable choices for many biomedical applications in recent years, including the production of novel nanotherapeutic platforms [48,49]. Furthermore, the degree of hydrophobicity can be modulated by changing the generation or peripheral functionalization of these dendrimers. In a seminal study, the importance of this particular dendritic structure in drug delivery was highlighted by Fréchet and Szoka [50]. The flexibility and ease of functionalization of polyester dendrons were validated by introducing doxorubicin (DOX) drug to their surface through acid labile hydrazone linkers. These dendrons were conjugated to a 3-arm-PEG-star core forming a high molecular weight 3-arm PEG–dendron hybrid (>20 kDa) for DOX delivery. As expected the rate of drug release was affected by pH of the environment, where acidic pH resulted in DOX release into the surrounding media while the conjugate retained its stability at neutral pH. The dendritic conjugate displayed effective cellular toxicity towards all cell lines. Importantly, *in vivo* experiments revealed improved plasma half-life and organ biodistribution profiles in comparison to free DOX treatments. Although, not a nanoparticulate formulation, this early example of dendron-polymer based DDS suggested the advantages of combining dendritic and polymeric building blocks.

Understandably, the size of individual dendrimers limits the amount of drug that can be encapsulated or conjugated. Dendrimers employed as unimolecular micelles generally display hydrodynamic sizes of only a few nanometers [51]. Since plasma clearance can be regulated by increasing the size of DDS, where using constructs with high hydrodynamic volumes enables escaping from renal clearance. Thus, the approach to improve blood circulation time depends on increasing the size of the dendrimer. However, to increase size of dendritic delivery system by increasing generation is difficult since production of high generation dendrimers is rather time-consuming and it is possible to diverge from the well-defined structure at higher generations. As a solution to this problem, dendritic polymer conjugates with amphiphilic character were designed to provide larger containers like self-assembled NPs or micelles [32]. Through combination of dendritic structures with polymers, a variety of amphiphilic conjugates can be prepared (Scheme 1). Self-assembly of these polymeric conjugates in aqueous environment to nanosized aggregates provides an efficient tool to fabricate drug delivery platforms. The interior and exterior domains of these micellar aggregates can be loaded with variety of therapeutic agents and conjugated with targeting units to achieve specific delivery to the tumor site. The subsequent sections will highlight examples from literature to provide the reader with a glimpse of how dendron-polymer conjugate based polymeric materials with different architectures have been harnessed to engineer effective carriers for delivery of therapeutic agents.



Scheme 1. Illustration of various dendron-polymer conjugates assembling to form nano-sized drug delivery vehicles.

2. Nano-Sized Aggregates from Polymer-Dendron Diblock Conjugates

Formation of micellar structures from the assembly of amphiphilic dendron polymer conjugates was reported by Fréchet and coworkers in 1992 [52]. Diblock and triblock copolymers were synthesized using a linear PEG-based hydrophilic segment and poly(aryl ether) dendron based hydrophobic segment. Mono and bifunctional PEGs were end-capped with dendrons containing a benzylic bromide unit at their focal point. Micelle formation from these constructs was probed using $^1\text{H-NMR}$ in various deuterated solvents, where the two blocks possessed different solubility. Since then several dendron-polymer conjugates have been designed to serve as efficient delivery platforms. Subsequent paragraphs illustrates with a few examples to provide an overview of current state of these systems.

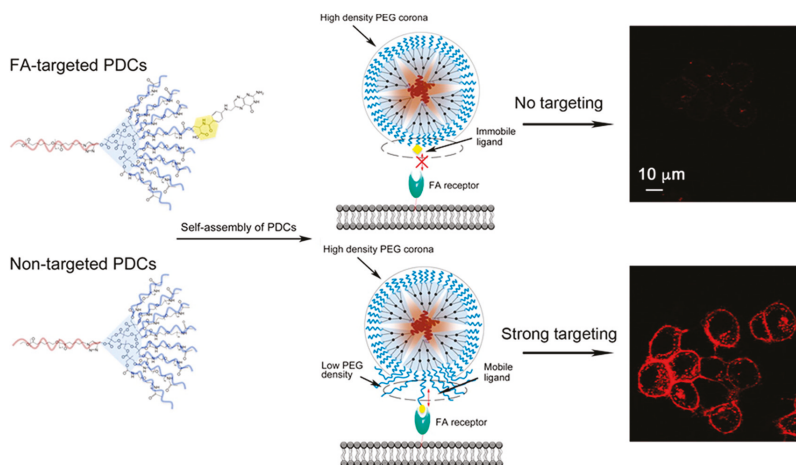
2.1. Nanoparticles Obtained with Hydrophilic Dendron and Hydrophobic Polymer Based Conjugates

In a very recent example, Wei and coworkers reported a micellar DDS system encapsulating 5-fluorouracil (5-FU) and DOX generated using an amphiphilic–dendron diblock conjugate from a generation 3.5 PAMAM dendron conjugated to a linear poly(D,L-lactide) (PDLL) block [53]. In this amphiphilic system, the dendritic moiety was hydrophilic, while the polymer segment was hydrophobic. The resulting drug loaded dendritic micelles (5-FU/Dox-DNM) displayed hydrodynamic size around 70 nm and drug loading capacity of 32% and 16% by weight for 5-FU and DOX respectively. Showing pH dependent drug release profiles as expected due to their PDLL segment, micelles were stable in cell media. MDA-MB-231 cells treated with 5-FU/Dox-DNM exhibited improved apoptotic potential compared to free drugs or single drug DNMs. Additionally, the cell populations were observed at late apoptotic quadrants indicating the synergetic potential of 5-FU/Dox-DNM formulation. When tested in MDA-MB-231 tumor xenograft models, 5-FU/Dox-DNM was able to almost inhibit tumor growth with minimal bodyweight change over the course of 14 days, even though organ accumulation of 5-FU/Dox-DNM were notable in liver, spleen and lung.

Hong and coworkers generated a micellar system based on dendron-polymer conjugates of hydrophilic PEG decorated G3 polyester dendrons conjugated to linear poly- ϵ -caprolactone (PCL) polymers acting as the hydrophobic block [54]. Critical micelle concentrations (CMC) of these conjugates were tuned by employing different sizes for PCL block and varying the PEG chains decorating the G3 dendrons periphery. When compared to linear micelle forming counterparts with similar hydrophilic–lipophilic balance, micelles from dendritic conjugates possessed 1–2 orders of magnitude lower CMC values. They further explored this DDS by fixing the PCL and PEG size to 3.5 kDa and 2 kDa respectively. To explore the effect of peripheral functional groups in terms of cellular interactions amine, carboxyl and acetyl terminated PEG segments were added to the study in addition to the former constructs with methoxy terminated PEGs [55]. The general characteristic were similar in terms of CMC or size, ranging between 20 to 60 nm, except that the zeta potentials of micelles with amino terminated PEGs was 23 mV, which were significantly higher in contrast to others. However, none of the constructs displayed notable difference in cell uptake of rhodamine by KB cells. The low level of internalization especially for micelles with amino terminated PEGs in contrast to the positive control PAMAM were explained as sequestration of the charges by PEG backbone, thereby inhibiting non-specific cell interactions. So decorating dendrons with PEG polymers and thereby achieving very high PEG density on micelle coronas might minimize cellular internalization regardless to surface charge of NPs. Later the authors used this DDS for topical delivery of endoxifen against breast cancer to minimize its toxic effect during oral administration [56]. Among the employed dendron-polymer conjugates, best drug loading was obtained from carboxy-terminated PEGs. Similarly carboxyl terminated vehicles displayed that these micelles enhanced endoxifen delivery through hairless mice skin samples 9 times better compared to ethanol controls, whereas liposomal endoxifen formulation achieved only 2.6 enhancement.

A later report by the same group highlighted the importance of the disposition and the density of targeting groups on the micellar surface in affecting their interaction with cells (Scheme 2). A targeting group, folic acid (FA), was introduced to the abovementioned system and the effect of FA ligand density, cluster formation and length of PEG polymers were evaluated in terms of selectivity of cellular interactions [57]. Covalent conjugation of synthetic PEG to DDS platforms provide not only improved solubility, stability and plasma residence, but also immunogenicity of the nanostructure is reduced significantly [58]. When covered with PEG, nanoparticles are able to escape serum components and reach their destination fairly uninterrupted [59,60]. However, it was observed that the presence of high density PEG layer might hinder association with cells furthermore impair the potential of conjugated ligand by shielding them from their targeted receptors as well [61]. To overcome the “PEG dilemma” PCL-G3-PEG PEGylated dendron-based copolymer (PDC) conjugates with different PEG sizes, namely 0.6 kDa, 1 kDa, and 2 kDa and FA content were synthesized [57]. One type of each PDC and FA conjugated PDCs (PDC-FA) were then mixed at various weight ratios (0%, 5%, 10%,

25%) to obtain a family of micelles. Folate receptor overexpressing KB cells (KBFR) were treated with different rhodamine labeled micelles containing same PDC-FA weight ratio but different PEG size. The cell interactions were minimal when PEG size of PDC and PDC-FA was same, however when 0.6 kDa PEG conjugated PDC were combined with 2 kDa PEG conjugated PDC-FA the resulting DMs showed 25-fold enhanced cellular associated fluorescent values compared to non-targeted counterparts.



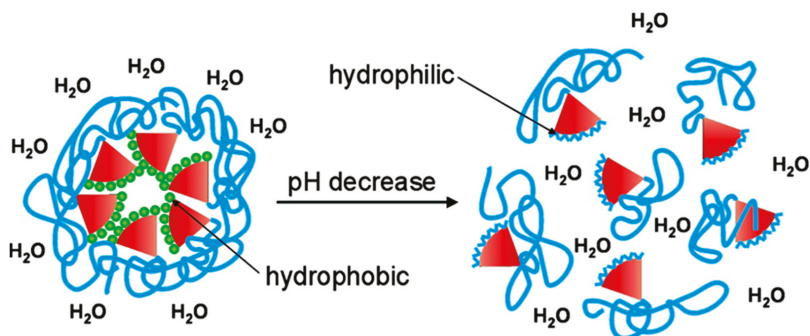
Scheme 2. Nanoparticle formation from dendron-polymer diblocks and the effect of targeting group configuration in internalization. Adapted with permission from [57]. Copyright (2016) American Chemical Society.

Another study that explored the effect of FA clusters on cell uptake utilizing a construct with polybenzyl-L-aspartate (PBLA) as hydrophobic block combined to a G4 polyester dendron with 0.6 kDa PEG chains on the periphery was reported by Hammond and coworkers [62]. They also generated a family of labeled mixed micelles with similar amount of FA ligands by combining dendritic conjugates functionalized with 0% to 100% folate groups (0%FA to 100%FA) with FA free dendritic conjugates at different weight ratios. When KBFR cells were treated with these micelles, the cell uptake increased initially by increasing cluster ratio to 20%. However, when the cluster density was further increased and weight ratio of FA containing dendritic conjugates were decreased in the final mixed micelle, cell association of these NPs decreased gradually. Three of these mixed micelles were injected to mice xenografts with two separate tumors at each flank namely the FA positive KBFR and FA negative A375 tumors. All targeted micelles showed improved accumulation in KBFR tumors relative to non-targeted controls, whereas no significant difference was reported with A375 tumors. Also, the normalized tumor fluorescence value was observed highest for mixed micelles with lowest cluster density.

2.2. Nanoparticles Obtained with Hydrophobic Dendron and Hydrophilic Polymer Based Conjugates

A different strategy that is widely followed for dendron-polymer conjugates utilizes installation of the hydrophobic dendrons at the core of the micellar structures, so that the linear hydrophilic polymer forms a moderately dense corona at the NP surface [63–65]. Linear-dendritic block copolymers utilizing PEG as hydrophilic block and either substituted polylysine or polyester dendrons as hydrophobic component were synthesized by Fréchet and coworkers, where the hydrophobic groups were attached to dendron peripheries via acid-labile cyclic acetal linkages [66]. These dendritic conjugates self-assembled to micelles in aqueous environment and were sensitive to pH. Micelle dissociation occurred through hydrolysis of acetals under acidic conditions, which is encountered in tumor environment or endosomal compartments (Scheme 3). Exhibiting fairly low CMC values in comparison

to micelles formed from linear block copolymer, these micelles were stable at neutral pH. The dendritic biodegradable core was efficient for encapsulating various hydrophobic drugs; hence these polyester dendron based micellar systems embodied several desirable qualities of DDS platforms.



Scheme 3. Micellar disassembly triggered by pH change. Reprinted with permission from [66]. Copyright (2004) American Chemical Society.

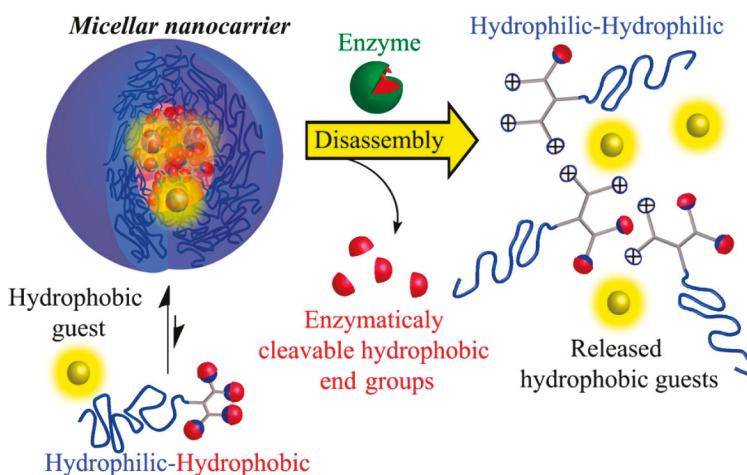
A study by Ambade and coworkers employed linear-dendritic conjugates prepared from 2 kDa PEG conjugated G2 bis-MPA dendrons decorated with alkyl chains for improved core hydrophobicity [67]. Interestingly, two stimuli responsive elements were introduced to the system, a photo-cleavable *o*-nitrobenzyl unit and an acid-labile acetal group between dendron and PEG block so that shell shedding via internal or external stimuli can be achieved to control and tune the drug delivery at the location of interest. The UV-responsive behavior of construct were demonstrated through light scattering experiments, where after 30 min UV irradiation a shift in hydrodynamic size from 90 to 30 nm was observed. Incubation of these NPs in acidic buffer for 7 days resulted in minor increase in degradation at pH 5.0 showing slower cleavage potential of acetal linkages relative to *o*-nitrobenzyl groups. The cellular uptake of DOX was also studied and a 30 min UV irradiation led to an increase of DOX incorporation by 40%. Another light responsive system was reported by Dong and coworkers who reported fabrication of micelles from linear-dendritic diblock constructs composed of generation 3 PAMAM dendron decorated with hydrophobic dye diazonaphthoquinone (DNQ) and linear PEG [68]. Exposure of micelles to UV or near infra-red (NIR) irradiation disrupted the micelles to release the encapsulated drug, doxorubicin, through transformation of the hydrophobic DNQ fragment to a hydrophilic 3-indenecarboxylic acid unit via the Wolff rearrangement. The NIR-triggered cytotoxicity of the drug loaded micelles was also demonstrated through in vitro studies with HeLa cells.

Malkoch and coworkers developed a micellar DDS using similar amphiphilic linear-dendritic polymeric conjugates utilizing rhodamine bound 10 kDa PEG tail conjugated to a G4 polyester dendron decorated with 16 cholesterol groups. Cholesterol, a naturally occurring highly hydrophobic bulky lipid was chosen to improve the drug loading capacity as well as micelle core stability [69]. The linear-dendritic conjugates formed micellar aggregates (NC20) with hydrodynamic size of 172 nm and DOX loading content of 18.8 ± 1.3 by weight. Decrease of mitochondrial function indicating the loss of cell viability was explored in drug resistant resi-MCF-7 cell line. DOX-NC20 micelles showed significant reduction in mitochondrial function in comparison to DOX only controls. An additional decrease was also achieved by co-delivery of triptolide (TPL) drug with DOX in TPL-DOX-NC20 micelles.

Dendrons other than those based on bis-MPA have also been employed as a biodegradable block. In a recent study Wei and coworkers used a linear-dendritic conjugate that was synthesized by combining methoxy-terminated PEG (mPEG) and glycolic acid oligomer-based, 4-benzyloxy-4-oxobutanate terminated G3 polyester dendrons [70]. DOX encapsulated micelles were

prepared with drug content of 21.2% and size around 150 nm. These micelles displayed pH dependent DOX release profiles due to their acid sensitive polyester backbones. DOX release increased to 39% when incubated at pH 5.0 buffer, as compared to 20% release upon incubation at pH 7.4 for 96 h.

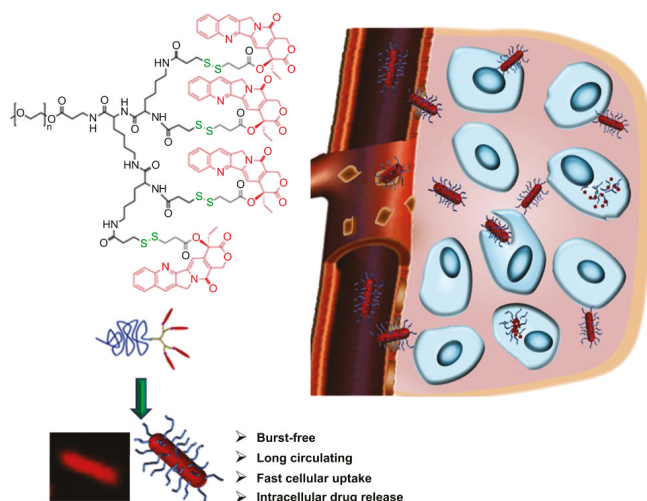
In a very elegant approach, an enzyme cleavable linear dendritic polymer conjugate system was reported by Amir and coworkers [71]. Different size PEG blocks (2, 5 or 10 kDa) were conjugated to a generation 2 dendron which was decorated with four phenyl acetamide molecules at the periphery acting as ligands to penicillin G amidase (PGA) enzyme (Scheme 4). The hydrodynamic size of assembled micellar NPs were determined before and after PGA incubation where dissociation of 2 and 5 kDa PEG micelles was completed after 8 h, whereas it took only 4 h for 10 kDa PEG micelles. Moreover the dissociation rates by fluorescence assays indicated faster enzyme triggered disassembly for micelles with longer PEG chain at the corona explained by a hypothesized equilibrium between “monomeric” and micellar polymeric states. In a subsequent study, the authors reported a micellar system with lower CMC and enhanced stability towards enzymatic degradation by introducing a thiol group on the dendritic fraction. The reversible dimerization of the thiol group to form disulfides imparts the added stability to these self-assembled nanostructures [72].



Scheme 4. Micellar disassembly and drug release via PGA enzyme cleavage. Reprinted with permission from [71]. Copyright (2014) American Chemical Society.

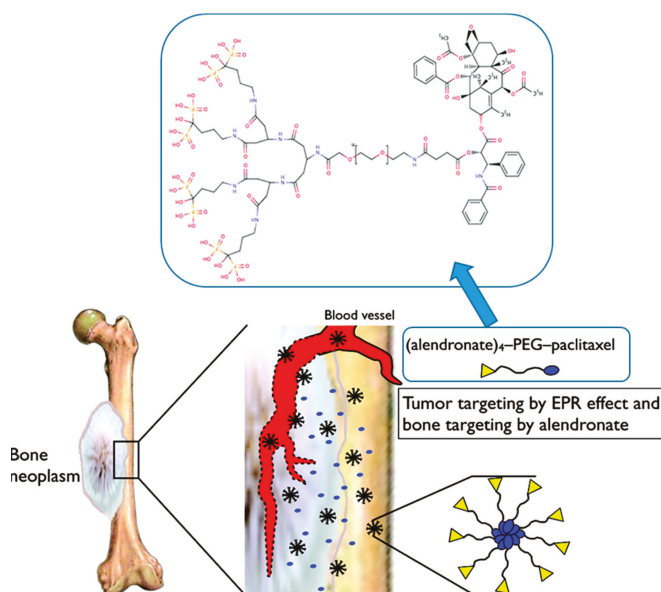
Lam, Luo and coworkers employed PEG (5 kDa) conjugated to a third generation of dendritic polylysine block which was further modified with cholic acid, to generate an amphiphilic PEG5k-CA8 telodendrimer [73]. This linear-dendritic block copolymer achieved high paclitaxel (PTX) encapsulation capacity up to 35% by weight and displayed stability over six months through addition of cholic acid that is a natural surfactant. Biodistribution studies in female athymic nude mice with SKOV3-luc cells subcutaneous xenografts indicated an almost 2.5 fold increase at 12 h in accumulation of DiD (1,1'-dioctadecyl-3,3,3',3'-tetramethylindodicarbocyanine 4-chlorobenzene-sulfonate) dye loaded DiD-PTX-NPs in tumor environment in comparison to free dye treatment and this difference was maintained at 72 h. DiD fluorescence levels at multiple tissues were evaluated *ex vivo* highlighting again improved tumor accumulation but also with notable lung and liver accumulation as well. However, PTX-PEG5k-CA8 NPs displayed improved therapeutic activity in both subcutaneous and orthotopic ovarian cancer models compared to Taxol[®] as well Abraxane[®] with evident decrease in tumor volume or increase in median survival days.

In an interesting study, Shen and coworkers demonstrated nanorod formation of linear dendritic conjugates composed of a 2 kDa mPEG segment attached to generation 2–3 polylysine dendrons bearing camptothecin (CPT) drugs on their periphery attached through disulfide linkers (Scheme 5) [74]. Depending on dendron, CPT incorporation as high as 38.9% was possible. CMC values also showed generation dependence and they were as low as 0.025 mg/mL for micelles prepared from G3 dendron containing conjugates (PEG₄₅-OctaCPT). DOX was also loaded to micelle to evaluate internalization by MCF7/ADR cell and a dendron generation dependent fluorescence signal increase was noted for PEG₄₅-x-CPT/DOX micelles. Biodistribution and pharmacokinetic (PK) properties of NPs were also tested. PEG₄₅-TetraCPT nanorods with G2 dendrons showed highest plasma clearance half-life of 5.82 h and all micelles showed spleen accumulation after 24 h. The ex vivo imaging of dissected tumors indicated poor tumor accumulation for micron-sized PEG₄₅-OctaCPT rods, whereas highest accumulation was reported for PEG₄₅-TetraCPT with medium lengths (<500 nm).



Scheme 5. Illustration of internalization of DOX loaded sized PEG₄₅-OctaCPT nanorods. Reprinted with permission from [74]. Copyright (2013) Elsevier.

Pasut and coworkers reported β -glutamic acid dendrons to introduce multiple bone targeting groups. A linear dendritic construct was prepared by conjugating a 5 kDa PEG polymer with an amino-bisphosphonate alendronate (ALN) modified generation 2 β -glutamic acid dendron, where PTX was attached to the other end of PEG through an ester group [75]. The ALN groups were utilized both to target the micellar assemblies of PTX-PEG-ALN conjugate to bone through high affinity of ALN towards bone-mineral hydroxyapatite (HA), as well as to exert apoptotic and anti-angiogenic effect towards bone metastases (Scheme 6) [75]. On Matrigel environment both the non-targeted PTX-PEG and targeted PTX-PEG-ALN micelles were able to inhibit tube formation of HUVECs up to 50%. Similar reduction in microvessel density for both micellar formulations were reported from immunohistochemical analysis of 4T1 tumors in tibia. However, an enhanced apoptotic effect was reported of PTX-PEG-ALN micelles by the significant increase in counts of apoptotic circulating endothelial cells detected in blood indicating the selective targeting of these NPs against metastatic cells. Targeted micelles also displayed improved accumulation after 8 h of injections in MDA-MB-231 mammary tumors in mice tibia, and longest plasma elimination half-lives, resulting in 50% tumor growth inhibition compared to saline controls [76].



Scheme 6. Illustration of bone tumor targeted micellar constructs from PTX-PEG-ALN. Adapted with permission from [75]. Copyright (2011) American Chemical Society.

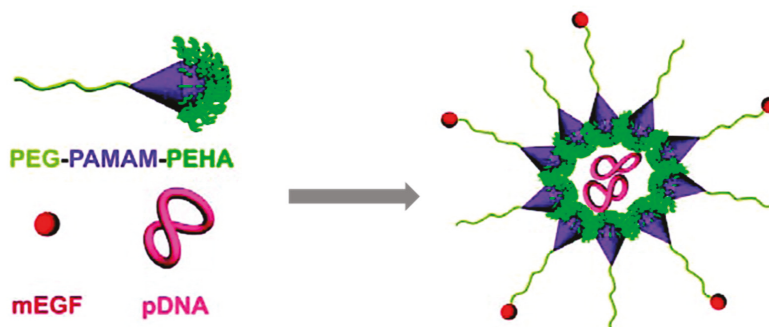
While a majority of studies reported to date have utilized PEG-based polymers as the hydrophilic segment, a few studies have also focused on utilization of other hydrophilic polymers. Recently, Bi and coworkers reported thermoresponsive micellar aggregates prepared from diblock constructs composed of poly(benzyl ether) dendrons and linear poly(*N*-vinylcaprolactam) [77]. Dendritic poly(benzyl ether) blocks containing a benzyl chloride group at their focal point were used as initiators for atom transfer radical polymerization of *N*-vinylcaprolactam. The self-assembled structures in aqueous media varied from irregular spherical micelles, vesicles to rod-like large compound vesicles depending on the generation of the dendritic component. These amphiphilic copolymers could undergo thermally-induced phase transition in aqueous media. These copolymers were found to be nontoxic toward mouse L929 fibroblast cells, thus suggesting their biocompatible nature. As an alternative to PEG as a hydrophilic component, Hoogenboom and coworkers reported the synthesis of dendron-polymer diblock conjugates obtained through conjugation of hydrophilic poly(2-ethyl-2-oxazoline) polymer to acetal protected hydrophobic polyester dendrons [78]. Degradation of micelles at acidic pH was confirmed through light scattering experiments.

2.3. Nanoparticles Obtained with Hydrophilic Dendron and Hydrophilic Polymer Based Conjugates

Gene therapy is another area for employment of dendrimers since they can provide well-defined, compact structures decorated with multiple terminal groups where surface functionalization with relevant moieties can be achieved easily [79]. As an alternative to viral vector systems which suffer from problems such as high toxicity and immunogenicity [80], cationic polymers especially dendrimers and dendritic conjugates can form stable complexes with nucleic acids such as plasmid DNA or siRNA via multivalent electrostatic interactions. The electrostatic complex formation eliminates the need for amphiphilic copolymers [81]. Since nucleic acids carry negative charge that challenges cellular internalization, and also can be cleared from blood stream rapidly by serum nucleases [80], it is crucial to combine them into dendriplexes to achieve safe and efficient transfection to targeted cells [82,83].

An example of polymer-dendron diblock conjugates for genetic material reported by Hammond, Langer and coworkers focused on generation of a PAMAM-PEG dendritic copolymer family for targeted delivery of plasmid DNA (pDNA). Different generations of PAMAM dendron were screened and it was observed that polyplex formation was favored by increasing generation due to higher charge density [84]. Furthermore, by addition of mannose or galactose targeting groups through the PEG segment increased transfection efficiency. Improved transfection of HepG2 hepatocytes via galactose targeted PAMAM polyplexes compared to commercially available PEI counterparts was observed.

These constructs are very versatile since it is possible to modify the dendron periphery as well as the linear polymeric part to add desirable properties to these DDS. Yu and coworkers reported a mouse endothelial growth factor (mEGF) targeted dendron-polymer conjugate for delivery of pDNA (Scheme 7) [85]. Generation 3.5 PAMAM dendrons were modified with different oligoamines to improve their transfection efficiency, where best results were provided by the pentaethylenhexamine (PEHA) substituent. The PAMAM-PEHA conjugates were further modified with EGF-PEG block to benefit from the anti-biofouling effect of PEG and active targeting of EGF receptor overexpressing tumor cells. The final EGF ligand conjugated polyplexes, bearing luciferase pDNA in their core were able to selectively improve gene delivery by 10-fold on EGFR overexpressing HuH-7 cells in comparison to their non-targeted counterparts.



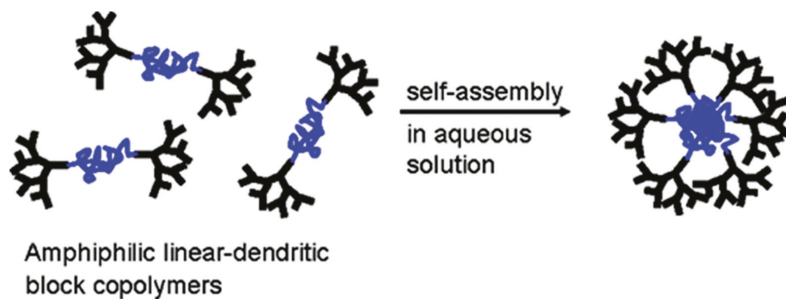
Scheme 7. Delivery of pDNA using a non-amphiphilic dendron-polymer conjugate. Reprinted with permission from [85]. Copyright (2011) American Chemical Society.

It must be noted that while oligonucleotide based materials have been used as a cargo, dendrimeric constructs composed of oligonucleotides have been synthesized. For example, Tomalia and coworkers used complementary DNA strands at focal points of dendrons to assemble dendrimers through self-assembly [86]. Likewise, other dendrimer structures that are purely composed using oligonucleotides have been synthesized by various groups [87,88].

3. Nano-Sized Aggregates from Polymer-Dendron Triblock Conjugates

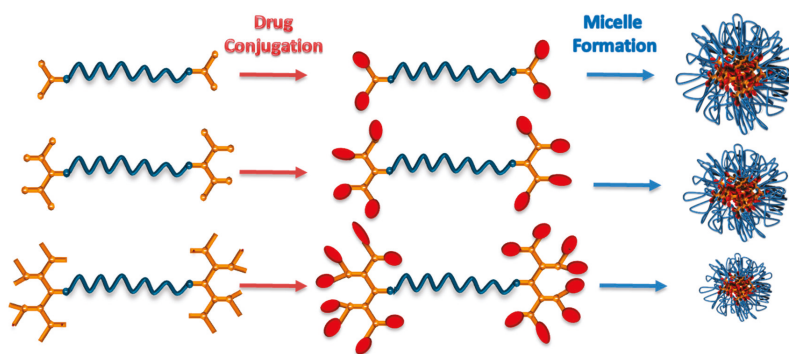
As mentioned earlier, formation of micellar structures from diblock and triblock copolymers was reported by Fréchet and coworkers in 1992 [52]. A more detailed study of amphiphilic dendron-polymer-dendron triblock conjugates assembly was later reported by Gitsov and coworkers [89]. The construct was composed of linear PEG chain flanked by hydrophobic dendritic poly(benzyl ester)s and was synthesized using a divergent growth strategy. It was observed that while the conjugates with second generation dendrons with hydrophobic groups at their exterior self-assembled in water at low concentrations (10^{-6} mol/L), their counterparts where the peripheral groups were removed to expose hydroxyl groups were soluble under similar conditions. The authors postulated the potential of these self-assembled aggregates for possible applications in drug delivery.

This study was followed by a report by Nguyen and Hammond who reported the assembly of a ABA-type dendron-polymer-dendron conjugate composed of PAMAM dendrons as hydrophilic components and poly(propylene oxide) as the hydrophobic middle block [90]. Notably, such constructs provide structures where the dendritic wedges are on the outside of the nanostructure as opposed to being buried inside as in abovementioned example (Scheme 8). PAMAM dendrons were divergently synthesized from an amine group containing telechelic poly(propylene oxide) polymer. Assembly in water resulted in formation of nanoparticles in the size range of 9–18 nm. To demonstrate its utility as a viable drug delivery system, a hydrophobic drug, triclosan, was encapsulated with loading efficiencies of 79–86% *w/w*.



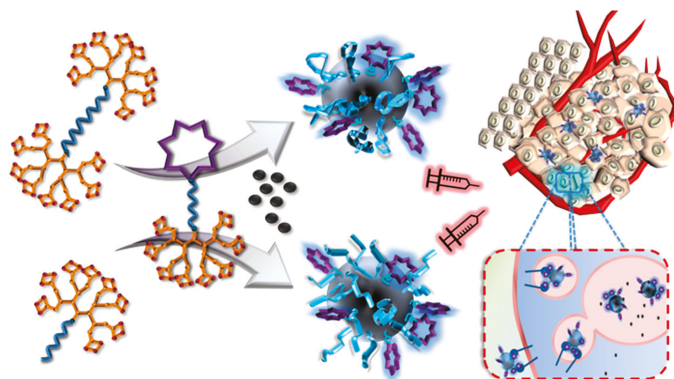
Scheme 8. Self-assembly of ABA-type dendron-polymer-dendron conjugate with hydrophilic dendrons and hydrophobic middle segment. Reprinted with permission from [90]. Copyright (2006) American Chemical Society.

Sanyal and coworkers used an ABA type dendron-polymer-dendron conjugate with 10 kDa middle PEG segment connecting two identical polyester dendrons with generation 1–3. The dendron surfaces were further modified with combretastatin-A4 anti-angiogenic drug (Scheme 9) [91]. Size and CMC values of prepared Comb-Gx-PEG and Gx-PEG micelles displayed dendron generation and drug content related trends. Even though combretastatin-A4 release occurred faster at acidic pH as expected, it took approximately 4 days to achieve high cumulative release results even at acidic environment, which indicates their potential as a slow drug releasing system. The Comb-G3-PEG micelles were further exhibited dose dependent anti-angiogenic effect in tube formation assay on HUVECs.



Scheme 9. Illustration of combretastatin-A4 conjugation to ABA type dendron-polymer-dendron conjugates and micelle formation.

Nanostructured delivery agents can also be fabricated using a combination of diblock and triblock dendron-polymer conjugates. In a recent study, Sanyal and coworkers reported a modular micellar system for delivery of docetaxel. An AB type diblock dendron polymer conjugate was used to introduce targeting RGD (arginine-glycine-aspartic acid) peptides onto NP surface (Scheme 10) [92]. The peptide targeting group containing diblock copolymer was composed of a linear PEG polymer appended with an acetal protected hydrophobic polyester dendron at one end and the cyclic RGD peptide targeting unit at the other end. Either an ABA type triblock conjugate composed of two acetal protected G4 polyester dendrons with a 6 kDa PEG middle segment or an AB type copolymer composed of a G4 polyester dendron conjugated to a 2 kDa mPEG polymer was mixed with the diblock polymer-dendron conjugate modified with the RGD peptide. Both AB and ABA PEG-based micelles possessed similar CMC values and drug loading contents with hydrodynamic sizes in the range of 170–230 nm. While both AB and ABA micelles were stable even after more than 1000-fold dilutions beyond their CMCs, only the AB micelles could retain their size in the presence of 10% FBS, whereas aggregate formation was observed for the ABA system. The cell internalization studies indicated that AB micelles showed higher association with MDA-MB-231 cells relative to the ABA ones, while presence of RGD increased cellular internalization in both cases.



Scheme 10. Illustration of drug loaded, RGD targeted micellar NPs via “Mix-and-Match” approach employing AB and ABA type dendron–polymer constructs. Reprinted with permission from [92]. Copyright (2017) American Chemical Society.

Although a majority of studies to date have focused on the delivery of anti-cancer drugs, these dendritic conjugates can also be utilized as delivery platforms for drugs against different diseases such as malaria. To overcome the high drug resistance of malaria parasites, provide improved cellular delivery of antimalarial drugs and achieve sustained drug release micellar assemblies were prepared using different Janus-like dendrons or ABA type dendritic-linear-dendritic conjugates [93]. Enhanced cellular association and decreased IC_{50} values for primaquine and chloroquine were reported for assemblies formed using dendritic-linear-dendritic conjugates. Additionally, improved plasma circulation times and survival times were noted relative to free drugs in malaria infected mice.

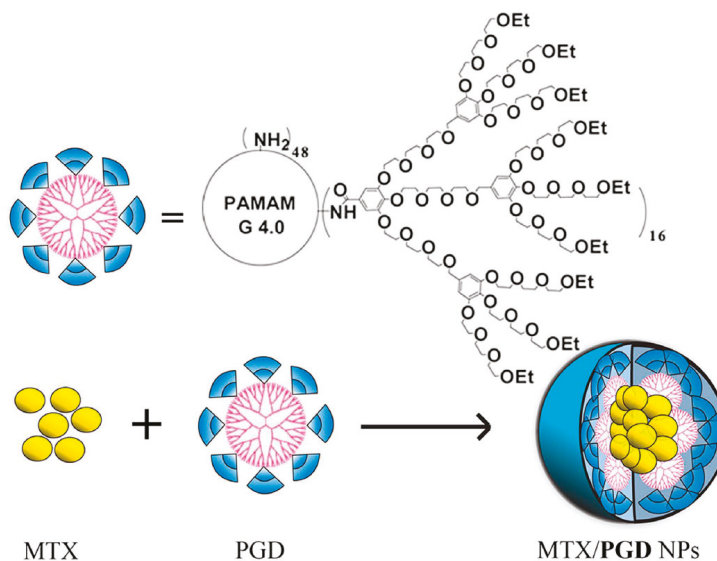
4. Nano-Sized Aggregates from Star Type Architectures

The star shaped structure of a dendrimer allows them to act as drug carriers through two different modes. These structures can either encapsulate drug molecules in their internal voids through non-covalent interactions, or the drug can be covalently conjugated onto their periphery. Dendrimers like PAMAM and PEI have been utilized to encapsulate drug molecules through stabilizing electrostatic or hydrogen bonding interactions [94,95]. Another example includes,

biodegradable dendrimers based on glycerol and succinic anhydride reported by Grinstaff and coworkers which could encapsulate various camptothecin derivatives, with exhibited superior in vitro performance than free drugs [96]. Attachment of drugs through non-covalent and covalent modes have both pros and cons and such comparisons have been recently reported in terms of drug release profiles, systemic toxicity and anti-tumor efficacy [97,98]. The limitation in drug loading, as well as facile release from dendrimers due to their small size promoted modification of dendrimer peripheries with polymer chains. Several drug delivery vehicles based on PAMAM dendrimers modified with PEG chains and other hydrophilic polymers have been reported to date [99–101]. Additionally, attachment of PEG also reduces the toxicity of PAMAM dendrimers containing amine groups at the periphery [102,103]. Furthermore, improving their in vivo performance such as prolonged circulation time and increased accumulation at tumor site is also possible, e.g., upon modification with PEG chains bearing targeting groups such as folic acid [104]. It must be noted though that such dendrimer-polymer constructs generally act as unimolecular micellar containers. Since the focus of this review is self-assembled nanostructures based on conjugates of dendron/dendrimer with polymers, such unimolecular constructs are not included here. Micellar constructs from star shaped amphiphilic constructs with dendrimers as core unit are rare. Fang and coworkers reported star shaped polymers composed of a G2 PAMAM core, from which a hydrophobic poly(ϵ -caprolactone) was grafted from using ring-opening polymerization, followed by conjugation to linear PEG chains as outer blocks [105]. These 16-arm PAMAM cored star polymers produced a mixture of unimolecular micelles and micellar aggregates as determined using dynamic light scattering experiments. Anti-cancer drug indomethacin, doxorubicin and etoposide loaded micelles were prepared using either dialysis or oil/water emulsion method. The authors reported a subsequent study where they used a 32-arm PAMAM dendrimer as a core to synthesize PAMAM-PCL-PEG and PAMAM-PLA-PEG star polymers containing the PCL and poly(L-lactide) (PLA) based middle blocks, respectively. These polymers also yielded a mixture of unimolecular micelles and micellar aggregates in aqueous environment, which could be loaded with an anti-cancer drug, etoposide, with higher loading in the PCL-containing construct. Interestingly, the 32-arm PAMAM-PCL-PEG constructs exhibited lower drug loading for etoposide than the 16-arm counterpart, which authors suggest could be a result of higher PCL chain density in the star polymers obtained with the higher generation dendrimer [106].

Another interesting architecture that has been recently reported is not strictly a star like linear polymer-dendrimer construct but a dendron appended dendrimer. This example cleverly illustrates that it is possible to utilize two types of dendritic fragments in the same delivery platform to benefit from characteristics of both types. Wang and coworkers developed a methotrexate (MTX) encapsulating PAMAM and oligoethylene glycols dendron (PGD) based co-dendrimer through conjugation of oligoethylene glycols (OEG) dendrons onto a G4 PAMAM dendrimer surface (Scheme 11) [107]. The PAMAM core in the dendronized dendrimer PGD provides as a reservoir for MTX. Moreover, the OEG dendrons act as solubilization agents, as well as they can diminish the cytotoxic potential of PAMAM dendrimers. The MTX release displayed dependence on the thermosensitive characteristics i.e., temperature dependence of solubility of the OEG dendrons. Also depending of concentrations, the PGD particles displayed a hydrodynamic size of 8 nm for unimeric form and around 110 nm for aggregates. They also reported that the number of conjugated OEG dendrons or decoration degree affect the drug loading capacity and the interaction of PGD NPs with cells. Among the various co-dendrimers, best results were obtained for those with decoration number 16 and 32 [108]. The authors further optimized the drug loading content up to 85.2% via employing an anti-solvent precipitation method augmented by ultra-sonication [109]. The MTX/PGD NPs displayed improved cytotoxic profiles both in MCF-7 and 4T1 cells in comparison to MTX only. Similarly, internalization of cy5.5 loaded PGD NPs showed significant cell uptake. In vivo tumor inhibition studies using BALB/c mice 4T1 breast tumor xenografts showed significant tumor growth limitation even at 2 mg/kg MTX/PGD NPs. On the other hand, the control samples displayed 23-fold volume increase whereas tumor volume increase with 8 mg/kg MTX/PGD NPs treated mice was 9.6-fold in 10 days.

For evaluating biodistribution of NPs *ex vivo* fluorescent imaging studies indicated significant increase in tumor accumulation of NPs however similar increase in NP accumulation was also observed with organs of RES as liver, spleen, and kidneys.



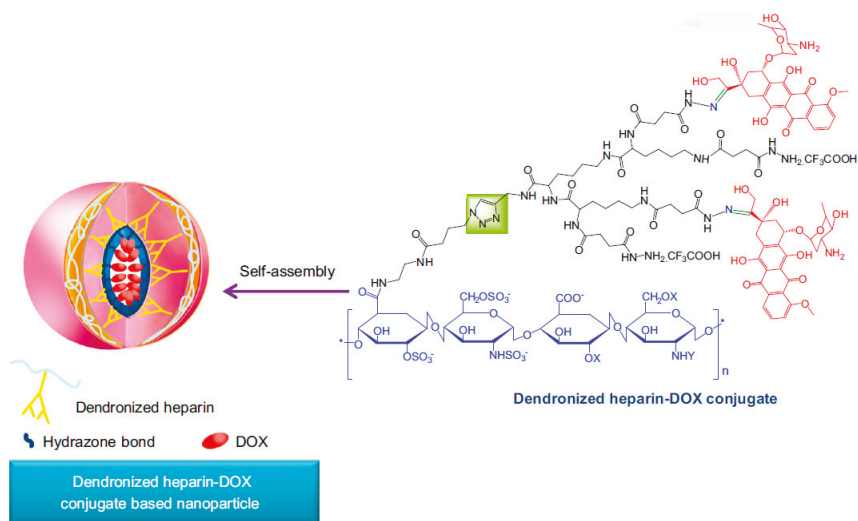
Scheme 11. Structure of unimeric PGD and MTX encapsulating MTX/PGD nanoparticles. Reprinted with permission from [109]. Copyright (2016) Springer Nature.

5. Nano-Sized Aggregates from Miscellaneous Dendron-Polymer Architectures

Dendronized polymers are another emerging class of macromolecular architecture that have been frequently utilized in recent years to obtain nanomaterials for drug delivery. These constructs comprise of dendrons conjugated as side chain residues along the backbone of a polymer. In a simple approach, amphiphilic constructs are obtained when hydrophilic synthetic or natural polymers are appended with dendrons that are either inherently hydrophobic or become so upon attachment of hydrophobic drug molecules.

In a recent example, Gu and coworkers generated dendronized polymers composed of heparin backbone decorated with G2 lysine-based dendrons bearing DOX molecules (Scheme 12) [110]. A Huisgen type 'click' reaction between an azide-containing heparin and lysine-based dendrons bearing an alkyne at their focal points catalyzed by a Cu(I) catalyst yielded the dendronized polymers. Interestingly, even prior to the attachment of drug, the parent dendron-heparin conjugates self-assembled into NPs with hydrodynamic size of 250 nm, presumably due to hydrogen bonding interactions between the charged amine groups on the dendrons with the sulfo and carboxyl groups on the biopolymer. Upon conjugation of the drug, the size of NPs decreased to 90 nm, which was attributed to introduction of additional interactions such as pi-pi stacking etc. from the drug. As expected, drug release in a pH responsive manner was observed, since acid-sensitive hydrazone linkages were used for conjugating DOX to dendrons periphery. High levels of anti-angiogenic and anti-tumor activity for the drug loaded NPs compared to free drug was demonstrated through *in vivo* experiments.

The same group reported another dendronized copolymer composed of a 20 kDa dextran decorated with fluorinated G2 lysine dendrons as side chains conjugated to polymer backbone via acid-labile hydrazone linkers [111]. Dextran was chosen for providing improved biodistribution for bioconjugates, and trifluoromethyl groups were introduced on the dendrons in order to increase hydrophobicity of the construct to enable efficient encapsulation of hydrophobic drug molecules. The drug loading content of DOX was 20.4 ± 3.1 for this system and the drug was released in a pH sensitive manner.

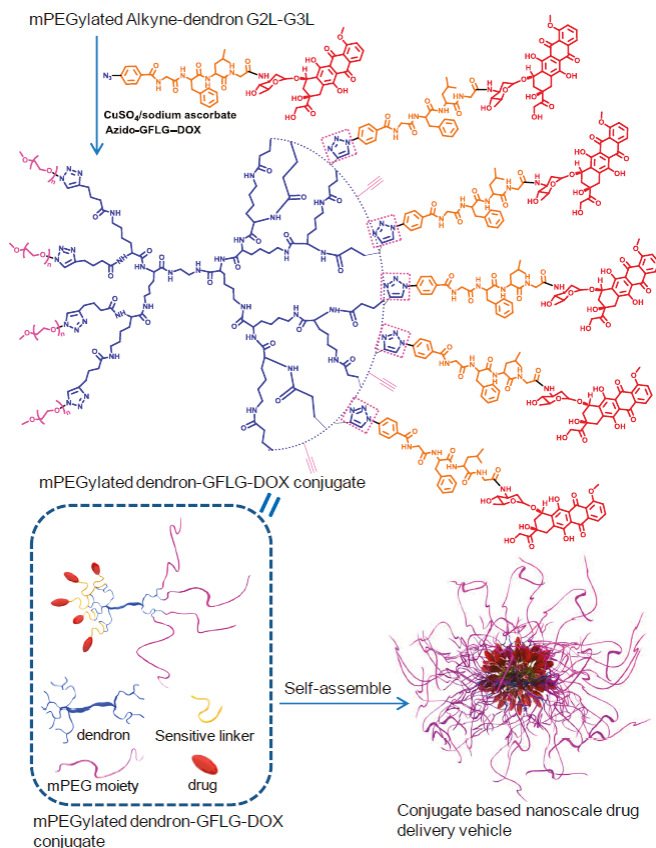


Scheme 12. Illustration of self-assembly of DOX conjugated dendronized heparin NPs. Reprinted with permission from [110]. Copyright (2013) Elsevier.

In an alternative assembly strategy, Gu et al. used a G3 lysine dendron functionalized with DOX via hydrazone linkages appended with two mPEG tails at the dendron focal group [112]. The dendron-PEG conjugates with 14% drug content assemble into NPs with hydrodynamic size of ~220 nm and possess a neutral surface charge. In contrast to the negligible drug release at physiological conditions, incubation at pH 5.0 led to an initial burst release and more sustained type release profile reaching up to 80% in 54 h. Antitumor activity of DOX NPs was studied through treatment of mice with 4T1 breast tumors every four days for 13 days. Significant inhibition of tumor growth, as well as almost no decrease in body weight of treated mice were reported for DOX NPs relative to saline control and free DOX treatments.

In a subsequent study, the authors further modified this NP system by using a G2 lysine dendron and thickening their PEG corona by using four 2 kDa PEG tails [113]. Additionally, instead of acid labile hydrazone linkers for dendron functionalization, an enzyme responsive GFLG peptide based linker was employed (Scheme 13). This allows triggering of drug release after cellular internalization since the GFLG peptide sequence is cleaved by the enzyme cathepsin B, a lysosomal cysteine protease that is upregulated in various tumors [114]. DOX-conjugated GFLG responsive NPs with 9.6% drug loading content were shown to release their cargo strictly in the presence of sequence specific proteases. The NPs displayed significant tumor growth inhibition relative to free DOX and saline controls. Moreover, the anti-angiogenic and especially anti-apoptotic effect of these drug loaded NPs was confirmed via immune-histochemical staining assays.

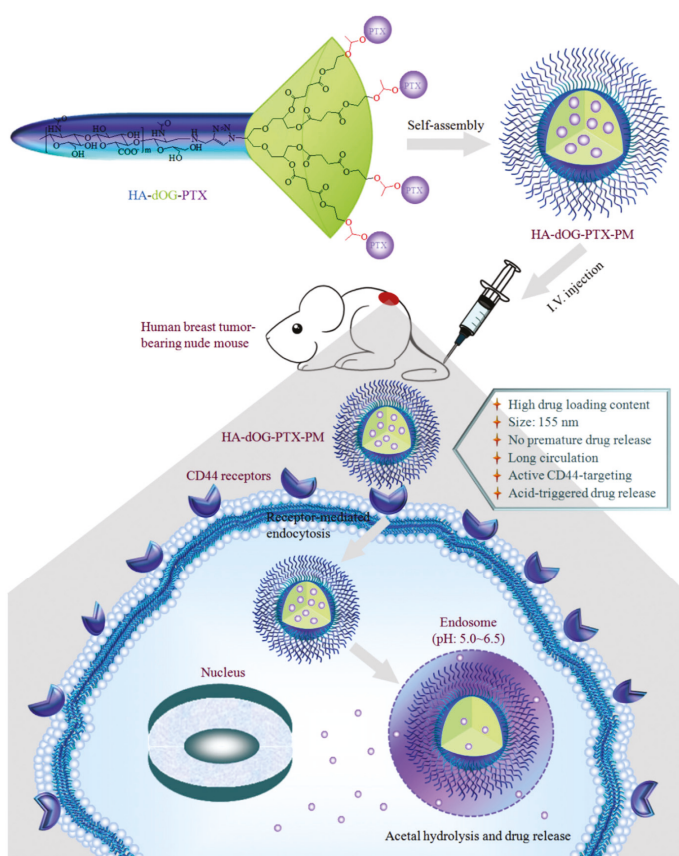
A conceptually different type of dendronized polymers was reported by Guan and coworkers [115]. They employed polymeric constructs containing peptide-based dendrons as siRNA delivery agents. In an interesting approach, they generated a linear peptide backbone consisting of dicysteine and L-lysine units thereby introducing an oxidation responsive disulfide linkage along the polymeric backbone. Thereafter, the backbone was further modified with G1 or G2 poly(L-lysine) dendrons with peripheral modifications with different hydrophobic or hydrophilic amino acids, thereby creating a combinatorial library of dendronized peptide polymers for siRNA delivery to NIH 3T3 cells.



Scheme 13. Illustration of self-assembly of PEGylated GFLG-DOX conjugated lysine dendrons. Reprinted with permission from [113]. Copyright (2014) Elsevier.

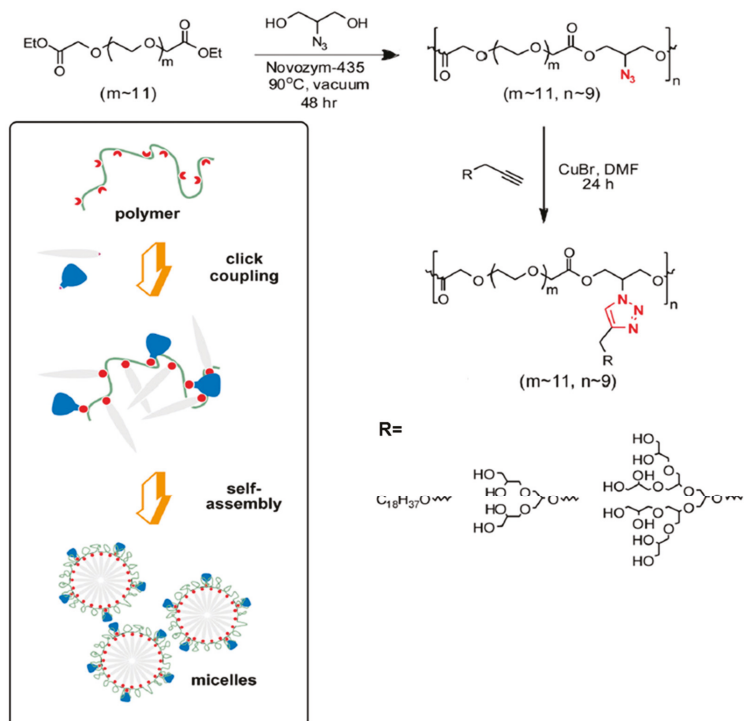
The siRNA complexation with various dendronized polymers resulted in spherical NPs with diameters below 100 nm, which disintegrated upon treatment with glutathione (GSH) and released the siRNA. The *in vitro* transfection efficiency of NIH 3T3 cells with an anti-GFP siRNA demonstrated that polyplexes formed with the G2 construct containing 75 mol% histidine and 25 mol% tryptophan residue at dendron periphery at 80 primary amine/siRNA phosphate (N/P) ratio were able to provide improved GFP down regulation especially at lower serum conditions in comparison the lipofectamine. The effect of different amino acids at dendron periphery on the complex formation and transfection efficiency was evaluated.

Dendritic polyglycerol (dOG) unit appended polymers are appealing building blocks with polyether internal cavities, biocompatibility similar to PEG and multiple hydroxyl groups enabling surface functionalization. Haag and coworkers conjugated polyglycerol dendrons modified with paclitaxel (PTX) through acetal linkages to hyaluronic acid (HA) to prepare HA-dOG-PTX-PM micelles. The HA shell serves as a protective natural polysaccharide layer, as well as enables active targeting of CD44 positive cancer cells (Scheme 14) [116]. The micellar assemblies dissociated under acidic environment, as suggested from DLS analysis, and triggered the release of PTX. Internalization of DOX loaded HA-dOG-PTX-PM by CD44 positive MCF7 cells were higher than free DOX, and a notable decrease in DOX internalization was observed by addition of excess HA as a competitor. Similar improvements in PK and biodistribution of micellar PTX was also reported; for instance, plasma elimination half-lives of micellar PTX and Taxol was 4.32 and 0.23 h, respectively. The therapeutic effect of micellar constructs were studied on nude mice bearing MCF-7 tumor xenografts. Excellent tumor progression inhibition with no eminent body weight loss was noted, thus highlighting the therapeutic potential of this PTX delivery system against CD44 positive breast tumors.



Scheme 14. Micellar constructs based on polyglycerol-hyaluronic acid conjugate. Reprinted with permission from [116]. Copyright (2016) Elsevier.

The dendritic polyglycerol unit has also been used as side chain appendages in dendronized polymers. A hydrophobic polymer bearing glycerol dendrons as side chains self-assemble to generate micellar NPs (Scheme 15). Haag and coworkers used click chemistry to conjugate dendritic polyglycerols dendrons modified with octadecyl chains to an enzymatically synthesized condensation polymer from azido-glycerol and PEG600 diethyl ester [117]. Obtained NPs displayed low hydrodynamic sizes ranging between 14–20 nm, with polydispersity index (PDI) values between 0.427–0.603. Their potential as drug delivery agents were evaluated by pyrene encapsulation experiments. In a following study, similar constructs with PEG1000 diethyl ester and an additional hyperbranched polyglycerol dendron was used and a set of self-assembling dendronized polymers were prepared [118]. QGP-1 cells were treated with Nile red encapsulated dendronized polymers displayed enhanced dye incorporation than free Nile red or Nile red loaded linear polymer-dendron diblock conjugate counterparts. Furthermore these micellar NPs demonstrated minimal cytotoxicity at concentrations as high as 500 $\mu\text{g}/\text{mL}$ after 72 h. A system using fluorinated version of the hydrocarbon chain was later used as a curcumin delivery system [119].



Scheme 15. Synthesis of dendronized polymers and their self-assembly into NPs. Reprinted with permission from [117]. Copyright (2013) WILEY-VCH Verlag GmbH & Co. KGaA, Weinheim.

A recent study from Imae and Chung and coworkers demonstrated that apart from using homopolymers components, diblock polymers where one of the block is dendronized can be used as building blocks for NPs effective for drug delivery. A linear polyelectrolyte block conjugated to a hydrophobic block with pendant dendrons assembled into micelles [120]. DOX loading capacities as high as 95% was reported. Interestingly, these micelles showed improved cytotoxicity with lower IC₅₀ of 0.12 μM against 4T1 cells, compared to free DOX. Usually, in general, the free DOX is observed to

possess more cytotoxicity in in vitro studies. Drug loaded micelles demonstrated 1.5 fold improved tumor growth inhibition relative to free DOX in BALB/c mice bearing 4T1 mammary tumors [121].

The brief survey of the abovementioned diverse polymeric structures that can be obtained through combination and dendrons and polymers, and are different than the classic AB and ABA type block copolymer systems, illustrate that variations in macromolecular architecture can yield novel NP based delivery vehicles.

6. Conclusions

A diverse collection of nanosized aggregates can be obtained from macromolecular architectures derived from dendron-polymer conjugate based on simple combinations of dendritic and polymeric building blocks. Since their inception more than two decades ago, advances in synthetic polymer and dendrimer chemistry have witnessed the evolution of these dendron-polymer conjugate based nanosized aggregates as simple containers for therapeutic agents to smart drug delivery systems. The abovementioned examples provide a glimpse of how clever design of the discrete dendron-polymer conjugate yields through self-assembly a 'more than the sum' aggregate that brings novel attributes which qualifies these nanoparticles as viable drug delivery platforms. The confluence of organic chemistry and polymer science is enabling the design of dynamic constructs that are responsive to intrinsic and external cues to yield stimuli-responsive systems. Incorporation of bioactive motifs onto these nano-objects which would allow more specificity for triggered release will further advance these systems. To date, while the efficiency of most systems have been evaluated in vitro, a few examples in recent years have demonstrated through in vivo studies the promise that these self-assembled nanosized aggregates hold for shaping the future of nanotherapeutics. One of the challenges in the area of nanoparticle technology relates to large scale synthesis of the particles with homogenous properties such as size and polydispersity. For developing practical applications, it is important that delivery vehicles can be prepared in large amounts within certain specifications for preclinical and clinical test phases. To address such issues, may be new technologies such as continuous manufacturing techniques such as use of microfluidic flow systems can provide access to large amounts of homogenous nanoparticles. For a chemist, the flexibility in the chemical design of both dendritic and polymeric components, as well as the final dendron-polymer conjugates offers plenty of room for creativity to tailor effective drug delivery platforms.

Funding : This research received no external funding.

Acknowledgments: APC was sponsored by MDPI.

Conflicts of Interest: The authors declare no conflict of interest.

References

1. Parveen, S.; Misra, R.; Sahoo, S.K. Nanoparticles: A boon to drug delivery, therapeutics, diagnostics and imaging. *Nanomed. Nanotechnol. Biol. Med.* **2012**, *8*, 147–166. [[CrossRef](#)] [[PubMed](#)]
2. Sirova, M.; Mrkvan, T.; Etrych, T.; Chytil, P.; Rossmann, P.; Ibrahimova, M.; Kovar, L.; Ulbrich, K.; Rihova, B. Preclinical evaluation of linear HPMA-doxorubicin conjugates with pH-sensitive drug release: Efficacy, safety, and immunomodulating activity in murine model. *Pharm. Res.* **2010**, *27*, 200–208. [[CrossRef](#)] [[PubMed](#)]
3. Kannan, R.M.; Nance, E.; Kannan, S.; Tomalia, D.A. Emerging concepts in dendrimer-based nanomedicine: From design principles to clinical applications. *J. Intern. Med.* **2014**, *276*, 579–617. [[CrossRef](#)] [[PubMed](#)]
4. Murray, J.C.; Weiner, L.M.; Shuptrine, C.W. Antibody-Based Immunotherapy of Cancer. *Cell* **2012**, *148*, 1081–1084.
5. Peer, D.; Karp, J.M.; Hong, S.; Farokhzad, O.C.; Margalit, R.; Langer, R. Nanocarriers as an emerging platform for cancer therapy. *Nat. Nanotechnol.* **2007**, *2*, 751–760. [[CrossRef](#)] [[PubMed](#)]
6. Ferrari, M. Cancer nanotechnology: Opportunities and challenges. *Nat. Rev. Cancer* **2005**, *5*, 161–171. [[CrossRef](#)] [[PubMed](#)]

7. Xiao, H.; Song, H.; Yang, Q.; Cai, H.; Qi, R.; Yan, L.; Liu, S.; Zheng, Y.; Huang, Y.; Liu, T.; et al. A prodrug strategy to deliver cisplatin(IV) and paclitaxel in nanomicelles to improve efficacy and tolerance. *Biomaterials* **2012**, *33*, 6507–6519. [[CrossRef](#)] [[PubMed](#)]
8. Duncan, R. Development of HPMA copolymer-anticancer conjugates: Clinical experience and lessons learnt. *Adv. Drug Deliv. Rev.* **2009**, *61*, 1131–1148. [[CrossRef](#)] [[PubMed](#)]
9. Kopecek, J.; Kopecková, P. HPMA copolymers: Origins, early developments, present, and future. *Adv. Drug Deliv. Rev.* **2010**, *62*, 122–149. [[CrossRef](#)] [[PubMed](#)]
10. Yang, D.; Van, S.; Shu, Y.; Liu, X.; Ge, Y.; Jiang, X.; Jin, Y.; Yu, L. Synthesis, characterization, and in vivo efficacy evaluation of PGG-docetaxel conjugate for potential cancer chemotherapy. *Int. J. Nanomed.* **2012**, *7*, 581–589. [[CrossRef](#)]
11. Sharma, A.; Kakkar, A. Designing Dendrimer and Mikroarm Polymer Based Multi-Tasking Nanocarriers for Efficient Medical Therapy. *Molecules* **2015**, *20*, 16987–17015. [[CrossRef](#)] [[PubMed](#)]
12. Biswas, S.; Torchilin, V.P. Nanopreparations for organelle-specific delivery in cancer. *Adv. Drug Deliv. Rev.* **2014**, *66*, 26–41. [[CrossRef](#)] [[PubMed](#)]
13. Kakkar, A.; Traverso, G.; Farokhzad, O.C.; Weissleder, R.; Langer, R. Evolution of macromolecular complexity in drug delivery systems. *Nat. Rev. Chem.* **2017**, *1*, 0063. [[CrossRef](#)]
14. Zhao, Z.; Harris, B.; Hu, Y.; Harmon, T.; Pentel, P.R.; Ehrich, M.; Zhang, C. Rational incorporation of molecular adjuvants into a hybrid nanoparticle-based nicotine vaccine for immunotherapy against nicotine addiction. *Biomaterials* **2018**, *155*, 165–175. [[CrossRef](#)] [[PubMed](#)]
15. Zhao, Z.; Hu, Y.; Hoerle, R.; Devine, M.; Raleigh, M.; Pentel, P.; Zhang, C. A nanoparticle-based nicotine vaccine and the influence of particle size on its immunogenicity and efficacy. *Nanomed. Nanotechnol. Biol. Med.* **2017**, *13*, 443–454. [[CrossRef](#)] [[PubMed](#)]
16. Zhao, Z.; Powers, K.; Hu, Y.; Raleigh, M.; Pentel, P.; Zhang, C. Engineering of a hybrid nanoparticle-based nicotine nanovaccine as a next-generation immunotherapeutic strategy against nicotine addiction: A focus on haptent density. *Biomaterials* **2017**, *123*, 107–117. [[CrossRef](#)] [[PubMed](#)]
17. Zhao, Z.; Hu, Y.; Harmon, T.; Pentel, P.; Ehrich, M.; Zhang, C. Rationalization of a nanoparticle-based nicotine nanovaccine as an effective next-generation nicotine vaccine: A focus on haptent localization. *Biomaterials* **2017**, *138*, 46–56. [[CrossRef](#)] [[PubMed](#)]
18. Eetezadi, S.; Ekdawi, S.N.; Allen, C. The challenges facing block copolymer micelles for cancer therapy: In vivo barriers and clinical translation. *Adv. Drug Deliv. Rev.* **2015**, *91*, 7–22. [[CrossRef](#)] [[PubMed](#)]
19. Nel, A.E.; Mädler, L.; Velegol, D.; Xia, T.; Hoek, E.M.V.; Somasundaran, P.; Klaessig, F.; Castranova, V.; Thompson, M. Understanding biophysicochemical interactions at the nano–bio interface. *Nat. Mater.* **2009**, *8*, 543–557. [[CrossRef](#)] [[PubMed](#)]
20. Monopoli, M.P.; Åberg, C.; Salvati, A.; Dawson, K.A. Biomolecular coronas provide the biological identity of nanosized materials. *Nat. Nanotechnol.* **2012**, *7*, 779–786. [[CrossRef](#)] [[PubMed](#)]
21. Li, S.-D.; Huang, L. Pharmacokinetics and Biodistribution of Nanoparticles. *Mol. Pharm.* **2008**, *5*, 496–504. [[CrossRef](#)] [[PubMed](#)]
22. Frank, M.M.; Fries, L.F. The role of complement in inflammation and phagocytosis. *Immunol. Today* **1991**, *12*, 322–326. [[CrossRef](#)]
23. Owens, D.E.; Peppas, N.A. Opsonization, biodistribution, and pharmacokinetics of polymeric nanoparticles. *Int. J. Pharm.* **2006**, *307*, 93–102. [[CrossRef](#)] [[PubMed](#)]
24. van Vlerken, L.E.; Vyas, T.K.; Amiji, M.M. Poly(ethylene glycol)-modified Nanocarriers for Tumor-targeted and Intracellular Delivery. *Pharm. Res.* **2007**, *24*, 1405–1414. [[CrossRef](#)] [[PubMed](#)]
25. Flory, P.J. Molecular Size Distribution in Three Dimensional Polymers. VI. Branched Polymers Containing A—R—B_{f-1} Type Units. *J. Am. Chem. Soc.* **1952**, *74*, 2718–2723. [[CrossRef](#)]
26. Buhleier, E.; Wehner, W.; Vögtle, F. “Cascade”- and “Nonskid-Chain-like” Syntheses of Molecular Cavity Topologies. *Synthesis* **1978**, *1978*, 155–158. [[CrossRef](#)]
27. Denkewalter, R.G.; Kolc, J.; Lukasavage, W.J. Macromolecular Highly Branched Homogeneous Compound Based on Lysine Units. U.S. Patent 4289872, 6 April 1979.
28. Tomalia, D.A.; Baker, H.; Dewald, J.; Hall, M.; Kallos, G.; Martin, S.; Roeck, J.; Ryder, J.; Smith, P. A New Class of Polymers: Starburst-Dendritic Macromolecules. *Polym. J.* **1985**, *17*, 117–132. [[CrossRef](#)]
29. Tomalia, D.A.; Dewald, J.R. Dense Star Polymers Having Core, Core Branches, Terminal Groups. U.S. Patent 4507466A, 7 January 1983.

30. Newkome, G.R.; Yao, Z.; Baker, G.R.; Gupta, V.K. Micelles. Part 1. Cascade molecules: A new approach to micelles. A [27]-arborol. *J. Org. Chem.* **1985**, *50*, 2003–2004. [[CrossRef](#)]
31. Ambade, A.V.; Savariar, E.N.; Thayumanavan, S. Dendrimeric Micelles for Controlled Drug Release and Targeted Delivery. *Mol. Pharm.* **2005**, *2*, 264–272. [[CrossRef](#)] [[PubMed](#)]
32. Gillies, E.R.; Fréchet, J.M.J. Dendrimers and dendritic polymers in drug delivery. *Drug Discov. Today* **2005**, *10*, 35–43. [[CrossRef](#)]
33. Medina, S.H.; El-Sayed, M.E.H. Dendrimers as carriers for delivery of chemotherapeutic agents. *Chem. Rev.* **2009**, *109*, 3141–3157. [[CrossRef](#)] [[PubMed](#)]
34. Zeng, F.; Zimmerman, S.C. Dendrimers in Supramolecular Chemistry: From Molecular Recognition to Self-Assembly. *Chem. Rev.* **1997**, *97*, 1681–1712. [[CrossRef](#)] [[PubMed](#)]
35. Patri, A.K.; Majoros, I.J.; Baker, J.R. Dendritic polymer macromolecular carriers for drug delivery. *Curr. Opin. Chem. Biol.* **2002**, *6*, 466–471. [[CrossRef](#)]
36. Newkome, G.R.; Moorefield, C.N.; Baker, G.R.; Saunders, M.J.; Grossman, S.H. Unimolecular Micelles. *Angew. Chem. Int. Ed. Engl.* **1991**, *30*, 1178–1180. [[CrossRef](#)]
37. Cho, K.; Wang, X.; Nie, S.; Chen, Z.G.; Shin, D.M. Therapeutic nanoparticles for drug delivery in cancer. *Clin. Cancer Res.* **2008**, *14*, 1310–1316. [[CrossRef](#)] [[PubMed](#)]
38. Svenson, S. Dendrimers as versatile platform in drug delivery applications. *Eur. J. Pharm. Biopharm.* **2009**, *71*, 445–462. [[CrossRef](#)] [[PubMed](#)]
39. Menjoge, A.R.; Kannan, R.M.; Tomalia, D.A. Dendrimer-based drug and imaging conjugates: Design considerations for nanomedical applications. *Drug Discov. Today* **2010**, *15*, 171–185. [[CrossRef](#)] [[PubMed](#)]
40. Sideratou, Z.; Tsiourvas, D.; Paleos, C.M. Quaternized Poly(propylene imine) Dendrimers as Novel pH-Sensitive Controlled-Release Systems. *Langmuir* **2000**, *16*, 1766–1769. [[CrossRef](#)]
41. Sideratou, Z.; Tsiourvas, D.; Paleos, C.M. Solubilization and Release Properties of PEGylated Diaminobutane Poly(propylene imine) Dendrimers. *J. Colloid Interface Sci.* **2001**, *242*, 272–276. [[CrossRef](#)]
42. Grayson, S.M.; Jayaraman, M.; Fréchet, J.M.J.; Verkade, J.G.; Gianasi, E.; Strohm, J.; Duncan, R. Convergent synthesis and ‘surface’ functionalization of a dendritic analog of poly(ethylene glycol). *Chem. Commun.* **1999**, *112*, 1329–1330. [[CrossRef](#)]
43. Liu, M.; Kono, K.; Fréchet, J.M.J. Water-soluble dendrimer-poly(ethylene glycol) starlike conjugates as potential drug carriers. *J. Polym. Sci. Part A Polym. Chem.* **1999**, *37*, 3492–3503. [[CrossRef](#)]
44. Carlmark, A.; Malmström, E.; Malkoch, M. Dendritic architectures based on bis-MPA: Functional polymeric scaffolds for application-driven research. *Chem. Soc. Rev.* **2013**, *42*, 5858–5879. [[CrossRef](#)] [[PubMed](#)]
45. Ihre, H.R.; de Jesús, O.L.P.; Szoka, F.C.; Fréchet, J.M.J. Polyester Dendritic Systems for Drug Delivery Applications: Design, Synthesis, and Characterization. *Bioconjug. Chem.* **2002**. [[CrossRef](#)]
46. Grinstaff, M.W. Biodendrimers: New Polymeric Biomaterials for Tissue Engineering. *Chem. A Eur. J.* **2002**, *8*, 2838. [[CrossRef](#)]
47. Feliu, N.; Walter, M.V.; Montañez, M.I.; Kunzmann, A.; Hult, A.; Nyström, A.; Malkoch, M.; Fadeel, B. Stability and biocompatibility of a library of polyester dendrimers in comparison to polyamidoamine dendrimers. *Biomaterials* **2012**, *33*, 1970–1981. [[CrossRef](#)] [[PubMed](#)]
48. Oelker, A.M.; Berlin, J.A.; Wathier, M.; Grinstaff, M.W. Synthesis and characterization of dendron cross-linked PEG hydrogels as corneal adhesives. *Biomacromolecules* **2011**, *12*, 1658–1665. [[CrossRef](#)] [[PubMed](#)]
49. Lundberg, P.; Walter, M.V.; Montañez, M.I.; Hult, D.; Hult, A.; Nyström, A.; Malkoch, M. Linear dendritic polymeric amphiphiles with intrinsic biocompatibility: Synthesis and characterization to fabrication of micelles and honeycomb membranes. *Polym. Chem.* **2011**, *2*, 394–402. [[CrossRef](#)]
50. Padilla De Jesús, O.L.; Ihre, H.R.; Gagne, L.; Fréchet, J.M.J.; Szoka, F.C. Polyester Dendritic Systems for Drug Delivery Applications: In Vitro and In Vivo Evaluation. *Bioconjug. Chem.* **2002**, *13*, 453–461. [[CrossRef](#)] [[PubMed](#)]
51. Lee, C.C.; MacKay, J.A.; Fréchet, J.M.J.; Szoka, F.C. Designing dendrimers for biological applications. *Nat. Biotechnol.* **2005**, *23*, 1517–1526. [[CrossRef](#)] [[PubMed](#)]
52. Gitsov, I.; Wooley, K.L.; Fréchet, J.M.J. Novel Polyether Copolymers Consisting of Linear and Dendritic Blocks. *Angew. Chem. Int. Ed. Engl.* **1992**, *31*, 1200–1202. [[CrossRef](#)]

53. Han, R.; Sun, Y.; Kang, C.; Sun, H.; Wei, W. Amphiphilic dendritic nanomicelle-mediated co-delivery of 5-fluorouracil and doxorubicin for enhanced therapeutic efficacy. *J. Drug Target.* **2017**, *25*, 140–148. [[CrossRef](#)] [[PubMed](#)]
54. Bae, J.W.; Pearson, R.M.; Patra, N.; Sunoqrot, S.; Vuković, L.; Král, P.; Hong, S. Dendron-mediated self-assembly of highly PEGylated block copolymers: A modular nanocarrier platform. *Chem. Commun.* **2011**, *47*, 10302–10304. [[CrossRef](#)] [[PubMed](#)]
55. Pearson, R.M.; Patra, N.; Hsu, H.J.; Uddin, S.; Král, P.; Hong, S. Positively charged dendron micelles display negligible cellular interactions. *ACS Macro Lett.* **2013**, *2*, 77–81. [[CrossRef](#)] [[PubMed](#)]
56. Yang, Y.; Pearson, R.M.; Lee, O.; Lee, C.W.; Chatterton, R.T.; Khan, S.A.; Hong, S. Dendron-based micelles for topical delivery of endoxifen: A potential chemo-preventive medicine for breast cancer. *Adv. Funct. Mater.* **2014**, *24*, 2442–2449. [[CrossRef](#)]
57. Pearson, R.M.; Sen, S.; Hsu, H.; Pasko, M.; Gaske, M.; Král, P.; Hong, S. Tuning the Selectivity of Dendron Micelles Through Variations of the Poly(ethylene glycol) Corona. *ACS Nano* **2016**, *10*, 6905–6914. [[CrossRef](#)] [[PubMed](#)]
58. Harris, J.M.; Chess, R.B. Effect of pegylation on pharmaceuticals. *Nat. Rev. Drug Discov.* **2003**, *2*, 214–221. [[CrossRef](#)] [[PubMed](#)]
59. Veronese, F.M.; Pasut, G. PEGylation, successful approach to drug delivery. *Drug Discov. Today* **2005**, *10*, 1451–1458. [[CrossRef](#)]
60. Sousa-Herves, A.; Riguera, R.; Fernandez-Megia, E. PEG-dendritic block copolymers for biomedical applications. *New J. Chem.* **2012**, *36*, 205. [[CrossRef](#)]
61. Hak, S.; Helgesen, E.; Hektoen, H.H.; Huuse, E.M.; Jarzyna, P.A.; Mulder, W.J.M.; Haraldseth, O.; Davies, C.D.L. The Effect of Nanoparticle Polyethylene Glycol Surface Density on Ligand-Directed Tumor Targeting Studied in Vivo by Dual Modality Imaging. *ACS Nano* **2012**, *6*, 5648–5658. [[CrossRef](#)] [[PubMed](#)]
62. Poon, Z.; Chen, S.; Engler, A.C.; Lee, H. II; Atas, E.; Von Maltzahn, G.; Bhatia, S.N.; Hammond, P.T. Ligand-clustered “patchy” nanoparticles for modulated cellular uptake and in vivo tumor targeting. *Angew. Chem. Int. Ed.* **2010**, *49*, 7266–7270. [[CrossRef](#)] [[PubMed](#)]
63. Wu, P.; Malkoch, M.; Hunt, J.N.; Vestberg, R.; Kaltgrad, E.; Finn, M.G.; Fokin, V.V.; Sharpless, K.B.; Hawker, C.J. Multivalent, bifunctional dendrimers prepared by click chemistry. *Chem. Commun.* **2005**, 5775. [[CrossRef](#)] [[PubMed](#)]
64. Dong, C.-M.; Liu, G. Linear-dendritic biodegradable block copolymers: From synthesis to application in bionanotechnology. *Polym. Chem.* **2013**, 46–52. [[CrossRef](#)]
65. del Barrio, J.; Oriol, L.; Alcalá, R.; Sánchez, C. Azobenzene-Containing Linear–Dendritic Diblock Copolymers by Click Chemistry: Synthesis, Characterization, Morphological Study, and Photoinduction of Optical Anisotropy. *Macromolecules* **2009**, *42*, 5752–5760. [[CrossRef](#)]
66. Gillies, E.R.; Jonsson, T.B.; Fréchet, J.M.J. Stimuli-responsive supramolecular assemblies of linear-dendritic copolymers. *J. Am. Chem. Soc.* **2004**, *126*, 11936–11943. [[CrossRef](#)] [[PubMed](#)]
67. Kalva, N.; Parekh, N.; Ambade, A.V. Controlled micellar disassembly of photo- and pH-cleavable linear-dendritic block copolymers. *Polym. Chem.* **2015**, *6*, 6826–6835. [[CrossRef](#)]
68. Sun, L.; Zhu, B.; Su, Y.; Dong, C.-M. Light-responsive linear-dendritic amphiphiles and their nanomedicines for NIR-triggered drug release. *Polym. Chem.* **2014**, *5*, 1605–1613. [[CrossRef](#)]
69. Andrén, O.C.J.; Zhang, Y.; Lundberg, P.; Hawker, C.J.; Nyström, A.M.; Malkoch, M. Therapeutic Nanocarriers via Cholesterol Directed Self-Assembly of Well-Defined Linear-Dendritic Polymeric Amphiphiles. *Chem. Mater.* **2017**, *29*, 3891–3898. [[CrossRef](#)]
70. Wang, H.; Wu, Y.; Liu, G.; Du, Z.; Cheng, X. A Biodegradable and Amphiphilic Linear-Dendritic Copolymer as a Drug Carrier Platform for Intracellular Drug Delivery. *Macromol. Chem. Phys.* **2016**, *217*, 2004–2012. [[CrossRef](#)]
71. Harnoy, A.J.; Rosenbaum, I.; Tirosh, E.; Ebenstein, Y.; Shaharabani, R.; Beck, R.; Amir, R.J. Enzyme-Responsive Amphiphilic PEG-Dendron Hybrids and Their Assembly into Smart Micellar Nanocarriers. *J. Am. Chem. Soc.* **2014**, *136*, 7531–7534. [[CrossRef](#)] [[PubMed](#)]
72. Rosenbaum, I.; Avinery, R.; Harnoy, A.J.; Slor, G.; Tirosh, E.; Hananel, U.; Beck, R.; Amir, R.J. Reversible Dimerization of Polymeric Amphiphiles Acts as a Molecular Switch of Enzymatic Degradability. *Biomacromolecules* **2017**, *18*, 3457–3468. [[CrossRef](#)] [[PubMed](#)]

73. Xiao, K.; Luo, J.; Fowler, W.L.; Li, Y.; Lee, J.S.; Xing, L.; Cheng, R.H.; Wang, L.; Lam, K.S. A self-assembling nanoparticle for paclitaxel delivery in ovarian cancer. *Biomaterials* **2009**, *30*, 6006–6016. [[CrossRef](#)] [[PubMed](#)]
74. Zhou, Z.; Ma, X.; Jin, E.; Tang, J.; Sui, M.; Shen, Y.; Van Kirk, E.A.; Murdoch, W.J.; Radosz, M. Linear-dendritic drug conjugates forming long-circulating nanorods for cancer-drug delivery. *Biomaterials* **2013**, *34*, 5722–5735. [[CrossRef](#)] [[PubMed](#)]
75. Clementi, C.; Miller, K.; Mero, A.; Satchi-Fainaro, R.; Pasut, G. Dendritic Poly(ethylene glycol) Bearing Paclitaxel and Alendronate for Targeting Bone Neoplasms. *Mol. Pharm.* **2011**, *8*, 1063–1072. [[CrossRef](#)] [[PubMed](#)]
76. Miller, K.; Clementi, C.; Polyak, D.; Eldar-Boock, A.; Benayoun, L.; Barshack, I.; Shaked, Y.; Pasut, G.; Satchi-Fainaro, R. Poly(ethylene glycol)-paclitaxel-alendronate self-assembled micelles for the targeted treatment of breast cancer bone metastases. *Biomaterials* **2013**, *34*, 3795–3806. [[CrossRef](#)] [[PubMed](#)]
77. Tang, G.; Hu, M.; He, F.; You, D.; Qian, Y.; Bi, Y. Dendritic poly(benzyl ether)-b-poly(N-vinylcaprolactam) block copolymers: Self-organization in aqueous media, thermoresponsiveness and biocompatibility. *J. Polym. Sci. Part A Polym. Chem.* **2018**, *56*, 300–308. [[CrossRef](#)]
78. Kempe, K.; Onbulak, S.; Schubert, U.S.; Sanyal, A.; Hoogenboom, R. pH degradable dendron-functionalized poly(2-ethyl-2-oxazoline) prepared by a cascade “double-click” reaction. *Polym. Chem.* **2013**, *4*, 3236. [[CrossRef](#)]
79. Tomalia, D.A. Birth of a new macromolecular architecture: Dendrimers as quantized building blocks for nanoscale synthetic polymer chemistry. *Prog. Polym. Sci.* **2005**, *30*, 294–324. [[CrossRef](#)]
80. Verma, I.M.; Somia, N. Gene therapy—Promises, problems and prospects. *Nature* **1997**, *389*, 239–242. [[CrossRef](#)] [[PubMed](#)]
81. Mintzer, M.A.; Simanek, E.E. Nonviral vectors for gene delivery. *Chem. Rev.* **2009**, *109*, 259–302. [[CrossRef](#)] [[PubMed](#)]
82. Dufes, C.; Uchegbu, I.F.; Schatzlein, A.G. Dendrimers in Gene Delivery. *Adv. Drug Deliv. Rev.* **2005**, *57*, 2177–2202. [[CrossRef](#)] [[PubMed](#)]
83. Hu, J.; Hu, K.; Cheng, Y. Tailoring the dendrimer core for efficient gene delivery. *Acta Biomater.* **2016**, *35*, 1–11. [[CrossRef](#)] [[PubMed](#)]
84. Wood, K.C.; Little, S.R.; Langer, R.; Hammond, P.T. A Family of Hierarchically Self-Assembling Linear-Dendritic Hybrid Polymers for Highly Efficient Targeted Gene Delivery. *Angew. Chem. Int. Ed.* **2005**, *44*, 6704–6708. [[CrossRef](#)] [[PubMed](#)]
85. Yu, H.; Nie, Y.; Dohmen, C.; Li, Y.; Wagner, E. Epidermal Growth Factor–PEG Functionalized PAMAM-Pentaethylenhexamine Dendron for Targeted Gene Delivery Produced by Click Chemistry. *Biomacromolecules* **2011**, *12*, 2039–2047. [[CrossRef](#)] [[PubMed](#)]
86. Demattei, C.R.; Huang, B.; Tomalia, D.A. Designed Dendrimer Syntheses by Self-Assembly of Single-Site, ssDNA Functionalized Dendrons. *Nano Lett.* **2004**, *4*, 771–777. [[CrossRef](#)]
87. Zhang, H.; Ma, Y.; Xie, Y.; An, Y.; Huang, Y.; Zhu, Z.; Yang, C.J. A Controllable Aptamer-Based Self-Assembled DNA Dendrimer for High Affinity Targeting, Bioimaging and Drug Delivery. *Sci. Rep.* **2015**, *5*, 10099. [[CrossRef](#)] [[PubMed](#)]
88. Meng, H.-M.; Zhang, X.; Lv, Y.; Zhao, Z.; Wang, N.-N.; Fu, T.; Fan, H.; Liang, H.; Qiu, L.; Zhu, G.; et al. DNA Dendrimer: An Efficient Nanocarrier of Functional Nucleic Acids for Intracellular Molecular Sensing. *ACS Nano* **2014**, *8*, 6171–6181. [[CrossRef](#)] [[PubMed](#)]
89. Lambrych, K.R.; Gitsov, I. Linear–Dendritic Poly(ester)-block-poly(ether)-b lock-poly(ester) ABA Copolymers Constructed by a Divergent Growth Method 1. *Macromolecules* **2003**, *36*, 1068–1074. [[CrossRef](#)]
90. Nguyen, P.M.; Hammond, P.T. Amphiphilic Linear-Dendritic Triblock Copolymers Composed of Poly(amidoamine) and Poly(propylene oxide) and Their Micellar-Phase and Encapsulation Properties. *Langmuir* **2006**, *22*, 7825–7832. [[CrossRef](#)] [[PubMed](#)]
91. Sumer Bolu, B.; Manavoglu Gecici, E.; Sanyal, R. Combretastatin A-4 Conjugated Antiangiogenic Micellar Drug Delivery Systems Using Dendron–Polymer Conjugates. *Mol. Pharm.* **2016**, *13*, 1482–1490. [[CrossRef](#)] [[PubMed](#)]
92. Bolu, B.S.; Golba, B.; Boke, N.; Sanyal, A.; Sanyal, R. Designing Dendron-Polymer Conjugate Based Targeted Drug Delivery Platforms with a “mix-and-Match” Modularity. *Bioconjug. Chem.* **2017**, *28*, 2962–2975. [[CrossRef](#)] [[PubMed](#)]

93. Movellan, J.; Urbán, P.; Moles, E.; de la Fuente, J.M.; Sierra, T.; Serrano, J.L.; Fernández-Busquets, X. Amphiphilic dendritic derivatives as nanocarriers for the targeted delivery of antimalarial drugs. *Biomaterials* **2014**, *35*, 7940–7950. [[CrossRef](#)] [[PubMed](#)]
94. Svenson, S.; Chauhan, A.S. Dendrimers for enhanced drug solubilization. *Nanomedicine* **2008**, *3*, 679–702. [[CrossRef](#)] [[PubMed](#)]
95. Esfand, R.; Beezer, A.E.; Mitchell, J.C.; Twyman, L.J. Synthesis, Complexation and Pharmaceutical Applications of Tetra-directional Cascade Dendrimers. *Pharm. Pharmacol. Commun.* **1996**, *2*, 157–159. [[CrossRef](#)]
96. Morgan, M.T.; Nakanishi, Y.; Kroll, D.J.; Griset, A.P.; Carnahan, M.A.; Wathier, M.; Oberlies, N.H.; Manikumar, G.; Wani, M.C.; Grinstaff, M.W. Dendrimer-Encapsulated Camptothecins: Increased Solubility, Cellular Uptake, and Cellular Retention Affords Enhanced Anticancer Activity In vitro. *Cancer Res.* **2006**, *66*, 11913–11921. [[CrossRef](#)] [[PubMed](#)]
97. Patri, A.K.; Kukowskalatallo, J.; Baker, J. Targeted drug delivery with dendrimers: Comparison of the release kinetics of covalently conjugated drug and non-covalent drug inclusion complex. *Adv. Drug Deliv. Rev.* **2005**, *57*, 2203–2214. [[CrossRef](#)] [[PubMed](#)]
98. Kaminskas, L.M.; McLeod, V.M.; Porter, C.J.H.; Boyd, B.J. Association of Chemotherapeutic Drugs with Dendrimer Nanocarriers: An Assessment of the Merits of Covalent Conjugation Compared to Noncovalent Encapsulation. *Mol. Pharm.* **2012**, *9*, 355–373. [[CrossRef](#)] [[PubMed](#)]
99. Luong, D.; Kesharwani, P.; Deshmukh, R.; Mohd Amin, M.C.I.; Gupta, U.; Greish, K.; Iyer, A.K. PEGylated PAMAM dendrimers: Enhancing efficacy and mitigating toxicity for effective anticancer drug and gene delivery. *Acta Biomater.* **2016**, *43*, 14–29. [[CrossRef](#)] [[PubMed](#)]
100. Liu, M.; Kono, K.; Fréchet, J.M. Water-soluble dendritic unimolecular micelles: Their potential as drug delivery agents. *J. Control. Release* **2000**, *65*, 121–131. [[CrossRef](#)]
101. Kojima, C.; Kono, K.; Maruyama, K.; Takagishi, T. Synthesis of Polyamidoamine Dendrimers Having Poly(ethylene glycol) Grafts and Their Ability To Encapsulate Anticancer Drugs. *Bioconjug. Chem.* **2000**, *11*, 910–917. [[CrossRef](#)] [[PubMed](#)]
102. El-Sayed, M.; Ginski, M.; Rhodes, C.; Ghandehari, H. Transepithelial transport of poly(amidoamine) dendrimers across Caco-2 cell monolayers. *J. Control. Release* **2002**, *81*, 355–365. [[CrossRef](#)]
103. Luo, D.; Haverstick, K.; Belcheva, N.; Han, E.; Saltzman, W.M. Poly(ethylene glycol)-Conjugated PAMAM Dendrimer for Biocompatible, High-Efficiency DNA Delivery. *Macromolecules* **2002**, *35*, 3456–3462. [[CrossRef](#)]
104. Singh, P.; Gupta, U.; Asthana, A.; Jain, N.K. Folate and Folate-PEG-PAMAM Dendrimers: Synthesis, Characterization, and Targeted Anticancer Drug Delivery Potential in Tumor Bearing Mice. *Bioconjug. Chem.* **2008**, *19*, 2239–2252. [[CrossRef](#)] [[PubMed](#)]
105. Wang, F.; Bronich, T.K.; Kabanov, A.V.; Rauh, R.D.; Roovers, J. Synthesis and Evaluation of a Star Amphiphilic Block Copolymer from Poly(ϵ -caprolactone) and Poly(ethylene glycol) as a Potential Drug Delivery Carrier. *Bioconjug. Chem.* **2005**, *16*, 397–405. [[CrossRef](#)] [[PubMed](#)]
106. Wang, F.; Bronich, T.K.; Kabanov, A.V.; Rauh, R.D.; Roovers, J. Synthesis and Characterization of Star Poly(ϵ -caprolactone)-b-Poly(ethylene glycol) and Poly(L-lactide)-b-Poly(ethylene glycol) Copolymers: Evaluation as Drug Delivery Carriers. *Bioconjug. Chem.* **2008**, *19*, 1423–1429. [[CrossRef](#)] [[PubMed](#)]
107. Guo, Y.; Zhao, Y.; Zhao, J.; Han, M.; Zhang, A.; Wang, X. Codendrimer from polyamidoamine (PAMAM) and oligoethylene dendron as a thermosensitive drug carrier. *Bioconjug. Chem.* **2014**, *25*, 24–31. [[CrossRef](#)] [[PubMed](#)]
108. Zhao, Y.; Zhao, J.; Li, R.; Han, M.; Zhu, C.; Wang, M.; Guo, Y.; Wang, X. A series of codendrimers from polyamidoamine (PAMAM) and oligoethylene glycols (OEG) dendrons as drug carriers: The effect of OEG dendron decoration degree. *RSC Adv.* **2015**, *5*, 85547–85555. [[CrossRef](#)]
109. Zhao, Y.; Guo, Y.; Li, R.; Wang, T.; Han, M.; Zhu, C.; Wang, X. Methotrexate Nanoparticles Prepared with Codendrimer from Polyamidoamine (PAMAM) and Oligoethylene Glycols (OEG) Dendrons: Antitumor Efficacy In Vitro and in Vivo. *Sci. Rep.* **2016**, *6*, 1–11. [[CrossRef](#)] [[PubMed](#)]
110. She, W.; Li, N.; Luo, K.; Guo, C.; Wang, G.; Geng, Y.; Gu, Z. Dendronized heparin-doxorubicin conjugate based nanoparticle as pH-responsive drug delivery system for cancer therapy. *Biomaterials* **2013**, *34*, 2252–2264. [[CrossRef](#)] [[PubMed](#)]

111. Ma, S.; Zhou, J.; Wali, A.R.M.; He, Y.; Xu, X.; Tang, J.Z.; Gu, Z. Self-assembly of pH-sensitive fluorinated peptide dendron functionalized dextran nanoparticles for on-demand intracellular drug delivery. *J. Mater. Sci. Mater. Med.* **2015**, *26*. [[CrossRef](#)] [[PubMed](#)]
112. She, W.; Luo, K.; Zhang, C.; Wang, G.; Geng, Y.; Li, L.; He, B.; Gu, Z. The potential of self-assembled, pH-responsive nanoparticles of mPEGylated peptide dendron-doxorubicin conjugates for cancer therapy. *Biomaterials* **2013**, *34*, 1613–1623. [[CrossRef](#)] [[PubMed](#)]
113. Li, N.; Li, N.; Yi, Q.; Luo, K.; Guo, C.; Pan, D.; Gu, Z. Amphiphilic peptide dendritic copolymer-doxorubicin nanoscale conjugate self-assembled to enzyme-responsive anti-cancer agent. *Biomaterials* **2014**, *35*, 9529–9545. [[CrossRef](#)] [[PubMed](#)]
114. Mohamed, M.M.; Sloane, B.F. Cysteine cathepsins: Multifunctional enzymes in cancer. *Nat. Rev. Cancer* **2006**, *6*, 764–775. [[CrossRef](#)] [[PubMed](#)]
115. Zeng, H.; Little, H.C.; Tiambeng, T.N.; Williams, G.A.; Guan, Z. Multifunctional Dendronized Peptide Polymer Platform for Safe and Effective siRNA Delivery. *J. Am. Chem. Soc.* **2013**, *135*, 4962–4965. [[CrossRef](#)] [[PubMed](#)]
116. Zhong, Y.; Goltsche, K.; Cheng, L.; Xie, F.; Meng, F.; Deng, C.; Zhong, Z.; Haag, R. Hyaluronic acid-shelled acid-activatable paclitaxel prodrug micelles effectively target and treat CD44-overexpressing human breast tumor xenografts in vivo. *Biomaterials* **2016**, *84*, 250–261. [[CrossRef](#)] [[PubMed](#)]
117. Gupta, S.; Schade, B.; Kumar, S.; Böttcher, C.; Sharma, S.K.; Haag, R. Non-ionic Dendronized Multiamphiphilic Polymers as Nanocarriers for Biomedical Applications. *Small* **2013**, *9*, 894–904. [[CrossRef](#)] [[PubMed](#)]
118. Kumari, M.; Gupta, S.; Achazi, K.; Böttcher, C.; Khandare, J.; Sharma, S.K.; Haag, R. Dendronized Multifunctional Amphiphilic Polymers as Efficient Nanocarriers for Biomedical Applications. *Macromol. Rapid Commun.* **2015**, *36*, 254–261. [[CrossRef](#)] [[PubMed](#)]
119. Parshad, B.; Kumari, M.; Achazi, K.; Böttcher, C.; Haag, R.; Sharma, S. Chemo-Enzymatic Synthesis of Perfluoroalkyl-Functionalized Dendronized Polymers as Cyto-Compatible Nanocarriers for Drug Delivery Applications. *Polymers* **2016**, *8*, 311. [[CrossRef](#)]
120. Viswanathan, G.; Hsu, Y.-H.; Voon, S.H.; Imae, T.; Siriviriyun, A.; Lee, H.B.; Kiew, L.V.; Chung, L.Y.; Yusa, S. A Comparative Study of Cellular Uptake and Subcellular Localization of Doxorubicin Loaded in Self-Assemblies of Amphiphilic Copolymers with Pendant Dendron by MDA-MB-231 Human Breast Cancer Cells. *Macromol. Biosci.* **2016**, *16*, 882–895. [[CrossRef](#)] [[PubMed](#)]
121. Voon, S.H.; Kue, C.S.; Imae, T.; Saw, W.S.; Lee, H.B.; Kiew, L.V.; Chung, L.Y.; Yusa, S. Ichi Doxorubicin-loaded micelles of amphiphilic diblock copolymer with pendant dendron improve antitumor efficacy: In vitro and in vivo studies. *Int. J. Pharm.* **2017**, *534*, 136–143. [[CrossRef](#)] [[PubMed](#)]



© 2018 by the authors. Licensee MDPI, Basel, Switzerland. This article is an open access article distributed under the terms and conditions of the Creative Commons Attribution (CC BY) license (<http://creativecommons.org/licenses/by/4.0/>).

Article

Design and Synthesis of Dendrimers with Facile Surface Group Functionalization, and an Evaluation of Their Bactericidal Efficacy

Elizabeth Ladd ^{1,2,3}, Amir Sheikhi ^{1,2,3}, Na Li ^{1,3}, Theo G.M. van de Ven ^{1,2,3,*} and Ashok Kakkar ^{1,3,*}

¹ Department of Chemistry, McGill University, 801 Sherbrooke St. West, Montreal, QC H3A 0B8, Canada; elizabeth.ladd@mail.mcgill.ca (E.L.); amir.sheikhi@mail.mcgill.ca (A.S.); Blinan04st@gmail.com (N.L.)

² Pulp and Paper Research Centre, McGill University, 3420 rue University, Montreal, QC H3A 2A7, Canada

³ Centre for Self-Assembled Chemical Structures, McGill University, 801 Sherbrooke St. West, Montreal, QC H3A 0B8, Canada

* Correspondence: theo.vandeven@mcgill.ca (T.G.M.v.d.V.); ashok.kakkar@mcgill.ca (A.K.); Tel.: +1-514-398-6912 (A.K.)

Academic Editor: Derek J. McPhee

Received: 5 May 2017; Accepted: 18 May 2017; Published: 24 May 2017

Abstract: We report a versatile divergent methodology to construct dendrimers from a tetrafunctional core, utilizing the robust copper(I) catalyzed alkyne-azide cycloaddition (CuAAC, “click”) reaction for both dendrimer synthesis and post-synthesis functionalization. Dendrimers of generations 1–3 with 8–32 protected or free OH and acetylene surface groups, were synthesized using building blocks that included acetylene- or azide-terminated molecules with carboxylic acid or diol end groups, respectively. The acetylene surface groups were subsequently used to covalently link cationic amino groups. A preliminary evaluation indicated that the generation one dendrimer with terminal NH₃⁺ groups was the most effective bactericide, and it was more potent than several previously studied dendrimers. Our results suggest that size, functional end groups and hydrophilicity are important parameters to consider in designing efficient antimicrobial dendrimers.

Keywords: dendrimers; hyperbranched macromolecules; synthesis; click chemistry; bactericide

1. Introduction

Dendrimers are well-defined hyperbranched macromolecules in which structural regularity arises from the controlled layer-by-layer build-up, with each additional layer leading to an exponential increase in the number of surface groups [1–7]. The overall structure and properties of dendrimers get contributions from their core, backbone, and the surface groups at the periphery [8]. The number of reactive ends at the core molecule influences the density of end units at each generation that primarily interact with the outside environment [9]. For example, a third generation dendrimer with a tetrafunctional core has 32 surface groups, while a corresponding dendrimer with a trifunctional core has 24. Flexibility of both the core and backbone also has a significant effect on the conformation of the structure [10,11]. A rigid backbone of the dendrimer leads to an open structure, while more flexible core and backbones correspond to more compact, globular dendrimers, as the arms can fold back on themselves [12,13]. The synthetic versatility and our ability to tailor their surfaces are some of the features, which make these monodisperse macromolecules attractive for a wide variety of applications.

One of the topical areas of interest in which dendrimers are becoming increasingly important is their ability to act as bactericides [14]. Multivalent surfaces of these hyperbranched macromolecules offer opportunities to tailor the efficacy of antimicrobial agents using a single scaffold [15–19].

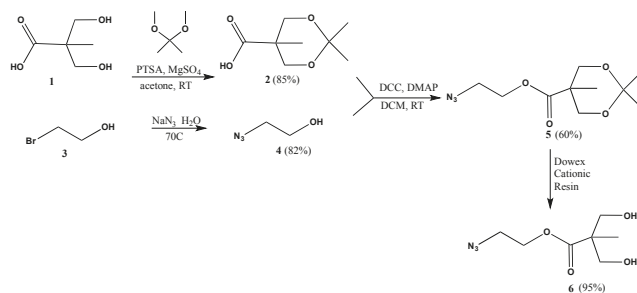
Cationic amino groups are well known to exert bactericidal effect by disrupting the integrity of bacterial cell membranes, eventually leading to cell lysis and death [18,20]. It has been shown that amine- and ammonium-terminated carbosilane dendrimers act as bactericides against Gram-positive and -negative bacteria, with almost two orders of magnitude less minimum inhibitory concentration (MIC) and minimum bactericidal concentration (MBC), than their monofunctional counterparts. However, these dendrimers can only be solubilized in water when a small amount of DMSO (1%) is added [21]. In another study, polyamidoamine (PAMAM) dendrimers were functionalized with nitric oxide (NO) releasing quaternary ammonium groups, which showed enhanced bactericidal activity and anti-biofilm formation properties as compared to non-NO releasing counterparts [22,23]. Hyaluronic acid/PAMAM multilayered dendrimers have also been used as antibacterial materials [24]. These studies suggest that by carefully designing dendrimers, one could achieve high efficacy through tailoring of desired functions [25].

We have developed a versatile synthetic methodology to dendrimers utilizing highly efficient alkyne-azide “click” chemistry [26–28], which leads to surface terminated OH or acetylene groups. The synthesis of dendrimers required the design of multifunctional building blocks including the one bearing a diol at one end and an azide at the other. The azide can be clicked to the peripheral alkynes of the growing dendrimer, regenerating the original alcohol functionality. The sequence can then be repeated to construct subsequent generations in a divergent manner. These dendrimers provide a facile method to introduce a variety of desired peripheral moieties, and we demonstrate the simplicity of this approach by functionalizing the surfaces of these dendrimers with cationic amino groups. We have evaluated the potential of these water-soluble cationic dendrimers for bactericidal activity, and we demonstrate that a balance of size, the terminal end groups and hydrophilicity plays an important role in their efficacy. Dendrimers functionalized with cationic amino groups were found to be highly potent antimicrobial agents, and the generation 1 dendrimer with surface NH_3^+ groups was the most efficient bactericide among such macromolecules.

2. Results and Discussion

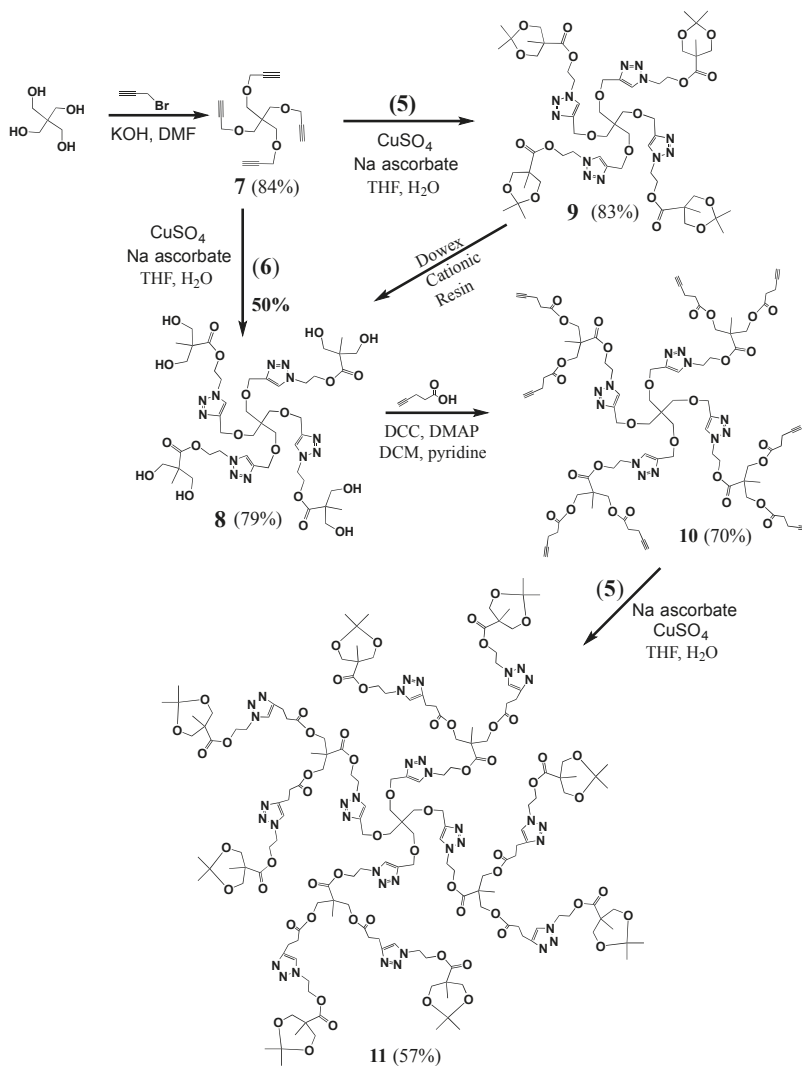
2.1. Synthesis

The synthesis of dendrimers was carried out using a careful design of building blocks with compatible functionalities. Since we intended to employ click chemistry both in the synthesis and functionalization of our dendrimers, we selected two building units, one with an acetylene moiety and another with an azide. The azide functionalized 2,2-bis(hydroxymethyl)propanoic acid (bis-MPA, Scheme 1) was prepared from bis-MPA (1) and bromoethanol (3). The diol terminal of the bis-MPA unit was first protected with an acetonide group, to yield 2, which could be purified easily by neutralizing with *p*-toluenesulfonic acid, followed by filtration.



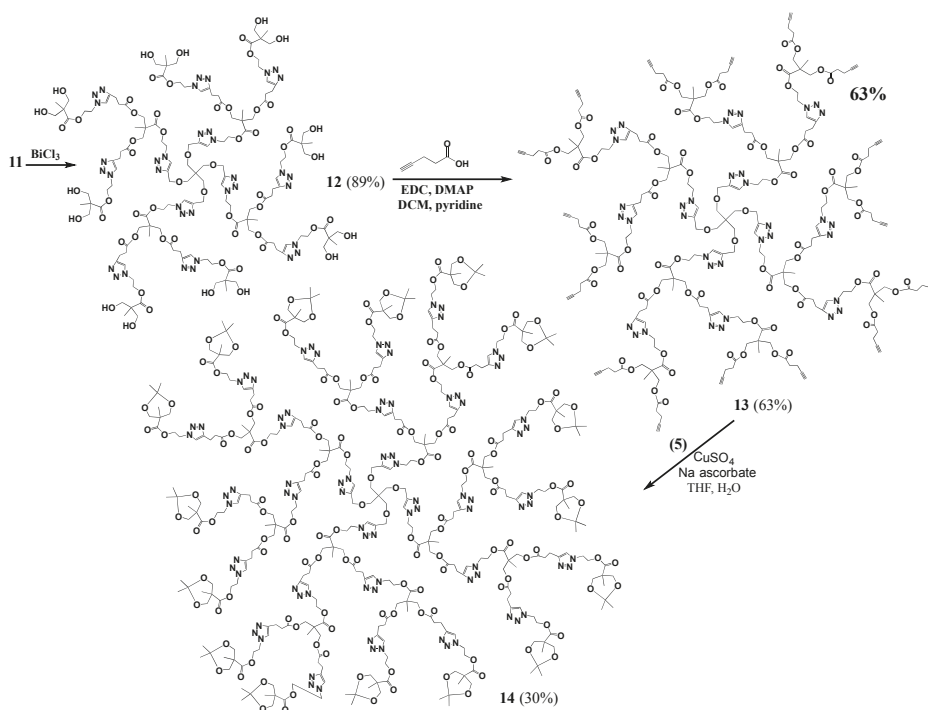
Scheme 1. Synthesis of building blocks.

Bromoethanol (**3**) was reacted with sodium azide to yield **4**, which was then coupled with **2** using *N,N'*-dicyclohexylcarbodiimide (DCC)/4-dimethylaminopyridine (DMAP), to yield **5**, a bifunctional molecule with a protected diol at one end and an azide at the other. It was deprotected to yield **6**, with azide and diol terminals. Propargyl bromide was coupled to the pentaerythritol core, yielding the tetra-acetylene terminated G0 dendrimer **7** (Scheme 2). The azide functionalized bis-MPA **6** was then clicked to G0 using CuAAC reaction to yield G1 dendrimer **8** with eight terminal hydroxide groups. It can also be prepared by first reacting core **7** with protected version of the azide functionalized bis-MPA **5** using CuAAC reaction to give **9**, followed by deprotection. This method gave better yields than the first route.



Scheme 2. Synthesis of G0-G2 dendrimers.

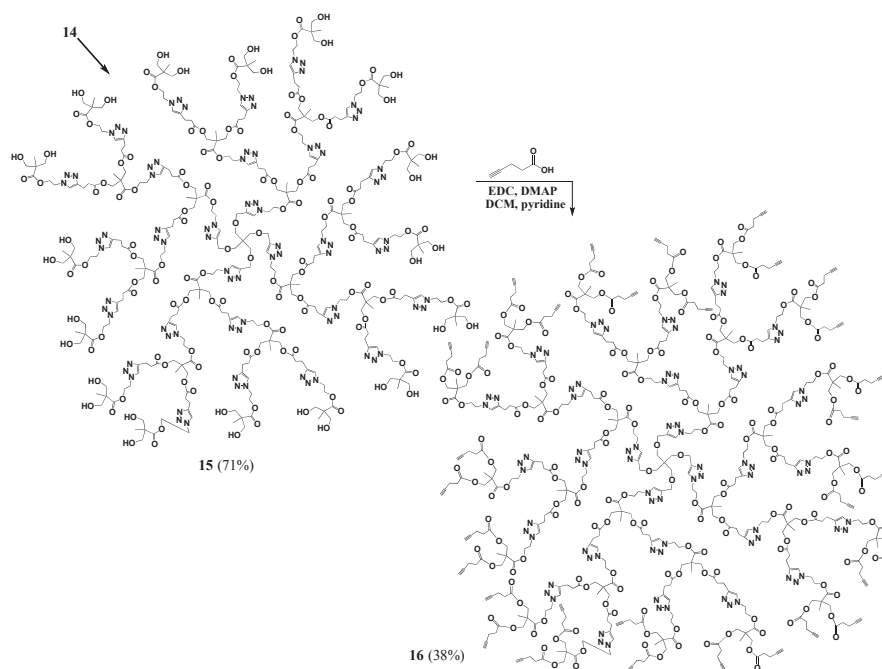
Several attempts to covalently link propargyl bromide to G1 dendrimer **8** using a similar procedure to that used to prepare G0 **7** failed. Since the important component was that the structure has acetylene termini, we considered a variation on this structure. An esterification with 4-pentynoic acid was carried out to prepare G1 (compound **10** with eight terminal acetylene groups). Compound **5** was then clicked onto the dendrimer to yield protected G2 dendrimer (p-G2, **11**), with sixteen terminal protected hydroxides, which was purified by dialysis. The deprotection using bismuth trichloride was employed to give the desired hydroxide terminated G2 dendrimer. A simple filtration to remove the remaining salts was the only purification necessary to yield G2 (**12**, Scheme 3). Another esterification with 4-pentynoic acid was then carried out to generate **13**, with sixteen terminal acetylenes. The purification of **13** was quite simple, employing only washing and filtration steps. A click reaction was then used to attach an additional layer of **5** onto **13**, generating pG3 **14**, with protected hydroxide groups, which was purified by precipitation. The compound was then deprotected to yield G3 (**15**, Scheme 4) with thirty two terminal hydroxyls, which were used to introduce terminal acetylene groups through esterification (**16**, Scheme 4).



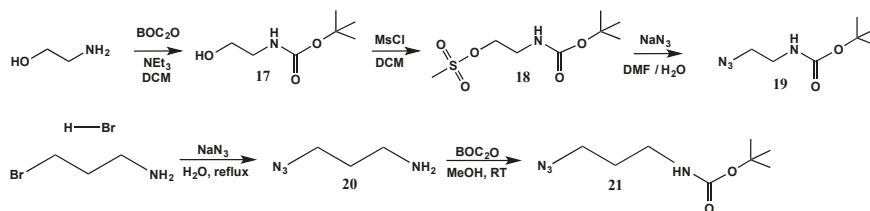
Scheme 3. Synthesis of G2-G3 dendrimers.

Dendrimers with positively charged amine groups on the surface were synthesized from the acetylene terminated dendrimers, by reacting them with protected amino-azides. The latter were synthesized from the commercially available amino alcohol. The amine was first protected with a t-butoxycarbonyl (BOC) group to yield **17** (Scheme 5), which was purified by washing in sequence with a basic followed by an acidic solution, brine and finally water. The alcohol group of **17** was then converted to a mesylate upon reaction with methane sulfonyl chloride to yield **18**, which was subsequently azidified to afford **19**. The amino-azide with a longer arm was prepared from commercially available amino-bromide by reacting it with sodium azide to yield **20**, which was

purified by a basic work-up, followed by extraction (Scheme 5). The amine moiety of **20** was then protected with ^tBOC to yield **21**.



Scheme 4. Synthesis of G3 dendrimer with terminal OH and acetylene groups.



Scheme 5. Synthesis of protected amine-azides.

The protected amine-azides **19** and **21** were clicked on to the acetylene terminated dendrimers **7**, **10** and **13**, and the surface amine groups on the resulting dendrimers were deprotected using trifluoroacetic acid (TFA), to yield the desired cationic amino terminated dendrimers (Figure 1: G0-NH₃⁺ **22**, G1-NH₃⁺ **23**, and G2-NH₃⁺ **24**). We used amine **21** that was one carbon longer for G1-2 dendrimers to reduce any steric hinderance on the surface for the larger dendrimers.

2.2. Bactericidal Activity of Dendrimers

We explored the bactericidal efficacy of the cationic amine terminated dendrimers, and one of the hydroxide terminated water soluble dendrimer ((G1-OH), Figure 1) for comparison purposes, as it is known that hydroxide terminated molecules may also show bactericidal effect [20]. Bactericidal efficacy was assessed using two parameters: minimum inhibitory concentration (MIC), and minimum bactericidal concentration (MBC). MIC is the lowest concentration of the antimicrobial (in this study,

the dendrimer) that inhibits the growth of a microorganism after overnight incubation. It gives a measure of the inhibition of the growth of bacteria as a function of concentration. MBC is the lowest concentration of the dendrimer that will prevent the growth of bacteria, and MBC is always larger than MIC. Aqueous solutions of dendrimers with a range of different concentrations were prepared, and then added to aliquots of bacteria solution. *Escherichia coli* (*E. coli*) with standard Gram-negative ATCC 11229TM strain were chosen for bactericidal activity experiments in this study, as these are the most widely studied microorganisms, and have a much faster growth rate which simplifies the time scale of the experiments. The initial optical density (OD) of the solutions was measured, and they were subsequently incubated overnight. After 18–24 h had elapsed, the OD was measured again. The relative absorbance of solutions as a function of bactericide concentration for G2-NH₃⁺ is shown in Figure 2. The minimum inhibitory concentration (MIC) was determined as the lowest concentration point where the curve drops sharply to zero.

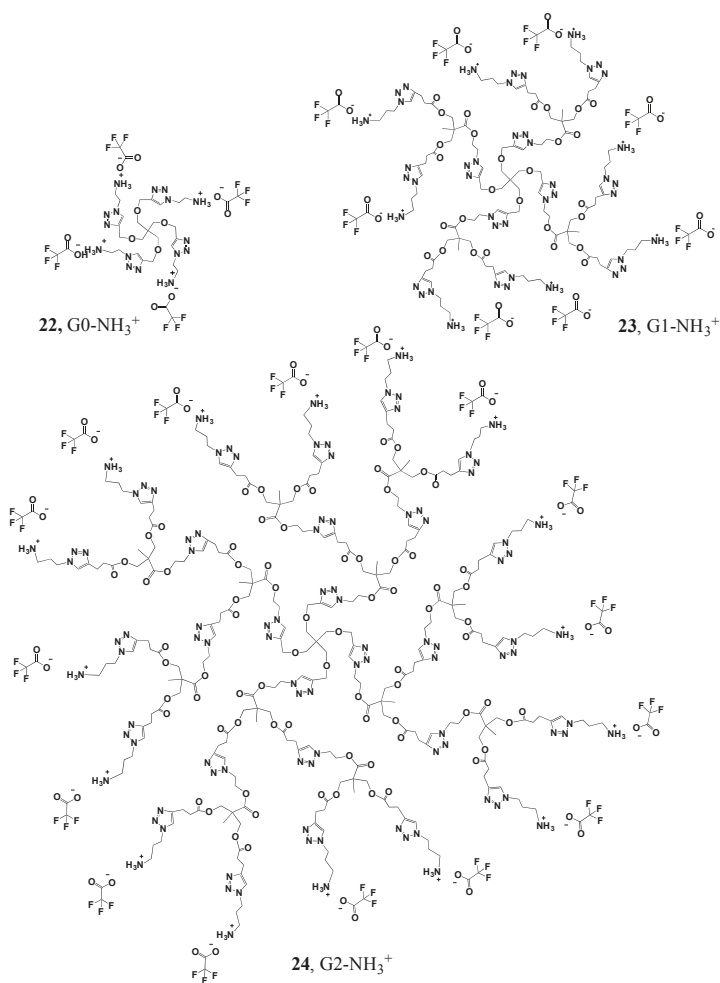


Figure 1. Dendrimers with positively charged surface groups.

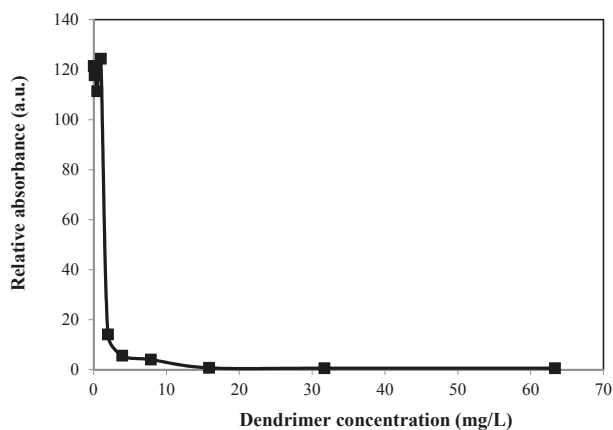


Figure 2. Relative absorbance versus dendrimer concentration curve for the determination of MIC for G2-NH₃⁺.

The bactericidal efficacies of four different dendrimers, three of them functionalized with cationic amino groups (G0-NH₃⁺, G1-NH₃⁺ & G2-NH₃⁺), and the fourth with hydroxide surface groups (G1-OH) are shown in Table 1. The most efficient bactericide was the generation one cationic amine terminated dendrimer, G1-NH₃⁺ (MIC = 0.9 mg/L, 8 NH₃⁺ groups, Table 1), and the least effective was the smallest structure, G0-NH₃⁺ (MIC = 32–64 mg/L, 4 NH₃⁺ groups, Table 1). Dendrimer G1-OH was found to have no bactericidal action at any of the concentrations tested (MIC > 64 mg/L, 8 OH groups, Table 1), which clearly suggests the importance of cationic surface groups for bactericidal activity. Since G1-NH₃⁺ was more effective in its bactericidal activity than both the lower (G0-NH₃⁺ 4 NH₃⁺ groups, MIC = 32–64 mg/L,) and higher (G2-NH₃⁺ 16 NH₃⁺ groups, MIC = 1–16 mg/L) generation dendrimers with the same backbone and type of end groups, it indicated that G1-NH₃⁺ provides the best balance between the number of bactericidal end groups and biopermeability. These results may also suggest that the generation 2 dendrimer is past the tipping point where the gain in bactericidal activity obtained from additional charged end groups, is outweighed by the loss of biopermeability. The MBC for G1-NH₃⁺ (4–8 mg/L, 8 NH₃⁺ groups, Table 1) followed the expected pattern of MBC > MIC for a given structure.

Table 1. MIC and MBC values of dendrimers for *E. coli* (ATCC 11229TM strain).

Structure	Type of End Groups	No. of End Groups	M _w (g/mol)	MIC (mg/L)	MIC (μM)	MBC (mg/L)	MBC (μM)
G1-OH	-OH	8	1101.1	>64	>58	>64	>58
G0-NH ₃ ⁺	-NH ₃ ⁺ TFA ⁻	4	1088.5	32–64	29–59	>64	>59
G1-NH ₃ ⁺	-NH ₃ ⁺ TFA ⁻	8	3454.9	0.9 ± 0.1	0.26 ± 0.03	4–8	1.1–2.3
G2-NH ₃ ⁺	-NH ₃ ⁺ TFA ⁻	16	8075.0	1–16	0.12–2	-	-

To better evaluate the bactericidal efficacy of our dendrimers, a comparison with dendrimers for which bactericidal activity has been reported earlier was carried out, and the data is presented in Table 2. The data corresponds only to dendrimers that function by the membrane disruptive mechanism (as opposed to anti-adhesive), where an MIC was measured [14]. Our best performing dendrimer, G1-NH₃⁺ (8 NH₃⁺ groups), is a more effective bactericide than any of the dendrimers (4–32 end groups) presented in Table 2. Comparable both in size and number of charged end groups to the generation 2 carbosilane dendrimer (MIC = 64 mg/L, 8 NMe₃⁺ groups, Table 2) [21], G1-NH₃⁺ (MIC = 0.9 mg/L, 8 NH₃⁺ groups, Table 1) is more effective by almost two orders of magnitude.

Equally comparable in size and number of charged end groups are the generation one carbosilane dendrimers (MIC = 4 mg/L, 4 NR₃⁺ groups), and G0-NH₃⁺ (MIC = 32–64 mg/L, 4 NR₃⁺ groups, Table 1). Interestingly, however, the trend is reversed in this case, with the generation one carbosilane dendrimer showed about an order of magnitude more bactericidal effect than G0-NH₃⁺. Since both sets of structures present the same number of charged amino groups, approximately the same molecular weight, and were tested against the same bacteria, the only major difference between the two dendrimer backbones seems to be in their hydrophilicity. It is known that structures which present more hydrophobic units can permeate the bacterial structure more easily to arrive at their site of action [14]. These results may suggest that for dendrimers with hydrophilic backbones, such as the ones presented here, the peak bactericidal efficiency is reached at a higher generation than for dendrimers with hydrophobic backbones, such as carbosilane.

Table 2. Comparative MIC values for dendrimers.

Generation & Backbone	No. End Groups	Type of End Groups	MW (g/mol)	MIC (mg/L)	MIC (μM)	Type of Bacteria
G3 PAMAM	31	-NH ₂	6859	6.3	0.92	<i>Pseudomonas aeruginosa</i> (PA)
G5 PAMAM	110	-NH ₂	26 373	12.5	0.47	PA
G1 Carbosilane	4	-N(Me) ₃ ⁺ I ⁻	1470.4	4	2.7	<i>Escherichia coli</i> (E coli)
G2 Carbosilane	8	-N(Me) ₃ ⁺ I ⁻	3493.8	64	18.3	<i>E coli</i>

The bactericidal efficacy of the neutral amine terminated generation three PAMAM dendrimer (MIC = 6.3 mg/L, 31 NH₂ groups Table 2) and generation five (12.5 mg/L, 110 NH₂ groups), both fall into the wide range determined for our G2-NH₃⁺ (MIC = 1–16 mg/L, 16 NH₃⁺ groups, Table 1) dendrimer. The molecular mass of G2-NH₃⁺ is comparable to that of the generation three PAMAM dendrimer. It is difficult to draw definite conclusions about these results due to the fact that the structures have different backbones, number of end groups, type of end groups, and were tested against different bacteria. Interestingly, the neutral structures that were previously tested (generations three and five PAMAM dendrimers) both performed better than the only neutral structure tested in this study, G1-OH (MIC > 64 mg/L, 8 OH groups, Table 1).

Our results, as well as those for the dendrimers previously evaluated [29,30], indicate that higher generation number may not be a necessary and important factor for bactericidal action. Although a detailed evaluation is necessary in order to determine structure-property relationships, it should be noted that the largest structure, the generation 5 PAMAM dendrimer with 110 peripheral amino groups, is the least effective bactericide. This suggests that a balance between the size of the dendrimer and the number of end groups is a key factor.

3. Materials and Methods

3.1. General Information

The reagents and solvents were purchased from Sigma-Aldrich (St. Louis, MO, USA) and Fisher Scientific (Hampton, NH, USA), and used as received. NMR spectral acquisitions were carried out on Mercury instruments (Varian, Palo Alto, CA, USA) and operated using VNMRJ 2.2D (Chempack 5) and VNMRJ 2.3A (Chempack 5) software using a 5 mm Smart Probe. The chemical shifts in ppm are reported relative to tetramethylsilane (TMS) as an internal standard for ¹H, and ¹³C. Mass spectra analyses (HRMS, ESI) were performed and analysed on an Exactive Plus Orbitrap-API (Thermo Scientific, Waltham, MA, USA) high resolution mass spectrometer and on MALDI Autoflex III-TOF (Bruker, Billerica, MA, USA). Procedures for the MIC and MBC determination were followed as described in [31]. The Compounds 2,2,5-trimethyl-1,3-dioxane-5-carboxylic acid

(2) [32], azidoethanol [33], and propargylated pentaerythritol [34], were prepared by adopting and modifying the procedures reported earlier.

3.2. Building Blocks

2,2,5-Trimethyl-1,3-dioxane-5-carboxylic acid (2): *p*-Toluenesulfonic acid (0.5975 g, 0.003141 mol) was added to a stirred solution of 2,2-bis(hydroxymethyl)propanoic acid (**1**, 8.4265 g, 0.06282 mol) in acetone (34 mL) in a 250 mL round bottom flask, under nitrogen. 2,2-Dimethoxypropane (9.8141 g, 0.09423 mol) and magnesium sulfate (0.7562 g, 0.006282 mol) were then added, and the reaction mixture was left to stir for 48 h. A solution of ammonia in dioxane (6.27 mL, 0.5 M) was added to neutralize the acid. The crude mixture was filtered, and the solvent evaporated to yield the product as a white powder (9.30 g, 0.0534 mol, 85% yield). ¹H-NMR (400 MHz, CDCl₃): δ = 1.20 (s, 3H, -CO-C-CH₃), 1.40 (s, 3H, -O-C-CH₃), 1.43 (s, 3H, -O-C-CH₃), 3.67 (t, 2H, -O-CH₂-C-CO-), 4.18 (d, 2H, -O-CH₂-C-CO-) ppm. ¹³C{¹H}-NMR (300 MHz, CDCl₃): δ = 18.42 (-CO-C-CH₃), 22.03 (-O-C-CH₃), 25.07 (-O-C-CH₃), 41.71 (-CO-C-), 65.81 (-O-CH₂-C-), 98.28 (-O-C-(CH₃)₂), 180.15 (-CO-) ppm.

Azidoethanol (4): A mixture of bromoethanol (**3**, 2.3742 g, 0.01900 mol) and sodium azide (2.4700 g, 0.03800 mol) in water (4 mL) was left stirring overnight at 70 °C. The reaction mixture was then extracted with DCM, the organic layer was isolated and dried with magnesium sulfate. The solvent was then evaporated to yield the product as yellow oil (1.36 g, 0.01561 mol, 82% yield). ¹H-NMR (400 MHz, CDCl₃): δ = 3.46 (t, 2H, N₃-CH₂-CH₂-), 3.79 (q, 2H, N₃-CH₂-CH₂-) ppm. ¹³C{¹H}-NMR (300 MHz, CDCl₃): δ = 53.6 (N₃-CH₂-CH₂-), 61.6 (N₃-CH₂-CH₂-) ppm.

2-Azidoethyl 2,2,5-trimethyl-1,3-dioxane-5-carboxylate (5): A solution of azidoethanol (**4**, 0.74 g, 0.008498 mol), 2,2,5-trimethyl-1,3-dioxane-5-carboxylic acid (**2**, 2.2204 g, 0.01275 mol) and DMAP (0.5191 g, 0.004249 mol) in anhydrous DCM (10 mL) was stirred for 5 min under nitrogen. DCC (2.1041 g, 0.01020 mol) was then added to the reaction mixture, and stirred under nitrogen, at room temperature, overnight. The precipitate was filtered off, and the solvent was evaporated to yield a residue that was purified by column chromatography (1:7 ethyl acetate–hexanes) to yield the product as a white solid (1.25 g, 0.005139 mol, 60% yield). ¹H-NMR (400 MHz, CDCl₃): δ = 1.21 (s, 3H, -CO-C-CH₃), 1.39 (s, 3H, -O-C-CH₃), 1.44 (s, 3H, -O-C-CH₃), 3.49 (t, 2H, N₃-CH₂-CH₂-), 3.68 (d, 2H, -O-CH₂-C-CO-), 4.21 (d, 2H, -O-CH₂-C-CO-), 4.33 (t, 2H, N₃-CH₂-CH₂-) ppm. ¹³C{¹H}-NMR (300 MHz, CDCl₃): δ = 18.5 (-CO-C-CH₃), 22.3 (-O-C-CH₃), 24.9 (-O-C-CH₃), 42.0 (-C-CH₃), 49.8 (N₃-CH₂-CH₂-), 63.6 (N₃-CH₂-CH₂-), 65.9 (-O-CH₂-C-), 98.1 (-C-CH₃), 174.0 (-CO-) ppm.

2-Azidoethyl 3-hydroxy-2-(hydroxymethyl)-2-methylpropanoate (6): A spoonful of Dowex cationic resin was added to a solution of **5** (0.301 g, 0.001728 mol) in methanol (6 mL). The mixture was left stirring overnight at room temperature. The supernatant was decanted off and the resin was rinsed several times with methanol. The supernatant was then combined with rinsing and the solvent was evaporated to yield the product as colorless oil (0.238 g, 0.001171 mol, 95% yield). ¹H-NMR (400 MHz, CDCl₃): δ = 1.09 (s, 3H, -CO-C-CH₃), 2.47 (s, 2H, -OH), 3.41 (m, 2H, N₃-CH₂-CH₂-), 3.50 (dd, 2H, -C-CH₂-OH), 3.80 (dd, 2H, -C-CH₂-OH), 4.28 (t, 2H, N₃-CH₂-CH₂-) ppm. ¹³C{¹H}-NMR (300 MHz, CDCl₃): δ = 17.0 (CH₃-C-), 49.3 (CH₃-C), 49.8 (N₃-CH₂-CH₂-), 63.5 (N₃-CH₂-CH₂-), 68.2 (CH₂-OH), 175.5 (-CO-) ppm.

Generation 0 (7): Anhydrous DMF (25 mL) was added by syringe to a round bottom flask containing pentaerythritol (**2** g, 0.01469 mol) and KOH (12.5 g, 0.2228 mol), with stirring, under nitrogen. The mixture was stirred for 5 min, under nitrogen, at 0 °C. A solution of propargyl bromide (20 g, 0.1681 mol) in toluene (80%) was then added dropwise to the reaction mixture over 30 min. The reaction was heated at 40 °C overnight, under nitrogen. Water (100 mL) was added to the mixture, which was then extracted with diethyl ether (3 × 50 mL). The organic layers were isolated, combined, and washed with water (3 × 50 mL) and brine (3 × 50 mL). The organic layer was isolated and dried with sodium sulfate. The solvent was removed to yield an orange oil which was purified by column chromatography (2:8 ethyl acetate–hexanes) to give the product as an orange-brown solid (1.7468 g,

0.006058 mol, 84% yield). $^1\text{H-NMR}$ (400 MHz, CDCl_3): δ = 2.40 (t, 4H, CH-C-CH_2 -), 3.53 (s, 8H, $-\text{C-CH}_2\text{-O-}$), 4.12 (d, 8H, CH-C-CH_2 -) ppm. $^{13}\text{C}\{^1\text{H}\}$ -NMR (300 MHz, CDCl_3): δ = 44.7 ($-\text{C-CH}_2\text{-O-}$), 58.7 (CH-C-CH_2), 69.0 ($-\text{C-CH}_2\text{-O-}$), 74.0 (CH-C-CH_2), 80.0 (CH-C-CH_2) ppm. ESI-MS: m/z = 311.1 [$\text{M} + \text{Na}^+$].

Protected Generation 1 (**pG1**, **9**): A solution of $\text{CuSO}_4 \cdot 5\text{H}_2\text{O}$ (0.0191 g, 0.00007669 mol) in water (0.5 mL) was added to a round bottom flask containing a stirred solution of **7** (0.0768 g, 0.0002663 mol) and **5** (0.2683 g, 0.001103 mol) in tetrahydrofuran (THF) (0.5 mL). Sodium ascorbate (0.0317 g, 0.0001598 mol) was added, and the mixture was allowed to react overnight. The product was purified by column chromatography (100% methanol) to yield a yellow oil (0.2778 g, 0.0002202 mol, 83% yield). $^1\text{H-NMR}$ (400 MHz, CD_3OD): δ = 1.00 (s, 3H, $-\text{CO-C-CH}_3$), 1.22 (s, 3H, $-\text{O-C-(CH}_3)_2$), 1.39 (s, 3H, $-\text{O-C-(CH}_3)_2$), 3.44 (s, 2H, $-\text{C-CH}_2\text{-O-CH}_2$), 3.63 (dd, 2H, $-\text{CO-C-CH}_2\text{-O-}$), 4.07 (dd, 2H, $-\text{CO-C-CH}_2\text{-O-}$), 4.51 (s, 2H, $-\text{O-CH}_2\text{-C-N-}$), 4.54 (t, 2H, $-\text{N-CH}_2\text{-CH}_2\text{-O-}$), 4.72 (s, 2H, $-\text{N-CH}_2\text{-CH}_2\text{-O-}$), 8.04 (s, 1H, $-\text{C-CH-N-}$) ppm. $^{13}\text{C}\{^1\text{H}\}$ -NMR (300 MHz, CD_3OD): δ = 17.19 ($-\text{C-CH}_3$), 20.52 ($-\text{O-C-(CH}_3)_2$), 24.93 ($-\text{O-C-(CH}_3)_2$), 41.78 ($-\text{C-C-CH}_3$), 45.11 ($-\text{C-CH}_2\text{-O-}$), 48.90 ($-\text{N-CH}_2\text{-CH}_2\text{-O-}$), 62.63 ($-\text{N-CH}_2\text{-CH}_2\text{-O-}$), 64.06 ($-\text{CH}_2\text{-O-CH}_2\text{-C-N-}$), 65.47 ($-\text{C-CH}_2\text{-O-C-}$), 68.65 ($-\text{C-CH}_2\text{-O-CH}_2\text{-C-N-}$), 97.97 ($-\text{O-C-(CH}_3)_2$), 124.07 ($-\text{C-CH-N-}$), 145.00 ($-\text{C-N-}$), 173.80 ($-\text{C-O-CH}_2$ -) ppm. MALDI-MS: m/z = 1267.3 [$\text{M} + \text{Li}^+$].

Generation 1 (**G1**, **8**). A solution of $\text{CuSO}_4 \cdot 5\text{H}_2\text{O}$ (0.0191 g, 0.00007669 mol) in water (0.5 mL) was added to a round bottom flask containing a stirred solution of **7** (0.0768 g, 0.0002663 mol) and **6** (0.2597 g, 0.001278 mol) in THF (0.5 mL). Sodium ascorbate (0.0317 g, 0.0001598 mol) was then added and the mixture was allowed to react overnight. The product was purified by column chromatography (100% methanol) to yield an orange oil (0.1479 g, 0.0001343 mol, 50% yield).

G1 (**8**) from **pG1** (**9**): Dowex Cationic Resin (6.72 g) was added to a solution of **pG1** (**9**, 9.69 g, 0.0077 mol) in methanol (485 mL). The mixture was then left stirring overnight. The resin was then filtered off and the solvent evaporated to yield **8** as a viscous orange oil (6.68 g, 0.0061 mol, 79% yield). $^1\text{H-NMR}$ (400 MHz, CD_3OD): δ = 1.08 (s, 3H, $-\text{CO-C-CH}_3$), 3.45 (s, 2H, $-\text{C-CH}_2\text{-O-}$), 3.61 (q, 4H, $-\text{C-CH}_2\text{-OH}$), 4.51 (t, 4H, $-\text{O-CH}_2\text{-C-N-}$), 4.52 (s, 2H, $-\text{N-CH}_2\text{-CH}_2\text{-O-}$), 4.70 (t, 2H, $-\text{N-CH}_2\text{-CH}_2\text{-O-}$), 8.04 (s, 1H, $-\text{C-CH-N-}$) ppm. $^{13}\text{C}\{^1\text{H}\}$ -NMR (300 MHz, CD_3OD): δ = 17.40 ($-\text{C-CH}_3$), 46.53 ($\text{C-CH}_2\text{-O-}$), 50.42 ($-\text{C-CH}_3$), 51.78 ($-\text{N-CH}_2\text{-CH}_2\text{-O-}$), 63.86 ($-\text{N-CH}_2\text{-CH}_2\text{-O-}$), 65.40 ($-\text{O-CH}_2\text{-C-N-}$), 65.85 ($-\text{C-CH}_2\text{-OH-}$), 70.09 ($\text{C-CH}_2\text{-O-}$), 125.77 ($-\text{C-CH-N-}$), 146.35 ($-\text{O-CH}_2\text{-C-N-}$), 176.06 ($-\text{C-CO-O-}$) ppm. MALDI-MS: m/z = 1107.6 [$\text{M} + \text{Li}^+$].

G1-ester-acetylene (**10**). DMAP (2.97 g, 0.0243 mol) was added to a stirred mixture of **G1** (**8**, 6.68 g, 0.0061 mol) in anhydrous DCM (267 mL) in a 500 mL round bottom flask under nitrogen. DCC (15.02 g, 0.0728 mol), pyridine (133 mL) and 4-pentynoic acid (7.14 g, 0.0728 mol) were added, and the reaction mixture was then left stirring, under nitrogen, overnight. The crude mixture was filtered and the solvent evaporated. The product was purified by column chromatography (ethyl acetate) to yield the product as a yellow oil (7.39 g, 0.0042 mol, 70% yield). $^1\text{H-NMR}$ (400 MHz, CD_3OD): δ = 1.19 (s, 3H, $-\text{C-CH}_3$), 2.26 (t, 2H, $-\text{C-CH}$), 2.46–2.53 (m, 8H, $-\text{O-C-CH}_2\text{-CH}_2\text{-C-}$), 3.45 (s, 2H, $-\text{C-CH}_2\text{-O-CH}_2$ -), 4.22 (q, 4H, $-\text{C-(CH}_2\text{-O-C-)}_2$), 4.54 (s, 2H, $-\text{C-CH}_2\text{-O-CH}_2\text{-C-}$), 4.55 (t, 2H, $-\text{CH-N-CH}_2\text{-CH}_2$ -), 4.73 (t, 2H, $-\text{C-CH-N-CH}_2$ -), 8.01 (s, 1H, $-\text{N-CH-}$) ppm. $^{13}\text{C}\{^1\text{H}\}$ -NMR (300 MHz, CD_3OD): δ = 15.10 ($-\text{CH}_2\text{-C-CH}$), 18.20 ($-\text{C-CH}_3$), 34.31 ($-\text{CH}_2\text{-CH}_2\text{-C-CH}$), 46.57 ($-\text{C-CH}_2\text{-O-CH}_2\text{-C-N-}$), 47.70 ($-\text{C-CH}_3$), 50.22 ($-\text{N-CH}_2\text{-CH}_2\text{-O-}$), 64.51 ($-\text{N-CH}_2\text{-CH}_2\text{-O-}$), 65.59 ($-\text{C-CH}_2\text{-O-CH}_2\text{-C-N-}$), 66.61 ($-\text{C-CH}_2\text{-O-C-}$), 70.19 ($-\text{C-CH}_2\text{-O-CH}_2\text{-C-N-}$), 70.55 ($-\text{C-CH}$), 83.54 ($-\text{C-CH}$), 125.49 ($-\text{C-CH-N-}$), 146.51 ($-\text{C-CH-N-}$), 172.84 ($-\text{O-C-CH}_2$ -), 173.72 (O-C-C-) ppm. MALDI-MS: m/z = 1747.5 [$\text{M} + \text{Li}^+$].

Protected Generation 2 (**pG2**, **11**). A solution of $\text{CuSO}_4 \cdot 5\text{H}_2\text{O}$ (0.1463 g, 0.000586 mol) in water (10 mL) was added to a round bottom flask containing a stirred solution of **10** (1.70 g, 0.0009766 mol) and **5** (2.2807 g, 0.009375 mol) in THF (10 mL). Sodium ascorbate (0.2322 g, 0.001172 mol) was added and the mixture was allowed to react overnight. The product mixture was evaporated,

dissolved in a minimum of methanol and run through a silica plug to remove the copper salts. The product was then purified by dialysis (MWCO = 1000 Da, methanol) to yield a brown solid (2.05 g, 0.000556 mol, 57% yield). $^1\text{H-NMR}$ (400 MHz, CD_3OD): δ = 1.02 (s, 6H, $\text{CH}_3\text{-C-O-CH}_2\text{-C-CH}_3$), 1.10 (s, 3H, $\text{C-C-O-CH}_2\text{-C-CH}_3$), 1.28 (s, 6H, $\text{CH}_3\text{-C-O-CH}_2\text{-C-CH}_3$), 1.39 (s, 6H, $\text{CH}_3\text{-C-O-CH}_2\text{-C-CH}_3$), 2.68 (t, 4H, $-\text{O-C-CH}_2\text{-CH}_2-$), 2.94 (t, 4H, t, 4H, $-\text{O-C-CH}_2\text{-CH}_2-$), 3.43 (s, 2H, $-\text{C-CH}_2\text{-O-CH}_2\text{-C-N-}$), 3.64 (dd, 4H, $-\text{C-CH}_2\text{-O-C-CH}_3$), 4.07 (dd, 4H, $-\text{C-CH}_2\text{-O-C-CH}_3$), 4.10 (s, 4H, $-\text{C-CH}_2\text{-O-C-CH}_2$), 4.50 (m, 8H, $-\text{N-CH}_2\text{-CH}_2\text{-O-C-C-CH}_2\text{-O-C-CH}_3$, $-\text{O-CH}_2\text{-C-CH-N-CH}_2\text{-CH}_2-$), 4.68 (m, 6H, $-\text{N-CH}_2\text{-CH}_2\text{-O-C-C-CH}_2\text{-O-C-CH}_3$, $-\text{O-CH}_2\text{-C-CH-N-CH}_2\text{-CH}_2-$), 7.85 (s, 1H, $-\text{O-CH}_2\text{-C-CH-N-}$), 8.02 (s, 2H, $-\text{C-CH}_2\text{-CH}_2\text{-C-CH-N-}$) ppm. $^{13}\text{C}\{^1\text{H}\}\text{-NMR}$ (300 MHz, CD_3OD): δ = 18.10, 18.68, 21.85, 26.49, 34.24, 43.24, 46.57, 47.67, 50.03, 50.17, 50.27, 64.15, 64.48, 65.59, 66.51, 67.04, 70.22, 99.44, 124.20, 125.51, 146.45, 147.69, 173.37, 173.68, 175.31 ppm. MALDI-MS: m/z = 3710.1[M + Na⁺].

Generation 2 (G2, 12): BiCl_3 (0.0009 g, 0.00000285 mol) and a drop of water were added to a stirred solution of pG2 (11, 0.025 g, 0.00000678 mol) in acetonitrile (1.1 mL). The reaction mixture was left stirring for 60 h at 45 °C. The product mixture was evaporated, dissolved in methanol, and filtered to remove the bismuth salts. The solvent was evaporated to yield a brown oil (0.020 g, 0.00000604 mol, 89% yield). $^1\text{H-NMR}$ (400 MHz, CD_3OD): δ = 1.10 (s, 9H, $-\text{C-CH}_3$), 2.69 (t, 4H, $-\text{C-CH}_2\text{-CH}_2\text{-C-N-}$), 2.95 (t, 4H, $-\text{C-CH}_2\text{-CH}_2\text{-C-N-}$), 3.43 (s, 2H, $-\text{C-CH}_2\text{-O-CH}_2\text{-C-N-}$), 3.60 (q, 8H, $-\text{C-CH}_2\text{-OH}$), 4.10 (s, 4H, $-\text{C-CH}_2\text{-O-C-}$), 4.48 (m, 8H, $-\text{N-CH}_2\text{-CH}_2\text{-O-C-C-CH}_2\text{-OH}$, $-\text{O-CH}_2\text{-C-CH-N-CH}_2\text{-CH}_2\text{-O-}$), 4.66 (m, 4H, $-\text{N-CH}_2\text{-CH}_2\text{-O-C-C-CH}_2\text{-OH}$), 4.71 (s, 2H, $-\text{O-CH}_2\text{-C-CH-N-CH}_2\text{-CH}_2\text{-O-}$, $-\text{O-CH}_2\text{-C-CH-N-CH}_2\text{-CH}_2\text{-O-}$), 7.86 (s, 2H, $-\text{CH}_2\text{-CH}_2\text{-C-CH-N-}$), 8.03 (s, 1H, $-\text{O-CH}_2\text{-C-CH-N-}$) ppm. $^{13}\text{C}\{^1\text{H}\}\text{-NMR}$ (300 MHz, CD_3OD): δ = ppm 17.41, 18.08, 34.18, 46.53, 47.65, 49.99, 50.17, 50.34, 51.79, 63.91, 64.45, 65.51, 65.86, 66.51, 70.13, 124.35, 125.61, 146.37, 147.58, 173.47, 173.70, 176.08. MALDI-MS: m/z = 3388.5[M + K⁺].

G2-ester-acetylene (13). DMAP (0.1586 g, 0.001298 mol) was added to a stirred mixture of 12 (0.2732 g, 0.00008113 mol) in anhydrous DCM (6.6 mL), under nitrogen. 1-ethyl-(3-dimethylaminopropyl)-carbodiimide hydrochloride (EDC) (0.3732 g, 0.001947 mol), pyridine (3.3 mL) and 4-pentynoic acid (0.1911 g, 0.001947 mol) were added to the flask. The reaction mixture was left stirring, under nitrogen, overnight. The crude product mixture was then washed with methanol, dissolved in chloroform and filtered to yield the product as brown oil (0.27 g, 0.0000581 mol, 63% yield). $^1\text{H-NMR}$ (400 MHz, CDCl_3): δ = 1.12 (s, 3H, $-\text{N-C-CH}_2\text{-CH}_2\text{-C-O-CH}_2\text{-C-CH}_3$), 1.20 (s, 6H, $-\text{CH-C-CH}_2\text{-CH}_2\text{-C-O-CH}_2\text{-C-CH}_3$), 1.98 (s, 4H, $-\text{C-CH}$), 2.50 (m, 16H, $-\text{C-CH}_2\text{-CH}_2\text{-C-CH}$), 2.70 (t, 4H, $-\text{O-C-CH}_2\text{-CH}_2\text{-C-N-}$), 2.97 (t, 4H, $-\text{O-C-CH}_2\text{-CH}_2\text{-C-N-}$), 3.42 (s, 2H, $-\text{C-CH}_2\text{-O-CH}_2-$), 4.10 (m, 4H, $-\text{C-CH}_2\text{-O-C-CH}_2\text{-CH}_2\text{-C-N-}$), 4.21 (m, 8H, $-\text{C-CH}_2\text{-O-C-CH}_2\text{-CH}_2\text{-C-CH}$), 4.51 (m, 8H, $-\text{CH}_2\text{-CH}_2\text{-C-N-N-N-CH}_2\text{-CH}_2\text{-O-}$, $-\text{C-CH}_2\text{-O-CH}_2\text{-C-CH-N-CH}_2\text{-CH}_2-$), 4.59 (m, 4H, $-\text{C-CH}_2\text{-O-CH}_2\text{-C-CH-N-CH}_2\text{-CH}_2-$), 4.65 (m, 2H, $-\text{C-CH}_2\text{-O-CH}_2\text{-C-CH-N-CH}_2\text{-CH}_2-$), 7.48 (s, 2H, $-\text{O-C-CH}_2\text{-CH}_2\text{-C-CH-N-}$), 7.78 (s, 1H, $-\text{CH}_2\text{-O-CH}_2\text{-C-CH-N-}$) ppm. $^{13}\text{C}\{^1\text{H}\}\text{-NMR}$ (300 MHz, CDCl_3): δ = ppm 14.26, 17.58, 17.68, 20.76, 33.11, 33.15, 43.19, 45.17, 46.27, 46.29, 48.67, 63.10, 64.75, 65.10, 65.25, 69.02, 69.34, 77.20, 82.26, 121.87, 123.31, 145.29, 146.22, 171.09, 171.98, 172.09, 172.14. MALDI-MS: m/z = 4669.1 [M + Na⁺].

pG3 (14). A solution of $\text{CuSO}_4 \cdot 5\text{H}_2\text{O}$ (0.0081 g, 0.000586 mol) in water (2 mL) was added to a round bottom flask containing a stirred solution of 13 (0.1262 g, 0.00002715 mol) and 5 (0.1268 g, 0.0005212 mol) in THF (2 mL). Sodium ascorbate (0.0129 g, 0.00006515 mol) was added and the mixture was allowed to react overnight. The product mixture was evaporated, dissolved in a minimum of methanol and run through a silica plug to remove the copper salts. The product was precipitated out of chloroform with hexanes, and dried to yield a yellow oil (0.067 g, 0.00000785 mol, 30% yield). $^1\text{H-NMR}$ (400 MHz, CDCl_3): δ = 1.04 (s, 12H, $\text{CH}_3\text{-C-O-CH}_2\text{-C-CH}_3$), 1.11 (s, 3H, $\text{C-C-O-CH}_2\text{-C-CH}_3$), 1.12 (s, 6H, $\text{C-C-O-CH}_2\text{-C-CH}_3$), 1.33 (s, 12H, $\text{CH}_3\text{-C-O-CH}_2\text{-C-CH}_3$), 1.41 (s, 12H, $\text{CH}_3\text{-C-O-CH}_2\text{-C-CH}_3$), 2.69 (t, 12H, $-\text{O-C-CH}_2\text{-CH}_2-$), 2.97 (t, 12H, $-\text{O-C-CH}_2\text{-CH}_2-$), 3.40 (s, 2H, $\text{C-CH}_2\text{-O-CH}_2-$), 3.62 (dd, 8H, $-\text{C-CH}_2\text{-O-C-CH}_3$), 4.10 (s, 12H, $-\text{C-CH}_2\text{-O-C-CH}_2$), 4.12 (dd, 8H, $-\text{C-CH}_2\text{-O-C-CH}_3$), 4.40–4.75 (m, 30H, $-\text{CH}_2\text{-CH}_2\text{-C-N-N-N-CH}_2\text{-CH}_2\text{-O-}$, $-\text{C-CH}_2\text{-O-CH}_2\text{-C-CH-N-CH}_2\text{-CH}_2-$,

-N-CH₂-CH₂-O-C-C-CH₂-O-C-CH₃), 7.56 (s, 2H, -CH-N-CH₂-CH₂-O-C-C-CH₂-O-C-CH₂-), 7.61 (s, 4H, -CH-N-CH₂-CH₂-O-C-C-CH₂-O-C-CH₃), 7.88 (s, 1H, -CH₂-O-CH₂-C-CH-N-) ppm. ¹³C{¹H}-NMR (300 MHz, CDCl₃): δ = ppm 17.48, 18.12, 20.71, 20.86, 26.22, 33.05, 41.98, 46.19, 48.68, 48.99, 62.82, 62.94, 65.04, 65.85, 68.41, 77.20, 98.05, 122.22, 146.71, 171.86, 171.98, 172.05, 173.70. MALDI-MS: *m/z* = 8580.6 [M + K⁺].

G3 (15). Dowex Cationic Resin (0.0629 g) was added to a solution of **pG3 (14)**, 0.1531 g, 0.0000179 mol in methanol (8.5 mL). The mixture was left stirring for three days at 45 °C. The resin was then filtered off and the solvent evaporated to yield the product as a yellow oil (0.0983 g, 0.0000124 mol, 71% yield). ¹H-NMR (400 MHz, CD₃OD): δ = 1.09 (s, 21H, -C-CH₃), 2.69 (m, 12H, -O-C-CH₂-CH₂-C-N-), 2.95 (m, 12H, -O-C-CH₂-CH₂-C-N-), 3.43 (s, 2H, -C-CH₂-O-CH₂-C-), 3.60 (q, 16H, -C-CH₂-OH), 4.10 (m, 12H, -C-CH₂-O-C-), 4.48 (m, 16H, -C-CH₂-O-CH₂-C-N-, -N-CH₂-CH₂-O-), 4.66 (m, 14H, -N-CH₂-CH₂-O-), 7.82–8.07 (m, 7H, -C-CH-N-) ppm. ¹³C{¹H}-NMR (300 MHz, DMSO-*d*₆): δ = ppm 16.65, 16.85, 16.89, 20.38, 32.69, 45.77, 45.80, 48.05, 48.34, 48.53, 50.24, 51.25, 62.24, 62.94, 63.06, 63.68, 63.84, 64.82, 122.31, 122.44, 123.98, 144.08, 145.22, 145.26, 171.50, 171.83, 174.20. MALDI-MS: *m/z* = 7894.2 [M + H⁺].

G3-ester-acetylene (16). DMAP (0.0266 g, 0.0002181 mol) was added to a stirred mixture of **G3** (0.0713 g, 0.000006814 mol) in anhydrous DCM (3.3 mL), under nitrogen. EDC (0.0627 g, 0.0003271 mol), pyridine (1.7 mL) and 4-pentynoic acid (0.0796 g, 0.0003271 mol) were added and the reaction mixture was left stirring, under nitrogen, overnight. The crude product mixture was dissolved in DCM and filtered to remove the salts. The product was then precipitated out of DCM with hexanes. Ether and hexanes washes were then performed to obtain a light brown oil (38% yield). ¹H-NMR (400 MHz, CDCl₃): δ = 1.07–1.24 (m, 32H, -CH₃), 1.99 (s, 8H, -CH), 2.43–2.55 (m, 32H, -CO-CH₂-CH₂-C-CH), 2.71 (m, 12H, -CO-CH₂-CH₂-C-N-), 2.96 (m, 12H, -CO-CH₂-CH₂-C-N-), 3.42 (s, 2H, -C-CH₂-O-CH₂-C-N-), 4.11 (s, 12H, CH₃-C-CH₂-O-CO-CH₂-CH₂-C-N-), 4.17–4.26 (m, 16H, CH₃-C-CH₂-O-CO-CH₂-CH₂-C-CH), 4.49–4.66 (m, 30H, -N-CH₂-CH₂-O-, -C-CH₂-O-CH₂-C-N-), 7.48–7.80 (m, 7H, -C-CH-N-) ppm. ¹³C{¹H}-NMR (300 MHz, CDCl₃): δ = ppm 14.29, 17.29, 17.62, 17.72, 20.9, 29.69, 33.14, 43.60, 45.22, 46.33, 48.68, 48.98, 62.95, 63.14, 64.82 (-C-CH₂-O-CH₂-C-N-N-CH₂-CH₂-), 64.97, 65.14, 65.28, 65.80, 69.39, 77.21, 82.30, 121.91, 121.98, 122.38, 146.18, 146.25, 146.29, 171.12, 172.01, 172.05, 172.13, 172.15, 172.18. MALDI-MS: *m/z* = 10,000–11,000 (theoretical mass = 10,456).

Amine functionalization: tert-butyl (2-hydroxyethyl)carbamate (17). Di-*tert*-butyl dicarbonate (BOC₂O) (7.86 g, 0.036 mol) was added slowly in a portionwise fashion to a stirred solution of ethanolamine (2.0 g, 0.033 mol) in DCM and triethylamine (5 mL), at 0 °C. The mixture was allowed to react overnight, at room temperature. The crude mixture was washed with an aqueous potassium carbonate solution, followed by an aqueous hydrochloric acid solution, brine, and finally water. The organic phase was isolated, dried with magnesium sulfate, and the solvent evaporated to yield the product as a colourless oil (3.70 g, 0.023 mol, 70% yield). ¹H-NMR (400 MHz, CDCl₃): δ = 1.47 (s, 9H, -C-(CH₃)₃), 3.26 (s, 2H, -CH₂-NH-), 3.67 (s, 2H, -CH₂-OH), 5.04 (s, 1H, -NH-) ppm. ¹³C{¹H}-NMR (300 MHz, CDCl₃): δ = 28.6 (s, -C-(CH₃)₃), 43.4 (s, -CH₂-NH-), 62.8 (s, -CH₂-OH), 79.9 (C-(CH₃)₃), 157.1 (-NH-CO-O-) ppm.

2-((tert-Butoxycarbonyl)amino)ethyl methanesulfonate (18). Methanesulfonyl chloride (9.42 g, 0.0822 mol) was added very slowly in a dropwise fashion to a stirred solution of (17) (12.8713 g, 0.0798 mol) in anhydrous DCM (500 mL) and triethylamine (20 mL) at 0 °C, under nitrogen. The reaction was left stirring, under nitrogen at room temperature overnight. The crude mixture was then washed with water (2 × 250 mL) and brine (2 × 250 mL). The organic layer was isolated, dried with magnesium sulfate and the solvent evaporated to yield the product as a yellow oil (17.95 g, 0.075 mol, 94% yield). ¹H-NMR (400 MHz, CDCl₃): δ = 1.44 (s, 9H, -C-(CH₃)₃), 3.03 (s, 3H, -S-CH₃), 3.46 (m, 2H, -CH₂-NH-), 4.28 (m, 2H, -CH₂-O-), 4.92 (s, 1H, -NH-) ppm. ¹³C{¹H}-NMR (300 MHz, CDCl₃): δ = 28.6 (-C-(CH₃)₃), 37.6 (-CH₂-NH-), 40.2 (-S-CH₃), 69.1 (-CH₂-O-), 80.2 (-C-(CH₃)₃) 158 (-NH-CO-O-) ppm.

tert-Butyl (2-azidoethyl)carbamate (**19**): Sodium azide (27.30 g, 0.4199 mol) was added to a stirred solution of (**18**) (19.98 g, 0.0835 mol) in DMF (100 mL) and water (100 mL), under nitrogen. The reaction was left stirring, at 80 °C overnight, under nitrogen. The crude product mixture was extracted with ethyl acetate (3 × 100 mL), the organic layers were isolated and combined and washed with water (3 × 100 mL) and brine (2 × 100 mL). The organic layer was isolated, dried with magnesium sulfate and the solvent evaporated to yield the product as a yellow oil (9.93 g, 0.0533 mol, 64% yield). ¹H-NMR (400 MHz, CDCl₃): δ = 1.44 (s, 9H, -C-(CH₃)₃), 3.28 (m, 2H, -CH₂-NH-), 3.40 (m, 2H, N₃-CH₂-), 4.82 (s, 1H, -NH-) ppm. ¹³C{¹H}-NMR (300 MHz, CDCl₃): δ = 28.3 (-C-(CH₃)₃), 40.0 (-CH₂-NH-), 51.2 (-CH₂-N₃), 79.8 (-C-(CH₃)₃), 155.70 (-NH-CO-O-) ppm.

3-Azidopropylamine (**20**). A solution of sodium azide (3.39 g, 0.05215 mol) in water (11 mL) was added to a stirred solution of 3-bromopropylamine hydrobromide (3.42 g, 0.01566 mol) in water (8 mL). The reaction was refluxed overnight, and 2/3 of the solvent was then evaporated and the crude mixture was placed in an ice bath. Potassium hydroxide (4.2 g, 0.0749 mol) and ether (50 mL) were added, the aqueous phase was isolated and washed with ether (3 × 35 mL). The organic phases were isolated, combined and dried with magnesium sulfate to yield the product as a yellow oil (1.38 g, 0.0138 mol, 88% yield). ¹H-NMR (400 MHz, CDCl₃): δ = 1.42 (s, 2H, -NH₂), 1.72 (q, 2H, -CH₂-CH₂-CH₂-), 2.79 (t, 2H, NH₂-CH₂-CH₂-CH₂-N₃), 3.36 (t, 2H, NH₂-CH₂-CH₂-CH₂-N₃) ppm. ¹³C{¹H}-NMR (300 MHz, CDCl₃): δ = 30.54 (-CH₂-CH₂-CH₂-), 36.13 (N₃-CH₂-CH₂-CH₂-NH₂), 51.12 (N₃-CH₂-CH₂-CH₂-NH₂) ppm.

tert-Butyl (3-azidopropyl)carbamate (**21**). A solution of BOC₂O (1.0899 g, 0.004994 mol) in methanol (6 mL) was added dropwise to a solution of (**20**) (0.500 g, 0.004994 mol) in triethylamine (3.48 mL) and methanol (20 mL). The reaction was left stirring, overnight at room temperature. The product mixture was filtered, and the solvent evaporated. The mixture was purified by column chromatography (chloroform) to yield the product as a yellow oil (0.5457 g, 0.00273 mol, 55% yield). ¹H-NMR (400 MHz, CDCl₃): δ = 1.41 (s, 9H, -C-(CH₃)₃), 1.74 (q, 2H, -CH₂-CH₂-CH₂-), 3.17 (t, 2H, -CH₂-CH₂-CH₂-N₃), 3.33 (t, 2H, -CH₂-CH₂-CH₂-N₃), 4.75 (s, 1H, -NH-) ppm. ¹³C{¹H}-NMR (300 MHz, CDCl₃): δ = 28.39 (C-(CH₃)₃), 29.87 (-CH₂-CH₂-CH₂-), 48.13 (N₃-CH₂-CH₂-CH₂-NH-), 53.93 (N₃-CH₂-CH₂-CH₂-NH-), 79.74 (-C-(CH₃)₃), 155.47 (-NH-COO-) ppm.

G0-NHBOC. A solution of CuSO₄·5H₂O (0.0754 g, 0.000302 mol) in water (2.5 mL) was added to a round bottom flask containing a stirred solution of **7** (0.300 g, 0.00104 mol) and **19** (0.8528 g, 0.00458 mol) in THF (2.5 mL). Sodium ascorbate (0.1236 g, 0.000624 mol) was added and the mixture was allowed to react overnight. The product mixture was evaporated and purified by column chromatography (acetone) to yield an orange solid (0.9041 g, 0.000875 mol, 97% yield). ¹H-NMR (400 MHz, CDCl₃): δ = 1.36 (s, 9H, -C-(CH₃)₃), 3.41 (s, 2H, -C-CH₂-O-), 3.55 (q, 2H, -N-CH₂-CH₂-NH-), 4.43 (t, 2H, -N-CH₂-CH₂-NH-), 4.47 (s, 2H, -C-CH₂-O-CH₂-), 5.62 (t, 1H, -NH-), 7.56 (s, 1H, -C-CH-N-) ppm. ¹³C{¹H}-NMR (300 MHz, CDCl₃): δ = 28.66 (-C-(CH₃)₃), 40.29 (-CH-N-CH₂-CH₂-), 46.47 (-C-CH₂-O-CH₂-C-N-), 48.52 (-CH-N-CH₂-CH₂-), 65.44 (-C-CH₂-O-CH₂-C-N-), 70.25 (-C-CH₂-O-CH₂-C-N-), 80.21 (-C-(CH₃)₃), 126.40 (-CH-), 147.20 (-C-CH-), 154.93 (-CO-) ppm. ESI-MS: *m/z* = 1056.5 [M + Na⁺].

G1-NHBOC. A solution of CuSO₄·5H₂O (0.0081 g, 0.00003232 mol) in water (2 mL) was added to a round bottom flask containing a stirred solution of **10** (0.0987 g, 0.0000567 mol) and **20** (0.1655 g, 0.0006804 mol) in THF (2 mL). Sodium ascorbate (0.0135 g, 0.00006804 mol) was added and the mixture was allowed to react overnight. The product mixture was evaporated and purified by column chromatography (acetone) to yield a sticky yellow solid (0.095 g, 0.0000284 mol, 50% yield). ¹H-NMR (400 MHz, CD₃OD): δ = 1.09 (s, 3H, -C-C-CH₃), 1.42 (s, 18H, -C-(CH₃)₃), 2.03 (m, 4H, -N-CH₂-CH₂-CH₂-NH-), 2.68 (t, 4H, -O-C-CH₂-CH₂-C-N-), 2.94 (t, 4H, -O-C-CH₂-CH₂-C-N-), 3.05 (t, 4H, -N-CH₂-CH₂-CH₂-NH-), 3.42 (s, 2H, -C-CH₂-O-), 4.09 (q, 4H, CH₃-C-CH₂-O-), 4.38 (t, 4H, -N-CH₂-CH₂-CH₂-NH-), 4.51 (m, 4H, -CH₂-O-CH₂-C-CH-N-CH₂-), 4.71 (t, 2H, -N-CH₂-CH₂-O-), 6.69 (t, 2H, -NH-),

7.77 (s, 2H, $-\underline{\text{C}}\text{H}-\text{N}-\text{CH}_2-\text{CH}_2-\text{CH}_2-$), 8.03 (s, 1H, $-\text{CH}_2-\text{O}-\text{CH}_2-\text{C}-\underline{\text{C}}\text{H}-\text{N}-$) ppm. $^{13}\text{C}\{^1\text{H}\}$ -NMR (300 MHz, CDCl_3): δ = 18.08 ($\text{CH}_3-\text{C}-\text{CH}_2-$), 21.84 ($-\text{CH}_2-\underline{\text{C}}\text{H}_2-\text{C}-\text{N}-$), 28.87 ($-\text{C}-\text{C}(\text{CH}_3)_3$), 31.67 ($-\text{CH}_2-\text{CH}_2-\text{NH}-$), 34.22 ($-\text{CH}_2-\text{CH}_2-\text{C}-\text{N}-$), 38.52 ($-\text{CH}_2-\text{NH}-$), 46.55 ($-\text{C}-\text{CH}_2-\text{O}-\text{CH}_2-\text{C}-\text{N}-$), 47.67 ($-\text{CH}_2-\underline{\text{C}}-\text{CH}_3$), 49.90 ($-\text{N}-\text{CH}_2-\text{CH}_2-\text{O}-$), 50.16 ($-\text{N}-\text{CH}_2-\text{CH}_2-\text{CH}_2-\text{NH}-$), 64.45 ($-\text{N}-\text{CH}_2-\text{CH}_2-\text{O}-$), 65.58 ($-\text{C}-\text{CH}_2-\text{O}-\text{CH}_2-\text{C}-\text{N}-$), 66.48 ($-\text{CH}_2-\text{C}-\text{CH}_3$), 70.18 ($-\text{C}-\text{CH}_2-\text{O}-\text{CH}_2-\text{C}-\text{N}-$), 80.12 ($-\text{C}-\text{C}(\text{CH}_3)_3$), 123.73 ($-\text{C}-\text{CH}-\text{N}-\text{CH}_2-\text{CH}_2-\text{CH}_2-$), 125.52 ($-\text{C}-\text{CH}_2-\text{O}-\text{CH}_2-\text{C}-\underline{\text{C}}\text{H}-\text{N}-$), 146.45 ($-\text{C}-\text{CH}_2-\text{O}-\text{CH}_2-\underline{\text{C}}-\text{CH}-\text{N}-$), 147.43 ($-\underline{\text{C}}-\text{CH}-\text{N}-\text{CH}_2-\text{CH}_2-\text{CH}_2-$), 158.45 ($-\text{CO}-\text{O}-\text{C}-\text{C}(\text{CH}_3)_3$), 173.43 ($-\text{O}-\underline{\text{C}}\text{O}-\text{CH}_2-$), 173.67 ($-\text{O}-\underline{\text{C}}\text{O}-\text{C}-$) ppm. MALDI-MS: m/z = 3365.1 $[\text{M} + \text{Na}^+]$.

G2-NHBOC. A solution of $\text{CuSO}_4 \cdot 5\text{H}_2\text{O}$ (0.0059 g, 0.00002349 mol) in water (1 mL) was added to a round bottom flask containing a stirred solution of **13** (0.091 g, 0.00001958 mol) and **20** (0.0941 g, 0.0004698 mol) in THF (1 mL). Sodium ascorbate (0.0093 g, 0.00004698 mol) was added and the mixture was allowed to react overnight. The product mixture was evaporated and filtered in DCM to remove the salts. The product was precipitated out of DCM using ether, isolated and dried to yield a viscous yellow oil (0.0429 g, 0.000005463 mol, 28% yield). ^1H -NMR (400 MHz, CDCl_3): δ = 1.11 (s, 9H, $-\text{O}-\text{C}-\text{C}-\text{CH}_3$), 1.41 (s, 36H, $-\text{C}-\text{C}(\text{CH}_3)_3$), 2.04 (q, 8H, $-\text{N}-\text{CH}_2-\text{CH}_2-\text{CH}_2-\text{NH}-$), 2.69 (t, 12H, $-\text{O}-\text{C}-\text{CH}_2-\text{CH}_2-\text{C}-\text{N}-$), 2.97 (t, 12H, $-\text{O}-\text{C}-\text{CH}_2-\text{CH}_2-\text{C}-\text{N}-$), 3.10 (m, 8H, $-\text{N}-\text{CH}_2-\text{CH}_2-\text{CH}_2-\text{NH}-$), 3.46 (s, 2H, $-\text{C}-\text{CH}_2-\text{O}-\text{CH}_2-$), 4.10 (m, 12H, $\text{CH}_3-\text{C}-\text{CH}_2-\text{O}-\text{C}-$), 4.36 (t, 8H, $-\text{N}-\text{CH}_2-\text{CH}_2-\text{CH}_2-\text{NH}-$), 4.48 (m, 8H, $-\text{CH}_2-\text{CH}_2-\text{C}-\text{N}-\text{N}-\text{CH}_2-\text{CH}_2-\text{O}-$), 4.58 (t, 4H, $-\text{CH}_2-\text{O}-\text{CH}_2-\text{C}-\text{N}-\text{N}-\text{CH}_2-\text{CH}_2-\text{O}-$), 4.65 (s, 2H, $-\text{C}-\text{CH}_2-\text{O}-\text{CH}_2-$), 5.14 (s, 4H, $-\text{NH}-$), 7.47 (s, 4H, $-\text{CH}-\text{N}-\text{CH}_2-\text{CH}_2-\text{CH}_2-\text{NH}-$), 7.54 (s, 2H, $-\text{C}-\text{CH}_2-\text{CH}_2-\text{C}-\underline{\text{C}}\text{H}-\text{N}-\text{CH}_2-\text{CH}_2-\text{O}-$), 7.83 (s, 1H, $-\text{O}-\text{CH}_2-\text{C}-\underline{\text{C}}\text{H}-\text{N}-$) ppm. $^{13}\text{C}\{^1\text{H}\}$ NMR (300 MHz, CDCl_3): δ = 17.58 ($-\text{CH}_2-\text{C}-\text{CH}_3$), 20.76 ($-\text{CO}-\text{CH}_2-\underline{\text{C}}\text{H}_2-\text{C}-\text{CH}-\text{N}-\text{CH}_2-\text{CH}_2-\text{O}-$), 20.81 ($-\text{CH}_2-\text{C}-\text{CH}-\text{N}-\text{CH}_2-\text{CH}_2-\text{CH}_2-$), 28.36 ($-\text{C}-\text{C}(\text{CH}_3)_3$), 30.62 ($-\text{N}-\text{CH}_2-\text{CH}_2-\text{CH}_2-$), 33.17 ($-\text{CO}-\underline{\text{C}}\text{H}_2-\text{CH}_2-\text{C}-\text{CH}-\text{N}-\text{CH}_2-\text{CH}_2-\text{O}-$), 33.28 ($-\text{CH}_2-\text{CH}_2-\text{C}-\text{CH}-\text{N}-\text{CH}_2-\text{CH}_2-\text{CH}_2-$), 37.36 ($-\text{N}-\text{CH}_2-\text{CH}_2-\underline{\text{C}}\text{H}_2-$), 45.18 ($-\text{C}-\text{CH}_2-\text{O}-\text{CH}_2-\text{C}-\text{N}-$), 46.26 ($-\text{C}-\text{CH}_2-\text{O}-\text{CH}_2-\text{C}-\text{CH}-\text{N}-\underline{\text{C}}\text{H}_2-\text{CH}_2-$), 46.30 ($-\text{CO}-\text{CH}_2-\text{CH}_2-\text{C}-\text{CH}-\text{N}-\text{CH}_2-\text{CH}_2-\text{O}-$), 47.47 ($-\text{N}-\underline{\text{C}}\text{H}_2-\text{CH}_2-\text{CH}_2-$), 48.68 ($-\text{C}-\text{CH}_2-\text{O}-\text{CO}-\text{CH}_2-\text{CH}_2-\text{C}-\text{CH}-\text{N}-\text{CH}_2-\text{CH}_2-\text{CH}_2-$), 48.75 ($-\text{C}-\text{CH}_2-\text{O}-\text{CO}-\text{CH}_2-\text{CH}_2-\text{C}-\text{CH}-\text{N}-\text{CH}_2-\text{CH}_2-\text{O}-$), 63.05 ($-\text{CO}-\text{CH}_2-\text{CH}_2-\text{C}-\text{CH}-\text{N}-\text{CH}_2-\underline{\text{C}}\text{H}_2-\text{O}-$), 63.11 ($-\text{C}-\text{CH}_2-\text{O}-\text{CH}_2-\text{C}-\text{CH}-\text{N}-\text{CH}_2-\underline{\text{C}}\text{H}_2-$), 64.75 ($-\text{C}-\text{CH}_2-\text{O}-\underline{\text{C}}\text{H}_2-\text{C}-\text{N}-$), 65.14 ($-\text{C}-\underline{\text{C}}\text{H}_2-\text{O}-\text{CO}-\text{CH}_2-\text{CH}_2-\text{C}-\text{CH}-\text{N}-\text{CH}_2-\text{CH}_2-\text{CH}_2-$), 69.05 ($-\text{C}-\underline{\text{C}}\text{H}_2-\text{O}-\text{CH}_2-\text{C}-\text{N}-$), 70.50 ($-\text{C}-\underline{\text{C}}\text{H}_2-\text{O}-\text{CO}-\text{CH}_2-\text{CH}_2-\text{C}-\text{CH}-\text{N}-\text{CH}_2-\text{CH}_2-\text{O}-$), 79.32 ($-\text{C}-\text{C}(\text{CH}_3)_3$), 121.67 ($-\text{C}-\text{CH}-\text{N}-\text{CH}_2-\text{CH}_2-\text{CH}_2-$), 122.10 ($-\text{CO}-\text{CH}_2-\text{CH}_2-\text{C}-\underline{\text{C}}\text{H}-\text{N}-\text{CH}_2-\text{CH}_2-\text{O}-$), 123.50 ($-\text{C}-\text{CH}_2-\text{O}-\text{CH}_2-\text{C}-\text{CH}-\text{N}-$), 146.01 ($-\text{CO}-\text{CH}_2-\text{CH}_2-\underline{\text{C}}-\text{CH}-\text{N}-\text{CH}_2-\text{CH}_2-\text{O}-$), 146.15 ($-\text{C}-\text{CH}-\text{N}-\text{CH}_2-\text{CH}_2-\text{CH}_2-$), 149.93 ($-\text{C}-\text{CH}_2-\text{O}-\text{CH}_2-\text{C}-\text{CH}-\text{N}-$), 156.12 ($-\text{CO}-\text{O}-\text{C}-\text{C}(\text{CH}_3)_3$), 171.96 ($-\text{CO}-\text{CH}_2-\text{CH}_2-\text{C}-\text{CH}-\text{N}-\text{CH}_2-\text{CH}_2-\text{O}-$), 172.01 ($-\text{CO}-\text{CH}_2-\text{CH}_2-\text{C}-\text{CH}-\text{N}-\text{CH}_2-\text{CH}_2-\text{CH}_2-$), 172.12 ($-\text{CO}-\text{CH}_2-\text{CH}_2-\text{C}-\text{CH}-\text{N}-\text{CH}_2-\text{CH}_2-\text{O}-\underline{\text{C}}\text{O}-$), 172.15 ($-\text{C}-\text{CH}_2-\text{O}-\text{CH}_2-\text{C}-\text{CH}-\text{N}-\text{CH}_2-\text{CH}_2-\text{O}-\underline{\text{C}}\text{O}-$) ppm. MALDI-MS: m/z = 7881.9 $[\text{M} + \text{Na}^+]$.

G0-NH₃⁺ (22). TFA (5 mL) was added dropwise to a solution of **G0-NHBOC** (0.9041 g, 0.000875 mol) in DCM (5 mL). The reaction was left stirring for 5 min, the solvent was evaporated and the product was dissolved in methanol. The methanol was evaporated, bringing the remaining TFA with it. This methanol addition and evaporation cycle was then repeated several times to ensure that all remaining TFA had been evaporated. The product was obtained as a sticky orange solid (0.800 g, 0.000735 mol, 84% yield). ^1H -NMR (400 MHz, CD_3OD): δ = 1.80 (s, 3H, $-\text{NH}_3$), 3.47 (s, 2H, $-\text{C}-\underline{\text{C}}\text{H}_2-\text{O}-$), 3.59 (t, 2H, $-\text{N}-\text{CH}_2-\underline{\text{C}}\text{H}_2-\text{NH}_3$), 4.53 (s, 2H, $-\text{C}-\text{CH}_2-\text{O}-\underline{\text{C}}\text{H}_2-$), 4.76 (t, 2H, $-\text{N}-\underline{\text{C}}\text{H}_2-\text{CH}_2-\text{NH}_3$), 8.06 (s, 1H, $-\text{C}-\underline{\text{C}}\text{H}-\text{N}-$) ppm. $^{13}\text{C}\{^1\text{H}\}$ -NMR (300 MHz, CD_3OD): δ = 40.30 ($-\text{CH}-\text{N}-\text{CH}_2-\underline{\text{C}}\text{H}_2-$), 46.48 ($-\text{C}-\text{CH}_2-\text{O}-\text{CH}_2-\text{C}-\text{N}-$), 48.54 ($-\text{CH}-\text{N}-\underline{\text{C}}\text{H}_2-\text{CH}_2-$), 65.46 ($-\text{C}-\text{CH}_2-\text{O}-\underline{\text{C}}\text{H}_2-\text{C}-\text{N}-$), 70.27 ($-\text{C}-\underline{\text{C}}\text{H}_2-\text{O}-\text{CH}_2-\text{C}-\text{N}-$), 119.20 ($-\text{CF}_3$), 126.40 ($-\text{CH}-$), 147.22 ($-\underline{\text{C}}-\text{CH}-$), 162.95 ($-\text{CO}-$) ppm. ESI-MS: m/z = 633.3 $[\text{M} - 4\text{TFA} + \text{H}^+]$.

G1-NH₃⁺ (23). TFA (0.5 mL) was added dropwise to a solution of **G1-NHBOC** (0.05 g, 0.000015 mol) in DCM (0.5 mL). The reaction was left stirring for 5 min, the solvent was evaporated and the product was dissolved in methanol. The methanol was then evaporated, bringing the remaining TFA with it. This methanol addition and evaporation cycle was then repeated several times to ensure

that all remaining TFA had been evaporated. The product was obtained as a sticky yellow solid (0.041 g, 0.000012 mol, 80% yield). $^1\text{H-NMR}$ (400 MHz, CD_3OD): δ = 1.10 (s, 3H, $-\text{C-CH}_3$), 2.27 (q, 4H, $-\text{N-CH}_2\text{-CH}_2\text{-CH}_2\text{-NH}_3$), 2.69 (t, 4H, $-\text{O-C-CH}_2\text{-CH}_2\text{-C-N-}$), 2.95 (t, 4H, $-\text{O-C-CH}_2\text{-CH}_2\text{-C-N-}$), 3.00 (t, 4H, $-\text{N-CH}_2\text{-CH}_2\text{-CH}_2\text{-NH}_3$), 3.42 (s, 2H, $-\text{C-CH}_2\text{-O-CH}_2\text{-}$), 4.08 (s, 4H, $\text{CH}_3\text{-C-CH}_2\text{-O-}$), 4.51 (t, 8H, $-\text{CH}_2\text{-O-CH}_2\text{-C-}$), 4.71 (t, 2H, $-\text{N-CH}_2\text{-CH}_2\text{-O-C-}$, $-\text{N-CH}_2\text{-CH}_2\text{-CH}_2\text{-NH}_3$), 7.80 (s, 2H, $-\text{CH-N-CH}_2\text{-CH}_2\text{-CH}_2\text{-}$), 8.04 (s, 1H, $-\text{CH}_2\text{-O-CH}_2\text{-C-CH-N-}$) ppm. $^{13}\text{C}\{^1\text{H}\}\text{-NMR}$ (300 MHz, CD_3OD): δ = 18.03 ($\text{CH}_3\text{-C-CH}_2\text{-}$), 21.74 ($-\text{CH}_2\text{-CH}_2\text{-C-N-}$), 29.18 ($-\text{CH}_2\text{-CH}_2\text{-NH}_3$), 34.14 ($-\text{CH}_2\text{-CH}_2\text{-C-N-}$), 38.17 ($-\text{CH}_2\text{-NH}_3$), 46.55 ($-\text{C-CH}_2\text{-O-CH}_2\text{-C-N-}$), 47.63 ($-\text{CH}_2\text{-C-CH}_3$), 49.90 ($-\text{N-CH}_2\text{-CH}_2\text{-O-}$), 50.20 ($-\text{N-CH}_2\text{-CH}_2\text{-CH}_2\text{-NH}_3\text{-}$), 64.44 ($-\text{N-CH}_2\text{-CH}_2\text{-O-}$), 65.48 ($-\text{C-CH}_2\text{-O-CH}_2\text{-C-N-}$), 66.41 ($-\text{CH}_2\text{-C-CH}_3$), 70.15 ($-\text{C-CH}_2\text{-O-CH}_2\text{-C-N-}$), 119.08 ($-\text{C-F}_3$), 123.91 ($-\text{C-CH-N-CH}_2\text{-CH}_2\text{-CH}_2\text{-}$), 125.64 ($-\text{C-CH}_2\text{-O-CH}_2\text{-C-CH-N-}$), 146.39 ($-\text{C-CH}_2\text{-O-CH}_2\text{-C-CH-N-}$), 147.69 ($-\text{C-CH-N-CH}_2\text{-CH}_2\text{-CH}_2\text{-}$), 162.57 ($-\text{CO-O-C-F}_3$), 173.46 ($-\text{O-CO-CH}_2\text{-}$), 173.69 ($-\text{O-CO-C-}$) ppm. MALDI-MS: m/z = 2563.6 [$\text{M} - 8\text{TFA} + \text{Na}^+$].

G2-NH₃⁺ (24). TFA (1 mL) was added dropwise to a solution of **G2-NHBOC** (0.0429 g, 0.000005463 mol) in DCM (1 mL). The reaction was left stirring for 5 min, the solvent was evaporated and the product was dissolved in methanol. The methanol was then evaporated, bringing the remaining TFA with it. This methanol addition and evaporation cycle was repeated several times to ensure that all remaining TFA had been evaporated. The product was obtained as a sticky yellow solid (0.034 g, 0.00000421 mol, 77% yield). $^1\text{H-NMR}$ (400 MHz, CD_3OD): δ = 1.10 (s, 9H, $-\text{O-C-C-CH}_3$), 2.27 (q, 8H, $-\text{N-CH}_2\text{-CH}_2\text{-CH}_2\text{-NH}_3$), 2.68 (t, 12H, $-\text{O-C-CH}_2\text{-CH}_2\text{-C-N-}$), 2.97 (t, 12H, $-\text{O-C-CH}_2\text{-CH}_2\text{-C-N-}$), 3.01 (m, 8H, $-\text{N-CH}_2\text{-CH}_2\text{-CH}_2\text{-NH}_3$), 3.41 (s, 2H, $-\text{C-CH}_2\text{-O-CH}_2\text{-}$), 4.08 (m, 12H, $\text{CH}_3\text{-C-CH}_2\text{-O-C-}$), 4.50 (m, 8H, $-\text{CH}_2\text{-CH}_2\text{-C-N-N-N-CH}_2\text{-CH}_2\text{-O-}$, $-\text{N-CH}_2\text{-CH}_2\text{-CH}_2\text{-NH}_3$), 4.66 (t, 4H, $-\text{CH}_2\text{-O-CH}_2\text{-C-N-N-N-CH}_2\text{-CH}_2\text{-O-}$), 4.70 (s, 2H, $-\text{C-CH}_2\text{-O-CH}_2\text{-}$), 4.88 (s, 12H, $-\text{NH}_3$), 7.82 (s, 4H, $-\text{CH-N-CH}_2\text{-CH}_2\text{-CH}_2\text{-NH-}$), 7.86 (s, 2H, $-\text{C-CH}_2\text{-CH}_2\text{-C-CH-N-CH}_2\text{-CH}_2\text{-O-}$), 8.07 (s, 1H, $-\text{O-CH}_2\text{-C-CH-N-}$) ppm. $^{13}\text{C}\{^1\text{H}\}\text{-NMR}$ (300 MHz, CD_3OD): δ = 16.55 ($-\text{CH}_2\text{-CH}_2\text{-CH}_2\text{-N-N-N-C-CH}_2\text{-CH}_2\text{-CO-O-CH}_2\text{-C-CH}_3$), 16.63 ($\text{O-CH}_2\text{-CH}_2\text{-N-N-N-C-CH}_2\text{-CH}_2\text{-CO-O-CH}_2\text{-C-CH}_3$), 20.30 ($-\text{CH}_2\text{-C-CH-N-CH}_2\text{-CH}_2\text{-CH}_2\text{-}$), 20.35 ($-\text{CO-CH}_2\text{-CH}_2\text{-C-CH-N-CH}_2\text{-CH}_2\text{-O-}$), 27.71 ($-\text{N-CH}_2\text{-CH}_2\text{-CH}_2\text{-}$), 32.70 ($-\text{CO-CH}_2\text{-CH}_2\text{-C-N-}$), 36.72 ($-\text{N-CH}_2\text{-CH}_2\text{-CH}_2\text{-}$), 45.05 ($-\text{C-CH}_2\text{-O-CH}_2\text{-C-N-}$), 46.17 ($-\text{CO-CH}_2\text{-CH}_2\text{-C-CH-N-CH}_2\text{-CH}_2\text{-O-}$), 46.19 ($-\text{C-CH}_2\text{-O-CH}_2\text{-C-CH-N-CH}_2\text{-CH}_2\text{-}$), 46.85 ($-\text{N-CH}_2\text{-CH}_2\text{-CH}_2\text{-}$), 48.73 ($\text{CH}_3\text{-C-CH}_2\text{-O-CO-}$), 62.97 ($-\text{N-CH}_2\text{-CH}_2\text{-O-}$), 64.05 ($-\text{C-CH}_2\text{-O-CH}_2\text{-C-N-}$), 64.97 ($-\text{C-CH}_2\text{-O-CO-CH}_2\text{-CH}_2\text{-C-CH-N-CH}_2\text{-CH}_2\text{-CH}_2\text{-}$), 65.05 ($-\text{C-CH}_2\text{-O-CO-CH}_2\text{-CH}_2\text{-C-CH-N-CH}_2\text{-CH}_2\text{-O-}$), 68.75 ($-\text{C-CH}_2\text{-O-CH}_2\text{-C-N-}$), 118.50 ($-\text{CF}_3$), 122.48 ($-\text{C-CH-N-}$), 146.08 ($-\text{C-CH-N-}$), 161.39 ($-\text{CO-O-CF}_3$), 171.98 ($-\text{CO-O-CH}_2\text{-C-CH}_3$), 172.24 ($-\text{CO-CH}_2\text{-CH}_2\text{-C-CH-N-CH}_2\text{-CH}_2\text{-O-CO-}$), 172.29 ($-\text{C-CH}_2\text{-O-CH}_2\text{-C-CH-N-CH}_2\text{-CH}_2\text{-O-CO-}$) ppm.

3.3. Determination of MIC

Aqueous solutions with dendrimer concentrations ranging from 0.025–64 mg/L were prepared. Initial testing was performed with these solutions, with subsequent tests carried out with a more narrow range around the initially determined MIC, in order to increase accuracy. Mueller Hinton Broth (MHB) (85 mL) was inoculated with one colony of *Escherichia coli* (*E. coli*) ATCC11229 and incubated with shaking (150 rpm) at 37 °C, for 18–24 h. Fresh MHB (85 mL) was then inoculated with overnight culture (300 μL) and incubated for 2 h, with shaking (150 rpm), at 37 °C. The OD of the culture was then measured at 625 nm. The bacterial solution was subsequently diluted in water until its OD lay in the range of 0.08–0.13, and then 100-fold in 15% MHB/85% H_2O . This diluted solution of bacteria (3 mL) was then added in a 1:1 ratio to the prepared dendrimer solutions, in duplicate. The initial OD at 625 nm of each dendrimer treated bacteria sample was then measured. Subsequently, the samples were incubated with shaking (150 rpm) at 37 °C, for 18–24 h, when the OD was again measured. Bacterial controls ensured that each sample contained 5×10^5 colony forming units (CFU). Experiments were repeated to ensure reproducibility. The OD values of the bacterial solutions taken

18–24 h after dendrimer addition relative to the initial OD were plotted as a function of dendrimer concentration. The MIC was evaluated as the concentration where the relative OD drops sharply to zero.

3.4. Determination of MBC

The same dendrimer treated bacterial samples used to evaluate the MIC were also employed to determine the MBC. After their OD had been measured at 625 nm, 18–24 h after exposure, the samples were plated on agar. The MBC was determined as the lowest concentration showing no bacterial growth after incubation for 18–24 h at 37 °C.

4. Conclusions

We have developed a synthetic methodology to hydroxide and acetylene terminated dendrimers that can be easily functionalized with a variety of surface groups including cationic amine moieties for application as bactericides. The introduction of tetravalent core molecule in the design of dendrimers reduces the number of generations required to obtain the appropriate number of functional groups at their periphery. It also reduces the number of steps required in their synthesis, and it may facilitate their large scale preparation. Availability of terminal acetylene groups allows covalent linking of any desired functional group using “click” chemistry. We have demonstrated the introduction of cationic end groups, and have evaluated the potential of these dendrimers as bactericides. However, the scope of functionalization is not limited, and these dendrimers offer an advantageous platform to design nanocarriers for varied applications in a diverse range of areas. Our studies suggest that while designing antimicrobial dendrimers, the dendrimer generation, the functional groups at the periphery and their permeability (and thus hydrophilicity) plays an important role in enhancing their efficacy.

Acknowledgments: We would like to thank Natural Sciences and Engineering Research Council (NSERC, Canada), Fonds de Recherche du Qu’ebec Nature et technologies (FRQNT, QC, Canada), and Center for Self-assembled Chemical Structures (FQRNT, QC, Canada) for financial support. We would like to thank Cristina Motillo and Tiffany Hua, for their help with bactericidal activity experiments.

Author Contributions: A. Kakkar and T. van de Ven conceived and designed the experiments, E. Ladd performed majority of the experiments together with N. Li and A. Sheikhi. All the authors contributed to writing of this manuscript.

Conflicts of Interest: The authors declare no conflict of interest.

References

- Tomalia, D.A.; Khanna, S.N. A systematic framework and nanoperiodic concept for unifying nanoscience: Hard/Soft nanoelements, superatoms, meta-atoms, New emerging properties, periodic property patterns, and predictive Mendeleev-like nanoperiodic tables. *Chem. Rev.* **2016**, *116*, 2705–2774. [[CrossRef](#)] [[PubMed](#)]
- Grayson, S.M.; Frechet, J.M.J. Convergent dendrons and dendrimers: From synthesis to application. *Chem. Rev.* **2001**, *101*, 3819–3868. [[CrossRef](#)] [[PubMed](#)]
- Mignani, S.; Kazzouil, S.E.; Bousmina, M.M.; Majoral, J.-P. Dendrimer space exploration: An assessment of dendrimers/dendritic scaffolding as inhibitors of protein–protein interactions, a potential new area of pharmaceutical development. *Chem. Rev.* **2014**, *114*, 1327–1342. [[CrossRef](#)] [[PubMed](#)]
- Mintzer, M.A.; Grinstaff, M.W. Biomedical applications of dendrimers: A tutorial. *Chem. Soc. Rev.* **2011**, *40*, 173–190. [[CrossRef](#)] [[PubMed](#)]
- Hourani, R.; Kakkar, A. Advances in the elegance of chemistry in designing dendrimers. *Macromol. Rapid Commun.* **2010**, *31*, 947–974. [[CrossRef](#)] [[PubMed](#)]
- Wang, D.; Deraedt, C.; Ruiz, J.; Astruc, D. Magnetic and dendritic catalysts. *Acc. Chem. Res.* **2015**, *48*, 1871–1880. [[CrossRef](#)] [[PubMed](#)]
- Roy, R.; Shiao, T.C. Glycodendrimers as powerful scaffolds and building blocks for the rapid construction of multifaceted, dense and chiral dendrimers. *Chem. Soc. Rev.* **2015**, *44*, 3924–3941. [[CrossRef](#)] [[PubMed](#)]
- Caminade, A.-M.; Ouali, A.; Laurent, R.; Turrin, C.-O.; Majoral, J.-P. The dendritic effect illustrated with phosphorus dendrimers. *Chem. Soc. Rev.* **2015**, *44*, 3890–3899. [[CrossRef](#)] [[PubMed](#)]

9. Carlmark, A.; Malmstrom, E.; Malkoch, M. Dendritic architectures based on bis-MPA: Functional polymeric scaffolds for application-driven research. *Chem. Soc. Rev.* **2013**, *42*, 5858–5879. [[CrossRef](#)] [[PubMed](#)]
10. Newkome, G.R.; Shreiner, C. Dendrimers derived from 1–3 branching motifs. *Chem. Rev.* **2010**, *110*, 6338–6442. [[CrossRef](#)] [[PubMed](#)]
11. Sun, H.-J.; Zhang, S.; Percec, V. From structure to function via complex supramolecular dendrimer systems. *Chem. Soc. Rev.* **2015**, *44*, 3900–3923. [[CrossRef](#)] [[PubMed](#)]
12. Turp, D.; Nguyen, T.-T.-T.; Baumgarten, M.; Mullen, K. Uniquely versatile: Nano-site defined materials based on polyphenylene dendrimers. *New J. Chem.* **2012**, *36*, 282–298. [[CrossRef](#)]
13. Frechet, J.M.J.; Tomalia, D.A. *Dendrimers and Other Dendritic Polymers*; John Wiley & Sons: Corchester, UK, 2002.
14. Castonguay, A.; Ladd, E.; van de Ve, T.G.M.; Kakkar, A. Dendrimers as bactericides. *New J. Chem.* **2012**, *36*, 199–204. [[CrossRef](#)]
15. Chen, C.Z.; Cooper, S.L. Recent advances in antimicrobial dendrimers. *Adv. Mater.* **2000**, *12*, 843–846. [[CrossRef](#)]
16. Branderhorst, H.M.; Liskamp, R.M.J.; Visser, G.M.; Pieters, R.J. Strong inhibition of cholera toxin binding by galactose dendrimers. *Chem. Commun.* **2007**, *47*, 5043–5045. [[CrossRef](#)] [[PubMed](#)]
17. Calabretta, M.K.; Kumar, A.; McDermott, A.M.; Cai, C. Antibacterial activities of poly (amidoamine) dendrimers terminated with amino and poly (ethylene glycol) groups. *Biomacromolecules* **2007**, *8*, 1807–1811. [[CrossRef](#)] [[PubMed](#)]
18. Chen, C.Z.; Cooper, S.L. Interactions between dendrimer biocides and bacterial membranes. *Biomaterials* **2002**, *23*, 3359–3368. [[CrossRef](#)]
19. Chen, C.Z.; Beck-Tan, N.C.; Dhurjati, P.; van Dyk, T.K.; LaRossa, R.A.; Cooper, S.L. Quaternary ammonium functionalized poly (propylene imine) dendrimers as effective antimicrobials: Structure-activity studies. *Biomacromolecules* **2000**, *1*, 473–480. [[CrossRef](#)] [[PubMed](#)]
20. Denyer, S.P. Mechanisms of action of biocides. *Int. Biodeterior. Biodegrad.* **1990**, *26*, 89–100. [[CrossRef](#)]
21. Fuentes-Paniagua, E.; Sanchez-Nieves, J.; Hernandez-Ros, J.M.; Fernandez-Ezequiel, A.; Soliveri, J.; Copa-Patino, J.L.; Gómez, R.; de la Mata, F.J. Structure-activity relationship study of cationic carbosilane dendritic systems as antibacterial agents. *RSC Adv.* **2016**, *6*, 7022–7033. [[CrossRef](#)]
22. Worley, B.V.; Slomberg, D.L.; Schoenfisch, M.H. Nitric oxide releasing quaternary ammonium modified poly (amido amine) dendrimers as dual action antibacterial agents. *Bioconjug. Chem.* **2014**, *25*, 918–927. [[CrossRef](#)] [[PubMed](#)]
23. Worley, B.V.; Schilly, K.M.; Schoenfisch, M.H. Anti-biofilm efficacy of dual action nitric oxide releasing alkyl chain modified poly (amidoamine) dendrimers. *Mol. Pharm.* **2015**, *12*, 1573–1583. [[CrossRef](#)] [[PubMed](#)]
24. Zhan, J.; Wang, L.; Liu, S.; Chen, J.; Ren, L.; Wang, Y. Antimicrobial hyaluronic acid/poly (amidoamine) dendrimer multilayer on poly (3-hydroxybutyrate-co-4-hydroxybutyrate) prepared by a layer-by-layer self-assembly method. *ACS Appl. Mater. Interfaces* **2015**, *7*, 13876–13881. [[CrossRef](#)] [[PubMed](#)]
25. Carmona-Ribeiro, A.M.; de Melo Carrasco, L.D. Cationic antimicrobial polymers and their assemblies. *Int. J. Mol. Sci.* **2013**, *14*, 9906–9946. [[CrossRef](#)] [[PubMed](#)]
26. Kolb, H.C.; Finn, M.G.; Sharpless, K.B. Click chemistry: Diverse chemical function from a few good reactions. *Angew. Chem. Int. Ed.* **2001**, *40*, 2004–2021. [[CrossRef](#)]
27. Franc, G.; Kakkar, A.K. Click methodologies: Efficient, simple and greener routes to design dendrimers. *Chem. Soc. Rev.* **2010**, *39*, 1536–1544. [[CrossRef](#)] [[PubMed](#)]
28. Arseneault, M.; Wafer, C.; Morin, J.-F. Recent advances in click chemistry applied to dendrimer synthesis. *Molecules* **2015**, *20*, 9263–9294. [[CrossRef](#)] [[PubMed](#)]
29. Ortega, P.; Copa-Patiño, J.L.; Muñoz-Fernandez, M.A.; Soliveri, J.; Gomez, R.; de la Mata, F.J. Amine and ammonium functionalization of chloromethylsilane-ended dendrimers. Antimicrobial activity studies. *Org. Biomol. Chem.* **2008**, *6*, 3264–3269. [[CrossRef](#)] [[PubMed](#)]
30. Lopez, A.I.; Reins, R.Y.; McDermott, A.M.; Trautner, B.W.; Cai, C. Antibacterial activity and cytotoxicity of PEGylated poly (amidoamine) dendrimers. *Mol. Biosyst.* **2009**, *5*, 1148–1156. [[CrossRef](#)] [[PubMed](#)]
31. Andrews, J.M. Determination of minimum inhibitory concentrations. *J. Antimicrob. Chemother.* **2001**, *48*, 5–16. [[CrossRef](#)] [[PubMed](#)]
32. Vieyres, A.; Lam, T.; Gillet, R.; Franc, G.; Castonguay, A.; Kakkar, A. Combined Cu(I)-catalysed alkyne-azide cycloaddition and furan-maleimide Diels-Alder “click” chemistry approach to thermoresponsive dendrimers. *Chem. Commun.* **2010**, *46*, 1875–1877. [[CrossRef](#)] [[PubMed](#)]

33. Zhao, Y.-L.; Dichtel, W.R.; Trabolsi, A.; Saha, S.; Aprahamian, I.; Stoddart, J.F. A redox-switchable alpha-cyclodextrin-based [2]rotaxane. *J. Am. Chem. Soc.* **2008**, *130*, 11294–11296. [[CrossRef](#)] [[PubMed](#)]
34. Touaibia, M.; Wellens, A.; Shiao, T.C.; Wang, Q.; Sirois, S.; Bouckaert, J.; Roy, R. Mannosylated G(0) Dendrimers with Nanomolar Affinities to Escherichia coli FimH. *Chem. Med. Chem.* **2007**, *2*, 1190–1201. [[CrossRef](#)] [[PubMed](#)]

Sample Availability: Not available.



© 2017 by the authors. Licensee MDPI, Basel, Switzerland. This article is an open access article distributed under the terms and conditions of the Creative Commons Attribution (CC BY) license (<http://creativecommons.org/licenses/by/4.0/>).

Article

Epitaxially Grown Ultra-Flat Self-Assembling Monolayers with Dendrimers

Takane Imaoka^{1,2,3}, Noriko Bukeo¹ and Kimihisa Yamamoto^{1,2,*}

¹ Laboratory for Chemistry and Life Science, Institute of Innovative Research, Tokyo Institute of Technology, Yokohama 225-8503, Japan; timaoka@res.titech.ac.jp (T.I.); norinya13@hotmail.com (N.B.)

² ERATO, Japan Science and Technology Agency, Chiyoda 102-0076, Japan

³ PRESTO, Japan Science and Technology Agency, Chiyoda 102-8666, Japan

* Correspondence: yamamoto@res.titech.ac.jp; Tel.: +81-45-924-5260

Received: 17 January 2018; Accepted: 14 February 2018; Published: 23 February 2018

Abstract: Mono-molecular films formed by physical adsorption and dendrimer self-assembly were prepared on various substrate surfaces. It was demonstrated that a uniform dendrimer-based monolayer on the subnanometer scale can be easily constructed via simple dip coating. Furthermore, it was shown that an epitaxially grown monolayer film reflecting the crystal structure of the substrate (highly ordered pyrolytic graphite (HOPG)) can also be formed by aligning specific conditions.

Keywords: dendrimers; epitaxial growth; self-assembling monolayers; surface modification

1. Introduction

Self-assembled monolayers (SAMs) comprise a fundamental bottom-up nanotechnology technique widely used for applications such as interface control and solid surface functionalization. The most commonly used method for such bottom-up fabrication consists in SAM films utilizing thiol chemisorption on the Au substrate surface [1]. Despite being an extremely simple method that does not require any special equipment, it is robust and causes few defects (pinhole or line defect) under appropriate conditions [2,3]. However, there are limitations with these techniques in terms of the substrates and depositing materials. Therefore, generic SAM forming technology that can be used in all situations is in high demand. Here we present a new strategy of preparing such SAMs utilizing dendrimers.

2. Results and Discussion

Although dendrimers are a class of macromolecules, they have a single molecular weight and a single structure [4–6]. Their compact structures allow for the formation of various higher order self-assembling structure owing to the weak and omnidirectional intermolecular interactions [7,8]. The material used in this study is phenylazomethine dendrimers with a zinc porphyrin core (**1**) [9–11]. Furthermore, this dendrimer has a capability for the precise accumulation for various metal ions [12] and organic molecules [13,14] in the interior. Therefore, it is a suitable molecule with many potential post-functionalization such as templated cluster synthesis [15–19], molecular shape recognition [11], anisotropic charge transfer [10,20–22], and further extension of the structural dimensions [23,24]. The dendrimer **1** (Figure 1) was synthesized according to a literature method [9] and deposited on the atomically flat surfaces of substrates including mica, HOPG (highly ordered pyrolytic graphite), and Au(111). We employed a dip-coating method to fabricate the dendrimer adlayer on these surfaces via immersion of **1** into a dilute solution ($1 \mu\text{mol L}^{-1}$) in benzene for 1 min under ambient conditions.

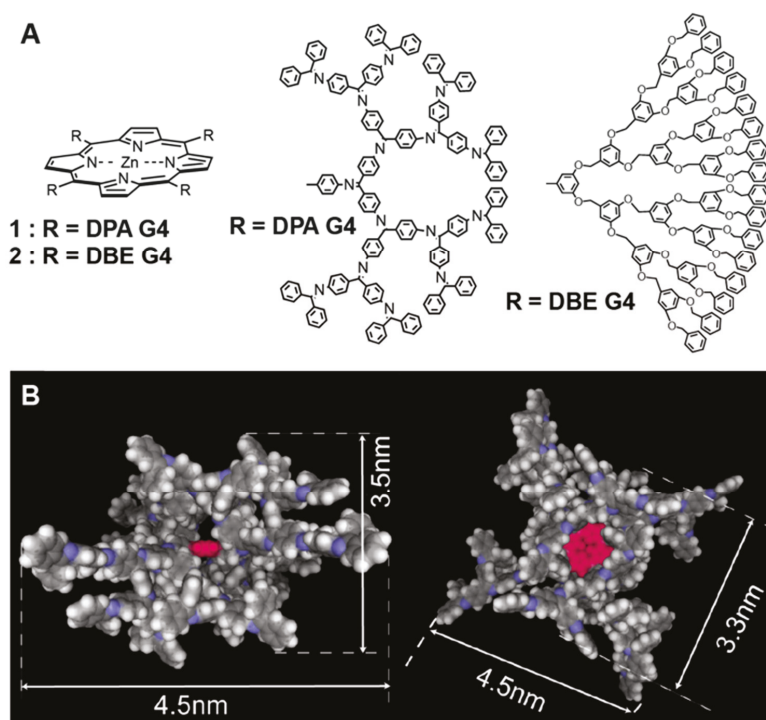


Figure 1. Structure of phenylazomethine dendrimer with a zinc porphyrin core (**1**). (a) Side view; (b) top view.

Non-contact AFM (atomic-force microscopy) observations were carried out on the resulting surfaces modified with **1**, and topographic images are shown in Figure 2. Results of the mica substrates showed a highly coated flat surface modified with **1**, of which roughness was less than 0.1 nm, which is a level comparable to or higher than those previously reported [25,26]. Although a few pinholes were observed, the surface coverage factor was 98.8%, which can increase to 99.5% if toluene, instead of benzene, is used as the solvent. When the non-dehydrated grade of the solvent was used, the number and area of the pinholes increased. This means that pinholes are due to trace amounts of water in the solvents. The coverage of the SAMs was unexpectedly high. Even though SAMs via alkane thiols are well-established, many defects (holes) generally form on gold surfaces via immersion at room temperature [2,3]. In contrast, with this dendrimer, SAMs can be produced with low defects, even at room temperature. For the control experiment, a fourth-generation benzylether dendrimer (**2**) with the same zinc porphyrin core [27] and a similar molecular weight and hydrophobicity was employed. However, as opposed to monolayer films such as phenylazomethine dendrimers under the same conditions, many aggregates with a height of about 10 nm were observed (Figure S1).

These deposits are regarded as a monolayer of **1** because the maximum height of each step at the pinholes was ca. 1 nm. Because the step height of the surface layer observed at the place intentionally scratched in the contact mode was the same height of the pinhole, the pinhole was considered to have penetrated the substrate surface. The height of about 1 nm observed was shorter than the shorter axis of the dendrimer molecule and appeared to be inconsistent. However, as previously reported, it is not appropriate to approximate a dendrimer as a rigid sphere. It is natural to consider that the shrinking structure observed was a result of the repulsive force from the cantilever. When the concentration was reduced to 1/10, the depth remained at 1 nm, but the surface coverage drastically decreased

(Figure S2). This means that a depth of 1 nm corresponds to one molecule of the dendrimer, which cannot be divided. On the other hand, when a dendrimer solution concentration one or two orders higher (10 or 100 $\mu\text{mol L}^{-1}$) was used for the coating, the depth of the adlayer was increased to 2 or 4 nm, respectively (Figure S2). It is worth noting that the thickness of a smooth deposited layer at the molecular level can be freely changed at the level of 1 nm simply by changing the concentration of the solution. A similar SAM was also observed on highly oriented pyrolytic graphite (HOPG). XPS results indicating the presence of zinc atoms (Figure S3) on a modified surface of HOPG also proved the existence of **1**. In addition, cyclic voltammograms of the SAM-modified HOPG electrode (Figure S4) demonstrated that this assumption was valid. Total faradaic charge (0.62 μC) observed as one-electron oxidation of the zinc porphyrin core at 0.3 V vs. Ag/AgCl was equivalent to the calculated value (0.61 μC). The theoretical value was calculated on the assumption that a hexagonal close-packing monolayer of the dendrimer with a spacing of 4.4 nm formed on the electrode, the diameter of which was 9 nm. This spacing is based on a doubling of the hydrodynamic radii of the dendrimer.

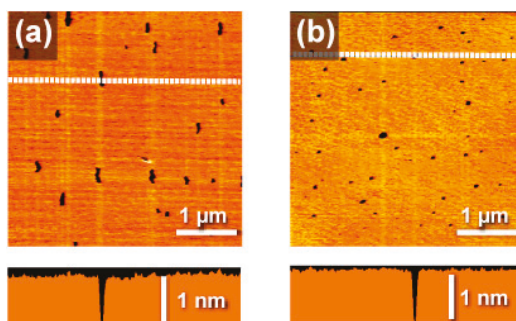


Figure 2. AFM (atomic-force microscopy) topographic images of the self-assembled monolayer (SAM) of **1** on mica. The fabrication was carried out through a dip-coating in a benzene (a) or toluene (b) solution of **1** (1 $\mu\text{mol L}^{-1}$). Lower images are the cross section along the dashed lines shown in the topographic images.

More interestingly, unique surface textures, as shown in Figure 3a, were occasionally found when the HOPG was used as the substrate for the benzene solution. The topography includes two different altitudes of terrace. The lower altitude sections that look like a valley were surrounded by a very flat 1 nm depth adlayer corresponding to the dendrimer monolayer. According to a higher magnification image (Figure S5), the lower layer is considered to be the surface of the HOPG because it is flat at the atomic level, whereas the higher layer is considered to be a layer of dendrimers since it shows slight irregularities.

Valleys in the monolayer lead to three specific directions. Angles between each direction were all 120° (or 60°), suggesting that the texture includes the regularity of C_3 symmetry. Symmetric dendrimers including phenylazomethine dendrimers, like the carbon atoms in HOPG, are known to form a hexagonal close-packing (hcp) crystal on a flat surface. Based on this idea, we speculated that the surface monolayer formed through an epitaxial growth along the crystal structure of HOPG. However, it is not clear whether this mesophase structure was observed as an incompleteness of the crystal growth or the thermodynamically stable structure.

To explain the origin of the geometric pattern, we examined different conditions of the fabrication. First, the immersion time was varied from 30 s to 10 min. However, no dependence on time was observed in the formation of the SAM of the dendrimer. Similarly, no variation was found when the concentration was reduced to 0.5 $\mu\text{mol L}^{-1}$, indicating that the formation of the SAM reached an equilibrium condition. Therefore, we determined that the valleys originated from factors that prevented the adsorption of **1**.

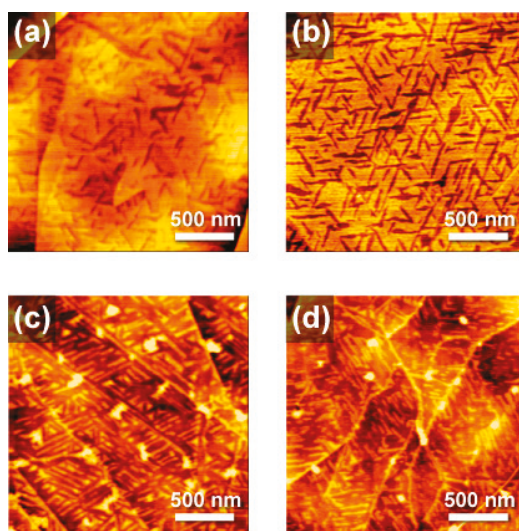


Figure 3. AFM topographic images of the SAM of **1** on highly oriented pyrolytic graphite (HOPG). The fabrication was carried out through dip-coating in a benzene solution of **1** ($1 \mu\text{mol L}^{-1}$) in the absence (a) and presence of naphthalene (b–d). The concentration of naphthalene was $50 \mu\text{mol L}^{-1}$ (b), $100 \mu\text{mol L}^{-1}$ (c) and $200 \mu\text{mol L}^{-1}$ (d).

Benzene molecules weakly adsorb to monocrystalline surfaces [28], including those of HOPG [29]. If solvent adsorption is a primary factor, this surface pattern should only appear with certain solvents such as benzene. For the control experiment, the same modification procedure was tested using toluene as the solvent. Because no characteristic pattern was found except for the flat dendrimer monolayer (Figure S6), the idea that the benzene molecule plays an important role in pattern formation was supported. This idea was further supported by additional experiments employing the other adsorbate. In particular, the naphthalene molecule was found to be a good candidate for the co-adsorbate. As shown in Figure 3b–d, the SAM prepared in the presence of naphthalene ($100 \mu\text{mol L}^{-1}$) clearly showed the geometric pattern, and the texture was controllable by the concentration of naphthalene. When the concentration of naphthalene was increased to $200 \mu\text{mol L}^{-1}$, a significant decrease in the coverage ratio was shown, which was confirmed by lowering the bright area that the dendrimer SAM covered. In this case, discrete line-shaped islands (bright area) of the SAM 1 nm high were formed on the HOPG surface (dark area). A much lower concentration ($50 \mu\text{mol L}^{-1}$) of naphthalene resulted in a higher coverage ratio, but the coverage was still lower than that formed without naphthalene. In this case, a periodic SAM that included many valleys formed. In any case, the islands or clacks were aligned in three specific directions, suggesting the epitaxial growth along the HOPG structure. In contrast to the case where naphthalene was used as a co-adsorbing molecule, no characteristic pattern was observed in any of the other extended π electron-based compounds. In these cases, only a simple monomolecular film was formed. This result suggests that the balance of adsorption energy of the dendrimer and the co-adsorption molecule to the substrate is important for the pattern formation.

3. Materials and Methods

The fourth-generation poly-phenylazomethine dendrimer (**1**) [9] and the poly-benzylether dendrimer (**2**) [27], both bearing a zinc porphyrin core, were synthesized according to a previously reported method. Other chemicals and solvents were purchased from Kantoh Kagaku Co. Ltd. (Tokyo, Japan). Natural mica substrates were purchased from Nilaco Co. (Tokyo, Japan), and the surfaces were

cleaved just before use. Other substrates including HOPG (NT-MDT) and Au(111) on mica (Phasis) were purchased as commercial products.

The surfaces of mica and HOPG were cleaved just before processing. The dip-coating of dendrimers on a substrate was carried out by simply dipping the substrate into each dendrimer solution (solvent and concentration are shown in the main text) for 1 min. After the substrate was lifted out of the solution, excess solution was removed, and the sample substrates were dried under vacuum for 12 h at room temperature. The resulting surfaces were observed by non-contact atomic force microscopy (AFM) with a scanning probe microscope (SPI3800N, SII) using a standard silicon cantilever with Al coating (SI-DF-40P2, SII). Fast Fourier transform (FFT) processing was carried out using built-in software.

Electrochemical measurements were performed using a multipurpose electrochemical workstation (ALS-750b, CH Instruments, Austin, TX, USA). A vassal-plane carbon disk electrode (3.0 mm diameter purchased from BAS Inc., Tokyo, Japan.) was used as the working electrode. The electrode surface was polished with diamond and alumina paste and then rinsed in methanol with ultrasonication prior to use. Similar to the mica or HOPG substrates, the electrode surface was modified with the dendrimer 1. An Ag/AgCl electrode in 3 mol L⁻¹ NaCl_{aq} and a platinum coil were used as the quasi-reference and counter electrodes, respectively. Cyclic voltammetry (CV) and RDV measurements were conducted in an aqueous KPF₆ solution (0.1 mol L⁻¹), which was thoroughly bubbled with O₂ or N₂ gas prior to the measurements.

XPS were obtained using a spectrometer (JEOL, JPS-9000MC) with Mg K α radiation. For the XPS measurement, gold powder was deposited on a glassy carbon substrate (Tokai Carbon Co., Ltd., Tokyo, Japan) as an internal standard with the cluster sample, and the Au 4f_{7/2} (84.0 eV) peak was used to offset the electron binding energy.

4. Conclusions

In summary, we have successfully prepared a dendrimer-based SAM on various substrates. The formation of a highly oriented texture pattern can be implemented through a simple dip-coating method. Employment of the co-adsorbate such as naphthalene, probably due to the epitaxy, can control this texture pattern. Although an example of epitaxial adsorption has been reported with respect to small organic molecules [30], this is the first epitaxy of a dendrimer to the best of our knowledge. The present results suggest that islands of the co-adsorbate molecule play a role as a guide for the patterning. Although the adsorption of benzene or naphthalene molecules to the HOPG surface is relatively weak, phase segregation between the packing structure of the dendrimer and the co-adsorbate should be considered an important factor for mesophase patterning. Similar to self-assembling phenomena reported elsewhere [31], a moderate balance between the intermolecular and interfacial adsorption energy might be essential for the production of a higher-order architecture.

Supplementary Materials: Supplementary materials are available online.

Acknowledgments: This study was supported by JST ERATO Grant Number JPMJER1503, Japan (K.Y.), JST PRESTO Grant Number JPMJPR1511, Japan (T.I.), JSPS KAKENHI Grant Nos. JP 15H05757 (K.Y.), and JP 16H04115 (T.I.). We thank Yoko Hayashi (Tokyo Institute of Technology) for assistance in AFM observations.

Author Contributions: N.B. and T.I. synthesized the dendrimers. N.B. carried out the AFM observations. T.I. and K.Y. conceived experiments and co-wrote the manuscript.

Conflicts of Interest: The founding sponsors had no role in the design of the study; in the collection, analyses, or interpretation of data; in the writing of the manuscript; or in the decision to publish the results.

References

1. Love, J.C.; Estroff, L.A.; Kriebel, J.K.; Nuzzo, R.G.; Whitesides, G.M. Self-Assembled Monolayers of Thiolates on Metals as a Form of Nanotechnology. *Chem. Rev.* **2005**, *105*, 1103–1170. [[CrossRef](#)] [[PubMed](#)]
2. Poirier, G.E. Characterization of Organosulfur Molecular Monolayers on Au(111) using Scanning Tunneling Microscopy. *Chem. Rev.* **1997**, *97*, 1117–1128. [[CrossRef](#)] [[PubMed](#)]

3. Yamada, R.; Sakai, H.; Uosaki, K. Solvent Effect on the Structure of the Self-Assembled Monolayer of Alkanethiol. *Chem. Lett.* **1999**, *28*, 667–668. [[CrossRef](#)]
4. Tomalia, D.A.; Naylor, A.M.; Goddard, W.A. Starburst Dendrimers: Molecular-Level Control of Size, Shape, Surface Chemistry, Topology, and Flexibility from Atoms to Macroscopic Matter. *Angew. Chem. Int. Ed.* **1990**, *29*, 138–175. [[CrossRef](#)]
5. Tomalia, D.A.; Khanna, S.N. A Systematic Framework and Nanoperiodic Concept for Unifying Nanoscience: Hard/Soft Nanoelements, Superatoms, Meta-Atoms, New Emerging Properties, Periodic Property Patterns, and Predictive Mendeleev-like Nanoperiodic Tables. *Chem. Rev.* **2016**, *116*, 2705–2774. [[CrossRef](#)] [[PubMed](#)]
6. Tomalia, D.A. Dendrons/dendrimers: Quantized, nano-element like building blocks for soft-soft and soft-hard nano-compound synthesis. *Soft Matter* **2010**, *6*, 456–474. [[CrossRef](#)]
7. Rosen, B.M.; Wilson, C.J.; Wilson, D.A.; Peterca, M.; Imam, M.R.; Percec, V. Dendron-Mediated Self-Assembly, Disassembly, and Self-Organization of Complex Systems. *Chem. Rev.* **2009**, *109*, 6275–6540. [[CrossRef](#)] [[PubMed](#)]
8. Percec, V.; Wilson, D.A.; Leowanawat, P.; Wilson, C.J.; Hughes, A.D.; Kaucher, M.S.; Hammer, D.A.; Levine, D.H.; Kim, A.J.; Bates, F.S.; et al. Self-Assembly of Janus Dendrimers into Uniform Dendrimersomes and Other Complex Architectures. *Science* **2010**, *328*, 1009–1014. [[CrossRef](#)] [[PubMed](#)]
9. Imaoka, T.; Tanaka, R.; Arimoto, S.; Sakai, M.; Fujii, M.; Yamamoto, K. Probing Stepwise Complexation in Phenylazomethine Dendrimers by a Metallo-Porphyrin Core. *J. Am. Chem. Soc.* **2005**, *127*, 13896–13905. [[CrossRef](#)] [[PubMed](#)]
10. Imaoka, T.; Ueda, H.; Yamamoto, K. Enhancing the photoelectric effect with a potential-programmed molecular rectifier. *J. Am. Chem. Soc.* **2012**, *134*, 8412–8415. [[CrossRef](#)] [[PubMed](#)]
11. Imaoka, T.; Kawana, Y.; Kurokawa, T.; Yamamoto, K. Macromolecular semi-rigid nanocavities for cooperative recognition of specific large molecular shapes. *Nat. Commun.* **2013**, *4*, 2581. [[CrossRef](#)] [[PubMed](#)]
12. Yamamoto, K.; Imaoka, T. Dendrimer complexes based on fine-controlled metal assembling. *Bull. Chem. Soc. Jpn.* **2006**, *79*, 511–526. [[CrossRef](#)]
13. Ochi, Y.; Fujii, A.; Nakajima, R.; Yamamoto, K. Stepwise Radial Complexation of Triphenylmethylions on a Phenylazomethine Dendrimer for Organic–Metal Hybrid Assembly. *Macromolecules* **2010**, *43*, 6570–6576. [[CrossRef](#)]
14. Ochi, Y.; Suzuki, M.; Imaoka, T.; Murata, M.; Nishihara, H.; Einaga, Y.; Yamamoto, K. Controlled storage of ferrocene derivatives as redox-active molecules in dendrimers. *J. Am. Chem. Soc.* **2010**, *132*, 5061–5069. [[CrossRef](#)] [[PubMed](#)]
15. Yamamoto, K.; Imaoka, T. Precision synthesis of subnanoparticles using dendrimers as a superatom synthesizer. *Acc. Chem. Res.* **2014**, *47*, 1127–1136. [[CrossRef](#)] [[PubMed](#)]
16. Yamamoto, K.; Imaoka, T.; Chun, W.-J.; Enoki, O.; Katoh, H.; Takenaga, M.; Sono, A. Size-specific catalytic activity of platinum clusters enhances oxygen reduction reactions. *Nat. Chem.* **2009**, *1*, 397–402. [[CrossRef](#)] [[PubMed](#)]
17. Imaoka, T.; Kitazawa, H.; Chun, W.-J.; Yamamoto, K. Finding the Most Catalytically Active Platinum Clusters with Low Atomcity. *Angew. Chem. Int. Ed.* **2015**, *127*, 9948–9953. [[CrossRef](#)]
18. Takahashi, M.; Koizumi, H.; Chun, W.-J.; Kori, M.; Imaoka, T.; Yamamoto, K. Finely controlled multimetallic nanocluster catalysts for solvent-free aerobic oxidation of hydrocarbons. *Sci. Adv.* **2017**, *3*, e1700101. [[CrossRef](#)] [[PubMed](#)]
19. Imaoka, T.; Kitazawa, H.; Chun, W.-J.; Omura, S.; Albrecht, K.; Yamamoto, K. Magic Number Pt₁₃ and Misshapen Pt₁₂ Clusters: Which One is the Better Catalyst? *J. Am. Chem. Soc.* **2013**, *135*, 13089–13095. [[CrossRef](#)] [[PubMed](#)]
20. Imaoka, T.; Inoue, N.; Yamamoto, K. Electron-transfer through potential gradient based on a dendrimer architecture. *Chem. Commun.* **2012**, *48*, 7235–7237. [[CrossRef](#)] [[PubMed](#)]
21. Imaoka, T.; Kobayashi, H.; Katsurayama, M.; Yamamoto, K. A potential gradient along the layer-by-layer architecture for electron transfer rectification. *Dalton Trans.* **2015**, *44*, 15116–15120. [[CrossRef](#)] [[PubMed](#)]
22. Imaoka, T.; Inoue, N.; Yamamoto, K. Extended Potential-Gradient Architecture of a Phenylazomethine Dendrimer. *Org. Lett.* **2013**, *15*, 1810–1813. [[CrossRef](#)] [[PubMed](#)]
23. Albrecht, K.; Hirabayashi, Y.; Otake, M.; Mendori, S.; Tobar, Y.; Azuma, Y.; Majima, Y.; Yamamoto, K. Polymerization of a divalent/tetravalent metal-storing atom-mimicking dendrimer. *Sci. Adv.* **2016**, *2*, e1601414. [[CrossRef](#)] [[PubMed](#)]

24. Imaoka, T.; Bukeo, N.; Yamamoto, K. A Self-Assembling Dendritic Reactor: Versatile Formation of Characteristic Patterns with Nanoscale Dimension. *Macromol. Rapid Commun.* **2015**, *36*, 616–620. [[CrossRef](#)] [[PubMed](#)]
25. Tsukruk, V.V.; Rinderspacher, F.; Bliznyuk, V.N. Self-Assembled Multilayer Films from Dendrimers. *Langmuir* **1997**, *13*, 2171–2176. [[CrossRef](#)]
26. Hierlemann, A.; Campbell, J.; Baker, L.; Crooks, R.M.; Ricco, A.J. Structural Distortion of Dendrimers on Gold Surfaces: A Tapping-Mode AFM Investigation. *J. Am. Chem. Soc.* **1998**, *120*, 5323–5324. [[CrossRef](#)]
27. Pollak, K.W.; Leon, J.W.; Frechet, J.M.J.; Maskus, M.; Abruña, H.D. Effects of Dendrimer Generation on Site Isolation of Core Moieties: Electrochemical and Fluorescence Quenching Studies with Metalloporphyrin Core Dendrimers. *Chem. Mater.* **1998**, *10*, 30–38. [[CrossRef](#)]
28. Wan, L.; Itaya, K. In situ scanning tunnelling microscopy of benzene, naphthalene, and anthracene adsorbed on Cu(111) in solution. *Langmuir* **1997**, *13*, 7173–7179. [[CrossRef](#)]
29. Chakarova-Kack, S.; Schroder, E.; Lundqvist, B.; Langreth, D. Application of van der Waals density functional to an extended system: Adsorption of benzene and naphthalene on graphite. *Phys. Rev. Lett.* **2006**, *96*, 146107. [[CrossRef](#)] [[PubMed](#)]
30. Miyamoto, Y.; Nemoto, T.; Yoshida, K.; Kurata, H.; Isoda, S. In situ atomic force microscopy observation of the desorption process from monomolecular organic layers of a naphthalene derivative. *Jpn. J. Appl. Phys.* **2004**, *43*, 4606–4609. [[CrossRef](#)]
31. Elemans, J.A.A.W.; Lei, S.; de Feyter, S. Molecular and Supramolecular Networks on Surfaces: From Two-Dimensional Crystal Engineering to Reactivity. *Angew. Chem. Int. Ed.* **2009**, *48*, 7298–7332. [[CrossRef](#)] [[PubMed](#)]

Sample Availability: All the reported data and samples are available from the corresponding authors on reasonable request.



© 2018 by the authors. Licensee MDPI, Basel, Switzerland. This article is an open access article distributed under the terms and conditions of the Creative Commons Attribution (CC BY) license (<http://creativecommons.org/licenses/by/4.0/>).

Article

Cation, Anion and Ion-Pair Complexes with a G-3 Poly(ethylene imine) Dendrimer in Aqueous Solution

Matteo Savastano ¹, Carla Bazzicalupi ¹, Claudia Giorgi ¹, Paola Gratteri ² and Antonio Bianchi ^{1,*}

¹ Department of Chemistry “Ugo Schiff”, via della Lastruccia 3, 50019 Sesto Fiorentino, Italy;

matteo.savastano@unifi.it (M.S.); carla.bazzicalupi@unifi.it (C.B.); Claudia.giorgi@unifi.it (C.G.)

² NEUROFARBA Department, Pharmaceutical and Nutraceutical Section, and Laboratory of Molecular Modeling Cheminformatics & QSAR, University of Florence, Via Ugo Schiff 6, 50019 Sesto Fiorentino, Italy; paola.gratteri@unifi.it

* Correspondence: antonio.bianchi@unifi.it; Tel.: +39-055-457-3254

Academic Editor: Ashok Kakkur

Received: 12 April 2017; Accepted: 12 May 2017; Published: 16 May 2017

Abstract: The G-3 poly(ethylene imine) ligand L2 shows a multifaceted coordination ability, being able to bind metal cations, anions and ion-pairs. The equilibrium constants for the formation of metal (Cu^{2+} , Zn^{2+}), anion (SO_4^{2-}) and ion-pair ($\text{Cu}^{2+}/\text{SO}_4^{2-}$) complexes were determined in 0.1 M Me_4NCl aqueous solution at 298.1 ± 0.1 K by means of potentiometric titrations. Thanks to its dendrimeric nature, L2 can form highly nucleated metal complexes, such as $\text{Cu}_5\text{L}2^{10+}$ and $\text{Zn}_4\text{L}2^{8+}$, in successive and well-defined complexation steps. Protonated forms of L2 give rise to relatively weak anion complexes with SO_4^{2-} , but the addition of Cu^{2+} significantly enhances the binding ability of the ligand toward this anion below pH 9. In more alkaline solutions, an opposite trend is observed. The coordination properties of L2 are discussed with the support of modelling calculations. According to results, L2 is a promising molecule for the preparation of solid supported materials for the recovery of cations and anions from aqueous media and/or for applications in heterogeneous catalysis.

Keywords: copper; zinc; dendrimers; poly(ethylene imine); polynuclear complexes; anion complexes; ion-pair complexes

1. Introduction

In recent papers, we showed that the G-2 poly(ethylene imine) dendrimer L1 (Figure 1) and its variously protonated forms are able to assemble stable cation, anion and ion-pair complexes in aqueous solution [1–4]. Such ability appears to be a propagation and an enhancement of the properties of the parent ligand tris(2-aminoethyl)amine (*tren*), which is historically known to bind metal complexes and, more recently, has also been accredited as a rather efficient anion receptor [5]. Indeed, regarding the coordination of metal ions, while *tren* forms stable mononuclear complexes, L1 can bind two metal ions such as Ni^{2+} , Zn^{2+} and Cd^{2+} and up to three Cu^{2+} and Hg^{2+} ions [1,4]. L1 and its metal complexes are also able to bind inorganic anions [2] as well as the anionic forms of AMP, ADP and ATP nucleotides acting as catalysts that enhance significantly ATP dephosphorylation in aqueous solution [3]. Construction of a third generation of ethylamino branches around L1 gave rise to the G-3 poly(ethylene imine) dendrimer L2 (Figure 1) that is also able to bind anions, such as PO_4^{3-} , $\text{P}_2\text{O}_7^{4-}$ and $\text{P}_3\text{O}_{10}^{5-}$, and AMP, ADP and ATP nucleotides. In particular, L2 showed an unprecedented behaviour toward ATP, the dendrimer being able to enhance or inhibit dephosphorylation of the nucleotide depending on the solution pH [6].

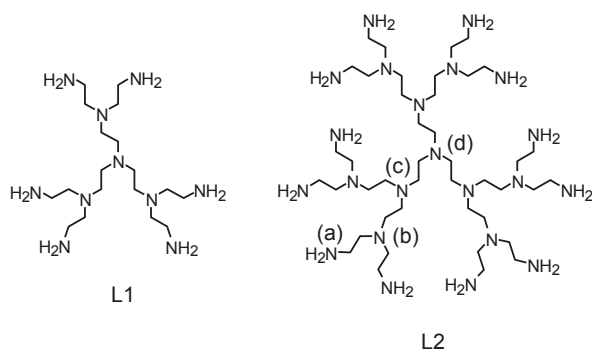


Figure 1. G-2 (L1) and G-3 (L2) poly(ethylene imine) dendrimers.

Despite the discovery of such properties towards nucleotide and phosphate type anions, the ability of L2 to bind metal cations, inorganic anions and ion-pairs remains unexplored. Actually, L2 is a very interesting ligand for the formation of metal complexes, in particular of polynuclear assemblies, since it contains a large number (22) of nitrogen donor atoms in its molecular structure, and accordingly, it should be able to form complexes of greater nuclearity than the smaller homologous L1. It is worth of note that there is a great deal of interest toward polynuclear metal complexes, especially for their catalytic properties and/or for their use in the generation of metal nanoparticle-based catalysts [7–10].

This has aroused our interest in performing a detailed analysis of the complexation equilibria involving L2, metal cations and anions in aqueous solution. As previously noted [1], to study similar complexation systems is an arduous task, due to the many equilibria involving the stepwise coordination of several metal ions involving several protonation states for each complexation step. Attempts to perform the speciation of complex systems and determining the equilibrium constants for complexation equilibria with other poly(ethylene imine) dendrimers were made by considering the repeating triamine units of the dendrimer as identical independent ligand molecules, under the implicit assumption that these repeating units were uniformly distributed in solution, in contrast to their actual localization within the same dendrimer molecule [11]. These studies were performed under conditions approaching the ligand coordinative saturation, the metal-to-triamine unit ratios being closed to 1:1 and extending it, at most, up to 1:4.

Despite such an approximation, the results of these studies can be functional for the purposes for which they are developed, although they furnish an incomplete picture of the complexation systems. In particular, this approach leads to the identification of a limited number of complex species relative to the many that these dendrimers can form. For instance, dendrimers containing large numbers of amino groups are expected to bind metal ions even when they are extensively protonated. Some of the missing species could have interesting properties, like the ability of highly protonated Zn(II) complexes with L1 to promote the binding and the dephosphorylation of ATP [3].

In this paper, we report the results of a detailed analysis of the complexation systems formed by L2 with Zn^{2+} and Cu^{2+} that led to the identification of 35 and 42 complex species for Zn^{2+} and Cu^{2+} , respectively, the ligand achieving the stepwise coordination of 4 Zn^{2+} or 5 Cu^{2+} ions. Once these complexation systems were clearly defined, we analysed the ability of L2 to interact with SO_4^{2-} both in the absence and in the presence of Cu^{2+} .

2. Results and Discussion

2.1. Formation of Metal Complexes

Speciation of $\text{L2}/\text{Cu}^{2+}$ and $\text{L2}/\text{Zn}^{2+}$ complex systems and determination of the relevant stability constants were performed by means of pH-metric (potentiometric) titrations (0.1 M Me_4NCl ,

298.1 ± 0.1 K) and analysis of the associated data by means of the computer program HYPERQUAD [12] which furnished the stability constants collected in Tables 1 and 2 for Cu²⁺ and Zn²⁺, respectively. Distribution diagrams of the complexes formed are reported in Figures S1 and S2.

As shown by these tables, the G-3 dendrimer L2 is able to bind in successive steps from one to five Cu²⁺ cations and from one to four Zn²⁺ ions. According to the presence of many (22) nitrogen donor atoms in the ligand, all complexes but Cu₅L2¹⁰⁺ are able to bind protons, and the number of protonated species they form decreases with increasing complex nuclearity. It was previously reported that protonation of the primary amine groups of L2 is associated with protonation constants logK ≥ 8.3 [6]. Considering this value as the limiting value for protonation of primary amine groups also in L2 complexes, we can deduce from the equilibrium data in Table 1 that, in CuL2²⁺, there are nine primary amine groups, out of 12, that are not involved in metal coordination. By similar reasoning, and taking into account the experimental errors on the determined equilibrium constants, the number of uncoordinated primary nitrogens can be reasonably estimated as six in Cu₂L2⁴⁺, five in Cu₃L2⁶⁺, three in Cu₄L2⁸⁺, and none in Cu₅L2¹⁰⁺. The equilibrium constants for the successive binding of the first and the second Cu²⁺ ions are very high (logK = 23.66 and 22.9, Table 1) and consistent with the stability of hexacoordinated Cu²⁺ complexes of polyamines [13,14]. Accordingly, the first two Cu²⁺ ions binding L2 should be coordinated by three primary and three secondary amine groups near the surface of the G-3 dendrimer. The third coordination stage causes a greater involvement of the inner dendrimer region, since only one primary amine group is involved in the equilibrium Cu₂L2⁴⁺ + Cu²⁺ = Cu₃L2⁶⁺. This appears to be a poorly favourable coordination step as shown by the surprisingly low value of the corresponding equilibrium constant (logK = 10.0, Table 1).

Table 1. Stability constants of Cu²⁺ complexes with L2. 0.1 M Me₄NCl, 298.1 ± 0.1 K. Values in parentheses are standard deviation on the last significant figure.

Equilibria	logK	Equilibria	logK
Cu ²⁺ + L2 = CuL2 ²⁺	23.66 (5)	Cu ₂ H ₇ L2 ¹¹⁺ + H ⁺ = Cu ₂ H ₈ L2 ¹²⁺	7.46 (8)
CuL2 ²⁺ + 2H ⁺ = CuH ₂ L2 ⁴⁺	22.88 (7)	Cu ₂ H ₈ L2 ¹²⁺ + H ⁺ = Cu ₂ H ₉ L2 ¹³⁺	6.25 (8)
CuH ₂ L2 ⁴⁺ + H ⁺ = CuH ₃ L2 ⁵⁺	9.93 (5)	Cu ₂ H ₉ L2 ¹³⁺ + H ⁺ = Cu ₂ H ₁₀ L2 ¹⁴⁺	4.98 (7)
CuH ₃ L2 ⁵⁺ + H ⁺ = CuH ₄ L2 ⁶⁺	10.07 (5)	Cu ₂ H ₁₀ L2 ¹⁴⁺ + H ⁺ = Cu ₂ H ₁₁ L2 ¹⁵⁺	4.07 (7)
CuH ₄ L2 ⁶⁺ + H ⁺ = CuH ₅ L2 ⁷⁺	9.42 (3)		
CuH ₅ L2 ⁷⁺ + H ⁺ = CuH ₆ L2 ⁸⁺	9.21 (7)	3Cu ²⁺ + L2 = Cu ₃ L2 ⁶⁺	56.55 (7)
CuH ₆ L2 ⁸⁺ + H ⁺ = CuH ₇ L2 ⁹⁺	9.09 (7)	Cu ₂ L2 ⁴⁺ + Cu ²⁺ = Cu ₃ L2 ⁶⁺	10.0 (1)
CuH ₇ L2 ⁹⁺ + H ⁺ = CuH ₈ L2 ¹⁰⁺	8.63 (5)	Cu ₃ L2 ⁶⁺ + 2H ⁺ = Cu ₃ H ₂ L2 ⁸⁺	22.72 (6)
CuH ₈ L2 ¹⁰⁺ + H ⁺ = CuH ₉ L2 ¹¹⁺	8.50 (4)	Cu ₃ H ₂ L2 ⁸⁺ + H ⁺ = Cu ₃ H ₃ L2 ⁹⁺	10.31 (7)
CuH ₉ L2 ¹¹⁺ + H ⁺ = CuH ₁₀ L2 ¹²⁺	8.13 (4)	Cu ₃ H ₃ L2 ⁹⁺ + H ⁺ = Cu ₃ H ₄ L2 ¹⁰⁺	8.87 (8)
CuH ₁₀ L2 ¹²⁺ + H ⁺ = CuH ₁₁ L2 ¹³⁺	7.49 (4)	Cu ₃ H ₄ L2 ¹⁰⁺ + H ⁺ = Cu ₃ H ₅ L2 ¹¹⁺	8.50 (8)
CuH ₁₁ L2 ¹³⁺ + H ⁺ = CuH ₁₂ L2 ¹⁴⁺	5.87 (4)	Cu ₃ H ₅ L2 ¹¹⁺ + H ⁺ = Cu ₃ H ₆ L2 ¹²⁺	7.39 (7)
CuH ₁₂ L2 ¹⁴⁺ + H ⁺ = CuH ₁₃ L2 ¹⁵⁺	5.18 (4)	Cu ₃ H ₆ L2 ¹²⁺ + H ⁺ = Cu ₃ H ₇ L2 ¹³⁺	6.82 (8)
CuH ₁₃ L2 ¹⁵⁺ + H ⁺ = CuH ₁₄ L2 ¹⁶⁺	3.94 (5)	Cu ₃ H ₇ L2 ¹³⁺ + H ⁺ = Cu ₃ H ₈ L2 ¹⁴⁺	5.81 (8)
CuH ₁₄ L2 ¹⁶⁺ + H ⁺ = CuH ₁₅ L2 ¹⁷⁺	2.59 (5)		
CuH ₁₅ L2 ¹⁷⁺ + H ⁺ = CuH ₁₆ L2 ¹⁸⁺	2.89 (6)	4Cu ²⁺ + L2 = Cu ₄ L2 ⁸⁺	72.6 (1)
		Cu ₃ L2 ⁶⁺ + Cu ²⁺ = Cu ₄ L2 ⁸⁺	16.0 (1)
2Cu ²⁺ + L2 = Cu ₂ L2 ⁴⁺	46.53 (7)	Cu ₄ L2 ⁸⁺ + 2H ⁺ = Cu ₄ H ₂ L2 ¹⁰⁺	22.5 (1)
CuL2 ²⁺ + Cu ²⁺ = Cu ₂ L2 ⁴⁺	22.9 (1)	Cu ₄ H ₂ L2 ¹⁰⁺ + H ⁺ = Cu ₄ H ₃ L2 ¹¹⁺	8.54 (1)
Cu ₂ L2 ⁴⁺ + H ⁺ = Cu ₂ HL2 ⁵⁺	11.51 (6)	Cu ₄ H ₃ L2 ¹¹⁺ + H ⁺ = Cu ₄ H ₄ L2 ¹²⁺	7.3 (1)
Cu ₂ HL2 ⁵⁺ + H ⁺ = Cu ₂ H ₂ L2 ⁶⁺	10.20 (7)	Cu ₄ H ₄ L2 ¹²⁺ + H ⁺ = Cu ₄ H ₅ L2 ¹³⁺	6.9 (1)
Cu ₂ H ₂ L2 ⁶⁺ + H ⁺ = Cu ₂ H ₃ L2 ⁷⁺	9.24 (7)	Cu ₄ H ₅ L2 ¹³⁺ + H ⁺ = Cu ₄ H ₆ L2 ¹⁴⁺	3.9 (1)
Cu ₂ H ₃ L2 ⁷⁺ + H ⁺ = Cu ₂ H ₄ L2 ⁸⁺	9.61 (6)		
Cu ₂ H ₄ L2 ⁸⁺ + H ⁺ = Cu ₂ H ₅ L2 ⁹⁺	8.31 (7)	5Cu ²⁺ + L2 = Cu ₅ L2 ¹⁰⁺	82.0 (2)
Cu ₂ H ₅ L2 ⁹⁺ + H ⁺ = Cu ₂ H ₆ L2 ¹⁰⁺	8.22 (7)	Cu ₄ L2 ⁸⁺ + Cu ²⁺ = Cu ₅ L2 ¹⁰⁺	9.4 (3)
Cu ₂ H ₆ L2 ¹⁰⁺ + H ⁺ = Cu ₂ H ₇ L2 ¹¹⁺	8.18 (7)	Cu ₅ L2 ¹⁰⁺ + 2OH ⁻ = [Cu ₅ L2(OH) ₂] ⁸⁺	8.5 (2)

Such a drop of the metal ion binding constant is, most likely, determined by an important structural rearrangement that the very stable Cu₂L2⁴⁺ complex must bear to accommodate the third Cu²⁺ ion. Conversely, Cu₃L2⁶⁺ displays a greater binding ability toward Cu²⁺ than Cu₂L2⁴⁺ (Cu₃L2⁶⁺ + Cu²⁺ = Cu₄L2⁸⁺, logK = 16.0, Table 1), that is, the coordination of the third Cu²⁺ ion is not very favourable but generates the structural conditions for a favourable continuation of the

stepwise binding process. Two of the 5 free primary amine groups of $\text{Cu}_3\text{L}_2^{6+}$ become coordinated in $\text{Cu}_4\text{L}_2^{8+}$, while no primary amine group appears to be available for protonation in $\text{Cu}_5\text{L}_2^{10+}$. The formation of the latter from the tetranuclear complex is accompanied by a small equilibrium constant ($\text{Cu}_4\text{L}_2^{8+} + \text{Cu}^{2+} = \text{Cu}_5\text{L}_2^{10+}$, $\log K = 9.4$, Table 1) in agreement with the high electrostatic repulsion exerting between the five metal ions and the reduced number of donor atoms remaining available for coordination in $\text{Cu}_4\text{L}_2^{8+}$. As a matter of fact, the ligand is not able to fulfil the coordination sphere of all five metal ions in $\text{Cu}_5\text{L}_2^{10+}$ and facile dissociation of coordinated water molecules generates the hydroxo complex $[\text{Cu}_5\text{L}_2(\text{OH})_2]^{8+}$.

In contrast to Cu^{2+} , in the case of Zn^{2+} complexation, the equilibrium constants for the successive binding of metal ions to form ZnL_2^{2+} , $\text{Zn}_2\text{L}_2^{4+}$, $\text{Zn}_3\text{L}_2^{6+}$ and $\text{Zn}_4\text{L}_2^{8+}$ ($\log K = 17.8, 13.2, 11.0, 10.7$, Table 2) display a more regular trend. The loss of stability from the mono- to the binuclear complex ($\log K = 17.8, 13.2$, Table 2) is greater than for the corresponding equilibria with Cu^{2+} . Nevertheless, also the stability constants for the formation of ZnL_2^{2+} and $\text{Zn}_2\text{L}_2^{4+}$ are consistent with the stability of hexacoordinated Zn^{2+} complexes with polyamines [15,16]. According to the criterium based on complex protonation constants, the number of uncoordinated primary amine group should be 9 in ZnL_2^{2+} and 6 in $\text{Zn}_2\text{L}_2^{4+}$, in agreement with a coordination sphere constituted by three primary and three tertiary nitrogen atoms for both metal ions. Binding of the third Zn^{2+} ion takes place with further decrease of stability ($\text{Zn}_2\text{L}_2^{4+} + \text{Zn}^{2+} = \text{Zn}_3\text{L}_2^{6+}$, $\log K = 11.0$, Table 2). At this stage, another three primary amine groups become involved in metal binding, suggesting a similar hexacoordination for all three metal ions in $\text{Zn}_3\text{L}_2^{6+}$. An insignificant decrease of binding constant is instead observed at the fourth coordination step ($\text{Zn}_3\text{L}_2^{6+} + \text{Zn}^{2+} = \text{Zn}_4\text{L}_2^{8+}$, $\log K = 10.7$, Table 2) even though an important reorganization of the trinuclear complex must occur to accommodate the fourth Zn^{2+} ion. According to protonation data in Table 2, two primary nitrogen atoms should remain uncoordinated in $\text{Zn}_4\text{L}_2^{8+}$.

Table 2. Stability constants of Zn^{2+} complexes with L2. 0.10 M Me_4NCl , 298.1 \pm 0.1 K. Values in parentheses are standard deviation on the last significant figure.

Equilibria	logK	Equilibria	logK
$\text{Zn}^{2+} + \text{L}_2 = \text{ZnL}_2^{2+}$	17.18 (5)	$\text{Zn}_2\text{H}_6\text{L}_2^{10+} + \text{H}^+ = \text{Zn}_2\text{H}_7\text{L}_2^{11+}$	8.13 (8)
$\text{ZnL}_2^{2+} + 2\text{H}^+ = \text{ZnH}_2\text{L}_2^{4+}$	22.50 (8)	$\text{Zn}_2\text{H}_7\text{L}_2^{11+} + \text{H}^+ = \text{Zn}_2\text{H}_8\text{L}_2^{12+}$	7.36 (7)
$\text{ZnH}_2\text{L}_2^{4+} + \text{H}^+ = \text{ZnH}_3\text{L}_2^{5+}$	10.04 (5)	$\text{Zn}_2\text{H}_8\text{L}_2^{12+} + \text{H}^+ = \text{Zn}_2\text{H}_9\text{L}_2^{13+}$	6.47 (5)
$\text{ZnH}_3\text{L}_2^{5+} + \text{H}^+ = \text{ZnH}_4\text{L}_2^{6+}$	9.59 (6)		
$\text{ZnH}_4\text{L}_2^{6+} + \text{H}^+ = \text{ZnH}_5\text{L}_2^{7+}$	10.01 (7)	$3\text{Zn}^{2+} + \text{L}_2 = \text{Zn}_3\text{L}_2^{6+}$	41.36 (5)
$\text{ZnH}_5\text{L}_2^{7+} + 2\text{H}^+ = \text{ZnH}_7\text{L}_2^{9+}$	18.14 (7)	$\text{Zn}_2\text{L}_2^{4+} + \text{Zn}^{2+} = \text{Zn}_3\text{L}_2^{6+}$	11.0 (1)
$\text{ZnH}_7\text{L}_2^{9+} + \text{H}^+ = \text{ZnH}_8\text{L}_2^{10+}$	8.25 (6)	$\text{Zn}_3\text{L}_2^{6+} + 2\text{H}^+ = \text{Zn}_3\text{H}_2\text{L}_2^{8+}$	22.52 (6)
$\text{ZnH}_8\text{L}_2^{10+} + \text{H}^+ = \text{ZnH}_9\text{L}_2^{11+}$	8.64 (7)	$\text{Zn}_3\text{H}_2\text{L}_2^{8+} + \text{H}^+ = \text{Zn}_3\text{H}_3\text{L}_2^{9+}$	9.34 (8)
$\text{ZnH}_9\text{L}_2^{11+} + \text{H}^+ = \text{ZnH}_{10}\text{L}_2^{12+}$	7.97 (6)	$\text{Zn}_3\text{H}_3\text{L}_2^{9+} + \text{H}^+ = \text{Zn}_3\text{H}_4\text{L}_2^{10+}$	8.12 (8)
$\text{ZnH}_{10}\text{L}_2^{12+} + \text{H}^+ = \text{ZnH}_{11}\text{L}_2^{13+}$	6.92 (5)	$\text{Zn}_3\text{H}_4\text{L}_2^{10+} + \text{H}^+ = \text{Zn}_3\text{H}_5\text{L}_2^{11+}$	8.00 (8)
$\text{ZnH}_{11}\text{L}_2^{13+} + \text{H}^+ = \text{ZnH}_{12}\text{L}_2^{14+}$	5.75 (4)	$\text{Zn}_3\text{H}_5\text{L}_2^{11+} + \text{H}^+ = \text{Zn}_3\text{H}_6\text{L}_2^{12+}$	6.94 (6)
$\text{ZnH}_{12}\text{L}_2^{14+} + \text{H}^+ = \text{ZnH}_{13}\text{L}_2^{15+}$	5.38 (5)	$\text{Zn}_3\text{H}_6\text{L}_2^{12+} + \text{H}^+ = \text{Zn}_3\text{H}_7\text{L}_2^{13+}$	6.26 (6)
$2\text{Zn}^{2+} + \text{L}_2 = \text{Zn}_2\text{L}_2^{4+}$	30.35 (7)	$4\text{Zn}^{2+} + \text{L}_2 = \text{Zn}_4\text{L}_2^{8+}$	52.08 (8)
$\text{ZnL}_2^{2+} + \text{Zn}^{2+} = \text{Zn}_2\text{L}_2^{4+}$	13.2 (1)	$\text{Zn}_3\text{L}_2^{6+} + \text{Zn}^{2+} = \text{Zn}_4\text{L}_2^{8+}$	10.7 (1)
$\text{Zn}_2\text{L}_2^{4+} + \text{H}^+ = \text{Zn}_2\text{HL}_2^{5+}$	11.27 (8)	$\text{Zn}_4\text{L}_2^{8+} + \text{H}^+ = \text{Zn}_4\text{HL}_2^{9+}$	9.48 (8)
$\text{Zn}_2\text{HL}_2^{5+} + \text{H}^+ = \text{Zn}_2\text{H}_2\text{L}_2^{6+}$	11.44 (8)	$\text{Zn}_4\text{HL}_2^{9+} + \text{H}^+ = \text{Zn}_4\text{H}_2\text{L}_2^{10+}$	8.90 (8)
$\text{Zn}_2\text{H}_2\text{L}_2^{6+} + \text{H}^+ = \text{Zn}_2\text{H}_3\text{L}_2^{7+}$	9.53 (8)	$\text{Zn}_4\text{H}_2\text{L}_2^{10+} + \text{H}^+ = \text{Zn}_4\text{H}_3\text{L}_2^{11+}$	8.24 (8)
$\text{Zn}_2\text{H}_3\text{L}_2^{7+} + \text{H}^+ = \text{Zn}_2\text{H}_4\text{L}_2^{8+}$	9.54 (8)	$\text{Zn}_4\text{H}_3\text{L}_2^{11+} + \text{H}^+ = \text{Zn}_4\text{H}_4\text{L}_2^{12+}$	7.35 (9)
$\text{Zn}_2\text{H}_4\text{L}_2^{8+} + \text{H}^+ = \text{Zn}_2\text{H}_5\text{L}_2^{9+}$	8.80 (9)	$\text{Zn}_4\text{L}_2^{8+} + \text{OH}^- = [\text{Zn}_4\text{L}_2(\text{OH})]^{7+}$	2.2 (1)
$\text{Zn}_2\text{H}_5\text{L}_2^{9+} + \text{H}^+ = \text{Zn}_2\text{H}_6\text{L}_2^{10+}$	8.60 (8)		

To get insight into the structural properties of these Zn^{2+} polynuclear complexes, we performed molecular modelling calculations on $\text{Zn}_2\text{L}_2^{4+}$, $\text{Zn}_3\text{L}_2^{6+}$ and $\text{Zn}_4\text{L}_2^{8+}$ in a simulated implicit water environment. The lower energy structures obtained for these complexes are shown in Figure 2. According to these structures, in $\text{Zn}_2\text{L}_2^{4+}$ (Figure 2a) and $\text{Zn}_3\text{L}_2^{6+}$ (Figure 2b) each metal ion is coordinated, in a distorted octahedral environment, to six nitrogen atoms pertaining to one arm of the ligand originating from the central tertiary amine group. In agreement with the deductions drawn above from the equilibrium constants, the number of primary nitrogen atoms remaining not

coordinated is six in Zn_2L2^{4+} (Figure 2a) and three in Zn_3L2^{6+} (Figure 2b). Indeed, the addition of the fourth Zn^{2+} ion causes a major rearrangement of the trinuclear complex. The ligand displays a great ability to minimize the electrostatic repulsion between metal cations bringing them at long distance from each other (Figure 2c). Only one of the Zn^{2+} ions retains the octahedral coordination environment seen in the trinuclear complex, while the other three metal cations are: one pentacoordinated by ligand nitrogen atoms, one pentacoordinated by four ligand donors and a water molecule, one tetracoordinated by two ligand donors and two water molecules. The last coordination environment requires some cautionary considerations. In this complex unit, the ligand forms an 8-membered chelate ring including a not coordinated nitrogen atom. A similar arrangement is unlikely to occur in a real solution, since chelate rings of such size are poorly stable. In the simulated implicit water environment of our calculations, however, an overestimation of electrostatic repulsions could have forced the Zn^{2+} ion to stay as far as possible from the other three cations, instead of involving the third nitrogen atom in the formation of two stable 5-membered chelate rings, which is the situation that we expect to occur in water. Nevertheless, the calculated structure of Zn_4L2^{8+} (Figure 2c) seems very representative of the overall organization of this complex, as shown by the fact that it implicates the presence of two not coordinated primary nitrogen atoms in agreement with the results deduced above from equilibrium data.

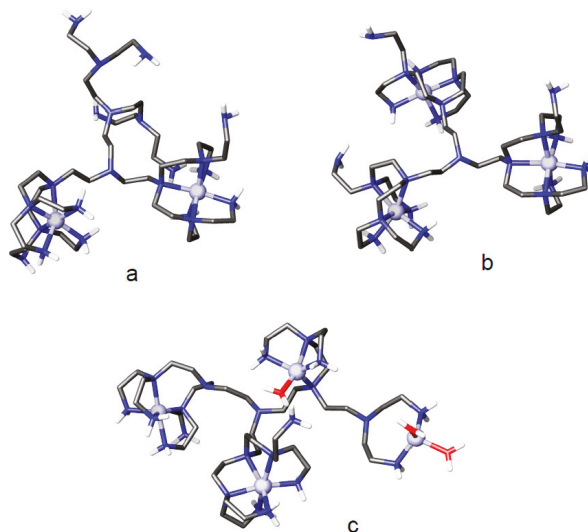


Figure 2. Minimum energy conformations calculated for (a) Zn_2L2^{4+} ; (b) Zn_3L2^{6+} and (c) Zn_4L2^{8+} .

2.2. Formation of Anion and Ion-Pair Complexes

The detailed analysis of metal complexation equilibria with L2 makes it possible to further investigate such equilibrium systems. For instance, it is possible to analyse the ability of L2 complexes to interact with other species in the environment. We have already seen that protonated forms of L2 can bind PO_4^{3-} , $P_2O_7^{4-}$, $P_3O_{10}^{5-}$, and nucleotides (AMP, ADP, ATP) anions in solution [6], and we have already seen that the G-2 dendrimer L1 is able to form both anion and ion-pair complexes [2,3]. We have now studied the equilibria involving L2 and SO_4^{2-} both in the absence and in the presence of Cu^{2+} ions by means of pH-metric (potentiometric) titrations (0.1 M Me_4NCl , 298.1 ± 0.1 K). Indeed, the potentiometric data, treated with the computer program HYPERQUAD [12], revealed that many protonated forms of L2 are able to bind both the SO_4^{2-} anion alone and the Cu^{2+}/SO_4^{2-} ion-pair. The equilibrium constants for the formation of SO_4^{2-} complexes are reported in Table 3 (see Figure S3

for a distribution diagram). This table includes the overall constants (β values) for the binding of SO_4^{2-} along with the constants for the equilibria of anion binding by protonated ligand species ($\text{H}_n\text{L}2^{n+} + \text{SO}_4^{2-} = [\text{H}_n\text{L}2(\text{SO}_4)]^{(n-2)+}$) that could be calculated from the former by using the ligand protonation constants [6]. It is to be noted that the constants for the latter equilibria could not be calculated for complexes $[\text{H}_n\text{L}2(\text{SO}_4)]^{(n-2)+}$ with $n < 11$ (Table 3), since it was not possible to resolve as single proton binding processes the protonation equilibria involving $\text{H}_n\text{L}2^{n+}$ species with $n < 11$ [6]. Nonetheless, the stability constants that are available for the binding of SO_4^{2-} to the protonated ligand forms show some peculiarities of this ligand. The stability of anion complexes of polyammonium ligands is generally determined by electrostatic attraction and hydrogen bonding [17–21]. Conversely, the ability of L2 to bind SO_4^{2-} appears to be unaffected by its positive charge, that is, by its protonation state. Actually, the equilibrium constants for the anion binding vary in a very reduced range and their values are very small, on consideration of the high positive ligand charge and in comparison with SO_4^{2-} complexes of other polyammonium ligands [22]. A similar behaviour was also observed for phosphate and phosphate-like anion complexes with L2, although, in several cases, the stability of these complexes was significantly higher, probably due to the greater hydrogen bond ability of phosphate-like anions [6]. Also the trend of stability is particular: the stability constants decrease from $\text{H}_{11}\text{L}2^{11+}$ ($\log K = 3.10$) to $\text{H}_{13}\text{L}2^{13+}$ ($\log K = 2.46$), then steadily increase up to the formation of the complex with $\text{H}_{18}\text{L}2^{18+}$ ($\log K = 3.32$).

Table 3. Stability constants of the anion complexes formed by L2 with SO_4^{2-} . 0.1 M Me_4NCl , 298.1 ± 0.1 K. Values in parentheses are standard deviation on the last significant figure.

Equilibria	logK	Equilibria	logK
$\text{L}2 + 3\text{H}^+ + \text{SO}_4^{2-} = [\text{H}_3\text{L}2(\text{SO}_4)]^+$	38.09 (5)	$\text{H}_{11}\text{L}2^{11+} + \text{SO}_4^{2-} = [\text{H}_{11}\text{L}2(\text{SO}_4)]^{9+}$	3.10 (7)
$\text{L}2 + 5\text{H}^+ + \text{SO}_4^{2-} = [\text{H}_5\text{L}2(\text{SO}_4)]^{3+}$	57.88 (5)	$\text{H}_{12}\text{L}2^{12+} + \text{SO}_4^{2-} = [\text{H}_{12}\text{L}2(\text{SO}_4)]^{10+}$	2.81 (7)
$\text{L}2 + 7\text{H}^+ + \text{SO}_4^{2-} = [\text{H}_7\text{L}2(\text{SO}_4)]^{5+}$	76.63 (5)	$\text{H}_{13}\text{L}2^{13+} + \text{SO}_4^{2-} = [\text{H}_{13}\text{L}2(\text{SO}_4)]^{11+}$	2.46 (7)
$\text{L}2 + 9\text{H}^+ + \text{SO}_4^{2-} = [\text{H}_9\text{L}2(\text{SO}_4)]^{7+}$	94.62 (5)	$\text{H}_{15}\text{L}2^{15+} + \text{SO}_4^{2-} = [\text{H}_{15}\text{L}2(\text{SO}_4)]^{13+}$	2.59 (7)
$\text{L}2 + 11\text{H}^+ + \text{SO}_4^{2-} = [\text{H}_{11}\text{L}2(\text{SO}_4)]^{9+}$	111.54 (5)	$\text{H}_{16}\text{L}2^{16+} + \text{SO}_4^{2-} = [\text{H}_{16}\text{L}2(\text{SO}_4)]^{14+}$	2.76 (7)
$\text{L}2 + 12\text{H}^+ + \text{SO}_4^{2-} = [\text{H}_{12}\text{L}2(\text{SO}_4)]^{10+}$	119.58 (5)	$\text{H}_{17}\text{L}2^{17+} + \text{SO}_4^{2-} = [\text{H}_{17}\text{L}2(\text{SO}_4)]^{15+}$	2.91 (7)
$\text{L}2 + 13\text{H}^+ + \text{SO}_4^{2-} = [\text{H}_{13}\text{L}2(\text{SO}_4)]^{11+}$	127.24 (5)	$\text{H}_{18}\text{L}2^{18+} + \text{SO}_4^{2-} = [\text{H}_{18}\text{L}2(\text{SO}_4)]^{16+}$	3.32 (7)
$\text{L}2 + 15\text{H}^+ + \text{SO}_4^{2-} = [\text{H}_{15}\text{L}2(\text{SO}_4)]^{13+}$	139.90 (5)		
$\text{L}2 + 16\text{H}^+ + \text{SO}_4^{2-} = [\text{H}_{16}\text{L}2(\text{SO}_4)]^{14+}$	145.53 (5)		
$\text{L}2 + 17\text{H}^+ + \text{SO}_4^{2-} = [\text{H}_{17}\text{L}2(\text{SO}_4)]^{15+}$	149.44 (5)		
$\text{L}2 + 18\text{H}^+ + \text{SO}_4^{2-} = [\text{H}_{18}\text{L}2(\text{SO}_4)]^{16+}$	152.12 (5)		

To get information about the possibility that such behaviour originates from the structural characteristics of the anion complexes, we performed a molecular modelling calculation on the $[\text{H}_6\text{L}2(\text{SO}_4)]^{4+}$, $[\text{H}_{12}\text{L}2(\text{SO}_4)]^{10+}$ and $[\text{H}_{15}\text{L}2(\text{SO}_4)]^{13+}$ species, assuming that the localization of H^+ ions in the protonated ligand forms is as previously established by $^1\text{H-NMR}$ spectroscopy [6], that is, the first 12 H^+ ions bind the 12 primary N(a) atoms (Figure 1), while in $\text{H}_{15}\text{L}2^{15+}$ the three additional protons involve the three tertiary N(c) nitrogen atoms. In $[\text{H}_6\text{L}2(\text{SO}_4)]^{4+}$, protonation was assumed to occur on primary amine groups located as far apart as possible from each other. The minimum energy structures calculated for these complexes, reported in Figure 3, show that the ligand molecule becomes increasingly expanded while becoming increasingly protonated, as a consequence of the increasing electrostatic repulsion exerting between the ammonium groups. In the minimum energy structures of $[\text{H}_6\text{L}2(\text{SO}_4)]^{4+}$ (Figure 3a) and $[\text{H}_{12}\text{L}2(\text{SO}_4)]^{10+}$ (Figure 3b), the SO_4^{2-} anion forms four salt-bridges (charge reinforced hydrogen bonds) with four ammonium groups of the ligand, while in $[\text{H}_{15}\text{L}2(\text{SO}_4)]^{13+}$ (Figure 3c) such interactions drop to three and become longer. Most likely, the two opposite trends developing with increasing ligand protonation, namely (i) the favourable contribution due to the increasing ligand charge; (ii) the unfavourable contribution determined by ligand expansion, are responsible for the particular trend of complex stability showing a minimum for SO_4^{2-} binding by $\text{H}_{13}\text{L}2^{13+}$ ($\log K = 2.46$, Table 3).

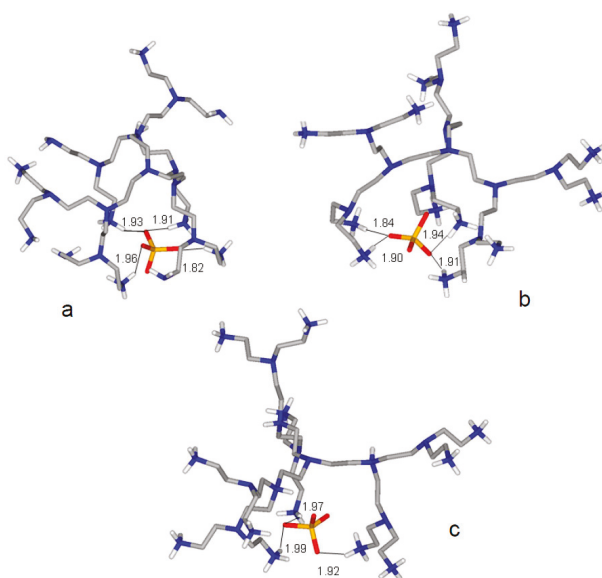


Figure 3. Minimum energy conformations calculated for (a) $[\text{H}_6\text{L}_2(\text{SO}_4)]^{4+}$; (b) $[\text{H}_{12}\text{L}_2(\text{SO}_4)]^{10+}$ and (c) $[\text{H}_{15}\text{L}_2(\text{SO}_4)]^{13+}$. Distances are in Å.

As anticipated above, L2 can bind SO_4^{2-} and Cu^{2+} , simultaneously, forming ion-pair complexes. The equilibrium constants determined for such complexes are presented in Table 4 in the form of equilibrium constants for SO_4^{2-} binding the by Cu^{2+} complexes of L2 (see Figure S4 for a distribution diagram). The analysis of the $\text{L}_2/\text{Cu}^{2+}/\text{SO}_4^{2-}$ system was limited to the formation of ion-pair complexes containing a single metal ion (see the experimental section). Nevertheless, even under the appropriate conditions, the $[\text{Cu}_2\text{L}_2(\text{SO}_4)]^{2+}$ complex was also found (Table 4), evidencing that more complex ion-pair species including more than one Cu^{2+} ion can be formed in solution. However, the analysis of such systems, requiring consideration of more than 92 equilibria, did not produced univocal results. This is the reason why we limited our study to ion-pair complexes with a single metal ion.

As can be seen from Table 4, the ability of the protonated Cu^{2+} complexes to bind SO_4^{2-} increases almost steadily with the positive charge of the metal complex, that is with its protonation state, the unique exception being represented by $[\text{CuH}_{10}\text{L}_2(\text{SO}_4)]^{10+}$, whose formation constant appears to be a little bit smaller than that of $[\text{CuH}_9\text{L}_2(\text{SO}_4)]^{9+}$. An assessment of the ability of the ligand to bind the anion in the absence or in the presence of Cu^{2+} ions can be performed by direct comparison of the equilibrium constants in Tables 3 and 4, limited to species with $\text{H}_{11}\text{L}_2^{11+}$ to $\text{H}_{18}\text{L}_2^{18+}$ ligand forms. Such comparison shows that the presence of Cu^{2+} enhances the ability of these ligand species to bind SO_4^{2-} , the increment growing with increasing ligand protonation. For instance, if we consider SO_4^{2-} binding by species with equal positive charge, such as $\text{H}_{18}\text{L}_2^{18+}$ and $\text{CuH}_{16}\text{L}_2^{18+}$, we observed an increase in stability from $\log K = 3.32$ ($\text{H}_{18}\text{L}_2^{18+} + \text{SO}_4^{2-} = [\text{H}_{18}\text{L}_2(\text{SO}_4)]^{16+}$) to $\log K = 5.20$ ($\text{CuH}_{16}\text{L}_2^{18+} + \text{SO}_4^{2-} = [\text{CuH}_{16}\text{L}_2(\text{SO}_4)]^{16+}$), corresponding to a free energy increment of 11 kJ/mol. For ligand species in lower protonation state than $\text{H}_{11}\text{L}_2^{11+}$, a similar comparison cannot be performed due to the already mentioned impossibility of expressing in the form $\text{H}_n\text{L}_2^{n+} + \text{SO}_4^{2-} = [\text{H}_n\text{L}_2(\text{SO}_4)]^{(n-2)+}$ the formation constants of $[\text{H}_n\text{L}_2(\text{SO}_4)]^{(n-2)+}$ complexes with $n < 11$. To overcome this problem, we can make use of the so called conditional (effective) stability constants that can be calculated for each system, as a function of pH, in the form $K_{\text{eff}} = \Sigma[\text{AH}_i\text{L}]/(\Sigma[\text{H}_j\text{L}] \times [\text{A}])$, for anion complexes ($\text{A} = \text{SO}_4^{2-}$), and $K_{\text{eff}} = \Sigma[\text{CuAH}_k\text{L}]/(\Sigma[\text{CuH}_l\text{L}] \times [\text{A}])$, for ion-pair complexes, where i, j, k and l are

the number of acidic protons on the ligand in the different species [23]. As can be seen from Figure 4, which shows the variation with pH of the effective stability constants calculated for SO_4^{2-} and ion-pair complexes, the presence of Cu^{2+} promotes the binding of SO_4^{2-} below pH 9, while in the range $9 < \text{pH} < 10.5$ there is a preference for the metal-free ligand. This behaviour suggests the involvement of the metal ion in the binding of SO_4^{2-} in the ion-pair complexes of higher protonation state. At high pH values, the ligand is poorly protonated and thus it is able to fulfil the coordination sphere of Cu^{2+} , preventing metal coordination to SO_4^{2-} . The ligand wraps around the metal ion leaving less space for SO_4^{2-} . Upon protonation of the Cu^{2+} complex, the ligand becomes less involved in the coordination to the metal and the increasing positive charge of the complex expands its structure, thus making space for the anion to get in contact with Cu^{2+} and form an increasing number of salt-bridges with ligand ammonium groups. At the break point of these trends (pH 9), the main ion-pair species in solution is $[\text{CuH}_7\text{L}_2(\text{SO}_4)]^{7+}$ (Figure S4). Below pH 6.5, the separation between the two curves in Figure 4, becomes about 2 logarithm units, which corresponds to the 11 kJ/mol free energy increment observed above for the binding of SO_4^{2-} to $\text{CuH}_{16}\text{L}_2^{18+}$ relative to $\text{H}_{18}\text{L}_2^{18+}$. The formation of contact ion-pair complexes was previously reported for the G-2 dendrimer L1, and is corroborated for L2 by the fact that the binuclear $\text{Cu}_2\text{L}_2^{4+}$ complex binds SO_4^{2-} (Table 4) in the absence of ligand ammonium groups (ligand protonation).

Table 4. Stability constants of the ion-pair complexes formed by L2 with Cu^{2+} and SO_4^{2-} . 0.1 M Me_4NCl , 298.1 ± 0.1 K. Values in parentheses are standard deviation on the last significant figure.

Equilibria	logK
$\text{CuH}_3\text{L}_2^{5+} + \text{SO}_4^{2-} = [\text{CuH}_3\text{L}_2(\text{SO}_4)]^{3+}$	3.10 (8)
$\text{CuH}_5\text{L}_2^{7+} + \text{SO}_4^{2-} = [\text{CuH}_5\text{L}_2(\text{SO}_4)]^{5+}$	3.33 (5)
$\text{CuH}_7\text{L}_2^{9+} + \text{SO}_4^{2-} = [\text{CuH}_7\text{L}_2(\text{SO}_4)]^{7+}$	3.51 (5)
$\text{CuH}_9\text{L}_2^{11+} + \text{SO}_4^{2-} = [\text{CuH}_9\text{L}_2(\text{SO}_4)]^{9+}$	3.62 (5)
$\text{CuH}_{10}\text{L}_2^{12+} + \text{SO}_4^{2-} = [\text{CuH}_{10}\text{L}_2(\text{SO}_4)]^{10+}$	3.44 (5)
$\text{CuH}_{11}\text{L}_2^{13+} + \text{SO}_4^{2-} = [\text{CuH}_{11}\text{L}_2(\text{SO}_4)]^{11+}$	3.69 (5)
$\text{CuH}_{12}\text{L}_2^{14+} + \text{SO}_4^{2-} = [\text{CuH}_{12}\text{L}_2(\text{SO}_4)]^{12+}$	3.96 (5)
$\text{CuH}_{13}\text{L}_2^{15+} + \text{SO}_4^{2-} = [\text{CuH}_{13}\text{L}_2(\text{SO}_4)]^{13+}$	4.31 (5)
$\text{CuH}_{14}\text{L}_2^{16+} + \text{SO}_4^{2-} = [\text{CuH}_{14}\text{L}_2(\text{SO}_4)]^{14+}$	4.64 (5)
$\text{CuH}_{16}\text{L}_2^{18+} + \text{SO}_4^{2-} = [\text{CuH}_{16}\text{L}_2(\text{SO}_4)]^{16+}$	5.20 (5)
$[\text{CuH}_{16}\text{L}_2(\text{SO}_4)]^{16+} + \text{H}^+ = [\text{CuH}_{17}\text{L}_2(\text{SO}_4)]^{17+}$	2.78 (5)
$\text{Cu}_2\text{L}_2^{4+} + \text{SO}_4^{2-} = [\text{Cu}_2\text{L}_2(\text{SO}_4)]^{2+}$	4.01 (5)

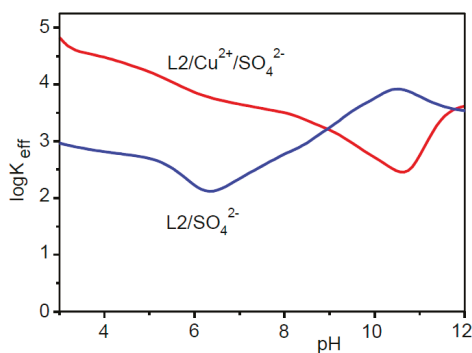


Figure 4. Logarithms of the conditional stability constants of anion (SO_4^{2-}) and ion-pair ($\text{Cu}^{2+}/\text{SO}_4^{2-}$) complexes with L2.

3. Materials and Methods

3.1. General Information

All starting materials were high purity compounds purchased from commercial sources and used as supplied. Ligand L2 was synthesized according to a previously described procedure [24].

3.2. Potentiometric Measurements

Potentiometric (pH-metric) titrations, employed to determine equilibrium constants, were performed in 0.1 M Me₄NCl aqueous solution at 298.1 ± 0.1 K by using an automated system and a procedure already described [25]. The combined Metrohm 6.0262.100 electrode (Metrohm AG, Herisau, Switzerland) was calibrated as a hydrogen-ion concentration probe by titration of previously standardized amounts of HCl with CO₂-free NMe₄OH solutions and determining the equivalent point by Gran's method [26], which gives the standard potential, E° , and the ionic product of water ($pK_w = 13.83$ (1) in 0.1 M Me₄NCl at 298.1 ± 0.1 K). The computer program HYPERQUAD [12] was used to calculate complex stability constants. All experiments were performed in the pH range 2.5–11.0 with 1×10^{-3} M ligand concentration. Six titrations in the case of Cu²⁺ complexation, and five in the case of Zn²⁺, were performed with metal concentration varying in the ranges $0.5[L] \leq [Cu^{2+}] \leq 4.5[L]$ and $0.5[L] \leq [Zn^{2+}] \leq 3.5[L]$. Metal to ligand molar ratios greater than 5 for Cu²⁺ and 4 for Zn²⁺ were also tested: precipitation of metal hydroxide was observed in alkaline solution, while the analysis of the acidic branches of the titrations confirmed the maximum nuclearity of 5 for Cu²⁺ and 4 for Zn²⁺. Three titrations were performed for anion binding with SO₄²⁻ concentration in the range $2[L] \leq [SO_4^{2-}] \leq 5[L]$. Three titrations were performed for ion-pair binding with $[Cu^{2+}] = 0.8[L]$ and SO₄²⁻ concentration $2[L] \leq [SO_4^{2-}] \leq 5[L]$. The different titration curves, obtained for metal, anion and ion-pair complexation experiments, respectively, were treated as separated curves without significant variations in the values of the common stability constants. Finally, the sets of data were merged together and treated simultaneously to give the final stability constants. Different equilibrium models for the complex systems were generated by eliminating and introducing different species. Only those models for which the HYPERQUAD program furnished a variance of residuals $\sigma^2 \leq 9$ were accepted. This condition was unambiguously met by a single model. Ligand protonation constants were taken from the literature [6].

3.3. Molecular Modelling

Molecular modelling investigations on [H₆L2(SO₄)]⁴⁺, [H₁₂L2(SO₄)]¹⁰⁺ and [H₁₅L2(SO₄)]¹³⁺ complexes were performed by means of the empirical force field method AMBER3 as implemented in the Hyperchem 7.51 package [27], using an implicit simulation of aqueous environment ($\epsilon = 4$ r) and atomic charges evaluated at the semiempirical level of theory (PM3) [28,29]. Potential energy surface of all the systems were explored by means of simulated annealing (T = 600 K, equilibration time = 10 ps, run time = 10 ps and cooling time = 10 ps, time step = 1.0 fs). For each studied system, 80 conformations were sampled.

As for the Zn(II) complexes, the trinuclear Zn₃L2⁶⁺ species was firstly analysed. Starting coordinates were built from the crystal structure of the Ni²⁺ complex of L1 [1], containing Ni²⁺ ions hexacoordinated in distorted octahedral environments to six out of the seven nitrogen atoms constituting a portion of L1 that is identical to the three branches of L2 growing from the central N(c) atom (Figure 1). The nitrogen atom remaining uncoordinated is a primary one. This structural motif was chosen taking into account that, according to the equilibrium data discussed before, all three metal ions of Zn₃L2⁶⁺ should be hexacoordinated and three primary amine groups of the complex should not be involved in metal coordination. This crystallographic structural unit was firstly modified by replacing Ni²⁺ with Zn²⁺ and completing each coordination environment with water molecules.

The starting coordinates for the binuclear Zn₂L2⁴⁺ complex were obtained by deleting one zinc ion in the QM minimized structure of Zn₃L2⁶⁺. The tetranuclear Zn₄L2⁸⁺ complex was instead obtained

from the QM minimized binuclear complex by adding to its metal-free branch two QM minimized pentacoordinated Zn^{2+} complexes, one in square pyramidal and one in bipyramidal geometry, taken from the crystallographic structure of the trinuclear Cu^{2+} complex of L1 [1] and successively modified by replacing Cu^{2+} with Zn^{2+} .

The starting coordinates for each polynuclear complexes were firstly optimized by using the OPLS2005 forcefield implemented in the Impact software [30], with completely frozen metals and coordination environments. Then, each MM minimized structure was fully optimized at the DFT/M06 level of theory [31,32] by using the 6–31 g(tm) basis set [33–37] and the implicit simulation for the aqueous environment [38]. The nature of stationary points as true minima was checked by frequency calculations.

4. Conclusions

The ability of L2 to form stable highly nucleated complexes over a large pH range, as a consequence of its dendrimeric nature and of the many amine groups in its structure, make this compound a promising candidate for the preparation of solid supported materials to be used in the recovery of metal ions from aqueous media. This could find applications in both decontamination of waste waters and in the extraction of precious metals. Indeed, it was recently reported that activated carbon functionalized with randomly structured poly(ethylene imine) dendrimers are efficient scavenger of Pd^{2+} cations [39]. Moreover, L2 is also a promising candidate for catalytic purposes. The use of molecules with well-defined molecular structures, such as L2, has the advantage that with such molecules it is possible to perform a confident speciation of the complexes they form in solution, thus getting a fundamental instrument for the tailoring of appropriate receptors for substrates binding and activation. This is of special interest when the supported complex is used for catalytic purposes. Considering the ability of L2 to form complexes with many metal centres that may promote the binding of further species from the medium, we are particularly interested in developing carbon materials (activated carbons, carbon nanotubes, graphene) functionalized with L2 and testing them for catalytic applications in reaction for the formation of carbon-carbon bonds, such as the Sonogashira cross coupling.

Supplementary Materials: The following are available online: Figure S1: Distribution diagrams of the Cu^{2+} complexes of L2, Figure S2: Distribution diagrams of the Zn^{2+} complexes of L2, Figure S3: Distribution diagrams of the anion complexes formed by L2 with SO_4^{2-} , Figure S4: Distribution diagrams of the ion-pair complexes formed by L2 with Cu^{2+} and SO_4^{2-} complexes of L2.

Acknowledgments: Financial support from the Italian MIUR (project 2015MP34H3) is gratefully acknowledged.

Author Contributions: All authors conceived and designed the experiments; M.S. performed the synthesis and part of the potentiometric measurements; C.B. and P.G. performed the modelling calculations; C.G. performed part of the potentiometric measurements and took care of the graphical presentation of results; A.B. wrote the paper.

Conflicts of Interest: The authors declare no conflict of interest.

References

- Bazzicalupi, C.; Bianchi, A.; Giorgi, C.; Gratteri, P.; Mariani, P.; Valtancoli, B. Metal ion binding by a G-2 Poly(ethylene imine) dendrimer. Ion-directed self-assembling of hierarchical mono- and two-dimensional nanostructured materials. *Inorg. Chem.* **2013**, *52*, 2125–2137. [[CrossRef](#)] [[PubMed](#)]
- Bazzicalupi, C.; Bianchi, A.; Giorgi, C.; Gratteri, P.; Mariani, P.; Valtancoli, B. Anion and ion-pair binding by a G-2 Poly(ethylene imine) dendrimer. *Dalton Trans.* **2013**, *42*, 12130–12138. [[CrossRef](#)] [[PubMed](#)]
- Bazzicalupi, C.; Bianchi, A.; Giorgi, C.; Valtancoli, B. Zn(II) enhances nucleotide binding and dephosphorilation in the presence of a Poly(ethylene imine) dendrimer. *Inorg. Chim. Acta* **2014**, *417*, 163–170. [[CrossRef](#)]
- Salvador Serrano, E.; Savastano, M.; Bianchi, A. Inorganic Mercury Sequestration by a Poly(ethylene imine) Dendrimer in Aqueous Solution. *Molecules* **2015**, *20*, 3783–3790. [[CrossRef](#)] [[PubMed](#)]
- Bazzicalupi, C.; Bencini, A.; Bianchi, A.; Danesi, A.; Giorgi, C.; Valtancoli, B. Anion Binding by Protonated Forms of the Tripodal Ligand Tren. *Inorg. Chem.* **2009**, *48*, 2391–2398. [[CrossRef](#)] [[PubMed](#)]

6. Bazzicalupi, C.; Bianchi, A.; Giorgi, C.; Savastano, M.; Morales-Lara, F. ATP dephosphorylation can be either enhanced or inhibited by pH-controlled interaction with a dendrimer molecule. *Chem. Commun.* **2015**, *51*, 3907–3910. [[CrossRef](#)] [[PubMed](#)]
7. Astruc, D.; Wang, D.; Deraedt, C.; Liang, L.; Ciganda, R.; Ruiz, J. Catalysis Inside Dendrimers. *Synthesis* **2015**, *47*, 2017–2031. [[CrossRef](#)]
8. Wang, D.; Astruc, D. Dendritic catalysis—Basic concepts and recent trends. *Coord. Chem. Rev.* **2013**, *257*, 2317–2334. [[CrossRef](#)]
9. Myers, V.S.; Weir, M.G.; Carino, E.V.; Yancey, D.F.; Pande, S.; Crooks, R.M. Dendrimer-encapsulated nanoparticles: New synthetic and characterization methods and catalytic applications. *Chem. Sci.* **2011**, *2*, 1632–1646. [[CrossRef](#)]
10. Hwang, S.-H.; Shreiner, C.D.; Moorefield, C.N.; Newkome, G.W. Recent progress and applications for metalodendrimers. *New J. Chem.* **2007**, *31*, 1192–1217. [[CrossRef](#)]
11. Jarvis, N.V.; Wagener, J.M. Mechanistic studies of metal ion binding to water-soluble polymers using potentiometry. *Talanta* **1995**, *42*, 219–226. [[CrossRef](#)]
12. Gans, P.; Sabatini, A.; Vacca, A. Investigation of equilibria in solution. Determination of equilibrium constants with the HYPERQUAD suite of programs. *Talanta* **1996**, *43*, 1739–1753. [[CrossRef](#)]
13. Aragón, J.; Bencini, A.; Bianchi, A.; Garcia-España, E.; Micheloni, M.; Paoletti, P.; Ramirez, J.A.; Paoli, P. Interaction of “long” open-chain polyazaalkanes with hydrogen and copper(II) ions. *Inorg. Chem.* **1991**, *30*, 1843–1849. [[CrossRef](#)]
14. Bencini, A.; Bianchi, A.; Micheloni, M.; Paoletti, P.; Garcia-España, E.; Niño, M.A. Co-ordination tendency of [3k]aneN_k polyazacycloalkanes. Thermodynamic study of solution equilibria. *J. Chem. Soc. Dalton Trans.* **1991**, 1171–1174. [[CrossRef](#)]
15. Aragón, J.; Bencini, A.; Bianchi, A.; Garcia-España, E.; Micheloni, M.; Paoletti, P.; Ramirez, J.A.; Rodriguez, A. Interaction of long polyazaalkanes with zinc(II) and cadmium(II) ions. A thermodynamic and ¹³C nuclear magnetic resonance study. *J. Chem. Soc. Dalton Trans.* **1991**, 3077–3083. [[CrossRef](#)]
16. Bencini, A.; Bianchi, A.; Dapporto, P.; Garcia-España, E.; Micheloni, M.; Paoletti, P. Polynuclear zinc(II) complexes with large polyazacycloalkanes. 2. Equilibrium study and crystal structure of the binuclear complex [Zn₂LCl₂](Cl)ClO₄·H₂O (L = 1,4,7,10,13,16,19,22-octaazacyclotetrasosane). *Inorg. Chem.* **1989**, *28*, 1188–1191. [[CrossRef](#)]
17. *Anion Coordination Chemistry*; Bowman-James, K., Bianchi, A., García-España, E., Eds.; Wiley-VCH: New York, NY, USA, 2012.
18. Mateus, P.; Bernier, N.; Delgado, R. Recognition of anions by polyammonium macrocyclic and cryptand receptors: Influence of the dimensionality on the binding behavior. *Coord. Chem. Rev.* **2010**, *254*, 1726–1747. [[CrossRef](#)]
19. Bowman-James, K. Alfred Werner Revisited: The Coordination Chemistry of Anions. *Acc. Chem. Res.* **2005**, *38*, 671–678. [[CrossRef](#)] [[PubMed](#)]
20. Garcia-España, E.; Díaz, P.; Llinares, J.M.; Bianchi, A. Anion coordination chemistry in aqueous solution of polyammonium receptors. *Coord. Chem. Rev.* **2006**, *250*, 2952–2986. [[CrossRef](#)]
21. Bianchi, A.; Micheloni, M.; Paoletti, P. Supramolecular interaction between adenosine 5′-triphosphate (ATP) and polycharged tetraazamacrocycles. Thermodynamic and ³¹P NMR studies. *Inorg. Chim. Acta* **1988**, *151*, 269–272. [[CrossRef](#)]
22. Arranz, P.; Bencini, A.; Bianchi, A.; Díaz, P.; Garcia-España, E.; Giorgi, C.; Luis, S.V.; Querol, M.; Valtancoli, B. Thermodynamics of sulfate anion binding by macrocyclic polyammonium receptors. *J. Chem. Soc. Perkin Trans.* **2001**, 1765–1770. [[CrossRef](#)]
23. Bazzicalupi, C.; Bianchi, A.; Giorgi, C.; Clares, M.P.; Garcia-España, E. Addressing selectivity criteria in binding equilibria. *Coord. Chem. Rev.* **2011**, *256*, 13–27. [[CrossRef](#)]
24. Lee, S.H.; Kim, D.-J.; Chang, C.-C.; Hah, S.S.; Suh, J. An efficient synthesis of ethylenimine dendrimer. *Bull. Korean Chem. Soc.* **1998**, *19*, 1270–1273.
25. Bazzicalupi, C.; Bianchi, A.; Biver, T.; Giorgi, C.; Santarelli, S.; Savastano, M. Formation of double-strand dimetallic helicates with a terpyridine-based macrocycle. *Inorg. Chem.* **2014**, *53*, 12215–12224. [[CrossRef](#)] [[PubMed](#)]
26. Gran, G. Determination of the equivalence point in potentiometric titration, Part II. *Analyst* **1952**, *77*, 661–671. [[CrossRef](#)]

27. *Hyperchem, Release 7.51 for Windows MM System*; Hypercube, Inc.: Gainesville, FL, USA, 2002.
28. Stewart, J.J.P. Optimization of parameters for semiempirical methods I. Method. *J. Comput. Chem.* **1989**, *10*, 209–220. [[CrossRef](#)]
29. Stewart, J.J.P. Optimization of parameters for semiempirical methods II. Applications. *J. Comput. Chem.* **1989**, *10*, 221–264. [[CrossRef](#)]
30. Banks, J.L.; Beard, H.S.; Cao, Y.; Cho, A.E.; Damm, W.; Farid, R.; Felts, A.K.; Halgren, T.A.; Mainz, D.T.; Maple, J.R.; et al. Integrated Modeling Program, Applied Chemical Theory (IMPACT). *J. Comput. Chem.* **2005**, *26*, 1752–1780. [[CrossRef](#)] [[PubMed](#)]
31. Kohn, W.; Sham, L.J. Self-Consistent Equations Including Exchange and Correlation Effects. *Phys. Rev.* **1965**, *140*, A1133–A1138. [[CrossRef](#)]
32. Zhao, Y.; Truhlar, D.G. The M06 suite of density functionals for main group thermochemistry, thermochemical kinetics, noncovalent interactions, excited states, and transition elements: Two new functionals and systematic testing of four M06-class functionals and 12 other functionals. *Theor. Chem. Acc.* **2008**, *120*, 215–241.
33. Ditchfield, R.; Hehre, W.J.; Pople, J.A. Self-Consistent Molecular-Orbital Methods. IX. An Extended Gaussian-Type Basis for Molecular-Orbital Studies of Organic Molecules. *J. Chem. Phys.* **1971**, *54*, 724–728. [[CrossRef](#)]
34. Hehre, W.J.; Pople, J.A. Self-Consistent Molecular Orbital Methods. XIII. An Extended Gaussian Type Basis for Boron. *J. Chem. Phys.* **1972**, *56*, 4233–4234. [[CrossRef](#)]
35. Binkley, J.S.; Pople, J.A. Self-Consistent Molecular Orbital Methods. XIX. Split Valence Gaussian-type Basis Sets for Beryllium. *J. Chem. Phys.* **1977**, *66*, 879–880. [[CrossRef](#)]
36. Hariharan, P.C.; Pople, J.A. The Influence of Polarization Functions on Molecular Orbital Hydrogenation Energies. *Theor. Chim. Acta* **1973**, *28*, 213–222. [[CrossRef](#)]
37. Mitin, A.V.; Baker, J.; Pulay, P. An improved 6–31G* basis set for first-row transition metals. *J. Chem. Phys.* **2003**, *119*, 7775–7782. [[CrossRef](#)]
38. Cortis, M.C.; Friesner, R.A. Poisson-Boltzmann Calculations of Nonspecific Salt Effects on Protein-Protein Binding Free Energies. *J. Comput. Chem.* **1997**, *18*, 1591–1608. [[CrossRef](#)]
39. Peñas-Sanjuán, A.; López-Garzón, R.; López-Garzón, J.; Pérez-Mendoza, M.; Melguizo, M. Preparation of a poly-alkylamine surface-functionalized carbon with excellent performance as a Pd(II) scavenger. *Carbon* **2012**, *50*, 2350–2352. [[CrossRef](#)]

Sample Availability: Samples of the compound **L2** is available from the authors.



© 2017 by the authors. Licensee MDPI, Basel, Switzerland. This article is an open access article distributed under the terms and conditions of the Creative Commons Attribution (CC BY) license (<http://creativecommons.org/licenses/by/4.0/>).

Article

Poly(alkylideneimine) Dendrimers Functionalized with the Organometallic Moiety $[\text{Ru}(\eta^5\text{-C}_5\text{H}_5)(\text{PPh}_3)_2]^+$ as Promising Drugs Against *Cisplatin*-Resistant Cancer Cells and Human Mesenchymal Stem Cells

Marisol Gouveia ¹, João Figueira ², Manuel G. Jardim ¹, Rita Castro ¹, Helena Tomás ¹, Kari Rissanen ³ and João Rodrigues ^{1,4,*}

¹ CQM—Centro de Química da Madeira, MMRG, Universidade da Madeira, Campus da Penteada, 9000-390 Funchal, Portugal; marisolgouveia5@gmail.com (M.G.); mgjardim@uma.pt (M.G.J.); ritacastro@uma.pt (R.C.); lenat@uma.pt (H.T.)

² Department of Chemistry, ScilifeLab, Umeå University, KBC-Building, Linnaeus väg 6, 90736 Umeå, Sweden; joao.figueira@umu.se

³ Department of Chemistry, University of Jyväskylä, P.O. Box. 35, FI-40014 Jyväskylä, Finland; kari.t.rissanen@jyu.fi

⁴ School of Materials Science and Engineering/Center for Nano Energy Materials, Northwestern Polytechnical University, Xi'an 710072, China

* Correspondence: joaor@uma.pt or joaor@nwpu.edu.cn; Tel.: +351-291-705-100

Received: 5 May 2018; Accepted: 12 June 2018; Published: 17 June 2018

Abstract: Here and for the first time, we show that the organometallic compound $[\text{Ru}(\eta^5\text{-C}_5\text{H}_5)(\text{PPh}_3)_2\text{Cl}]$ (RuCp) has potential to be used as a metallodrug in anticancer therapy, and further present a new approach for the cellular delivery of the $[\text{Ru}(\eta^5\text{-C}_5\text{H}_5)(\text{PPh}_3)_2]^+$ fragment via coordination on the periphery of low-generation poly(alkylideneimine) dendrimers through nitrile terminal groups. Importantly, both the RuCp and the dendrimers functionalized with $[\text{Ru}(\eta^5\text{-C}_5\text{H}_5)(\text{PPh}_3)_2]^+$ fragments present remarkable toxicity towards a wide set of cancer cells (Caco-2, MCF-7, CAL-72, and A2780 cells), including cisplatin-resistant human ovarian carcinoma cell lines (A2780*cis*R cells). Also, RuCp and the prepared metallodendrimers are active against human mesenchymal stem cells (hMSCs), which are often found in the tumor microenvironment where they seem to play a role in tumor progression and drug resistance.

Keywords: dendrimers; nanocarriers; metallodrugs; ruthenium; platinum; *cisplatin*; cancer treatment; hMSCs; toxicity; nanomedicine

1. Introduction

Despite their complexity and diversity, oncologic diseases are mainly characterized by the abnormal growth of cells which can gain the potential to invade tissues and disseminate (metastasize) to distant locations in the body [1,2]. According to the U.S. National Cancer Institute, and despite encouraging indicators [3], the number of deaths caused by cancer is expected to increase to 22 million in the next two decades [4], which justifies the current pursuit of new treatments.

The discovery of *cis*-diamminedichloroplatinum (II) (commonly abbreviated as DDP, cisplatin or *cis*Pt) anticancer properties by Rosenberg et al. [5] in 1965, as well as its approval by Food and Drug Administration (FDA) to clinical use in 1978, has triggered the investigation of metal complexes as anticancer chemotherapeutic agents [6,7]. Cisplatin and its second and third-generation platinum drug analogues, *cis*-diammine(1,1-cyclobutanedicarboxylato)platinum(II) (carboplatin) and

[(1*R*,2*R*)-cyclohexane-1,2-diamine](ethanedioato-*O*,*O'*)platinum(II) (oxaliplatin), respectively, are the only metal complexes currently used in chemotherapeutic regimes of patients with cancer, being employed alone or in combination with other drugs [8–15]. However, the administration of these platinum-based drugs has been limited due to their substantial adverse side effects (e.g., neurotoxicity) [16–20], incapacity to prevent cancer relapse [20,21], and development of intrinsic or acquired resistance by several types of cancer [16,22–26]. For these reasons, efforts have been made to develop non-platinum metallodrugs with the same objective [6–11,13,14,16,23,27–29].

Among several metallodrugs that have been explored as anticancer agents, ruthenium compounds have emerged in recent years as promising candidates [27–31]. Some relevant characteristics of ruthenium compounds that have sparked the attention for their application include: (i) the diversity of oxidation states accessible in physiological medium, namely Ru(II), Ru(III) and Ru(IV) [30]; (ii) the slow ligand-exchange kinetics, which can be adjusted by the variation of the nature of the ligands coordinated to the metal [32,33], and (iii) the reduced systemic toxicity. This last property has been associated with the ability of ruthenium to mimic iron in binding several biological molecules, like transferrin and albumin. Thereafter, because cancer cells possess a high number of transferrin receptors on their surface, theoretically, a high level of ruthenium complexes will be delivered preferentially to these cells by transferrin [30,34,35]. Furthermore, it is believed that the inert Ru(III) complexes can be activated to the corresponding cytotoxic forms of Ru(II) in the tumors that possess a reducing environment and, consequently, present a higher selectivity to cancer cells [36].

Many families of ruthenium complexes have been studied against several different types of cancer [28,37,38]. Specifically, the Ru(III) complexes have shown promising results in clinical trials against solid tumors. For example, the imidazolium *trans*-[tetrachlorido(1*H*-imidazole)(*S*-dimethyl sulfoxide)ruthenate(III)] (NAMI-A, an acronym for New Anti-tumour Metastasis Inhibitor A) has concluded the clinical phase I [39] and entered, in combination with gemcitabine (2',2'-difluoro deoxycytidine), in phase I/II [40]. However, this study is currently suspended due to the toxicity profile and the unclear efficiency of the combination of these drugs [31,40,41]. Other promising Ru(III) compounds are the indazolium *trans*-[tetrachloridobis(1*H*-indazole)ruthenate(III)] (KP1019 or FFC14A) and its analogue sodium *trans*-[tetrachloridobis(1*H*-indazole)ruthenate(III)] (NKP-1339 or IT-139). Both compounds have completed the clinical phase I [42–44] but, since NKP-1339 presents higher solubility in water than KP1019, the clinical trials have proceeded only with the former, which is water-soluble [44–46]. Also, the incorporation of ruthenium complexes to form multinuclear and supramolecular structures has also been successfully tested on several platforms such as polymers (e.g., polymeric micelles [47]), lipid-based systems [48–51], and polymer-peptide conjugates [52] with the aim of improving the chemotherapeutic action of these potential drugs.

Among the organoruthenium(II) compounds, the half-sandwich organometallic ruthenium compounds with η^6 -arene [53] or η^5 -cyclopentadienyl [54–56] exhibited attracting pharmacological properties to be applied in cancer therapy. In these cases, the aromatic ligand present in the structure of the half sandwich compounds allows the stability and protection of the metal Ru(II) [57,58].

Dendrimers constitute a class of synthetic polymeric macromolecules that possess a hyperbranched structure at the nanosize scale, low polydispersity, and a multifunctional surface [59]. These nanoparticles may be good drug carriers due to the possibility of encapsulating drugs in their interior and/or covalently link them at their surface terminal groups [59–62]. Besides the potential for carrying multiple drugs and high drug loads, the dendritic multivalency provides increasing interaction with receptors of the therapeutic target [60]. Also, the nanoscale size of the dendrimers allows their selective accumulation in the tumors by the “enhanced permeability and retention” (EPR) effect [61,63].

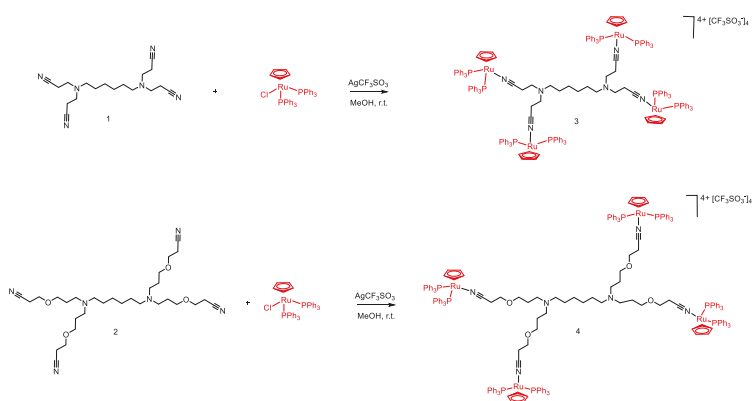
The incorporation of metal complexes in dendritic scaffolds, thus originating metallodendrimers, can increase the activity and selectivity of drugs based on transition metals [64]. Indeed, metallodendrimers can combine the anticancer potential of metal complexes with the features of the dendrimers as nanocarriers, and were described as having promising cytotoxicity against different cancer cell lines [65–79].

In the present work, we started by preparing and characterizing low-generation ruthenium(II) metallo dendrimers based on poly(alkylideneimine) dendritic scaffolds peripherally functionalized with the nitrile group and the fragment $[\text{Ru}(\eta^5\text{-C}_5\text{H}_5)(\text{PPh}_3)_2]^+$. Then, the cytotoxicity of the organometallic compound $[\text{Ru}(\eta^5\text{-C}_5\text{H}_5)(\text{PPh}_3)_2\text{Cl}]$ (abbreviated by RuCp), the core dendrimers, and the prepared tetrakis-ruthenium dendrimers were tested against five human cancer cell lines: a colorectal adenocarcinoma cell line (Caco-2), an osteosarcoma cell line (CAL-72), a breast adenocarcinoma cell line (MCF-7), and two ovarian carcinoma cell lines (A2780 and A2780cisR, the last one resistant to cisplatin), and in healthy human mesenchymal stem cells (hMSCs). In fact, hMSCs are more and more being proposed as a promising target for anticancer drug delivery since many pieces of evidence are arising pointing out their role in tumor development [80–82]. hMSCs are known to be recruited into tumors where their action is often described in the literature as pro-tumor, or tumor-supporting, including suppression of the immune response, promotion of angiogenesis, inhibition of apoptosis, stimulation of epithelial to mesenchymal transition and tumor metastasis. Results not only showed that the organometallic moiety $[\text{Ru}(\eta^5\text{-C}_5\text{H}_5)(\text{PPh}_3)_2]^+$ has an important anticancer activity by itself, but also that its coordination on the periphery of the dendrimers can be used as a successful drug delivery strategy. Furthermore, the present experiments also revealed that both RuCp and the developed dendrimers functionalized with $[\text{Ru}(\eta^5\text{-C}_5\text{H}_5)(\text{PPh}_3)_2]^+$ fragments presented remarkable toxicity towards cancer cells resistant to cisplatin which is considered a standard in anticancer therapy.

2. Results and Discussion

2.1. Synthesis and Characterization of $[\text{Ru}(\eta^5\text{-C}_5\text{H}_5)(\text{PPh}_3)_2]^+$ Functionalized Poly(alkylideneimine) Dendrimers

Two low generation poly(alkylideneimine) dendrimer cores having nitrile groups at their periphery and distinct in size and flexibility (Scheme 1, dendrimers 1 and 2) were used to prepare two different $[\text{Ru}(\eta^5\text{-C}_5\text{H}_5)(\text{PPh}_3)_2]^+$ functionalized poly(alkylideneimine) dendrimers (Scheme 1, metallo dendrimers 3 and 4). The synthesis followed a methodology previously developed by our group [83]. However, because the use of thallium compounds may result in unwanted cytotoxicity, thus hampering the results, in the current work, the prepared compounds were synthesized using a slight modification of the original procedure. AgCF_3SO_3 was used as chloride abstractor instead of TlPF_6 . As such, the reaction of a methanolic solution of $[\text{Ru}(\eta^5\text{-C}_5\text{H}_5)(\text{PPh}_3)_2\text{Cl}]$ and AgCF_3SO_3 with the nitrile functionalized poly(alkylideneimine) dendrimers 1 or 2, at room temperature, afforded the metallo dendrimers 3 or 4, respectively (Scheme 1). These metallo dendrimers were isolated as green powders and were characterized by NMR (^1H , ^{31}P , and ^{19}F) and infrared (FTIR) spectroscopy, mass spectrometry (MS) and elemental analysis (EA).



Scheme 1. Synthesis of the tetrakis-ruthenium dendrimers 3 and 4.

As is evident in the $^1\text{H-NMR}$ spectra of both tetranuclear metallo dendrimers **3** and **4** (Figures 1 and 2, respectively), the presence of only one singlet at 4.48 and 4.44 ppm, respectively, that can be assigned to the protons of the cyclopentadienyl ligand, indicates that the four ruthenium fragments were equivalently coordinated with each dendritic core.

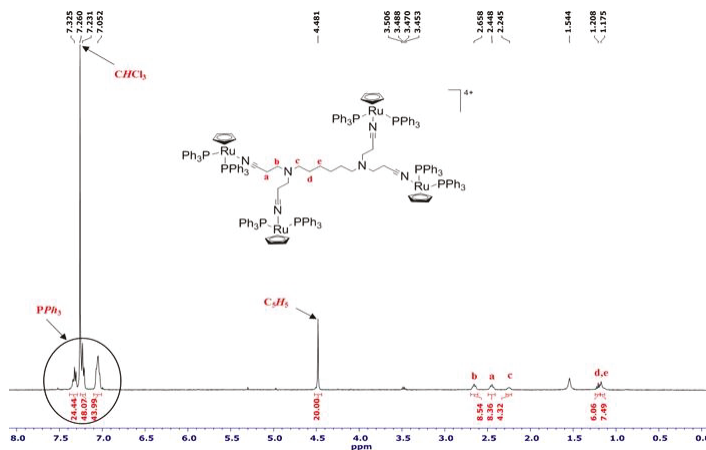


Figure 1. $^1\text{H-NMR}$ spectrum of $[[(\eta^5\text{-C}_5\text{H}_5)(\text{PPh}_3)_2\text{Ru}]_4(1)][\text{CF}_3\text{SO}_3]_4$ (**3**), in CDCl_3 .

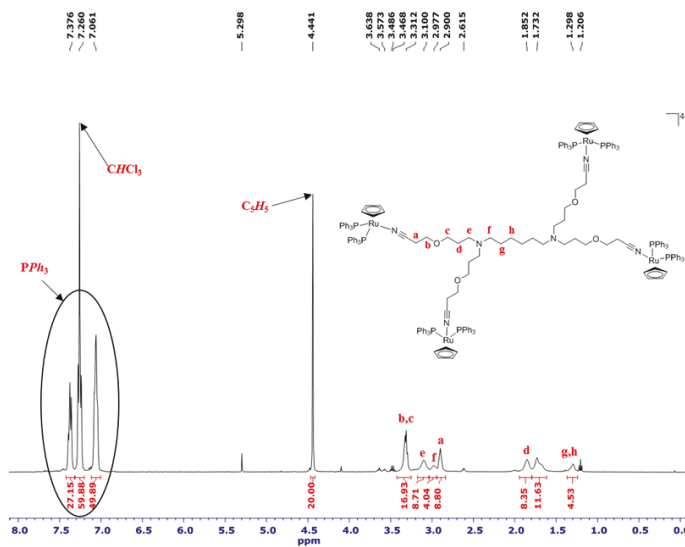


Figure 2. $^1\text{H-NMR}$ spectrum of $[[(\eta^5\text{-C}_5\text{H}_5)(\text{PPh}_3)_2\text{Ru}]_4(2)][\text{CF}_3\text{SO}_3]_4$ (**4**), in CDCl_3 .

The formation of these compounds was also sustained by the $^{31}\text{P-NMR}$ studies (Supplementary Material, Figures S1 and S5) that display a singlet at 41.89 and 41.60 ppm, coming from the resonance of the phosphorus atoms of phosphine ligands, in the spectrum of metallo dendrimer **3** and **4**, respectively. The metallo dendrimers **3** and **4** presented moderate stability in organic solvents, which was even lower in halogenated solvents, being impossible to obtain $^{13}\text{C-NMR}$ spectra for these compounds. The $^{19}\text{F-NMR}$ spectra of metallo dendrimers **3** and **4** (Supplementary Material, Figures S2 and S6)

revealed, respectively, a singlet at -81.78 and at -81.95 ppm that was attributed to the fluorine atoms of the $[\text{CF}_3\text{SO}_3]^-$ counterions.

The FTIR analysis for both metallodendrimers (**3** and **4**) show, outside the fingerprint zone, similar spectra (Supplementary Material, Figures S3 and S7). The presence of a single nitrile peak shifted to higher wavelengths relative to the position in the free ligand is a clear sign of the formation of the desired compound. Furthermore, the absence of the free $\nu(\text{CN})$ in the FTIR spectra supports the complete coordination of all nitrile groups present in the dendritic termini. In terms of values, the nitrile stretching band in compound **3** arises at 2271 cm^{-1} while in compound **4** it arises at 2269 cm^{-1} . The vibration bands of the $[\text{CF}_3\text{SO}_3]^-$ counter ion appear in the FTIR spectra around 1274 cm^{-1} and 700 cm^{-1} for metallodendrimer **3**, and ca. 1286 and 697 cm^{-1} for metallodendrimer **4**.

The analysis of the mass spectrum of metallodendrimer **3** (Supplementary Material, Figure S4) shows that the standard fragmentation is consistent with the loss of two counter ions, $m/z = 1694.5096$ $[\text{M}-2\text{CF}_3\text{SO}_3]^{2+}$, and three counter ions, $m/z = 1081.0131$ $[\text{M}-3\text{CF}_3\text{SO}_3]^{3+}$, revealing the presence of the desired metallodendrimer. Similar conclusions can be taken from the mass spectrum of metallodendrimer **4** (Supplementary Material, Figure S8) that exhibited the expected isotopic distribution for $[\text{M}-2\text{CF}_3\text{SO}_3]^{2+}$ ($m/z = 1810.9692$), and $[\text{M}-3\text{CF}_3\text{SO}_3]^{3+}$ ($m/z = 1157.9568$).

Finally, the results of the elemental analysis confirmed the integrity of the structure of the prepared metallodendrimers **3** and **4** since the calculated theoretical values showed good agreement with those obtained experimentally (data shown in the Section 3).

2.2. Biological Activity Assays

The 3-(4,5-dimethylthiazol-2-yl)2,5-diphenyltetrazolium bromide (MTT) assay was used to explore the in vitro cytotoxic potential of the metallodendrimers **3** and **4**. This assay is based on the principle that only cells that are alive are metabolically active, that is, can reduce MTT. For this purpose and in order to cover a broad spectra of cancer types, the response of five human tumor cell lines were investigated, namely a colorectal adenocarcinoma cell line (Caco-2), an osteosarcoma cell line (CAL-72), a breast adenocarcinoma cell line (MCF-7) and two ovarian carcinoma cell lines (A2780 and A2780*cisR*). The cytotoxic effect of the prepared compounds was also evaluated in primary human mesenchymal stem cells (hMSCs). For comparison, the cytotoxicity profile of dendrimers **1** and **2**, $[\text{Ru}(\eta^5\text{-C}_5\text{H}_5)(\text{PPh}_3)_2\text{Cl}]$ (abbreviated as RuCp), and PPh_3 were also investigated using the same cell types. Since we also wanted to compare the anticancer potential of metallodendrimers **3** and **4** with that of cisplatin (abbreviated as *cisPt*), the cytotoxic effect of *cisPt* was evaluated in A2780 (a cancer cell line sensitive to *cisPt*) and A2780*cisR* (a cancer cell line resistant to *cisPt*) cells. In all these assays, the used concentration range for the tested compounds was 0.05 to $50\text{ }\mu\text{M}$. For RuCp and metallodendrimers **3** and **4**, the concentrations $\geq 25\text{ }\mu\text{M}$ are only indicative due to solubility issues. The metabolic activity as a function of compound concentration are shown for all compounds in the Supplementary Material (Figures S10 and S11). Figure 3 highlights the data for A2780 and A2780*cisR* cells, as well as for hMSCs.

From Figure S11, it is clear that dendrimer **1** and dendrimer **2** present low cytotoxicity in the range of concentrations studied for all the cancer cell lines. When their concentration is increased, the cellular metabolic activity values remain quite constant. On the contrary, RuCp and metallodendrimers **3** and **4** showed high cytotoxicity which, as expected, generally increased with increasing compound concentration and was cell type-dependent (Figure 3 and Figure S10).

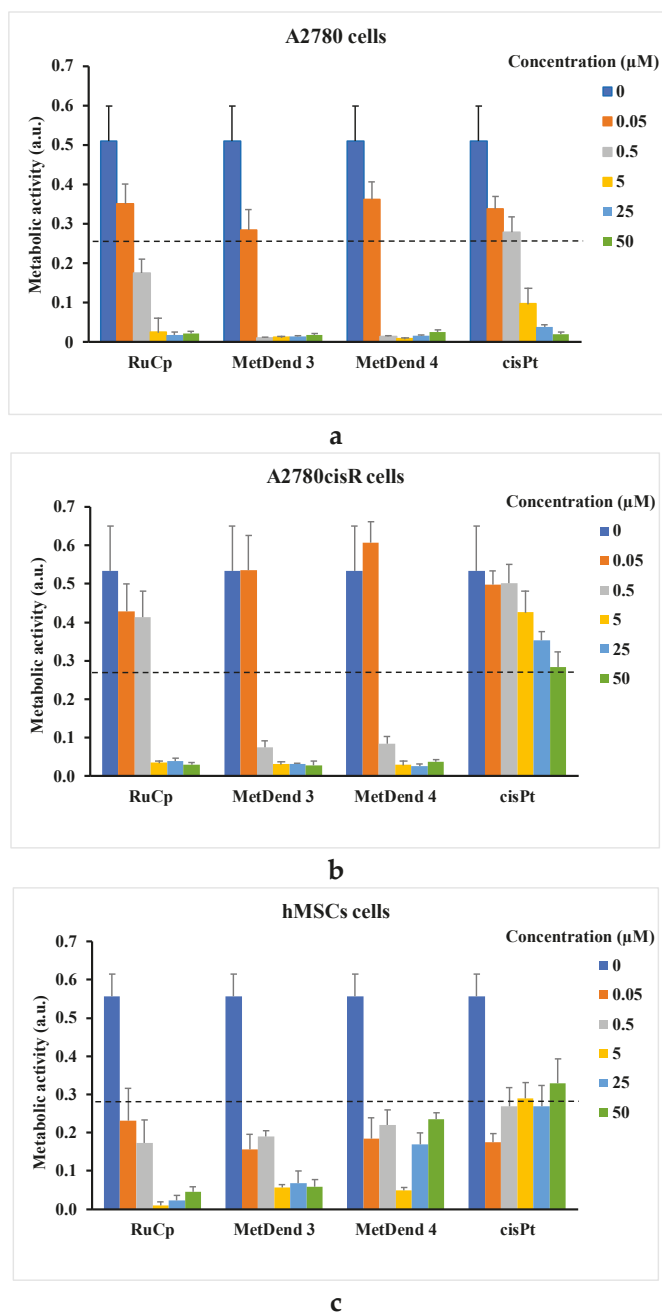


Figure 3. Effect of increasing concentrations of RuCp, metallodendrimers 3 and 4, and *cisPt* on the cellular metabolic activity (an indirect measure of cell viability) of (a) A2780 and (b) A2780*cisR* tumor cell lines, and on (c) hMSCs. The dashed line corresponds to 50% of cellular metabolic activity compared to the control. Values are presented as a mean \pm standard deviation.

The concentration required to obtain 50% of cell growth inhibition in vitro (IC_{50} value) was determined for these compounds, and as well as for *cisPt* (when applicable). These results are summarized in Table 1.

Table 1. IC_{50} values (in μM) of RuCp, metallodendrimers **3** and **4**, and *cisPt* observed for Caco-2, CAL 72, MCF-7, A2780 and A2780*cisR* cancer cells, as well as for hMSCs, after 72 h of exposition to the compounds.

Compound	Cell Type (IC_{50} Values in μM) ¹					
	Caco-2	CAL-72	MCF-7	A2780	A2780 <i>cisR</i>	hMSCs
RuCp	14.7	2.4	4.4	0.3	2.3	<0.05
Metallodendrimer 3	3.4	0.6	2.5	0.1	0.3	<0.05
Metallodendrimer 4	3.2	1.4	3.0	0.2	0.3	<0.05
<i>cisPt</i>	8.9 [84]	- ²	7.6 [85]	1.1	>50	<0.05

¹ The IC_{50} values were determined by linear interpolation between the two nearest neighbour experimental points. The standard deviation was always less than 10% of the IC_{50} value. ² Not reported in the literature.

Among all cancer cell types studied, the Caco-2 cells were the less sensitive, showing IC_{50} values of 14.7, 3.4 and 3.2 μM for RuCp, metallodendrimer **3** and **4**, respectively. The most sensitive cancer cells were the A2780 cells with IC_{50} values of 0.3, 0.1 and 0.2 μM for RuCp, metallodendrimer **3** and **4**, respectively. The hMSCs that are non-cancer cells were highly sensitive to all ruthenium compounds, and to *cisPt* also, presenting IC_{50} values lower than the lowest concentration tested (0.05 μM). Interestingly, although these cells seem to be very sensitive to low concentrations of the metallodrugs, an increase in drug concentration above 0.05 μM does not always imply a concomitant decrease in cell viability. This was especially evident for metallodendrimer **4** and *cisPt*. Likely, either the cellular internalization of these compounds is limited to low concentration values (of the order of magnitude of 0.05 μM) or these cells have internal mechanisms capable of excreting them. Although the role of hMSCs in tumor development is still not well understood and may even involve opposing effects [86–88], most of the literature in this subject indicate that they are attracted to cancer sites where they have an overall positive action in tumor progression and metastasis. In some cases, hMSCs even counter-act against anticancer chemotherapeutics [89]. Thus, it is very important to assess the effect of anticancer drugs in these cells. Our results show that RuCp, metallodendrimer **3** and **4** are not only cytotoxic for cancer cell lines, but also for hMSCs, which should contribute to their overall efficiency in anticancer therapeutics.

A significant problem in cancer therapy is the occurrence of drug resistance that requires a continuous search for new therapeutics. All three ruthenium compounds under study presented an anticancer activity towards A2780 cells about one order of magnitude lower than *cisPt* ($IC_{50} = 1.1 \mu M$) that is a drug already under use in the clinic scenario. Importantly, they were also remarkably active against A2780*cisR* cells—the anticancer activity was more than 22 and 166 times higher than *cisPt*, respectively, for RuCp and both metallodendrimers. For the Caco-2 and MCF-7 cancer cell lines, the anticancer behaviour of the prepared metallodendrimers **3** and **4** was ca. 3 times better than *cisPt*. Thus, RuCp, metallodendrimers **3** and **4** could be good candidates for the therapy of *cisPt* resistant tumors. As far as we know and despite being a compound widely used in organometallic chemistry as a starting material for different applications, including metallodrugs [55–57,59], the anticancer activity of RuCp was never reported in the literature and particularly referred as an active compound against tumors resistant to *cisPt*.

The IC_{50} values of RuCp were always higher than those of metallodendrimers that possess four coordinated $[Ru(\eta^5-C_5H_5)(PPh_3)_2]^+$ organometallic fragments. Possibly, for the metallodendrimers, the mechanism of drug cytotoxicity involves the release (de-coordination) of ruthenium containing fragments from the organic cores. Therefore, the organic dendrimer core serves as a vehicle for the cellular delivery of several $[Ru(\eta^5-C_5H_5)(PPh_3)_2]^+$ “toxic” fragments. Furthermore, we

previously showed by ^{31}P NMR spectroscopy that these metallodendrimers could suffer a degradation process at 37 °C [90]. Since the organic cores and PPh_3 did not show relevant toxicity by themselves (Supplementary Material, Figure S11), $[\text{Ru}(\eta^5\text{-C}_5\text{H}_5)(\text{PPh}_3)_2]^+$ should certainly be among the metallodendrimer degradation products. Also, the de-coordination of PPh_3 was not supported by NMR studies.

An additional observation of the present work was that the difference in the structure of the core (dendrimer **2** is more extensive and flexible than dendrimer **1**) had no especial impact over the cytotoxic behavior of the metallodendrimers which were both strongly cytotoxic.

Despite the usual differences between reported experimental conditions, the metallodendrimers **3** and **4** present IC_{50} values lower than other metallodendrimers reported in the literature, including high generation metallodendrimers (see some examples in Appendix A, Figure A1). For instance, by comparison with the fourth-generation of the chelating *N,O*-ruthenium(II)-arene-PTA metallodendrimers [72], our compounds were found to be 3.7 to 20 times more active against A2780 and A2780*cis*R cells. Interesting is also to compare, our IC_{50} values for metallodendrimers **3** and **4** with non-dendrimeric systems containing ruthenium complexes. For example, our simple metallodendrimers **3** and **4**, with four coordinated $[\text{Ru}(\eta^5\text{-C}_5\text{H}_5)(\text{PPh}_3)_2]^+$ organometallic fragments, when compared with cyclic peptide–polymer self-assembling nanotubes conjugated to ruthenium(II)-arene complex $[\text{Ru}(\eta^6\text{-p-cymene})\text{Cl}_2(\text{pta})]$ (RAPTA-C, a very active drug against metastases *in vivo*), were about 74 times more active against A2780 and A2780*cis*R cells [52]. They were also 65 times more cytotoxic than NAMI-A block copolymer micelles against the A2780 cancer cell line [47]. Even with the necessary reservations, the *in vitro* results obtained for metallodendrimers **3** and **4**, with the $[\text{Ru}(\eta^5\text{-C}_5\text{H}_5)(\text{PPh}_3)_2]^+$ organometallic fragment, compared with the published metallodendrimers or other multinuclear and supramolecular structures involving ruthenium-complexes, seem to be very promising and worthy of further study.

3. Materials and Methods

3.1. General Remarks

Unless otherwise noted, chemicals were used as received. The solvents diethyl ether (VWR), and dichloromethane (HPLC grade, Fisher Scientific, Hampton, NH, USA,) were distilled from sodium/benzophenone ketyl and calcium hydride (ACROS/Thermo Fisher Scientific, Waltham, MA USA), respectively, under a nitrogen atmosphere before use. Absolute methanol (Sigma-Aldrich, St. Louis, MO, USA) and benzene (PanReac, Barcelona, Spain) were degassed before use by bubbling with nitrogen. Dimethylsulfoxide (DMSO) for biological assays and AgCF_3SO_3 were purchased from VWR (Radnor, PA, USA) and ACROS, respectively. Deuterated solvents (CDCl_3 , DMSO- D_6 , D_2O) were purchased from EURISO-TOP (Saint-Aubin, France).

All reactions and manipulations involved in the preparation of the dendrimers $[\text{N}\equiv\text{C}(\text{CH}_2)_2]_2\text{N}(\text{CH}_2)_6\text{N}[(\text{CH}_2)_2\text{C}\equiv\text{N}]_2$ (**1**) and $[\text{N}\equiv\text{C}(\text{CH}_2)_2\text{O}(\text{CH}_2)_3]_2\text{N}(\text{CH}_2)_6\text{N}[(\text{CH}_2)_3\text{O}(\text{CH}_2)_2\text{C}\equiv\text{N}]_2$ (**2**), and the metallodendrimers **3** and **4** were executed under a dry nitrogen atmosphere by applying standard Schlenk-tube techniques. The starting materials $[\text{Ru}(\eta^5\text{-C}_5\text{H}_5)(\text{PPh}_3)_2\text{Cl}]$ [91] and the dendrimers **1** and **2** were prepared by following published methods [83].

3.2. Physical Measurements

^1H (400 MHz), $^{13}\text{C}\{^1\text{H}\}$ (100 MHz), $^{31}\text{P}\{^1\text{H}\}$ (161 MHz) and $^{19}\text{F}\{^1\text{H}\}$ (376 MHz) NMR spectra were recorded on an Avance II⁺ 400 spectrometer (Bruker, Wissembourg, France) at 299 K (probe temperature). The chemical shifts are reported in parts per million (δ , ppm) and referenced to residual solvent peaks for ^1H (CDCl_3 : $\delta = 7.26$ ppm). The ^{31}P - and ^{19}F -NMR were referenced to the external aqueous solution of 85% H_3PO_4 and KF at 0.5 M, respectively in CDCl_3 (or in a mixture of DMSO- D_6 / D_2O for PPh_3 spectra—see Supplementary Material, Figure S9). The IR spectra were measured on an Avatar 360 FTIR (Nicolet, Thermo Scientific, Waltham, MA, USA) in KBr pellets; only significant bands are mentioned in the text. The mass spectra (ESI-TOF) were recorded with a Micromass LCT mass spectrometer (Waters, Milford, MA, USA).

Elemental analyses (C, H, N) were performed in a VariolEL instrument from Elementar Analysensysteme (Langensfeld, Germany). In the processing of the elemental analysis results of compound **3** and **4**, the theoretical values were calculated taking into account the addition of dichloromethane molecules since their presence is observed in the $^1\text{H-NMR}$ spectra of both compounds. This situation arises from the inclusion of solvent molecules and/or inorganic salts in the dendritic structures during the isolation of the compound by precipitation.

3.3. Synthesis

3.3.1. Synthesis of $[(\eta^5\text{-C}_5\text{H}_5)(\text{PPh}_3)_2\text{Ru}]_4(1)[\text{CF}_3\text{SO}_3]_4$ (**3**)

The compound was prepared by reaction of $[\text{Ru}(\eta^5\text{-C}_5\text{H}_5)(\text{PPh}_3)_2\text{Cl}]$ (0.32 g, 0.44 mmol) with compound **1** (0.04 g, 0.11 mmol) and AgCF_3SO_3 (0.15 g, 0.58 mmol) in methanol (59 mL). The yellow-green suspension was stirred for 76 h at room temperature and protected from light. After the reaction, the resulting brown suspension was filtered, and the solid was extracted with dichloromethane. Then, the addition of diethyl ether to the resulting solution afford the precipitation of the desired compound. The solvent was removed, and the product was washed several times with diethyl ether and dried in under vacuum, resulting in a pale green powder. Yield: 0.14 g (35%). $^1\text{H-NMR}$ (CDCl_3): $\delta = 7.40\text{--}6.90$ (m, 24H + 48H + 48H, *PPh*₃), 4.48 (s, 20 H, *C*₅*H*₅), 2.66 (br., 8H), 2.45 (br., 8H), 2.24 (br., 4H), 1.18 (br., 8H) ppm. $^{31}\text{P-NMR}$ (CDCl_3): $\delta = 41.89$ (s, *PPh*₃) ppm. $^{19}\text{F-NMR}$ (CDCl_3): $\delta = -81.78$ ppm. FTIR (KBr): $\tilde{\nu} = 2271$ (ν_{CN}) and 1274 ($\nu_{\text{CF}_3\text{SO}_3}$) cm^{-1} . TOF-MS(ESI+): $m/z = 1694.5096$ $[\text{M}-2\text{CF}_3\text{SO}_3]^{2+}$, 1081.0131 $[\text{M}-3\text{CF}_3\text{SO}_3]^{3+}$. EA(%): $\text{C}_{186}\text{H}_{168}\text{F}_{12}\text{N}_6\text{O}_{12}\text{P}_8\text{Ru}_4\text{S}_4 \cdot 1.3\text{CH}_2\text{Cl}_2$ (3715.98): calcd. C 59.23, H 4.53, N 2.21; found C 59.21, H 4.54, N 2.20.

3.3.2. Synthesis of $[(\eta^5\text{-C}_5\text{H}_5)(\text{PPh}_3)_2\text{Ru}]_4(2)[\text{CF}_3\text{SO}_3]_4$ (**4**)

Compound **4** was prepared by reaction of $[\text{Ru}(\eta^5\text{-C}_5\text{H}_5)(\text{PPh}_3)_2\text{Cl}]$ (0.46 g, 0.63 mmol), compound **2** (0.07 g, 0.13 mmol) and AgCF_3SO_3 (0.17 g, 0.66 mmol) in methanol (42 mL). The resulting brown suspension was stirred for 66 h at room temperature under protection from light. The reaction mixture was filtered and dried under vacuum. Then, the yellow-brown solid was extracted with dichloromethane, dried and washed with diethyl ether and benzene. The dark green product was dissolved in dichloromethane, and the resulting solution was filtered and then concentrated under reduced pressure. The addition of diethyl ether to the previous solution originated the formation of dark green oil. This oil was isolated by removing the solvent and then washed with diethyl ether giving a bright green powder. Yield: 0.13 g (25%). $^1\text{H-NMR}$ (CDCl_3): $\delta = 7.50\text{--}7.00$ (m, 24H + 48H + 48H, *PPh*₃), 4.44 (s, 20H, *C*₅*H*₅), 3.31 (br., 8H + 8H), 3.10 (br., 8H), 2.98 (br., 4H), 2.90 (br., 8H), 1.85 (br., 8H), 1.30 (br., 4H) ppm. $^{31}\text{P-NMR}$ (CDCl_3): $\delta = 41.60$ (s, *PPh*₃) ppm. $^{19}\text{F-NMR}$ (CDCl_3): $\delta = -81.95$ ppm. FTIR (KBr): $\tilde{\nu} = 2269$ (ν_{CN}), 1286 and 697 ($\nu_{\text{CF}_3\text{SO}_3}$) cm^{-1} . TOF-MS(ESI+): $m/z = 1810.9692$ $[\text{M}-2\text{CF}_3\text{SO}_3]^{2+}$ and 1157.9568 $[\text{M}-3\text{CF}_3\text{SO}_3]^{3+}$. ES(%): $\text{C}_{198}\text{H}_{192}\text{F}_{12}\text{N}_6\text{O}_{16}\text{P}_8\text{Ru}_4\text{S}_4 \cdot 3\text{CH}_2\text{Cl}_2$ (4174.8): calcd. C 57.83, H 4.78, N 2.01; found C 57.79, H 4.79, N 2.04.

3.4. Cytotoxicity Studies

3.4.1. Cell Culture

The human cell lines Caco-2, CAL-72, and MCF-7 were purchased from German Collection of Microorganisms and Cell Cultures (DSMZ, Braunschweig, Germany), whereas A2780 and A2780cisR human cell lines were obtained from European Collection of Cell Cultures (ECACC, Salisbury, UK). The hMSCs were obtained from patient trabecular bone samples collected during surgical interventions performed after traumatic events (the only bone that would have been discarded was used). For this, the approval of the Ethics Committee of Dr. Nélio Mendonça Hospital (Funchal, Madeira main hospital) was obtained.

Caco-2 cells were grown in MEM medium supplemented with 20% (*v/v*) fetal bovine serum (FBS), 1% (*v/v*) nonessential amino acids (NEAA, from 100× ready-to-use stock solution) and 1% (*v/v*) antibiotic-antimycotic (AA, from 100× solution). CAL-72 cells were grown in DMEM medium enriched with 10% (*v/v*) FBS, 1% (*v/v*) insulin-transferrin-sodium selenite (ITS, from 100× solution), 2 mM L-glutamine and 1% antibiotic-antimycotic (AA, from 100× solution). MCF-7 cells were grown in RPMI 1640 medium supplemented with 20% (*v/v*) FBS, 1% (*v/v*) nonessential amino acids (NEAA, from 100× solution), 1 mM sodium pyruvate, 3.3 µg/mL human insulin and 1% (*v/v*) antibiotic-antimycotic (AA, from 100× solution). A2780 and A2780*cisR* were grown in RPMI 1640 medium supplemented with 10% (*v/v*) FBS, 2 mM L-glutamine and 1% (*v/v*) antibiotic-antimycotic (AA, from 100× solution). The hMSCs were grown in α-MEM medium supplemented with 10% (*v/v*) FBS and 1% (*v/v*) antibiotic-antimycotic (AA, from 100× solution). All cells were maintained at 37 °C in an incubator under a humidified atmosphere containing 5% CO₂.

3.4.2. Cell Viability Evaluation

The cell viability was indirectly determined by the MTT assay, which measures the mitochondrial dehydrogenase activity as an indication of cell survival.

Cells were counted using a hemocytometer and were seeded in 96-well plates by the addition of 100 µL of cell solution per well at the following cellular densities: 2×10^3 (Caco-2 and CAL-72), 4.2×10^3 (MCF-7), 5×10^3 (A2780 and A2780*cisR*) and 4.8×10^3 (hMSCs). The tested compounds were prepared in a stock solution of DMSO and serially diluted, in the same solvent, to different concentrations. Then, the resulting solutions were diluted in complete culture medium to the desired concentrations with a final DMSO concentration of 0.5% (*v/v*).

After 24 h of preincubation of the cells plates at 37 °C and 5% CO₂, the medium was aspirated, and 100 µL/well of complete medium containing the compound under test was added to the cells. Control experiments were done with cells cultured in complete culture medium with 0.5% (*v/v*) of DMSO. All tested conditions were accomplished in replicates of eight. All these culture plates were incubated for 72 h at 37 °C and 5% CO₂. After this period, the culture medium was aspirated and 100 µL of culture medium solution with 10% (*v/v*) of MTT solution (5 mg/mL) was added to each well. Then, after 3 to 4 h of incubation of the plates with MTT, the culture medium was aspirated, and DMSO was added to dissolve the formed purple formazan crystals. The absorbance reading was performed at 550 nm in a microplate reader (Victor3 1420, Perkin Elmer, Waltham, MA, USA) and the cell viability was determined. The concentration that inhibited 50% of the cellular metabolic activity (IC₅₀) was calculated by linear interpolation between the two experimental points closer to the point correspondent to 50% of the cellular metabolic activity shown by the control.

4. Conclusions

In summary, low-generation ruthenium (II) metallodendrimers based on two nitrile poly(alkylideneimine) dendritic scaffolds (differing in size and flexibility) and containing at the periphery the organometallic fragment $[\text{Ru}(\eta^5\text{-C}_5\text{H}_5)(\text{PPh}_3)_2]^+$ were synthesized and characterized. The core dendrimers **1** and **2** presented low cytotoxicity on all the cancer cell lines studied. Opposite behavior was observed for the prepared metallodendrimers and compound $[\text{Ru}(\eta^5\text{-C}_5\text{H}_5)(\text{PPh}_3)_2\text{Cl}]$ that revealed, a high anticancer activity towards different cancer cell lines (Caco-2, CAL-72, and MCF-7) and a high inhibitory effect on the viability of hMSCs *in vitro* (cells that are believed to be implicated in tumor progression). The latter compounds also presented high activity against cell lines resistant to *cisPt* (A2780*cisR*), with its anticancer activity being 22 and 166 times more higher than *cisPt*, respectively, for RuCp and both metallodendrimers, tackling an important and real problem in the context of anticancer therapy. Also, the IC₅₀ values of the prepared dendrimers are lower than other metallodendrimers reported in the literature, and 3.7 to 20 times more active against A2780 and A2780*cisR* cells.

With this work and to the best of our knowledge for the first time, we present evidences of the potential of an old organometallic complex, the $[\text{Ru}(\eta^5\text{-C}_5\text{H}_5)(\text{PPh}_3)_2\text{Cl}]$, as an anticancer drug, but also that the toxic fragment $[\text{Ru}(\eta^5\text{-C}_5\text{H}_5)(\text{PPh}_3)_2]^+$ could be delivered into cells using nitrile poly(alkylideneimine) dendritic scaffolds. We hypothesize that the delivery of these “new” drugs directly in the tumor site (local delivery) or, in the alternative, their association with nanomaterials for targeted and controlled delivery into tumors [92,93], would be the right strategy for their use in cancer therapy. Indeed, the high toxicity of these compounds towards different cancer cells and hMSCs can potentially be exploited but like happens with other anticancer drugs, undesired off-target effects must be avoided. Currently, we are focused on the design of nanocarriers dendrimers based on the targeted delivery of RuCp, as well as on the study of the possible mechanisms underlying their anticancer activity and pharmacokinetic behavior.

Supplementary Materials: The following are available online. Characterization data and Cytotoxicity assays of synthesized and studied compounds.

Author Contributions: Conceptualization, J.R.; Formal analysis, M.G., J.F., H.T. and J.R.; Funding acquisition, J.R.; Investigation, M.G., M.G.J. and R.C.; Methodology, H.T. and J.R.; Project administration, J.R.; Resources, H.T., K.R. and J.R.; Supervision, H.T. and J.R.; Validation, M.G., J.F., H.T. and J.R.; Visualization, M.G., H.T. and J.R.; Writing—original draft, M.G., H.T. and J.R.; Writing—review & editing, J.R. All authors have given approval to the final version of the manuscript.

Funding: This research was funded by Fundação para a Ciência e a Tecnologia (FCT), grant number PEst-OE/QUI/UI0674/2013, by the Madeira 14–20 Program, project PROEQUIPRAM—Reforço do Investimento em Equipamentos e Infraestruturas Científicas na RAM (grant number M1420-01-0145-FEDER-000008) and by ARDITI—Agência Regional para o Desenvolvimento da Investigação, Tecnologia e Inovação, grant number M1420-01-0145-FEDER-000005—Centro de Química da Madeira—CQM⁺ (Madeira 14–20 Program).

Acknowledgments: This work was supported by Fundação para a Ciência e a Tecnologia (FCT) with Portuguese Government funds through the CQM Strategic Project PEst-OE/QUI/UI0674/2013 and the Madeira 14–20 Program, project PROEQUIPRAM—Reforço do Investimento em Equipamentos e Infraestruturas Científicas na RAM (M1420-01-0145-FEDER-000008). ARDITI—Agência Regional para o Desenvolvimento da Investigação Tecnologia e Inovação is also acknowledged through the project M1420-01-0145-FEDER-000005—CQM⁺ (Madeira 14–20 Program).

Conflicts of Interest: The authors declare no conflict of interest and communicate that the founding sponsors had no role in the design of the study; in the collection, analyses, or interpretation of data; in the writing of the manuscript, and in the decision to publish the results.

Appendix A

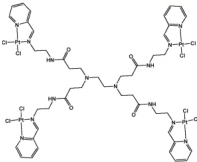
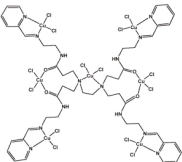
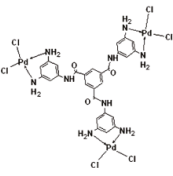
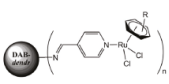
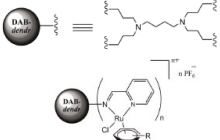
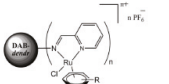
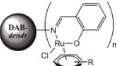
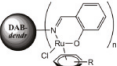
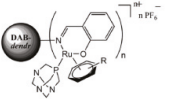
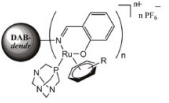
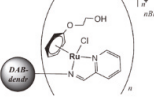
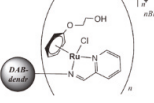
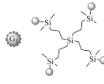
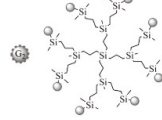
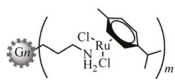
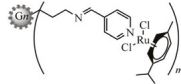
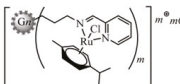
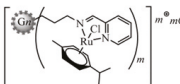
	 MCF-7^a \approx inactive		 MCF-7^a 10.2		 MCF-7^b 50	
IC₅₀						
	 A2780 (IC₅₀)^c		 A2780 (IC₅₀)^d		 A2780cisR (IC₅₀)^d	
	 A2780 (IC₅₀)^{d,e}		 A2780cisR (IC₅₀)^{d,e}			
n	<i>p</i> -cym	HMB	<i>p</i> -cym	HMB	<i>p</i> -cym	HMB
4	43	40	>200	32	>200	42
8	21	20	23	4	76	4
16						
32						
	 A2780 (IC₅₀)^e		 A2780 cisR (IC₅₀)^e		 A2780 (IC₅₀)^f	
	 A2780cisR (IC₅₀)^f					
n	<i>p</i> -cym	HMB	<i>p</i> -cym	HMB		
4	174	8.9	72.8	25	25.8	50
8	9.3	6.2	19.3	11.8	>100	>100
16	1.4	2.9	3.6	2	16.7	19
32	0.8	2	2.7	1.1	5	17.3
	 HeLa (IC₅₀)^g		 HeLa (IC₅₀)^h			
	 MCF-7 (IC₅₀)^g		 MCF-7 (IC₅₀)^h			
	 HT-29 (IC₅₀)^g		 HT-29 (IC₅₀)^h			
	n=1, m=4	n=2, m=8	n=1, m=4	n=2, m=8	n=1, m=4	n=1, m=8
HeLa (IC₅₀)^g	6.3	68.8	4.4	9.1	8.1	6.9
MCF-7 (IC₅₀)^g	3.6	19.9	2.5	3.4	6.9	8.5
HT-29 (IC₅₀)^g	6.6	14.4	3.3	7	5.6	13.4
MDA-MB-231 (IC₅₀)^g	4.5		4.9	6.7	6.1	10.1
HL-60 (IC₅₀)^h	12.01		12.05	29.81	11.57	12.94

Figure A1. IC₅₀ values (in μ M) of some metallodendrimers reported in the literature. (a) [68]; (b) [71]; (c) [67]; (d) [69]; (e) [72]; (f) [77]; (g) [78] and (h) [79].

References

- Ruddon, R.W. *Cancer Biology*, 4th ed.; Oxford University Press: New York, NY, USA, 2007; ISBN 978-0195175448.
- Hesketh, R. *Introduction to Cancer Biology: A Concise Journey from Epidemiology Through Cell and Molecular Biology to Treatment and Prospects*; Cambridge University Press: New York, NY, USA, 2013; ISBN 978-1-107-60148-2.
- Cronin, K.A.; Lake, A.J.; Scott, S.; Sherman, R.L.; Noone, A.; Howlader, N.; Henley, S.J.; Anderson, R.N.; Firth, A.U.; Ma, J.; et al. Annual Report to the Nation on the Status of Cancer, part I: National cancer statistics. *Cancer* **2018**. [[CrossRef](#)] [[PubMed](#)]
- National Cancer Institute—Cancer Statistics. Available online: <https://www.cancer.gov/about-cancer/understanding/statistics> (accessed on 26 April 2018).
- Rosenberg, B.; Van Camp, L.; Krigas, T. Inhibition of Cell Division in Escherichia Coli by Electrolysis Products from a Platinum Electrode. *Nature* **1965**, *205*, 698–699. [[CrossRef](#)] [[PubMed](#)]
- Trudu, F.; Amato, F.; Vañhara, P.; Pivetta, T.; Peña-Méndez, E.M.; Havel, J. Coordination Compounds in Cancer: Past, Present and Perspectives. *J. Appl. Biomed.* **2015**, *13*, 79–103. [[CrossRef](#)]
- Monneret, C. Platinum Anticancer Drugs. From Serendipity to Rational Design. *Ann. Pharm. Françaises* **2011**, *69*, 286–295. [[CrossRef](#)] [[PubMed](#)]
- Besse, B.; Adjei, A.; Baas, P.; Meldgaard, P.; Nicolson, M.; Paz-Ares, L.; Reck, M.; Smit, E.F.; Syrigos, K.; Stahel, R.; et al. 2nd ESMO Consensus Conference on Lung Cancer: Non-Small-Cell Lung Cancer First-Line/second and Further Lines of Treatment in Advanced Disease. *Ann. Oncol.* **2014**, *25*, 1475–1484. [[CrossRef](#)] [[PubMed](#)]
- Gahart, B.L.; Nazareno, A.R. *2015 Intravenous Medications: A Handbook for Nurses and Health Professionals; Intravenous Medications*, 31st ed.; Elsevier Health Sciences: St. Louis Missouri, USA, 2014.
- Partridge, A.H.; Rumble, R.B.; Carey, L.A.; Come, S.E.; Davidson, N.E.; Di Leo, A.; Gralow, J.; Hortobagyi, G.N.; Moy, B.; Yee, D.; et al. Chemotherapy and Targeted Therapy for Women With Human Epidermal Growth Factor Receptor 2—Negative (or Unknown) Advanced Breast Cancer: American Society of Clinical Oncology Clinical Practice Guideline. *J. Clin. Oncol.* **2014**, *32*, 3307–3329. [[CrossRef](#)] [[PubMed](#)]
- Hanna, N.H.; Einhorn, L.H. Testicular Cancer—Discoveries and Updates. *N. Engl. J. Med.* **2014**, *371*, 2005–2016. [[CrossRef](#)] [[PubMed](#)]
- Ghosn, M.; Kourie, H.R.; El Rassy, E.; Chebib, R.; El Karak, F.; Hanna, C.; Nasr, D. Optimum Chemotherapy for the Management of Advanced Biliary Tract Cancer. *World J. Gastroenterol.* **2015**, *21*, 4121–4125. [[CrossRef](#)] [[PubMed](#)]
- Pignata, S.; Scambia, G.; Katsaros, D.; Gallo, C.; Pujade-Lauraine, E.; De Placido, S.; Bologna, A.; Weber, B.; Raspagliesi, F.; Panici, P.B.; et al. Carboplatin plus Paclitaxel Once a Week versus Every 3 Weeks in Patients with Advanced Ovarian Cancer (MITO-7): A Randomised, Multicentre, Open-Label, Phase 3 Trial. *Lancet Oncol.* **2014**, *15*, 396–405. [[CrossRef](#)]
- Liao, B.-C.; Shao, Y.-Y.; Chen, H.-M.; Shau, W.-Y.; Lin, Z.-Z.; Kuo, R.N.; Lai, C.-L.; Chen, K.-H.; Cheng, A.-L.; Yang, J.C.-H.; et al. Comparative Effectiveness of First-Line Platinum-Based Chemotherapy Regimens for Advanced Lung Squamous Cell Carcinoma. *Clin. Lung Cancer* **2015**, *16*, 137–143. [[CrossRef](#)] [[PubMed](#)]
- Smith, J.J.; Garcia-Aguilar, J. Advances and Challenges in Treatment of Locally Advanced Rectal Cancer. *J. Clin. Oncol.* **2015**, *33*, 1797–1808. [[CrossRef](#)] [[PubMed](#)]
- Rabik, C.A.; Dolan, M.E. Molecular Mechanisms of Resistance and Toxicity Associated with Platinating Agents. *Cancer Treat. Rev.* **2007**, *33*, 9–23. [[CrossRef](#)] [[PubMed](#)]
- Langer, T.; am Zehnhoff-Dinnesen, A.; Radtke, S.; Meitert, J.; Zolk, O. Understanding Platinum-Induced Ototoxicity. *Trends Pharmacol. Sci.* **2013**, *34*, 458–469. [[CrossRef](#)] [[PubMed](#)]
- Avan, A.; Postma, T.J.; Ceresa, C.; Avan, A.; Cavaletti, G.; Giovannetti, E.; Peters, G.J. Platinum-Induced Neurotoxicity and Preventive Strategies: Past, Present, and Future. *Oncologist* **2015**, *20*, 411–432. [[CrossRef](#)] [[PubMed](#)]
- Krüger, K.; Thomale, J.; Stojanović, N.; Osmak, M.; Henninger, C.; Bormann, S.; Fritz, G. Platinum-Induced Kidney Damage: Unraveling the DNA Damage Response (DDR) of Renal Tubular Epithelial and Glomerular Endothelial Cells Following Platinum Injury. *Biochim. Biophys. Acta Mol. Cell Res.* **2015**, *1853*, 685–698. [[CrossRef](#)] [[PubMed](#)]
- McWhinney, S.R.; Goldberg, R.M.; McLeod, H.L. Platinum Neurotoxicity Pharmacogenetics. *Mol. Cancer Ther.* **2009**, *8*, 10–16. [[CrossRef](#)] [[PubMed](#)]

21. Martin, L.P.; Hamilton, T.C.; Schilder, R.J. Platinum Resistance: The Role of DNA Repair Pathways. *Clin. Cancer Res.* **2008**, *14*, 1291–1295. [[CrossRef](#)] [[PubMed](#)]
22. Davis, A.; Tinker, A.V.; Friedlander, M. “Platinum Resistant” Ovarian Cancer: What Is It, Who to Treat and How to Measure Benefit? *Gynecol. Oncol.* **2014**, *133*, 624–631. [[CrossRef](#)] [[PubMed](#)]
23. Moutinho, C.; Martínez-Cardús, A.; Santos, C.; Navarro-Pérez, V.; Martínez-Balibrea, E.; Musulen, E.; Carmona, F.J.; Sartore-Bianchi, A.; Cassingena, A.; Siena, S.; et al. Epigenetic Inactivation of the BRCA1 Interactor SRBC and Resistance to Oxaliplatin in Colorectal Cancer. *J. Natl. Cancer Inst.* **2014**, *106*, djt322. [[CrossRef](#)] [[PubMed](#)]
24. Siddik, Z.H. Cisplatin: Mode of Cytotoxic Action and Molecular Basis of Resistance. *Oncogene* **2003**, *22*, 7265–7279. [[CrossRef](#)] [[PubMed](#)]
25. Jacobsen, C.; Honecker, F. Cisplatin Resistance in Germ Cell Tumours: Models and Mechanisms. *Andrology* **2015**, *3*, 111–121. [[CrossRef](#)] [[PubMed](#)]
26. Horibe, S.; Matsuda, A.; Tanahashi, T.; Inoue, J.; Kawauchi, S.; Mizuno, S.; Ueno, M.; Takahashi, K.; Maeda, Y.; Maegouchi, T.; et al. Cisplatin Resistance in Human Lung Cancer Cells Is Linked with Dysregulation of Cell Cycle Associated Proteins. *Life Sci.* **2015**, *124*, 31–40. [[CrossRef](#)] [[PubMed](#)]
27. Bergamo, A.; Gaiddon, C.; Schellens, J.H.; Beijnen, J.H.; Sava, G. Approaching Tumour Therapy beyond Platinum Drugs: Status of the Art and Perspectives of Ruthenium Drug Candidates. *J. Inorg. Biochem.* **2012**, *106*, 90–99. [[CrossRef](#)] [[PubMed](#)]
28. Zeng, L.; Gupta, P.; Chen, Y.; Wang, E.; Ji, L.; Chao, H.; Chen, Z.-S. The Development of Anticancer Ruthenium(II) Complexes: From Single Molecule Compounds to Nanomaterials. *Chem. Soc. Rev.* **2017**, *46*, 5771–5804. [[CrossRef](#)] [[PubMed](#)]
29. Lazarević, T.; Rilak, A.; Bugarić, Ž.D. Platinum, palladium, gold and ruthenium complexes as anticancer agents: Current clinical uses, cytotoxicity studies and future perspectives. *Eur. J. Med. Chem.* **2017**, *142*, 8–31. [[CrossRef](#)] [[PubMed](#)]
30. Allardyce, C.S.; Dyson, P.J. Ruthenium in Medicine: Current Clinical Uses and Future Prospects. *Platin. Met. Rev.* **2001**, *45*, 62–69. [[CrossRef](#)]
31. Alessio, E.; Guo, Z. Metal Anticancer Complexes—Activity, Mechanism of Action, Future Perspectives. *Eur. J. Inorg. Chem.* **2017**, 1549–1560. [[CrossRef](#)]
32. Reedijk, J. Metal-Ligand Exchange Kinetics in Platinum and Ruthenium Complexes. *Platin. Met. Rev.* **2008**, *52*, 2–11. [[CrossRef](#)]
33. Bruijninx, P.C.A.; Sadler, P.J. Controlling Platinum, Ruthenium, and Osmium Reactivity for Anticancer Drug Design. *Adv. Inorg. Chem.* **2009**, *61*, 1–62. [[CrossRef](#)] [[PubMed](#)]
34. Pongratz, M.; Schluga, P.; Jakupec, M.A.; Arion, V.B.; Hartinger, C.G.; Allmaier, G.; Keppler, B.K. Transferrin Binding and Transferrin-Mediated Cellular Uptake of the Ruthenium Coordination Compound KP1019, Studied by Means of AAS, ESI-MS and CD Spectroscopy. *J. Anal. At. Spectrom.* **2004**, *19*, 46–51. [[CrossRef](#)]
35. Guo, W.; Zheng, W.; Luo, Q.; Li, X.; Zhao, Y.; Xiong, S.; Wang, F. Transferrin Serves As a Mediator to Deliver Organometallic Ruthenium(II) Anticancer Complexes into Cells. *Inorg. Chem.* **2013**, *52*, 5328–5338. [[CrossRef](#)] [[PubMed](#)]
36. Antonarakis, E.S.; Emadi, A. Ruthenium-Based Chemotherapeutics: Are They Ready for Prime Time? *Cancer Chemother. Pharmacol.* **2010**, *66*, 1–9. [[CrossRef](#)] [[PubMed](#)]
37. Ang, W.H.; Dyson, P.J. Classical and Non-Classical Ruthenium-Based Anticancer Drugs: Towards Targeted Chemotherapy. *Eur. J. Inorg. Chem.* **2006**, *2006*, 4003–4018. [[CrossRef](#)]
38. Levina, A.; Mitra, A.; Lay, P.A. Recent Developments in Ruthenium Anticancer Drugs. *Metallomics* **2009**, *1*, 458–470. [[CrossRef](#)] [[PubMed](#)]
39. Rademaker-Lakhai, J.M.; van den Bongard, D.; Pluim, D.; Beijnen, J.H.; Schellens, J.H.M. A Phase I and Pharmacological Study with Imidazolium-Trans-DMSO-Imidazole-Tetrachlororuthenate, a Novel Ruthenium Anticancer Agent. *Clin. Cancer Res.* **2004**, *10*, 3717–3727. [[CrossRef](#)] [[PubMed](#)]
40. Leijen, S.; Burgers, S.; Baas, P.; Pluim, D.; Tibben, M.; van Werkhoven, E.; Alessio, E.; Sava, G.; Beijnen, J.; Schellens, J.M. Phase I/II Study with Ruthenium Compound NAMI-A and Gemcitabine in Patients with Non-Small Cell Lung Cancer after First Line Therapy. *Investig. New Drugs* **2015**, *33*, 201–214. [[CrossRef](#)] [[PubMed](#)]
41. Bergamo, A.; Sava, G. Linking the Future of Anticancer Metal-Complexes to the Therapy of Tumour Metastases. *Chem. Soc. Rev.* **2015**, *44*, 8818–8835. [[CrossRef](#)] [[PubMed](#)]

42. Hartinger, C.G.; Jakupec, M.A.; Zorbas-Seifried, S.; Groessl, M.; Egger, A.; Berger, W.; Zorbas, H.; Dyson, P.J.; Keppler, B.K. KP1019, A New Redox-Active Anticancer Agent—Preclinical Development and Results of a Clinical Phase I Study in Tumor Patients. *Chem. Biodivers.* **2008**, *5*, 2140–2155. [[CrossRef](#)] [[PubMed](#)]
43. Lentz, F.; Drescher, A.; Lindauer, A.; Henke, M.; Hilger, R.A.; Hartinger, C.G.; Scheulen, M.E.; Dittrich, C.; Keppler, B.K.; Jaehde, U. Research-EWIV, in collaboration with C. E. S. for A. D. Pharmacokinetics of a Novel Anticancer Ruthenium Complex (KP1019, FFC14A) in a Phase I Dose-Escalation Study. *Anticancer Drugs* **2009**, *20*, 97–103. [[CrossRef](#)] [[PubMed](#)]
44. Trondl, R.; Heffeter, P.; Kowol, C.R.; Jakupec, M.A.; Berger, W.; Keppler, B.K. NKP-1339, the First Ruthenium-Based Anticancer Drug on the Edge to Clinical Application. *Chem. Sci.* **2014**, *5*, 2925–2932. [[CrossRef](#)]
45. Chellan, P.; Sadler, P.J. The Elements of Life and Medicines. *Philos. Trans. Ser. A Math. Phys. Eng. Sci.* **2015**, *373*. [[CrossRef](#)] [[PubMed](#)]
46. Dömötör, O.; Hartinger, C.; Bytzek, A.; Kiss, T.; Keppler, B.; Enyedy, E. Characterization of the Binding Sites of the Anticancer ruthenium(III) Complexes KP1019 and KP1339 on Human Serum Albumin via Competition Studies. *BIC J. Biol. Inorg. Chem.* **2013**, *18*, 9–17. [[CrossRef](#)] [[PubMed](#)]
47. Blunden, B.M.; Rawal, A.; Lu, H.; Stenzel, M.H. Superior Chemotherapeutic Benefits from the Ruthenium-Based Anti-Metastatic Drug NAMI-A through Conjugation to Polymeric Micelles. *Macromolecules* **2014**, *47*, 1646–1655. [[CrossRef](#)]
48. Montesarchio, D.; Mangiapia, G.; Vitiello, G.; Musumeci, D.; Irace, C.; Santamaria, R.; D'Errico, G.; Paduano, L. A new design for nucleolipid-based Ru(III) complexes as anticancer agents. *Dalton Trans.* **2013**, *42*, 16697–16708. [[CrossRef](#)] [[PubMed](#)]
49. Vitiello, G.; Luchini, A.; D'Errico, G.; Santamaria, R.; Capuozzo, A.; Irace, C.; Montesarchio, D.; Paduano, L. Cationic Liposomes as Efficient Nanocarriers for the Drug Delivery of an Anticancer Cholesterol-Based Ruthenium Complex. *J. Mater. Chem. B* **2015**, *3*, 3011–3023. [[CrossRef](#)]
50. Irace, C.; Misso, G.; Capuozzo, A.; Piccolo, M.; Riccardi, C.; Luchini, A.; Caraglia, M.; Paduano, L.; Montesarchio, D.; Santamaria, R. Antiproliferative effects of ruthenium-based nucleolipidic nanoaggregates in human models of breast cancer in vitro: Insights into their mode of action. *Sci. Rep.* **2017**, *7*, 45236. [[CrossRef](#)] [[PubMed](#)]
51. Riccardi, C.; Musumeci, D.; Irace, C.; Paduano, L.; Montesarchio, D. Ru^{III} Complexes for Anticancer Therapy: The Importance of Being Nucleolipidic. *Eur. J. Org. Chem.* **2017**, 1100–1119. [[CrossRef](#)]
52. Blunden, B.M.; Chapman, R.; Daniai, M.; Lu, H.; Jolliffe, K.A.; Perrier, S.; Stenzel, M.H. Drug Conjugation to Cyclic Peptide-Polymer Self-Assembling Nanotubes. *Chem. Eur. J.* **2014**, *20*, 12745–12749. [[CrossRef](#)] [[PubMed](#)]
53. Suss-Fink, G. Arene Ruthenium Complexes as Anticancer Agents. *Dalton Trans.* **2010**, *39*, 1673–1688. [[CrossRef](#)] [[PubMed](#)]
54. Garcia, M.H.; Morais, T.S.; Florindo, P.; Piedade, M.F.; Moreno, V.; Ciudad, C.; Noe, V. Inhibition of Cancer Cell Growth by ruthenium(II) Cyclopentadienyl Derivative Complexes with Heteroaromatic Ligands. *J. Inorg. Biochem.* **2009**, *103*, 354–361. [[CrossRef](#)] [[PubMed](#)]
55. Tomaz, A.I.; Jakusch, T.; Morais, T.S.; Marques, F.; de Almeida, R.F.M.; Mendes, F.; Enyedy, É.A.; Santos, I.; Pessoa, J.C.; Kiss, T.; et al. [Ru^{II}(η⁵-C₅H₅)(bipy)(PPh₃)]⁺, a Promising Large Spectrum Antitumor Agent: Cytotoxic Activity and Interaction with Human Serum Albumin. *J. Inorg. Biochem.* **2012**, *117*, 261–269. [[CrossRef](#)] [[PubMed](#)]
56. Morais, T.S.; Santos, F.C.; Jorge, T.F.; Côte-Real, L.; Madeira, P.J.A.; Marques, F.; Robalo, M.P.; Matos, A.; Santos, I.; Garcia, M.H. New Water-Soluble ruthenium(II) Cytotoxic Complex: Biological Activity and Cellular Distribution. *J. Inorg. Biochem.* **2014**, *130*, 1–14. [[CrossRef](#)] [[PubMed](#)]
57. Peacock, A.F.A.; Sadler, P.J. Medicinal Organometallic Chemistry: Designing Metal Arene Complexes as Anticancer Agents. *Chem. An Asian J.* **2008**, *3*, 1890–1899. [[CrossRef](#)] [[PubMed](#)]
58. Morais, T.S.; Silva, T.J.L.; Marques, F.; Robalo, M.P.; AVECILLA, F.; Madeira, P.J.A.; Mendes, P.J.G.; Santos, I.; Garcia, M.H. Synthesis of Organometallic ruthenium(II) Complexes with Strong Activity against Several Human Cancer Cell Lines. *J. Inorg. Biochem.* **2012**, *114*, 65–74. [[CrossRef](#)] [[PubMed](#)]
59. Kesharwani, P.; Jain, K.; Jain, N.K. Dendrimer as Nanocarrier for Drug Delivery. *Prog. Polym. Sci.* **2014**, *39*, 268–307. [[CrossRef](#)]
60. Nanjwade, B.K.; Bechra, H.M.; Derkar, G.K.; Manvi, F.V.; Nanjwade, V.K. Dendrimers: Emerging Polymers for Drug-Delivery Systems. *Eur. J. Pharm. Sci.* **2009**, *38*, 185–196. [[CrossRef](#)] [[PubMed](#)]

61. Pérez-Herrero, E.; Fernández-Medarde, A. Advanced Targeted Therapies in Cancer: Drug Nanocarriers, the Future of Chemotherapy. *Eur. J. Pharm. Biopharm.* **2015**, *93*, 52–79. [[CrossRef](#)] [[PubMed](#)]
62. Mignani, S.; Rodrigues, J.; Tomas, T.; Roy, R.; Shi, X.; Majoral, J.-P. Bench-to-bedside translation of dendrimers: Reality or utopia? A concise analysis. *Adv. Drug Deliv. Rev.* **2017**, in press. [[CrossRef](#)] [[PubMed](#)]
63. Kesharwani, P.; Iyer, A.K. Recent Advances in Dendrimer-Based Nanovectors for Tumor-Targeted Drug and Gene Delivery. *Drug Discov. Today* **2015**, *20*, 536–547. [[CrossRef](#)] [[PubMed](#)]
64. Govender, P.; Therrien, B.; Smith, G.S. Bio-Metallo-dendrimers—Emerging Strategies in Metal-Based Drug Design. *Eur. J. Inorg. Chem.* **2012**, *2012*, 2853–2862. [[CrossRef](#)]
65. Jansen, B.A.J.; van der Zwan, J.; Reedijk, J.; den Dulk, H.; Brouwer, J. A Tetranuclear Platinum Compound Designed to Overcome Cisplatin Resistance. *Eur. J. Inorg. Chem.* **1999**, *1999*, 1429–1433. [[CrossRef](#)]
66. Hurley, A.L.; Mohler, D.L. Organometallic Photonuclases: Synthesis and DNA-Cleavage Studies of Cyclopentadienyl Metal-Substituted Dendrimers Designed To Increase Double-Strand Scission. *Org. Lett.* **2000**, *2*, 2745–2748. [[CrossRef](#)] [[PubMed](#)]
67. Govender, P.; Antonels, N.C.; Mattsson, J.; Renfrew, A.K.; Dyson, P.J.; Moss, J.R.; Therrien, B.; Smith, G.S. Anticancer Activity of Multinuclear Arene Ruthenium Complexes Coordinated to Dendritic Polypyridyl Scaffolds. *J. Organomet. Chem.* **2009**, *694*, 3470–3476. [[CrossRef](#)]
68. Zhao, X.; Loo, S.C.J.; Lee, P.P.-F.; Tan, T.T.Y.; Chu, C.K. Synthesis and Cytotoxic Activities of chloropyridylimineplatinum(II) and chloropyridyliminecopper(II) Surface-Functionalized Poly(amidoamine) Dendrimers. *J. Inorg. Biochem.* **2010**, *104*, 105–110. [[CrossRef](#)] [[PubMed](#)]
69. Govender, P.; Renfrew, A.K.; Clavel, C.M.; Dyson, P.J.; Therrien, B.; Smith, G.S. Antiproliferative Activity of Chelating *N,O*- and *N,N*-Ruthenium(II) Arene Functionalised Poly(propyleneimine) Dendrimer Scaffolds. *Dalton Trans.* **2011**, *40*, 1158–1167. [[CrossRef](#)] [[PubMed](#)]
70. Robilotto, T.J.; Alt, D.S.; von Recum, H.A.; Gray, T.G. Cytotoxic Gold(I)-Bearing Dendrimers from Alkyne Precursors. *Dalton Trans.* **2011**, *40*, 8083–8085. [[CrossRef](#)] [[PubMed](#)]
71. Ahamad, T.; Mapolie, S.F.; Alshehri, S. Synthesis and Characterization of Polyamide Metallo-dendrimers and Their Anti-Bacterial and Anti-Tumor Activities. *Med. Chem. Res.* **2012**, *21*, 2023–2031. [[CrossRef](#)]
72. Govender, P.; Sudding, L.C.; Clavel, C.M.; Dyson, P.J.; Therrien, B.; Smith, G.S. The Influence of RAPTA Moieties on the Antiproliferative Activity of Peripheral-Functionalised Poly(salicylaldehyde) Metallo-dendrimers. *Dalton Trans.* **2013**, *42*, 1267–1277. [[CrossRef](#)] [[PubMed](#)]
73. Payne, R.; Govender, P.; Therrien, B.; Clavel, C.M.; Dyson, P.J.; Smith, G.S. Neutral and Cationic Multinuclear Half-Sandwich Rhodium and Iridium Complexes Coordinated to Poly(propyleneimine) Dendritic Scaffolds: Synthesis and Cytotoxicity. *J. Organomet. Chem.* **2013**, *729*, 20–27. [[CrossRef](#)]
74. El Brahmī, N.; El Kazzouli, S.; Mignani, S.M.; Essassi, E.M.; Aubert, G.; Laurent, R.; Caminade, A.-M.; Bousmina, M.M.; Cresteil, T.; Majoral, J.-P. Original Multivalent Copper(II)-Conjugated Phosphorus Dendrimers and Corresponding Mononuclear Copper(II) Complexes with Antitumoral Activities. *Mol. Pharm.* **2013**, *10*, 1459–1464. [[CrossRef](#)] [[PubMed](#)]
75. Sudding, L.C.; Payne, R.; Govender, P.; Edeaf, F.; Clavel, C.M.; Dyson, P.J.; Therrien, B.; Smith, G.S. Evaluation of the in Vitro Anticancer Activity of Cyclometalated Half-Sandwich Rhodium and Iridium Complexes Coordinated to Naphthaldehyde-Based Poly(propyleneimine) Dendritic Scaffolds. *J. Organomet. Chem.* **2014**, *774*, 79–85. [[CrossRef](#)]
76. Govender, P.; Edeaf, F.; Makhubela, B.C.E.; Dyson, P.J.; Therrien, B.; Smith, G.S. Neutral and Cationic osmium(II)-Arene Metallo-dendrimers: Synthesis, Characterisation and Anticancer Activity. *Inorg. Chim. Acta* **2014**, *409*, 112–120. [[CrossRef](#)]
77. Govender, P.; Riedel, T.; Dyson, P.J.; Smith, G.S. Higher Generation Cationic *N,N*-ruthenium(II)-Ethylene-Glycol-Derived Metallo-dendrimers: Synthesis, Characterization and Cytotoxicity. *J. Organomet. Chem.* **2015**, *799–800*, 38–44. [[CrossRef](#)]
78. Maroto-Díaz, M.; Elie, B.T.; Gomez-Sal, P.; Perez-Serrano, J.; Gomez, R.; Contel, M.; Javier de la Mata, F. Synthesis and Anticancer Activity of Carbosilane Metallo-dendrimers Based on Arene Ruthenium(II) Complexes. *Dalton Trans.* **2016**, *45*, 7049–7066. [[CrossRef](#)] [[PubMed](#)]
79. Michlewska, S.; Ionov, M.; Shcharbin, D.; Maroto-Díaz, M.; Gomez Ramirez, R.; Javier de la Mata, F.; Bryszewska, M. Ruthenium Metallo-dendrimers with Anticancer Potential in an Acute Promyelocytic Leukemia Cell Line (HL60). *Eur. Polym. J.* **2017**, *87*, 39–47. [[CrossRef](#)]

80. Reagan, M.R.; Kaplan, D.L. Concise Review: Mesenchymal Stem Cell Tumor-Homing: Detection Methods in Disease Model Systems. *Stem Cells* **2011**, *29*, 920–927. [[CrossRef](#)] [[PubMed](#)]
81. Chang, A.I.; Schwertschkow, A.H.; Nolta, J.A.; Wu, J. Involvement of Mesenchymal Stem Cells in Cancer Progression and Metastases. *Curr. Cancer Drug Targets* **2015**, *15*, 88–98. [[CrossRef](#)] [[PubMed](#)]
82. Rhee, K.-J.; Lee, I.J.; Eom, W.Y. Mesenchymal Stem Cell-Mediated Effects of Tumor Support or Suppression. *Int. J. Mol. Sci.* **2015**, *16*, 30015–30033. [[CrossRef](#)] [[PubMed](#)]
83. Jardim, M.G.; Rissanen, K.; Rodrigues, J. Preparation and Characterization of Novel Poly(alkylideneamine) Nitrile Ruthenium Metallodendrimers. *Eur. J. Inorg. Chem.* **2010**, *2010*, 1729–1735. [[CrossRef](#)]
84. Van Geelen, C.M.M.; de Vries, E.G.E.; Le, T.K.P.; van Weeghel, R.P.; de Jong, S. Differential Modulation of the TRAIL Receptors and the CD95 Receptor in Colon Carcinoma Cell Lines. *Br. J. Cancer* **2003**, *89*, 363–373. [[CrossRef](#)] [[PubMed](#)]
85. Tolan, D.; Gandin, V.; Morrison, L.; El-Nahas, A.; Marzano, C.; Montagner, D.; Erxleben, A. Oxidative Stress Induced by Pt(IV) Pro-drugs Based on the Cisplatin Scaffold and Indole Carboxylic Acids in Axial Position. *Sci. Rep.* **2016**, *6*, 29367. [[CrossRef](#)] [[PubMed](#)]
86. Klopp, A.H.; Gupta, A.; Spaeth, E.; Andreeff, M.; Marini, F. Concise Review: Dissecting a Discrepancy in the Literature: Do Mesenchymal Stem Cells Support or Suppress Tumor Growth? *Stem Cells* **2011**, *29*, 11–19. [[CrossRef](#)] [[PubMed](#)]
87. Bartosh, T.J.; Ullah, M.; Zeitouni, S.; Beaver, J.; Prockop, D.J. Cancer Cells Enter Dormancy after Cannibalizing Mesenchymal Stem/stromal Cells (MSCs). *Proc. Natl. Acad. Sci. USA* **2016**, *113*, E6447–E6456. [[CrossRef](#)] [[PubMed](#)]
88. Hong, I.-S.; Lee, H.-Y.; Kang, K.-S. Mesenchymal Stem Cells and Cancer: Friends or Enemies? *Mutat. Res.* **2014**, *768*, 98–106. [[CrossRef](#)] [[PubMed](#)]
89. Houthuijzen, J.M.; Daenen, L.G.M.; Roodhart, J.M.L.; Voest, E.E. The Role of Mesenchymal Stem Cells in Anti-Cancer Drug Resistance and Tumour Progression. *Br. J. Cancer* **2012**, *106*, 1901–1906. [[CrossRef](#)] [[PubMed](#)]
90. Rodrigues, J.; Jardim, M.G.; Figueira, J.; Gouveia, M.; Tomas, H.; Rissanen, K. Poly(alkylideneamines) Dendrimers as Scaffolds for the Preparation of Low-Generation Ruthenium Based Metallodendrimers. *New J. Chem.* **2011**, *35*, 1938–1943. [[CrossRef](#)]
91. Bruce, M.I.; Windsor, N.J. Cyclopentadienyl-Ruthenium and -Osmium Chemistry. IV. Convenient High-Yield Synthesis of Some Cyclopentadienyl Ruthenium or Osmium Tertiary Phosphine Halide Complexes. *Aust. J. Chem.* **1977**, *30*, 1601–1604. [[CrossRef](#)]
92. Blunden, B.M.; Stenzel, M.H. Incorporating Ruthenium into Advanced Drug Delivery Carriers—An Innovative Generation of Chemotherapeutics. *J. Chem. Technol. Biotechnol.* **2015**, *90*, 1177–1195. [[CrossRef](#)]
93. Thangavel, P.; Viswanath, B.; Kim, S. Recent developments in the nanostructured materials functionalized with ruthenium complexes for targeted drug delivery to tumors. *Int. J. Nanomed.* **2017**, *12*, 2749–2758. [[CrossRef](#)] [[PubMed](#)]

Sample Availability: Samples of the compounds 1–4 are available from the authors.



© 2018 by the authors. Licensee MDPI, Basel, Switzerland. This article is an open access article distributed under the terms and conditions of the Creative Commons Attribution (CC BY) license (<http://creativecommons.org/licenses/by/4.0/>).

Article

Preferential and Increased Uptake of Hydroxyl-Terminated PAMAM Dendrimers by Activated Microglia in Rabbit Brain Mixed Glial Culture

Yossef Alnasser ^{1,†,‡}, Siva P. Kambhampati ^{2,†}, Elizabeth Nance ^{1,§}, Labchan Rajbhandari ³, Shiva Shrestha ³, Arun Venkatesan ³, Rangaramanujam M. Kannan ^{2,*} and Sujatha Kannan ^{1,2,*}

¹ Department of Anesthesiology and Critical Care Medicine, Johns Hopkins University School of Medicine, Baltimore, MD 21205, USA; yossefalnasser@gmail.com (Y.A.); eanance@gmail.com (E.N.)

² Center for Nanomedicine, Wilmer Eye Institute, Department of Ophthalmology, Johns Hopkins, University School of Medicine, Baltimore, MD 21205, USA; skpramodh@gmail.com

³ Department of Neurology, Johns Hopkins University School of Medicine, Baltimore, MD 21205, USA; labchanr@gmail.com (L.R.); shivashrestha09@gmail.com (S.S.); avenkat2@jhmi.edu (A.V.)

* Correspondence: krangar1@jhmi.edu (R.M.K.); skannan3@jhmi.edu (S.K.); Tel.: +1-443-287-8634 (R.M.K.); +1-410-955-7610 (S.K.)

† Co-first authors, the authors contributed equally to this work.

‡ Current Address: Department of Pediatrics, BC Children's Hospital, University of British Columbia, Vancouver, BC V6H 3N1, Canada.

§ Current Address: Department of Chemical Engineering, University of Washington, Seattle, WA 98195, USA.

Received: 20 March 2018; Accepted: 20 April 2018; Published: 27 April 2018

Abstract: Polyamidoamine (PAMAM) dendrimers are multifunctional nanoparticles with tunable physicochemical features, making them promising candidates for targeted drug delivery in the central nervous system (CNS). Systemically administered dendrimers have been shown to localize in activated glial cells, which mediate neuroinflammation in the CNS. These dendrimers delivered drugs specifically to activated microglia, producing significant neurological improvements in multiple brain injury models, including in a neonatal rabbit model of cerebral palsy. To gain further insight into the mechanism of dendrimer cell uptake, we utilized an in vitro model of primary glial cells isolated from newborn rabbits to assess the differences in hydroxyl-terminated generation 4 PAMAM dendrimer (D4-OH) uptake by activated and non-activated glial cells. We used fluorescently-labelled D4-OH (D-Cy5) as a tool for investigating the mechanism of dendrimer uptake. D4-OH PAMAM dendrimer uptake was determined by fluorescence quantification using confocal microscopy and flow cytometry. Our results indicate that although microglial cells in the mixed cell population demonstrate early uptake of dendrimers in this in vitro system, activated microglia take up more dendrimer compared to resting microglia. Astrocytes showed delayed and limited uptake. We also illustrated the differences in mechanism of uptake between resting and activated microglia using different pathway inhibitors. Both resting and activated microglia primarily employed endocytotic pathways, which are enhanced in activated microglial cells. Additionally, we demonstrated that hydroxyl terminated dendrimers are taken up by primary microglia using other mechanisms including pinocytosis, caveolae, and aquaporin channels for dendrimer uptake.

Keywords: PAMAM hydroxyl dendrimers; activated microglia; mixed primary glial cultures; intracellular trafficking; enhanced cellular uptake; neuroinflammation

1. Introduction

Dendrimers are unique nanodevices with great potential as drug delivery vehicles and diagnostic tools [1,2]. Their tree-like architecture offers many advantageous characteristics such as monodispersity, biocompatibility, multivalency, and customizable chemical properties [3,4]. In particular, polyamidoamine (PAMAM) dendrimers have been successfully used as drug, gene, and peptide delivery vehicles, as well as contrast agents [5–7].

Delivery of drugs across central nervous system (CNS) barriers such as the blood-brain barrier (BBB) and the blood-retinal barrier (BRB), to specifically target cells in the brain, is a major challenge for nanoparticles [8–13]. Huang et al. illustrated the ability of modified PAMAM dendrimers to cross the intact BBB [14]. Our group has reported that PAMAM dendrimers, particularly generation 4 hydroxyl-terminated dendrimers (D4-OH), upon systemic administration can cross the BBB/BRB and selectively target and co-localize in activated microglia/macrophages in the brain and retina [11,15–18] without the need for targeting moieties. Furthermore, systemic dendrimer-drug therapies have shown significantly enhanced efficacy in attenuating neuroinflammation than free drugs in multiple small and large animal models [11,17–20]. This enhanced cellular uptake and efficacy can be attributed to (1) the size and surface functionality of D4-OH, (2) the ability of D4-OH to cross impaired CNS barriers, and (3) the combined effects of increased phagocytic activity of activated microglia/macrophages and the intrinsic targeting ability of dendrimers.

We have previously shown that the intracellular uptake and trafficking of dendrimers with different surface charges follow different cellular pathways [21]. Generation 4 PAMAM dendrimers (neutral, anionic, and cationic) majorly employ non-specific, clathrin-independent fluid phase endocytosis. However, it is known that different cells employ different endocytosis mechanisms, which may be further modified in the presence of an inflammatory stimulus. Additionally, *in vitro* studies have reported that dendrimer-drug treatment resulted in enhanced anti-inflammatory activity in LPS-activated microglial cells, compared to free drugs [22–25]. This can be attributed to increased cellular uptake of dendrimer-drug conjugates in activated microglial cells compared to free drugs that may typically utilize a receptor-mediated process. In multiple preclinical brain injury models, there was a significant increase in the activated microglia and astrocyte uptake of D4-OH PAMAM compared to healthy controls [26,27]. However, the mechanisms by which this uptake occurs and the differences between ‘activated’ and ‘quiescent’ glial cells remain unexplored. Although it has been reported that the intracellular internalization of PAMAM dendrimers occurs via endocytosis, further investigation to determine the mechanisms of increased uptake by activated glial cells is necessary [28,29]. Recent studies have shown that besides the three key factors (surface charge, molecular weight, and generation), PAMAM dendrimer internalization may also be dependent on the targeted cell type [20,30].

In this study, we hypothesized that glial cells utilize more than one route of cell entry for uptake of hydroxyl-terminated PAMAM dendrimers and that the uptake mechanisms may vary depending on the activation status of the cell. We also hypothesized that cell internalization is time-dependent and varies between the different types of glial cells. We labelled D4-OH dendrimers with near IR fluorescent dye cyanine 5 (Cy5) and studied their uptake by primary glial cells using quantitative and qualitative measures. Various pharmacological inhibitors for different cell entry pathways were adopted to clarify the mode of glial cell internalization of the dendrimer. Understanding the mechanism of glial cell uptake will provide information necessary to further optimize dendrimer-based drug delivery vehicles for targeting specific glial cells in the presence of disease pathologies.

2. Materials and Methods

DMEM low glucose media (Corning Cellgro, Manassas, VA, USA); HI-FBS, Penicillin/Streptomycin (antibiotics) and DAPI (Invitrogen, Carlsbad, CA, USA); glass-bottom culture dishes (MatTek, Ashland, MA, USA), poly-L-lysine hydrobromide, genestine, sucrose, acetazolamide, and amiloride (Sigma-Aldrich, St. Louis, MO, USA); anti-Glial Fibrillary Acidic Protein Fluor

488 (GFAP) (eBioscience, San Diego, CA, USA); and Tomato Lectin (Vectorlabs, Burlingame, CA, USA) were purchased. The synthesis of Cy5-labelled D4-OH dendrimers has been established and reported previously [17]. Lipopolysaccharides from *E. coli* 0127:B8 (lot#081M4071V) was purchased from Sigma-Aldrich.

2.1. Primary Glial Cell Culture and Cell Treatment

All procedures used in this study were approved by the Johns Hopkins University Animal Care and Use Committee and followed according to approved animal protocols. The cerebral cortices from PND2 New Zealand white rabbits were excised, meninges were removed carefully, and cortices were suspended in 5 mL of 0.05% trypsin for 15 min. The trypsin reaction was neutralized using Dulbecco's Modified Eagle's Medium (DMEM) low glucose medium (Corning Cellgro, Manassas, VA, USA) supplemented with 20% heat inactivated fetal bovine serum (HI-FBS) (Invitrogen Corp., Carlsbad, CA, USA) and 2% antibiotics (penicillin/streptomycin) (Invitrogen Corp., Carlsbad, CA, USA). The cortices were minced and triturated into small pieces to separate the cells using sterile cell culture pipettes. The cell suspension was filtered through a 0.2 µm sterile cell strainer (BD Biosciences, San Jose, CA, USA) to remove debris and fibrous layers. The filtered cell suspension was centrifuged at 1000 rpm for 5 min at 4 °C, and the pellet was resuspended in DMEM medium containing 4.5 g/L glucose and 1.4 mM L-glutamine (Corning Cellgro, Manassas, VA, USA) with 10% FBS and 1% antibiotics. The cells were plated into glass-bottom culture dishes or 12-well plates coated with poly-L-lysine hydrobromide (Sigma Aldrich, St Louis, MO, USA) and incubated at 37 °C and 5% CO₂ atmosphere. Medium was changed every two days, and cells were allowed to reach 90% confluence (day 9–13). Subsequently, planned wells and dishes were treated with LPS in culture medium at 100 ng/mL for glial cell activation. Following overnight incubation with LPS, cells were treated with D-Cy5 at 20 µg/mL with or without cell uptake inhibitors to evaluate the mode of cellular entry.

To study the mechanism of primary glial cell uptake, cells were initially pretreated with inhibitors to block specific cell uptake pathways, followed by D-Cy5 treatment. The inhibitors used were (1) genistein at a concentration of 100 nM to block caveolae-mediated endocytosis, (2) sucrose at 450 nM to impede fluid phase endocytosis, (3) amiloride at 10 µM to prevent macropinocytosis, and (4) acetazolamide at 100 nM to obstruct aquaporin channels. The inhibitors were dissolved in DMEM medium and incubated with primary glial cells for one hour prior to treatment with D-Cy5.

2.2. Cell Cytotoxicity Assay

The effects of the inhibitor treatment on cell viability were evaluated by MTT assay (Invitrogen, Grand Island, NY, USA). Metabolically active cells reduce the yellow tetrazolium MTT in part by the action of dehydrogenase enzymes, to generate reducing equivalents such as NADH and NADPH. The resulting intracellular purple formazan is solubilized and quantified by spectrophotometry to determine the fraction of viable cells. Briefly, primary glial cells were seeded at 10⁴ cells/well in 96 well-plates incubated for 24 h and then treated with the cell inhibitors and LPS, followed by D4-OH dendrimer treatment. The MTT assay was done as previously described by our group and as per manufacturer instructions [22]. Absorbance was read at 540 nm using a micro-plate reader (SynergyMix, BioTek, Winooski, VT, USA) and percent viability compared to untreated controls was calculated.

2.3. Cell Imaging

Cells in glass-bottom culture dishes were used at day 8–12 of primary glial cell culture. After treatments, cells were washed with dPBS twice and fixed using 4% paraformaldehyde for 15 min. Tomato Lectin (1:500) (Vectorlabs, Burlingame, CA, USA) was co-incubated with anti-GFAP (1:500) (eBioScience, San Diego, CA, USA) overnight at 4 °C to stain microglia and astrocytes, respectively. The cells were washed twice with dPBS for 5 min, stained with 4',6-diamidino-2-phenylindole (DAPI) (1:1000) (Invitrogen, Grand Island, NY, USA) for 15 min, and imaged under an LSM 710 confocal

microscope (Carl Zeiss, Hertfordshire, UK) for identification of the dendrimers in microglia and astrocytes. A 633 nm laser was used to image dendrimer (D-Cy5) localization, while Tomato lectin and GFAP imaged by 594 and 488 lasers, respectively. The laser intensity levels were kept identical and constant for all the images for appropriate comparison. Images were acquired at 20× magnification and were processed using Zen software (Carl Zeiss) at identical settings. For semi-quantitative analysis, cell signals intensities were analyzed utilizing ImageJ software (NIH, Bethesda, MD, USA).

2.4. Flow Cytometry

At various time points (30 min through 24 h), dendrimer-treated cells along with untreated controls were isolated using 0.05% Trypsin. Cells were spun down to pellet out at 1500 rpm in an Eppendorf benchtop centrifuge for 5 min and washed once with FACS buffer (1× PBS with 10% FBS). Each condition contained 1×10^5 cells, which were stained for 30 min on ice with mouse anti-rabbit Fluorescein *Lycopersicon Esculentum* (Tomato) Lectin antibody (1:500, Victorlabs, Burlingame, CA, USA) in 100 µL of FACS buffer to label microglia. For labeling astrocytes, Anti-Glial Fibrillary Acidic Protein Fluor 488 (GFAP) (1:500, eBioscience, San Diego, CA, USA) was used at similar conditions. Unstained glial cells were used to obtain gating data according to their light scattering characteristics. After incubation, both non-labeled and labeled Lectin and GFAP cells were washed once by adding 1000 µL of FACS buffer and centrifuged at 1500 rpm for 5 min before re-suspending in 250 µL of FACS buffer. The total cell population to FL-3 channel (Cy3, Lectin) to find out the microglial population and to assess the percentage of microglia taking up dendrimer was evaluated by gating the lectin +ve cells and analyzing the D-Cy5 fluorescence in the FL-4 channel. A total of 30,000 events was collected for each condition using a BD Accuri C6 Flow Cytometer (BD Biosciences, San Diego, CA, USA). Analysis of fluorescence was performed using CFlow software.

2.5. Statistical Analysis

Data were analyzed using analysis of variance (ANOVA) followed by student's *t*-test using Prism Graphpad. A *p* value less than or equal to 0.05 was considered statically significant. The graphs were constructed using KelidaGraph version 4.1.1 (Synergy, PA, USA). The values are represented as means ± standard error of mean (SEM).

3. Results

3.1. Selective Uptake of Dendrimers by Microglia in Primary Mixed Glial Cultures

We used mixed glial cultures derived from neonatal rabbit cortices to investigate the cellular uptake kinetics of the D4-OH. Before beginning the dendrimer uptake experiments, we analyzed the purity of glial cultures using flow cytometry and cell counts using confocal microscopy images. We used GFAP for labelling astrocytes and tomato lectin for labelling microglia/macrophages. Flow cytometry analysis revealed that ~60–70% of the cells in the mixed glial culture were astrocytes (GFAP +ve both in flow and imaging), ~20–25% were microglia/macrophages (lectin +ve both in flow and imaging), and ~8–10% were found to be other cell types (+ve DAPI and –ve GFAP and lectin). The numbers were similar upon cell counting from confocal microscopy images (Figure 1A–C). The other cells may be oligodendrocytes and fibroblasts, since we expect neuronal cells will not survive in our culture conditions, as they require neuronal specific growth supplements and medium.

We used varying D-Cy5 concentrations (1, 5, 10, 20, 40, and 100 µg/mL) to investigate dendrimer uptake. We found out that a concentration of 20 µg/mL of D-Cy5 was optimal, as increasing the concentration beyond that caused high fluorescence signals and difficulty in evaluating the time-dependent uptake. Dendrimer (D-Cy5) was selectively taken up by microglia/macrophages both in resting (no-LPS) and activated (LPS) conditions (Figure 2). As time increased, the population of microglia/macrophages internalizing dendrimers increased from ~15% to ~80% within 3 h (Figures 2, 3 and 4A). Dendrimer uptake by microglia/macrophages peaked at 6 h after incubation with ~95% of

the population positive for D-Cy5 signal both in flow cytometry (Figure 4A) and confocal microscopy (Figure 5). The dendrimers were retained in microglia/macrophages up to 24 h post-dendrimer incubation. In contrast, no dendrimers were found co-localized or internalized by any GFAP-positive astrocytes or other cell populations in mixed glial culture until 6 h post-dendrimer incubation. We found that ~8.5% of the total astrocyte population internalized dendrimers after 24 h of dendrimer (D-Cy5) incubation (Figure 4C).

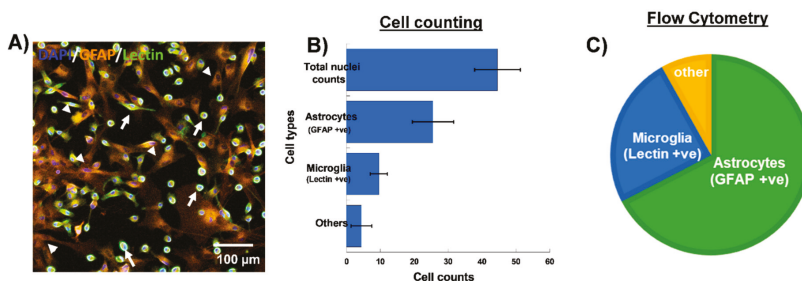


Figure 1. Characterization of mixed glial cell culture from neonatal rabbit brains. (A) Confocal microscopy image of mixed glial culture showing microglia/macrophages (Green stained with lectin, white arrows), astrocytes (Orange, stained with GFAP, white arrow heads) and the cell nuclei stained with DAPI (Blue). (B) Evaluation of different cell population using cell counting from confocal microscopy images. (C) Evaluation of percentages of different cell populations present in the mixed primary glial culture using flow cytometry. Scale bar 100 μ m.

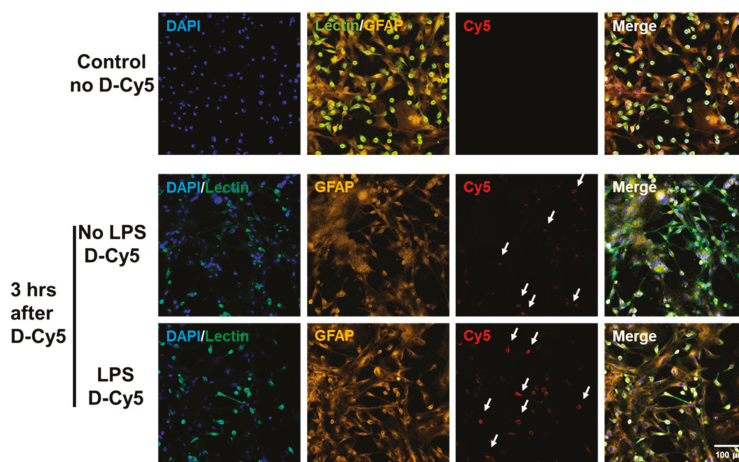


Figure 2. Preferential and selective cellular uptake of G4-OH dendrimers (D-Cy5) activated microglia/macrophages. Cy5-labeled D4-OH PAMAM dendrimers (D-Cy5) were used to evaluate the selective uptake of dendrimers by microglial cells. Microglial cells stained with lectin (Green), Astrocytes were stained using GFAP (Orange), and nuclei were stained using DAPI (Blue). The activated microglial cells (LPS) group demonstrated a higher number of microglial +ve for dendrimers (D-Cy5, white arrows) compared to resting microglia (No LPS). Interestingly, the signal intensity of D-Cy5 is higher in activated microglial cells compared to the D-Cy5 intensity in resting microglial cells, suggesting higher amount of dendrimer uptake. The signal intensities for all channels are kept constant for all conditions. DAPI/Lectin channel is used to better demonstrate the microglia/macrophage population in mixed glial culture taken-up dendrimers, as shown in Cy5 channel. Scale bar 100 μ m.

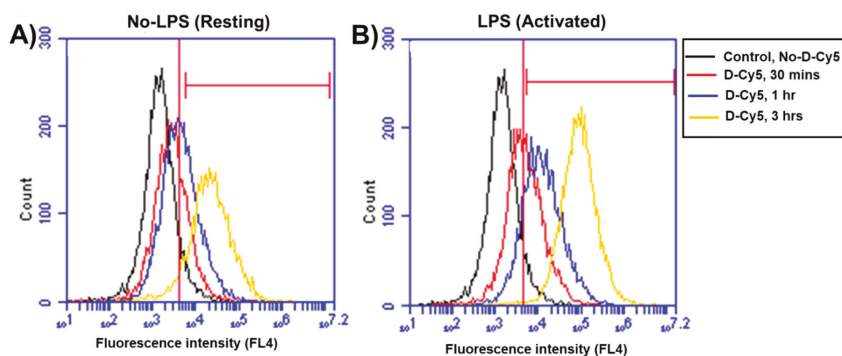


Figure 3. Flow cytometry analysis of time-dependent differential uptake of dendrimer (D-Cy5) by lectin stained microglia/macrophages population in mixed glial culture. (A,B) Histograms of lectin +Ve cells (Microglia/macrophages) showing minimal D-Cy5 uptake (Red) at 30 min in both resting and activated conditions compared to controls (Black). Shift in histograms of lectin +Ve cells (Microglia/macrophages) show increased dendrimer uptake at 3 h. A larger percentage of the activated microglia/macrophage population (~85%) shows D-Cy5 uptake, whereas only ~60% of cells show D-Cy5 uptake in the group without LPS treatment.

3.2. Differential Uptake of Dendrimers by Microglial Cells

To determine if there are any differences in the rate and amount of dendrimer uptake between resting and activated microglial cells, we treated the cells with LPS (100 ng/mL) for 6 h to ‘activate’ the microglia/macrophages to a pro-inflammatory phenotype (to ‘mimic’ neuroinflammation in vivo). At 30 min post-dendrimer treatment, both the ‘resting’ and LPS-activated microglia/macrophages population showed similar dendrimer uptake (~15% and ~12% of cells, respectively) (Figures 4A and 5). We also used the mean fluorescence intensity (MFI) to measure the amount of fluorescence in the cells. The MFI is proportional to amount of dendrimer (D-Cy5) in the cells (Figure 4B). At thirty minutes post-dendrimer incubation, the MFI was also similar for both activated and resting microglia/macrophages. One-hour post-dendrimer incubation, a greater percentage of the activated microglia/macrophages population (~38%) demonstrated dendrimer uptake, compared to non-LPS treated cells (~28%) ($F(4,30) = 292.2, p < 0.01, n = 4$) (Figure 4A).

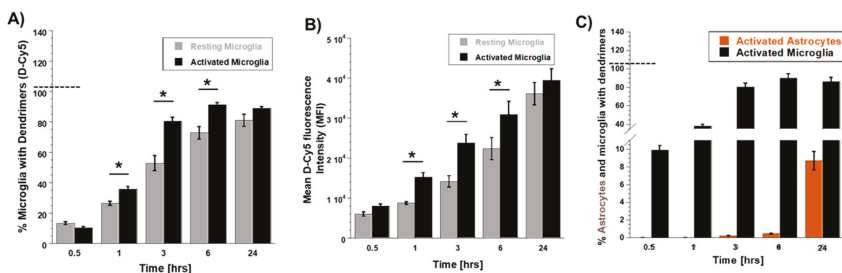


Figure 4. Evaluation of differential dendrimer (D-Cy5) uptake by resting and activated microglial cells in mixed glial culture. (A) Flow cytometry analysis of time-dependent differential uptake of dendrimers by resting (non-LPS treated) and activated (LPS treated) microglia/macrophage populations. (B) Mean intensity fluorescence (MIF) measurements of FL4 channel showing differential amount of dendrimer uptake or intracellular D-Cy5 in resting and activated microglial cells. (C) Delayed and limited dendrimer uptake by astrocyte population (~8.5%) 24 h post dendrimer treatment. All the values are represented as mean \pm SEM, $n = 4$, * $p < 0.01$, student *t*-test.

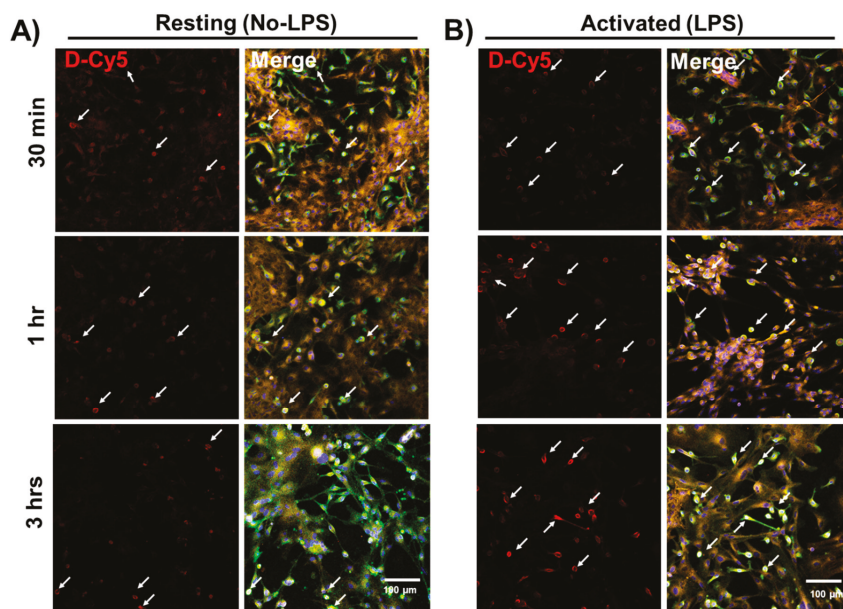


Figure 5. Time-dependent (30 min–3 h) and differential dendrimer uptake between resting and activated microglial cells in mixed glial cultures from neonatal rabbit brain. The mixed glial cultures were activated using LPS (100 ng/mL) and treated with 20 μ g/mL of D-Cy5. At different time points (0.5, 1, 3, 6, and 24 h) post-D-Cy5 treatment, the cells were fixed and stained with lectin for microglia (Green), GFAP for astrocytes (Orange), and DAPI for nucleus (Blue). (A) Resting (no-LPS) microglia/macrophages show less dendrimer uptake compared to (B) activated (LPS) microglia/macrophages at all time points (white arrows). Scale bar 100 μ m.

MFI measurements also confirmed higher amounts of intracellular dendrimer uptake (~1.8-fold increase) compared to non-LPS treated cells (Figure 4B). Interestingly, more than 80% of the LPS-activated microglia/macrophage population demonstrated dendrimer uptake at 3 h after dendrimer treatment (Figure 4A). In contrast, ‘resting’ microglial cells demonstrated dendrimer uptake in only ~58% of the total microglial cell population ($F(4,30) = 9.22, p < 0.01, n = 4$) (Figures 4A and 5). At 24 h, the proportion of microglia/macrophages population demonstrating dendrimer uptake was almost equivalent in both activated and ‘resting’ cells (Figures 4A and 6). MFI measurements suggest that LPS-treated microglia have increased intracellular fluorescence (in other terms, greater intracellular dendrimer amount) at 1, 3, and 6 h post D-Cy5 treatment compared to non-LPS treated cells ($F(4,30) = 2.11, p < 0.01, n = 4$) (Figure 4B). Qualitative measurements of the intracellular fluorescence from the confocal images demonstrate that there is ~2-fold increase in magnitude of D-Cy5 uptake in LPS activated microglial cells (Figures 5 and 6).

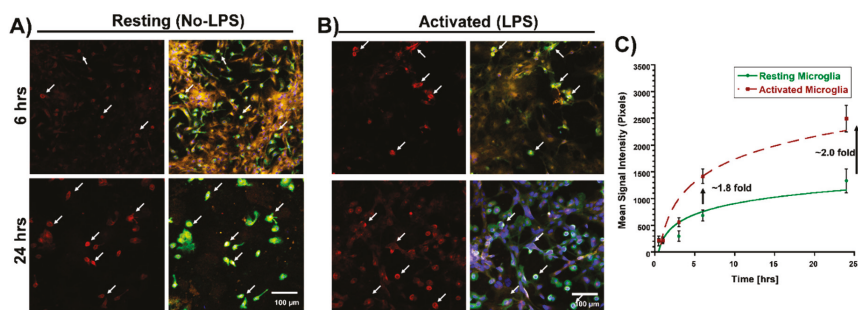


Figure 6. Time-dependent (6 and 24 h) and differential dendrimer uptake between resting and activated microglial cells in mixed glial cultures from neonatal rabbit brain. (A) Resting (no-LPS) microglia show time-dependent increase in dendrimer uptake (white arrows). (B) Activated (LPS) microglial cells show higher uptake of D-Cy5 (white arrows) compared to resting microglial cells, and this phenomenon is consistent as the time increases. (C) Mean signal intensity measurements of intracellular dendrimers (D-Cy5) from confocal images, suggesting relatively higher magnitude of dendrimer (D-Cy5) uptake in activated microglial cells ($n = 4$). Scale bar 100 μm .

Astrocytes showed a delayed and limited uptake at 24 h, which was observed both in LPS and non-LPS treated groups. We did not observe dendrimer uptake in GFAP-positive cells (astrocytes), irrespective of LPS treatment until 6 h post-dendrimer incubation. At 24 h, ~8% of the total astrocyte population exhibited dendrimer uptake in both LPS and non-LPS treated cells (Figure 4C).

3.3. Effect of Inhibitors on Dendrimer Uptake in Primary Mixed Glial Cells

We next investigated the mechanisms underlying the entry of dendrimers into microglia based on the microglial activation state. Previously, our group investigated the cell uptake mechanism of PAMAM dendrimers with different surface groups (Neutral -OH, Cationic -NH₂, and anionic -COOH) by human lung adenocarcinoma epithelial cells (A549) cells [21]. Neutral dendrimers' cell entry was shown to be primarily facilitated by non-caveolae, non-clathrein fluid phase endocytosis. In this current study, we investigated the uptake mechanism by the microglial population in rabbit brain primary mixed glial cells to see the effect of activation on dendrimer uptake. We treated the cells with various inhibitors to block the cell entry pathways. Cell viability above 85% was considered to be acceptable (Supplementary Figure S1). None of the treatments decreased primary mixed glial cell viability beyond 85%. Since the size of dendrimers ranges from 4–10 nm (G3-G10), we hypothesized that dendrimers were taken up by the cells via endocytosis and pinocytosis. We used sucrose (450 nM) to inhibit fluid phase endocytosis. Sucrose treatment lowered dendrimer uptake in both resting (~40% lower) and, to a higher extent, in activated microglia (~60% lower) ($F(6,42) = 2.66, p < 0.01, n = 4$) (Figure 7). The magnitude of decrease in percent of microglia was greater upon sucrose treatment in the activated cells (~2.5-fold decrease vs ~1.6-fold decrease in resting cells ($F(6,42) = 2.35, p < 0.01, n = 4$) compared to the no treatment group (No LPS and LPS only). MFI measurements also show that the amount of dendrimer taken up by the cells was significantly decreased (~3-fold decrease in activated cells vs ~2-fold decrease in resting cells) compared to the resting microglial cells ($p < 0.01$) (Figure 7).

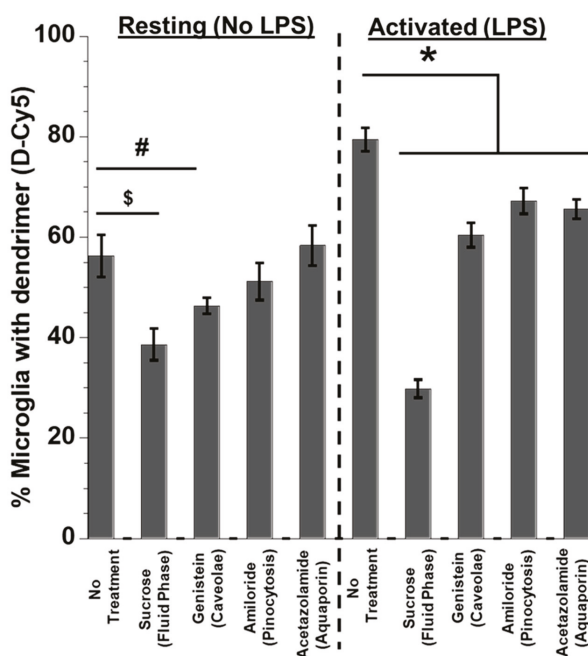


Figure 7. Evaluation of dendrimer uptake using flow cytometry after treatment with various cell entry pathway inhibitors. The mixed glial cultures were activated with LPS, various cell entry pathways were blocked using inhibitors, and the D-Cy5 uptake changes were evaluated using flow cytometry. D-Cy5 uptake was significantly reduced after blocking different endocytosis pathways (fluid phase and Caveolae-mediated endocytosis), suggesting that the cell entry of dendrimer majorly happens via endocytosis. In the case of LPS-activated cell population, D-Cy5 uptake was significantly inhibited when pinocytosis, aquaporin, and mannose pathways were blocked, suggesting that dendrimers may employ multiple pathways for cell entry in activated microglia. All the values are represented as mean \pm SEM, $n = 4$, \$ t -test, $p < 0.01$, and # t -test $p < 0.001$. * Two-way ANOVA, $p < 0.001$ (no-LPS or LPS treated (Resting or Activated) no inhibitors (no treatment) (vs.) no-LPS or LPS-treated (resting or activated) with inhibitors).

Upon blocking caveolae-mediated endocytosis using genistein, the percentage of microglia with D-Cy5 was decreased by ~17% in the 'resting' cells. In activated microglia, inhibiting caveolae-mediated endocytosis resulted in a decrease of the microglia population containing D-Cy5 by ~25% (Figure 7). Blocking pinocytosis, and aquaporin pathways did not significantly decrease the dendrimer uptake by 'resting' microglia, but there was a significant decrease in percent of activated microglia expressing dendrimer signal by ~15% (Amiloride, pinocytosis) ($p < 0.05$) and ~18% (Acetazolamide, aquaporins) ($p < 0.05$) compared to the no-treatment group, respectively (Figure 7). This suggests that activated microglia may be able to employ the above-mentioned pathways other than endocytosis for dendrimer uptake.

4. Discussions

Dendrimer-enabled drug delivery to activated glial cells is opening new opportunities for therapies in CNS disorders [4]. Understanding the mode by which dendrimers get internalized by glial cells will help in designing appropriate dendrimer-based drug delivery nanodevices and optimizing their use for multiple CNS applications, particularly in diseases in which neuroinflammation plays a role. Many studies have shown that cationic (amine terminated) PAMAM dendrimers demonstrate

cell toxicity and platelet aggregation, and partial masking of the surface amine groups reduces the neurotoxicity [31,32]. In contrast, neutral dendrimers show low cell toxic profile, which does not induce complement activation nor platelet aggregation [33]. In this study, we used neutral, hydroxyl-terminated, generation 4 PAMAM dendrimers, which showed low cytotoxicity on primary glial cells, which was supported by earlier findings on different cell lines [16,34,35]. Along with D4-OH dendrimers, all of the cell entry pathway inhibitors had no effect on cell viability. These findings were similar to multiple *in vitro* and *in vivo* studies [36–38]. Glial cells are crucial for maintaining the homeostatic balance of the CNS and exhibit a surveillance function [39]. Among microglia/macrophages and astrocytes, microglial/macrophages cells are the ones accountable for recognition of invaders and immunological stimulators [40–42]. This may explain the more rapid and greater uptake of D4-OH by microglia rather than by astrocytes and other glial cell species in the mixed glial cell cultures. The earliest D4-OH PAMAM dendrimers primary glial cell internalization at 30 min was comparable to data previously reported previously by our group in immortalized BV2 mouse microglial cells [16,29]. Similar to our previous studies, we find that by 3 h most of the microglial cells have taken up the dendrimer [16,21,27]. It has been previously reported that dendrimer uptake is an active process, as decrease in temperature resulted in decrease in dendrimer uptake by ~90% [21]. These studies used cell lines, and in these the initial uptake is more rapid. However, the mechanisms of uptake are similar to those published by our group for A549 lung epithelial cells in which fluid phase endocytosis played a major role in the uptake of the neutral, hydroxyl terminated dendrimer [21].

In this work, we further illustrated differences in the cellular uptake kinetics of dendrimers between resting and activated primary microglial cells. LPS-activated microglia/macrophages showed higher dendrimer uptake compared to non-LPS-treated cells. This can be attributed to increased endocytosis in activated microglia/macrophages [43,44]. LPS treatment activates the toll-like receptors (TLR) pathway, which has been reported previously to increase endocytosis in microglial cells [45–47], and which can contribute to a higher dendrimer uptake. Astrocytes, irrespective of their activation state, exhibited limited and delayed dendrimer uptake in primary mixed glial culture. We have previously studied the cellular uptake pattern of D4-OH dendrimers *in vivo* at 24 h after subarachnoid injections [26]. The results are in good agreement with our current study demonstrating delayed and relatively lower uptake in astrocytes [48]. Mechanisms of cell uptake in the astrocytes are not studied here and will be explored in the future. It is possible that other mechanisms including exosomal or microsomal transport may occur between microglia and astrocytes that transport the dendrimer to astrocytes [49].

Endocytosis is an active cell transport mechanism that cells primarily adopt to internalize extracellular materials through the plasma membrane [50,51]. In the current scenario, our results indicate that fluid phase endocytosis constitutes the main pathway for internalization for D4-OH PAMAM dendrimers in microglial cells. Several studies have been reported that activation of microglia via various stimulants such as LPS, IL-4, and INF- γ will enhance various cell uptake mechanisms such as fluid phase micropinocytosis, caveolae-mediated endocytosis, and phagocytosis [44,52–54]. Therefore, other independent endocytosis mechanisms such as caveolae, clathrin-mediated endocytosis, and macropinocytosis, which can also play a significant role in cellular internalization, should be taken into account [55,56]. Glucose treatment resulted in significant inhibition of dendrimer uptake in both resting and activated microglia/macrophages. These data are similar to our previous studies in a lung epithelial cell line (A549) in which non-specific fluid phase endocytosis (hypertonic sucrose inhibition) had a major role to play in cell uptake of the neutral, hydroxyl-terminated D4 PAMAM dendrimer. On the other hand, it is important to note that exposing the cells to hypertonic conditions may result in non-selective inhibition of other cell uptake pathways, particularly in activated cells. Blocking caveolae-mediated endocytosis using genistein also impeded dendrimer uptake in activated microglia. This can be attributed to an increase in endocytosis activity in activated microglial cells; therefore, blocking endocytosis pathways resulted in decreased dendrimer uptake. The aforementioned pathways have been well documented as modes of cellular

entry for hydroxyl-terminated dendrimers in different cell lines [21,28,36,51]. Some of the most integral membrane proteins, which bring extracellular water and small solutes to the internal compartments of cells, are the aquaporin channels [57]. Blocking aquaporin channels using acetazolamide resulted in reduced dendrimer uptake in LPS-activated microglial cells. It has to be taken into account that LPS is known to downregulate certain types of aquaporin channels [58]. On the other hand, we cannot exclude other receptor pathway such as mannose receptors, toll-like receptors (TLR), macrophage scavenger receptors (MSR-1), or other complement receptors that are also reported to be upregulated in activated microglia/macrophages [59]. Additional studies investigating transport in specific knockout animals will help to fully characterize potential receptor candidates on the microglia/macrophage surface. Our results suggest that microglia/macrophages in their activated state may use more than one pathway that potentially contributes to dendrimer targeting and its cellular internalization. Since microglia/macrophages are implicated in multiple CNS neuroinflammatory diseases such as multiple sclerosis, cerebral palsy, Alzheimer disease, Parkinson's disease, and amyotrophic lateral sclerosis (ALS), appropriate design and manipulation of studied dendrimer nanodevices may be harnessed as potential treatment options for diverse CNS diseases.

5. Conclusions

Our study demonstrates early uptake of D4-OH dendrimers exclusively by primary microglia/macrophages in mixed glial cultures, compared to astrocytes. Activated microglia showed faster and increased dendrimer uptake when compared to resting microglia, although the overall extent of uptake at 24 h was similar between resting and activated microglia. At 24 h, astrocytes displayed restricted uptake at a similar rate in both the resting and activated cells. Both resting and activated microglial/macrophage cells primarily employ fluid phase endocytosis for dendrimer uptake. Activated microglial cells appear to employ more than one mechanism to take up the hydroxyl-terminated generation 4 dendrimer. This can be attributed to increased overall endocytotic processes in the pro-inflammatory microglia/macrophages. Cellular dendrimer uptake can also happen via aquaporin channels, but further studies and other modes of activation are necessary to clarify the role of aquaporin channels and other receptor pathways such as mannose in D4-OH PAMAM dendrimer uptake by primary glial cells. These findings may give us important insights for improving the selective targeting characteristics of dendrimers and delivering therapeutic agents to microglia for attenuating neuroinflammation in a wide range of CNS diseases.

Supplementary Materials: The following are available online.

Author Contributions: A.Y. performed all the flow cytometry experiments and contributed for manuscript preparation. K.S.P. performed all the imaging experiments and manuscript preparation. L.R. and S.S. helped in flow cytometry experimental setup. S.K., E.N., A.V. and R.M.K designed the experiments, data interpretation and preparation of the manuscript.

Acknowledgments: This study was supported by the funds from NIH NIBIBRO1EB018306-01-(RMK, SK), NEIRO1EY025304 (RMK) and NICHDR01HD076901 (SK, RMK). The authors also thank Wilmer Core Module from Microscopy and Imaging for allowing us to use LSM710 confocal. The Wilmer core flow cytometry facility is also highly acknowledged.

Conflicts of Interest: The authors declare no conflict of interest.

References

1. Esfand, R.; Tomalia, D.A. Poly (amidoamine)(PAMAM) dendrimers: From biomimicry to drug delivery and biomedical applications. *Drug Discov. Today* **2001**, *6*, 427–436. [[CrossRef](#)]
2. Menjoge, A.R.; Kannan, R.M.; Tomalia, D.A. Dendrimer-based drug and imaging conjugates: Design considerations for nanomedical applications. *Drug Discov. Today* **2010**, *15*, 171–185. [[CrossRef](#)] [[PubMed](#)]
3. Lee, C.C.; MacKay, J.A.; Fréchet, J.M.; Szoka, F.C. Designing dendrimers for biological applications. *Nat. Biotechnol.* **2005**, *23*, 1517–1526. [[CrossRef](#)] [[PubMed](#)]

4. Labieniec, M.; Watala, C. PAMAM dendrimers—Diverse biomedical applications. Facts and unresolved questions. *Cent. Eur. J. Biol.* **2009**, *4*, 434–451. [[CrossRef](#)]
5. Stiriba, E.S.; Frey, H.; Haag, R. Dendritic polymers in biomedical applications: From potential to clinical use in diagnostics and therapy. *Angew. Chem. Int. Ed.* **2002**, *41*, 1329–1334. [[CrossRef](#)]
6. Murta, V.; Schilrreff, P.; Rosciszewski, G.; Morrilla, M.J.; Ramos, A.J. G5G2. 5 core-shell tecto-dendrimer specifically targets reactive glia in brain ischemia. *J. Neurochem.* **2018**, *144*, 748–760. [[CrossRef](#)] [[PubMed](#)]
7. Breger, J.C.; Muttenthaler, M.; Delehanty, J.B.; Thompson, D.A.; Oh, E.; Susumu, K.; Deschamps, J.R.; Anderson, G.P.; Field, L.D.; Walper, S.A. Nanoparticle cellular uptake by dendritic wedge peptides: Achieving single peptide facilitated delivery. *Nanoscale* **2017**, *9*, 10447–10464. [[CrossRef](#)] [[PubMed](#)]
8. Azad, T.D.; Pan, J.; Connolly, I.D.; Remington, A.; Wilson, C.M.; Grant, G.A. Therapeutic strategies to improve drug delivery across the blood-brain barrier. *Neurosurg. Focus* **2015**, *38*, E9. [[CrossRef](#)] [[PubMed](#)]
9. Aryasomayajula, B.; Sriraman, S.K.; Torchilin, V.P. Crossing the Endothelial Barrier. *Drug Deliv. Across Physiol. Barriers* **2016**, *15*, 209.
10. Peluffo, H.; Unzueta, U.; Negro-Demontel, M.L.; Xu, Z.; Vázquez, E.; Ferrer-Miralles, N.; Villaverde, A. BBB-targeting, protein-based nanomedicines for drug and nucleic acid delivery to the CNS. *Biotechnol. Adv.* **2015**, *33*, 277–287. [[CrossRef](#)] [[PubMed](#)]
11. Kambhampati, S.P.; Clunies-Ross, A.J.; Bhutto, I.; Mishra, M.K.; Edwards, M.; McLeod, D.S.; Kannan, R.M.; Luty, G. Systemic and Intravitreal Delivery of Dendrimers to Activated Microglia/Macrophage in Ischemia/Reperfusion Mouse Retina Retinal Microglia Uptake of Dendrimers. *Investig. Ophthalmol. Vis. Sci.* **2015**, *56*, 4413–4424. [[CrossRef](#)] [[PubMed](#)]
12. Pardridge, W.M. Crossing the blood-brain barrier: Are we getting it right? *Drug Discov. Today* **2001**, *6*, 1–2. [[CrossRef](#)]
13. Oh, E.; Delehanty, J.B.; Sapsford, K.E.; Susumu, K.; Goswami, R.; Blanco-Canosa, J.B.; Dawson, P.E.; Granek, J.; Shoff, M.; Zhang, Q. Cellular uptake and fate of PEGylated gold nanoparticles is dependent on both cell-penetration peptides and particle size. *ACS Nano* **2011**, *5*, 6434–6448. [[CrossRef](#)] [[PubMed](#)]
14. Huang, R.-Q.; Qu, Y.-H.; Ke, W.-L.; Zhu, J.-H.; Pei, Y.-Y.; Jiang, C. Efficient gene delivery targeted to the brain using a transferrin-conjugated polyethyleneglycol-modified polyamidoamine dendrimer. *EASEB J.* **2007**, *21*, 1117–1125. [[CrossRef](#)] [[PubMed](#)]
15. Kannan, S.; Dai, H.; Navath, R.S.; Balakrishnan, B.; Jyoti, A.; Janisse, J.; Romero, R.; Kannan, R.M. Dendrimer-based postnatal therapy for neuroinflammation and cerebral palsy in a rabbit model. *Sci. Transl. Med.* **2012**, *4*, 130ra46. [[CrossRef](#)] [[PubMed](#)]
16. Kannan, S.; Kolhe, P.; Raykova, V.; Glibatec, M.; Kannan, R.M.; Lieh-Lai, M.; Bassett, D. Dynamics of cellular entry and drug delivery by dendritic polymers into human lung epithelial carcinoma cells. *J. Biomater. Sci. Polym. Ed.* **2004**, *15*, 311–330. [[CrossRef](#)] [[PubMed](#)]
17. Lesniak, W.G.; Mishra, M.K.; Jyoti, A.; Balakrishnan, B.; Zhang, F.; Nance, E.; Romero, R.; Kannan, S.; Kannan, R.M. Biodistribution of fluorescently labeled PAMAM dendrimers in neonatal rabbits: Effect of neuroinflammation. *Mol. Pharm.* **2013**, *10*, 4560–4571. [[CrossRef](#)] [[PubMed](#)]
18. Mishra, M.K.; Beaty, C.A.; Lesniak, W.G.; Kambhampati, S.P.; Zhang, F.; Wilson, M.A.; Blue, M.E.; Troncoso, J.C.; Kannan, S.; Johnston, M.V. Dendrimer brain uptake and targeted therapy for brain injury in a large animal model of hypothermic circulatory arrest. *ACS Nano* **2014**, *8*, 2134–2147. [[CrossRef](#)] [[PubMed](#)]
19. Nance, E.; Porambo, M.; Zhang, F.; Mishra, M.K.; Buelow, M.; Getzenberg, R.; Johnston, M.; Kannan, R.M.; Fatemi, A.; Kannan, S. Systemic dendrimer-drug treatment of ischemia-induced neonatal white matter injury. *J. Control. Release* **2015**, *214*, 112–120. [[CrossRef](#)] [[PubMed](#)]
20. Nance, E.; Zhang, F.; Mishra, M.K.; Zhang, Z.; Kambhampati, S.P.; Kannan, R.M.; Kannan, S. Nanoscale effects in dendrimer-mediated targeting of neuroinflammation. *Biomaterials* **2016**, *101*, 96–107. [[CrossRef](#)] [[PubMed](#)]
21. Perumal, O.P.; Inapagolla, R.; Kannan, S.; Kannan, R.M. The effect of surface functionality on cellular trafficking of dendrimers. *Biomaterials* **2008**, *29*, 3469–3476. [[CrossRef](#)] [[PubMed](#)]
22. Kambhampati, S.P.; Mishra, M.K.; Mastorakos, P.; Oh, Y.; Luty, G.A.; Kannan, R.M. Intracellular delivery of dendrimer triamcinolone acetonide conjugates into microglial and human retinal pigment epithelial cells. *Eur. J. Pharm. Biopharm.* **2015**, *95*, 239–249. [[CrossRef](#)] [[PubMed](#)]

23. Nance, E.; Kambhampati, S.P.; Smith, E.S.; Zhang, Z.; Zhang, F.; Singh, S.; Johnston, M.V.; Kannan, R.M.; Blue, M.E.; Kannan, S. Correction to: Dendrimer-mediated delivery of N-acetyl cysteine to microglia in a mouse model of Rett syndrome. *J. Neuroinflamm.* **2018**, *15*, 14. [[CrossRef](#)] [[PubMed](#)]
24. Soiberman, U.; Kambhampati, S.P.; Wu, T.; Mishra, M.K.; Oh, Y.; Sharma, R.; Wang, J.; Al Towerki, A.E.; Yiu, S.; Stark, W.J.; et al. Subconjunctival injectable dendrimer-dexamethasone gel for the treatment of corneal inflammation. *Biomaterials* **2017**, *125*, 38–53. [[CrossRef](#)] [[PubMed](#)]
25. Wang, B.; Navath, R.S.; Romero, R.; Kannan, S.; Kannan, R. Anti-inflammatory and anti-oxidant activity of anionic dendrimer–N-acetyl cysteine conjugates in activated microglial cells. *Int. J. Pharm.* **2009**, *377*, 159–168. [[CrossRef](#)] [[PubMed](#)]
26. Dai, H.; Navath, R.S.; Balakrishnan, B.; Guru, B.R.; Mishra, M.K.; Romero, R.; Kannan, R.M.; Kannan, S. Intrinsic targeting of inflammatory cells in the brain by polyamidoamine dendrimers upon subarachnoid administration. *Nanomedicine* **2010**, *5*, 1317–1329. [[CrossRef](#)] [[PubMed](#)]
27. Kannan, G.; Kambhampati, S.P.; Kudchadkar, S.R. Effect of anesthetics on microglial activation and nanoparticle uptake: Implications for drug delivery in traumatic brain injury. *J. Control. Release* **2017**, *263*, 192–199. [[CrossRef](#)] [[PubMed](#)]
28. Albertazzi, L.; Serresi, M.; Albanese, A.; Beltram, F. Dendrimer internalization and intracellular trafficking in living cells. *Mol. Pharm.* **2010**, *7*, 680–688. [[CrossRef](#)] [[PubMed](#)]
29. Liaw, K.; Gök, O.; DeRidder, L.B.; Kannan, S.; Kannan, R.M. Quantitative assessment of surface functionality effects on microglial uptake and retention of PAMAM dendrimers. *J. Nanopart. Res.* **2018**, *20*, 111. [[CrossRef](#)]
30. Fan, Z.; Nance, E.; Zhang, Z.; Jasty, V.; Kambhampati, S.P.; Mishra, M.K.; Burd, I.; Romero, R.; Kannan, S.; Kannan, R.M. Surface functionality affects the biodistribution and microglia-targeting of intra-amniotically delivered dendrimers. *J. Control. Release* **2016**, *237*, 61–70.
31. Vidal, F.; Vásquez, P.; Cayamán, F.R.; Díaz, C.; Fuentealba, J.; Aguayo, L.G.; Yévenes, G.E.; Alderete, J.; Guzmán, L. Prevention of Synaptic Alterations and Neurotoxic Effects of PAMAM Dendrimers by Surface Functionalization. *Nanomaterials* **2017**, *8*, 7. [[CrossRef](#)] [[PubMed](#)]
32. Enciso, A.E.; Neun, B.; Rodriguez, J.; Ranjan, A.P.; Dobrovolskaia, M.A.; Simanek, E.E. Nanoparticle effects on human platelets in vitro: A comparison between PAMAM and triazine dendrimers. *Molecules* **2016**, *21*, 428. [[CrossRef](#)] [[PubMed](#)]
33. Dobrovolskaia, M.A. Dendrimers effects on the immune system: Insights into toxicity and therapeutic utility. *Curr. Pharm. Des.* **2017**, *23*, 3134–3141. [[CrossRef](#)] [[PubMed](#)]
34. Jevprasesphant, R.; Penny, J.; Jalal, R.; Attwood, D.; McKeown, N.; D'emanuele, A. The influence of surface modification on the cytotoxicity of PAMAM dendrimers. *Int. J. Pharm.* **2003**, *252*, 263–266. [[CrossRef](#)]
35. Kitchens, K.M.; Kolhatkar, R.B.; Swaan, P.W.; Eddington, N.D.; Ghandehari, H. Transport of poly (amidoamine) dendrimers across Caco-2 cell monolayers: Influence of size, charge and fluorescent labeling. *Pharm. Res.* **2006**, *23*, 2818–2826. [[CrossRef](#)] [[PubMed](#)]
36. Dos Santos, T.; Varela, J.; Lynch, I.; Salvati, A.; Dawson, K.A. Effects of transport inhibitors on the cellular uptake of carboxylated polystyrene nanoparticles in different cell lines. *PLoS ONE* **2011**, *6*, e24438. [[CrossRef](#)] [[PubMed](#)]
37. Mokhtari, R.B.; Kumar, S.; Islam, S.S.; Yazdanpanah, M.; Adeli, K.; Cutz, E.; Yeger, H. Combination of carbonic anhydrase inhibitor, acetazolamide, and sulforaphane, reduces the viability and growth of bronchial carcinoid cell lines. *BMC Cancer* **2013**, *13*, 378. [[CrossRef](#)] [[PubMed](#)]
38. Kempfski, O.; Staub, F.; Jansen, M.; Schödel, F.; Baethmann, A. Glial swelling during extracellular acidosis in vitro. *Stroke* **1988**, *19*, 385–392. [[CrossRef](#)] [[PubMed](#)]
39. Hanisch, U.K. Microglia as a source and target of cytokines. *Glia* **2002**, *40*, 140–155. [[CrossRef](#)] [[PubMed](#)]
40. Liu, B.; Wang, K.; Gao, H.M.; Mandavilli, B.; Wang, J.Y.; Hong, J.S. Molecular consequences of activated microglia in the brain: Overactivation induces apoptosis. *J. Neurochem.* **2001**, *77*, 182–189. [[CrossRef](#)] [[PubMed](#)]
41. Perez, A.P.; Cosaka, M.L.; Romero, E.L.; Morilla, M.J. Uptake and intracellular traffic of siRNA dendriplexes in glioblastoma cells and macrophages. *Int. J. Nanomed.* **2011**, *6*, 2715–2718.
42. Higa, L.H.; Jerez, H.E.; de Farias, M.A.; Portugal, R.V.; Romero, E.L.; Morilla, M.J. Ultra-small solid archaeolipid nanoparticles for active targeting to macrophages of the inflamed mucosa. *Nanomedicine* **2017**, *12*, 1165–1175. [[CrossRef](#)] [[PubMed](#)]

43. Martinez, O.F.; Helming, L.; Gordon, S. Alternative activation of macrophages: An immunologic functional perspective. *Ann. Rev. Immunol.* **2009**, *27*, 451–483. [[CrossRef](#)] [[PubMed](#)]
44. Varin, A.; Gordon, S. Alternative activation of macrophages: Immune function and cellular biology. *Immunobiology* **2009**, *214*, 630–641. [[CrossRef](#)] [[PubMed](#)]
45. Arroyo, D.S.; Soria, J.A.; Gaviglio, E.A.; Rodriguez-Galan, M.C.; Iribarren, P. Toll-like receptors are key players in neurodegeneration. *Int. Immunopharmacol.* **2011**, *11*, 1415–1421. [[CrossRef](#)] [[PubMed](#)]
46. Blanco, A.M.; Perez-Arago, A.; Fernandez-Lizarbe, S.; Guerri, C. Ethanol mimics ligand-mediated activation and endocytosis of IL-1RI/TLR4 receptors via lipid rafts caveolae in astroglial cells. *J. Neurochem.* **2008**, *106*, 625–639. [[CrossRef](#)] [[PubMed](#)]
47. Kagan, J.C.; Su, T.; Horng, T.; Chow, A.; Akira, S.; Medzhitov, R. TRAM couples endocytosis of Toll-like receptor 4 to the induction of interferon- β . *Nat. Immunol.* **2008**, *9*, 361–368. [[CrossRef](#)] [[PubMed](#)]
48. Pinkernelle, J.; Calatayud, P.; Goya, G.F.; Fansa, H.; Keilhoff, G. Magnetic nanoparticles in primary neural cell cultures are mainly taken up by microglia. *BMC Neurosci.* **2012**, *13*, 32. [[CrossRef](#)] [[PubMed](#)]
49. Drago, F.; Lombardi, M.; Prada, I.; Gabrielli, M.; Joshi, P.; Cojoc, D.; Franck, J.; Fournier, I.; Vizioli, J.; Verderio, C. ATP Modifies the Proteome of Extracellular Vesicles Released by Microglia and Influences Their Action on Astrocytes. *Front. Pharmacol.* **2017**, *8*, 910. [[CrossRef](#)] [[PubMed](#)]
50. Dutta, D.; Donaldson, J.G. Search for inhibitors of endocytosis: Intended specificity and unintended consequences. *Cell. Logist.* **2012**, *2*, 203–208. [[CrossRef](#)] [[PubMed](#)]
51. Peñaloza, J.P.; Márquez-Miranda, V.; Cabaña-Brunod, M.; Reyes-Ramírez, R.; Llancahuen, F.M.; Vilos, C.; Maldonado-Biermann, F.; Velásquez, L.A.; Fuentes, J.A.; González-Nilo, F.D. Intracellular trafficking and cellular uptake mechanism of PHBV nanoparticles for targeted delivery in epithelial cell lines. *J. Nanobiotechnol.* **2017**, *15*, 1. [[CrossRef](#)] [[PubMed](#)]
52. Mandrekar, S.; Jiang, Q.; Lee, C.D.; Koenigsnecht-Talboo, J.; Holtzman, D.M.; Landreth, G.E. Microglia mediate the clearance of soluble A β through fluid phase macropinocytosis. *J. Neurosci.* **2009**, *29*, 4252–4262. [[CrossRef](#)] [[PubMed](#)]
53. Schnurr, M.; Then, F.; Galambos, P.; Scholz, C.; Siegmund, B.; Endres, S.; Eigler, A. Extracellular ATP and TNF- α synergize in the activation and maturation of human dendritic cells. *J. Immunol.* **2000**, *165*, 4704–4709. [[CrossRef](#)] [[PubMed](#)]
54. Fernandez-Lizarbe, S.; Pascual, M.; Guerri, C. Critical role of TLR4 response in the activation of microglia induced by ethanol. *J. Immunol.* **2009**, *183*, 4733–4744. [[CrossRef](#)] [[PubMed](#)]
55. Kerr, M.C.; Teasdale, R.D. Defining macropinocytosis. *Traffic* **2009**, *10*, 364–371. [[CrossRef](#)] [[PubMed](#)]
56. Pelkmans, L.; Helenius, A. Endocytosis via caveolae. *Traffic* **2002**, *3*, 311–320. [[CrossRef](#)] [[PubMed](#)]
57. Yool, J.A.; Brown, E.A.; Flynn, G.A. Roles for novel pharmacological blockers of aquaporins in the treatment of brain oedema and cancer. *Clin. Exp. Pharmacol. Physiol.* **2010**, *37*, 403–409. [[CrossRef](#)] [[PubMed](#)]
58. Lehmann, G.L.; Carreras, F.I.; Soria, L.R.; Gradilone, S.A.; Marinelli, R.A. LPS induces the TNF- α -mediated downregulation of rat liver aquaporin-8: Role in sepsis-associated cholestasis. *Am. J. Physiol. Gastrointest. Live Physiol.* **2008**, *294*, G567–G575. [[CrossRef](#)] [[PubMed](#)]
59. Boche, D.; Perry, V.; Nicoll, J. Review: Activation patterns of microglia and their identification in the human brain. *Neuropathol. Appl. Neurobiol.* **2013**, *39*, 3–18. [[CrossRef](#)] [[PubMed](#)]



© 2018 by the authors. Licensee MDPI, Basel, Switzerland. This article is an open access article distributed under the terms and conditions of the Creative Commons Attribution (CC BY) license (<http://creativecommons.org/licenses/by/4.0/>).

Article

Dendrimeric Antigens for Drug Allergy Diagnosis: A New Approach for Basophil Activation Tests

Noemi Molina ^{1,2,†}, Angela Martin-Serrano ^{2,3,†}, Tahia D. Fernandez ^{2,3}, Amene Tesfaye ^{2,3}, Francisco Najera ^{1,2}, María J. Torres ^{2,4}, Cristobalina Mayorga ^{2,3,4}, Yolanda Vida ^{1,2,*}, Maria I. Montañez ^{2,3,*} and Ezequiel Perez-Inestrosa ^{1,2,*}

¹ Departamento de Química Orgánica, Universidad de Málaga—IBIMA, 29071 Málaga, Spain; nmolina@uma.es (N.M.); najera@uma.es (F.N.)

² Andalusian Centre for Nanomedicine and Biotechnology-BIONAND, Parque Tecnológico de Andalucía, 29590 Málaga, Spain; amso_almaden@hotmail.com (A.M.-S.); tahia.fernandez@ibima.eu (T.D.F.); amenet2009@gmail.com (A.T.); mjttoresj@ibima.eu (M.J.T.); mayorga.lina@gmail.com (C.M.)

³ Research Laboratory, IBIMA—Regional University Hospital of Málaga—UMA, 29009 Málaga, Spain

⁴ Allergy Unit, IBIMA—Regional University Hospital of Málaga—UMA, 29009 Málaga, Spain

* Correspondence: yolvida@uma.es (Y.V.); maribel.montanez@ibima.eu (M.I.M.); inestrosa@uma.es (E.P.-I.); Tel.: +34-952137565 (E.P.-I.)

† These authors contributed equally to this work.

Academic Editor: Ashok Kakkur

Received: 5 March 2018; Accepted: 20 April 2018; Published: 24 April 2018

Abstract: Dendrimeric Antigens (DeAns) consist of dendrimers decorated with multiple units of drug antigenic determinants. These conjugates have been shown to be a powerful tool for diagnosing penicillin allergy using *in vitro* immunoassays, in which they are recognized by specific IgE from allergic patients. Here we propose a new diagnostic approach using DeAns in cellular tests, in which recognition occurs through IgE bound to the basophil surface. Both IgE molecular recognition and subsequent cell activation may be influenced by the tridimensional architecture and size of the immunogens. Structural features of benzylpenicilloyl-DeAn and amoxicilloyl-DeAn (G2 and G4 PAMAM) were studied by diffusion Nuclear Magnetic Resonance (NMR) experiments and are discussed in relation to molecular dynamics simulation (MDS) observations. IgE recognition was clinically evaluated using the basophil activation test (BAT) for allergic patients and tolerant subjects. Diffusion NMR experiments, MDS and cellular studies provide evidence that the size of the DeAn, its antigen composition and tridimensional distribution play key roles in IgE-antigen recognition at the effector cell surface. These results indicate that the fourth generation DeAns induce a higher level of basophil activation in allergic patients. This approach can be considered as a potential complementary diagnostic method for evaluating penicillin allergy.

Keywords: PAMAM; dendrimeric antigens; penicillin; drug allergy; basophil activation tests

1. Introduction

Dendrimers are highly branched and regular macromolecules with well-defined structures that attract considerable interest due to their potential applications in many fields of science. The three-dimensional architecture of dendrimeric systems confers them various intrinsic features such as structural homogeneity, integrity, controlled composition and high-density multidentate homogeneous terminal groups, ready for conjugation. These characteristics, added to their stability and versatility, mean that dendrimers have been used for many applications, such as sensing, catalysis, molecular electronics and photonics [1]. Moreover, dendrimer and dendron nanostructures represent ideal scaffolds for numerous bioapplications and hold great promise for the future of nanomedicine [2,3]. One important application is related to the study of allergic drug reactions.

Allergic drug reactions are one of the most important health problems nowadays. Betalactam (BL) allergy is self-reported by approximately 10% of adverse drug reaction sufferers. A high proportion of these cases are mediated by immunoglobulin E (IgE), leading to a range of symptoms, from simple skin involvement to anaphylactic shock [4,5]. However, a variety of factors make the study of these reactions difficult, such as a lack of knowledge of the actual drug derivatives involved, changes to the pattern of hapten recognition over time in selected populations, the possibility of cross-reactivity between related chemical structures and a general increase in adverse patient responses due to environmental and genetic factors [6–8].

In addition, BL allergy has a complex diagnosis which is still not correctly addressed. Many BLs with different chemical structures exist and each patient has a unique IgE response. An individual can be allergic to one BL only, or cross-reactive, being allergic to BLs with the same or similar side chains, or to multiple, potentially structurally diverse BLs from different families [9–11]. A complete diagnostic procedure includes a detailed clinical history, which can be unreliable, followed by *in vivo* tests, including skin tests, which can have low sensitivity, and drug provocation testing, which poses some patient-risk, especially for severe reactions [12].

In vitro testing represents a more rational alternative, as it can potentially identify the drug responsible, allowing the physician to find a safe alternative and reducing the need to perform drug provocation testing. However, it is necessary to confirm the sensitivity, specificity and negative and positive predictive values for these *in vitro* tests in order to enable their implementation in clinical practice. The most common *in vitro* tests are based on the detection of specific IgE, either in serum (immunoassays) or bound to receptors on the surface of effector cells (basophil activation tests) [13].

BLs are haptens that need to be bound covalently to a carrier protein to induce an immune response. This hapten-carrier conjugate is used in immunoassays to quantify drug specific IgE (sIgE) in serum. The immunoassay is the most widely used *in vitro* test for the diagnosis of drug allergy. However, it has certain disadvantages, such as low sensitivity and the limited availability of commercial kits for a small range of BLs. Among non-commercial ones, Radio Allergo Sorbent Test (RAST) is the most commonly employed in research laboratories.

The nature of the carrier molecule is important for the development of an *in vitro* test for the detection of drug sIgE antibodies, as the conjugate it forms can influence IgE recognition. Poly-L-Lysine is the most widely used carrier molecule for the RAST, due to its accessibility, multivalency and ease of chemical functionalization for different haptens [14,15]. However, its inherent polydispersity complicates its precise chemical characterization and affects the reproducibility of the formed conjugate. To avoid these handicaps and to produce dense and reproducible hapten-carrier conjugates we proposed the use of PAMAM dendrimers [16] as carrier molecules. Their potential for emulating the carrier protein in hapten-carrier conjugates for IgE recognition in BL allergy has been confirmed using dendrimeric antigens (DeAns). DeAns were synthesized by incorporating benzylpenicilloyl (BPO, the antigenic determinant of benzylpenicillin) or amoxicilloyl (AXO; the equivalent of amoxicillin) groups in the dendrimer periphery. Bi-epitope DeAns have also been designed, including both BPO and AXO on the same macromolecule, which enabled the detection of sIgE from selective and cross-reactive patients [17]. The coupling of DeAns to different solid supports (cellulose disks, zeolites and silica particles) have allowed the determination of sIgE to penicillins by RAST, and this has been shown to have potential for diagnosis [18–23].

Although the nanotechnological advances achieved in immunoassay design are very promising [24,25], RAST assays have certain limitations, such as dependencies on a radioactive isotope, specific facilities and trained personnel. Thus, other techniques avoiding radioactivity are preferred by many research groups. Consequently, the basophil activation test (BAT), another *in vitro* diagnostic technique, has received increasing attention for the diagnosis of drug allergy [12,13].

Like other functional assays, BAT tries to mimic *in vivo* IgE-mediated cell activation and mediator release. This test is useful for evaluating IgE-mediated reactions for a variety of injectable drugs since there is no need to use drug-carrier conjugates. BAT is also valuable for the identification of

the drug responsible for a reaction. However, its sensitivity depends on the drug involved, with values of around 55% reported for BLs [26–28].

BAT is based on the determination of activation markers expressed on basophil surface after the interaction of the drug with sIgE [13]. However, the lack of knowledge of activation mechanisms has hampered a wider clinical application. BLs are not capable of activating basophils by themselves. They require conjugation to a carrier molecule, generally present in the blood, that is big enough to allow cross-linking of two sIgE bound to the basophil surface. However, no information about the size and compositions of these conjugates is available. The use of well-defined hapten-carrier conjugates would be a valuable tool for the investigation of the mechanism through which the activation occurs.

In this paper, we analyze BAT results in a group of patients with immediate allergic reactions to BLs using various DeAns as immunogens. We compare the results to those obtained using the free drug or hapten. We further analyze these results taking into account the structural features of the DeAns, using diffusion Nuclear Magnetic Resonance (NMR) and molecular dynamics simulation (MDS).

2. Results

In the penicillin allergy scenario, the formation of the antigenic determinant structures (or epitopes) is based on the nucleophilic attack by the amino groups of lysine residues in proteins on the electrophilic β -lactam ring. The antigenic determinants of benzylpenicillin and amoxicillin, BPO and AXO, respectively, have been previously characterized [17,21]. Their excellent stability enables their use for both clinical diagnostic purposes and in research. These antigenic determinants have been used to decorate dendrimers, generating BPO-DeAn and AXO-DeAn, respectively. Those conjugates were used to evaluate basophil activation in vitro in blood samples from confirmed allergic patients.

2.1. Synthesis and Characterization of DeAn

PAMAM dendrimers of different generations (G2 and G4) were peripherally functionalized with either BPO or AXO units, generating four DeAns, namely BPO-DeAn-G2, BPO-DeAn-G4, AXO-DeAn-G2 and AXO-DeAn-G4 (Figure 1a). All conjugates were fully characterized to confirm complete functionalization by means of ^1H and ^{13}C NMR [17,21].

The MDS study provided information on the size and shape of the DeAn conjugates. Both DeAn-G2 conjugates were found to be similar in size, as quantified by the radius of gyration (R_g), Table 1. The DeAn-G4 conjugates were also found to be similar sizes to each other. The shape of the macromolecules is indicated by the asphericities values (δ). Values can range between 1 (for a linear arrangement of atoms) and 0 (for shapes with high 3D similarity). The observed values (Table 1) imply that higher generation conjugates have more globular structures.

The conjugates were examined by diffusion NMR to estimate their size in aqueous solution. Diffusion coefficients (D) were determined with DOSY (diffusion-ordered spectroscopy) experiments and used to estimate size in \AA by calculating the hydrodynamic radius (R_H) using the Stokes-Einstein equation (Table 1) [29,30]. As expected, the larger DeAn-G4 conjugates diffused more slowly, resulting in higher R_H values than the smaller DeAn-G2 conjugates.

The values calculated by MDS are in broad agreement with those obtained from the DOSY experiments, showing values of $\sim 14 \text{ \AA}$ for DeAn-G2 and $\sim 20\text{--}22 \text{ \AA}$ for DeAn-G4.

Table 1. Radius of gyration R_g , aspect ratios (I_z/I_x and I_z/I_y), asphericities (δ) [calculated by MDS] [17,21], diffusion coefficients (D) and hydrodynamic radius (R_H) [determined by NMR experiments] of DeAns.

Dendrimer	MDS				NMR Experiments	
	R_g (\AA)	I_z/I_x	I_z/I_y	δ	D (m^2s^{-1})	R_H (\AA)
BPO-DeAn-G2	14.20	2.40	2.40	0.054	1.38×10^{-10}	14.50
BPO-DeAn-G4	21.90	1.25	1.17	0.005	1.00×10^{-10}	20.04
AXO-DeAn-G2	13.65	1.74	1.20	0.024	1.40×10^{-10}	14.32
AXO-DeAn-G4	22.03	1.61	1.07	0.019	1.00×10^{-10}	20.04

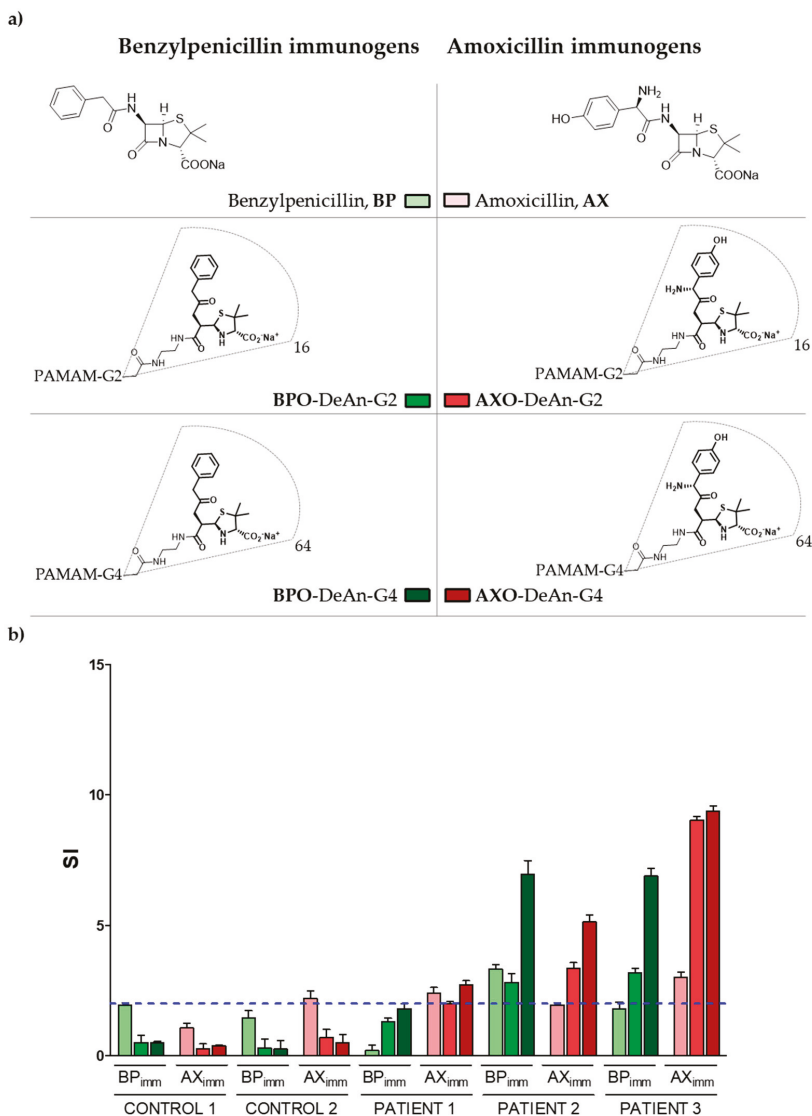


Figure 1. Immunogen structures and BAT results: (a) Chemical structure of the series of immunogens evaluated: the free drugs, BP and AX; DeAn-G2 decorated with BPO (BPO-DeAn-G2) or AXO (AXO-DeAn-G2) and DeAn-G4 decorated with BPO (BPO-DeAn-G4) or AXO (AXO-DeAn-G4); (b) Evaluation of BAT performed with different immunogens related to BP and AX: individual BAT results expressed as SI of each structure for patients and controls. BAT represents the mean of five determinations plus the mean + SEM (Standard Error of the Mean).

2.2. Clinical Evaluation

In order to study the potential of the different DeAns to be used as antigen in the BAT for the diagnosis of benzylpenicillin and amoxicillin allergy, we evaluated basophil activation through specific IgE recognition at the cell surface. This was achieved using BAT with blood samples from

three amoxicillin-allergic patients and two individuals tolerant to this drug (Table 2), according to conventional diagnostic protocols applied in clinical practice (European Network of Drug Allergy, ENDA) [31].

Table 2. Classification and clinical characteristics of controls and patients diagnosed with an immediate allergic reaction to AX included in the study.

Subject	Sex	Age (Years)	Reaction	Responsible Drug	Int R-S	Skin Test				RAST	
						BP-OL	MD	AX	+to Other Drug	BPO-PLL	AXO-PLL
Contr 1	F	43	Urticaria/AE	Cefaclor	5	–	–	–	Cefaclor	–	–
Contr 2	F	48	Anaphylaxis	Cefur	3	–	–	–	Cefur	–	–
Pat 1	M	28	Anaphylaxis	AX	5	–	–	+	nd	–	–
Pat 2	M	30	Anaphylaxis	AX	5	nd	nd	nd	nd	+	+
Pat 3	F	18	Anaphylaxis	BP	6	+	–	+	nd	+	+

Abbreviations. Contr: Control; Pat: Patient; F: female; M: male; AE: Angioedema; AX: Amoxicillin; BP: Benzylpenicillin; Cefur: Cefuroxime; Int R-S: Time interval between reaction and in vitro study (months); BP-OL: benzylpenicilloyl-octa-L-lysine; MD: benzylpenicillin minor determinant; (–): negative; (+): positive; nd: not determined; RAST: Radioallergosorbent test; BPO-PLL: benzylpenicilloyl-poly-L-lysine; AXO-PLL: amoxicilloyl-poly-L-lysine.

BAT results (Figure 1b) were considered positive when the stimulation index (SI) was greater than two to at least one of the concentrations used. SI was calculated as the ratio between the percentage of activated basophils with the different immunogens (free drugs and DeAns), compared to the percentage activated with the negative control. Results for patient 1, who is allergic to AX but not BP, showed positive BAT results to the free drug (AX), as well as to the DeAn conjugates decorated with AXO units. Negative values were obtained with BP and both BP-derived DeAn conjugates. Results for patient 2, who is a cross-responder to BP and AX, showed a positive SI to only one free drug, BP, and all the DeAns. Similarly, data obtained for patient 3, a cross-responder to BP and AX, showed positivity to only one of the free drugs, in this case AX, and all the DeAn conjugates. In all cases, higher values of SI were obtained for DeAn-G4 than DeAn-G2.

When analyzing the data for tolerant individuals (i.e., control subjects allergic to neither AX nor BP), a positive BAT result is observed in control 2 for the free molecule of AX, yielding a false positive result. However, it is important to note that negative test results were obtained using DeAns for both control individuals, even though they are allergic to other BLs (cephalosporins). Similarly, patient 1 only showed a positive BAT for the AX-derived molecules with no activation of any BP-derived conjugates. In terms of the chemical structure, additional amino and hydroxyl groups on the benzyl side chain of AX compared to the side chain of BP may explain the differential activation through IgE recognition at basophil surfaces. These preliminary results indicate a high specificity of the BAT when using DeAns as immunogens. The high specificity of sIgE recognition for BPO-DeAn and AXO-DeAn has already been demonstrated in immunoassays [17], however this is the first time they have been evaluated in cellular assays.

We evaluated whether the inclusion of these DeAns can improve the potential of BAT for diagnosing penicillin allergic patients. Employing the current available approach using the free drug alone, of the three patients allergic to AX (patients 1, 2 and 3) basophil activation occurred in two of them (patients 1 and 3), and of the two patients allergic to BP (patients 2 and 3) only patient 2 showed positive results. These ratios increase to three of three of patients using AXO-DeAn and two of two using BPO-DeAn, respectively. Thus, all patients were correctly diagnosed as allergic, demonstrating that the inclusion of DeAns improves test sensitivity. Moreover, sensitivity was also better than that obtained by RAST, which could only diagnose two of the three patients correctly (Table 2).

3. Discussion

The diagnosis of penicillin allergy is complex and there is a large and unmet need from health-care professionals for better in vitro methods. The sensitivity of the tests can be influenced by the structure of the immunogen and is related to the underlying mechanisms involved in the allergic process.

Activation of effector cells, mast cells and basophils, requires antigens of a certain size [32] and may be negatively affected by the separation between the antigenic determinants [32,33]. In the case of drugs, they are thought to act as haptens, as they are considered too small to induce allergy by themselves. To reach the adequate size to induce reactions, penicillins must bind proteins covalently, forming conjugates [34–36]. The simultaneous recognition of a penicillin-protein conjugate by at least two sIgE molecules bound to adjacent FcεRI at the cellular surface is known as cross-linking. This induces degranulation of the effector cells, leading to the release of inflammatory mediators responsible for the reaction [35].

In the BAT scenario, the free drugs (AX or BP) are assumed to bind proteins present in blood covalently through β-lactam reactivity, forming a big enough conjugate to achieve cross-linking. This approach attempts to emulate *in vivo* conditions, however it lacks information about the chemical composition of the conjugate inducing the activation. By using DeAns, one has more control over conjugate size, multivalence and the structure of peripheral antigenic determinants, allowing more reproducible assays. The use of the appropriate DeAn structure ensure the optimal interaction between the drug moieties and sIgE on the basophil surface, inducing more potent basophil degranulation and improving BAT sensitivity.

These relationships between cell activation and immunogen structure have been recently explored in *in vitro* studies performed in animal models using 2,4-dinitrophenyl (DNP) as a model hapten. It was found that the number of epitopes and the distance between them in synthetic nanostructures have different effects on mast cell degranulation [32,37–39]. One of these studies, using dendrimers decorated with DNP epitopes, showed that larger DNP₁₆-dendrimers (64 Å) trigger mast cell degranulation by cross-linking IgE-receptor complexes, whereas smaller DNP-dendrimers are inhibitory [39]. Other studies have analyzed these relationships in BLs using monovalent haptens, which could be recognized by IgE but unable to bind two adjacent antibodies simultaneously. These structures were shown to inhibit the development of an allergic reaction [31,40,41], for both *in vitro* and *in vivo* tests in BP allergic patients, however this finding has not been further explored in a clinical setting. Most of our current knowledge regarding the activation of nanostructures in effector cell degranulation is based on studies performed with model ligands and animal mast cells. To the best of our knowledge, no studies employing this strategy have been used with real haptens or in human samples.

These studies have provided much needed information about the requirements necessary to activate effector cells, which cannot be deduced using the free drug alone. In fact, little is known about the nature of the adduct that activates basophils in the assay. In this context, the size of the actual carrier protein, the number of reactive sites, and the proximity between them are considered key factors that influence the cross-linking process, and their evaluation would be very complex. The use of well-defined nanostructures with consistent sizes and epitope density will provide a valuable tool to study the structural parameters required for these cell processes. We evaluated the ability of these nanostructures to stimulate basophils and we found that DeAns were able to induce activation in a selective and specific way. Interestingly, basophils from allergic patients follow similar patterns regarding generation: DeAn-G4 produces higher SI than DeAn-G2; this could be due to the size, valence or proximity between epitopes in the immunogen: compared to DeAn-G2, DeAn-G4 have a higher size (~20 Å vs. ~14 Å), an increased density of epitopes (64 vs. 16) and a higher proximity between them, favoring the IgE cross-linking on cell surface, and enhancing activation. This preliminary data suggests that using a size of approximately 20 Å as well as a higher density of epitopes may better resemble the IgE molecular recognition that occurs with penicillin-protein conjugates formed *in vivo*.

4. Materials and Methods

4.1. Molecular Dynamic Simulation (MDS)

Dendrimer Building. AXO-DeAn-G2 was produced using the previously described procedure [17].

Simulation Details. Full atomistic simulation was performed in water as explicit solvent at neutral pH. We used the AMBER 12 MD software package for all calculations [42]. To preserve overall charge neutrality and represent more realistic conditions, an appropriate number of Na⁺ and Cl⁻ counterions were added and the molecules hydrated, using the TIP3P water model [43], in a truncated octahedral cell. The dimensions of the cell were chosen to provide a minimum 10 Å solvation shell around the dendrimer structure.

Solvated structures were minimized as described previously [44], using six cycles of conjugated gradient minimization. During the initial cycle, dendrimers were kept in their starting conformation using a harmonic constraint with a force constant of 500 kcal/mol-Å². This was followed by another five periods of minimization while decreasing the harmonic restraint force constant from 20 kcal/mol-Å² to zero in steps of 5 kcal/mol-Å². To allow a slow relaxation of the assembled dendrimer-solvent system, the minimized structure was heated slowly from 0 to 300 K with three steps of 40 ps of MD, the first of them under conditions of constant volume-constant temperature (NVT) and the rest under constant pressure-constant temperature (NPT) conditions. Initially, we applied a weak 20 kcal/mol-Å² harmonic constraint to the solute starting structure and slowly decreased it to zero in 5 kcal/mol-Å² steps. At this point the dendrimer relaxation was determined from the autocorrelation function of the squared radius-of-gyration.

Finally, we carried out 2 ns of unconstrained MD simulation in NPT ensemble to equilibrate the system at 300 K. To solve the motion equation we used the Verlet leapfrog algorithm [44], with an integration step of 2 fs. Bond lengths involving bonds to hydrogen atoms were constrained using the SHAKE algorithm [45], using a geometrical tolerance of 5×10^{-4} Å.

Finally, starting from the configurations generated by the above procedure, production runs of 20 ns trajectories were performed under an NPT ensemble. Temperature regulation was achieved using the Berendsen weak coupling method (1 ps time constant for heat bath coupling and 0.5 ps for pressure relaxation time) [46]. The particle-mesh Ewald (PME) algorithm was employed to treat long-range electrostatic interactions [47], with a real space cut off of 9 Å. The same cutoff was used for van der Waals interactions. For the structural analyses (*Rg*, *dendrimer shape*, etc.), the last 1 ns equilibrated trajectory was used. Amber modules ptraj and cpptraj were used to accomplish these analyses. VMD software was used for the calculation of molecular surfaces [48].

4.2. DOSY Nuclear Magnetic Resonance (NMR) Experiments

The samples were prepared in deuterium oxide at a concentration of 0.5 mM (within the infinite dilution range for similar samples at 0.1–2.1 mM) [30]. The experiments have been performed on a The Bruker AscendTM 400 MHz spectrometer, equipped with a 5 mm BBFO^{PLUS} probe with ²H “lock” channel and z gradient. The spectrometer is also equipped with a control temperature unit prepared to work at temperatures ranging from 0 °C to +50 °C. Gradient strength was calibrated by measuring the diffusion rate of pure water of residual protons in D₂O. All experiments were conducted at 300 K. The samples were allowed to equilibrate for no fewer than 15 min.

To determine the diffusion rates, a 2D sequence using double stimulated echo for convection compensation and LED using bipolar gradient pulses for diffusion was used.

The diffusion coefficients determined were used to calculate the hydrodynamic radius via the Stokes-Einstein equation: $R_H = K_B T / 6\pi\eta D$, where K_B is the Boltzmann constant, T is the temperature and η is the viscosity of the solution (1.0963 cP for D₂O viscosity) [30].

4.3. Patients

Subjects, 2 tolerant and 3 with an immediate allergic reaction to penicillins, were included in the study. Diagnosis was confirmed following the European Academy of Allergy and Clinical Immunology (EAACI)/European Network for Drug Allergy (ENDA) guidelines [49]. Patients were classified into two groups: cross-reactors when they recognized AX as well as major and minor determinants of BP by skin testing, RAST or drug provocation test; and selective reactors when positive to AX, although negative to determinants of BP.

The study was conducted according to the Declaration of Helsinki principles and was approved by the Provincial Ethics Committee of Malaga. All subjects included in the study were informed orally and signed the corresponding informed consent.

4.4. Basophil Activation Tests

Basotest (Orpegen Pharma, Heidelberg, Germany) was used following the manufacturer's recommendations and previous procedures [26]. Briefly, 100 μ L of heparinized whole blood was incubated with stimulation buffer for 10 min at 37 °C in a water bath. After this, 100 μ L of the washing solution was added to the negative control tube and fMLP (chemotactic peptide *N*-Formyl-Met-Leu-Phe) to the positive control tube. Samples were incubated with two immunogen concentrations: BP at 2 and 0.5 mg/mL; AX at 1.2 and 0.25 mg/mL and DeAns at 1 and 0.1 mg/mL (chosen on the basis of previous dose–response curves and cytotoxicity studies). The samples were incubated for 20 min at 37 °C in a water bath. The degranulation was stopped by incubating the samples on ice for 5 min and then 20 μ L of staining reagent containing two monoclonal antibodies, anti-IgE PE and anti-gp53 FITC (gp53 is a glycoprotein expressed on activated basophils), was added to each tube and incubated for 20 min in an ice bath covered to prevent exposure to light. The cells were analyzed in a flow cytometer by acquiring at least 1000 basophils per sample. Results were considered as positive when the SI, calculated as the ratio between the percentage of degranulated basophils with the different haptens and the negative control, was greater than two to at least one of the dilutions mentioned above. When the percentage of spontaneously activated basophils was less than 2.5%, the percentage of basophils activated after contact with the antigen should be equal to or greater than 5%. The BAT selection strategy of representative samples for a patient and a control is shown in Figure 2.

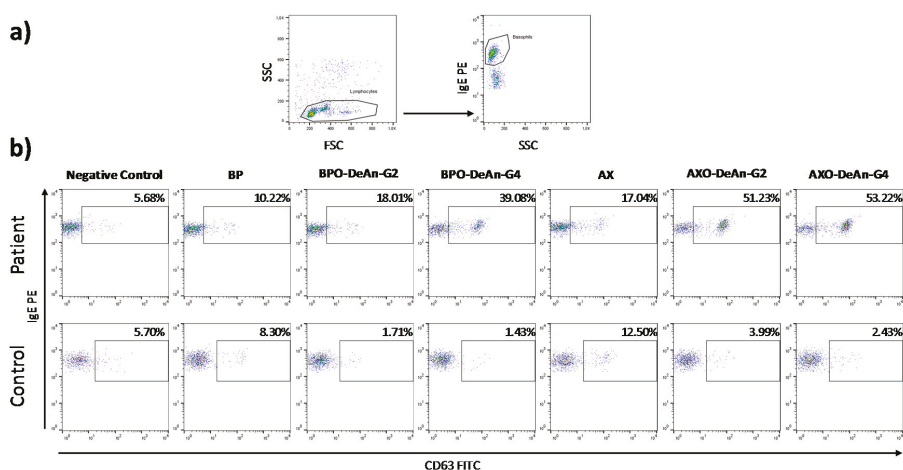


Figure 2. Cytometry dot plots showing: (a) basophils selection strategy; (b) a representative example (patient 3 and control 2) of results for all the immunogens tested, including native drug and DeAns.

5. Conclusions

The study of the structural requirements of conjugates for basophil activation can define the suitable molecules needed to perform BAT with increased sensitivity. Structural properties of DeAn have shown to be appropriate for intra-molecular cross-linking of sIgE bound to FcεRI on basophils. This preliminary study has allowed, for the first time, the performance of BAT with molecules other than the free drug, which enhances the response by way of a better control of the method in terms of reproducibility regarding the immunogen size and density of epitopes. Nothing similar designed at the nanoscale focused on basophils has been undertaken, and potential application to diagnosis are foreseeing, in terms of sensitivity of the test.

Author Contributions: E.P.-I., M.I.M. and Y.V. conceived and designed the experiments; N.M., A.M.-S. and A.T. performed the chemical synthesis and analysis of the compounds; F.N. performed molecular dynamic simulation studies; C.M. and T.D.F. performed cellular tests and analyzed BAT data; M.J.T. evaluated and selected patients and controls; Y.V., M.I.M. and T.D.F. analyzed all the data and wrote the paper with input from E.P.-I.

Acknowledgments: We thank James R. Perkins for his help with the final English language version of this manuscript. The present study has been supported by State Secretariat for Research, Development and Innovation of the Ministry of Economy and Competitiveness (grants cofunded by European Regional Development Fund (ERDF)): MINECO CTQ2016-75870P; by Institute of Health “Carlos III” (ISCIII) of MINECO (grants cofunded by ERDF): PI12/02529, PI15/01206, CP15/00103, PI17/01237, RETICs RIRAAF RD12/0013/0001 and 0003 and RETIC ARADYAL RD16/0006/0001 and 0012; by Andalusian Regional Ministry of Economy and Knowledge (grants cofunded by ERDF): CTS-06603; by Andalusian Regional Ministry Health (grants: PI-0699-2011, PI-0179-2014, PI-0241-2016 and PI-0250-2016), and “Premio UNICAJA a la innovación en biomedicina y salud”. NM holds a FPU grant of MECD (FPU15/00641). TDF hold a “Ramon y Cajal” research contract from MINECO (RYC-2013-13138). AT has received funding from the European Union’s H2020 research and innovation programme under the Marie Skłodowska-Curie grant agreement No 713721. CM holds a ‘Nicolas Monardes’ research contract by Andalusian Regional Ministry Health: C-0044-2012 SAS 2013. MIM holds a “Miguel Servet I” (CP15/00103) contract by ISCIII of MINECO (grants cofunded by European Social Fund (ESF)). Partially supported by Open Access Funds from “Universidad de Málaga”.

Conflicts of Interest: The authors declare no conflict of interest.

References

1. Astruc, D.; Boisselier, E.; Ornelas, C. Dendrimers Designed for Functions: From Physical, Photophysical, and Supramolecular Properties to Applications in Sensing, Catalysis, Molecular Electronics, Photonics, and Nanomedicine. *Chem. Rev.* **2010**, *110*, 1857–1959. [[CrossRef](#)] [[PubMed](#)]
2. Mintzer, M.A.; Grinstaff, M.W.; Paetsch, I.; Hunold, P.; Mahler, M.; Shamsi, K.; Nagel, E.; Price, C.F.; Clark, L.J.; Paull, J.R.A.; et al. Biomedical applications of dendrimers: a tutorial. *Chem. Soc. Rev.* **2011**, *40*, 173–190. [[CrossRef](#)] [[PubMed](#)]
3. Mignani, S.; Rodrigues, J.; Tomas, H.; Zablocka, M.; Shi, X.; Caminade, A.-M.; Majoral, J.-P. Dendrimers in combination with natural products and analogues as anti-cancer agents. *Chem. Soc. Rev.* **2018**, *47*, 514–532. [[CrossRef](#)] [[PubMed](#)]
4. Uetrecht, J. Idiosyncratic Drug Reactions: Past, Present, and Future. *Chem. Res. Toxicol.* **2008**, *21*, 84–92. [[CrossRef](#)] [[PubMed](#)]
5. Uetrecht, J. Immune-Mediated Adverse Drug Reactions. *Chem. Res. Toxicol.* **2009**, *22*, 24–34. [[CrossRef](#)] [[PubMed](#)]
6. Ebo, D.G.; Leysen, J.; Mayorga, C.; Rozieres, A.; Knol, E.F.; Terreehorst, I. The in vitro diagnosis of drug allergy: status and perspectives. *Allergy* **2011**, *66*, 1275–1286. [[CrossRef](#)] [[PubMed](#)]
7. Moggs, J.G.; Terranova, R.; Kammüller, M.E.; Chibout, S.-D.; Chapman, V.; Dearman, R.J.; Kimber, I. Regulation of Allergic Responses to Chemicals and Drugs: Possible Roles of Epigenetic Mechanisms. *Toxicol. Sci.* **2012**, *130*, 60–69. [[CrossRef](#)] [[PubMed](#)]
8. Akdis, C.A. Allergy and hypersensitivity: Mechanisms of allergic disease. *Curr. Opin. Immunol.* **2006**, *18*, 718–726. [[CrossRef](#)] [[PubMed](#)]
9. Antunez, C.; Martin, E.; Cornejo-Garcia, J.; Blanca-Lopez, N.; R-Pena, R.; Mayorga, C.; Torres, M.; Blanca, M. Immediate Hypersensitivity Reactions to Penicillins and Other Betalactams. *Curr. Pharm. Des.* **2006**, *12*, 3327–3333. [[CrossRef](#)] [[PubMed](#)]

10. Ariza, A.; Barrionuevo, E.; Mayorga, C.; Montañez, M.I.; Perez-Inestrosa, E.; Ruiz-Sánchez, A.; Rodríguez-Guéant, R.M.; Fernández, T.D.; Guéant, J.L.; Torres, M.J.; et al. IgE to penicillins with different specificities can be identified by a multiepitope macromolecule: Bihaptenic penicillin structures and IgE specificities. *J. Immunol. Methods* **2014**, *406*, 43–50. [[CrossRef](#)] [[PubMed](#)]
11. Montañez, M.I.; Ariza, A.; Mayorga, C.; Fernandez, T.D.; Torres, M.J. Cross-Reactivity in Betalactam Allergy: Alternative Treatments. *Curr. Treat. Opt. Allergy* **2015**, *2*, 141–154. [[CrossRef](#)]
12. Fernandez, T.D.; Mayorga, C.; Salas, M.; Barrionuevo, E.; Posadas, T.; Ariza, A.; Laguna, J.J.; Moreno, E.; Torres, M.J.; Doña, I.; et al. Evolution of diagnostic approaches in betalactam hypersensitivity. *Expert Rev. Clin. Pharmacol.* **2017**, *10*, 671–683. [[CrossRef](#)] [[PubMed](#)]
13. Doña, I.; Torres, M.J.; Montañez, M.I.; Fernández, T.D. In vitro diagnostic testing for antibiotic allergy. *Allergy Asthma Immunol. Res.* **2017**, *9*, 288–298. [[CrossRef](#)] [[PubMed](#)]
14. Blanca, M.; Mayorga, C.; Perez, E.; Suau, R.; Juarez, C.; Vega, J.M.; Carmona, M.J.; Perez-Estrada, M.; Garcia, J. Determination of IgE antibodies to the benzyl penicilloyl determinant. A comparison between poly-l-lysine and human serum albumin as carriers. *J. Immunol. Methods* **1992**, *153*, 99–105. [[CrossRef](#)]
15. Torres, M.J.; Mayorga, C.; Pamies, R.; Juarez, C.; Blanca, M.; Romano, A. Immunologic response to different determinants of benzylpenicillin, amoxicillin, and ampicillin. Comparison between urticaria and anaphylactic shock. *Allergy* **1999**, *54*, 936–943. [[CrossRef](#)] [[PubMed](#)]
16. Fréchet, J.M.J.; Tomalia, D.A. *Dendrimers and Other Dendritic Polymers*; Wiley: Hoboken, NJ, USA, 2001; ISBN 9780470845820.
17. Montañez, M.I.; Najera, F.; Mayorga, C.; Ruiz-Sanchez, A.J.; Vida, Y.; Collado, D.; Blanca, M.; Torres, M.J.; Perez-Inestrosa, E. Recognition of multiepitope dendrimeric antigens by human immunoglobulin E. *Nanomed. Nanotechnol. Biol. Med.* **2015**, *11*, 579–588. [[CrossRef](#)] [[PubMed](#)]
18. Sánchez-Sancho, F.; Pérez-Inestrosa, E.; Suau, R.; Mayorga, C.; Torres, M.J.A.; Blanca, M. Dendrimers as Carrier Protein Mimetics for IgE Antibody Recognition. Synthesis and Characterization of Densely Penicilloylated Dendrimers. *Bioconjug. Chem.* **2002**, *13*, 647–653. [[CrossRef](#)] [[PubMed](#)]
19. Montañez, M.I.; Perez-Inestrosa, E.; Suau, R.; Mayorga, C.; Torres, M.J.; Blanca, M. Dendrimerized Cellulose as a Scaffold for Artificial Antigens with Applications in Drug Allergy Diagnosis. *Biomacromolecules* **2008**, *9*, 1461–1466. [[CrossRef](#)] [[PubMed](#)]
20. Montañez, M.I.; Mayorga, C.; Torres, M.J.; Blanca, M.; Perez-Inestrosa, E. Methodologies to anchor dendrimeric nanoconjugates to solid phase: toward an efficient in vitro detection of allergy to β -lactam antibiotics. *Nanomed. Nanotechnol. Biol. Med.* **2011**, *7*, 682–685. [[CrossRef](#)] [[PubMed](#)]
21. Montañez, M.I.; Najera, F.; Perez-Inestrosa, E. NMR Studies and Molecular Dynamic Simulation of Synthetic Dendritic Antigens. *Polymers* **2011**, *3*, 1533–1553. [[CrossRef](#)]
22. Ruiz-Sanchez, A.J.; Montanez, M.I.; Mayorga, C.; Torres, M.J.; Kehr, N.S.; Vida, Y.; Collado, D.; Najera, F.; De Cola, L.; Perez-Inestrosa, E. Dendrimer-modified solid supports: nanostructured materials with potential drug allergy diagnostic applications. *Curr. Med. Chem.* **2012**, *19*, 4942–4954. [[CrossRef](#)] [[PubMed](#)]
23. Vida, Y.; Montañez, M.I.; Collado, D.; Najera, F.; Ariza, A.; Blanca, M.; Torres, M.J.; Mayorga, C.; Perez-Inestrosa, E. Dendrimeric antigen–silica particle composites: an innovative approach for IgE quantification. *J. Mater. Chem. B* **2013**, *1*, 3044–3050. [[CrossRef](#)]
24. Montañez, M.I.; Ruiz-Sanchez, A.J.; Perez-Inestrosa, E. A perspective of nanotechnology in hypersensitivity reactions including drug allergy. *Curr. Opin. Allergy Clin. Immunol.* **2010**, *10*, 297–302. [[CrossRef](#)] [[PubMed](#)]
25. Mayorga, C.; Perez-Inestrosa, E.; Molina, N.; Montañez, M.I. Development of nanostructures in the diagnosis of drug hypersensitivity reactions. *Curr. Opin. Allergy Clin. Immunol.* **2016**, *16*, 300–307. [[CrossRef](#)] [[PubMed](#)]
26. Torres, M.J.; Padial, A.; Mayorga, C.; Fernández, T.; Sanchez-Sabate, E.; Cornejo-García, J.A.; Antúnez, C.; Blanca, M. The diagnostic interpretation of basophil activation test in immediate allergic reactions to betalactams. *Clin. Exp. Allergy* **2004**, *34*, 1768–1775. [[CrossRef](#)] [[PubMed](#)]
27. De Weck, A.L.; Sanz, M.L.; Gamboa, P.M.; Aberer, W.; Sturm, G.; Bilo, M.B.; Montroni, M.; Blanca, M.; Torres, M.J.; Mayorga, L.; et al. Diagnosis of Immediate-Type β -Lactam Allergy In Vitro by Flow-Cytometric Basophil Activation Test and Sulfidoleukotriene Production: A Multicenter Study. *J. Investig. Allergol. Clin. Immunol.* **2009**, *19*, 91.

28. Torres, M.J.; Ariza, A.; Mayorga, C.; Doña, I.; Blanca-Lopez, N.; Rondon, C.; Blanca, M. Clavulanic acid can be the component in amoxicillin-clavulanic acid responsible for immediate hypersensitivity reactions. *J. Allergy Clin. Immunol.* **2010**, *125*, 502–505.e2. [[CrossRef](#)] [[PubMed](#)]
29. Van Dongen, M.A.; Orr, B.G.; Banaszak Holl, M.M. Diffusion NMR Study of Generation-Five PAMAM Dendrimer Materials. *J. Phys. Chem. B* **2014**, *118*, 7195–7202. [[CrossRef](#)] [[PubMed](#)]
30. Jiménez, V.A.; Gavín, J.A.; Alderete, J.B. Scaling trend in diffusion coefficients of low generation G0–G3 PAMAM dendrimers in aqueous solution at high and neutral pH. *Struct. Chem.* **2012**, *23*, 123–128. [[CrossRef](#)]
31. De Weck, A.L.; Jeunet, F.; Schulz, K.H.; Louis, P.; Girard, J.P.; Grilliat, J.P.; Moneret-Vautrin, D.; Storck, H.; Wuthrich, B.; Spengler, H.; et al. Clinical trial of Ro 6-0787, a monovalent specific hapten inhibitor of penicillin allergy. *Z. Immunitätsforsch. Exp. Klin. Immunol.* **1975**, *150*, 138–160. [[PubMed](#)]
32. Paar, J.M.; Harris, N.T.; Holowka, D.; Baird, B. Bivalent ligands with rigid double-stranded DNA spacers reveal structural constraints on signaling by Fc epsilon RI. *J. Immunol.* **2002**, *169*, 856–864. [[CrossRef](#)] [[PubMed](#)]
33. Posner, R.G.; Subramanian, K.; Goldstein, B.; Thomas, J.; Feder, T.; Holowka, D.; Baird, B. Simultaneous cross-linking by two nontriggering bivalent ligands causes synergistic signaling of IgE Fc epsilon RI complexes. *J. Immunol.* **1995**, *155*, 3601–3609. [[PubMed](#)]
34. Ariza, A.; Mayorga, C.; Salas, M.; Doña, I.; Martín-Serrano, Á.; Pérez-Inestrosa, E.; Pérez-Sala, D.; Guzmán, A.E.; Montañez, M.I.; Torres, M.J. The influence of the carrier molecule on amoxicillin recognition by specific IgE in patients with immediate hypersensitivity reactions to betalactams. *Sci. Rep.* **2016**, *6*, 35113. [[CrossRef](#)] [[PubMed](#)]
35. Ariza, A.; Mayorga, C.; Fernández, T.D.; Barbero, N.; Martín-Serrano, A.; Pérez-Sala, D.; Sánchez-Gómez, F.J.; Blanca, M.; Torres, M.J.; Montanez, M.I. Hypersensitivity Reactions to β -Lactams: Relevance of Hapten-Protein Conjugates. *J. Investig. Allergol. Clin. Immunol.* **2015**, *25*, 12–25. [[PubMed](#)]
36. Ariza, A.; Collado, D.; Vida, Y.; Montañez, M.I.; Pérez-Inestrosa, E.; Blanca, M.; Torres, M.J.; Cañada, F.J.; Pérez-Sala, D. Study of protein haptentation by amoxicillin through the use of a biotinylated antibiotic. *PLoS ONE* **2014**, *9*, e90891. [[CrossRef](#)] [[PubMed](#)]
37. Gieras, A.; Linhart, B.; Roux, K.H.; Dutta, M.; Khodoun, M.; Zafred, D.; Cabauatan, C.R.; Lupinek, C.; Weber, M.; Focke-Tejkl, M.; et al. IgE epitope proximity determines immune complex shape and effector cell activation capacity. *J. Allergy Clin. Immunol.* **2016**, *137*, 1557–1565. [[CrossRef](#)] [[PubMed](#)]
38. Sil, D.; Lee, J.B.; Luo, D.; Holowka, D.; Baird, B. Trivalent Ligands with Rigid DNA Spacers Reveal Structural Requirements For IgE Receptor Signaling in RBL Mast Cells. *ACS Chem. Biol.* **2007**, *2*, 674–684. [[CrossRef](#)] [[PubMed](#)]
39. Baird, E.J.; Holowka, D.; Geoffrey, W.; Coates, A.; Baird, B. Highly Effective Poly(Ethylene Glycol) Architectures for Specific Inhibition of Immune Receptor Activation. *Biochemistry* **2003**, *42*, 12739–12748. [[CrossRef](#)] [[PubMed](#)]
40. Levine, B.B. *N*(alpha-D-penicilloyl) amines as univalent hapten inhibitors of antibodydependent allergic reactions to penicillin. *J. Med. Pharm. Chem.* **1962**, *91*, 1025–1034. [[CrossRef](#)] [[PubMed](#)]
41. De Weck, A.L.; Girard, J.P. Specific Inhibition of Allergic Reactions to Penicillin in Man by a Monovalent Hapten. *Int. Arch. Allergy Immunol.* **1972**, *42*, 798–815. [[CrossRef](#)]
42. Case, D.A.; Darden, T.A.; Cheatham, T.E., III; Simmerling, C.L.; Wang, J.; Duke, R.E.; Luo, R.; Walker, R.C.; Zhang, W.; Merz, K.M.; et al. *AMBER 12*; University of California: San Francisco, CA, USA, 2012.
43. Jorgensen, W.L.; Chandrasekhar, J.; Madura, J.D.; Impey, R.W.; Klein, M.L. Comparison of simple potential functions for simulating liquid water. *J. Chem. Phys.* **1983**, *79*, 926–935. [[CrossRef](#)]
44. Maingi, V.; Jain, V.; Bharatam, P.V.; Maiti, P.K. Dendrimer building toolkit: Model building and characterization of various dendrimer architectures. *J. Comput. Chem.* **2012**, *33*, 1997–2011. [[CrossRef](#)] [[PubMed](#)]
45. Ryckaert, J.-P.; Ciccotti, G.; Berendsen, H.J. Numerical integration of the cartesian equations of motion of a system with constraints: molecular dynamics of n-alkanes. *J. Comput. Phys.* **1977**, *23*, 327–341. [[CrossRef](#)]
46. Berendsen, H.J.C.; Postma, J.P.M.; van Gunsteren, W.F.; DiNola, A.; Haak, J.R. Molecular dynamics with coupling to an external bath. *J. Chem. Phys.* **1984**, *81*, 3684–3690. [[CrossRef](#)]
47. Darden, T.; York, D.; Pedersen, L. Particle mesh Ewald: An *N* log(*N*) method for Ewald sums in large systems. *J. Chem. Phys.* **1993**, *98*, 10089–10092. [[CrossRef](#)]

48. Humphrey, W.; Dalke, A.; Schulten, K. VMD: Visual molecular dynamics. *J. Mol. Graph.* **1996**, *14*, 33–38. [[CrossRef](#)]
49. Torres, M.J.; Blanca, M.; Fernandez, J.; Romano, A.; Weck, A.; Aberer, W.; Brockow, K.; Pichler, W.J.; Demoly, P. Diagnosis of immediate allergic reactions to beta-lactam antibiotics. *Allergy* **2003**, *58*, 961–972. [[CrossRef](#)] [[PubMed](#)]

Sample Availability: Samples of the compounds not are available from the authors.



© 2018 by the authors. Licensee MDPI, Basel, Switzerland. This article is an open access article distributed under the terms and conditions of the Creative Commons Attribution (CC BY) license (<http://creativecommons.org/licenses/by/4.0/>).

Article

Fluorescent Dendritic Micro-Hydrogels: Synthesis, Analysis and Use in Single-Cell Detection

Lisa Christadore ¹, Mark W. Grinstaff ^{1,2,*} and Scott E. Schaus ^{1,*}¹ Department of Chemistry, Boston University, Boston, MA 02215, USA; lmchristadore1@gmail.com² Departments of Biomedical Engineering and Medicine, Boston University, Boston, MA 02215, USA

* Correspondence: mgrin@bu.edu (M.W.G.); seschaus@bu.edu (S.E.S.);

Tel.: +1-617-358-3429 (M.W.G.); +1-617-353-2489 (S.E.S.)

Academic Editor: Ashok Kakkur

Received: 21 March 2018; Accepted: 11 April 2018; Published: 18 April 2018

Abstract: Hydrogels are of keen interest for a wide range of medical and biotechnological applications including as 3D substrate structures for the detection of proteins, nucleic acids, and cells. Hydrogel parameters such as polymer wt % and crosslink density are typically altered for a specific application; now, fluorescence can be incorporated into such criteria by specific macromonomer selection. Intrinsic fluorescence was observed at λ_{\max} 445 nm from hydrogels polymerized from lysine and aldehyde-terminated poly(ethylene glycol) macromonomers upon excitation with visible light. The hydrogel's photochemical properties are consistent with formation of a nitron functionality. Printed hydrogels of 150 μm were used to detect individual cell adherence via a decreased in fluorescence. The use of such intrinsically fluorescent hydrogels as a platform for cell sorting and detection expands the current repertoire of tools available.

Keywords: dendrimer; hydrogel; screening; crosslinking; fluorescence

1. Introduction

Dendrimers are well-defined macromolecules with unique properties that are advantageous for a wide range of applications [1–4], with particular utility in medical and biotechnological systems [5–10]. For example, dendrimer-based delivery vehicles for anticancer drugs provide new approaches to tune cellular uptake and pharmacokinetics [11–20]. Multifunctionalized dendritic macromonomers are of interest for the formation of crosslinked hydrogels to repair bone [21] and soft tissues [22–28], to engineer cartilage tissue scaffolds [29,30], to deliver drugs [31,32], and to prepare microarrays for screening protein and nucleic acid interactions [33]. The latter study led us to the discovery of intrinsic fluorescence emitted by hydrogels prepared from PEG-(CHO)₂ and PEG-(Lys)₂, PEG-(Lys)₂, or [G1]-Lys-NH₂ macromonomers. The macromonomers rapidly polymerized on aldehyde-coated slides to yield Schiff-base crosslinked hydrogels. When the hydrogel microarrays were analyzed with a fluorescent scanner, distinct fluorescence was observed that persisted over multiple days and washes with aqueous buffer. Herein, we describe the visible fluorescence, propose the origin of its emission, and develop a hydrogel label-free single-cell assay.

Previous studies described fluorescence from amine-containing poly(amido amine) and poly(propylene imine) dendrimers in solution with emission maximums between 440 and 450 nm upon excitation at \approx 380 nm [34–38]. Several groups reported that dendrimer fluorescence intensified with prolonged exposure to oxygen. Furthermore, emission intensities increased linearly with dendrimer concentrations and were unaffected by terminal group composition. These results suggested that the fluorescence was directly related to the dendrimers' common tertiary amine and/or amide backbones. Recent studies by Qian et al. suggest that the imine bond in the imidic acid group present within the

PAMAM structure is responsible for emission [39,40]. In our studies, we propose that aerobic oxidation of the imine may be responsible for the fluorescence observed from the Schiff-base crosslinked hydrogels.

2. Results and Discussion

We employed steady-state spectrofluorimetry and confocal fluorescence microscopy to analyze hydrogel fluorescence (Figure 1, top). Figure 1 middle depicts the excitation and emission fluorescence profiles of the Schiff-base crosslinked hydrogel. The excitation maximum was observed at 380 nm, and emission occurred over a broad range with a maximum at 445 nm. These results indicated a unique fluorescent structure existed within the hydrogel network that exhibited a relatively large Stokes shift (65 nm) and a wide emission bandwidth (FWHM = 89 nm). Fluorescence is not observed with amide-crosslinked hydrogels prepared from the reaction between Lys-terminated and PEG-(NHS)₂ macromonomers.

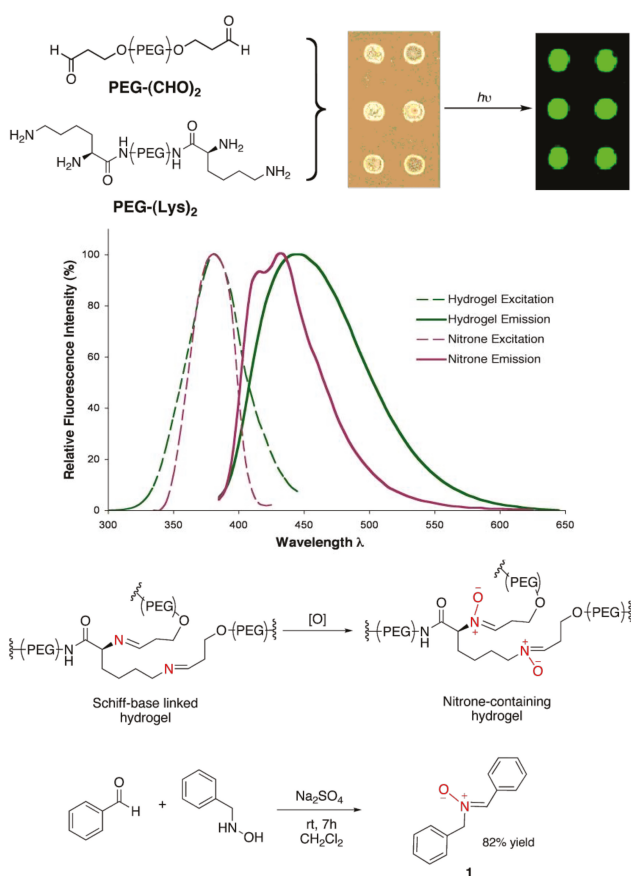


Figure 1. (top) PEG-(CHO)₂ and PEG-(Lys)₂ were mixed in situ and dispensed onto aldehyde-coated slides to form 150 μm hydrogel chambers using an OmniGrid accent microarrayer. Fluorescence emission was observed between 550–590 nm on a GenePix 4000B microarray scanner. (middle) Fluorescence spectra of the Schiff-base linked hydrogel, 14 wt % 2:1 PEG-(CHO)₂:PEG-(Lys)₂, polymerized in HEPES buffer pH 7.4 for 24 h (green), and (Z)-N-benzyl-α-phenylnitronone, **1**, in ethanol at 2.8 wt % immediately following solvation (purple) (bottom). Proposed air oxidation scheme of the hydrogel imine linkages to nitrones (top), and synthesis scheme of **1** (bottom).

We next addressed the possible chemical structure and mechanism responsible for the unique fluorescence properties of the hydrogel. Specifically, the imine functionality and the photochemical properties of its oxidation products were investigated. Previous studies have demonstrated nitron formation by aerobic oxidation of secondary amines and imines. Such syntheses have utilized oxygen and hydrogen peroxide as primary oxidants, typically in conjunction with transition metal [41–45] and flavin-derived [46,47] catalysts. Thus, we proposed that air oxidation of the imine to the nitron may be responsible for the observed hydrogel fluorescence (Figure 1, top).

Accordingly, a model nitron compound, (*Z*)-*N*-benzyl- α -phenylnitron **1**, was synthesized [48] to compare fluorescent properties (Figure 1, bottom). The excitation spectrum of **1** in ethanol showed a maximum at 380 nm, similar to the Schiff-base crosslinked hydrogel. Emission maxima were observed at 415 and 435 nm (Figure 1, middle). The dual emission peaks of the nitron were attributed to photochemical isomerization of the *Z* isomer to the oxaziridine intermediate via an excited singlet state.

The double emission peaks observed for **1** upon steady-state excitation are likely due to the nitron's rearrangement to an oxaziridine intermediate via the lowest singlet excited state. Various isomerization mechanisms and activation energy barriers have been published for aryl-substituted nitrons under photolysis conditions [49–56]. For example, photochemical-induced rearrangement of *N*, α -diphenyl- α -cyanonitron to its corresponding oxaziridine occurred from the lowest singlet excited state when irradiated with 313 nm light. Oxaziridine formation was indicated by the decrease in nitron absorbance at 322 nm and the emergence of a new band at 223 nm. Infrared spectra at 77 °K showed the disappearance of characteristic C=N and N \rightarrow O nitron stretching and the presence of oxaziridine ring vibrations [55]. Another group reported the photorearrangement of chiral aryl-substituted nitrons to optically active oxaziridines when excited at wavelengths greater than 300 nm [49]. Furthermore, photolysis studies of *N*, α -diphenylnitron indicated a 20 nm hypsochromic absorbance band shift that was attributed to the singlet transition of the nitron to its oxaziridine intermediate [52].

In the last decade, cell sorting and microfluidic technologies have enabled advancements on many fronts including the study of individual cells and the diagnosis of disease states [57–67]. Given both the favorable characteristics of hydrogels as artificial extracellular matrix scaffolds and the intrinsic fluorescence observed with these specific hydrogels, we evaluated this system to detect single cells via the abatement or loss of hydrogel fluorescence signal upon individual cell binding.

Specifically, printed hydrogel microarrays were treated with a bovine serum albumin (BSA) solution and excited by a 405 nm laser diode using a confocal microscope. The emission was monitored from 450 to 500 nm as transmitted through a beam splitter, and 3D photon surface plots of the hydrogel chambers were obtained (as shown in Figure 2a). Next, human A549 small cell lung carcinoma cells were incubated with the hydrogel microarrays and washed to remove unbound cells. As can be seen in the photon surface plots, the adhered cells significantly obstructed fluorescence throughout the entire hydrogel network with a hydrogel:cell signal-to-noise ratio of 3.4:1 (Figure 2b–d).

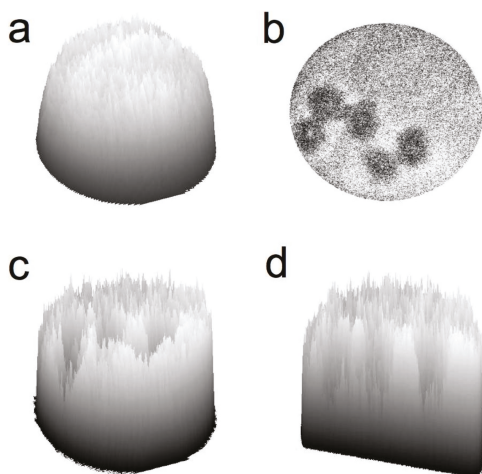


Figure 2. Scanning confocal microscopy images of BSA-treated hydrogels, 22 wt % 2:1 PEG-(CHO)₂:PEG-(Lys)₂. Emission was collected at 460 nm, subtracted from slide background, and normalized to 8-bits/pixel. (a) 3D surface plot of a hydrogel chamber in the absence of cell adhesion, (b) 2D depiction of cells masking hydrogel emission fluorescence, (c) 3D surface plot of the hydrogel shown in b, and (d) 3D cross-section of the hydrogel shown in b.

3. Materials and Methods

3.1. General Information

¹H-NMR was recorded on a Varian INOVA at 400 MHz at ambient temperature. Chemical shifts are reported in parts per million as follows: chemical shift, multiplicity (s = singlet, d = doublet, t = triplet, q = quartet, m = multiplet, br = broad) and integration. Infrared spectra were recorded on a Nicolet Nexus 670 FT-IR ESP spectrophotometer. Analytical thin layer chromatography was performed using EMD 0.25 mm silica gel 60-F plates. Reverse phase chromatography was performed on a C8-bonded silica extraction column (United Chemical Technologies, Horsham, PA, USA). Sub-micro fluorimeter quartz cells were supplied by Starna Cells, Inc. (Atascadero, CA, USA). All solvents were purchased from Pharmco-AAPER or Fisher Scientific as highest purity grade or dispensed dry from a solvent purification system (CH₂Cl₂). Other synthetic reagents were obtained from commercial sources and used without further purification unless indicated. Benzaldehyde was distilled prior to use. NanoPure™ water (Barnstead International, Dubuque, IA, USA) was used for all microarray and cell processing procedures. 384-well plates were purchased from Genetix (Boston, MA, USA) and SuperAldehyde slides were purchased from TeleChem International (Sunnyvale, CA, USA). Cell culture and seeding materials were supplied by Fisher Scientific (Hampton, NH, USA) and Invitrogen (Carlsbad, CA, USA). Hydrogel microarrays were produced using an OmniGrid Accent™ Microarrayer (GeneMachines, San Carlos, CA, USA). Scanner fluorescence images were obtained on a GenePix 4000B microarray scanner and data analysis was done using GenePix 3.0 software (Axon Instruments, Union City, CA, USA). Fluorescence spectra were taken on a QuantaMaster™ Luminescence spectrofluorimeter and data was analyzed using FeliX32™ software (Photon Technology International, Birmingham, NJ, USA) and Microsoft Office® Excel. Confocal fluorescence imaging of hydrogels was performed with an Olympus Fluoview™ 1000 scanning laser confocal microscope, controlled by Olympus FV10-ASW v1.61 software (Center Valley, PA, USA). Fluorescence emission data were acquired as the integrated photon intensity within a defined hydrogel region. Images were processed and analyzed with ImageJ [68].

3.2. Hydrogel Array Materials & Methods

Preparation of 2-iodoxybenzoic acid (IBX): Oxone (133.80 g, 0.218 mol) was added to a 1-L round bottom flask and suspended in 520 mL of distilled water. 2-iodobenzoic acid (30 g, 0.121 mol) was added in one portion and the reaction mixture heated to 70 °C and stirred for 3 h. The reaction was cooled to room temperature and then to 0 °C for 90 min to further precipitate the product. The resulting white solid was collected by filtration, washed with water (5 × 50 mL) and acetone (4 × 50 mL), and dried under vacuum to afford the pure product (27 g, 80% yield). The spectral data were in agreement with reported values [69].

Preparation of poly(ethylene glycol) dialdehyde (PEG-(CHO)₂) macromonomer (Figure 3): Poly(ethylene glycol) Mn = 3400 g/mol (3 g, 0.882 mmol) was dissolved in toluene (10 mL), concentrated under reduced pressure to a viscous residue, and dried under vacuum (2×). The residue was dissolved in a minimum of ethyl acetate (approx. 20 mL) and IBX (1.24 g, 4.4 mmol) was added in one portion. The reaction mixture was heated to 80 °C and stirred for 20 h. IBX was filtered over Celite and the filtrate was concentrated under reduced pressure to a thin residue. An additional filtration in ethyl acetate removed any remaining IBX. The product was concentrated under pressure and precipitated in cool ether for 2 h to afford crude PEG-(CHO)₂ (0.8 g, 27% yield). The crude product was purified by reversed phase chromatography using a C8-bonded silica endcapped column (elution with 10–90% acetonitrile in water), and the product was lyophilized to afford pure PEG-(CHO)₂. ¹H-NMR (400 MHz, CDCl₃): 3.62–3.72 (m, 340, CH₂ of PEG); 4.14 (m, 2, CH₂CHO); 9.71 (s, 1, CHO).

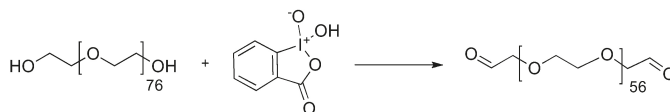


Figure 3. Synthesis scheme of the poly(ethylene glycol) dialdehyde (PEG-(CHO)₂) macromonomer.

Preparation of bis(2-amido-lysine)-poly(ethylene glycol) (PEG-(Lys)₂) macromonomer: According to literature procedure [70].

Printing of hydrogel microarrays: The hydrogel solution (22 wt % 2:1 PEG-(CHO)₂:PEG-(Lys)₂ in HEPES buffer pH 7.4) was printed on aldehyde-coated glass slides, polymerized for 24 h at room temperature and blocked with a 1% *w/v* BSA solution in water as previously reported [33]. Fluorescence measurements were performed as described below. Attempts to observe the nitrene in the gel by IR were unsuccessful.

A549 cell seeding conditions: Cells were cultured at 37 °C in a 5% CO₂ atmosphere in Dulbecco's modified Eagle medium (DMEM) supplemented with 10% fetal bovine serum and 10 µg/mL penicillin. Immediately prior to incubation with hydrogel microarrays, cells were detached from polystyrene culture flasks, centrifuged at 1000× *g* for 5 min, and re-suspended in the appropriate volume of phosphate buffered saline (PBS) to yield ~3 × 10⁴ cells/mL. The cell solution was slowly pipetted directly on top of the hydrogels in a 100 × 20 mm polystyrene culture dish and incubated for 20 min at 37 °C. Microarrays were then washed with PBS (10 mL) to remove unbound cells and tapped dry.

3.3. Fluorescence Image Analysis

GenePix 4000B microarray fluorescence scans: Following microarray printing, the macromonomers were allowed to polymerize for 24 h at room temperature. The crosslinked hydrogel chambers were excited with the microarray scanner and emission intensities were calculated as the mean intensity of the spot normalized to the background.

Steady-state fluorescence spectra: The hydrogel solution (14 wt % 2:1 PEG-(CHO)₂:PEG(Lys)₂) was contained in a 10 mm pathlength quartz cuvette under atmospheric conditions 24 h prior to fluorescence measurements. The samples were excited by a pulsed xenon lamp at a wavelength of

380 nm, and emission was monitored from 300–600 nm as the number of photon counts per second. Excitation and emission were controlled by a quarter-meter class, Czerny–Turner type monochromator with a standard 1200 line/mm ruled grating. Spectra data was corrected for solvent background, and counts per second were normalized to an arbitrary scale of 0–100.

Confocal fluorescence imaging: The hydrogel microarrays were printed and blocked with BSA solution as described above. For cell seeding hydrogel experiments, the microarray slides were further incubated with a solution of A549 human lung carcinoma cells for 20 min at 37 °C, washed with PBS, and tapped dry. Both blank and cell-seeded hydrogel arrays were imaged on a confocal scanning electron microscope with a 20× water-immersion objective lens. A 407 nm diode laser was used for excitation of the intrinsic hydrogel fluorescence, and detection was carried out between 450 and 500 nm at 20 μs/pixel resolution. Confocal emission spectra were generated using sequential emission imaging of the hydrogel at 5 nm bandpass between 440 and 600 nm. Maximum hydrogel emission, with minimal background interference, occurred at 460 nm.

Data were analyzed as the integrated pixel intensity (at 460 nm emission) within the area of a manually outlined hydrogel chamber, human cell, or background region. Fluorescence 2D images and 3D surface plots corresponding to the emission intensity of an outlined hydrogel chamber subtracted from slide background were constructed in ImageJ (Figure 2 in paper). Images were formatted to 8-bits per pixel (grayscale LUT) and contrast was enhanced. Signal-to-noise ratios were determined as the mean pixel intensity within a hydrogel area or cell area divided by the corresponding standard deviation.

3.4. Nitron Model

Preparation of *N*-benzylhydroxylamine [71]. A flame dried flask was charged with a stir bar and benzaldehyde oxime (1.00 g, 8.26 mmol) dissolved in methanol (9.03 mL, 0.223 mol) was added. Sodium cyanoborohydride (0.363 g, 5.78 mmol) was added and the pH was brought down to pH 4 with the addition of aqueous concentrated HCl. The reaction was stirred for 3 h. Solvent was concentrated under reduced pressure and crude product was diluted with 6 M potassium hydroxide and washed with brine. The organic layer was extracted with chloroform (3×) and dried over MgSO₄. The product was concentrated and ¹H-NMR spectroscopy showed sufficient purity to be used in the next reaction.

Preparation of (*Z*)-*N*-benzyl- α -phenylnitron (1; Figure 4): According to the procedure of Chang, et al. [48], a flame dried 5 mL round bottom flask was charged with a stir bar and flushed with nitrogen. To this flask was added anhydrous sodium sulfate (0.160 g, 1.125 mmol), *N*-benzylhydroxylamine (0.092 g, 0.75 mmol), benzaldehyde (0.111 g, 1.05 mmol), and dichloromethane (2.5 mL). The reaction was stirred under nitrogen at room temperature for 7 h. Sodium sulfate was filtered and the filtrate was concentrated under reduced pressure to give a light brown oil that solidified upon standing. The crude product was washed once with cold petroleum ether and recrystallized from hexane (2×) to afford 0.13 g (82% yield) of the *Z* isomer. The spectral data was in agreement with reported values [72].

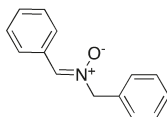


Figure 4. Chemical structure of nitron, 1.

Photochemical properties: Steady-state fluorescence spectra were taken of 1 (2.8 wt %, 0.13M) immediately following dissolution in either ethanol or dichloromethane. Fluorescence intensity was weaker and dual peak emission less pronounced in EtOH as compared to CH₂Cl₂ as result of the increased solvation of 1 due to H-bonding interactions. However, excitation and emission maxima

were consistent between both solvents, and EtOH solvent fluorescence data was used for hydrogel fluorescence comparisons. The nitrone solution was contained in a 10 mm pathlength quartz cuvette and fluorescence measurements were taken under the same conditions as described for the hydrogel. Spectra data was corrected for background, and counts per second were normalized to an arbitrary scale of 0–100.

4. Conclusions

In summary, fluorescence emission is observed from the hydrogels with a λ_{\max} at 445 nm. The photochemical properties of these hydrogels are consistent with emission from a nitrone functionality formed via oxidation of the imine crosslinkages within the hydrogel. A new cell microarray assay is described, whereby the reduction or obstruction of fluorescence is monitored upon individual cell adherence to the hydrogel chamber. Typically, hydrogel parameters such as polymer wt % and crosslink density are altered for a specific application; now, fluorescence can be incorporated into such criteria by specific macromonomer selection. Continued experimentation with multifunctional dendritic macromolecules will lead to new polymer structures, crosslinked networks, and properties broadening the investigation of these unique macromolecules for basic and clinical applications.

Acknowledgments: This research was supported by Boston University. We thank Michel Wathier and Phil Allen for help with the experiments.

Author Contributions: L.C., M.W.G. and S.E.S. conceived and designed the experiments; L.C. performed the experiments; L.C., M.W.G. and S.E.S. analyzed the data; L.C., M.W.G. and S.E.S. wrote the paper.

Conflicts of Interest: The authors declare no conflict of interest.

References

1. Caminade, A.M.; Ouali, A.; Laurent, R.; Turrin, C.O.; Majoral, J.P. Coordination chemistry with phosphorus dendrimers. Applications as catalysts, for materials, and in biology. *Coord. Chem. Rev.* **2016**, *308*, 478–497. [[CrossRef](#)]
2. Sun, H.J.; Zhang, S.; Percec, V. From structure to function via complex supramolecular dendrimer systems. *Chem. Soc. Rev.* **2015**, *44*, 3900–3923. [[CrossRef](#)] [[PubMed](#)]
3. Wang, D.; Astruc, D. Dendritic catalysis—Basic concepts and recent trends. *Coord. Chem. Rev.* **2013**, *257*, 2317–2334. [[CrossRef](#)]
4. Newkome, G.R.; Shreiner, C.D. Poly(amidoamine), polypropylenimine, and related dendrimers and dendrons possessing different 1/2 branching motifs: An overview of the divergent procedures. *Polymer* **2008**, *49*, 1–173. [[CrossRef](#)]
5. Molla, M.R.; Rangadurai, P.; Pavan, G.M.; Thayumanavan, S. Experimental and theoretical investigations in stimuli responsive dendrimer-based assemblies. *Nanoscale* **2015**, *7*, 3817–3837. [[CrossRef](#)] [[PubMed](#)]
6. Kannan, R.M.; Nance, E.; Kannan, S.; Tomalia, D.A. Emerging concepts in dendrimer-based nanomedicine: From design principles to clinical applications. *J. Intern. Med.* **2014**, *6*, 579–617. [[CrossRef](#)] [[PubMed](#)]
7. Mintzer, M.A.; Grinstaff, M.W. Biomedical Applications of Dendrimers: A Tutorial. *Chem. Soc. Rev.* **2011**, *40*, 173–190. [[CrossRef](#)] [[PubMed](#)]
8. Lee, C.C.; MacKay, J.A.; Fréchet, J.M.J.; Szoka, F.C. Designing Dendrimers for Biological Applications. *Nat. Biotechnol.* **2005**, *23*, 1517–1526. [[CrossRef](#)] [[PubMed](#)]
9. Svenson, S.; Tomalia, D.A. Dendrimers in Biomedical Application—Reflections on the Field. *Adv. Drug Deliv. Rev.* **2005**, *57*, 2106–2129. [[CrossRef](#)] [[PubMed](#)]
10. Grinstaff, M.W. Biodendrimers: New Polymeric Materials for Tissue Engineering. *Chem. Eur. J.* **2002**, *8*, 2838–2846. [[CrossRef](#)]
11. Shaunak, S. Perspective: Dendrimer drugs for infection and inflammation. *Biochem. Biophys. Res. Commun.* **2015**, *468*, 435–441. [[CrossRef](#)] [[PubMed](#)]
12. Wu, L.P.; Ficker, M.; Christensen, J.B.; Trohopoulos, P.N.; Moghimi, S.M. Dendrimers in Medicine: Therapeutic Concepts and Pharmaceutical Challenges. *Bioconj. Chem.* **2015**, *26*, 1198–1211. [[CrossRef](#)] [[PubMed](#)]

13. Bugno, J.; Hsu, H.; Hong, S. Recent advances in targeted drug delivery approaches using dendritic polymers. *Biomater. Sci.* **2015**, *3*, 1025–1034. [[CrossRef](#)] [[PubMed](#)]
14. Wolinsky, J.B.; Grinstaff, M.W. Therapeutic and Diagnostic Applications of Dendrimers for Cancer Treatment. *Adv. Drug Deliv. Rev.* **2008**, *60*, 1037–1055. [[CrossRef](#)] [[PubMed](#)]
15. Gillies, E.R.; Fréchet, J.M. Dendrimers and dendritic polymers in drug delivery. *Drug Discov. Today* **2005**, *10*, 35–43. [[CrossRef](#)]
16. Lee, C.C.; Gillies, E.R.; Fox, M.E.; Guillaudeu, S.J.; Fréchet, J.M.J.; Dy, E.E.; Szoka, F.C. A single dose of doxorubicin-functionalized bow-tie dendrimer cures mice bearing C-26 colon carcinoma. *Proc. Natl. Acad. Sci. USA* **2006**, *103*, 16649–16654. [[CrossRef](#)] [[PubMed](#)]
17. Lim, J.; Simanek, E.E. Synthesis of water-soluble dendrimers based on melamine bearing 16 paclitaxel groups. *Org. Lett.* **2008**, *10*, 201–204. [[CrossRef](#)] [[PubMed](#)]
18. Gurdag, S.; Khandare, J.S.S.; Matherly, L.H.; Kannan, R.M. Activity of dendrimer methotrexate conjugates on methotrexate-sensitive and resistant cell lines. *Bioconj. Chem.* **2006**, *17*, 275–283. [[CrossRef](#)] [[PubMed](#)]
19. Morgan, M.T.; Nakanishi, Y.; Kroll, D.J.; Griset, A.P.; Carnahan, M.A.; Wathier, M.; Oberlies, N.H.; Manikumar, G.; Wani, M.C.; Grinstaff, M.W. Dendrimer-encapsulated camptothecins: Increased solubility, cellular uptake, and cellular retention afford enhanced anticancer activity in vitro. *Cancer Res.* **2006**, *66*, 11913–11921. [[CrossRef](#)] [[PubMed](#)]
20. Morgan, M.T.; Carnahan, M.A.; Immoos, C.E.; Ribeiro, A.A.; Finkelstein, S.; Lee, S.J.; Grinstaff, M.W. Dendritic molecular capsules for hydrophobic compounds. *J. Am. Chem. Soc.* **2003**, *125*, 15485–15489. [[CrossRef](#)] [[PubMed](#)]
21. Hed, Y.; Oberg, K.; Berg, S.; Nordberg, A.; von Holst, H.; Malkoch, M. Multipurpose heterofunctional dendritic scaffolds as crosslinkers towards functional soft hydrogels and implant adhesives in bone fracture applications. *J. Mater. Chem. B* **2013**, *1*, 6015–6019. [[CrossRef](#)]
22. Ghobril, C.; Grinstaff, M.W. The Chemistry and Engineering of Polymeric Hydrogel Adhesives for Wound Closure: A Tutorial. *Chem. Soc. Rev.* **2015**, *44*, 1820–1835. [[CrossRef](#)] [[PubMed](#)]
23. Ghobril, C.; Charoen, K.; Rodriguez, E.K.; Nazarian, A.; Grinstaff, M.W. A Dendritic Thioester Hydrogel Based on Thiol-Thioester Exchange as a Dissolvable System for Wound Closure. *Angew. Chem. Int. Ed.* **2013**, *52*, 14070–14074. [[CrossRef](#)] [[PubMed](#)]
24. Oelker, A.M.; Grinstaff, M.W. Ophthalmic Adhesives: A Materials Chemistry Perspective. *J. Mater. Chem.* **2008**, *18*, 2521–2536. [[CrossRef](#)]
25. Wathier, M.; Jung, P.J.; Carnahan, M.A.; Kim, T.; Grinstaff, M.W. Dendritic Macromers as In Situ Polymerizing Biomaterials for Securing Cataract Incisions. *J. Am. Chem. Soc.* **2004**, *126*, 12744–12745. [[CrossRef](#)] [[PubMed](#)]
26. Carnahan, M.A.; Middleton, C.; Kim, J.; Kim, T.; Grinstaff, M.W. Hybrid Dendritic-Linear Polyester-ethers for In Situ Photopolymerization. *J. Am. Chem. Soc.* **2002**, *124*, 5291–5293. [[CrossRef](#)] [[PubMed](#)]
27. Wathier, M.; Johnson, S.M.; Kim, T.; Grinstaff, M.W. Hydrogels Formed by Multiple Peptide Ligation Reactions to Fasten Corneal Transplants. *Bioconj. Chem.* **2006**, *17*, 873–876. [[CrossRef](#)] [[PubMed](#)]
28. Berdahl, J.P.; Johnson, C.S.; Proia, A.D.; Grinstaff, M.W.; Kim, T. Comparison of Sutures and New Dendritic Polymer Adhesives for Corneal Laceration Repair in an In Vivo Chicken Model. *Arch. Ophthalmol.* **2009**, *127*, 442–447. [[CrossRef](#)] [[PubMed](#)]
29. Degoricija, L.; Söntjens, S.H.M.; Bansal, P.N.; Takahashi, M.; Joshi, N.; Snyder, B.; Grinstaff, M.W. Hydrogels for Osteochondral Regeneration Based on Photo-crosslinkable Carbamate Dendrimers. *Biomacromolecules* **2008**, *9*, 2863–2872. [[CrossRef](#)] [[PubMed](#)]
30. Sontjens, S.H.M.; Nettles, D.L.; Carnahan, M.A.; Setton, L.A.; Grinstaff, M.W. Biodendrimer-based hydrogel scaffolds for cartilage tissue repair. *Biomacromolecules* **2006**, *7*, 310–316. [[CrossRef](#)] [[PubMed](#)]
31. Navath, R.S.; Menjoge, A.R.; Dai, H.; Romero, R.; Kannan, S.; Kannan, R.M. Injectable PAMAM dendrimer-PEG hydrogels for the treatment of genital infections: Formulation, in-vitro and in-vivo evaluation. *Mol. Pharm.* **2011**, *8*, 1209–1223. [[CrossRef](#)] [[PubMed](#)]
32. Yang, H.; Tyagi, P.; Kadam, R.S.; Holden, C.A.; Kompella, U.B. Hybrid dendrimer hydrogel/PLGA nanoparticle platform sustains drug delivery for one week and antiglaucoma effects for four days following one-time topical administration. *ACS Nano* **2012**, *6*, 7595–7606. [[CrossRef](#)] [[PubMed](#)]
33. Dominguez, M.M.; Wathier, M.; Grinstaff, M.W.; Schaus, S.E. Immobilized Hydrogels for High Throughput Screening of Molecular Interactions. *Anal. Chem.* **2007**, *79*, 1064–1066. [[CrossRef](#)] [[PubMed](#)]

34. Larson, C.L.; Tucker, S.A. Intrinsic fluorescence of carboxylate-terminated polyamido amine dendrimers. *Appl. Spectrosc.* **2001**, *55*, 679–683. [[CrossRef](#)]
35. Lee, W.I.; Bae, Y.B.; Bard, A.J. Strong blue photoluminescence and ECL from OH-terminated PAMAM dendrimers in the absence of gold nanoparticles. *J. Am. Chem. Soc.* **2004**, *126*, 8358–8359. [[CrossRef](#)] [[PubMed](#)]
36. Wang, D.; Imae, T. Fluorescence emission from dendrimers and its pH dependence. *J. Am. Chem. Soc.* **2004**, *126*, 13204–13205. [[CrossRef](#)] [[PubMed](#)]
37. Wang, D.; Imae, T.; Miki, M. Fluorescence emission from PAMAM and PPI dendrimers. *J. Colloid Interface Sci.* **2007**, *306*, 222–227. [[CrossRef](#)] [[PubMed](#)]
38. Tsai, Y.J.; Hu, C.C.; Chu, C.C.; Imae, T. Intrinsically fluorescent PAMAM dendrimer as gene carrier and nanoprobe for nucleic acids delivery: Bioimaging and transfection study. *Biomacromolecules* **2011**, *12*, 4283–4290. [[CrossRef](#)] [[PubMed](#)]
39. Ji, Y.; Qian, Y. A study using quantum chemical theory methods on the intrinsic fluorescence emission and the possible emission mechanisms of PAMAM. *RSC Adv.* **2014**, *4*, 58788–58794. [[CrossRef](#)]
40. Ji, Y.; Yang, X.-L.; Qian, Y. Poly-amidoamine structure characterization: Amide resonance structure of imidic acid (HO-C[double bond, length as m-dash]N) and tertiary ammonium. *RSC Adv.* **2014**, *4*, 49535–49540. [[CrossRef](#)]
41. Ballistreri, F.P.; Barbuzzi, E.; Tomaselli, G.A.; Toscano, R.M.; Mol, J.C. Oxidation of *N*, *N*-benzylalkylamines to nitrones by Mo(VI) and W(VI) polyperoxo complexes. *Catal. A Chem.* **1997**, *114*, 229. [[CrossRef](#)]
42. Cardona, F.; Bonanni, M.; Soldaini, G.; Goti, A. One-Pot Synthesis of Nitrones from Primary Amines and Aldehydes Catalyzed by Methyltrioxorhenium. *ChemSusChem* **2008**, *1*, 327–332. [[CrossRef](#)] [[PubMed](#)]
43. Feuer, H. *Nitrile Oxides, Nitrones and Nitronates*; John Wiley & Sons, Inc.: Hoboken, NJ, USA, 2008.
44. Soldaini, G.; Cardona, F.; Goti, A. Catalytic Oxidation of Imines Based on Methyltrioxorhenium/Urea Hydrogen Peroxide: A Mild and Easy Chemo- and Regioselective Entry to Nitrones. *Org. Lett.* **2007**, *9*, 473–476. [[CrossRef](#)] [[PubMed](#)]
45. Thiel, W.R. Transition metal mediated oxygen transfer to organo nitrogen compounds. *Coord. Chem. Rev.* **2003**, *245*, 95–106. [[CrossRef](#)]
46. Imada, Y.; Iida, H.; Ono, S.; Murahashi, S. Flavin catalyzed oxidations of sulfides and amines with molecular oxygen. *J. Am. Chem. Soc.* **2003**, *125*, 2868–2869. [[CrossRef](#)] [[PubMed](#)]
47. Murahashi, S. Synthetic Aspects of Metal-Catalyzed Oxidations of Amines and Related Reactions. *Angew. Chem. Int. Ed.* **1995**, *34*, 2443–2465. [[CrossRef](#)]
48. Chang, Z.Y.; Coates, R.M. Diastereoselectivity of organometallic additions to nitrones bearing stereogenic *N*-substituents. *J. Org. Chem.* **1990**, *55*, 3464–3474. [[CrossRef](#)]
49. Boyd, D.R.; Campbell, P.B.; Grimshaw, J.; Neill, D.C.; Jennings, W.B. Dynamic stereochemistry of imines and derivatives. Part 18. Photosynthesis and photoracemization of optically active oxaziridines. *J. Chem. Soc. Perkin Trans.* **1985**, *1*, 849–855. [[CrossRef](#)]
50. Cik, G.; Sersen, F. A study of photolysis of *N*-(4-azidobenzylidene)aniline-*N*-oxide. *J. Imaging Sci.* **1991**, *35*, 14–19.
51. Cyr, D.R.; Mathew, T.; Ashok, K.; Das, P.K.; George, M.V. A laser flash photolysis study of aromatic nitrones. Triplet state properties and reactivity with singlet oxygen. *J. Photochem. Photobiol. A Chem.* **1991**, *60*, 161–174. [[CrossRef](#)]
52. Khoe, S.; Memarian, H.R. Fluorescence self-quenching of substituted *N*, α -diphenylnitrones in various solvents. *J. Photochem. Photobiol. A Chem.* **2006**, *177*, 276–285. [[CrossRef](#)]
53. Koyano, K.; Tanaka, I. The Photochemical and Thermal Isomerization of trans- and cis- α -Cyano- α -phenyl-*N*-phenylnitrones. *J. Phys. Chem.* **1965**, *69*, 2545–2550. [[CrossRef](#)]
54. Lamchen, M.; Mittag, T.W. Nitrones. Part VII. The photochemistry and cycloaddition of a monocyclic α -dinitrone. *J. Chem. Soc. C* **1968**, 1917–1921. [[CrossRef](#)]
55. Shinzawa, K.; Tanaka, I. The Photochemical Isomerization of α ,*N*-Diphenylnitronone. *J. Phys. Chem.* **1964**, *68*, 1205–1213. [[CrossRef](#)]
56. Splitter, J.S.; Calvin, M. Oxaziridines. I. The Irradiation Products of Several Nitrones. *J. Org. Chem.* **1965**, *30*, 3427–3436. [[CrossRef](#)]
57. Brehm-Stecher, B.F.; Johnson, E.A. Single-cell microbiology: Tools, technologies, and applications. *Microbiol. Mol. Biol. Rev.* **2004**, *68*, 538–559. [[CrossRef](#)] [[PubMed](#)]

58. Dittrich, P.S.; Manz, A. Lab-on-a-chip: Microfluidics in drug discovery. *Nat. Rev. Drug Discov.* **2006**, *5*, 210. [CrossRef] [PubMed]
59. El-Ali, J.; Sorger, P.K.; Jensen, K.F. Cells on chips. *Nature* **2006**, *442*, 403–411. [CrossRef] [PubMed]
60. Vilkner, T.; Janasek, D.; Manz, A. Micro Total Analysis Systems. Recent Developments. *Anal. Chem.* **2004**, *76*, 3373–3386. [CrossRef] [PubMed]
61. Wheeler, A.R.; Thronsdet, W.R.; Whelan, R.J.; Leach, A.M.; Zare, R.N.; Liao, Y.H.; Farrell, K.; Manger, I.D.; Daridon, A. Microfluidic device for single-cell analysis. *Anal. Chem.* **2003**, *75*, 3581–3586. [CrossRef] [PubMed]
62. Zare, R.N.; Kim, S. Microfluidic platforms for single-cell analysis. *Annu. Rev. Biomed. Eng.* **2010**, *12*, 187–201. [CrossRef] [PubMed]
63. Tan, S.J.; Li, Q.; Lim, C.T. Manipulation and isolation of single cells and nuclei. *Methods Cell Biol.* **2010**, *98*, 79–96. [PubMed]
64. Yershov, G.; Barsky, V.; Belgovskiy, A.; Kirillov, E.; Kreindlin, E.; Ivanov, I.; Parinov, S.; Guschin, D.; Drobyshev, A.; Dubiley, S.; et al. DNA analysis and diagnostics on oligonucleotide microchips. *Proc. Natl. Acad. Sci. USA* **1996**, *93*, 4913–4918. [CrossRef] [PubMed]
65. Zlatanova, J.; Mirzabekov, A. Gel-Immobilized Microarrays of Nucleic Acids and Proteins. Production and Application for Macromolecular Research. *Methods Mol. Biol.* **2001**, *170*, 17–38. [PubMed]
66. Beria, L.; Gevrek, T.N.; Erdog, A.; Sanyal, R.; Pasini, D.; Sanyal, A. Clickable Hydrogels for All: Facile Fabrication and Functionalization. *Biomater. Sci.* **2014**, *2*, 67–75. [CrossRef]
67. Kemp, M.M.; Weiwer, M.; Koehler, A.N. Unbiased binding assays for discovering small-molecule probes and drugs. *Bioorg. Med. Chem.* **2012**, *20*, 1979–1989. [CrossRef] [PubMed]
68. Rasband, W.S. *ImageJ. U. S.*; National Institutes of Health: Bethesda, MD, USA, 2008. Available online: <https://imagej.nih.gov/ij/> (accessed on 17 April 2018).
69. Frigerio, M.; Santagostino, M.; Sputore, S. A User-Friendly Entry to 2-Iodoxybenzoic Acid (IBX). *J. Org. Chem.* **1999**, *64*, 4537–4538. [CrossRef]
70. Wathier, M.; Johnson, M.S.; Carnahan, M.A.; Baer, C.; McCuen, B.W.; Kim, T.; Grinstaff, M.W. In situ polymerized hydrogels for repairing scleral incisions used in pars plana vitrectomy procedures. *ChemMedChem* **2006**, *1*, 821–825. [CrossRef] [PubMed]
71. Kainthan, R.K.; Mugabe, C.; Burt, H.M.; Brooks, D.E. Unimolecular micelles based on hydrophobically derivatized hyperbranched polyglycerols: Ligand binding properties. *Biomacromolecules* **2008**, *9*, 886–895. [CrossRef] [PubMed]
72. Murahashi, S.; Mitsui, H.; Shiota, T.; Tsuda, T.; Watanabe, S. Tungstate-catalyzed oxidation of secondary amines to nitrones. α -Substitution of secondary amines via nitrones. *J. Org. Chem.* **1990**, *55*, 1736–1744. [CrossRef]

Sample Availability: Samples of the compounds are available from the authors.



© 2018 by the authors. Licensee MDPI, Basel, Switzerland. This article is an open access article distributed under the terms and conditions of the Creative Commons Attribution (CC BY) license (<http://creativecommons.org/licenses/by/4.0/>).

Article

On-Demand Bioadhesive Dendrimers with Reduced Cytotoxicity

Feng Gao ¹, Ivan Djordjevic ², Oleksandr Pokholenko ³, Haobo Zhang ¹, Junying Zhang ^{1,*} and Terry W. J. Steele ^{3,*}

¹ School of Material Science and Engineering, Beijing University of Chemistry Technology, North Third Ring Road 15, Chaoyang District, Beijing 100029, China; gaofeng@mail.buct.edu.cn (F.G.); zhanghaobo9093@163.com (H.Z.)

² Escuela de Ingeniería y Ciencias, Tecnológico de Monterrey, Ave. Eugenio Garza Sada 2501, Monterrey 64849, NL, Mexico; idjordjevic@ntu.edu.sg

³ School of Materials Science and Engineering, Division of Materials Technology, Nanyang Technological University, Singapore 639798, Singapore; opokholenko@ntu.edu.sg

* Correspondence: wjsteele@ntu.edu.sg (T.W.J.S.); zhangjy@mail.buct.edu.cn (J.Z.); Tel.: +65-6592-7594 (T.W.J.S.); +86-10-6442-5439 (J.Z.)

Academic Editor: Ashok Kakkur

Received: 22 March 2018; Accepted: 27 March 2018; Published: 30 March 2018

Abstract: Tissue adhesives based on polyamidoamine (PAMAM) dendrimer, grafted with UV-sensitive aryldiazirine (PAMAM-g-diazirine) are promising new candidates for light active adhesion on soft tissues. Diazirine carbene precursors form interfacial and intermolecular covalent crosslinks with tissues after UV light activation that requires no premixing or inclusion of free radical initiators. However, primary amines on the PAMAM dendrimer surface present a potential risk due to their cytotoxic and immunological effects. PAMAM-g-diazirine formulations with cationic pendant amines converted into neutral amide groups were evaluated. In vitro toxicity is reduced by an order of magnitude upon amine capping while retaining bioadhesive properties. The in vivo immunological response to PAMAM-g-diazirine formulations was found to be optimal in comparison to standard poly(lactic-co-glycolic acid) (PLGA) thin films.

Keywords: PAMAM; dendrimers; bioadhesive; diazirine

1. Introduction

Adhesive hydrogels generated by crosslinking of polymers are designed to disperse mechanical stress and allow fluid transport through tissue interfaces [1]. Such formulations are considered to be useful to replace the suturing of delicate tissues and to avoid tissue piercing. This feature is particularly important for vascular anastomosis (Figure 1) where adhesive formulations should allow strong tissue fixation in order to replace traditional suturing fixation methods [2–5].

Although developed for more than half a century, non-invasive tissue fixation strategies still rely on cyanoacrylate [6] and the fibrin glue formulations [7]. Cyanoacrylate, also known as ‘super glue’, is able to generate reliable adhesion strength towards the surface of tissue after an in-situ crosslinking process in the presence of moisture [8]. However, the heat generated during the polymerization can burn the tissue [9] and the toxic degradation products limit the applications of cyanoacrylates to topical tissue fixations [6]. Fibrin glue is a protein-based adhesive that sets the adhesion strength through physical crosslinks with tissue interfaces of $\sim 0.5 \text{ N/cm}^2$. The in-situ crosslinking processes and swelling behavior of fibrin glue were found to be challenging for the hydrated tissue environment [7]. Tissue adhesives need to be able to bond both natural materials and synthetic films for applications involving implantable biosensors and drug depots [10–20]. Formation of covalent bonds between thin

film or hydrogel adhesive formulations and soft tissue substrates is a promising strategy to achieve a reliable adhesion strength [3,15,16,19]. This can be achieved by diazirine-functionalized polymer formulations that crosslink under low energy UV light or voltage as previously published by our group [21–24]. Diazirines can be covalently attached to a PAMAM backbone through the reaction with pendant amine ($-NH_2$) groups in a highly controlled manner. PAMAM-g-diazirine formulations resulted in tunable shear moduli of 1–100 kPa and maximum shear adhesion strength of 27 kPa when attached on wet, ex-vivo arteries, which is a promising in comparison to fibrin adhesives [25]. In vitro 3T3 fibroblasts cell culture test showed no leaching of potentially toxic components from the crosslinked adhesive. It should be noted that significant cytotoxicity was caused by the uncrosslinked parts of macromolecules and their inherent $-NH_2$ groups from the PAMAM dendrimer [21,22,24]. Positively charged amines are known to disrupt cell membranes [16]. In order to avoid direct contact of PAMAM with cells we have mediated the cytotoxic influence of $-NH_2$ groups by chemical capping. This is achieved by reacting free $-NH_2$ groups of PAMAM with acetyl chloride, which produces a neutral dendrimer free of cationic charge (Figure 2).

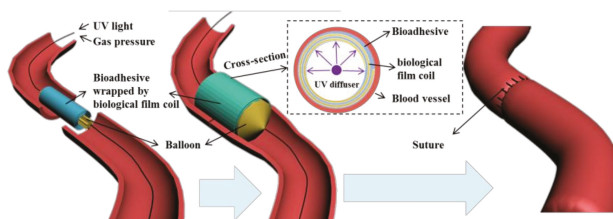


Figure 1. Proposed strategy for blood vessel fixation: UV crosslinked adhesive hydrogel is spread on the surface of bio-degradable film coil, wrapped around the balloon stent. Adhesives layer is in direct contact with blood vessel once the coil is expanded by balloon inflation. UV light is transferred through the stent and crosslinks the adhesive layer with the help of a light diffuser.

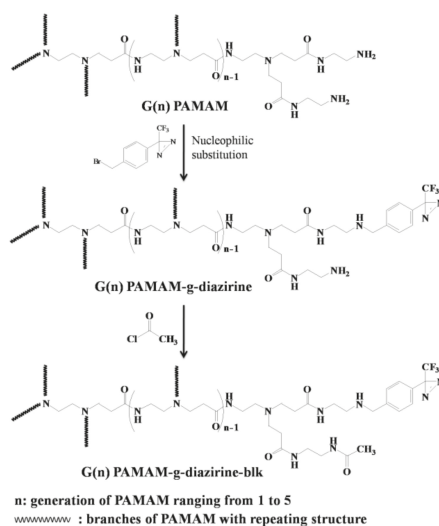


Figure 2. Synthesis pathway for PAMAM-g-diazirine and PAMAM-g-diazirine-block: the first step is conjugation of aromatic diazirine onto G1–G5 PAMAM macromolecules; the second step is the reaction between free $-NH_2$ groups and acetyl chloride resulting in a reduced number of free $-NH_2$ groups that can cause cytotoxicity.

The number of functional groups doubles during the divergent synthesis of PAMAM with each generation and the diameter of the molecule extends by only 1 nm [26]. Surface functional groups of PAMAM dendrimers exponentially increases with the next generation, likely correlating with toxicity. The work presented herein is based on the following hypotheses: (i) tissue adhesion is caused by UV-activated crosslinking of diazirine end-groups and the adhesion strength is dependent on diazirine concentration and not dendrimer size; (ii) the presence of protective amide groups (Figure 2) will not interfere with carbene crosslinking; and (iii) capping of $-NH_2$ groups (PAMAM-g-diazirine-blk) decreases both in vitro toxicity, and in vivo immunological response. The conjugation of acetyl chloride onto pendant $-NH_2$ groups of PAMAM reduces or removes the cationic charge, mediating cationic cytotoxicity without significantly lowering intermolecular crosslinking. PAMAM dendrimers (G1 to G5) were conjugated with diazirine (PAMAM-g-diazirine) and acetyl chloride (PAMAM-g-diazirine-blk) in order to examine new formulations both in vitro and in vivo [22,27]. Prior to biocompatibility tests, the conjugated dendrimer structures were characterized with size exclusion chromatography (SEC), nuclear magnetic resonance (1H -NMR) spectroscopy and amino-group quantitation. Dynamic mechanical properties of dendrimer adhesive formulations were monitored by photorheometry in real time in order to determine the dose dependent moduli.

2. Results and Discussion

Diazirine was conjugated on G1–G5 PAMAM via nucleophilic substitution reactions as demonstrated in Figure 2 and the formulations were analyzed for their molecular weight (SEC; Figure 3). Neat PAMAM macromolecules (G1–G5) were used as controls (Figure 3a). The solid lines in Figure 3a present the refractive index signals and are shifted from right to left indicating the increase of molecular weight with increasing dendrimer generation (G1 to G5). Dashed lines in Figure 3b represent the corresponding UV absorption at 350 nm caused by the conjugated diazirine. The UV absorption correlated with the increase of diazirine conjugation percentage (Table S1, see Supplementary Section). Similar to our previous work, diazirine conjugation onto PAMAM macromolecules is obtained with a high degree of control over the percentage of conjugation (Figure S1). G1–G5 PAMAM-g-diazirine conjugates with capped amines (Figure 2) were also analysed by SEC and compared to PAMAM-g-diazirine as presented in Figure 3b. As expected, the acetyl chloride blocking caused the increase of molecular weight of the conjugates as the peak value of refractive index signal of G5 PAMAM-g-diazirine-blk (blue) occurred earlier than that of G5 PAMAM-g-diazirine (Figure 3b).

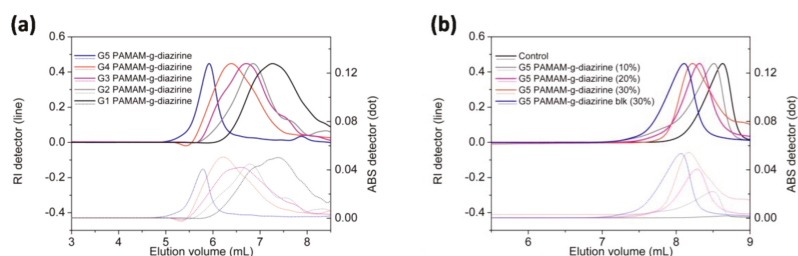


Figure 3. SEC-MALS-UV analysis of conjugated PAMAM dendrimers: (a) chromatographs of G1–G5 PAMAM-g-diazirine (solid lines stand for the normalized refractive index, and the corresponding dashed lines were the UV absorption caused by the conjugated diazirine on each conjugates injected); (b) chromatographs of G5 PAMAM-g-diazirine and its 'blocked' conjugate with acetyl chloride.

The percentage of residual non-reactive $-NH_2$ groups was calculated based on the increase of the molecular weight evaluated from the elution volume (Table S1; Supplementary Section). In order to confirm the concentration of free amines, all formulations were quantified for free amines with the

TNBS assay. TNBS reacts with -NH_2 groups in aqueous solution forming a complex with a maximum UV absorbance at 420 nm. The residual amine was examined by comparing the UV absorption at 420 nm of each conjugate (Figure 4). Note that only 6% of -NH_2 groups were detected for G5 PAMAM-g-diazirine-*blk*. Diazirine conjugation percentages were also calculated from TNBS results. For example, the residual free -NH_2 percentage was 75% for G5 PAMAM-g-diazirine, indicating that 25% of the -NH_2 groups were replaced by aromatic diazirines during the conjugation reaction (Table S1).

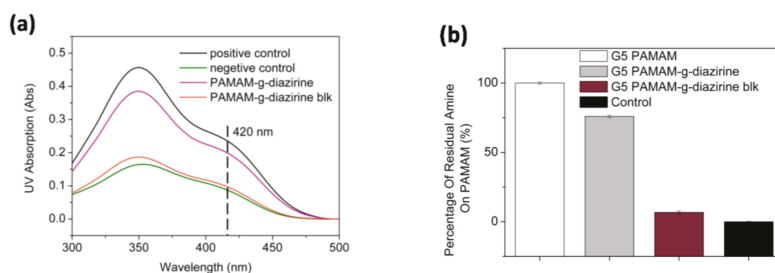


Figure 4. Primary amine concentration from PAMAM adhesive formulations analyzed with TNBS assay: (a) UV absorption curves of TNBS for the G5 PAMAM and its conjugates (pure G5 PAMAM was tested as positive control and negative control was 0.1 M NaHCO_3 buffer); (b) Percentage of residual -NH_2 .

The mechanical properties of PAMAM-g-diaziridene conjugates were monitored in real time with photorheometry as presented in Figure 5a. Dendrimer adhesive solution was placed in between the light transparent base and the rheometer probe and UV light was introduced by a waveguide (Figure 5a).

The irradiation intensity on the sample was adjusted to a constant value of $20 \pm 2 \text{ mW cm}^{-2}$ in all experiments. The curves in Figure 5b demonstrate the relationship between the storage moduli and irradiation (UV activation) time for G1–G5 PAMAM-g-diazirine. Stepwise shaped curves were detected for all the conjugates as well as the G5 PAMAM-g-diazirine-*blk* after several 1 min “ON/OFF” intervals of UV activation. The crosslinking process started immediately when UV light was ‘ON’ leading to a rapid increase of the storage modulus (G') and the loss modulus (G''). The crosslinking reaction stops immediately when UV was switched “OFF” thus resulting in flat line of G' vs. time (Figure 5b). This behavior is a result of instant, non-specific covalent insertion of carbenes without chain propagation during the crosslinking process [28]. Tunable and highly controllable mechanical properties are evident from our dendrimer adhesives, thus reducing the risks of substrate-adhesive modulus mismatch, potentially reducing the chances of adhesive failure under dynamic strains [29,30].

The relationships between G''/G' (tan delta) under continuous UV stimulation time for G1–G5 PAMAM-g-diazirine and G5 PAMAM-g-diazirine-*blk* are plotted in Figure 5c. All these ratios were greater than 1 before UV exposure, indicating the adhesives were viscous liquids. The liquid consistency enabled adhesives to wet and fill irregular surfaces of soft tissue before the sol/gel transition (when $G''/G' > 1$). G''/G' values for G1 and G2 PAMAM-g-diazirine (G2, 30% diazirine conjugation percentage, G1, 62.5% diazirine conjugation percentage) never fell below 1, indicating incomplete crosslinking. Lower order PAMAM generations reduce the surface functional group concentration and dendrimer to dendrimer interpenetration entanglement as well. Thus, the intermolecular crosslinking caused by carbene was insufficient for the formation of an elastic 3D network when the generation was lower than G3. The cohesive failures of G4 and G5 PAMAM-g-diazirine showed porous structures resulted from the formation of nitrogen indicating the consumption of diazirine.

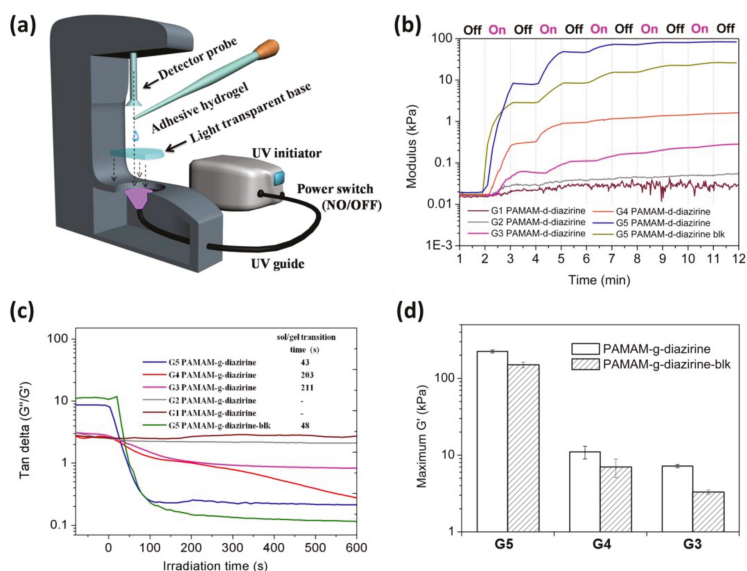


Figure 5. Photo-rheometry of PAMAM-g-diazirine adhesives: (a) schematic illustration of rheometry measurements with UV activation; (b) dynamic change of storage modulus (G') and loss modulus (G'') with UV activation (diazirine conjugation percentages were 20% for G2–G5 and 37.5% for G1; concentration for all conjugates was 50 wt % in PBS); (c) ratio between G' and G'' under continuous UV activation (inset: sol/gel transition time); (d) maximum G' obtained for each conjugate.

The time taken by sol/gel transition increased from 43 s to 211 s when the generation of PAMAM-g-diazirine dropped from G5 to G3 (Figure 5c inset). Note that there was a five-fold drop of the sol/gel transition time from 43 s to 203 s when the dendrimer generation increased from G4 to G5. The modulus of G4 PAMAM-g-diazirine reached maximum of 10 kPa, about 20 \times lower than G5. In terms of biomimetic mechanical integrity G1–G4 PAMAM-g-diazirine are recommended for subcutaneous adipose tissue $G' \approx 10$ kPa [31] or other soft tissues with matching moduli. In terms of control over adhesion strength, G5 PAMAM-g-diazirine could be crosslinked on demand to meet requirements of treated tissues by simple reduction of UV energy used for crosslinking.

According to previous research, the branches of PAMAM above G5 were densely packed, thus forming spherical shapes in solution [32]. The morphology of PAMAM from G1 to G4 is planar and elliptical [33] and therefore the branch interpenetration intensity for G5 is higher than those of G4 and G3. As a consequence, we detected a different mechanical profile for G4 and G5 PAMAM-g-diazirine, which may be explained by the close packed geometry. Figure 5d demonstrates how after 5 min of UV activation G' reached 225 kPa for G5 which were almost 20 times higher than that of G4 PAMAM-g-diazirine. Diazo functional group, also produced upon diazirine activation) is highly reactive towards nucleophiles such as $-NH_2$ groups on the surface of PAMAM-g-diazirine and this allows specific crosslinking versus non-specific carbene insertion where the solvent competes with intermolecular bonding. Removal of amines and thus diazo-specific crosslinking may explain the decreased storage modulus (G') of blocked PAMAM-g-diazirine presented in Figure 5d. The moduli change upon acetyl chloride blocking of G5 PAMAM-g-diazirine resulted in 225 kPa versus 151 kPa for amine capped. This value is still comparable to moduli of the soft tissues such as blood vessels (Table S2, supplementary section).

As the primary evaluation method for adhesion performance of adhesives for soft tissues (Figure 1) [8] a lap shear test was performed ex-vivo with the endothelial surface of swine aorta

procured from a local abattoir [34]. Conjugates with different formulations were prepared in PBS solution and sandwiched between PLGA film and fresh swine aorta. UV irradiation (5 min, 6 joules 365 nm) was applied for each group to ensure complete activation of conjugated diazirine. The stress/strain curves were recorded and plotted in Figure 6. The fracture occurred in the bulk of the adhesive indicating cohesive failure (Figure 6 inset) which is consistent with our previously reported results [21,22]. The adhesive strength decreased in the order of: G5 = 25.3 kPa, G4 = 7.4 kPa, and G3 = 3.4 kPa and this decrease in strength is consistent with the rheology data (Figure 5). The adhesive strength of G5 PAMAM-g-diazirine-blk was 17.1 kPa which is around 30% lower in comparison to the unblocked dendrimer formulation. It should be noted that the adhesion strength for G5 PAMMA-g-diazirine-blk is still significant higher than that of fibrin glue (5 kPa) [35]. Apart from relatively high adhesion strength, blocked dendrimer adhesive formulation is expected to significantly reduce cytotoxicity in vitro and in vivo.

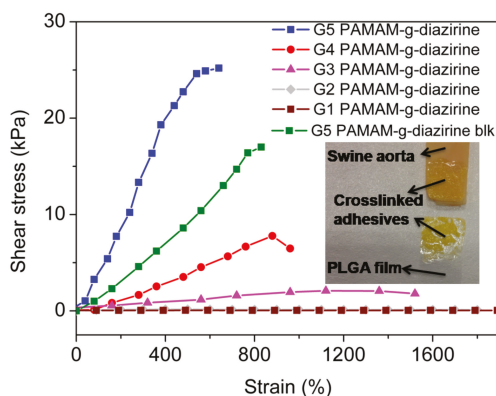


Figure 6. Ex-vivo lap shear adhesion test for PAMAM-g-diazirine bioadhesive formulations (inset: the ‘sandwich’ PLGA-adhesive-tissue structure and demonstration of cohesive failure).

The potential cytotoxicity of adhesive formulations was evaluated as the half maximal effective concentration (EC_{50}) of each formulation towards 3T3 fibroblasts cells. The cells were cultured with adhesive dendrimer solution and cell viability was evaluated with an Alamar Blue assay by comparing the cell reductivity with the negative control. Figure 7a,b show the cell viability when cultured with PAMAM-g-diazirine from G1 to G5 (the diazirine conjugation percentage was 30% for G2 to G5 and 37.5% for G1). EC_{50} values for each generation were fitted and plotted in Figure 7c. EC_{50} increased significantly from 2.4 $\mu\text{g}/\text{mL}$ (G5) to 7.3 $\mu\text{g}/\text{mL}$ (G1), indicating the decrease of cytotoxicity from reduced cell exposure to $-\text{NH}_2$ groups. Fibroblast viability rate was enhanced significantly for blocked PAMAM-g-diazirine formulations thus confirming the necessity of $-\text{NH}_2$ capping (Figure 2). The EC_{50} values for G1–G5 PAMAM-g-diazirine-blk are almost 15 times higher than the corresponding values of the PAMAM-g-diazirine.

PAMAM-g-diazirine conjugates were investigated in vivo in a subcutaneous implant animal model as displayed in Figure S2. Representative histology results are presented in Figure 8 and they show that all the implants (PLGA control, Figure 8a; and crosslinked adhesive formulations, Figure 8b,c) were surrounded by mononuclear cells (macrophages, lymphocytes and plasma cells), polymorphonuclear cells (mainly neutrophils), giant cells, fibrosis and neovascularization. The immunological response was more pronounced towards PAMAM-g-diazirine crosslinked formulations compared to PLGA control (Figure 8d).

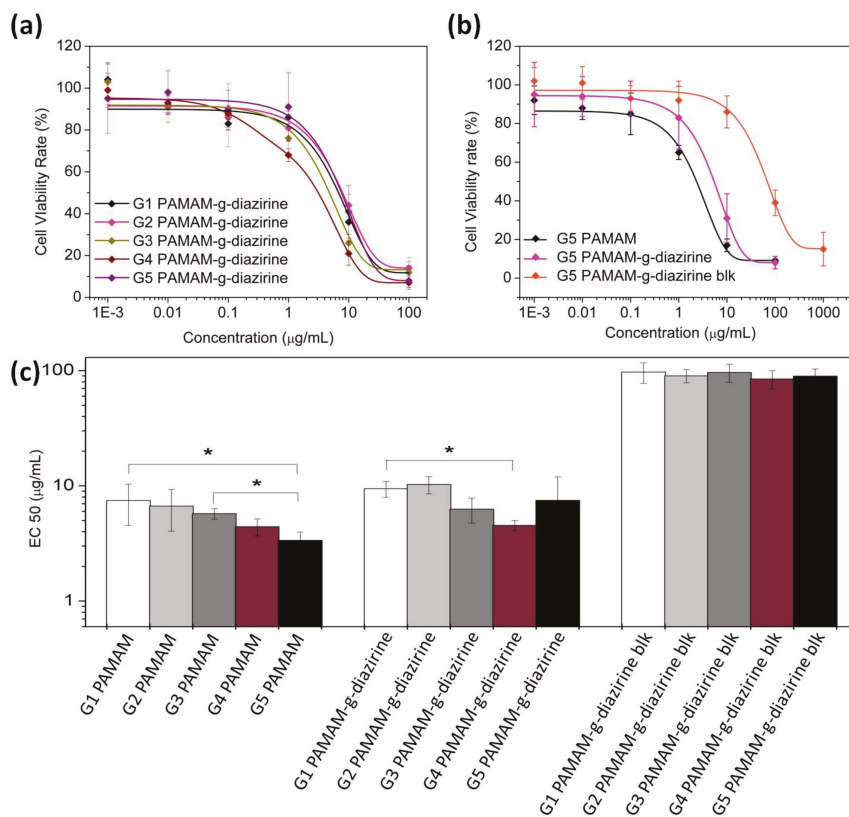


Figure 7. 3T3 fibroblasts cytotoxicity of PAMAM-g-diazirine (G2–G5) 20% conjugates and 37.5% conjugate of PAMAM G1, with DMEM as negative control: (a) cell viability in contact with G1–G5 PAMAM-g-diazirine; (b) cell viability comparison between neat G5 and blocked G5 PAMAM-g-diazirine; (c) EC50 values for PAMAM, PAMAM-g-diazirine and PAMAM-g-diazirine-blk.

Higher number of polymorph nuclear cells, lymphocytes, plasma cells and macrophages were detected along with intense fibrosis and neovascularization that was found on the interface with bioadhesive formulations (Figure 8b,c). As anticipated, mild immunological response was detected for blocked PAMAM-g-diazirine in comparison to neat formulation. This result is consistent with in vitro cytotoxicity of the same formulation (Figure 7) and is most likely a consequence of the cationic charge of pendant $-NH_2$ on the interface between PAMAM-g-diazirine adhesive and the subcutaneous tissue.

Dendrimer toxicity is generally reported as hemolytic toxicity, cytotoxicity and hematological toxicity [36]. Positively charged surface groups of PAMAM are known to destabilize negatively charged cell membranes causing lysis [37]. Processes like adsorptive endocytosis and paracellular transport are the major cause for PAMAM dendrimers to cross cell membranes with the aid of primary amine groups [38]. As a result, the degree of cytotoxicity is determined by the concentration of $-NH_2$ groups and therefore dendrimer-induced cytotoxicity increases with generation number.

Reduced cytotoxicity of amine-blocked PAMAM-g-diazirine (Figure 7) is a result of reduced exposure of fibroblast cells to a toxic effect of inherent primary amines from dendrimer structure. Moreover, the degrees of neovascularisation and fibrosis for PAMAM-g-diazirine-blk were even lower than the control, indicating lower degree of tissue reaction towards PAMAM-g-diazirine-blk than that of PLGA. However, the degree of infiltration of giant cells was reduced to none for PAMAM-g-diazirine

possibly due to the germicidal ability of $-NH_2$ groups [35,39]. These results indicate that the tissue adhesive warrants further investigation towards vascular patches, drug depots, and hydrogel biosensor implants [17,18,40–46].

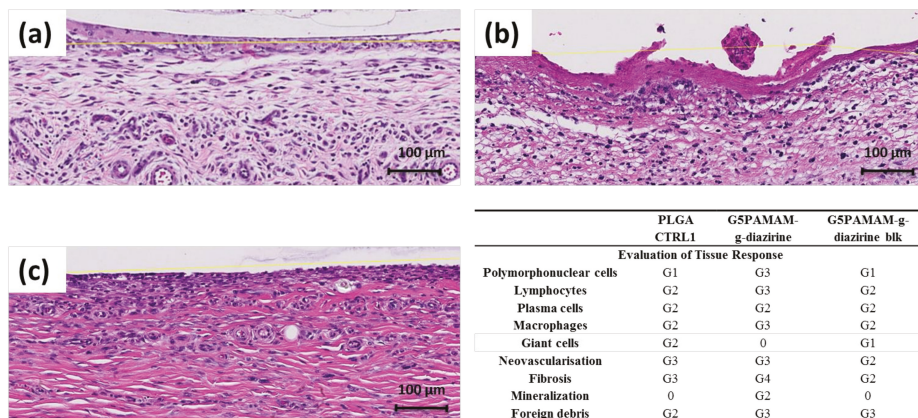


Figure 8. Histology results after 7 days of subcutaneous implantation in vivo by H&E staining methods: (a) PLGA control; (b) PAMAM-g-diazirine (15% diazirine conjugation, 75% wt % in PBS); (c) PAMAM-g-diazirine-blk (15% diazirine conjugation, 75% wt % in PBS); (d) immunological response evaluation: 0: No abnormalities detected (NAD); G1: minimal; G2: mild; G3: moderate; G4: marked; G5: severe.

3. Materials and Methods

Poly (amidoamine) (PAMAM, from 1st generation, G1 to 5th generation, G) were purchased from Dendritech, Midland, MI, USA and Chenyuan, Weihai, China. 3-(4-(Bromomethyl) phenyl)-3-(trifluoromethyl)-diazirine (aromatic-diazirine) was purchased from TCI, Tokyo, Japan. Methyl alcohol (MeOH), acetyl chloride and glacial acetic acid (AcOH) and THF were from TEDIA, Singapore. Poly-DL-lactide-co-glycolide (PLGA 53/47) from Sigma (Singapore) was used as received. Phosphate buffer saline (PBS; Gibco, Singapore) was employed in all experiments. Glass slides (25.4 × 76.2 mm, 1–1.2 mm thick) were purchased from CLP, Tianjin, China. 3T3 fibroblasts cells were from ATCC, Singapore. Dulbecco's modified Eagle medium (DMEM) and fetal bovine serum (FBS) were both purchased from Gibco, Singapore. 24 well plates were from Thermo Fisher Scientific, Shanghai, China. Alamar Blue was from Thermo Fisher Scientific Inc., Boston, MA, USA.

G1–G5 PAMAM MeOH solution (5 mL, 5 wt %) was prepared and aromatic diazirine was added to produce conjugation percentages ranged up to 30% for G2 to G5. The nucleophilic substitution reaction took 36 h under room temperature in dark. G1–G5 PAMAM-g-diazirine was dried under vacuum, as pale yellow viscous liquid. Conjugates were stored in dark under 4 °C. Solution was kept stirred in ice bath for 1 h. Acetyl chloride was dropped into the MeOH solution in ice bath dropwise. The temperature was monitored which was kept below 10 °C. Molar ratio between $-NH_2$ from PAMAM-g-diazirine and acetyl chloride was controlled as 1:5. The 'blocked' conjugates were precipitated out by addition of 30 mL THF after 24 h stirring in dark under room temperature.

Aromatic diazirine was prepared in MeOH with a concentration gradient (0.2, 0.4, 0.5, 0.8 and 1 mM). UV extinction coefficient of aromatic diazirine was the slope of the linear fitting curve of absorption at 350 nm against concentration. SEC-MALS-UV is connected in a line. AcOH aqueous solution (1% w/v, 166.7 mmol) with 0.2% (w/v) NaN_3 (30.8 mM) was prepared as the mobile phase. PAMAM as the control and PAMAM-g-diazirine samples were dissolved in 1 mL of mobile phase with a concentration of 2 mg/mL. All the samples were filtered by 0.22 µm filter and sealed in 1 mL

HPLC glass vials. RI, LS and UV absorption (350 nm) were obtained and processed by Wyatt ASTRA V. The dn/dc value of PAMAM was 0.185 [47]. The UV extinction coefficient of Br-diazirine in aqueous medium was measured as $1009.5 \text{ mL cm}^{-1} \text{ g}^{-1}$ at 350 nm which was used to calculate the experimental conjugation percentage. TNBS assay was performed according to the protocols provided by Thermo Fisher Scientific, but other methods may be applicable [48].

G1–G5 PAMAM, aromatic diazirine, and all PAMAM-g-diazirine were analyzed by NMR (Bruker Avance, Midland, ON, Canada) at 400 MHz with DMSO- d_6 as the solvent. H1 and C13 DEPT 135 HMQC HMBC NMR spectra were collected and analyzed. The peak assignment, 2D spectrum analysis and peak integration ($^1\text{H-NMR}$) were performed with SpinWorks 4.2 (Spin.works, Lisbon, Portugal).

G1–G5 PAMAM-g-diazirine and G1–G5 PAMAM-g-diazirine-blk with different generations and conjugation percentages were prepared in PBS (pH was balanced to 7.2), and there were three concentrations for each formulation (25, 50 and 75 wt %). Samples were pipetted onto the light transparent rheology testing base (P-PTD120/GL, Anton Paar, Singapore). The UV light was generated and transferred by a S1000-1B-3188 UV initiator (OmniCure, Plano, TX, USA) with 365 nm UV filter (019-01036) to the bottom of the base for activation of PAMAM-g-diazirine. The intensity of the UV light on the surface of the base was maintained at 21.3 mW/cm^2 . Dynamic mechanical analysis was assessed in real-time at 1% amplitude and 1 Hz with 8 mm diameter parallel stainless steel probe under $25 \text{ }^\circ\text{C}$ and the gap between probe and base was set as 100 μm . For continue activation, UV light source was turned “OFF” for 2 min in the beginning for the baseline collection. It was turned “ON” after that for 10 min. G' and G'' of the sample were recorded during the activation. For the “ON/OFF” intervals activation, UV light was turned “OFF” for 2 min in the beginning for the baseline collection. Then, it was turned “ON” for 1 min and turned “OFF” for 1 min. This cycle was repeated 5 times for each sample.

Shear adhesive performance measurements of PAMAM-g-diazirine were based on ASTM standard F2255-05 [34]. Fresh swine aorta from a local abattoir was cut into $40 \times 20 \text{ mm}$ slides. The fat on the opposite side of the aorta was removed, and the thickness of the slide was around 1 mm. The tissue with endothelial (intima) side was glued onto a glass slide using cyanoacrylate adhesive. PLGA thin films were prepared based on a previous publication [15] and cut into $40 \times 20 \text{ mm}$ squares, and these slides were glued onto glass slides with the help of cyanoacrylate. G1–G5 PAMAM-g-diazirine PBS solution (0.3 mL) with conjugation percentages and concentration were pipetted in between the PLGA film and swine aorta surface. This glass-tissue-adhesive-PLGA-glass system was sandwiched by two paper binder clips with an average force of $1.37 \pm 0.25 \text{ N/cm}^2$. This ‘sandwich’ structure was activated by UV light (365 nm) immediately, and the UV intensity at the surface of this structure was kept constant at 21.3 mW/cm^2 . Exact overlap area of the gel between PLGA and tissue surface was calculated by analyzing the digital photograph with the help of Adobe Photoshop CS2 (company, San Jose, CA, USA). Series Force Measurement System (Chatillon Force Measurement, Largo, FL, USA) was used for adhesive strength test with the controlled linear speed of 3 mm/min with 10 N loading cell ($n = 5$).

Cells were cultured in DMEM containing 10% PBS at $37 \text{ }^\circ\text{C}$ with 5% CO_2 . Cells were suspended via trypsinization and then counted and seeded on to 24 well plates. Cell number was controlled as 10,000 in each well of the plates ($n = 4$ for each sample). Cells attached to the bottom of the plates after 24 h incubation, and the medium was refreshed before the addition of PAMAM-g-diazirine. The concentrations of each formulation were as follows: 200, 1, 0.1, 0.01 and 0.001 $\mu\text{g/mL}$. G1–G5 PAMAM-g-diazirine, G1–G5 PAMAM-g-diazirine-blk conjugates were examined and the unmodified G1–G5 PAMAM were the positive controls. The viability of the cell in each well was quantitative measured via Alamar Blue assay, and the fluorescence strength of samples was measured by a microplate reader with 560EX nm/590EM nm filter settings (Infinite M200, TECAN, Männedorf, Switzerland). Values were considered to be significantly different if the P value was less than 0.05.

G5 PAMAM-g-diazirine (theoretical conjugation percentage is 15%) and the corresponding G5 PAMAM-g-diazirine-blk were implanted subcutaneously into Wistar female rats ($300 \pm 50 \text{ g}$, 10-weeks

old, InVivos Pte Ltd., Singapore). Mice were sedated with inhalation of isoflurane (2%) and the analgesic was administered by intraperitoneal (IP) injection (tramadol, 3 mg/kg). Experiments and the protocols were approved by Nanyang Technological University Animal Care and Use Committee (IACUC; Protocol: ARF-SBS/NIE-A0301). Hair of the mice was removed. The surgical area was sterilized using povidone iodine solution, and then washed by 70% ethanol. Four wounds with 1.5 cm length and 0.5 cm depth were cut on the dorsum of each rat exposing the muscle tissue. The two conjugates mentioned in the beginning of this section was prepared in PBS solution (50 wt %) and then applied onto PLGA patches (diameter = 6 mm; thickness = 0.1 mm). These patches were implanted directly on exposed muscle tissue, and the adhesive conjugates were sandwiched in between the patch and the tissue. PLGA patches without adhesives were implanted as the negative control. The adhesives were stimulated by UV light, generated and transferred by a S1000-1B-3188 UV initiator (OmniCure) with 365 nm UV filter (019-01036) at 20% power from approximately 1 cm distance (~100 mW/cm² for 1 min: 6 J/cm²). Then, the skin cuts were sealed by MaxonTM 3-0 sutures (the surgical procedures were demonstrated by Figure S2). Mice were kept monitored, and the body weight was recorded for one week. The two rates were sacrificed on the 7th day. The dermal suture implants, the internal implant material and the dissected samples of skin with epidermal were fixed in formalin. Entire implant site for each sample was sectioned perpendicular to the skin surface and parallel to plane of incision. Tissue was then processed by a Sakura VIP Tissue Processor (Lab X, Midland, ON, Canada) with increasing concentration of ethanol, xylene and finally paraffin. The processed tissue was embedded into paraffin block which was then sectioned into 5 µm thick slides by rotary microtome. Slides obtained were dried and stored in incubator (60 °C/15 min) before the H&E staining by an Autostainer XL (Lab X, Midland, ON, Canada). The reaction between implant material and deep dermal tissue was evaluated by a board-certified pathologist with the help of Ariol software/Slidepath Tissue IA software (Leica Microsystems, Buffalo Grove, IL, USA). The collagen extraction was confirmed by analysis of the sections stained by Masson trichrome histochemical.

4. Conclusions

We have produced bioadhesive formulations based on PAMAM dendrimers conjugated with diazirine that act as the UV-activated carbene precursor for polymer crosslinking. In order to maintain adhesion strength and to reduce the cytotoxicity of our formulations, capping of the pendant amines was established. The conversion of amines to amides resulted in a lowering of the adhesion strength of our formulation, the overall properties of the blocked conjugates still have considerable advantages. In vitro compatibility of amine-capped formulation with fibroblast cells was significantly improved by reducing the concentration of cationic amine groups. Our results demonstrated higher cytotoxicity for the higher generation of dendrimers as a consequence of higher amine concentration, consistent with other investigations. G5 dendrimer displayed rapid rise in storage modulus and had the highest shear modulus observed among the formulations tested. Blocked PAMAM-g-diazirine showed improved in vitro fibroblast compatibility and reduced immunological response in vivo while maintaining excellent tissue adhesion strength (ex vivo) of 17 kPa, several times higher than that of commercially available fibrin glue.

Supplementary Materials: The following are available online, Figure S1: 1H-NMR spectra of PAMAM and G1–G5 PAMAM-g-diazirine, Figure S2: the surgical procedures for in vivo histological analysis, Table S1: Structure characterization information for G1–G5 PAMAM-g-diazirine and G1–G5 PAMAM-g-diazirine-blk conjugates, Table S2: Rheological performance and adhesion strength of all the G5 PAMAM-g-diazirine and PAMAM-g-diazirine-blk conjugates.

Acknowledgments: Ministry of Education Tier 2 Grant: Tailored soft-tissue bioadhesives for site-specific therapy (MOE2012-T2-2-046); NTU-Northwestern Institute for Nanomedicine Grant: 3D-Printing of Electro-Curing Nanocomposite Living Electrodes for Cardiac Tissue Regeneration. Ministry of Education Tier 1 Grant: Coil Expanding Layers (COELS) For Intravascular Repairs. China Postdoctoral Science Foundation Grant 11300037027.

Author Contributions: All the experiments and work included in this manuscript were supervised by Terry W. J. Steele (mainly about structure design and characterization, biological performance evaluation) and

Zhang Junying (mainly about backbone selection, mechanical properties characterization). Terry W. J. Steele and Gao Feng conceived and designed the experiments; Gao Feng performed the synthesis and remaining experiments. Ivan Djordjevic did the in vivo immunological response analysis; Oleksandr Pokholenko did the ¹H-NMR analysis. Zhang Haobo did rheological analysis of G1–G4 PAMAM-g-diazirine-blk.

Conflicts of Interest: The authors declare no conflict of interest.

References

1. Nakamura, T.; Takashima, Y.; Hashidzume, A.; Yamaguchi, H.; Harada, A. A metal-ion-responsive adhesive material via switching of molecular recognition properties. *Nat. Commun.* **2014**, *5*, 4622. [[CrossRef](#)] [[PubMed](#)]
2. Bre, L.P.; Zheng, Y.; Pego, A.P.; Wang, W. Taking tissue adhesives to the future: From traditional synthetic to new biomimetic approaches. *Biomater. Sci.* **2013**, *1*, 239–253. [[CrossRef](#)]
3. Pocius, A.V. Adhesion and adhesives technology. In *Adhesion and Adhesives Technology*, 3rd ed.; Carl Hanser Verlag: Munich, Germany, 2012; pp. I–XVI.
4. O’Rorke, R.D.; Steele, T.W.J.; Taylor, H.K. Bioinspired fibrillar adhesives: A review of analytical models and experimental evidence for adhesion enhancement by surface patterns. *J. Adhes. Sci. Technol.* **2016**, *30*, 362–391. [[CrossRef](#)]
5. O’Rorke, R.D.; Pokholenko, O.; Gao, F.; Cheng, T.; Shah, A.; Mogal, V.; Steele, T.W. Addressing unmet clinical needs with uv bioadhesives. *Biomacromolecules* **2017**, *18*, 674–682. [[CrossRef](#)] [[PubMed](#)]
6. Peng, H.T.; Shek, P.N. Novel wound sealants: Biomaterials and applications. *Exp. Rev. Med. Dev.* **2010**, *7*, 639–659. [[CrossRef](#)] [[PubMed](#)]
7. Sierra, D.H. Fibrin sealant adhesive systems: A review of their chemistry, material properties and clinical applications. *J. Biomater. Appl.* **1993**, *7*, 309–352. [[CrossRef](#)] [[PubMed](#)]
8. Mehdizadeh, M.; Yang, J. Design strategies and applications of tissue bioadhesives. *Macromol. Biosci.* **2013**, *13*, 271–288. [[CrossRef](#)] [[PubMed](#)]
9. Leggat, P.A.; Smith, D.R.; Kedjarune, U. Surgical applications of cyanoacrylate adhesives: A review of toxicity. *ANZ J. Surg.* **2007**, *77*, 209–213. [[CrossRef](#)] [[PubMed](#)]
10. Subbu, V.; Kevin, K.; Yitzhak, R.; Yingying, H.; Terry, W.J.S.; Frank, A. Drug delivery systems for vascular disease therapy. In *Polymers for Vascular and Urogenital Applications*; CRC Press: Boca Raton, FL, USA, 2012; pp. 5–38.
11. Huang, C.L.; Kumar, S.; Tan, J.J.Z.; Boey, F.Y.C.; Venkatraman, S.S.; Steele, T.W.J.; Loo, J.S.C. Modulating drug release from poly(lactic-co-glycolic acid) thin films through terminal end-groups and molecular weight. *Polym. Degrad. Stabil.* **2013**, *98*, 619–626. [[CrossRef](#)]
12. Huang, C.L.; Steele, T.W.J.; Widjaja, E.; Boey, F.Y.C.; Venkatraman, S.S.; Loo, J.S.C. The influence of additives in modulating drug delivery and degradation of plga thin films. *NPG Asia Mater.* **2013**, *5*, e54. [[CrossRef](#)]
13. Steele, T.W.; Huang, C.L.; Nguyen, E.; Sarig, U.; Kumar, S.; Widjaja, E.; Loo, J.S.; Machluf, M.; Boey, F.; Vukadinovic, Z.; et al. Collagen-cellulose composite thin films that mimic soft-tissue and allow stem-cell orientation. *J. Mater. Sci. Mater. Med.* **2013**, *24*, 2013–2027. [[CrossRef](#)] [[PubMed](#)]
14. Cheng, T.; Ortiz, R.F.; Vedantham, K.; Naccache, R.; Vetrone, F.; Marks, R.S.; Steele, T.W. Tunable chemical release from polyester thin film by photocatalytic zinc oxide and doped liyf4 upconverting nanoparticles. *Biomacromolecules* **2014**, *16*, 364–373. [[CrossRef](#)] [[PubMed](#)]
15. Mogal, V.; Papper, V.; Chaurasia, A.; Feng, G.; Marks, R.; Steele, T. Novel on-demand bioadhesion to soft tissue in wet environments. *Macromol. Biosci.* **2014**, *14*, 478–484. [[CrossRef](#)] [[PubMed](#)]
16. Mogal, V.T.; Yin, C.S.; O’Rorke, R.; Boujday, S.; Methivier, C.; Venkatraman, S.S.; Steele, T.W. Tuning model drug release and soft-tissue bioadhesion of polyester films by plasma post-treatment. *ACS Appl. Mater. Interfaces* **2014**, *6*, 5749–5758. [[CrossRef](#)] [[PubMed](#)]
17. Schaller, T.; Wenner, T.; Agrawal, R.; Teoh, S.; Phua, L.; Loo, J.S.; Steele, T. High throughput screening of valganciclovir in acidic microenvironments of polyester thin films. *Materials* **2015**, *8*, 1714–1728. [[CrossRef](#)] [[PubMed](#)]
18. Bagheri, M.; Mohammadi, M.; Steele, T.W.J.; Ramezani, M. Nanomaterial coatings applied on stent surfaces. *Nanomedicine* **2016**, *11*, 1309–1326. [[CrossRef](#)] [[PubMed](#)]

19. Steele, T.; Loo, J.S.; Venkatraman, S. Ch3: Tailoring thin films for implant specific applications. In *Thin Film Coatings for Biomaterials and Biomedical Applications*; Griesser, H., Ed.; Woodhead Publishing: Cambridge, UK, 2016.
20. Cheng, T.; O'Rorke, R.; Ortiz, R.F.; Yan, T.Y.; Hemmer, E.; Vetrone, F.; Marks, R.S.; Steele, T.W.J. Self-assembled photoadditives in polyester films allow stop and go chemical release. *Acta Biomater.* **2017**, *54*, 186–200. [[CrossRef](#)] [[PubMed](#)]
21. Nanda, H.S.; Shah, A.H.; Wicaksono, G.; Pokhonenko, O.; Gao, F.; Djordjevic, I.; Steele, T.W.J. Nonthrombogenic hydrogel coatings with carbene-cross-linking bioadhesives. *Biomacromolecules* **2018**. [[CrossRef](#)] [[PubMed](#)]
22. Feng, G.; Djordjevic, I.; Mogal, V.; O'Rorke, R.; Pokhonenko, O.; Steele, T.W.J. Elastic light tunable tissue adhesive dendrimers. *Macromol. Biosci.* **2016**, *16*, 1072–1082. [[CrossRef](#)] [[PubMed](#)]
23. Lu, G.; Tan, C.; Steele, T. Incorporation of conductive internal additives within electrocuring adhesives. *ECS Trans.* **2017**, *77*, 981–988.
24. Nanda, H.; Singh, M.; Steele, T. Thrombogenic responses from electrocured tissue adhesives. *ECS Trans.* **2017**, *77*, 547–555. [[CrossRef](#)]
25. Gao Feng, V.M.; O'Rorke, R.; Djordjevic, I.; Steele, T.W.J. Dendrimer mediated bioadhesion of plga to soft tissues. In Proceedings of the Smart Materials and Surfaces-SMS Korea 2016, Incheon, Korea, 23–25 March 2016.
26. Tomalia, D.A.; Baker, H.; Dewald, J.; Hall, M.; Kallos, G.; Martin, S.; Roeck, J.; Ryder, J.; Smith, P. A new class of polymers: Starburst-dendritic macromolecules. *Polym. J.* **1985**, *17*, 117–132. [[CrossRef](#)]
27. Ping, J.; Gao, F.; Chen, J.L.; Webster, R.D.; Steele, T.W.J. Adhesive curing through low-voltage activation. *Nat. Commun.* **2015**, *6*, 8050. [[CrossRef](#)] [[PubMed](#)]
28. Satoh, K.; Kamigaito, M. Stereospecific living radical polymerization: Dual control of chain length and tacticity for precision polymer synthesis. *Chem. Rev.* **2009**, *109*, 5120–5156. [[CrossRef](#)] [[PubMed](#)]
29. Ebnesajjad, S. *Adhesives Technology Handbook*; William Andrew Pub: Norwich, UK, 2008.
30. Nijst, C.L.E.; Bruggeman, J.P.; Karp, J.M.; Ferreira, L.; Zumbuehl, A.; Bettinger, C.J.; Langer, R. Synthesis and characterization of photocurable elastomers from poly(glycerol-co-sebacate). *Biomacromolecules* **2007**, *8*, 3067–3073. [[CrossRef](#)] [[PubMed](#)]
31. Geerligs, M.; Peter, G.W.; Ackermans, P.A.; Oomens, C.W.; Baaijens, F.P. Linear viscoelastic behavior of subcutaneous adipose tissue. *Biorheology* **2008**, *45*, 677–688. [[PubMed](#)]
32. Ghobril, C.; Charoen, K.; Rodriguez, E.K.; Nazarian, A.; Grinstaff, M.W. A dendritic thioester hydrogel based on thiol–thioester exchange as a dissolvable sealant system for wound closure. *Angew. Chem. Int. Ed. Engl.* **2013**, *52*, 14070–14074. [[CrossRef](#)] [[PubMed](#)]
33. Malik, N.; Wiwattanapatapee, R.; Klopsch, R.; Lorenz, K.; Frey, H.; Weener, J.W.; Meijer, E.W.; Paulus, W.; Duncan, R. Erratum to “dendrimers: Relationship between structure and biocompatibility in vitro, and preliminary studies on the biodistribution of 125i-labelled polyamidoamine dendrimers in vivo” [journal of controlled release 65 (2000) 133–148]. *J. Control. Release* **2000**, *68*, 299–302. [[CrossRef](#)]
34. International, A. Astm f2255-05(2015). In *Standard Test Method for Strength Properties of Tissue Adhesives in Lap-Shear by Tension Loading*, ASTM International; PA: West Conshohocken, MT, USA, 2005.
35. Ryou, M.; Thompson, C.C. Tissue adhesives: A review. *Tech. Gastrointest. Endosc.* **2006**, *8*, 33–37. [[CrossRef](#)]
36. Jain, K.; Kesharwani, P.; Gupta, U.; Jain, N.K. Dendrimer toxicity: let's meet the challenge. *Int. J. Pharm.* **2010**, *394*, 122–142. [[CrossRef](#)] [[PubMed](#)]
37. Goldberg, M.; Langer, R.; JIA, X. Nanostructured materials for applications in drug delivery and tissue engineering. *J. Biomater. Sci. Polym. Ed.* **2007**, *18*, 241–268. [[CrossRef](#)] [[PubMed](#)]
38. Bhadra, D.; Bhadra, S.; Jain, S.; Jain, N.K. A pegylated dendritic nanoparticulate carrier of fluorouracil. *Int. J. Pharm.* **2003**, *257*, 111–124. [[CrossRef](#)]
39. Uzun, K.; Çevik, E.; Şenel, M.; Sözeri, H.; Baykal, A.; Abasıyanık, M.F.; Toprak, M.S. Covalent immobilization of invertase on pamam-dendrimer modified superparamagnetic iron oxide nanoparticles. *J. Nanopart. Res.* **2010**, *12*, 3057–3067. [[CrossRef](#)]
40. Lee, B.H.; Tin, S.P.; Chaw, S.Y.; Cao, Y.; Xia, Y.; Steele, T.W.; Seliktar, D.; Bianco-Peled, H.; Venkatraman, S.S. Influence of soluble peg-oh incorporation in a 3d cell-laden peg-fibrinogen (pf) hydrogel on smooth muscle cell morphology and growth. *J. Biomater. Sci. Polym. Ed.* **2014**, *25*, 394–409. [[CrossRef](#)] [[PubMed](#)]

41. Ping, J.; Zhou, Y.; Wu, Y.; Papper, V.; Boujday, S.; Marks, R.S.; Steele, T.W. Recent advances in aptasensors based on graphene and graphene-like nanomaterials. *Biosens. Bioelectron.* **2015**, *64C*, 373–385. [[CrossRef](#)] [[PubMed](#)]
42. Zhou, Y.; Chi, H.; Wu, Y.Y.; Marks, R.S.; Steele, T.W.J. Organic additives stabilize RNA aptamer binding of malachite green. *Talanta* **2016**, *160*, 172–182. [[CrossRef](#)] [[PubMed](#)]
43. Chen, J.L.; Steele, T.W.J.; Stuckey, D.C. Metabolic reduction of resazurin; Location within the cell for cytotoxicity assays. *Biotechnol. Bioeng.* **2017**, *115*, 351–358. [[CrossRef](#)] [[PubMed](#)]
44. Ortiz, R.; Chen, J.L.; Stuckey, D.C.; Steele, T.W.J. Poly(methyl methacrylate) surface modification for surfactant-free real-time toxicity assay on droplet microfluidic platform. *ACS Appl. Mater. Interface* **2017**, *9*, 13801–13811. [[CrossRef](#)] [[PubMed](#)]
45. Zhou, Y.; Wu, Y.; Pokholenko, O.; Papper, V.; Marks, R.S.; Steele, T.W.J. Stilbene switch activated by click chemistry. *Procedia Technol.* **2017**, *27*, 10–11. [[CrossRef](#)]
46. Zhou, Y.; Yuanyuan, W.; Pokholenko, O.; Grimsrud, M.; Sham, Y.; Papper, V.; Marks, R.; Steele, T. Aptamer adaptive binding assessed by stilbene photoisomerization towards regenerating aptasensors. *Sens. Actuators B Chem.* **2017**, *257*, 245–255. [[CrossRef](#)]
47. Sliz, R.; Suzuki, Y.; Fabritius, T.; Myllyla, R. Influence of temperature on wetting properties of thin films in organic solar cells applications. *Colloids Surf. A Physicochem. Eng. Asp.* **2013**, *443*, 182–187. [[CrossRef](#)]
48. Irvine, S.A.; Steele, T.W.J.; Bhuthalingam, R.; Li, M.; Boujday, S.; Prawirasatya, M.; Neoh, K.G.; Boey, F.Y.C.; Venkatraman, S.S. Quantification of aldehyde terminated heparin by sec-malls-uv for the surface functionalization of polycaprolactone biomaterials. *Colloids Surf. B Biointerfaces* **2015**, *132*, 253–263. [[CrossRef](#)] [[PubMed](#)]

Sample Availability: Samples of the compounds are available from the authors.



© 2018 by the authors. Licensee MDPI, Basel, Switzerland. This article is an open access article distributed under the terms and conditions of the Creative Commons Attribution (CC BY) license (<http://creativecommons.org/licenses/by/4.0/>).

Article

Dendrimers for Drug Delivery

Abhay Singh Chauhan

School of Pharmacy, Medical College of Wisconsin, 8701 W Watertown Plank Road, Milwaukee, WI 53226, USA; achauhan@mcw.edu; Tel.: +1-414-955-2863

Received: 26 March 2018; Accepted: 15 April 2018; Published: 18 April 2018

Abstract: Dendrimers have come a long way in the last 25 years since their inception. Originally created as a wonder molecule of chemistry, dendrimer is now in the fourth class of polymers. Dr. Donald Tomalia first published his seminal work on Poly(amidoamine) (PAMAM) dendrimers in 1985. Application of dendrimers as a drug delivery system started in late 1990s. Dendrimers for drug delivery are employed using two approaches: (i) formulation and (ii) nanoconstruct. In the formulation approach, drugs are physically entrapped in a dendrimer using non-covalent interactions, whereas drugs are covalently coupled on dendrimers in the nanoconstruct approach. We have demonstrated the utility of PAMAM dendrimers for enhancing solubility, stability and oral bioavailability of various drugs. Drug entrapment and drug release from dendrimers can be controlled by modifying dendrimer surfaces and generations. PAMAM dendrimers are also shown to increase transdermal permeation and specific drug targeting. Dendrimer platforms can be engineered to attach targeting ligands and imaging molecules to create a nanodevice. Dendrimer nanotechnology, due to its multifunctional ability, has the potential to create next generation nanodevices.

Keywords: dendrimer; PAMAM; Tomalia; solubility; stability; transdermal; multifunctional; targeting

1. Introduction

I work in exploring dendrimers as a drug delivery system and mainly use it for entrapment of drugs by non-covalent interactions. This article is a tribute to Dr. Donald Tomalia through my research journey with dendrimers for drug delivery.

While doing my Masters in Pharmacy (M. Pharm), my supervisor asked me to read about dendrimers for my research thesis. I was provided a research paper to read. That was the first time that I saw the dendrimer structure and a picture of a guy with a beard. From that time onwards, dendrimer and Don became synonymous to me.

I also selected dendrimers as my research area for my PhD. My fascination with dendrimers grew as new concepts entered my mind about using Poly(amidoamine) dendrimers (PAMAM) for drug delivery. While working on the dendrimer–indomethacin complex, I ‘discovered’ an inherent anti-inflammatory property of a few PAMAM dendrimers in 2001 (Patent: WO2003080121A1) [1]. I also published the first paper on using PAMAM dendrimers as a transdermal permeation enhancer [2]. Every time I found something interesting on dendrimers, I wanted to share that with Dr. Tomalia.

One of my senior colleagues advised me to send my anti-inflammatory dendrimer work to the International Dendrimer Symposium (IDS-3) in Berlin. Surprisingly, it was selected for a poster presentation. Somehow, as a student, I could arrange funds to travel from India to attend IDS-3 in Berlin. I had never met Don in person and was eagerly waiting for him to come and see my poster, but it did not happen until the end of the day. Then, Dr. Anil Patri visited my poster and brought Don to see my anti-inflammatory dendrimer poster. Don came with a beer mug in his hand. He was very impressed with my findings and, in the next fifteen minutes, he gave me an offer to work with him. I am not sure if it was my research or the beer! About a year later, I ended up joining Dendritic Nanotechnologies in Mount Pleasant, MI, USA.

I am a pharmacist by training and Don exposed me to the vast world of dendrimers and the chemistry behind it. Moreover, it was wonderful to know about the philosophy and history of dendrimers such as the idea that a three-dimensional structured polymer was inspired by a tree and its branches. As a drug delivery scientist, it is imperative to understand the architecture of dendrimers.

2. Discussion

2.1. Dendrimer-Drug Delivery Strategy

PAMAM dendrimers were first reported by Tomalia in 1985 [3,4]. PAMAM dendrimers are one of the most used dendrimers for drug delivery systems [5–7]. The dendrimer architecture has three main sites for drug entrapment by using various mechanisms: (i) void spaces (by molecular entrapment); (ii) branching points (by hydrogen bonding); and (iii) outside surface groups by (charge–charge interactions) (Figure 1).

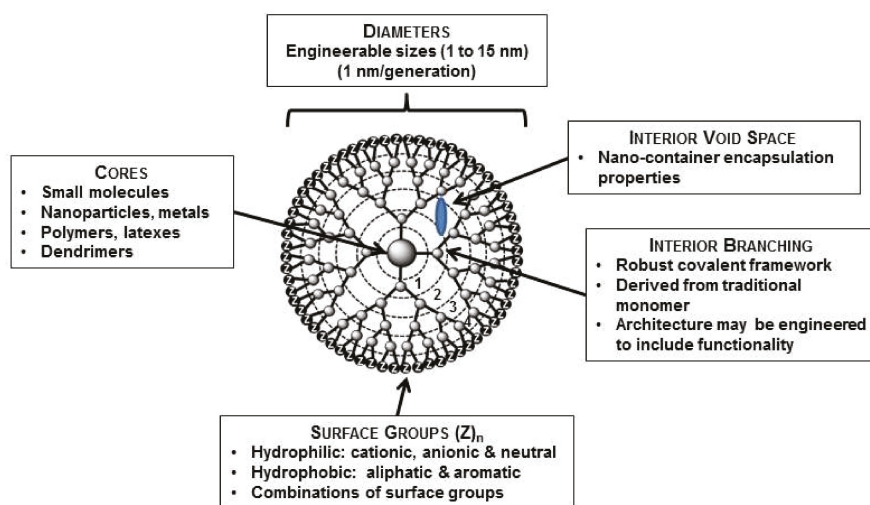
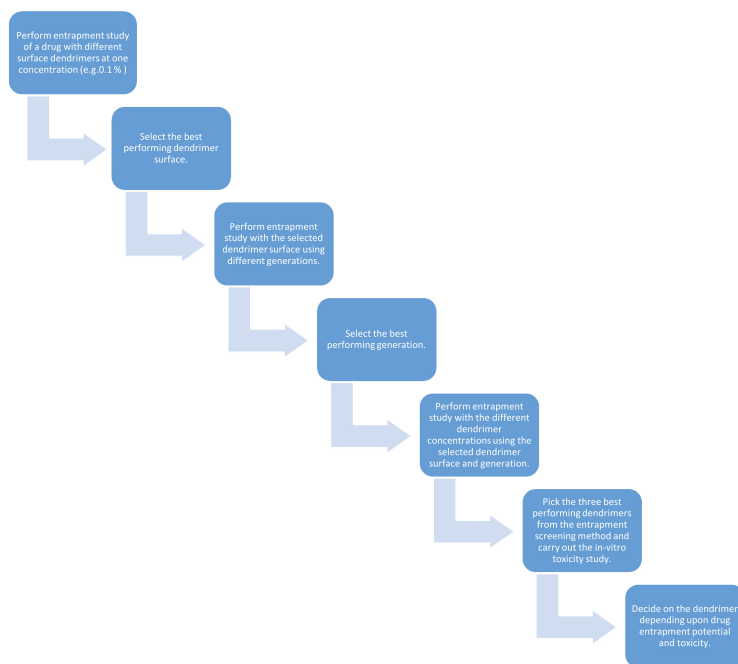


Figure 1. Schematic presentation of a G4 dendrimer containing four generations. Reproduced with permission [8].

Entrapment of a drug depends on the structures of both the dendrimer and the drug. Hence, it is important to understand the chemistry behind the dendrimer architecture. Designing or selecting an appropriate dendrimer is the main step for drug entrapment. As of now, we have no tools to predict the entrapment potential of a dendrimer for any drug. Hence, screening with different dendrimers is suggested to find the right combinations. PAMAM dendrimers are commercially available with amine, hydroxyl, carboxylate and pyrrolidinone surfaces along with corresponding generations. Here is a suggested strategy to find the appropriate dendrimer for a drug molecule (Scheme 1).



Scheme 1. Strategy to select dendrimers for drug entrapment.

2.2. Multifunctional Delivery System

A dendrimer can perform various jobs ranging from solubility enhancement to drug targeting. We envisaged that dendrimers would have the potential to be used as multifunctional excipients. My current research focus is to explore dendrimers for multifunctional capability by enhancing solubility, dissolution, gastrointestinal tract (GIT) permeability, bioavailability, stability, multiple drug entrapment, controlled delivery, and efficacy of drugs in a single formulation. Various interrelated approaches are investigated simultaneously to establish dendrimers as a multifunctional delivery system. Here is the classification of various categories and sub-categories to define the role of dendrimer:

- Pre-formulation: solubility, stability, storage and transport,
- Formulation: dissolution, stability, enzymatic and hydrolytic degradation, permeability and multiple drug entrapment,
- Advanced formulation: bioavailability, targeting, toxicity, transdermal, novel drug delivery.

a. *Solubility enhancers:* Some of the newly developed and even launched drugs are rejected by the pharmaceutical industry and/or exhibit sub-optimal performance because of low water solubility and hence low bioavailability. We have published one of the earlier works on aqueous solubility enhancement propensity of dendrimers [2,9,10].

PAMAM dendrimers are water-soluble molecules and their ability to entrap hydrophobic molecules makes them good solubility enhancers [11]. Hydrophobic molecules can be entrapped in dendrimers using mechanisms discussed before (Scheme 1). Indomethacin (Figure 2) is a weakly acidic drug and it was entrapped in different dendrimers. It showed the best solubility enhancement with G4-NH₂ and low performance with G4-COOH dendrimer. The carboxylate groups of indomethacin were associated with surface amine groups on G4-NH₂ dendrimers through charge–charge interactions,

which is not feasible with G4-COOH dendrimers. Nonetheless, some entrapment with G4-COOH dendrimers was observed due to the molecular encapsulation.

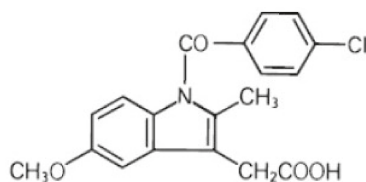


Figure 2. Structure of indomethacin.

Drug entrapment was also size dependent and increased with the increase in dendrimer generations (Figure 3). As charge–charge interactions represent one of the main mechanisms in drug entrapment, pH plays a vital role. We have shown that drug entrapment occurs best in a pH, where both dendrimer and drug are fully ionized [10]. It means that selecting an appropriate pH for entrapment is very crucial.

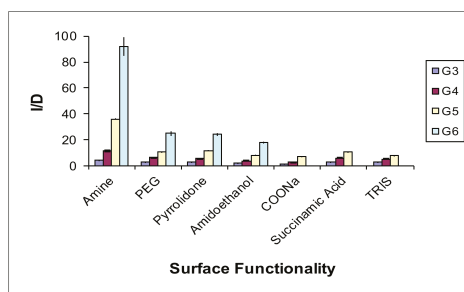


Figure 3. Effect of dendrimer surface and generation on entrapment potential (I/D) of dendrimers. Reproduced with permission [8].

Once dendrimer entraps/solubilizes a hydrophobic molecule, this dendrimer-drug complex can also be used to enhance drug dissolution, stability and bioavailability.

b. *Stability*: Dendrimers provide stability to the guest molecules in vitro and in vivo. Resveratrol is a hydrophobic molecule with stability issues. The entrapment of resveratrol in dendrimer enhanced its water solubility and stability (Figure 4) [12].

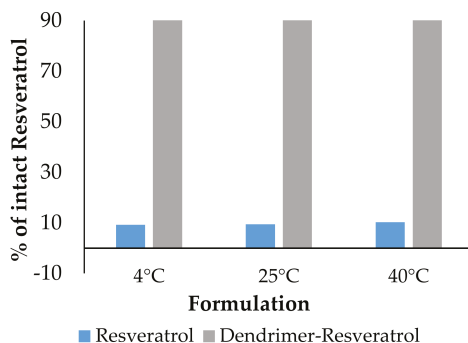


Figure 4. Percentage of intact resveratrol remaining in the formulations after Day 1.

c. *Dissolution*: Dendrimer-drug complexes showed very high and fast drug dissolution compared to the hydrophobic drug alone (Figure 5) [12].

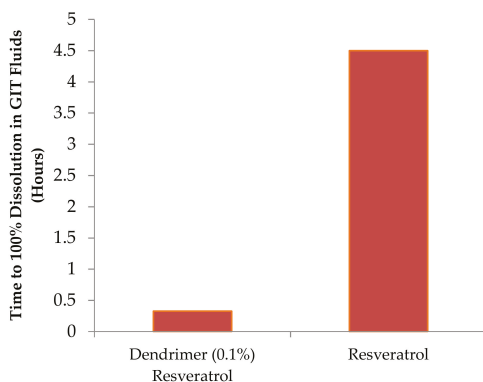


Figure 5. Dissolution profile of dendrimer–resveratrol formulations.

d. *Drug Release*: Release of drugs from dendrimers can be controlled by various means.

- (i) *Chemical modification of dendrimer*: Indomethacin showed slow release with G4-NH₂ dendrimer while fast release was observed with G4-COOH [13]. The slow release with G4-NH₂ dendrimer can be attributed to the strong interactions of drugs with dendrimers.
- (ii) *Physical loading*: Rate of drug release from dendrimers can also be modified by adjusting dendrimer-to-drug molar ratio. We have shown that, by changing cisplatin loading in PAMAM dendrimers, drug release can be controlled [14]. Cisplatin release from dendrimers showed fast release with higher cisplatin/dendrimer molar ratio formulation, whereas lowering the cisplatin/dendrimer molar ratio would provide slower release of cisplatin.

e. *Oral Bioavailability*: Entrapment of drugs in dendrimers helps to enhance solubility, stability and dissolution. These properties eventually help to enhance oral bioavailability of the drug. Simvastatin (SMV) was entrapped in PAMAM dendrimers to prepare a dendrimer–simvastatin (SMV) complex [15]. Dendrimer–SMV formulations showed better oral bioavailability than pure SMV suspension following oral administration [16]. Peak plasma SMV concentration increased from 2.3 µg/mL with pure SMV to 3.8 µg/mL with dendrimer formulations. The mean SMV residence time was 3–5 times better for the dendrimer–SMV formulation.

f. *Multiple drug delivery systems*: PAMAM dendrimers were evaluated to explore the potential of PAMAM dendrimers for multiple drug delivery. We have entrapped two anti-hypertensive drugs Ramipril (RAPL) and hydrochlorothiazide (HCTZ [17]). The results showed that the solubility of RAPL and HCTZ was dependent on dendrimer concentrations and pH of dendrimer solution. Formulations of dendrimer-drug complex and dendrimer-drug combinations (RAPL+HCTZ) displayed faster dissolution in simulated gastric fluid at pH 1.2 and United States Pharmacopeia (USP) dissolution medium at pH 7.0. We have demonstrated dendrimer’s capability for combination therapy with predictable dissolution profile by formulating RAPL and HCTZ for the treatment of hypertension.

2.3. Dendrimer-Mediated Transdermal Delivery

The transdermal delivery of indomethacin formulations with different dendrimers was studied and transdermal permeation potential was evaluated (Figure 6) [2]. The effect of concentrations of dendrimers was observed and it showed a linear increase in flux with an increasing concentration of each of the dendrimers. Transdermal permeation results showed contrasting behavior compared

to the solubility studies, where Higuchi's A_N solubility profile was noted [10]. The steady-state flux of the dendrimer-drug formulations showed 2–4.5 times enhancement factor compared to the pure drug formulation. Entrapment of resveratrol in dendrimer increases its solubility and stability and the dendrimer–resveratrol complex showed significantly higher (2.5 times) transdermal permeation compared to resveratrol alone.

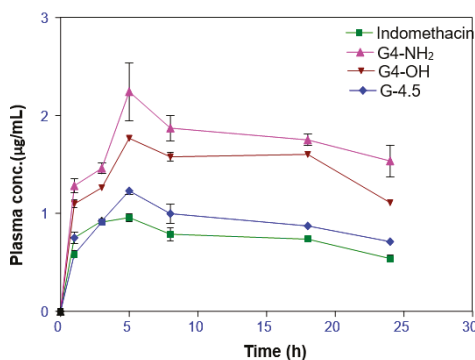


Figure 6. Transdermal delivery of dendrimer formulations (G4-NH₂, G4-OH, G4.5-COOH dendrimers, indomethacin). Reproduced with permission [2].

2.4. Engineered Dendrimers

Dendrimer platform can be engineered to develop various applications. We have developed thiolated dendrimers for enhanced mucoadhesion [18,19]. The thiol groups on the polymers form covalent bonds with the cysteine domains of the mucin to achieve mucoadhesion. Dendrimers were decorated with the thiol groups using its polyvalent architecture (Figure 7). Thiolated dendrimers were loaded with acyclovir and the dendrimer–drug complexes have shown encouraging results for drug loading, bio adhesion, and controlled release profile.

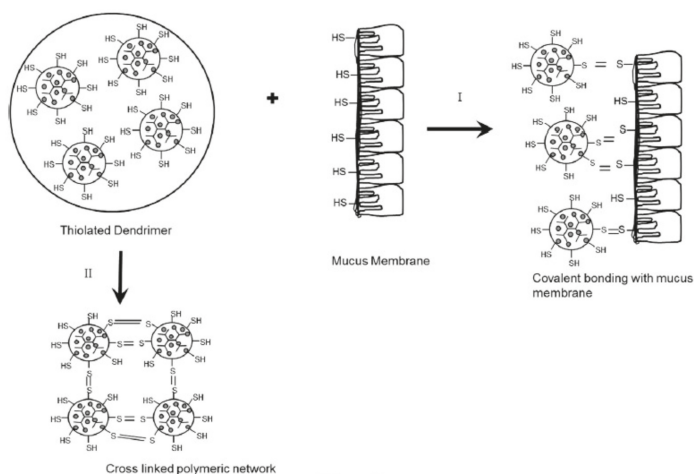


Figure 7. Schematic representation of muco-adhesiveness of thiolated dendrimers. (I) disulfide bond formation with glycoproteins of mucus membrane; (II) inter cross linking of thiolated dendrimers to form polymeric network. Reproduced with permission [19].

2.5. Hybrid Dendrimers

1. Dendrimer-nanoparticle nano-assembly: Dendrimers can be assembled with other delivery systems to create a novel nanostructure assembly. We have prepared a self-assembled nanostructure assembly by controlled electrostatic gelation of anionic albumin with 4.0 G PAMAM dendrimers [20]. Dendrimers were mainly utilized for loading of paclitaxel, and albumin nanoparticles were used to anchor folate as a targeting ligand (Figure 8). This dendrimer-nanoparticle assembly provides a novel way of targeting drugs to the cancer cells compared to paclitaxel and albumin nanoparticles.

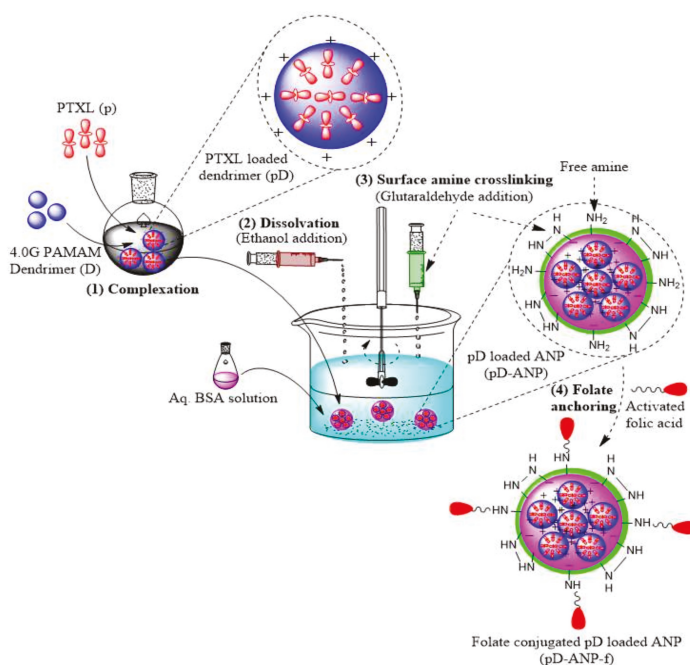


Figure 8. PAMAM dendrimer-Albumin nanoparticle nano-assembly for delivery of paclitaxel. Reproduced with permission [20].

2. Dendrimer-Dendrimer nano-assembly: We have demonstrated that PAMAM dendrimers with different surfaces can be assembled together to create hybrid dendrimers [18]. Each dendrimer portrays a characteristic release profile for a drug. For example, dendrimers with amine surface groups showed slow release and dendrimers with carboxylate surface depict fast release of indomethacin. Hence, two or more dendrimers can be combined to work in tandem in a formulation, thereby achieving a therapeutically desired release profile.

3. Conclusions

We have demonstrated that PAMAM dendrimers can enhance aqueous solubility, stability, dissolution, drug release, targeting and pharmacokinetics of various drugs. The future of drug delivery would be fabricating ‘nano-robots’ capable of doing multiple jobs inside the body. These ‘nano-robots’ can either be biodegradable or leave the body through excretion routes. Designing a sophisticated drug delivery platform needs an interdisciplinary approach involving chemistry, engineering and pharmacy disciplines. Dendrimer nanotechnology due to its multifunctional ability has the potential to create next generation drug delivery platforms. The future of dendrimers would be to exploit their

multifunctional capabilities and engineerable platforms. The idea that sprouted through the ‘tree branches’ has now taken ‘root’ in drug delivery.

Acknowledgments: Author would like to acknowledge School of Pharmacy, Medical College of Wisconsin for providing resources to write this article.

Conflicts of Interest: The author declares no conflict of interest.

References

1. Chauhan, A.S.; Diwan, P.V.; Jain, N.K.; Tomalia, D.A. Unexpected in vivo anti-inflammatory activity observed for simple, surface functionalized poly(amidoamine) dendrimers. *Biomacromolecules* **2009**, *10*, 1195–1202. [[CrossRef](#)] [[PubMed](#)]
2. Chauhan, A.S.; Sridevi, S.; Chalasani, K.B.; Jain, A.K.; Jain, S.K.; Jain, N.K.; Diwan, P.V. Dendrimer-mediated transdermal delivery: Enhanced bioavailability of indomethacin. *J. Control. Release* **2003**, *90*, 335–343. [[CrossRef](#)]
3. Tomalia, D.; Baker, H.; Dewald, J.; Hall, M.; Kallos, G.; Martin, S.; Roeck, J.; Ryder, J.; Smith, P. A New Class of Polymers: STARBURST®-Dendritic Macromolecules. *Polym. J.* **1985**, *17*, 117–132. [[CrossRef](#)]
4. Tomalia, D.; Naylor, A.M.; Goddard, W.A., III. STARBURST Dendrimers: Molecular Level Control of Size, Shape, Surface Chemistry, Topology and Flexibility from Atoms to Macroscopic Matter. *Angew. Chem. Int. Ed. Engl.* **1990**, *29*, 138–175. [[CrossRef](#)]
5. Tomalia, D.A. Dendrimer research. *Science* **1991**, *252*, 1231. [[CrossRef](#)] [[PubMed](#)]
6. Tomalia, D.A. In quest of a systematic framework for unifying and defining nanoscience. *J. Nanopart. Res.* **2009**, *11*, 1251–1310. [[CrossRef](#)] [[PubMed](#)]
7. Tomalia, D.A. Interview: An architectural journey: From trees, dendrons/dendrimers to nanomedicine. Interview by Hannah Stanwix. *Nanomedicine* **2012**, *7*, 953–956. [[CrossRef](#)] [[PubMed](#)]
8. Chauhan, A.S. Dendrimer nanotechnology for enhanced formulation and controlled delivery of resveratrol. *Ann. N. Y. Acad. Sci.* **2015**, *1348*, 134–140. [[CrossRef](#)] [[PubMed](#)]
9. Asthana, A.; Chauhan, A.S.; Diwan, P.V.; Jain, N.K. Poly(amidoamine) (PAMAM) dendritic nanostructures for controlled site-specific delivery of acidic anti-inflammatory active ingredient. *AAPS PharmSciTech* **2005**, *6*, E536–E542. [[CrossRef](#)] [[PubMed](#)]
10. Chauhan, A.S.; Jain, N.K.; Diwan, P.V.; Khopade, A.J. Solubility enhancement of indomethacin with poly(amidoamine) dendrimers and targeting to inflammatory regions of arthritic rats. *J. Drug Target.* **2004**, *12*, 575–583. [[CrossRef](#)] [[PubMed](#)]
11. Svenson, S.; Chauhan, A.S. Dendrimers for enhanced drug solubilization. *Nanomedicine* **2008**, *3*, 679–702. [[CrossRef](#)] [[PubMed](#)]
12. Chauhan, A.; Newenhouse, E.; Gerhardt, A. Compositions Comprising a Dendrimer-Resveratrol Complex and Methods for Making and Using the Same. U.S. Patent 9,855,223 B2, 2 January 2018.
13. Chauhan, A.; Svenson, S.; Reyna, L.; Tomalia, D. Solubility enhancement propensity of PAMAM nanoconstructs. *Mater. Matters Nanomater.* **2007**, *2*, 24–26.
14. Kulhari, H.; Pooja, D.; Singh, M.K.; Chauhan, A.S. Optimization of carboxylate-terminated poly(amidoamine) dendrimer-mediated cisplatin formulation. *Drug Dev. Ind. Pharm.* **2015**, *41*, 232–238. [[CrossRef](#)] [[PubMed](#)]
15. Kulhari, H.; Pooja, D.; Prajapati, S.K.; Chauhan, A.S. Performance evaluation of PAMAM dendrimer based simvastatin formulations. *Int. J. Pharm.* **2011**, *405*, 203–209. [[CrossRef](#)] [[PubMed](#)]
16. Kulhari, H.; Kulhari, D.P.; Prajapati, S.K.; Chauhan, A.S. Pharmacokinetic and pharmacodynamic studies of poly(amidoamine) dendrimer based simvastatin oral formulations for the treatment of hypercholesterolemia. *Mol. Pharm.* **2013**, *10*, 2528–2533. [[CrossRef](#)] [[PubMed](#)]
17. Singh, M.K.; Pooja, D.; Kulhari, H.; Jain, S.K.; Sistla, R.; Chauhan, A.S. Poly(amidoamine) dendrimer-mediated hybrid formulation for combination therapy of ramipril and hydrochlorothiazide. *Eur. J. Pharm. Sci.* **2017**, *96*, 84–92. [[CrossRef](#)] [[PubMed](#)]
18. Chauhan, A.; Svenson, S. Formulations Containing Hybrid Dendrimers. WO2007149500A9, 27 December 2007.

19. Yandrapu, S.K.; Kanujia, P.; Chalasani, K.B.; Mangamoori, L.; Kolapalli, R.V.; Chauhan, A. Development and optimization of thiolated dendrimer as a viable mucoadhesive excipient for the controlled drug delivery: An acyclovir model formulation. *Nanomedicine* **2013**, *9*, 514–522. [[CrossRef](#)] [[PubMed](#)]
20. Tekade, R.K.; Tekade, M.; Kumar, M.; Chauhan, A.S. Dendrimer-stabilized smart-nanoparticle (DSSN) platform for targeted delivery of hydrophobic antitumor therapeutics. *Pharm. Res.* **2015**, *32*, 910–928. [[CrossRef](#)] [[PubMed](#)]



© 2018 by the author. Licensee MDPI, Basel, Switzerland. This article is an open access article distributed under the terms and conditions of the Creative Commons Attribution (CC BY) license (<http://creativecommons.org/licenses/by/4.0/>).

Article

Hyperbranched Polyglycerol Derivatives as Prospective Copper Nanotransporter Candidates

Mohiuddin Quadir ^{1,*}, Susanne Fehse ², Gerhard Multhaup ³ and Rainer Haag ²¹ Department of Coatings and Polymeric Materials, North Dakota State University, Fargo, ND 58105, USA² Institute of Chemistry and Biochemistry, Freie Universität Berlin, Berlin 14195, Germany; fehse@zedat.fu-berlin.de (S.F.); haag@chemie.fu-berlin.de (R.H.)³ Department of Pharmacology and Therapeutics, McGill University, Montreal, QC H3A 0G4, Canada; gerhard.multhaup@mcgill.ca

* Correspondence: mohiuddin.quadir@ndsu.edu; Tel.: +1-701-231-6283

Received: 28 March 2018; Accepted: 17 May 2018; Published: 26 May 2018

Abstract: Hyperbranched polyglycerol (hPG) has been used as a multivalent scaffold to develop a series of nanocarriers capable of high-affinity encapsulation of copper (Cu). A rationally selected set of Cu-complexing motifs has been conjugated to hPG hydroxyl groups to render the constructs potentially usable as exogenous sources of Cu for addressing different pathological conditions associated with Cu-deficiency. We have utilized a newly discovered route to attach Cu-binding domains exclusively within a hPG core by selective differentiation between the primary and secondary hydroxyl groups of the polyol. These hPG-derivatives were found to form a stable complex with Cu ions depending on the type of immobilized ligands and corresponding degree of functionalization. In addition, these Cu-bearing nano-complexes demonstrated moderately cationic surface charge resulting in adjustable protein-binding characteristics and low cellular toxicity profile. We envision that these Cu-loaded hPG nanocarriers can be used as a stable platform to transport the metal ion across the systemic circulation to supply bioavailable quantity of Cu in disease-afflicted tissues.

Keywords: hyperbranched polyglycerol; nanocarrier; ion transport; Cu-deficiency disorders

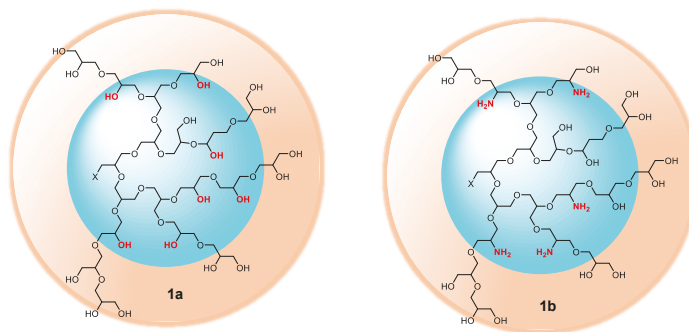
1. Introduction

Recapitulation of homeostatic level of electrolytes or trace element concentration is one of the mainstays of clinical management for a number of pathological conditions, including but not limited to blood disorders, renal failure, acute poisoning, cancer and skeletal system-related diseases. In biological systems, Cu ions are cofactors of several metalloenzymes and are essential for central nervous system (CNS) development [1–4]. For example, alterations in Cu balance have been linked, but not causally associated, to changes in senile plaque deposition in Alzheimer’s disease (AD) [5]. Currently in clinical trials, exogenous supply of Cu is mediated by soluble oral administration of soluble metal salts or metal complexes in disease conditions where Cu supplementation is required. For example, potential beneficial effects of oral intake of Cu (II)-orotate-dihydrate (8 mg Cu daily) were investigated in AD patients. Although results demonstrated that oral Cu intake has neither a detrimental nor a promoting effect on the progression of AD, Cu treatment stabilized plasma and CSF levels in AD patients and antagonized the unbalanced Cu levels likely by activating the homeostatic system [6,7]. Studies with the antibiotic clioquinol (CQ), an 8-OH quinoline with a moderate affinity for Cu²⁺ and Zn²⁺, the lipophilic chelator (DP109), isatin-Schiff base Cu (II)-complexes and metal bis(thiosemicarbazonato) complexes also confirmed that promoting Cu uptake is a reasonable treatment strategy [8–11] in Cu deficiency-related disorders. To offset the obvious pharmacokinetic challenges involved with these monovalent, small molecular Cu complexing agents pertaining to systemic toxicity due to complex instability, bioavailability, circulation lifetime and dosing frequency, we have reported a library

of macromolecular, multivalent, Cu-encapsulating nanocarrier platforms based on hyperbranched polyglycerol (hPG) [12–14]. Due to the presence of multiple chemically accessible hydroxyl groups and very stable ether backbone, as well as high compatibility, we found hPG as an ideal candidate to design Cu complexing systems for therapeutic use. Previously, we showed that the presence of multivalent Cu-complexing ligands on a hPG platform not only increased the affinity and stability of the ligands towards the metal ion, but also suppressed the risk of non-specific toxicity due to premature leaching of the metal ion from the complex. In addition, the synthesized hPG-derived Cu-nanocarriers showed permeation through human brain microvascular endothelial cell (HBMEC) model, which was established to investigate the engagement of these nanocarriers through the blood brain barrier (BBB). It was shown that, hPG-based nanocarriers crossed the BBB model two times more effectively than ^{14}C -sucrose and sodium fluorescein (NaFl) and up to $60\times$ better than Evans Blue labeled albumin (EBA), when the the permeability \times surface area product (PSe) of the nanocarrier and reference substances were compared [13]. As a polyether, hPG contains a large number of C-O bonds and hydroxyl groups, which makes the molecule highly hydrophilic. In addition, these polyether-based multi-functional scaffolds exhibited condensed three-dimensional structure with a hydrodynamic diameter typically within the range of 3–5 nm, high Cu-loading capacity, intracellular transport and inertness to ubiquitous biological components such as protein and phospholipid membranes. In this study, we elaborate the potential routes to generate hPG-scaffolds, which either complex Cu within a specific molecular domain, or, are decorated with ligands that can either impart superior biocompatibility and putative receptor engagement. The designed architectures were tested for formation of the metal-complex and thermodynamics of the complex stabilization. In addition, we have also investigated electrostatic and surface properties of these dendritic nano-constructs, and evaluated their cellular toxicity and uptake behavior in mammalian cell lines.

2. Results

Compared to linear polymers of analogous molecular weight, spatially globular architecture of hPGs gives rise to a number of interesting properties such as reduced viscosities and enhanced water solubility, both of which can be readily modulated by post-synthetic functionalization of peripheral hydroxyl functional group through classical alcohol-group chemistry [15–21]. Another salient feature that makes hPGs unique from its linear analogues is the fact that these macromolecules exhibit a distinct, convertible ‘interior’ supramolecular space [22], sterically shielded from the topological ‘exterior’ of the scaffold (Scheme 1) [23].



Scheme 1. Representative illustration of interior and exterior of hPG (**1a**) scaffold has been indicated by the blue and brown shaded spheres respectively. In structure (**1b**), the interior hydroxyl groups have been converted to amines.

We set out to modify the hPG core structure by orthogonally including/attaching: (a) a Cu encapsulating domain at a specific location within the molecule that can potentially complex Cu ion with substantial stability; and (b) a molecular species that can putatively suppress cytotoxicity and mediate cellular entry. Cu complexing nanocarriers designed in this study are presented in Table 1. We optimized the synthetic design of these hPG-derived metal ion nanocarriers and investigated their capacity to interact with Cu-ion in physiological settings.

Table 1. Library of hPG-based Cu-complexing nanocarriers. * Compound 3f indicates TMEDA bearing hPG systems at full functionalization level. Synthesis and characterization of compound 3f (at full functionalization level) has been reported earlier [13]. Different partial functionalization of hPG, wherever used in this study, has been specified accordingly.

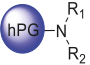
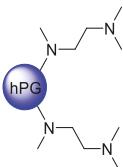
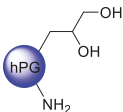
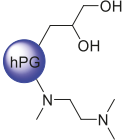
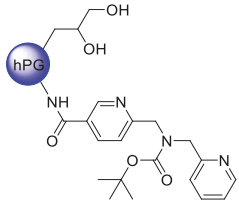
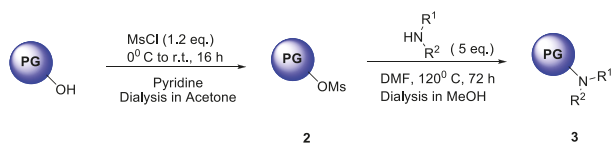
Compoundno.	Compound Code	Structure
		
3a	PG ₁₀ -DMA	R ₁ = R ₂ = -CH ₃
3b	PG ₁₀ -DEA	R ₁ = R ₂ = -CH ₂ -CH ₃
3c	PG ₁₀ -DPA	R ₁ = R ₂ = -CH ₂ -CH ₂ -CH ₃
3d	PG ₁₀ -DIPA	R ₁ = R ₂ = -CH(CH ₃) ₂
3e	PG ₁₀ -DBA	R ₁ = R ₂ = -CH ₂ -CH ₂ -CH ₂ -CH ₃
3f *	PG ₁₀ -(TMEDA) _x	
X = Degree of functionalization, for 3f, X = 1.0		
8	PG _m -cNH ₂	
8a	m = 10 kDa	
8b	m = 5 kDa	
10	PG ₁₀ -cTMEDA	
11	PG ₁₀ -NF135	

Table 1. Cont.

Compoundno.	Compound Code	Structure
12	PG ₁₀ -KR455	
14	PG ₁₀ -Mlt	
15	PG ₁₀ -GLNC	
16	PG ₁₀ -His	

2.1. Dialkylamine Modified hPG Synthesized through Nucleophilic Substitution Reaction

As a first approach, a reactive hPG was functionalized with different dialkyl amines (Scheme 2) to obtain a core-shell architecture where the tertiary nitrogen atom bearing alkyl chains acts as the Cu ion complexing modality within the molecule. Water-solubility of these architectures is critically governed by the degree of functionalization of the PG core. Synthetically, these systems were accessible in a straightforward two-step reaction protocol where both terminal (T) and linear (L) hydroxyl group of hPG can be converted to alkyl amine functionality (Scheme 2). Through the formation of an *O*-mesylpolyglycerol [15], compounds 3a–3e can be obtained with quantitative conversion at elevated temperature.



Scheme 2. Synthesis of dialkylamine functionalized PG. R¹ and R² can be similar or different.

The critical consideration in this reaction is the high volatility of dialkylamines and the requirement of relatively high temperature (over 100 °C) to carry out the reaction. We have synthesized a series of dialkylamine-substituted hPG following this reaction protocol with satisfactory yield as presented in Table 2.

Table 2. Designing dialkylamine terminated PG. Range of amine groups and yields. Compound **3f** has not been included, as chemical data of the molecule has been published earlier [13].

Compound	R ¹ = R ²	Yield (%)
3a	CH ₃ -	60
3b	CH ₃ CH ₂ -	86
3c	CH ₃ CH ₂ CH ₂ -	76
3d	(CH ₃) ₂ -CH-	56
3e	CH ₃ CH ₂ CH ₂ CH ₂ -	68

Figure 1 shows the ¹H-NMR spectrum of **3b**. The broadened signals of the protons of CH₃ at 1.31 ppm and CH₂ group from 2.32–2.81 ppm indicate the immobilization of dialkylamine moiety onto the PG scaffold. The degree of functionalization can be estimated from relative integration intensities of the signals from CH₃ group and that from PG scaffold (3.5–4.0 ppm). In the case of compounds **3c** to **3e**, the degree of functionalization could be easily determined by considering the terminal methyl proton as a reference for calculation. A full synthesis, chemical and biochemical characterization of compound **3f** has been published earlier [13]. Hence, limited experimental data has been presented for this compound for comparison purpose, while, synthetic, UV-spectroscopic, calorimetric and cell cytotoxicity experiment has been conducted and presented for other Cu-nanocarrier candidates.

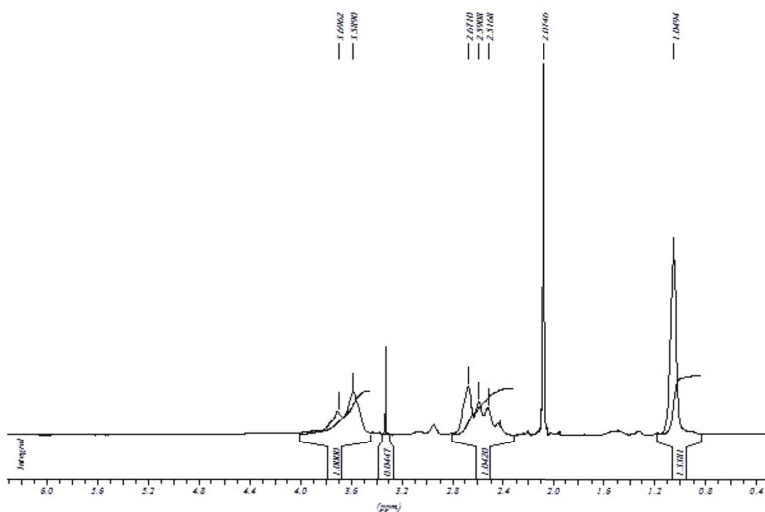


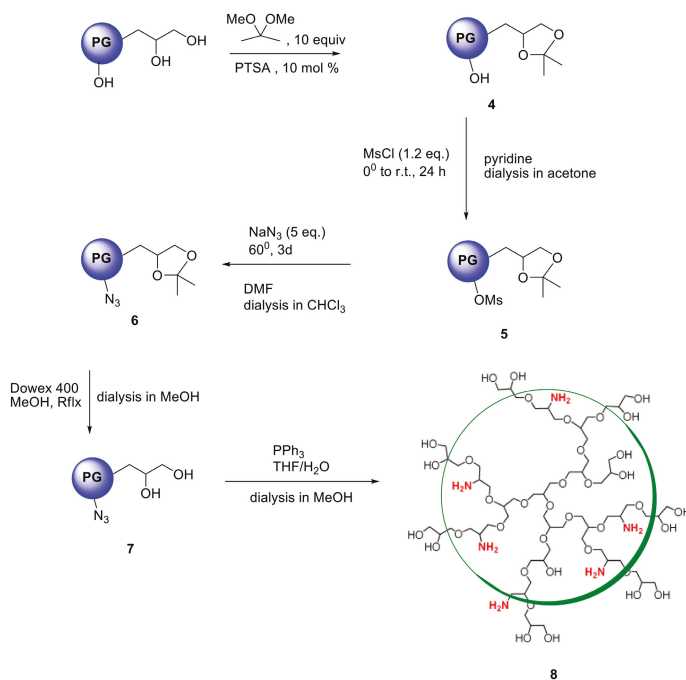
Figure 1. ¹H-NMR of diethylamine functionalized PG (**3b**) at quantitative functionalization level.

This is noteworthy that since the signals due to the protons belonging to the alkyl chain of dialkylamines, which are located next to nitrogen atom, overlap with PG signal, therefore the area corresponding to two protons should be subtracted from the PG signal integration to avoid the underestimation of the actual degree of functionalization. The absence of a signal at 3.12 ppm indicates the complete removal of the mesyl group from the PG backbone. Similar ¹H-NMR patterns were

observed with other secondary dialkylamines attached to PG. ^{13}C -NMR and IR spectra were also found to be confirmatory for the proposed product structures.

2.2. Selective Chemical Differentiation of Primary and Secondary Hydroxyl Groups of hPG: Cu-Binding Domains at hPG Core

In contrast to dendrimers, hyperbranched polymers showed no distinguishable interior and periphery. Hyperbranched PGs, however, possess two types of hydroxyl functional groups (generated from linear and terminal glycerol units), which can be chemically differentiated [24]. Although the linear units are randomly dispersed throughout the structure, they are predominantly present in the proximity of the focal or “core” unit of the macromolecule, when the polymers are prepared by slow monomer addition technique [25]. By following an earlier procedure developed by Haag et al. [22], a chemical differentiation strategy has been undertaken to synthesize core-aminated PG where the “focal-close” linear hydroxyl groups were selectively converted to amines keeping the terminal hydroxyl groups intact. These structural variants of PG were envisioned to encapsulate Cu ion through the nitrogen atoms present in the core, thereby shielding the encapsulation zone. With such structures, it was also possible to retain the required water solubility and biocompatibility profile of the complexes, which are mostly contributed through the “focal-distant” terminal hydroxyl groups. These hyperbranched scaffolds could be envisioned as the molecular chaperons observed in biological systems where the guest molecule is shielded from external environment. The outer hydroxyl group can further be functionalized with targeting moieties or biocompatible PEG shells. In the first step to construct this type of architecture, the terminal 1,2-diols of PG were regioselectively converted to polyacetal **4**. The complete conversion of 1,2-diols in PG was observed (according to ^{13}C - and ^1H -NMR) leaving approximately 40% of the hydroxyl groups unaffected [22]. The synthetic scheme of core-functionalized polyglycerolamine is presented in Scheme 3.



Scheme 3. Synthesis of core-functionalized polyglycerolamine **8**.

The conversion of **5** from **4** could be monitored by means of IR, by tracking the appearance of azide signal (at 2100 cm^{-1}) in polyglycerol azide, **6** [15]. Deprotection of acetals was carried out in the following step with acidic Dowex-400 resin, where the selective acid-catalyzed cleavage of the acetal groups proceeded with quantitative conversion yielding **7**. Core functionalized polyglycerolazide **7** synthesized in this way, where the azide groups are located only at the core of the hyperbranched molecule could also be envisioned as an useful substrate for metal assisted 1,3-Huisgen type “click” chemistry approach. Staudinger reduction of core-functionalized polyglycerolazide carried out in the presence of triphenylphosphine and water, yielded core-functionalized polyglycerolamine (**8**), as confirmed by complete elimination of azide signal in IR spectra. Usually Staudinger reaction is carried out in THF in the presence of small amount of water (5%). However, this is to note that, careful consideration is needed to maintain the ratio of THF to water during the course of the reaction, so that premature precipitation of compound **7** can be optimally minimized.

2.3. Amide Coupling for the Synthesis of hPG-Bispicolylamide Derivatives

Cu^{2+} complexation of a bispicolylamide entity is a widely studied phenomena in designing linker molecules for solid phase peptide synthesis [26]. In peptide chemistry, this type of complexation leads to a weakening of the N-C-amide bond, which can subsequently be cleaved under very mild condition by methanolysis [27–29]. In nature, metalloproteases use the same mechanism for hydrolytic cleavage of the peptide bond. Due to high affinity complexation capacity of bispicolylamide derivatives towards Cu, we hypothesized that, bispicolylamide derivatives bound to PG by a stable amide linkage will encapsulate Cu^{2+} ion in aqueous environment with substantial stability. Therefore two carboxylic acid terminated bispicolylamide derivatives, namely NF 135 and KR 455 (a kind gift from AG Bannawarth, Universität Freiburg, Freiburg, Germany) were coupled to core-aminated PG through an amide bond formation to synthesize compounds **11** and **12**, respectively. These derivatives were coupled to core-aminated PG, (**8**, $\text{PG}_{10}\text{-cNH}_2$) by EDCI/DMAP mediated coupling protocol. An overnight dialysis in methanol yielded pure compounds **11** and **12** in quantitative yield. $^1\text{H-NMR}$ conclusively proved the immobilization of the derivatives on to PG scaffold where the broadened signals of protons from the BOC group and those from aromatic pyridine moiety resonate around 1.39 ppm and from 7.0 to 8.57 ppm respectively. Degree of functionalization was limited to approximately 20% in both cases compared to all hydroxyl groups of PG to ensure water-solubility of the products.

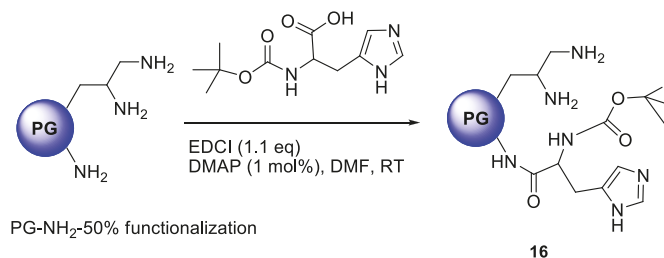
2.4. Reductive Amination Pathway towards the Synthesis of Mono-and Oligosaccharide Modified hPG-Amine

The coupling of mono- and oligosaccharide units to the outer shell of dendritic or hyperbranched architectures has been successful and the resulting amphiphilic macromolecules have been explored as carrier systems for drugs [30–32] and DNA [33,34]. These systems, in addition to the increase in biocompatibility, can utilize the molecular recognition potential of mono- and oligosaccharide units for enhanced and selective cell uptake [35–40]. PPI dendrimers with a densely organized oligosaccharide shell was proved to be a promising anti-prion agent and extensive studies on oligosaccharide shell coupling to PEI based hyperbranched polymers has been reported [41]. Previously it has been documented that the Cu^{2+} complexes of the polypeptide-shelled PPI dendrimers possess nearly the same stability constants as the Cu^{2+} complexes of the unmodified PPI ones [42]. The study suggested that the polypeptide chains do not alter the Cu^{2+} complexation ability of the dendritic PPI skeleton significantly. Thus, it can be assumed that the dendritic PPI skeleton is the driving force for the complexation of Cu^{2+} and it is independent of the attached peripheral chains as surface groups. In our study, it is therefore presumed that attachment of oligosaccharide shells onto polyglycerolamine will not adversely alter polyglycerolamine’s inherent Cu^{2+} complexation ability. To this end, maltose and *N*-acetylglucosamine have been coupled to polyglycerolamine to utilize the purported recognition potential of carbohydrate motif at glucose transferring receptor (GLUT) present in the BBB. Reductive amination was adopted to immobilize the saccharide units as surface group. This reaction can result in the simultaneous coupling of at least one (or two) saccharide units for one amino surface group with

minimized synthetic effort [43]. This synthetic approach has also been described by several authors in immobilizing oligosaccharide onto poly(lysine) and poly-(ornithine) monodendrons and dendrimers, PPI dendrimers [42] and PEI [44] based hyperbranched system. In our case, polyglycerolamine (**13**, fully functionalized, i.e., all hydroxyl groups of PG have been converted to primary amines) was synthesized by previously published procedure from PG by subsequent steps of mesylation, azidation and Staudinger reduction. The reductive amination of the polyglycerolamine with a large excess of maltose or *N*-acetylglucosamine was carried out with a borane-pyridine complex as a strong reducing agent in a sodium borate buffer, yielding *N*-acetyl-glucosamine linked polyglycerolamine (PG₁₀-GLNC, **14**) and maltose-modified polyglycerolamine (PG₁₀-Mlt, **15**). The ¹H-NMR spectrum of **14** showed signals in two characteristic regions: from 2.5 to 4.4 ppm (PG protons overlapped with those from sugar) and from 5.0 to 5.3 ppm (anomeric proton from maltose). On the other hand, ¹H-NMR spectrum of **15** displayed a broad signal in the range of 1.9–2.2 ppm (CH₃ group of the *N*-acetylglucosamine) followed by highly overlapping signals broadened from 2.5 to 4.5 ppm (proton from PG backbone overlapping with those from sugar units). The reductive amination reaction of the reducing unit of the parent (oligo-) saccharide yields a noncyclic unit partly restricted in mobility by its neighborhood to the PG scaffold and, therefore, generating signals with different extents of broadening. Additional broadening and splitting should be caused by different stereochemistry and by the substitution pattern of the neighboring amine nitrogen. Nevertheless, for compound **15**, signal at 22 ppm and for **14**, at 100 ppm in ¹³C spectra after dialysis indicated the immobilization of the saccharide residue onto the PG scaffold. It was difficult to conclude whether one or two units of sugar residues have been added per amino group, however from ¹H-NMR, the degree of functionalization was calculated which was typically within the range of 48% for **14** and 54% for **15**.

2.5. Attaching *N*- α -BOC-Histidine to Polyglycerolamine: BBB Targeted Nanocarriers

Brain microvascular endothelial cells (BMEC) are the major structural and functional components of the BBB that maintain the homeostasis of the central nervous system. The plasma membrane of BMEC has been shown to be the site of several carrier-mediated transport systems including those for glucose, monocarboxylic acids and amino acids [45,46]. Xiang et al., provided evidence for there being at least two pathways for L-histidine uptake into isolated choroids plexus, an Na⁺-independent and an Na⁺-dependent process. Hikichi et al., studied the stereoselective BBB transport of histidine using rat brain BMEC and reported the process to be saturable [47]. Their results suggested that L-histidine is actively taken up by a carrier-mediated mechanism into the BMEC with energy supplied by Na⁺. Considering these earlier data, we have immobilized a histidine analogue, *N*- α -BOC-Histidine was immobilized onto polyglycerolamine (50% amino functionalized) to yield compound **16** (PG₁₀-His) in an attempt to utilize the Cu complexing capability of both polyglycerolamine and imidazole ring system of the histidine moiety while exploiting the affinity of histidine nucleus towards System-L and System-N transporters in the BBB. In this system, *N*- α -BOC-Histidine serves as the targeting modality to target histidine transport receptors. The reaction chemistry is presented in Scheme 4.



Scheme 4. Coupling of *N*- α -BOC-histidine to polyglycerolamine.

N- α -BOC-histidine was coupled to polyglycerolamine by using EDCI as the coupling agent in the presence of catalytic amount of DMAP in DMF-water (1:1) mixture. An overnight dialysis in methanol yielded pure compounds in 78% yield. $^1\text{H-NMR}$ conclusively proves the immobilization of the derivatives onto PG scaffold where the nine protons from BOC signals resonate at 1.09 ppm while two protons from the imidazole rings of histidine nucleus appear at 6.52 and 7.84 ppm. The degree of functionalization was adjusted to 20%, which resulted in water-soluble product.

2.6. Synthesis of FITC-Labelled PG₁₀-TMEDA System

Compound **3f** (approximately 70% level of functionalization) was tagged with FITC in the presence of dibutyl tindilaurate as catalyst. Extensive dialysis in MeOH yielded the desired FITC labeled **3f** (FITC-PG₁₀-TMEDA) for cellular uptake studies. UV-Vis spectrophotometric methods and $^1\text{H-NMR}$ were used to characterize the labeled product.

2.7. Cu-Encapsulation by Synthesized hPG-Derived Nanocarriers: UV-Visible Spectroscopic Investigation

The primary objective of designing these synthetic constructs was to use them for complexing and delivering Cu ion across cell membranes. To this end, the hPG-based architectures were first tested for their Cu-complexing ability. UV/Vis spectroscopy is a method that is extensively used to investigate qualitative as well as quantitative changes in the coordination sphere of transition-metal complexes [48–51]. In the case of dendrimers, it was shown that dendritic structures can only encapsulate a maximum number of metal ions per molecule [52]. The maximum metal loading of the dendrimer and the value of the [metal ions]/[dendrimer] ratio determines the size of the formed nanoparticles [53]. In our case, a similar approach to investigate the metal loading capacity by PG based Cu encapsulating nanostructures was undertaken. Cu²⁺ encapsulated systems were prepared by mixing equal volume of aqueous CuSO₄ solution with respective polymer solution. An incubation time for metal uptake was standardized to be 24 h. The encapsulated Cu²⁺ ion was not reduced after complexation to form true nanoparticles since the therapeutic efficacy needs the Cu²⁺ ion to be delivered in ionic form. The evidence for Cu²⁺ encapsulation by the respective PG based Cu²⁺ encapsulating constructs resides in the fact that, in pure aqueous solution copper sulfate forms a light blue (aqua) copper complex, [Cu (H₂O)₆]²⁺, which has a wide absorbance maximum at 810 nm region. On the formation of a complex between the amine moieties of polymer scaffold, this absorbance maximum will be shifted to shorter wavelength. At this wavelength, a continuous variation plot of Cu to polymer ratio will provide the maximum number of Cu ions that can be encapsulated per mole of nanocarrier [54,55]. As a general procedure, to assess maximum metal-cargo capacity of dendrimers and hyperbranched polymers, an aqueous solution of the individual nanotransporter (at various concentrations calculated according to the M_n value) was mixed with an aqueous solution of Cu²⁺ to obtain a distinct molar [Cu²⁺ ions/nanotransporter] ratio within the range of 0–100. As a representative example, Figure 2a illustrates the complexation of copper ions with PG₁₀-TMEDA_{1,0} system. A more detailed biophysical and biochemical evaluation of Cu-complexing capacity of this candidate and related molecular species has been communicated in our earlier publications [12–14]. In the absence of a polymer with complexation capabilities, Cu²⁺ exists primarily as [Cu (H₂O)₆]²⁺ in aqueous solutions, which gave rise to a broad, weak absorption band at 810 nm associated with a d-d transition ($\epsilon \sim 10$). In the presence of **3f**, λ_{max} for the Cu²⁺ d-d transition was shifted to 735 nm. In addition, a strong ligand-to-metal-charge-transfer (LMCT) transition appeared at 280–300 nm regions (Figure 2a). With higher ratio of Cu²⁺ to polymer, the spectrum shows a tendency to shift towards the longer wavelength. This change in UV-Vis spectrum allows following the Cu²⁺ ion binding with different hyperbranched polymer systems bearing nitrogen atoms. In this experiment, the absorbance at λ_{max} at 735 nm increased with increasing [Cu²⁺]/[nanotransporter] ratio until a critical value is reached, above which the absorbance increased only slowly. The shift in the absorption maximum at 735 nm is mainly due to the complexed Cu ion co-ordinated within the four nitrogen system of TMEDA structure across the polymeric scaffold. Figure 2b represents the general architecture of such TMEDA

complexes with Cu^{2+} , where the metal ion is bound between the four nitrogen atoms of TMEDA moiety of compound **3f**. A different UV-Vis absorbance pattern was observed when compound PG_{10} -Mlt **14** or PG_{10} -GLNC **15** was titrated with Cu^{2+} . Figure 2c,d shows the absorption spectra of **14** in the presence of increasing amount of Cu^{2+} . The nanocarriers themselves do not absorb light significantly above 250 nm. In the presence of Cu^{2+} , a new peak at appears at 273 nm (Figure 2c for PG_{10} -Mlt system). This can be attributed to the ligand-to-metal charge-transfer (LMCT) transition of the Cu^{2+} encapsulated complexes [54,55]. This LMCT band were obtained when increasing amount of Cu^{2+} was added to PG_{10} -Mlt system in water.

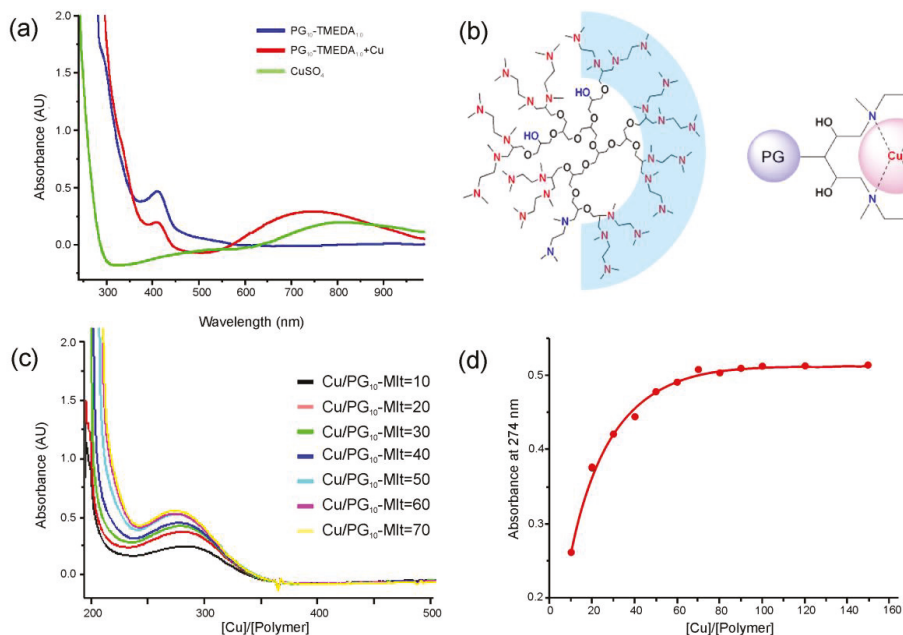


Figure 2. (a) Complexation of Cu^{2+} ion by PG_{10} -TMEDA_{1.0} system **3f** as indicated by shift of absorbance band at shorter wavelengths compared to that for free CuSO_4 (b) Idealized structure of compound **3f**, and the possible structure of the complex (c) Complexation of Cu^{2+} ion by PG_{10} -Mlt **14** can be followed by gradual increase of absorbance at 273 nm. Cu/Polymer ratio of 10–70 is presented (d) Two distinct region is present before and after maximum Cu loading by the PG_{10} -Mlt **14** system which diverges at $[\text{Cu}]/[\text{Polymer}] = 50$.

Comparative studies have been undertaken which revealed no interaction between maltose with Cu^{2+} . Therefore it can be assumed that the amino groups within the polymeric scaffold are responsible for complexing Cu^{2+} . Because of the low absorbance of d-d transitions (less than 0.12) at about 700 nm, which is also associated with high signal-to-noise ratio, the LMCT transition at 290 nm was used for quantitative evaluation of Cu^{2+} /polymer complex. Figure 2d shows the absorbances of PG_{10} -Maltose system as a function of Cu^{2+} concentration. At low Cu^{2+} concentration, a linear increase in absorbance at 274 nm was observed. In this region, an effective complexation takes place between Cu^{2+} ions and hPGs. This gradual increase of absorbance eventually diminishes into an approximately linear region. Here practically no complexation between Cu^{2+} and polymers takes place. The intersection point of these two regions can be estimated as the maximum molar capacity of these carbohydrate modified polyglycerolamine systems to load Cu^{2+} ions.

For PG₁₀-His system **16**, a shoulder band at 290 nm, which gradually increases with increasing Cu²⁺ concentration, was assigned as LMCT transition signals and similar procedures as mentioned above was followed to determine the Cu²⁺-loading capacity of these nanocarriers. The high signal-to-noise ratio of Cu²⁺/carrier complexes from 650 to 700 nm, associated with the problem of overlapping of the LMCT region by the structural features of the carriers themselves restricted the UV-Vis spectroscopic application to determine maximum metal-encapsulating capacity of PG₁₀-NF135 **11** and PG₁₀-KR 455 **12** systems. For these carriers, isothermal titration calorimetry (ITC) was used as a method of choice to investigate their encapsulation/complexation behaviour.

2.8. Thermodynamics of Cu-Ion Encapsulation by hPG Nanoconstructs: Isothermal Titration Calorimetry (ITC)

Isothermal titration calorimetry (ITC) has proven its efficiency for studying thermodynamic and kinetic properties of macromolecular interactions due to its ease of application and high level of accuracy. ITC technique was used to follow the enthalpic interactions between hPG-derived nanotransporter and Cu²⁺ ions, which in turn reflect the strength and extent of metal encapsulation properties of the selected species. The energetics of encapsulation is critically important for designing Cu-ion delivery systems as it governs the stability of the complex in fluctuating in vivo environment before it reaches the target tissue. Encapsulation of all nanotransporters was analysed by measuring the heat change during the titration of Cu²⁺ to nanotransporter solutions. The heat released or absorbed during the titration process is in direct proportion to the amount of binding between the macromolecule and the metal ion. In this experiment, isothermal titration calorimetry was performed in both orders, i.e., nanotransporters added to Cu²⁺ ion solution and vice-versa to investigate the encapsulation event quantitatively. It was found that, adding Cu²⁺ ion solution from the syringe to the nanotransporter solution in the cell gives a better representation of the saturation process of the polymers by Cu²⁺ ions. A series of concentration experiments has been done for each of the nanotransporters to fix the experiment parameters including the concentration of the hPG derivatives and the metal ion.

Figure 3 illustrates the isothermal titration calorimetric trace for PG-cNH₂ architecture **8**. Encapsulation stoichiometry of Cu²⁺ ions by these nanocarriers was found to be a function of the molecular weight of the PG core. Resulting binding isotherm representing the interaction of Cu²⁺ ions to this nanotransporter was hyperbolic in nature with an initial rapid release of heat in the negative side of titration baseline indicating exothermic interaction between Cu²⁺ ions and the nanocarriers.

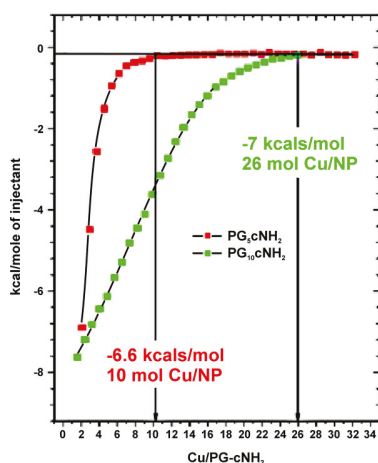


Figure 3. Binding isotherm of Cu²⁺ interaction with PG₅-cNH₂ **8a** and PG₁₀-cNH₂ **8b** systems. X-axis shows the amount of heat (kcal mol⁻¹) released upon encapsulation of Cu by the nanocarriers.

The enthalpic values, as illustrated in the figure, finally reached a plateau, which indicated the end-point of titration confirming that all or at least most of the accessible binding sites of the macromolecules have been saturated with the ligand. The negative value of apparent change in enthalpy (ΔH_{app}) indicated the predominant effect of charge-interaction in binding event. Different statistical and qualitative approaches were undertaken to analyse the binding isotherm resulting from calorimetric titration. In principle, the difference between the amount of energy liberated/absorbed at the onset of titration and that at the end of the saturation process, generally gives the first approximation of binding energy of interaction. Stoichiometry of binding can be calculated from the inflection point of the titration curve. The stoichiometry can also be evaluated from the intersection points of different kinetic regions within the binding isotherm before the saturation/plateau level of interaction is reached. From exothermic heat release profile, it can be concluded that both core-functionalized polyglycerolamines PG-cNH₂ **8** was complexing Cu²⁺ ions. PG₁₀-cNH₂ architecture was able to complex 26 mole of Cu ion per mol of polymer, whereas PG₅-cNH₂ was encapsulating only 10 mole of metal ion per mole of the nanocarrier. The heat of complex stabilization was almost of similar order for both variants, which is within the range of -6.5 to -7 kcal mol⁻¹ indicating considerably stable complexes between Cu²⁺ ions and the polymers. The binding isotherms of these two polymeric systems however showed that PG₅-cNH₂ is saturated with Cu²⁺ ions at a faster rate than that of its high molecular weight counterpart. The observation might be due to easier accessibility of the metal ions towards the linear amino groups for low molecular weight core. The change of complexation enthalpy as a function of [Cu²⁺] to [nanocarrier] ratio followed a similar pattern for other nanocarrier systems. The exothermic isotherms can be mainly attributed to the charge transfer based complexation between the amine groups of the molecule and Cu²⁺ ions. Of the two carbohydrate-coupled polyglycerolamines, PG₁₀-Mlt **14** showed different energetic behavior on its interaction with Cu²⁺. At the onset of titration, endothermic signals were generated which were gradually converted to exothermic heat flow (data not shown). The observed facts could be due to two separate energetic processes occurring during complexation. Similar effect was also reported previously where introducing larger oligosaccharide units onto the host polymer changes the binding mechanism of guest molecule [56].

PG₁₀-NF 135, **11** and PG₁₀-KR 455, **12** systems were analyzed micro-calorimetrically in the same manner to evaluate their Cu-complexing ability. Figure 4 shows the binding isotherms of these systems with Cu²⁺ ions. As observed from Figure 4a, approximately 13 kcal/mol of energy has been liberated on interaction of Cu²⁺ with PG₁₀-NF 135 system, which indicates the formation of considerably strong complex. On the other hand, Cu²⁺-PG₁₀-KR 455 complex stabilization energy was only within the range of 5 kcal/mol (Figure 4b). Intersection of the linear regions of binding isotherms affords the maximum Cu²⁺-loading efficiency of the nanocarriers. The figure also shows that PG₁₀-NF 135 (**11**) can encapsulate ~45 mol of Cu/mol of carrier, while PG₁₀-KR 455 (**12**) was able to bind ~55 mol of Cu/mol of carrier.

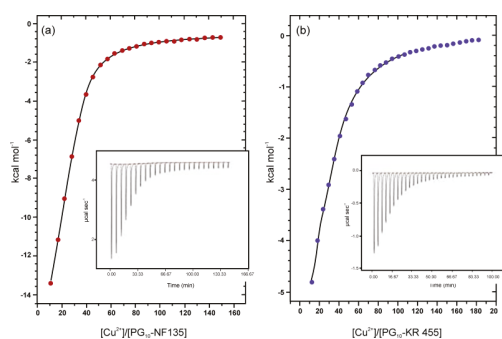


Figure 4. Binding isotherm for Cu²⁺ interaction with (a) PG₁₀-NF 135, **11** and (b) PG₁₀-KR 455, **12**.

Depending on the variation of molecular architecture, Cu^{2+} saturation level and complex stabilization energy varied with individual Cu^{2+} encapsulating systems. The binding isotherms of the different nanocarriers with Cu^{2+} ion allowed the determination of maximum $[\text{Cu}^{2+}]/[\text{nanocarrier}]$ ratio using the inflection method as per earlier published procedure [56]. Saturation stoichiometry of the nanotransporters towards Cu^{2+} generated by analysing the titration curves is presented in Table 3. The Cu-complexing capacity of compound **3f** (i.e., PG_{10} -TMEDA_{1,0}, fully functionalized) has been published in an earlier report [13]. Here we show that, compound **3f**, functionalized with TMEDA moiety at 50% and 10% functionalization level, also showed similar trend of Cu-encapsulation characteristics as per ITC and UV-Vis measurements.

Table 3. Cu^{2+} complexing stoichiometry as determined by ITC and UV-Vis spectroscopy.

Compound No.	Nanocarriers	Mole of Cu^{2+} /mol of Nanotransporter	
		ITC	UV-Vis
3f (50%) *	PG_{10} -TMEDA _{0,5}	31	36
3f (10%) *	PG_{10} -TMEDA _{0,1}	14	15
8a	PG_{10} -cNH ₂	26	31
8b	PG_5 -cNH ₂	10	17
11	PG_{10} -NF 135	45	40
12	PG_{10} -KR 455	55	48
14	PG_{10} -Mlt	N/D	40
15	PG_{10} -GLNC	N/D	42
16	PG_{10} -His	35	N/D

N/D: not determined; It was not possible to accurately determine the saturation stoichiometry of Cu^{2+} by PG_{10} -Mlt or PG_{10} -GLNC system by ITC (inadequate model fitting), and PG_{10} -His by UV-Vis spectroscopic techniques (very weak LMCT signal). * % value inside parenthesis indicates the degree of functionalization of total number of hydroxyl groups/mol of hPG.

2.9. Surface Charge Characteristics of Cu-Loaded hPG Nanocarriers

The surface charge, or zeta potential of nanocarriers governs a wide array of their biological activity, including cellular permeability, biocompatibility, systemic stability, enzyme interaction, metabolic degradation and toxicity. Hence, we have investigated the surface charge of the synthesized Cu-nanocarriers either alone or in Cu-encapsulated form. Zeta potentials of the PG_{10} -TMEDA nanocarrier solution in PBS of pH 7.4 were measured for different degree of functionalization of the construct. To assess the effect of Cu^{2+} on surface charge of PG_{10} -TMEDA systems, the nanocarriers were loaded with maximum stoichiometric amount of Cu (estimated from ITC and UV-Vis titration). For optimal loading of Cu, after incubation, free metal ion was removed from the polymer-encapsulated species by dialysis until a stabilized value of absorbance at 735 nm is obtained for the retentate solution. The freeze-dried, PBS resuspended solution of nanocarriers was subjected to zeta potential measurement. In case of PG_{10} -TMEDA systems protonation may occur at all nitrogen atoms and like amine terminated PAMAM dendrimers, the surface of the polyglycerolamines will be positively charged and zeta potentials will gradually increase with increased percentage of cationic groups. Typical results from the zeta potential measurements are illustrated in Figure 5a for PG_{10} -TMEDA system **3f** in buffered aqueous solution. It is clearly observed that at pH 7.4, these systems were positively charged and surface charge increases with increasing degree of functionalization of PG scaffold with TMEDA moiety from +10.4 mV to as high as +18.2 mV. Loading PG_{10} -TMEDA systems with saturating concentration of Cu load (as measured from ITC/UV calculations) decreases the zeta potential of the Cu-encapsulated complex. For example, PG_{10} -TMEDA_{1,0} **3f** system exhibits surface charge of +18.2 mV, which is decreased to 12.1 mV upon encapsulation of Cu^{2+} (Figure 5a). This charge neutralization of the carrier system by Cu^{2+} proves the location of the metal ion adjacent to TMEDA shell systems of the carrier molecule with probable involvement of the charge transfer mechanism. The higher the degree of functionalization, the stronger is the charge neutralization, most likely due to higher stoichiometric load of Cu ion within the polymer scaffold. Also considering the fact that,

CuSO_4 does not have any surface charge, the colloidal electrostatic charges of the resulting solution over entire $[\text{Cu}^{2+}]/[\text{PG}_{10}\text{-TMEDA}]$ functionalization range is essentially being contributed from the Cu-encapsulated $\text{PG}_{10}\text{-TMEDA}$ system. Surface charge properties of PG-cNH_2 8 system were found to be a function of molecular weight of the PG core. $\text{PG}_{10}\text{-cNH}_2$ derived from 10 kDa PG scaffold exhibit higher zeta potential (16.4 mV) than $\text{PG}_5\text{-cNH}_2$ species with 5 kDa PG core (10.4 mV). For carbohydrate-modified carriers, surface charge was substantially low.

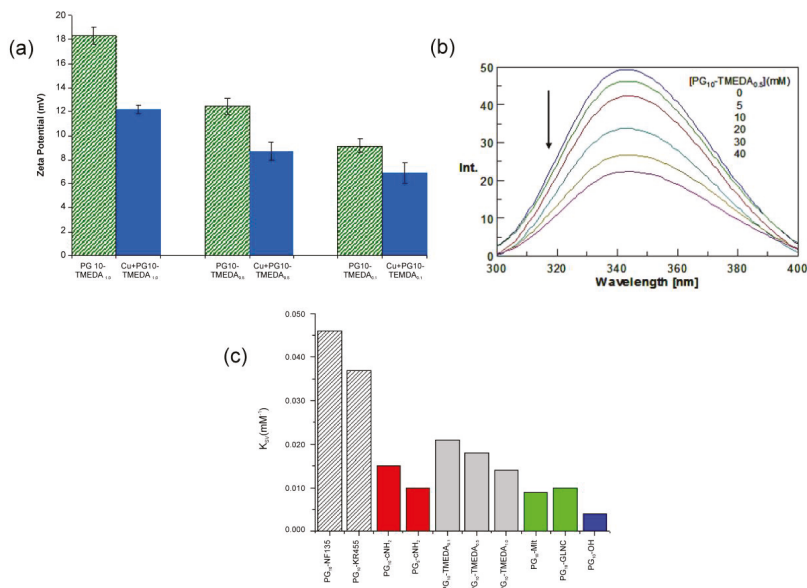


Figure 5. (a) Comparative zeta potential of $\text{PG}_{10}\text{-TMEDA}$ system alone and in the absence and presence of Cu^{2+} . Gradual decrease of zeta potential is observed with decreasing functionalization level of PG core by TMEDA moiety (b) Fluorescence spectra of BSA (emission maximum at 341 nm) in the presence of increasing concentration of $\text{PG}_{10}\text{-TMEDA}_{0.5}$ (c) Stern-Volmer constant (K_{SV}) of the nanocarriers with respect to PG ($\text{PG}_{10}\text{-OH}$).

Table 4 summarizes the zeta potential values of the studied nanocarriers:

Table 4. Zeta potential of PG based Cu-encapsulating systems.

Compound No.	Nanocarriers	Zeta Potential (mV)
11	$\text{PG}_{10}\text{-NF 135}$	(+) 36.0 ± 1.0
12	$\text{PG}_{10}\text{-KR 455}$	(+) 38.5 ± 0.5
3a	$\text{PG}_{10}\text{-DMA}$	(+) 28.0 ± 0.5
14	$\text{PG}_{10}\text{-Mlt}$	(-) 1.5 ± 1.0
15	$\text{PG}_{10}\text{-GLNC}$	(+) 5.0 ± 0.5
16	$\text{PG}_{10}\text{-His}$	(+) 8.5 ± 1.0

2.10. Interaction of Cu-Ion Encapsulating Systems with Plasma Albumin

The effectiveness of drug or delivery system candidates depends heavily on their interaction with naturally occurring plasma proteins within the systemic circulation. This is particularly critical when the polymeric architectures possess high surface charge, molecular weight, and have tendency to interact with biomacromolecules in blood due to their surface properties. In general, the extent

of interactions between bioactive molecules and serum is quantified by Stern-Volmer constants, reflecting tryptophan fluorescence quenching efficiency of the ligands, where the amino acid being the integral part of BSA construct. Furthermore, these interactions are measured in terms of binding constants or binding associations. Reported studies have been directed to realize the interactions of polyamidoamine (PAMAM) dendrimers (fatty acid free and loaded with fatty acids) with serum albumins (SA), for their physiological significance in developing nano-carrier systemic delivery system [57]. In our case, fluorescence spectroscopic studies were carried out in phosphate buffered saline solution. Emission spectra were recorded from 300 to 440 nm after excitation at 295 nm. In buffered aqueous solution, BSA exhibits a characteristic emission spectrum of the tryptophan fluorophore, with a distinct peak maximum at around 340 nm. In order to investigate the interaction between dendritic polyglycerols and BSA, changes in the intensity of the emission spectra of BSA upon addition of hPG-constructs were monitored. As can be seen from the spectra in Figure 5b, addition of PG₁₀-TMEDA_{0,5} **3f-b** to BSA in buffer led to a significant decrease in the intensity. When the PG₁₀-TMEDA_{0,1} **3f-c** carrier was added to the solution of BSA, the spectra showed only a slight decrease in the fluorescence intensity; therefore suggesting much weaker binding interactions to BSA indicating the interaction is operating mainly through the TMEDA groups coupled to PG. On the contrary, in the experiment with PG₁₀-Mlt, emission spectra of BSA were less affected by the presence of the attached maltose units onto PG scaffold (data not shown). The distinct decrease in the fluorescence intensity, as in Figure 5b, upon addition of polymers can be utilized in studying the interaction of PG based carriers with BSA quantitatively by using classical Stern–Volmer equation [58–60]:

$$F_0/F = 1 + k_q \times \tau_0 \times [Q] = 1 + K_{SV} \times [Q] \quad (1)$$

where F_0 and F are, respectively, BSA fluorescence intensities in the absence and presence of polymer, K_{SV} is the Stern–Volmer quenching constant, $[Q]$ is the concentration of polymer, k_q is the bimolecular quenching constant, and τ_0 is the lifetime of the fluorophore in the absence of quencher. If diffusion controlled, collisional quenching process is assumed, Equation (1) can be applied to properly fit the experimental data.

The slope of Stern-Volmer equation equals to K_{SV} and usually reveals the accessibility of the polymers to the albumin fluorophore, hence the interaction and potential protein binding capacity of the quencher [59]. More precisely, a linear plot is generally indicative of a single class of fluorophores, all equally accessible to the quencher molecules. Typical results of Stern-Volmer constants of other carriers are presented in Figure 5c. Spectroscopic results imply that the electrostatic interaction is the main driving force for binding of these nanocarriers to negatively charged BSA. For example, if the PG₁₀-TMEDA **3f** systems (light blue colour bars) are considered, it is clearly apparent that the extent of interaction which is quantified by Stern-Volmer constant, decreases with decreasing functionalization level of PG hydroxyl groups by TMEDA moiety. Similar trend can be observed with PG-cNH₂ system, where the K_{SV} value clearly depends on molecular weight of the PG core. Attachment of sugar residue onto PG scaffold essentially reduces the interaction with BSA. On the contrary, PG₁₀-NF 135 **11** and PG₁₀-KR 455 **12** system exhibited substantially high interaction with BSA probably due to the presence of heterocyclic ring, which facilitates non-specific attachment with BSA in addition to hydrophobic mediated interactions.

2.11. Cellular Toxicity and Uptake of Representative hPG-Derived Nanocarriers

Cellular toxicity studies of the architectures in human hematopoietic cell line U-937 are shown in Figure 6. A set of four parameters were considered for the evaluation of the Cu²⁺ nanocarrier systems: (a) Cell number; (b) MTT-test for metabolic activity (c) Cell viability and (d) Apoptosis in terms of cell diameter with respect to dexamethasone control. In all the cases, PG₁₀-His **16**, PG₁₀-Mlt **14** and PG₁₀-GLNC **15** showed substantial cell viability, unaltered cell diameter, normal metabolic activity and significant cellular biocompatibility than PG₁₀-DMA **3a**, PG₁₀-NF135 **11** and KR455 **12**,

and architectures. Figure 6 illustrates the representative cell-toxicity study obtained with PG₁₀-GLNC system 15. In addition to control, we have added dexamethasone to evaluate the effect of a known cytotoxic agent within the same concentration as that for our test samples. As evident from the figure, the number of viable cells, metabolic status and cell viability in general were virtually unaffected by PG₁₀-GLNC (15) or by PG₁₀-His systems (compound 16). This might be due to the biocompatibility of *N*-acetylglucosamine or histidine analogue that has been attached onto polyglycerolamine scaffold. On the other hand, PG₁₀-KR 455 12 system was found to be highly toxic to the U-937 cell line as illustrated in supporting information, and so was dimethylamine-substituted hPG (compound 3a). Cytotoxicity data of compound 3f has been published in our earlier report [13]. This observation might be attributed to extremely strong Cu-binding efficiency of these systems, which possibly depleted essential metal ions from cellular microenvironment. We have also studied a short-term incubation of PG₁₀-TMEDA 3f system with 90% level of functionalization and PG₁₀-cNH₂ with living neuronal SY5Y cell lines. When the cell lines were subjected to Cu loaded and FITC-labelled PG₁₀-TMEDA system, green fluorescence of FITC was observed around the DAPI stained nucleus on superimposing image, confirming the cellular uptake of the carrier system within the cytoplasm (Figure 6d) starts taking place within 30 min as observed in confocal microscopy based experiments. We have also reported a more extensive cellular and biochemical property of this system, which showed that, not only PG₁₀-TMEDA systems were capable of internalization inside cytosol, they were also able to engage with cytoplasmic metal processing machinery [13,14]. In a similar way, core-functionalized polyglycerolamine, PG₁₀-cNH₂ 8a tagged with FITC was investigated for cellular uptake in SH-SY5Y cell-line, and the dye-labelled nanoparticles were found to be associated to the nuclear membrane after 30 min of incubation period (data not shown). Since these cationic constructs do not contain any receptor-specific ligand, the observed cellular uptake of is most likely triggered by non-specific endocytosis, followed by endosomal escape through proton-sponge effect.

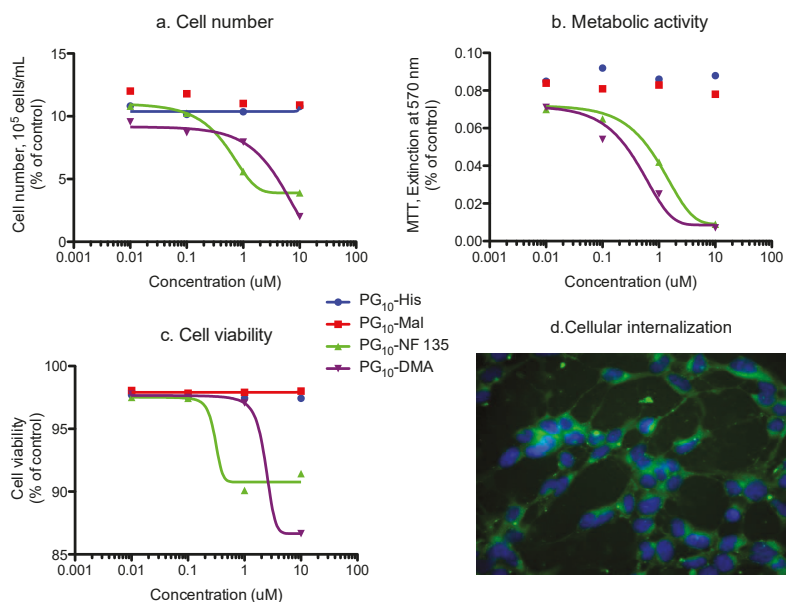


Figure 6. Cellular studies with U-937 cell-line treated with different hPG derivative Clock-wise: (a) Cell number (b) metabolic activity; and (c) Cell viability (d) Presence of FITC-labelled compound 3f in cytosol after 30 min incubation with SY5Y cell lines.

3. Discussion

We found that, bare hPGs do not encapsulate Cu ion to a significant extent. Modification of PG core is required to introduce Cu-encapsulating modalities within the molecule. This has been achieved either by activating the PG hydroxyl group to an efficient leaving group, following nucleophilic substitution with different dialkylamine moieties or, by step-wise conversion of PG hydroxyl groups to primary amines. Cu-encapsulating moiety can be strategically localized either within the core, or introduced statistically throughout the molecule. The complex formation of hPG-derivatives with the metal is believed to take place through the displacement of water molecules surrounding Cu^{2+} ion in aqueous solution. Along with typical mechanism of charge transfer from N-atom of the polymer towards Cu^{2+} ion, it is also assumable that there is an enthalpic-entropic compensation in the formation of such complexes. The role of entropic part in addition to enthalpic component in host-guest interaction [61–63] is a well-documented phenomena particularly in case of charge-interactions [64]. Encapsulation of a guest species, Cu in this case, resulted in reduced rotation of bonds and higher ordered structures applicable to all tested candidates. The partial/total loss of hydrate shell around Cu ion set water molecules free which increased entropy and might compensate for the loss of rotational freedom after encapsulation [65]. We have reported earlier, that compound **3f**, at full functionalization level, not only showed high affinity encapsulation of Cu^{2+} , but also a pH-dependent release in aqueous environment [13]. The stability of all tested complexes at pH 7.4 is important to retain the integrity of the complex in the blood stream before accumulation into target tissues. On the other hand, gradual release of Cu in acidic environment will be of critical importance in the liberation of Cu ion within the cytosol after endocytosis.

hPG-derivatives with primary amine groups at the core (compounds **8a** and **8b**), showed Cu-encapsulation efficiency as a function of the MW of the core. Heat of complex stabilization was almost similar for both molecular weight variants, however, the rate of saturation of nanocarriers were much faster in case of high MW PG-species **8** than their low MW counterparts (Figure 3). This can be attributed to the higher accessibility Cu towards the linear amino groups in case of low MW polyglycerolamine. Similarly, hPG-derived compounds, particularly those conjugated with bioactive ligands such as maltose, *N*-acetylglucosamine and histidine showed increased toxicity tolerance for free Cu (Figure 6) in the cell. Attaching carbohydrate functionalities to the core, i.e., maltose and *N*-acetylglucosamine, as in compounds **14** and **15** respectively, is a well-documented approach to increase compartmentalization of guest molecules and to exert biocompatibility. In this project, addition of carbohydrate fragments was envisioned to stabilize the Cu^{2+} complex formed within the polyglycerolamine scaffold. These architectures were found to be the most non-toxic of all the synthesized architectures in U-937 cell-line in terms of cell-viability, metabolism and apoptosis. Improvement of biocompatibility scenario through incorporation of carbohydrate shell has been reported before [56]. Attachment of bispicolylamide derivatives to PG improved the Cu^{2+} binding ability of PG based nanocarriers to a considerable extent (Figure 4). PG₁₀-NF135 **11** was found to be the strongest Cu^{2+} complexing nano-architectures among the synthesized candidates in terms of binding energy. Compound **11** was found to accommodate ~55 moles of Cu/mol of polymer with an energy range of 13 kcal mol⁻¹. Unfortunately, the bispicolylamide derivative immobilized PG nanocarriers exhibited substantial level of toxicity compared to control. This could be attributed to strong chelating ability of bispicolylamide towards Cu, and also to other metals that might have damaged normal metal homeostasis within cellular environment. Similar results were also reflected in binding experiments of nanocarriers with serum albumin. Stern-Volmer constant (K_{SV}), which is considered as a quantitative extent of interaction with BSA with a given quencher molecule, decreased gradually in the following order: PG₁₀-DMA, **3a** > PG₁₀-NF135, **11**, PG₁₀-KR 455, **12** > PG₁₀-TMEDA_{1.0}, **3f** > PG₁₀-His, **16**, PG₁₀-TMEDA_{0.5} **3f-b** > PG₁₀-Mlt, **14**, and PG₁₀-GLNC, **15**. When neuronal cells, such as SY5Y, were treated with FITC-tagged **3f** derivatives, FITC fluorescence from the nanocarriers were visualized near the DAPI stained nucleus indicating that the systems were uptaken by the

cells through non-specific endocytosis followed by endosomal escape. In case of core-functionalized polyglycerolamine, accumulation of the nanocarriers on or near nuclear membrane was evident.

The experimental significance of this work principally indicates that, it is possible to construct multivalent hPG-based ligand for spontaneous encapsulation of Cu ion to generate biocompatible Cu-complexing macromolecular constructs. The strength and complexation property can be optimized by selective functionalization of the hydroxyl groups of hPG scaffold by different structural modalities, which in turn also governs cellular uptake and toxicity of the nanocarriers. The optimized hPG-derived architectures can find potential application in addressing disease and nutritional deficiency conditions where exogenous administration of Cu is required.

4. Experimental Section

4.1. Materials

PG ($M_n = 10,000$ g/mol) synthesized from TMP starter, MWD = 1.7) was prepared by the Haag group according to a previously published procedure. All PG samples were concentrated and dried under vacuum ($50\text{ }^\circ\text{C}$, 1×10^{-2} mbar) until loss of weight was lower than 0.025 g per 1.0 g of the dried sample in 5 h drying periods. This process was accepted as a standard procedure followed also in previous works. Commercially available chemicals from standardized sources have been used and used as delivered. Solvents were purchased as reagent grade and distilled if necessary. Anhydrous solvents were either purchased as ultra dry solvent from Acros Organics® (Fisher Scientific, Im Heiligen Feld, Schwerte, Germany) or received from solvent purification system. The following spectrometers were used for recording $^1\text{H-NMR}$ and $^{13}\text{C-NMR}$ spectra: DRX 500 and AMX 500 spectrometers, (Bruker, Billerica, MA, USA). Typically, 10–30 mg of compound was used for recording $^1\text{H-NMR}$ while 50–100 mg of compounds were required for $^{13}\text{C-NMR}$. Deuterated solvents were used as standardized procedure. All spectra were recorded at r.t. and were analyzed with Win NMR® software (Bruker, Billerica, MA, USA). Benzoylated cellulose membrane purchased from Sigma-Aldrich (Munich, Germany), MWCO = 1000 was used to perform dialysis. Typically, dialysis was carried out for 24 h with 1 L of solvent that was exchanged after first 6 h of the process. Size exclusion chromatography (SEC) was performed with Sephadex LH 20 or Sephadex G 25 from GE Healthcare (Little Chalfont, UK). The material was activated by swelling in the respective eluent prior to performing chromatography. In case of using CHCl_3 , the beads were activated in the presence of 10% ethanol. TLC was performed on aluminium sheets with silica (corn size 60) and fluorescence marker (F_{254}) (Merck, Darmstadt, Germany). Flash column chromatography was performed on Merck silica (corn size 60).

4.2. UV-Vis Spectroscopy

UV/Vis spectra were recorded with a S-3150 instrument (Scinco, Seoul, Korea) range: 190–1100 nm, resolution 1024 points) in fast mode. Calibration was performed at 360.85 and 453.55 nm with holmium oxide glass. The spectra were recorded at r.t. and were evaluated with Labpro® Plus from Scinco Co., Ltd., Microsoft® Excel 2000 (Microsoft Inc., USA), and Origin® 7.0 from Origin Lab Corporation (Redwood City, MA, USA).

4.3. Isothermal Titration Calorimetry (ITC)

A Microcal VP-ITC microcalorimeter (MicroCal, LLC, Northampton, MA, USA) was used to carry out the calorimetric experiments. Experimental parameters for titration experiments were: number of injections 34, cell temperature $30\text{ }^\circ\text{C}$, stirring speed 290 rpm, cell volume 1.43 mL, injection volume $8\text{ }\mu\text{L}$, injection duration 16 s, spacing 300 s and filter speed 2 s and reference power $10\text{ }\mu\text{cal s}^{-1}$.

4.4. Zeta Potential Measurement

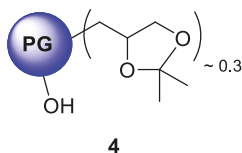
Zeta potential measurement were carried out on a Zetasizer Nano ZS analyzer with integrated 4 mW He-Ne laser, $\lambda = 633\text{ nm}$ (Malvern Instruments Ltd., Malvern, UK). Doppler anemometry

technique was used whereby electric field was applied across the sample solution. All measurements were carried out at 25 °C using folded capillary cells (DTS 1060). The medium was PBS (pH 7.4) and particle concentration used was 2 mg/mL.

4.5. Fluorescence Spectroscopic Studies

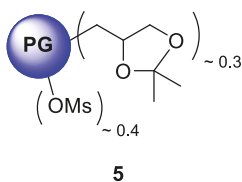
Fluorescence emission spectra were taken with a FP—6500 spectrofluorometer (Jasco, Deutschland, Pfungstadt, Germany) equipped with a thermostated cell holder, a DC-powered 150 W xenon lamp, a R 928 photomultiplier and a versatile slit system. For polymer-BSA interaction studies, emission spectra were recorded in from 300 nm to 440 nm after excitation at 295 nm. Both excitation and emission slits were set at 5 nm. The sample solutions used for fluorescence measurement were stirred thoroughly by using a laboratory vortex shaker and incubated for at least half an hour at 25 °C before measuring the fluorescence. All measurements were carried out at 25 °C.

4.6. Synthesis of Core-Functionalized Polyglycerolamine; Ketalization of PG: Protection of Terminal Diols 4



Ketalization of PG has been done following the already published procedure [22]. To a mixture of PG (10.0 g, 40.54 mmol of diol units, 1.0 eq.) and 0.4 mol (10.0 eq.) of acetone dimethyl acetal, 0.77 g (10 mol%) of PTSA was added. The reaction was allowed to run overnight under r.t. The crude product was diluted in chloroform and then extracted three times with saturated Na₂CO₃ solution to remove the remaining PTSA. The organic phase was dried over MgSO₄. Dialysis in chloroform for 48 h was carried out to remove the traces of dimethylacetal and PTSA. The purified product was dried under vacuum to yield the polyketal as viscous, yellowish, transparent oil in 93% yield. Conversion: quant. (all hPG diols, 30% of total hydroxyl groups were converted). ¹H-NMR (500 MHz, CDCl₃): δ (ppm) = 1.17 (s, CCH₃, ketal), 1.20 (s, CCH₃, ketal), 3.28–4.06 (PG-backbone); ¹³C-NMR: (CDCl₃): δ (ppm) = 26.1 (C-CH₃, ketal), 27.6 (C-CH₃, ketal), 64.2–80.1 (m, PG-backbone), 109 (C-CH₃, ketal); IR (KBr) $\bar{\nu}$ = 3440, 2980 (ketal; CH₃), 2920, 2865, 1210 cm⁻¹.

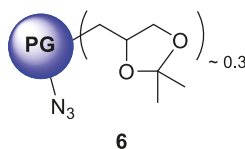
4.7. Mesylation of Ketal Protected PG 5



This reaction was carried out under an inert gas atmosphere and exclusion of water. Ketal protected PG (7.0 g, 32.7 mmol OH-groups, 1.0 eq.) in a three-necked 250 mL flask equipped with a drop funnel, thermometer and magnetic stirrer was dissolved in abs. pyridine (50 mL). The solution was cooled down to 0 °C by means of ice/NaCl bath and a solution of MsCl (3.0 mL, 4.5 g, 39.26 mmol, 1.2 eq.) in abs. pyridine (20 mL) was added drop-wise so that the temperature did not exceed 5 °C. The brown mixture was stirred for 16 h in the thawing ice bath. In case of full functionalization, after the reaction period, ice was added to the reaction mixture on which a dark brown solid precipitated, which was, after decantation of the liquid phase, washed with H₂O, dissolved and

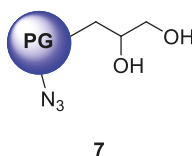
dialyzed in chloroform to give a brown honey-like product in 87% yield. Conversion: quant. $^1\text{H-NMR}$ (500 MHz, CDCl_3): δ (ppm) = 1.19 (s, CCH_3 , ketal), 1.22 (s, CCH_3 , ketal), 3.13 (bs, $-\text{CH}_3$), 3.28–4.26 (PG-backbone); $^{13}\text{C-NMR}$: (CDCl_3): δ (ppm) = 27.1 (C-CH_3 , ketal), 29.6 (C-CH_3 , ketal), 35.3 (CH_3), 64.2–82.1 (m, PG-backbone), 105 (C-CH_3 , ketal); IR (KBr) $\bar{\nu}$ = 3040, 2980 (ketal; CH_3), 2932, 2918, 2869, 2350, 1709, 1450, 1201 cm^{-1} .

4.8. Procedure for the Synthesis of Ketal Protected Polyglycerolazide 6



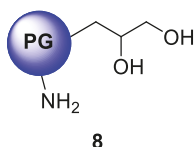
In a 250 mL one-necked flask with reflux condenser and magnetic stirrer was dissolved ketal protected *O*-mesylpolyglycerol (6.0 g, 18.06 mmol OMs-group, 1.0 eq.) in p.a. DMF. After complete dissolution of the mesylated derivative, NaN_3 (5.87 g, 90.32 mmol, 5.0 eq.) was added to the flask and the resulting suspension was heated at 60 °C for 3 days behind a transparent security wall. After cooling, filtration delivered a bright yellow filtrate and a white residue of excess NaN_3 . The filtrate was concentrated in vacuo at temperature below 40 °C and only handled with plastic spatula to avoid explosive degradation of polyazide. In case of complete functionalization, the residue was dissolved in CHCl_3 and extracted four times with water. The organic phase was dried over MgSO_4 and concentrated in vacuo. Further dialysis in CHCl_3 was carried out for 24 h to remove traces of DMF from the crude product. Extensive dialysis in CHCl_3 for 24–48 h was carried out to yield polyglycerolazide as brown-paste like compound. Yield: 75%; Conversion: quant. $^1\text{H-NMR}$ (500 MHz, CDCl_3): δ (ppm) = 1.18 (s, CCH_3 , ketal), 1.20 (s, CCH_3 , ketal), 3.41–4.26 (PG-backbone); $^{13}\text{C-NMR}$: (CDCl_3): δ (ppm) = 25.1 (C-CH_3 , ketal), 26.6 (C-CH_3 , ketal), 65.5–80.1 (m, PG-backbone), 107 (C-CH_3 , ketal); IR (KBr) $\bar{\nu}$ = 2976 (ketal; CH_3), 2870, 2350, 2101 (N_3), 1465, 1234 cm^{-1} .

4.9. Deprotection of Ketal Protected Polyglycerol Azide 7

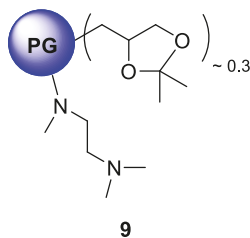


To a solution of ketal protected polyglycerolazide (1.77 g) in 25 mL MeOH, 2.0 g of Dowex-500 resin was added after activation. The mixture was stirred and heated at reflux for 18 h. The crude product was filtered, and the filtrate was concentrated, dried under vacuum and subjected to MeOH dialysis overnight. Yield: 70%; Conversion: quant. $^1\text{H-NMR}$ (500 MHz, CDCl_3): δ (ppm) = 1.81 (PG-starter), 3.41–4.26 (PG-backbone); $^{13}\text{C-NMR}$: (CDCl_3): 50.1 (functionalized primary PG-groups) 65.5–80.1 (m, PG-backbone); IR (KBr) $\bar{\nu}$ = 3300, 2802, 2365, 2101 (N_3), 1234 cm^{-1} .

4.10. Synthesis of Core-Functionalized Polyglycerolamine 8

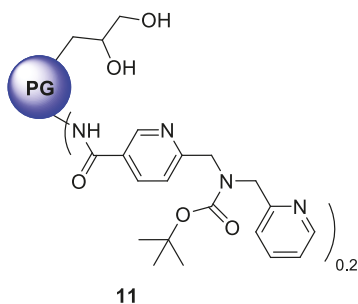


Deprotected polyglycerolazide (1.89 g, 7.79 mmol N_3 group, 1.0 eq.) was dissolved in p.a THF (40 mL) in 250 mL one-necked flask. H_2O (10 mL) and PPh_3 (2.04 g, 7.79 mmol, 1.0 eq.) were added and N_2 formation was observed. Volume of water was increased gradually by dropwise addition of water (30 mL) through a drop funnel to avoid precipitation of the partially reduced product. The reaction was continued until the azide signal at 2100 cm^{-1} is completely diminished. In most of the cases, depending on the level of functionalization of PG core, the complete reduction of N_3 to NH_2 group required 5 to 7 days. After that, the mixture was concentrated to in vacuo to smaller volume, $CHCl_3$ was added and the phases were separated using a separation funnel. The aqueous layer was extracted with $CHCl_3$ four times and then concentrated to dryness to deliver a brown honey-like product, which was dialyzed in MeOH. The purified product was not completely dried off MeOH, and stored under inert gas to avoid potential cross-linking. Yield: 65%; Conversion: quant.; 1H -NMR (500 MHz, CD_3OD): δ (ppm) = 4.01–3.25 (PG), 2.86–2.73 (m, broad, NH_2 functionalized-PG groups), 0.92 (PG-starter); ^{13}C -NMR: (CD_3OD): 58.3 (functionalized primary PG-groups) 67.5–76.1 (m, PG-backbone); IR (KBr) $\bar{\nu}$ = 3441, 2872, 1455, 1208, 1104 cm^{-1} .

4.11. Core Functionalization of PG Acetal with N^1,N^1,N^2 -Trimethylethane-1,2-Diamine 9

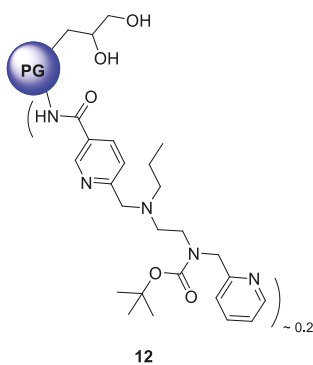
In a sealed tube, mesylated PG acetal (1.0 g, 2.10 mmol OMs group, 1.0 eq.) was dissolved in 10 mL of p.a. DMF. N^1,N^1,N^2 -trimethylethane-1,2-diamine (0.858 g, 8.40 mmol, 4.0 eq., 1.1 mL) was added slowly at RT and the resulting solution was heated at $120\text{ }^\circ C$ for 4 days. At the end of the reaction, the tube was cooled to RT and DMF was removed by cryo-distillation. The residue was dissolved and dialyzed in MeOH for 48 h to give the dark brown honey-like product. Yield: 64%; Conversion: quant (all hPG diols, 30% of total hydroxyl groups were converted); 1H -NMR (500 MHz, CD_3OD): δ (ppm) = 4.25–3.54 (PG-groups), 2.41–2.34 (d, broad, $-N-(CH_3)_2$), 1.41–1.35 (d, broad, $-CH_3$); ^{13}C -NMR: (CD_3OD): δ (ppm) = 112.4 (C- CH_3 , ketal), 80.1–64.3 (PG-backbone), 48.6–43.3 ($-N-CH_3$), 45.3–40.2 ($-N-(CH_3)_2$), 28.2 (C- CH_3 , ketal), 25.4 (C- CH_3 , ketal); IR (KBr) $\bar{\nu}$ = 3142, 2975 (ketal; CH_3), 2892, 2865, 1680, 1354, 1210 cm^{-1} .

4.12. Procedure for the Synthesis of PG-cNH₂ Containing 6-((*tert*-butoxycarbonyl(pyridin-2-ylmethyl)-amino)methyl)nicotinic Acid **11**



6-((*tert*-Butoxycarbonyl(pyridin-2-ylmethyl)amino)methyl)nicotinic acid (NF 135) (0.029 g, 0.087 mmol, 1.0 eq.) was dissolved in 3 mL p.a. DMF in a one necked 10 mL round-bottomed flask. To the resulting solution, EDCI (0.018 g, 0.096 mmol, 1.1 eq.) and catalytic amount of DMAP (0.001 mmol, 1 mol%) was added while stirring at 0 °C. After 15 min, a solution of PG-cNH₂ (0.1 g, 0.43 mmol NH₂ group, 20% of which will be functionalized with nicotinic acid moiety) in 1 mL p.a. DMF was added drop-wise to the reaction mixture for 30 min. The reaction was allowed to run for 24 h and the temperature was allowed to rise from 0 °C to r.t. The solvent was evaporated and the product was dialyzed in MeOH for 24 h. Yield: 72%; Conversion: quant.; ¹H-NMR (500 MHz, CD₃OD): δ (ppm) = 8.41 (1H, aromatic), 7.92–7.70 (3H, aromatic), 7.23–7.51 (3H, aromatic), 4.72–4.51 (functionalized primary PG-groups), 4.20–3.43 (PG-backbone), 2.53–2.22 (4H, -CH₂-), 1.37 (3H, CH₃) ¹³C-NMR: (CD₃OD): δ (ppm) = 169.2, 150.4, 148.6, 131.8, 119.6, 128.6, 75.1, 29.3; IR (KBr) $\bar{\nu}$ = 3564, 3121, 3002, 1745, 1645, 1599, 1409, 1326, 1089 cm⁻¹.

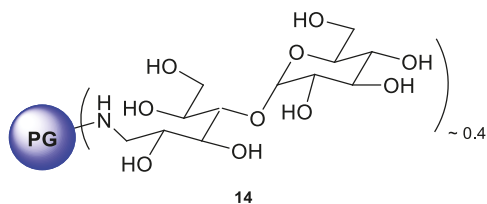
4.13. Procedure for the Synthesis of PG-cNH₂ Containing 6-(((2-*tert*-butoxycarbonyl(pyridin-2-ylmethyl)-amino)ethyl)(propyl)amino)methyl)nicotinic Acid **12**



6-(((2-*tert*-Butoxycarbonyl(pyridin-2-ylmethyl)amino)ethyl)(propyl)amino)methyl)nicotinic acid (KR 455), (0.050 g, 0.117 mmol, 1.0 eq.) was dissolved in 3 mL p.a. DMF in a one necked 10 mL round-bottomed flask. To the resulting solution, EDCI (0.025 g, 0.128 mmol, 1.1 eq.) and catalytic amount of DMAP (0.001 mmol, 1 mol%) was added while stirring at 0 °C. After 15 min, a solution of PG-cNH₂ (0.027 g, 0.117 mmol NH₂ group) in 1 mL p.a. DMF was added drop-wise to the reaction mixture for 30 min. The reaction was allowed to run for 24 h and the temperature was allowed to rise from 0 °C to r.t. The solvent was evaporated and the product was dialyzed in MeOH for 24 h. Yield:

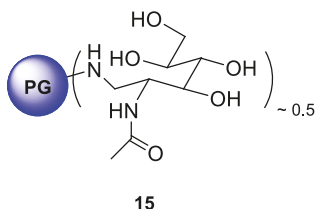
76%; Conversion: quant.; $^1\text{H-NMR}$ (500 MHz, CD_3OD): δ (ppm) = 8.77 (bs, 1H, aromatic), 8.43–8.11 (bs, 3H, aromatic), 7.78–7.62 (bs, 4H, aromatic), 7.12–6.91 (bs, 3H, aromatic), 4.51 (- $\text{CH}_2\text{-NHCO-}$), 4.01–3.34 (PG-backbone), 2.45–2.15 (- $\text{CH}_2\text{-NCH}_2\text{-CH}_2\text{-}$), 1.41–1.45 (bs, - CH_2 + CH_3 -, BOC), 0.84 (- CH_3) $^{13}\text{C-NMR}$: (CD_3OD): δ (ppm) = 167.1, 157.4, 153.5, 139.6, 127.8, 124.3, 79.4, 25.6; IR (KBr) $\bar{\nu}$ = 3363, 3065, 3027, 2878, 1698, 1543, 1435, 1276, 1121, 855 cm^{-1} . [An equivalent of 25% of all PG amino groups in the core were targeted, the functionalization ended up at ~20% after the reaction].

4.14. Procedure for the Synthesis of Maltose Modified PG Amine 14

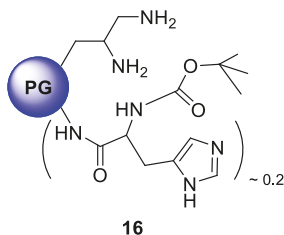


PG amine (0.25 g, 3.419 mmol NH_2 group), D-(+)-maltose monohydrate (12.319 g, 34.189 mmol, 10.0 eq.), and borane-pyridine complex (4.30 mL, 3.177 g, 34.189 mmol, 10 eq., 8 M solution) were dissolved in sodium borate buffer (40.0 mL, 0.1 M) solution. The reaction solution was stirred at 50 °C for 7 d. The crude product was transferred directly to dialysis tube and purified by dialysis towards deionized water for 3 d. Maltose modified PG amine was obtained after freeze drying. Yield: 65% Conversion: 48% of all glycidol units based on anomeric proton at 5.1 ppm. $^1\text{H-NMR}$ (500 MHz, D_2O): δ (ppm) = 5.10–5.33 (bs, 1H, Sugar), 4.42–2.56 (PG-backbone + Sugar); $^{13}\text{C-NMR}$: (D_2O): δ (ppm) = 100.4 (C-1), 81.7 (C-4), 75.8–69.3 (PG-backbone + C-maltose), 62.7–62.2 (6-C), 60.3 (6-C).

4.15. Procedure for the Synthesis of N-Acetylglucosamine Modified PG Amine 15



PG amine (0.25 g, 3.419 mmol NH_2 group), *N*-acetylglucosamine (12.319 g, 34.189 mmol, 10.0 eq.), and borane-pyridine complex (4.30 mL, 3.177 g, 34.189 mmol, 10 eq., 8 M solution) were dissolved in sodium borate buffer (40.0 mL, 0.1 M) solution. The reaction solution was stirred at 50 °C for 7 days. The crude yellow colored solution was transferred directly to dialysis tube and purified by dialysis towards acidified water for 3 days. *N*-acetylglucosamine modified PG amine was obtained after freeze drying. Yield: 58%; Conversion 54% of all glycidol units; $^1\text{H-NMR}$ (500 MHz, D_2O): δ (ppm) = 4.51–3.23 (PG-backbone + hexose unit); 2.23–1.85 (bs, - CH_3 -); $^{13}\text{C-NMR}$: (D_2O): δ (ppm) = 168.7 (C = O), 74.7–60.8 (PG-groups + Sugar unit), 58.7 (C-5), 53.2 (6-C), 48.7 (- $\text{CH}_2\text{NH-}$), 21.9 (- CH_3).

4.16. Procedure for the Synthesis of Polyglycerolamine Containing N- α -BOC-Histidine 16

N- α -BOC histidine (0.035 g, 0.136 mmol, 1.0 eq.) was dissolved in 2 mL p.a. DMF in a one necked 10 mL round-bottomed flask. To the resulting solution, EDCI (0.029 g, 0.150 mmol, 1.1 eq.) and catalytic amount of DMAP (0.001 mmol, 1 mol%) was added while stirring at 0 °C. After 15 min, a solution of PG amine (0.1 g, 0.68 mmol NH₂ group, 20% of which will be functionalized with histidine moiety) in 2 mL p.a. DMF:water (3:1) was added drop-wise to the reaction mixture for 30 min. The reaction was allowed to run for 24 h and the temperature was allowed to rise from 0 °C to r.t. The solvent was evaporated and the product was dialyzed in MeOH for 24 h. Yield: 70%; Conversion: quant. ¹H-NMR (500 MHz, CD₃OD): δ (ppm) = 7.62 (bs, 1H, imidazole ring), 6.91 (bs, 1H, imidazole ring), 4.42–3.97 (functionalized PG-groups), 3.95–3.41 (PG-backbone), 3.07 (bs, 1H, -CH-), 2.88 (2H, -CH₂-), 1.49 (bs, 3H, -CH₃); ¹³C-NMR: (CD₃OD): δ (ppm) = 160.8, 154.6, 143.5, 129.8, 124.3, 29.7; IR (KBr) $\bar{\nu}$ = 2982, 2769, 1745, 1612, 1587, 1523, 1434, 1369, 1275 cm⁻¹.

Author Contributions: R.H. and G.M. conceived the idea, R.H. and M.Q. designed the experiments; M.Q. performed the experiments; R.H., M.Q. analyzed the data; S.F. contributed to cell-based studies; M.Q. and R.H. wrote the paper.

Funding: APC was sponsored by MDPI.

Acknowledgments: We would like to acknowledge the support of Catharina Treiber for the cellular studies. R.H. thanks the German Science Foundation (DFG) for financial support through an Indo-German project. M.Q. is currently supported by NSF Grant No. IIA-1355466 from the North Dakota Established Program to Stimulate Competitive Research (EPSCoR) through the Center for Sustainable Materials Science, and NIH grant number P20 GM109024 (to M.Q.) from the National Institute of General Medicine (NIGMS). Authors would like to acknowledge the support of Kai Licha for providing with cytotoxicity data. We thank and are very grateful to Dr. Wiebke Fischer (Chemie/Biochemie, Freie Universität Berlin, Germany) for her contribution with data and graphical representation.

Conflicts of Interest: The authors declare no conflict of interest.

References

- Kim, B.-E.; Nevitt, T.; Thiele, D.J. Mechanism for copper acquisition, distribution and regulation. *Nat. Chem. Biol.* **2008**, *4*, 176–185. [[CrossRef](#)] [[PubMed](#)]
- Ponka, P. Hereditary causes of disturbed iron homeostasis in the central nervous system. *Ann. N. Y. Acad. Sci.* **2004**, *1012*, 267–281. [[CrossRef](#)] [[PubMed](#)]
- Waggoner, D.J.; Bartnikas, T.B.; Gitlin, J.D. The role of copper in neurodegenerative disease. *Neurobiol. Dis.* **1999**, *6*, 221–230. [[CrossRef](#)] [[PubMed](#)]
- de Bie, P.; Muller, P.; Wijmenga, C.; Klomp, L.W. Molecular pathogenesis of wilson and menkes disease: Correlation of mutations with molecular defects and disease phenotypes. *J. Med. Genet.* **2007**, *44*, 673–688. [[CrossRef](#)] [[PubMed](#)]
- Adlard, P.A.; Bush, A.I. Metals in alzheimer's disease. *J. Alzheimer's Dis.* **2006**, *10*, 145–163. [[CrossRef](#)]

6. Kessler, H.; Bayer, T.A.; Bach, D.; Schneider-Axmann, T.; Supprian, T.; Herrmann, W.; Haber, M.; Multhaup, G.; Falkai, P.; Pajonk, F.G. Intake of copper has no effect on cognition in patients with mild alzheimer's disease: A pilot phase 2 clinical trial. *J. Neural Transm.* **2008**, *115*, 1181–1187. [[CrossRef](#)] [[PubMed](#)]
7. Phinney, A.L.; Drisaldi, B.; Schmidt, S.D.; Lugowski, S.; Coronado, V.; Liang, Y.; Horne, P.; Yang, J.; Sekoulidis, J.; Coomaraswamy, J.; et al. In vivo reduction of amyloid-beta by a mutant copper transporter. *Proc. Natl. Acad. Sci.* **2003**, *100*, 14193–14198. [[CrossRef](#)] [[PubMed](#)]
8. Adlard, P.A.; Cherny, R.A.; Finkelstein, D.I.; Gautier, E.; Robb, E.; Cortes, M.; Volitakis, I.; Liu, X.; Smith, J.P.; Perez, K.; et al. Rapid restoration of cognition in alzheimer's transgenic mice with 8-hydroxy quinoline analogs is associated with decreased interstitial abeta. *Neuron* **2008**, *59*, 43–55. [[CrossRef](#)] [[PubMed](#)]
9. Filomeni, G.; Cerchiaro, G.; Da Costa Ferreira, A.M.; De Martino, A.; Pedersen, J.Z.; Rotilio, G.; Ciriolo, M.R. Pro-apoptotic activity of novel isatin-schiff base copper(ii) complexes depends on oxidative stress induction and organelle-selective damage. *J. Biol. Chem.* **2007**, *282*, 12010–12021. [[CrossRef](#)] [[PubMed](#)]
10. Lee, J.Y.; Friedman, J.E.; Angel, I.; Kozak, A.; Koh, J.Y. The lipophilic metal chelator dp-109 reduces amyloid pathology in brains of human beta-amyloid precursor protein transgenic mice. *Neurobiol. Aging* **2004**, *25*, 1315–1321. [[CrossRef](#)] [[PubMed](#)]
11. Treiber, C.; Simons, A.; Strauss, M.; Hafner, M.; Cappai, R.; Bayer, T.A.; Multhaup, G. Clioquinol mediates copper uptake and counteracts copper efflux activities of the amyloid precursor protein of alzheimer's disease. *J. Biol. Chem.* **2004**, *279*, 51958–51964. [[CrossRef](#)] [[PubMed](#)]
12. Albrecht, R.; Fehse, S.; Pant, K.; Nowag, S.; Stephan, H.; Haag, R.; Tzschucke, C.C. Polyglycerol-based copper chelators for the transport and release of copper ions in biological environments. *Macromol. Biosci.* **2016**, *16*, 412–419. [[CrossRef](#)] [[PubMed](#)]
13. Fehse, S.; Nowag, S.; Quadir, M.; Kim, K.S.; Haag, R.; Multhaup, G. Copper transport mediated by nanocarrier systems in a blood-brain barrier in vitro model. *Biomacromolecules* **2014**, *15*, 1910–1919. [[CrossRef](#)] [[PubMed](#)]
14. Nowag, S.; Frangville, C.; Multhaup, G.; Marty, J.-D.; Mingotaud, C.; Haag, R. Biocompatible, hyperbranched nanocarriers for the transport and release of copper ions. *J. Mater. Chem. B* **2014**, *2*, 3915–3918. [[CrossRef](#)]
15. Roller, S.; Zhou, H.; Haag, R. High-loading polyglycerol supported reagents for mitsunobu- and acylation-reaction and other polyglycerol derivatives. *Mol. Divers.* **2005**, *9*, 305–316. [[CrossRef](#)] [[PubMed](#)]
16. Wooley, K.L.; Fréchet, J.M.J.; Hawker, C.J. Influence of shape on the reactivity and properties of dendritic, hyperbranched and linear aromatic polyesters. *Polymer* **1994**, *35*, 4489–4495. [[CrossRef](#)]
17. Hawker, C.J.; Malmström, E.; Frank, C.W.; Kampf, J.P. Exact linear analogs of dendritic polyether macromolecules: design, synthesis, and unique properties. *J. Am. Chem. Soc.* **1997**, *119*, 9903–9904. [[CrossRef](#)]
18. Mourey, T.H.; Turner, S.R.; Rubinstein, M.; Fréchet, J.M.J.; Hawker, C.J.; Wooley, K.L. Unique behavior of dendritic macromolecules: intrinsic viscosity of polyether dendrimers. *Macromolecules* **1992**, *25*, 2401–2406. [[CrossRef](#)]
19. Wooley, K.L.; Hawker, C.J.; Pochan, J.M.; Fréchet, J.M.J. Physical properties of dendritic macromolecules: a study of glass transition temperature. *Macromolecules* **1993**, *26*, 1514–1519. [[CrossRef](#)]
20. Hawker, C.J.; Farrington, P.J.; Mackay, M.E.; Wooley, K.L.; Fréchet, J.M.J. Molecular ball bearings: the unusual melt viscosity behavior of dendritic macromolecules. *J. Am. Chem. Soc.* **1995**, *117*, 4409–4410. [[CrossRef](#)]
21. Grayson, S.M.; Fréchet, J.M.J. Convergent dendrons and dendrimers: from synthesis to applications. *Chem. Rev.* **2001**, *101*, 3819–3867. [[CrossRef](#)] [[PubMed](#)]
22. Haag, R.; Stumbé, J.-F.; Sunder, A.; Frey, H.; Hebel, A. An approach to core—Shell-type architectures in hyperbranched polyglycerols by selective chemical differentiation. *Macromolecules* **2000**, *33*, 8158–8166. [[CrossRef](#)]
23. Frey, H.; Haag, R. Dendritic polyglycerol: A new versatile biocompatible-material. *J. Biotechnol.* **2002**, *90*, 257–267. [[CrossRef](#)]
24. Kurniasih, I.N.; Liang, H.; Kumar, S.; Mohr, A.; Sharma, S.K.; Rabe, J.P.; Haag, R. A bifunctional nanocarrier based on amphiphilic hyperbranched polyglycerol derivatives. *J. Mater. Chem. B* **2013**, *1*, 3569–3577. [[CrossRef](#)]
25. Hanselmann, R.; Hölter, D.; Frey, H. Hyperbranched polymers prepared via the core-dilution/slow addition technique: computer simulation of molecular weight distribution and degree of branching. *Macromolecules* **1998**, *31*, 3790–3801. [[CrossRef](#)]

26. Bröhmer, M.C.; Bannawarth, W. Forced complexation of nitrogen leading to a weakening of amide bonds: Application to a new linker for solid-phase chemistry. *Eur. J. Org. Chem* **2008**, *2008*, 4412–4415. [[CrossRef](#)]
27. Sayre, L.M. Metal ion catalysis of amide hydrolysis. *J. Am. Chem. Soc.* **1986**, *108*, 1632–1635. [[CrossRef](#)]
28. Polzin, G.M.; Burstyn, J.N. Synthetic Cu(II) and Ni(II) peptidases. *Met. Ions Biol. Syst.* **2001**, *38*, 103–144. [[PubMed](#)]
29. Grant, K.B.; Kassari, M. Major advances in the hydrolysis of peptides and proteins by metal ions and complexes. *Curr. Org. Chem.* **2006**, *10*, 1035–1049. [[CrossRef](#)]
30. Bhadra, D.; Yadav, A.K.; Bhadra, S.; Jain, N.K. Glycodendrimeric nanoparticulate carriers of primaquine phosphate for liver targeting. *Int. J. Pharm.* **2005**, *295*, 221–233. [[CrossRef](#)] [[PubMed](#)]
31. Dutta, T.; Jain, N.K. Targeting potential and anti-HIV activity of lamivudine loaded mannosylated poly (propyleneimine) dendrimer. *Biochim. Biophys. Acta* **2007**, *1770*, 681–686. [[CrossRef](#)] [[PubMed](#)]
32. Kumar, P.V.; Asthana, A.; Dutta, T.; Jain, N.K. Intracellular macrophage uptake of rifampicin loaded mannosylated dendrimers. *J. Drug Target.* **2006**, *14*, 546–556. [[CrossRef](#)] [[PubMed](#)]
33. Arima, H.; Chihara, Y.; Arizono, M.; Yamashita, S.; Wada, K.; Hirayama, F.; Uekama, K. Enhancement of gene transfer activity mediated by mannosylated dendrimer/ α -cyclodextrin conjugate (generation 3, G3). *J. Control. Release* **2006**, *116*, 64–74. [[CrossRef](#)] [[PubMed](#)]
34. Kunath, K.; von Harpe, A.; Fischer, D.; Kissel, T. Galactose-PEI-DNA complexes for targeted gene delivery: degree of substitution affects complex size and transfection efficiency. *J. Control. Release* **2003**, *88*, 159–172. [[CrossRef](#)]
35. Baek, M.-K.; Roy, R. Synthesis and protein binding properties of T-antigen containing GlycoPAMAM dendrimers. *Bioorg. Med. Chem.* **2002**, *10*, 11–17. [[CrossRef](#)]
36. Kensinger, R.D.; Yowler, B.C.; Benesi, A.J.; Schengrund, C.-L. Synthesis of novel, multivalent glycodendrimers as ligands for HIV-1 gp120. *Bioconjug. Chem.* **2004**, *15*, 349–358. [[CrossRef](#)] [[PubMed](#)]
37. Köhn, M.; Benito, J.; Mellet, C.O.; Lindhorst, T.K.; Fernández, J.M.G. Functional Evaluation of Carbohydrate-Centred Glycoclusters by Enzyme-Linked Lectin Assay: Ligands for Concanavalin A. *ChemBioChem* **2004**, *5*, 771–777. [[CrossRef](#)] [[PubMed](#)]
38. Mangold, S.L.; Cloninger, M. Maximising multivalency effects in protein–Carbohydrate interactions. *Org. Biomol. Chem.* **2006**, *4*, 2458–2465. [[CrossRef](#)] [[PubMed](#)]
39. Marotte, K.; Preville, C.; Sabin, C.; Moume-Pymbock, M.; Imberty, A.; Roy, R. Synthesis and binding properties of divalent and trivalent clusters of the Lewis a disaccharide moiety to *Pseudomonas aeruginosa* lectin PA-III. *Org. Biomol. Chem.* **2007**, *5*, 2953–2961. [[CrossRef](#)] [[PubMed](#)]
40. Woller, E.K.; Walter, E.D.; Morgan, J.R.; Singel, D.J.; Cloninger, M.J. Altering the strength of lectin binding interactions and controlling the amount of lectin clustering using mannose/hydroxyl-functionalized dendrimers. *J. Am. Chem. Soc.* **2003**, *125*, 8820–8826. [[CrossRef](#)] [[PubMed](#)]
41. Quadir, M.A.; Radowski, M.R.; Kratz, F.; Licha, K.; Hauff, P.; Haag, R. Dendritic multishell architectures for drug and dye transport. *J. Control. Release* **2008**, *132*, 289–294. [[CrossRef](#)] [[PubMed](#)]
42. Appelhans, D.; Komber, H.; Kirchner, R.; Seidel, J.; Huang, C.-H.; Voigt, D.; Kuckling, D.; Chang, F.-C.; Voit, B. Polypeptide-Shelled Poly (propylene imine) Dendrimers and Their Complexing Properties towards Copper (II) Ions. *Macromol. Rapid Commun.* **2005**, *26*, 586–593. [[CrossRef](#)]
43. Baigude, H.; Katsuraya, K.; Okuyama, K.; Yachi, Y.; Sato, S.; Uryu, T. Synthesis of dicarboxylate oligosaccharide multilayer terminal functionality upon poly (lysine) dendrimer scaffolding. *J. Polym. Sci. Part A Polym. Chem.* **2002**, *40*, 3622–3633. [[CrossRef](#)]
44. Klajnert, B.; Appelhans, D.; Komber, H.; Morgner, N.; Schwarz, S.; Richter, S.; Brutschy, B.; Ionov, M.; Tonkikh, A.K.; Bryszewska, M.; et al. The influence of densely organized maltose shells on the biological properties of poly (propylene imine) dendrimers: new effects dependent on hydrogen bonding. *Chem. Eur. J.* **2008**, *14*, 7030–7041. [[CrossRef](#)] [[PubMed](#)]
45. Butt, A.M.; Jones, H.C. Effect of histamine and antagonists on electrical resistance across the blood-brain barrier in rat brain-surface microvessels. *Brain Res.* **1992**, *569*, 100–105. [[CrossRef](#)]
46. Pardridge, W.M. Transport of small molecules through the blood-brain barrier: Biology and methodology. *Adv. Drug Deliv. Rev.* **1995**, *15*, 5–36. [[CrossRef](#)]
47. Yamakami, J.; Sakurai, E.; Sakurada, T.; Maeda, K.; Hikichi, N. Stereoselective blood-brain barrier transport of histidine in rats. *Brain Res.* **1998**, *812*, 105–112. [[CrossRef](#)]

48. Brackman, W.; Gaasbeek, C.J. Spectra and equilibria of some complexes containing the Cu^{2+} (phen)₂ group. *J. Inorg. Nucl. Chem.* **1965**, *27*, 1793–1804. [[CrossRef](#)]
49. Faye, G.H. The correlation of absorption spectra and structure of pseudo-octahedral and trigonal bipyramidal copper (II)-1,10-phenanthroline complexes in acetone solutions. *Can. J. Chem.* **1966**, *44*, 2165–2171. [[CrossRef](#)]
50. James, B.R.; Parris, M.; Williams, R.J.P. Spectrophotometric and thermodynamic properties of some copper and iron complexes. *J. Chem. Soc.* **1961**, 4630–4637. [[CrossRef](#)]
51. Jorgensen, C.K. Comparative crystal field studies of some ligands and the lowest singlet state of paramagnetic nickel(II) complexes. *Acta Chem. Scand.* **1955**, *9*, 1362–1377. [[CrossRef](#)]
52. Zhao, M.; Sun, L.; Crooks, R.M. Preparation of Cu nanoclusters within dendrimer templates. *J. Am. Chem. Soc.* **1998**, *120*, 4877–4878. [[CrossRef](#)]
53. Esumi, K.; Suzuki, A.; Aihara, N.; Usui, K.; Torigoe, K. Preparation of gold colloids with UV irradiation using dendrimers as stabilizer. *Langmuir* **1998**, *14*, 3157–3159. [[CrossRef](#)]
54. Crooks, R.M.; Zhao, M.; Sun, L.; Chechik, V.; Yeung, L.K. Dendrimer-encapsulated metal nanoparticles: Synthesis, characterization, and applications to catalysis. *Acc. Chem. Res.* **2001**, *34*, 181–190. [[CrossRef](#)] [[PubMed](#)]
55. Krämer, M.; Perignon, N.; Haag, R.; Marty, J.-D.; Thomann, R.; Lauth-de Viguierie, N.; Mingotaud, C. Water-soluble dendritic architectures with carbohydrate shells for the templation and stabilization of catalytically active metal nanoparticles. *Macromolecules* **2005**, *38*, 8308–8315. [[CrossRef](#)]
56. Appelhans, D.; Komber, H.; Quadir, M.A.; Richter, S.; Schwarz, S.; van der Vlist, J.; Aigner, A.; Müller, M.; Loos, K.; Seidel, J.; et al. Hyperbranched pei with various oligosaccharide architectures: Synthesis, characterization, atp complexation, and cellular uptake properties. *Biomacromolecules* **2009**, *10*, 1114–1124. [[CrossRef](#)] [[PubMed](#)]
57. Klajnert, B.; Bryszewska, M. Dendrimers: Properties and applications. *Acta Biochim. Pol.* **2001**, *48*, 199–208. [[PubMed](#)]
58. Lakowicz, J.R. *Principles of Fluorescence Spectroscopy*, 2nd ed.; Kluwer Academic/Plenum Publishers: New York, NY, USA, 1999; pp. 238–255.
59. Eftink, M.J. Fluorescence quenching reactions: Probing biological macromolecular structures. In *Biophysical and Biochemical Aspects of Fluorescence Spectroscopy*; Dewey, T.G., Ed.; Plenum Press: New York, NY, USA, 1991; pp. 1–41.
60. Stern, O.; Volmer, M. Über die abklingzeit der fluoreszenz. *Phys. Z.* **1919**, *20*, 183–188.
61. Cram, D.J.; Choi, H.J.; Bryant, J.A.; Knobler, C.B. Host-guest complexation. 62. Solvophobic and entropic driving forces for forming velcraplexes, which are 4-fold, lock-key dimers in organic media. *J. Am. Chem. Soc.* **1992**, *114*, 7748–7765. [[CrossRef](#)]
62. Meissner, R.; Garcias, X.; Mecozzi, S.; Rebek, J.J. Synthesis and assembly of new molecular hosts: Solvation and the energetics of encapsulation. *J. Am. Chem. Soc.* **1997**, *119*, 77–85. [[CrossRef](#)]
63. Peschke, W.; Schmidtchen, F.P. Incremental rigidification of a foldable anion host: Does it help in guest binding? *Tetrahedron Lett.* **1995**, *36*, 5155–5158. [[CrossRef](#)]
64. Berger, M.; Schmidtchen, F.P. The binding of sulfate anions by guanidinium receptors is entropy-driven. *Angew. Chem. Int. Ed.* **1998**, *37*, 2694–2696. [[CrossRef](#)]
65. Schneider, H.J. Binding mechanisms in supramolecular complexes. *Angew. Chem. Int. Ed.* **2009**, *48*, 3924–3977. [[CrossRef](#)] [[PubMed](#)]

Sample Availability: Samples of the compounds can be made available upon re-synthesis.



© 2018 by the authors. Licensee MDPI, Basel, Switzerland. This article is an open access article distributed under the terms and conditions of the Creative Commons Attribution (CC BY) license (<http://creativecommons.org/licenses/by/4.0/>).

Article

Effect of Dendrimer Generation and Aglyconic Linkers on the Binding Properties of Mannosylated Dendrimers Prepared by a Combined Convergent and Onion Peel Approach

Celia Sehad ¹, Tze Chieh Shiao ¹, Lamyaa M. Sallam ¹, Abdelkrim Azzouz ¹ and René Roy ^{1,2,*}

¹ Department of Chemistry, University of Québec a Montréal, P.O. Box 8888, Succ. Centre-Ville, Montréal, QC H3C 3P8, Canada; celia_0709@hotmail.fr (C.S.); chichi_shiao@hotmail.com (T.C.S.); lsallam@yahoo.com (L.M.S.); azzouz.a@uqam.ca (A.A.)

² Glycovax Pharma Inc., 424 Guy, Suite 202, Montreal, QC H3J 1S6, Canada

* Correspondence: roy.rene@uqam.ca or rroy@glycovax.com; Tel.: +1-514-987-3000 (ext. 2546)

Academic Editor: Ashok Kakkur

Received: 5 July 2018; Accepted: 25 July 2018; Published: 28 July 2018

Abstract: An efficient study of carbohydrate-protein interactions was achieved using multivalent glycodendrimer library. Different dendrimers with varied peripheral sugar densities and linkers provided an arsenal of potential novel therapeutic agents that could be useful for better specific action and greater binding affinities against their cognate protein receptors. Highly effective click chemistry represents the basic method used for the synthesis of mannosylated dendrimers. To this end, we used propargylated scaffolds of varying sugar densities ranging from 2 to 18 for the attachment of azido mannopyranoside derivatives using copper catalyzed click cycloaddition. Mannopyranosides with short and pegylated aglycones were used to evaluate their effects on the kinetics of binding. The mannosylated dendrons were built using varied scaffolds toward the accelerated and combined “onion peel” strategy. These carbohydrates have been designed to fight *E. coli* urinary infections, by inhibiting the formation of bacterial biofilms, thus neutralizing the adhesion of FimH type 1 lectin present at the tip of their fimbriae against the natural multiantennary oligomannosides of uroplakin 1a receptors expressed on uroepithelial tissues. Preliminary DLS studies of the mannosylated dendrimers to cross-link the leguminous lectin Con A used as a model showed their high potency as candidates to fight the *E. coli* adhesion and biofilm formation.

Keywords: dendrimers; mannose; click chemistry; *E. coli*; UTIs; FimH; DLS

1. Introduction

Modern medicine is exploring several alternative strategies to overcome the impending antibiotic resistance problems. One of these goals is to find new ways to fight bacterial infections. Of particular interest are the recurrent urinary tract infections (UTIs). Half of women are affected by UTIs at least once in their lifetime. Hence, UTIs represent an important public health issue because of their frequent occurrence. UTIs are mostly caused by uropathogenic *Escherichia coli* strains (UPEC) that infest urinary epithelium through their type-1 pili (FimH). At the tips of their pili, *E. coli* possesses a carbohydrate binding domain called FimH that adhere to mannosylated glycoproteins receptors on the urinary epithelial cells [1–3]. In addition, through their quorum sensing molecules, *E. coli* can infest hosts cell and forms resilient biofilms. Once formed, bacteria become mature and readily acquire drugs resistance.

Besides, as the first defense mechanism against this infectious agent, the innate immune system exploits the structures of mannosides [4,5]. On the other hand, fimbriated *E. coli* receptor-binding site

(FimH) consists of a specific mannose-binding pocket, with a tyrosine gate (Tyr48, Tyr137) [6–8] that also recognizes and binds to the mannosides residues of uroplakin-1a, present at the surface of urothelial cells as a premise for bacterial infections causing cystitis and pyelonephritis. Ever since, considerable efforts have been devoted toward the development of new synthetic antiadhesive antagonists that could act as potent competitive inhibitors [9–13]. Since then, synthetic mono-mannopyranosides carrying various aglycones have been reported and their binding to FimH have been fully characterized. Amongst these, heptyl α -D-mannopyranoside (HM) as emerged as one of the strongest monovalent FimH binders described so far [3]. The studies supported that the hydrophobic HM's aglycone strongly interacted via van der Waals contacts and aromatic stacking with the tyrosine gates residues Tyr148 and Tyr137 [2,8,13].

However, monomeric carbohydrate residues interacting with proteins often occur with low-binding affinities [14–16]. Furthermore, multivalent carbohydrate-protein interactions have unequivocally displayed several advantages over monomeric ones, a process commonly used by nature to control a wide variety of cellular processes [17–19]. Hence, several glycodendrimers have been designed to address the issue of low affinity carbohydrate-protein interactions [5,20–27]. Mannosylated glycodendrimers were found to be excellent ligands against the leguminous lectin from *Canavalia ensiformis* (Concanavalin A) and to be excellent ligands toward the fimbriated *E. coli* K12 with nanomolar affinities [21,26,28,29]. Likewise, the glycoside cluster effect helps to enhance avidity, selectivity and affinity of a multivalent glycoside toward a protein that possess multiple carbohydrate recognition domains (CRDs). This phenomenon was characterized by strong stabilization of carbohydrate-protein interactions through macroscopic cross-linking effects [17,19]. Therefore, mannosylated glycodendrimers constitute excellent lead candidates for the treatment of *E. coli* infectious agents by the inhibition of bacterial adhesion and biofilm formation on cell surfaces [5,12,30].

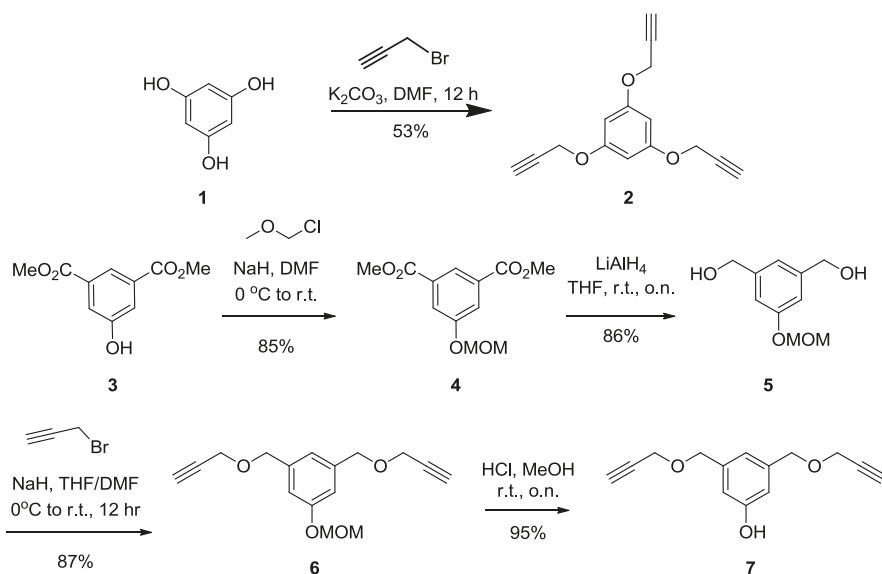
To these aim, a new variety of mannosylated dendrimers of different sugar densities and linker's properties have been developed to prevent infections spreading, by inhibiting *E. coli* adhesion and biofilm formations. Thus, we report herein a new class of glycodendrimers [5,20–22,25,28,31,32] that are built on aromatics, cyclotriphosphazene and pentaerythritol cores using high yielding click chemistry to anchor mannosylated azides onto the above alkyne-functionalized scaffolds. This synthetic strategy provides easy access to biodegradability and biocompatibility to the glycodendrimers. In addition, by using different scaffolds at each layer rather than the identical ones commonly used, we are providing another application of the so called “onion peel” approach. Hence, pegylated tetraethylene glycol spacers have been introduced as aglycones, because of the easy availability, water-solubility, biocompatibility and the variable chain length accessible that should enable good interactions with the multiple FimH binding pili present at the surface of *E. coli*. The relative affinities of the pegylated mannodendrimers were studied using diffraction light scattering measurements (DLS) in the presence of ConA, toward a better understanding of the multivalent binding interactions and the effect of the linkers. Although ConA is a leguminous lectin, it also binds natural multiantennary mannosylated glycosides that can also be advantageously replaced by synthetic monomeric derivatives harboring hydrophobic aglycones. Hence, it constitutes an appropriate model to evaluate the relative propensity of mannosylated dendrimers toward *E. coli* FimH.

2. Results and Discussion

2.1. Scaffold Syntheses

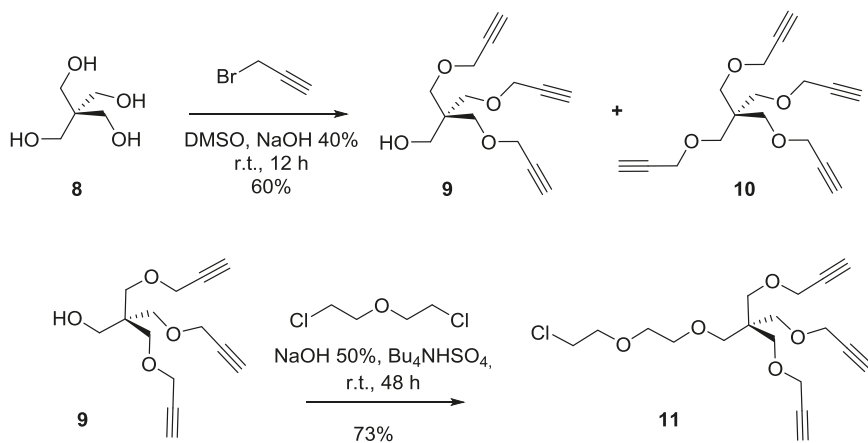
First, the syntheses of different propargylated aromatic scaffolds with valencies of 2 (7) and 3 (2) were achieved in moderate to good yields. Scaffolds 2 and 7 were obtained through propargylation (propargyl bromide, K_2CO_3 , DMF) of polyhydroxylated aromatic cores 1 and 5, respectively. The trimeric phloroglucinol 1 was commercially available and the dimeric compound 5 was synthesized after protection of the hydroxyl group of 5-hydroxy dimethyl isophthalate 3 with a MOM-protecting

group (MOMCl, NaH, DMF, 85%), followed by reduction of the intermediate esters of **4** to afford **5** using LiAlH_4 in 86% yield (Scheme 1).



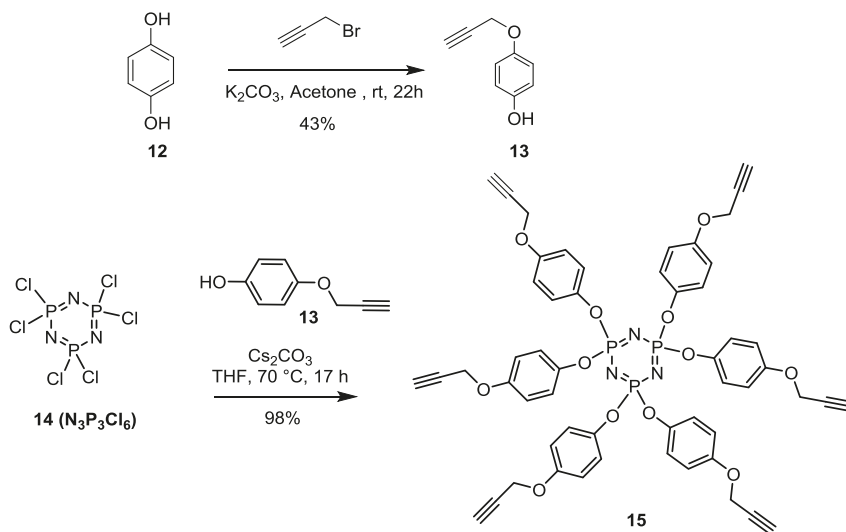
Scheme 1. Synthesis of *tris*-propargylated **2** and *bis*-propargylated **7** aromatic scaffolds.

Pentaerythritol **8** was next chosen as template for the synthesis of the desired *tris*-propargylated core **9** (propargyl bromide, DMSO/NaOH) (Scheme 2). It was accompanied by smaller quantities of the fully tetra-propargylated scaffold **10** which was readily separated by flash chromatography. The reaction mixture gave both **9** and **10** in a 2:1 ratio, respectively. An extended dendron precursor **11** was then obtained from **9** using bis(2-chloroethyl) ether under phase-transfer catalyzed conditions (PTC) (tetrabutylammonium hydrogensulfate (TBAHS), NaOH, r.t.) in 73% yield (Scheme 2).



Scheme 2. Synthesis of a tripropargylated dendron precursor **11** under PTC conditions.

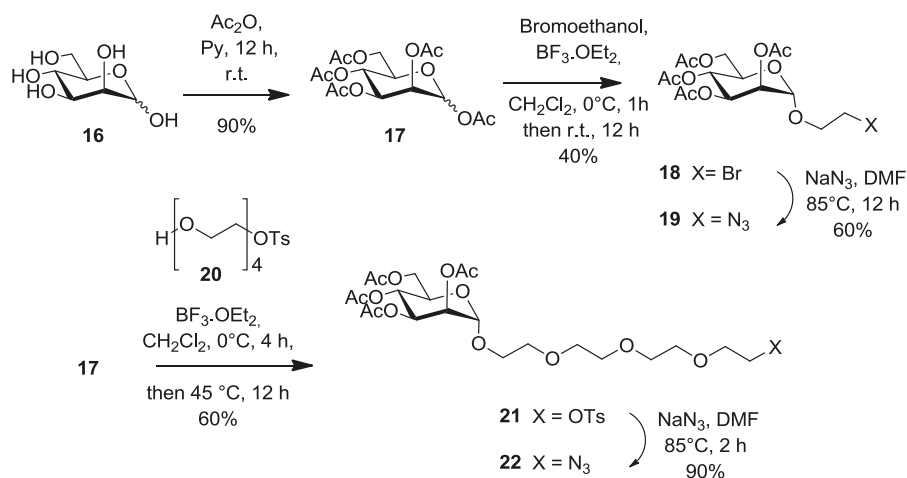
For our next scaffold, harboring six propargylated functionalities, we choose the previously described hexachlorocyclotriphosphazene core **14** ($N_3P_3Cl_6$) [28,33–35]. The choice for this dense hexavalent core was based on previous observations by the Majoral's group who showed that it was biologically favorable over several other scaffolds and that it can readily form dendrimers of very high generation [36–40]. Toward this goal, diol **12** was monopropargylated (propargyl bromide, K_2CO_3 , acetone, r.t., 12 h) to afford **13** (43%) (Scheme 3) which was treated with **14** under basic conditions (Cs_2CO_3 , THF, 70 °C, 17 h) to provide **15** in essentially quantitative yield (98%). The structural integrity of the fully substituted **15** was compared to its known 1H - and ^{31}P -NMR [28].



Scheme 3. Synthesis of a hexa-propargylated cyclotriphosphazene core **15**.

2.2. Sugar Precursors

It is well known that the aglyconic moiety of a given carbohydrate can affect the binding affinity and selectivity with lectins. This effect is achieved by either providing better accessibility of the sugar itself into the deep binding pocket of the lectin (linker effect) or by increasing the binding interactions network between neighboring amino acids (pharmacophore effect). Because of the high number of pili at the surface of *E. coli*, we figured that the linker effect would be a dominant aspect. For comparison purposes, we also built our mannoside residues with a short linker. Thus, known peracetylated mannose **17** was chosen as a starting point after treatment of commercial D-mannose **16** with acetic anhydride in pyridine (Scheme 4). Lewis acid treatment of **17** with bromoethanol in DCM ($BF_3 \cdot Et_2O$, DCM, 40%) provided known 2-bromoethyl α -D-mannopyranoside **18**. Nucleophilic substitution of the bromide by an azide group (NaN_3 , DMF, 85 °C, 12 h) afforded 2-azidoethyl α -D-mannopyranoside **19** in 60% yield. Similarly, using monotosylated tetraethylene glycol as the aglycone (**20**), analogous glycosidation of **17** gave tosylate **21** (60%), followed by displacement with azide to give extended mannoside **22** in 90% yield.



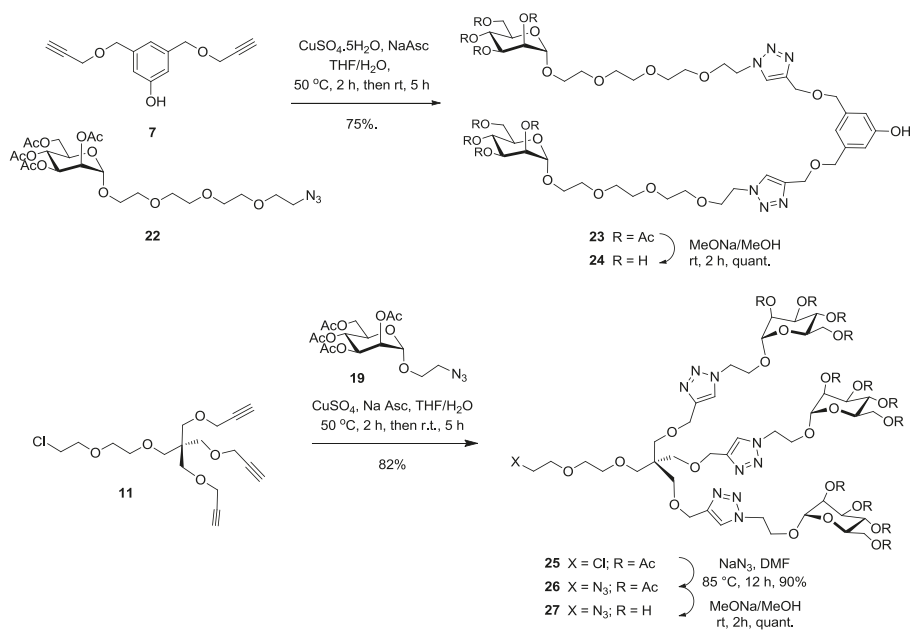
Scheme 4. Synthesis of azido mannoside precursors having a short (**19**) and a long spacer (**22**).

2.3. Glycodendron Syntheses

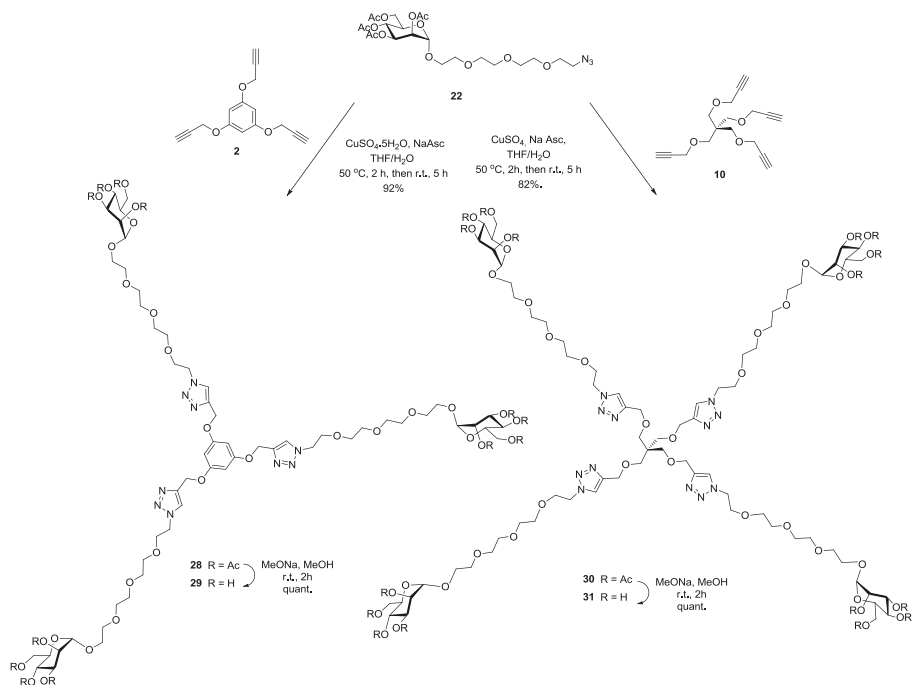
Having the di-(**7**) and tri-propargylated (**11**) scaffolds in hands, together with the two family of short (**19**) and long (**22**) azido mannosides, we were set for the convergent syntheses of our mannosylated dendrons using the efficacious [1,3]-dipolar copper-catalyzed azide-alkyne cycloaddition (CuAAC) (click chemistry) (Scheme 5). We first combined bis-propargylated scaffold **7** with elongated azido mannoside **22** under typical CuAAC conditions to obtain dimer **23** in 75% yield. Alternatively, the tri-mannosylated dendron was accomplished by treating chloride **11** with the short mannoside **19** under the above click conditions to provide dendron **25** (82%) having an orthogonal chloride functionality at the focal point. Displacement of the chloride by an azide as above gave **26** in 90% yield. Final sugar deprotection using the Zemplén transesterification procedure (NaOMe, MeOH) gave the necessary precursors **24** and **27** in quantitative yields. Completion of the reactions were evidenced by proton NMR spectroscopy, wherein complete disappearance of the propargylic CH signal at δ 2.40 ppm and the appearance of the newly formed singlet of the triazole moiety at δ 7.65 ppm.

2.4. Glycodendrimer Syntheses

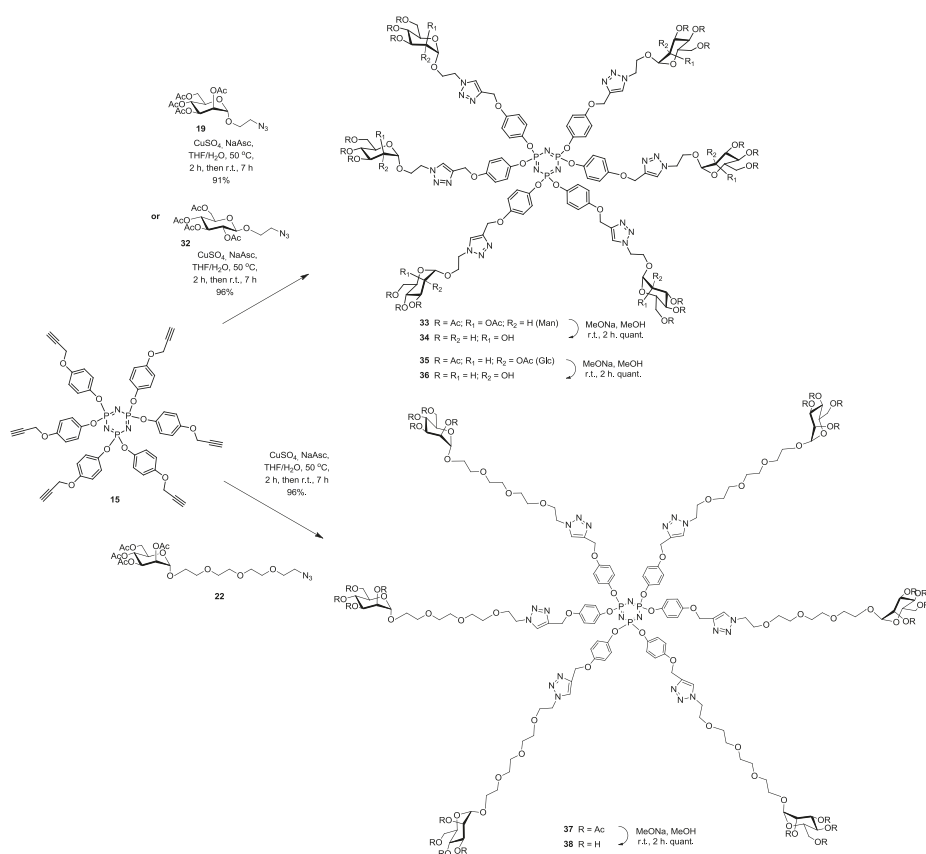
Multivalent binding interactions of glycodendrimers constitute a well-established strategy to enhanced binding efficacies toward their cognate lectins. We chose to prepare several dendrimers harboring from 2 to 18 mannopyranoside moieties to be evaluated as inhibitors against *E. coli* biofilm formation by using the highly efficient click chemistry. Azide-ending mannoside **22** was anchored to bis-propargylated aromatic scaffold **7** (Scheme 5), tris-propargylated aromatic scaffold **2**, tetrapropargylated scaffold **10** (Scheme 6) and hexa-propargylated phosphorus core **15** (Scheme 7) using CuAAC click reaction to afford **23**, **28**, **30** and **37** in good yields (75%, 92%, 82% and 96%, respectively). Completion of the reaction was evidenced by proton and phosphorus NMR spectroscopy, wherein complete disappearance of the propargylic CH signal and the appearance of the newly formed characteristic singlet of the triazole moieties were observed. Additionally, mass spectral analysis showed the presence of the required molecular ion peak (experimental section). All glycodendrimers were fully deprotected using Zemplén conditions providing the desired glyco-ligands **24**, **29**, **31** and **38** quantitatively.



Scheme 5. Synthesis of dimeric (**24**) and trimeric (**27**) mannodendrons using click chemistry.



Scheme 6. Synthesis of tri- (**29**) and tetra-valent (**31**) pegylated mannosylated clusters using click chemistry on trimer (**2**) and tetramer (**10**) scaffolds, respectively.

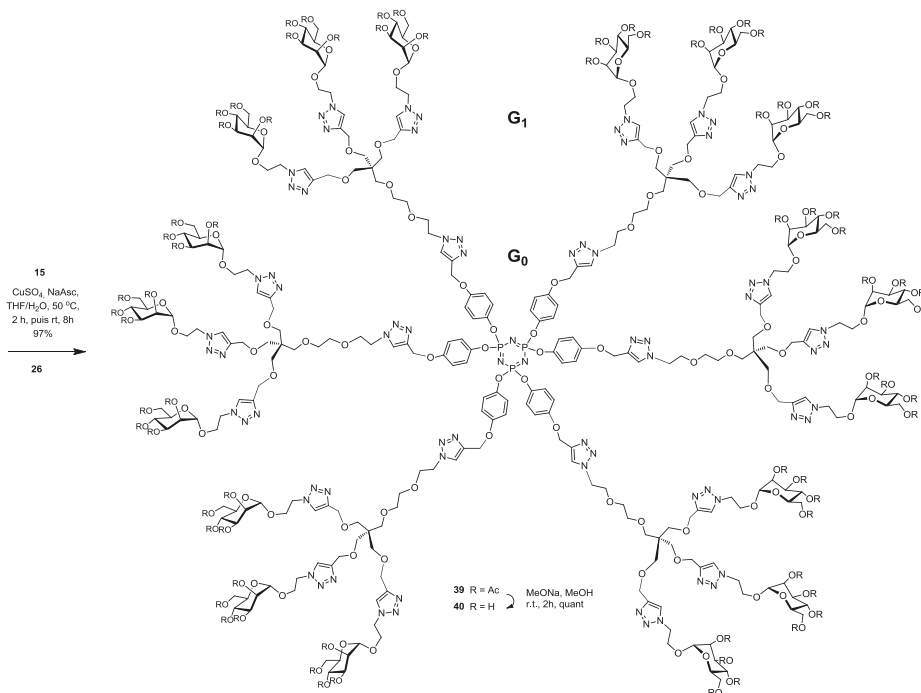


Scheme 7. Synthesis of hexavalent phosphorus glycodendrimers **34**, **36** and **38** using click chemistry on hexapropargylated core **15** and azido sugars **19**, **32** and **22** respectively.

Hexameric mannosylated clusters possessing a short (**19**) and the long pegylated (**22**) azido mannosides were anchored onto hexapropargylated phosphorus core **15** using CuAAC click reaction to afford **34** and **38** in good yields of 91% and 96% respectively (Scheme 7). In order to compare the role played by the sugar moiety in the subsequent bioassays, the known short 2-azidoethyl β -D-glucopyranoside **32** [41] was also coupled to the above scaffold **15** under the same reaction conditions to provide **36** also in an excellent 96% yield. Completion of the reactions was again readily evidenced through their respective proton and phosphorus NMR spectroscopy, wherein complete disappearance of the propargylic CH signal and the appearance of the newly formed characteristic singlet of the triazole moieties are showed. Additionally, mass spectral analysis showed the presence of the required molecular ion peak (experimental section). All clusters were fully deprotected using Zemplén reaction (NaOMe, MeOH) to provide the desired glycosylated hexamers **34**, **36** and **38** quantitatively.

A G1 glycodendrimer **39** possessing 18 mannoside moieties was synthesized in good yield of 97%, by anchoring the azide-ending tri-valent mannosylated dendron **26** to the hexa-propargylated phosphorus core **15** using CuAAC click reaction. Completion of the reaction was evidenced by proton and phosphorus NMR spectroscopy, wherein complete disappearance of the propargylic CH signal δ 2.52 ppm and the appearance of the newly formed characteristic singlet of the triazole

moieties δ 7.82 ppm, also the presence of one singlet phosphorus pick at δ 9.54 ppm fully support the homogeneity of the fully substituted cyclophosphazene core. Additionally, mass spectral analysis showed the presence of the required molecular ion peak (experimental section). Compound **39** was fully deprotected by using Zemplén reaction providing the desired G1 glycodendrimer **40** quantitatively (Scheme 8).



Scheme 8. Synthesis of phosphorus glycodendrimer **40** having 18 α -D-mannopyranoside residues using click chemistry and built around a cyclotriphosphazene core and a pentaerythritol scaffold at the next generation level.

2.5. Dynamic Light Scattering (DLS) Studies

The relative ability of the above glycodendrimers to react with a homotetrameric leguminous lectin such as Concanavalin A (ConA) from *Canavalia ensiformis* (jack bean) taken as a model and rapidly forming stable cross-linked lattices was monitored using dynamic light scattering (DLS). It was anticipated that the multivalent sugars at the peripheries of the dendrimers would facilitate the multidirectional interactions with its associated tetrameric protein as seen before with several other mannosylated structures [32,42–47]. Indeed, these multivalent glycodendrimer–protein complexes were shown to rapidly form large aggregates as a function of time. As seen in Figure 1, the complex resulting from the mannosylated dendrimers **24**, **27**, **29**, **31**, **38**, **40** and ConA resulted, within 1–3 min to nanometer sizes clusters having sizes ranging from 1400 to 4600 nm. When using the β -D-glucopyranoside dendrimer **36**, taken as negative control, no appreciable cross-linked lattice was observed. Clearly, the more highly dense mannodendrimer **40** (18 Man) reacted faster but also formed larger size aggregates than their hexameric cluster counterparts **34** and **38**. Interestingly, tetrameric mannoside **31** formed larger aggregates faster than trimer **29** but both smaller clusters plateaued at the same level of \sim 3000 nm size. Alternatively, tetramer **31** and hexamer **38** formed cross-linked lattices

almost equally rapidly but the denser structure **38** formed larger aggregates at the end of the process. As anticipated, hexamer **34**, harboring short mannopyranoside aglycone, formed aggregates of smaller size (2530 nm) when compared with hexamer **38** containing the tetraethyleneglycol linker (4090 nm) (see Supplementary Materials). In addition, **38** reached its plateau faster (204 s) in comparison to **34** (230 s), indicating the higher adaptability of the longer spacer to form stable cross-linked lattices.

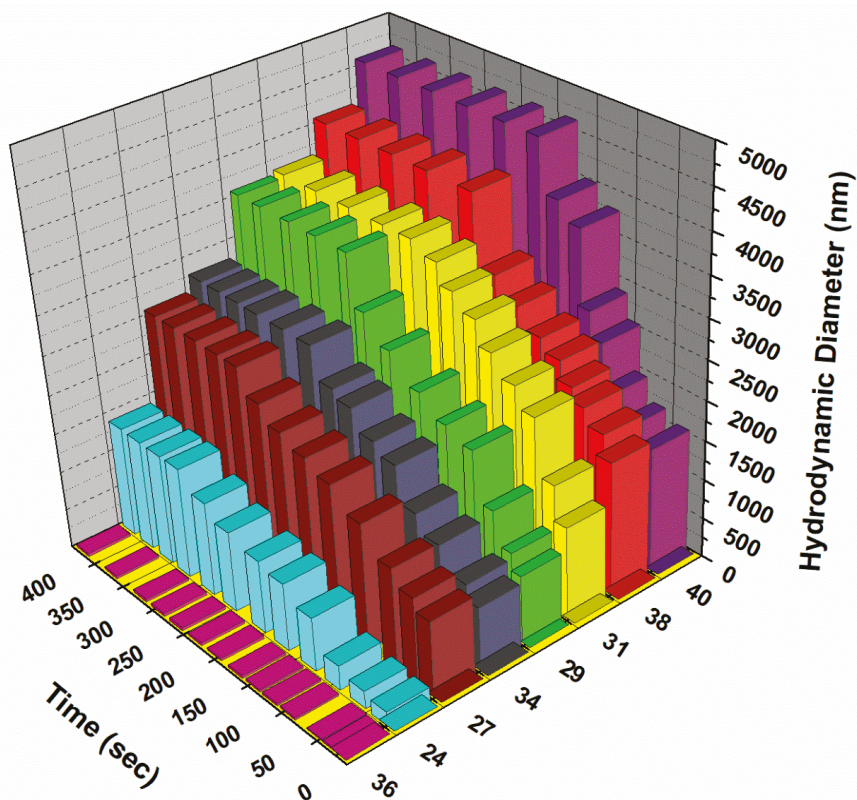


Figure 1. 3D DLS plots of the cross-linking kinetics of ConA in the presence of mannosylated dendrimers **24**, **27**, **29**, **31**, **34**, **38** and **40** and the glucosylated dendrimer **36** taken as negative control.

3. Materials and Methods

All reactions in organic medium were performed in standard oven dried glassware under an inert atmosphere of nitrogen using freshly distilled solvents stored over molecular sieves. Solvents were deoxygenated when necessary by bubbling nitrogen through the solution. All reagents were used as supplied without prior purification and obtained from Sigma-Aldrich Chemical Co. (Toronto, ON, Canada) Reactions were monitored by analytical thin-layer chromatography (TLC) using silica gel 60 F254 pre-coated plates (Merck, Darmstadt, Germany) and compounds were visualized by 254 nm light and/or by dipping into a mixture of sulfuric acid and methanol in water or into a mixture of KMnO_4 and K_2CO_3 in water followed by gentle warming with a heat-gun. Purifications were performed by flash column chromatography using silica gel from Canadian Life Science (60 Å, 40–63 μm) (Peterborough, ON, Canada) with the indicated eluent. $^1\text{H-NMR}$, $^{13}\text{C-NMR}$ and $^{31}\text{P-NMR}$ spectra were recorded at 300 and/or 600 MHz, 75 and/or 150 MHz and 122 and/or 243 MHz, respectively, on a Bruker spectrometer (300 MHz and 600 MHz) (Milton, ON, Canada) and Varian

spectrometer (600 MHz) (Milton, ON, Canada). All NMR spectra were measured at 25 °C in indicated deuterated solvents. Proton and carbon chemical shifts (δ) are reported in ppm and coupling constants (J) are reported in Hertz (Hz). The resonance multiplicity in the ^1H -NMR spectra are described as “s” (singlet), “d” (doublet), “t” (triplet) and “m” (multiplet) and broad resonances are indicated by “broad.” Residual protic solvent of CDCl_3 (^1H , 7.27 ppm; ^{13}C , 77.0 ppm (central resonance of the triplet)), D_2O (^1H , 4.80 ppm and 30.9 ppm for CH_3 of acetone for ^{13}C spectra), MeOD (^1H , 3.30 ppm and ^{13}C , 49.0 ppm), 85% H_3PO_4 was used as an external reference for ^{31}P -NMR. Two-dimensional homonuclear correlation ^1H - ^1H COSY and ^1H - ^{13}C HSQC experiments were used to confirm NMR peak assignments. Letters are used to NMR assignment. Accurate mass measurements (HRMS) were performed on a LC-MSD-TOF instrument from Agilent Technologies (Santa Clara, CA, USA) in positive electrospray mode. Either protonated molecular ions $[\text{M} + \text{nH}]^{\text{n}+}$ or adducts $[\text{M} + \text{nX}]^{\text{n}+}$ ($\text{X} = \text{Na}, \text{K}, \text{NH}_4$) were used for empirical formula confirmation. Light Scattering-Multiangle Laser Light Scattering (LS-MALLS) detection with performances verified with polystyrene 100 kDa and 2000 kDa were used to determine the number-average molecular weight (Min.) and polydispersity index (M_w/M_n). Calculations were performed with Zimm Plot (model). MALDI-TOF MS data were acquired on a Bruker Microflex LRF system (Bruker Daltonics, Billerica, MA, USA) equipped with a Compass 3.1 software platform. Acquisitions were performed in positive ion mode. Reflector mode was utilized for samples below 5 kDa and linear mode for samples above 5 kDa. Samples were dissolved in water (1 mg/mL) and mixed with 10 volumes of α -cyano-4-hydroxycinnamic acid matrix prepared at 10 mg/mL with 50% ACN/ H_2O 0.1% TFA. A volume of 2 μL was deposited on the target plate and dried. Representative acquisition parameters were: ion source 1, 19.5 kV; ion source 2, 18.05 kV; lens, 7.0 V; pulse ion extraction, 240 ns; detector, 1.905 kV. Approximately 200 laser shot/spectra were obtained with a 60 Hz N_2 -cartridge-laser set at 337 nm and the laser intensity adjusted according to the signal intensity. Sugar monomers were synthesized following the typical procedures found in literatures with a slight modification as describe below.

Dynamic Light Scattering

Particle size distribution (DLS) was measured in water with the help of Zetasizer Nano S90 from Malvern Instruments. Crosslinking studies were carried out in 1 mol/L phosphate buffered saline (PBS) for the plant lectin Concanavalin A (Sigma-Aldrich).

General procedure for the Cu(I) azide-alkyne cycloaddition reaction (I) (CuAAC) [28]. Solutions of alkyne (1 equiv.) and azide (1.5 equiv. per alkyne site) were prepared in minimum amount of THF. The resulting solutions were treated with an aqueous solution of CuSO_4 (0.3 equiv. per alkyne site) and sodium ascorbate solution in THF (0.35 equiv. per alkyne site). Biphasic mixture was then stirred at 50 °C for 2 h then left at room temperature until completion of the reaction as judged by the complete conversion of the limiting reagents (alkyne). After completion of the reaction, EtOAc was added, then Na_2SO_4 was added to quench the reaction by regenerating the $\text{CuSO}_4 \cdot 5\text{H}_2\text{O}$. The mixture was allowed to stir for 3 min then filtered before the solvent was removed under reduced pressure and the resulting viscous oil was subjected to silica gel column chromatography using the appropriate eluent system (0–10% MeOH in CH_2Cl_2) to afford the triazole products.

General procedure for the azide substitution (II) [28]. To a solution of the appropriate bromo/tosyl derivatives (1 equiv.) in DMF was added NaN_3 (1.5 equiv. per bromide). The reaction mixtures were stirred at 80 °C until completion of reaction as judged by TLC. The excess solvent was next removed under reduced pressure with heating at 60 °C until dryness. The residues were dissolved in EtOAc and washed successively with water and brine. The organic layer was separated and dried on Na_2SO_4 . The residue was subjected to silica gel flash chromatography to afford the desired azido derivative.

General Procedure for De-O-acetylation (III) (Zemplén reaction) [28]. An acetylated glycocluster (0.1 mmol) was dissolved in dry MeOH (3 mL) and a solution of sodium methoxide (1 M in MeOH, 0.5 equiv.) was added. The reaction mixture was stirred at room temperature until the starting material disappeared. The solution was neutralized by the addition of a cationic ion-exchange resin (H⁺), filtered and washed with MeOH and then the solvent was removed in vacuo. The residue was lyophilized to yield quantitatively the fully deprotected glycoclusters.

Synthesis of 2. Benzene-1,3,5-triol (1) [48] (2 g, 15.86 mmol) was dissolved in DMF (10 mL) followed by the addition of K₂CO₃ (3 g, 14.87 mmol). The mixture was reflux for 30 min, propargyl bromide (8.5 mL, 79.3 mmol, 5 equiv.) was added dropwise, then stirred over night at room temperature. The residue was dissolved in dichloromethane (DCM) and washed with water and brine. The organic layer was dried over Na₂SO₄, filtered, then concentrated under vacuum. The crude product was purified by silica gel flash chromatography using 0–20% EtOAc in Hexane as eluents to afford compound **2** as a white powder (2 g, 53%). *R*_f = 0.28 (EtOAc/Hexane, 1:4). ¹H-NMR (300 MHz, CDCl₃) δ 6.27 (s, 3H, k), 4.65 (d, *J* = 2.4 Hz, 6H, b), 2.53 (t, *J* = 2.4 Hz, 3H, c).

Synthesis of compound 9. To a solution of pentaerythritol **8** (2 g, 14.7 mmol) in dimethylsulfoxide (DMSO, 15 mL) were added an aqueous solution of NaOH (40 wt%, 10 mL). The solution was kept under magnetic stirring at room temperature for 30 min Propargyl bromide (97%, 12 mL, 135.18 mmol) was then added and the solution was kept at room temperature for an additional 24 h. Ethyl ether was added to the reaction mixture then washed with water. The organic layer was dried over Na₂SO₄. The crude product was purified by silica gel flash chromatography using 0–20% EtOAc in Hexane as eluents to afford compound **9** as a colorless oil (2.2 g, 60%). *R*_f = 0.25 (EtOAc/Hexane, 1:4). Compound **10** was obtained as a white powder (1.2 g, 28%). *R*_f = 0.35 (EtOAc/Hexane, 1:4). Tetrapropargylpentaerythritol **10** [49]. ¹H-NMR (300 MHz, CDCl₃) δ 4.08 (d, *J* = 2.3 Hz, 8H, OCH₂CCH), 3.48 (s, 8H, CH₂OCH₂CCH), 2.42 (d, *J* = 2.2 Hz, 4H, OCH₂CCH).

Tripargylpentaerythritol 9 [49]. ¹H-NMR (300 MHz, CDCl₃) δ 4.13 (d, *J* = 2.4 Hz, 6H, OCH₂CCH), 3.69 (s, 2H, CH₂OH), 3.56 (s, 6H, CH₂OCH₂CCH), 2.42 (t, *J* = 2.4 Hz, 3H, CCH).

Synthesis of compound 11. A solution of pentaerythritol propargyl ether (**9**) (2 g, 7.9 mmol, 1 equiv.), Bu₃NHSO₄ (5 g, 14.7 mmol, 1.8 equiv.), Bis(2-chloroethyl) ether (22 mL, 187.61 mmol) in NaOH 50% (30 mL), was stirred at room temperature for 24 h. DCM was added to the reaction mixture and the organic layer was washed successfully with water and brine, then dried over anhydrous sodium sulfate. The crude product was purified by silica gel flash chromatography using 0–20% EtOAc in Hexane as eluents to afford compound **11** as a colorless oil (2.1 g, 73%). *R*_f = 0.25 (EtOAc/Hexane, 1:4). ¹H-NMR (300 MHz, CDCl₃) δ 4.11 (d, *J* = 2.4 Hz, 6H, OCH₂CCH), 3.76 (dd, *J* = 8.8, 3.2 Hz, 2H, CH₂Cl), 3.67–3.56 (m, 6H, OCH₂-CH₂), 3.52 (s, 6H, CH₂OCH₂CCH), 3.46 (s, 2H, CH₂OCH₂), 2.40 (t, *J* = 2.4 Hz, 3H, CCH).

Monopropargyloxyphenol (13) [50]. Hydroquinone (10.28 g, 93.37 mmol) was dissolved in acetone (150 mL) followed by the addition of K₂CO₃ (15.42 g, 111.58 mmol). The mixture was reflux for 30 min, propargyl bromide (10.28 mL, 93.50 mmol, 0.98 equiv.) was added dropwise, then stirred over night at room temperature. Residue was dissolved in DCM (100 mL) and washed with water (3 × 50 mL) and brine (3 × 50 mL). The organic layer was dried over Na₂SO₄, filtered and concentrated under vacuum. The crude product was purified by silica gel flash chromatography using 0–30% EtOAc in Hexane as eluents to afford the mono substituted propargyl hydroquinone **13** as a brownish powder (3.11 g, 20.96 mmol, 43%). *R*_f = 0.35 (EtOAc/Hexane, 3:7). ¹H-NMR (300 MHz, CDCl₃) δ 6.85 (d, *J* = 9.1 Hz, 2H, aromatic), 6.78 (d, *J* = 9.1 Hz, 2H, aromatic), 4.66 (d, *J* = 1.4 Hz, 2H, CH₂), 2.53 (t, *J* = 2.4 Hz, 1H, ≡CH).

Synthesis of 15 [50–55]. Cs_2CO_3 (3.4 g, 10.4 mmol) is added into a reaction mixture of 4-(prop-2-yn-1-yloxy)phenol (**13**) (6.7 mmol) and $\text{N}_3\text{P}_3\text{Cl}_6$ (**14**) (0.6 mmol) in THF (20 mL). The mixture was heated at 40 °C for 17 h, then filtered on Celite and concentrated. The pure **15** was isolated as a white crystal yielding 98% after crystallization in EtOH. $^1\text{H-NMR}$ (300 MHz, CDCl_3) δ 6.87 (d, $J = 9.65$ Hz, 6H, $\text{OC}_6\text{H}_4\text{O}$), δ 6.80 (d, $J = 9.65$ Hz, 6H, $\text{OC}_6\text{H}_4\text{O}$), 4.65 (d, $J = 2.4$ Hz, 6H, OCH_2), 2.52 (t, $J = 2.4$ Hz, 3H, CH). $^{31}\text{P-NMR}$ (122 MHz, CDCl_3) δ 9.82 (s).

1,2,3,4,6-Penta-O-acetyl- α/β -D-mannopyranose (17). 1,2,3,4,6-penta-O-acetyl- α/β -D-mannopyranose was prepared according to the procedure reported [52] with a slight modification. D-Mannose **16** (3 g, 16.6 mmol), pyridine (40 mL) and acetic anhydride (32 mL, 333 mmol) were stirred at room temperature. After stirring for 12 h, the reaction mixture was diluted with ice-water and extracted with DCM. The combined organic layer was washed with 1 M aqueous HCl, saturated sodium bicarbonate solution (NaHCO_3), H_2O and Brine. The organic layer was dried over Na_2SO_4 and the solvent was removed under reduced pressure. The product **17** was obtained as colorless syrup (6 g, 15.4 mmol, 90%) which was a mixture of α and β anomers with a ratio of 3:1. This product was used in the next synthetic step without any further purification. $^1\text{H-NMR}$ (300 MHz, CDCl_3) δ 6.09 (d, $J = 1.8$ Hz, 3H, H-1a), 5.86 (d, $J = 1.1$ Hz, 1H, H-1b), 5.49 (dd, $J = 3.3, 1.1$ Hz, 1H), 5.38–5.33 (m, 6H), 5.32 (d, $J = 2.8$ Hz, 1H), 5.26 (t, $J = 2.0$ Hz, 3H), 5.13 (dd, $J = 10.0, 3.3$ Hz, 1H), 4.30 (ddd, $J = 12.4, 7.5, 5.1$ Hz, 5H), 4.18–4.02 (m, 8H), 3.80 (ddd, $J = 9.8, 5.3, 2.4$ Hz, 1H), 2.22 (s, 3H), 2.18 (s, 9H), 2.17 (s, 9H), 2.10 (s, 3H), 2.09 (s, 12H), 2.05 (s, 12H), 2.01 (s, 12H).

2-Bromoethyl 2,3,4,6-tetra-O-acetyl- α -D-manno-pyranoside (18) [27,51]. Compound **17** (5.37 g, 13.8 mmol) and 2-bromoethanol (0.98 mL, 13.8 mmol) were dissolved in DCM (50 mL). Then, boron trifluoride etherate (5.8 mL, 47.2 mmol) was added to the solution and stirred under a nitrogen atmosphere for 3 h and monitored by TLC (EtOAc/Hexane, 1:1). After addition of DCM (100 mL), the reaction mixture was neutralized by adding saturated sodium bicarbonate solution (100 mL) and the resulting solution was washed with water (2×200 mL). The combined organic layers were dried over Na_2SO_4 , filtered and concentrated to dryness under reduced pressure. The resulting oil was then purified using silica gel chromatography (EtOAc/Hexane, 1:1). The relevant fractions were collected, combined and concentrated to dryness under reduced pressure to yield **18** as a colorless powder (2.2 g, 40%). $^1\text{H-NMR}$ (300 MHz, CDCl_3) δ 5.39–5.18 (m, 4H, H-2, 3 and 4), 4.85 (d, $J = 1.6$ Hz, 1H, H-1), 4.27 (dd, $J = 12.2, 5.3$ Hz, 1H, H-6), 4.16–3.98 (m, 2H, H-6, H-5), 3.85 (ddd, $J = 10.6, 6.6, 4.0$ Hz, 1H, j), 3.72–3.60 (m, 1H, j'), 3.54–3.34 (m, 2H, CH_2Br), 2.12 (s, 3H, COCH_3), 2.08 (s, 3H, COCH_3), 2.03 (s, 3H, COCH_3), 1.97 (s, 3H, COCH_3).

2-Azidoethyl 2,3,4,6-tetra-O-acetyl- α -D-manno-pyranoside (19) [27,51]. Compound **18** (1.40 g, 3.0 mmol) and sodium azide (1.00 g, 15.4 mmol) were dissolved in anhydrous DMF (30 mL) and stirred at 80 °C for 5 h. The reaction mixture was filtered and concentrated to dryness under reduced pressure and further processed as given in general procedure (II) to afford compound **19** (0.75 g, 60%) as white powder. $^1\text{H-NMR}$ (300 MHz, CDCl_3) δ 5.48–5.11 (m, 3H, H-2, 3 and 4), 4.87 (d, $J = 1.6$ Hz, 1H, H-1), 4.29 (dd, $J = 12.3, 5.3$ Hz, 1H, H-6), 4.20–3.99 (m, 2H, H-6' and 5), 3.87 (m, 1H, j), 3.76–3.60 (m, 1H, j'), 3.56–3.36 (m, 2H, CH_2N_3), 2.16 (s, 3H, COCH_3), 2.11 (s, 3H, COCH_3), 2.06–2.03 (s, 3H, COCH_3), 2.00 (s, 3H, COCH_3).

Monotosylated tetraethylene glycol (20) [53]. To a solution of tetraethylene glycol (26.3 g, 135.4 mmol, 10 equiv.) in THF (60 mL) was added a solution of sodium hydroxide (1.79 g, 44.7 mmol, 3.3 equiv.) dissolved in water (5 mL). The mixture was cooled to 0 °C and toluenesulfonyl chloride (2.57 g, 16.54 mmol, 1 equiv.) in THF (5 mL) was added dropwise. The reaction was stirred at 0 °C for 2 h. The solution was poured into water and the aqueous layer was extracted with dichloromethane. The organic layers were washed with water, dried over Na_2SO_4 , filtered and concentrated under reduced pressure to yield **20** as a colorless oil (4.69 g, 97%) yield based on the *p*-toluenesulfonyl

chloride. $R_f = 0.25$ (in 100% EtOAc). $^1\text{H-NMR}$ (300 MHz, CDCl_3) δ 7.79 (d, $J = 8.0$ Hz, 2H, b), 7.33 (d, $J = 8.0$ Hz, 2H, d), 4.16 (t, $J = 4.7$ Hz, 2H, a), 3.75–3.55 (m, 14H, e), 2.44 (s, 3H, c).

2-(2-[2-[2-(2-Tosyloxy-ethoxy)-ethoxy]-ethoxy]-ethyl) 2,3,4,6-tetra-O-acetyl- α -D-mannopyranoside (**21**) [53]. Into a solution of pentaacetate mannose **17** (1.68 g, 4.31 mmol, 1 equiv.) in anhydrous CH_2Cl_2 (20 mL) was added boron trifluoride etherate (1.23 mL, 9.93 mmol, 2.3 equiv.) at room temperature under nitrogen atmosphere. The solution was stirred for 4 h before compound **20** (3.76 g, 10.79 mmol, 2.5 equiv.) was added. Glycosylation was completed after stirring at 40 °C overnight. The crude product was washed with NaHCO_3 sat, dried over Na_2SO_4 and concentrated under reduced pressure. Further purification was processed on silica gel flash chromatography using 0–20% EtOAc in Hexane as eluents to afford compound **21** as a colorless oil (1.8 g, 60%). $R_f = 0.35$ (EtOAc/Hexane, 1:4). $^1\text{H-NMR}$ (300 MHz, CDCl_3) δ 7.80 (d, $J = 8.3$ Hz, 2H, aromatic), 7.34 (d, $J = 8.0$ Hz, 2H, aromatic), 5.38–5.25 (m, 3H, H-3, 4 and 2), 4.87 (d, $J = 1.6$ Hz, 1H, H-1), 4.36–4.19 (m, 2H, H-6), 4.18–4.01 (m, 3H, c and H-5), 3.85–3.75 (m, 1H, j'), 3.73–3.56 (m, 13H, j, i, d, g, f, e), 2.45 (s, 3H, CH_3), 2.16 (d, 3H, COCH_3), 2.09 (s, 3H, COCH_3), 2.03 (s, 3H, COCH_3), 1.99 (s, 3H, COCH_3).

2-(2-[2-[2-(2-Azido-ethoxy)-ethoxy]-ethoxy]-ethyl) 2,3,4,6-tetra-O-acetyl- α -D-mannopyranoside (**22**) [53]. To a solution of **21** (520 mg, 0.766 mmol, 1 equiv.) in dry DMF (15 mL) under a nitrogen atmosphere were added sodium azide (996 mg, 15.3 mmol, 20 equiv.). After stirring at 80 °C for 2 h, the solution was diluted in EtOAc and further processed as given in general procedure (II) to afford compound **22** as a colorless oil (380 mg, 90%), $R_f = 0.4$ (EtOAc/Hexane, 1:4). $^1\text{H-NMR}$ (300 MHz, CDCl_3) δ 5.43–5.24 (m, 3H, H-3, 4 and 2), 4.87 (d, $J = 1.6$ Hz, 1H, H-1), 4.27 (td, $J = 12.6, 5.0$ Hz, 1H, H-6), 4.14–4.03 (m, 2H, H-6' and 5), 3.86–3.76 (m, 1H, j'), 3.71–3.64 (m, 13H, j, i, d, g, e, h, f), 3.39 (t, $J = 5.1$ Hz, 2H, $\text{CH}_2\text{-N}_3$), 2.15 (s, 3H, COCH_3), 2.10 (s, 3H, COCH_3), 2.04 (s, 3H, COCH_3), 1.99 (s, 3H, COCH_3).

Synthesis of 23. Into a solution of bispropargylated core (**7**) (30 mg, 0.13 mmol, 1.0 equiv.) in a mixture of THF/ H_2O (4 mL, 3:1, v/v), was added 2-(2-[2-[2-(2-Azido-ethoxy)-ethoxy]-ethoxy]-ethyl) 2,3,4,6-tetra-O-acetyl- α -D-mannopyranoside (**22**) (220 mg, 0.39 mmol, 3 equiv.), Na-ascorbate (18 mg, 0.09 mmol, 0.7 equiv.) and $\text{CuSO}_4 \cdot 5\text{H}_2\text{O}$ (19 mg, 0.08 mmol, 0.6 equiv.). The mixture was stirred at 50 °C for 2 h, then at room temperature for 5 h. Upon completion of the reaction, EtOAc was added to the reaction mixture and further processed as given in general procedure (I) to afford compound **23** (136 mg, 75%) as a white powder; $R_f = 0.35$ (with 5% MeOH in CH_2Cl_2 as eluents). $^1\text{H-NMR}$ (600 MHz, CDCl_3) δ 7.74 (s, 2H, H-triazole), 6.77 (s, 1H, H_P -aromatic), 6.74 (s, 2H, H_O -aromatic), 5.30 (dd, $J = 10.0, 3.4$ Hz, 2H, H-3), 5.25 (d, $J = 9.9$ Hz, 2H, H-4), 5.23–5.20 (m, 2H, H-2), 4.82 (s, 2H, H-1), 4.61 (s, 4H, b), 4.52–4.49 (m, 4H, c), 4.47 (s, 4H, m), 4.24 (dd, $J = 12.2, 4.8$ Hz, 2H, H-6), 4.05 (dd, $J = 12.3, 4.1$ Hz, 2H, H-6'), 4.03–3.99 (m, 2H, H-5), 3.83 (t, $J = 4.9$ Hz, 4H, d), 3.77–3.73 (m, 2H, j), 3.61 (m, 2H, j'), 3.60 (s, 4H, i), 3.58 (s, 16H, g, f, e, h), 2.11 (s, 6H, COCH_3), 2.05 (s, 6H, COCH_3), 1.99 (s, 6H, COCH_3), 1.94 (s, 6H, COCH_3). $^{13}\text{C-NMR}$ (150 MHz, CDCl_3) δ 170.6 (C=O), 169.9 (C=O), 169.8 (C=O), 169.6 (C=O), 156.8 (COH), 144.7 (C-triazole), 139.5 (C_m -aromatic), 123.8 (CH-triazole), 118.4 (C_p -aromatic), 113.9 (C_o -aromatic), 97.5 (C-1), 71.9 (C_m), 70.5 (C_d), 70.4 (C_g), 70.3 (C_f), 69.8 (C_e), 69.4 (C_h), 69.4 (C_i), 69.3 (C-2), 68.9 (C-3), 68.2 (C-4), 67.2 (C-5), 65.9 (C_j), 63.4 (C_b), 62.2 (C-6), 50.1 (C_c), 20.8 (COCH_3), 20.6 (COCH_3), 20.6 (COCH_3). ESI⁺-HRMS: $[\text{M} + \text{Na}]^+$ calcd for $\text{C}_{56}\text{H}_{86}\text{N}_6\text{NaO}_{29}$, 1329.5331; found: 1329.5395.

Synthesis of 24. Compound **23** (50 mg, 0.036 mmol) and sodium methoxide (16 μL from 1 M solution in MeOH) in 3 mL of methanol were stirred for 4 h and the mixture was treated following the general procedure (III) described above. Deprotected compound **24** (38 mg, quant.) was obtained as a colorless solid. $^1\text{H-NMR}$ (600 MHz, D_2O) δ 8.04 (s, 2H), 6.89 (s, 1H), 6.82 (s, 2H), 4.84 (s, 2H), 4.70 (s, 4H), 4.66–4.59 (m, 4H), 4.57 (s, 4H), 3.98–3.94 (m, 4H), 3.93–3.80 (m, 4H), 3.80–3.72 (m, 4H), 3.67–3.60 (m, 12H), 3.60–3.55 (m, 8H), 3.55–3.52 (m, 4H). $^{13}\text{C-NMR}$ (150 MHz, D_2O) δ 215.4, 155.9, 143.9, 139.3, 125.5,

120.1, 114.7, 99.8, 72.7, 71.7, 70.5, 69.9, 69.7, 69.6, 69.5, 69.4, 69.4, 68.7, 66.7, 66.3, 62.4, 60.9, 49.9, 30.2. ESI⁺-HRMS: [M + Na]⁺ calcd for C₄₀H₇₀N₆NaO₂₁, 993.4486; found: 993.4545.

Synthesis of 25. Into a solution of tripropargyl pentaerythritol core (**11**) (125 mg, 0.35 mmol, 1.0 equiv.) in a mixture of THF/H₂O (4 mL, 3:1, *v/v*), was added 2-azidoethyl 2,3,4,6-tetra-*O*-acetyl- α -D-mannopyranoside (**19**) (745 mg, 1.42 mmol, 5.1 equiv.), Na-ascorbate (70 mg, 0.29 mmol, 1.1 equiv.) and CuSO₄·5H₂O (78 mg, 0.31 mmol, 0.9 equiv.). The mixture was stirred at 50 °C for 2 h, then at room temperature for 5 h. Upon completion of the reaction, EtOAc was added to the reaction mixture and further processed as given in general procedure (I) to afford compound **25** (480 mg, 82%) as a white powder; *R*_f = 0.3 (with 5% MeOH in CH₂Cl₂ as eluents). ¹H-NMR (300 MHz, CDCl₃) δ 7.70 (s, 3H, H_B-triazole), 5.31–5.19 (m, 9H, H-3, 4 and 2), 4.81 (d, *J* = 1.3 Hz, 3H, H-1), 4.61 (m, 6H, i), 4.59 (s, 6H, h), 4.21 (dd, *J* = 12.3, 5.1 Hz, 3H, H-6), 4.13 (dt, *J* = 10.4, 4.9 Hz, 3H, j'), 4.04 (dd, *J* = 12.3, 2.3 Hz, 3H, H-6'), 3.91 (dt, *J* = 10.6, 5.2 Hz, 3H, j), 3.74 (m, 2H, d), 3.61 (m, 7H, H-5, f and CH₂-Cl), 3.57–3.53 (m, 2H, e), 3.49 (s, 6H, g'), 3.44 (s, 2H, g), 2.13 (s, 9H, COCH₃), 2.09 (s, 9H, COCH₃), 2.04 (s, 9H, COCH₃), 1.99 (s, 9H, COCH₃).

Synthesis of 26. To a solution of compound **25** (480 mg, 0.29 mmol, 1.0 equiv.) in dry DMF (2 mL) under a nitrogen atmosphere were added sodium azide (186 mg, 2.9 mmol, 10 equiv.). After stirring at 80 °C for 2 h, the solution was diluted in EtOAc and further processed as given in general procedure (II) to afford compound **26** as a white powder (430 mg, 90%). ¹H-NMR (300 MHz, CDCl₃) δ 7.65 (s, 3H, H_B-triazole), 5.28–5.09 (m, 9H, H-3, 4 and 2), 4.76 (d, *J* = 1.1 Hz, 3H, H-1), 4.6–4.57 (m, 6H, i), 4.53 (s, 6H, h), 4.15 (dd, *J* = 12.4, 5.1 Hz, 3H, H-6), 4.07 (dt, *J* = 10.5, 5.7 Hz, 3H, j'), 3.98 (dd, *J* = 12.3, 2.3 Hz, 3H, H-6'), 3.86 (dt, *J* = 10.4, 5.1 Hz, 3H, j), 3.63–3.59 (m, 2H, d), 3.56–3.53 (m, 5H, H-5, f), 3.49 (m, 2H, e), 3.44 (s, 6H, g'), 3.39 (s, 2H, g), 3.33–3.27 (m, 2H, c, CH₂-N₃), 2.07 (s, 9H, COCH₃), 2.03 (s, 9H, COCH₃), 1.98 (s, 9H, COCH₃), 1.94 (s, 9H, COCH₃). ¹³C-NMR (75 MHz, CDCl₃) δ 170.6 (C=O), 170.0 (C=O), 169.6 (C=O), 169.1 (C=O), 145.6 (C-triazole), 123.7 (CH_B-triazole), 97.6 (C-1), 77.2 (C_q), 71.0 (C_f), 70.3 (C_e), 70.0 (C_g), 69.2 (C-2), 69.1 (C-3), 68.9 (C-4), 66.3 (C-5), 65.7 (C_j), 64.8 (C_h), 62.2 (C-6), 51.8 (C_i), 50.8 (C_c), 49.5 (C_q), 20.8 (COCH₃), 20.7 (COCH₃).

Synthesis of 27. Compound **26** (200 mg, 0.02 mmol) and sodium methoxide (16 μ L from 1 M solution in MeOH) in 3 mL of methanol were stirred for 4 h and the mixture was treated following the general procedure (III) described above. Deprotected compound **27** (150 mg, quant.) was obtained as a white powder. ¹H-NMR (300 MHz, MeOD) δ 8.00 (s, 3H), 4.69–4.60 (m, 9H), 4.55 (s, 6H), 4.11 (dt, *J* = 10.3, 4.9 Hz, 3H), 3.88 (dt, *J* = 5.8, 4.6 Hz, 3H), 3.81–3.71 (m, 6H), 3.65 (ddd, *J* = 18.4, 7.4, 5.7 Hz, 18H), 3.58–3.49 (m, 4H), 3.46 (s, 6H), 3.40 (dd, *J* = 9.5, 4.3 Hz, 6H), 3.21 (dd, *J* = 7.6, 5.1 Hz, 4H). ¹³C-NMR (75 MHz, MeOD) δ 146.08, 126.31, 101.33, 79.41, 74.58, 72.26, 72.06, 71.69, 71.35, 70.99, 70.1, 68.1, 66.9, 65.2, 62.4, 51.8, 51.4, 50.1, 49.9, 49.6, 49.3, 49.0, 48.7, 48.4, 46.5, 31.3, 24.6. ESI⁺-HRMS: [M + 2H]²⁺ calcd for C₄₂H₇₂N₁₂O₂₃, 556.2418; found: 556.2470.

Synthesis of 28. Into a solution of tripropargylated core (**2**) (25 mg, 0.104 mmol, 1.0 equiv.) in a mixture of THF/H₂O (4 mL, 3:1, *v/v*), was added 2-(2-[2-[2-(2-Azido-ethoxy)-ethoxy]-ethoxy]-ethyl) 2,3,4,6-tetra-*O*-acetyl- α -D-mannopyranoside (**22**) (281 mg, 0.5 mmol, 5 equiv.), Na-ascorbate (22 mg, 0.11 mmol, 0.5 equiv.) and CuSO₄·5H₂O (23 mg, 0.09 mmol, 0.9 equiv.). The mixture was stirred at 50 °C for 2 h, then at room temperature for 5 h. Upon completion of the reaction, EtOAc was added to the reaction mixture and further processed as given in general procedure (I) to afford compound **28** (188 mg, 92%) as a white powder; *R*_f = 0.32 (with 5% MeOH in CH₂Cl₂ as eluents). ¹H-NMR (600 MHz, CDCl₃) δ 7.83 (s, 3H, H-triazole), 6.28 (s, 3H, k) 5.32 (dd, *J* = 10.0, 2.8 Hz, 3H, H-3), 5.27 (t, *J* = 10.0 Hz, 3H, H-4), 5.25 (dd, *J* = 3.0, 1.7 Hz, 3H, H-2), 5.12 (s, 6H, b), 4.85 (d, *J* = 1.4 Hz, 3H, H-1), 4.55 (t, *J* = 4.9 Hz, 6H, c), 4.27 (dd, *J* = 12.4, 5.1 Hz, 3H, H-6), 4.07 (d, *J* = 12.8 Hz, 3H, H-6'), 4.03 (dd, *J* = 5.7, 3.5 Hz, 3H, H-5), 3.89 (t, *J* = 4.9 Hz, 6H, d), 3.82–3.73 (m, 3H, j), 3.65 (m, 3H, j'), 3.63 (s, 6H, i), 3.61 (s, 24H, g, e, f, h), 2.13 (s, 9H, COCH₃), 2.07 (s, 9H, COCH₃), 2.01 (s, 9H, COCH₃), 1.96

(s, 9H, COCH₃). ¹³C-NMR (150 MHz, CDCl₃) δ 170.8 (C=O), 170.1 (C=O), 170.0 (C=O), 169.8 (C=O), 160.3 (COCH₃-aromatic), 143.7 (C-triazole), 124.2 (CH-triazole), 97.8 (C-1), 95.1 (C_k-aromatic), 70.8 (C_d), 70.7 (C_g), 70.6 (C_f), 70.1 (C_e), 69.7 (C_h), 69.6 (C_j), 69.5 (C-2), 69.2 (C-3), 68.5 (C-4), 67.5 (C-5), 66.2 (C_i), 62.5 (C_b), 62.1 (C-6), 50.4 (C_c), 21.0 (COCH₃), 20.9 (COCH₃), 20.8 (COCH₃), 20.8 (COCH₃). MALDI-TOF: [M + H]⁺ calcd for C₈₁H₁₁₈N₉O₄₂: 1888.737; found, 1888.789.

Synthesis of 29. Compound **28** (100 mg, 0.05 mmol) and sodium methoxide (16 μL from 1 M solution in MeOH) in 3 mL of methanol were stirred for 4 h and the mixture was treated following the general procedure (III) described above. Deprotected compound **29** (74 mg, quant.) was obtained as a white solid. ¹H-NMR (600 MHz, MeOD) δ 8.16 (s, 3H), 6.37 (s, 3H), 5.19 (s, 6H), 4.65–4.63 (m, 8H), 3.95–3.92 (m, 4H), 3.88–3.87 (m, 2H), 3.82 (m, 10.0, 3.1 Hz, 4H), 3.77–3.71 (m, 4H), 3.68–3.54 (m, 23H). ¹³C-NMR (150 MHz, MeOD) δ 159.9, 143.3, 125.4, 100.1, 95.5, 72.9, 70.9, 70.3, 69.9, 69.8, 69.8, 68.9, 66.9, 66.4, 61.1, 50.2, 48.5, 47.9, 47.9, 47.8, 47.8, 47.8. MALDI-TOF: [M]⁺ calcd for C₅₇H₉₂N₉O₃₀: 1382.592; found, 1382.801.

Synthesis of 30. Into a solution of tetrapropargyl pentaerythritol core (**10**) (67 mg, 0.23 mmol, 1.0 equiv.) in a mixture of THF/H₂O (4 mL, 3:1, *v/v*), was added 2-(2-[2-[2-(2-Azido-ethoxy)-ethoxy]-ethoxy]-ethyl) 2,3,4,6-tetra-*O*-acetyl- α -D-mannopyranoside (**22**) (790 mg, 1.4 mmol, 6 equiv.), Na-ascorbate (65 mg, 0.32 mmol, 1.4 equiv.) and CuSO₄·5H₂O (70 mg, 0.28 mmol, 1.2 equiv.). The mixture was stirred at 50 °C for 2 h, then at room temperature for 5 h. Upon completion of the reaction, EtOAc was added to the reaction mixture and further processed as given in general procedure (I) to afford compound **30** as a white powder (484 mg, 82%). *R*_f = 0.27 (with 5% MeOH in CH₂Cl₂ as eluents). ¹H-NMR (600 MHz, CDCl₃) δ 7.68 (s, 4H, *H*-triazole), 5.32 (dd, *J* = 10.0, 3.4 Hz, 4H, *H*-3), 5.26 (t, *J* = 10.0 Hz, 4H, *H*-2), 5.24 (dd, *J* = 3.2, 1.6 Hz, 4H, *H*-4), 4.85 (s, 4H, *H*-1), 4.52 (s, 8H, b), 4.51 (t, *J* = 5.5 Hz, 8H, c), 4.27 (dd, *J* = 12.2, 4.9 Hz, 4H, *H*-6), 4.07 (dd, *J* = 12.2, 2.2 Hz, 4H, *H*-6'), 4.04 (ddd, *J* = 9.8, 4.8, 2.3 Hz, 4H, *H*-5), 3.87 (t, *J* = 5.3 Hz, 8H, d), 3.81–3.75 (m, 4H, j), 3.66 (dd, *J* = 5.8, 3.7 Hz, 4H, j'), 3.64–3.63 (m, 8H, i), 3.62–3.58 (m, 32H, g, f, e, h), 3.45 (s, 8H, k), 2.13 (s, 12H, COCH₃), 2.08 (s, 12H, COCH₃), 2.01 (s, 12H, COCH₃), 1.96 (s, 12H, COCH₃). ¹³C-NMR (150 MHz, CDCl₃) δ 170.7 (C=O), 170.0 (C=O), 169.9 (C=O), 169.7 (C=O), 145.1 (C-triazole), 123.6 (CH-triazole), 97.7 (C-1), 70.7 (C_d), 70.6 (C_g), 70.5 (C_f), 69.9 (C_e), 69.6 (C_h), 69.5 (C_j), 69.5 (C-2), 69.2 (C_q), 69.1 (C-3), 68.4 (C-4), 67.4 (C-5), 66.1 (C_i), 64.9 (C_b), 62.4 (C-6), 50.1 (C_c), 45.3 (C_k), 20.9 (COCH₃), 20.8 (COCH₃), 20.7 (COCH₃), 20.7 (COCH₃). ESI⁺-HRMS: [M + 2H]²⁺ calcd for C₁₀₅H₁₆₂N₁₂O₅₆, 1244.5021; found: 1244.0172.

Synthesis of 31. Compound **30** (100 mg, 0.038 mmol) and sodium methoxide (16 μL from 1 M solution in MeOH) in 3 mL of methanol were stirred for 4 h and the mixture was treated following the general procedure (III) described above. Deprotected compound **31** (70 mg, quant.) was obtained as a colorless solid. ¹H-NMR (600 MHz, D₂O) δ 8.01 (s, 4H), 4.87 (s, 4H), 4.60 (t, *J* = 4.9 Hz, 8H), 4.52 (s, 8H), 3.95 (d, *J* = 4.8 Hz, 12H), 3.90–3.86 (m, 4H), 3.85 (dd, *J* = 7.4, 3.7 Hz, 4H), 3.81 (dd, *J* = 9.1, 3.2 Hz, 4H), 3.75 (dd, *J* = 12.2, 5.4 Hz, 4H), 3.72–3.65 (m, 12H), 3.65–3.60 (m, 24H), 3.60–3.57 (m, 16H), 3.40 (s, 8H). ¹³C-NMR (150 MHz, D₂O) δ 144.1, 125.3, 99.9, 72.7, 70.5, 69.9, 69.9, 69.7, 69.6, 69.5, 69.5, 68.7, 68.1, 66.7, 66.3, 63.5, 60.9, 49.9, 44.6. ESI⁺-HRMS: [M + 2H]²⁺ calcd for C₇₃H₁₃₀N₁₂O₄₀, 907.4248; found: 907.4258.

Synthesis of 33. Into a solution of hexapropargylated core (**15**) (30 mg, 0.03 mmol, 1.0 equiv.) in a mixture of THF/H₂O (4 mL, 3:1, *v/v*), was added **19** (152 mg, 0.29 mmol, 9.6 equiv.), Na-ascorbate (12 mg, 0.06 mmol, 1.98 equiv.) and CuSO₄·5H₂O (14 mg, 0.05 mmol, 1.8 equiv.). The mixture was stirred at 50 °C for 2 h, then at room temperature for 5 h. Upon completion of the reaction, EtOAc was added to the reaction mixture and further processed as given in general procedure (I) to afford compound **33** as a white powder (97 mg, 91%); *R*_f = 0.3 (with 5% MeOH in CH₂Cl₂ as eluents). ¹H-NMR (600 MHz, CDCl₃) δ 7.83 (s, 6H, *H*-triazole), 6.85 (d, *J* = 9.0 Hz, 12H, aromatic), 6.79 (d, *J* = 9.1 Hz, 12H, aromatic), 5.31–5.19 (m, 18H, *H*-2, 3 and 4), 5.16–5.08 (m, 12H, Ar-OCH₂), 4.82 (s, 6H, *H*-1), 4.64–4.54 (m, 12H, Man-OCH₂), 4.21 (dd, *J* = 12.3, 5.1 Hz, 6H, CHH'^N), 4.16–4.09 (m, 6H, *H*-6), 4.04 (dd, *J* = 12.3, 2.2 Hz,

6H, *H*-6'), 3.90 (dt, *J* = 10.4, 5.1 Hz, 6H, *CHH'*N), 3.65–3.58 (m, 6H, *H*-5), 2.13 (s, 18H, COCH₃), 2.09 (s, 18H, COCH₃), 1.98 (s, 18H, COCH₃), 1.97 (s, 18H, COCH₃). ¹³C-NMR (151 MHz, CDCl₃) δ 170.8 (C=O), 170.2 (C=O), 170.2 (C=O), 169.9 (C=O), 155.7 (CO-aromatic), 145.1 (C-triazole), 144.5 (C_p-aromatic), 124.5 (CH-triazole), 122.2 (C_m-aromatic), 115.7 (C_o-aromatic), 97.9 (C-1), 77.2 (C-2), 69.6 (C-3), 69.5 (C-4), 69.3 (C-5), 66.6 (C_j), 66.2 (C_b), 62.7 (C-6), 50.0 (C_i), 21.1 (COCH₃), 21.0 (COCH₃), 20.9 (COCH₃). ³¹P-NMR (243 MHz, CDCl₃) δ 9.84. ESI⁺-HRMS: [M + 3H]³⁺ calcd for C₁₅₀H₁₈₃N₂₁O₇₂P₃, 1174.34752; found: 1174.6753.

Synthesis of 34. Compound **33** (97 mg, 0.03 mmol) and sodium methoxide (16 μL from 1 M solution in MeOH) in 3 mL of methanol were stirred for 4 h and the mixture was treated following the general procedure (III) described above. Deprotected compound **34** (69 mg, quant.) was obtained as a white solid. ¹H-NMR (600 MHz, D₂O) δ 7.80 (s, 6H), 6.56 (s, 24H), 4.84 (s, 18H), 4.65 (s, 6H), 4.36 (s, 12H), 3.87 (s, 6H), 3.74 (s, 6H), 3.71–3.50 (m, 24H), 3.05 (d, *J* = 3.2 Hz, 6H). ¹³C-NMR (151 MHz, D₂O) δ 154.9, 143.8, 143.1, 125.1, 121.6, 115.5, 99.5, 72.8, 70.5, 69.9, 66.4, 65.2, 61.3, 60.6, 49.8. ³¹P-NMR (243 MHz, CDCl₃) δ 10.16. ESI⁺-HRMS: [M + 3H]³⁺ calcd for C₁₀₂H₁₃₅N₂₁O₄₈P₃, 838.26603; found: 838.5901.

Synthesis of 35. Into a solution of hexapropargylated core (**15**) (50 mg, 0.049 mmol, 1.0 equiv.) in a mixture of THF/H₂O (4 mL, 3:1, *v/v*), was added **32** (185 mg, 0.44 mmol, 6 equiv.), Na-ascorbate (20 mg, 0.1 mmol, 0.1 equiv.) and CuSO₄·5H₂O (22 mg, 0.28 mmol, 0.09 equiv.). The mixture was stirred at 50 °C for 2 h, then at room temperature for 5 h. Upon completion of the reaction, EtOAc was added to the reaction mixture and further processed as given in general procedure (I) to afford compound **35** as a white powder (171 mg, 96%); *R*_f = 0.2 (with 5% MeOH in CH₂Cl₂ as eluents). ¹H-NMR (600 MHz, CDCl₃) δ 7.74 (s, 6H, *H*-triazole), 6.92–6.74 (m, 24H, aromatic), 5.16 (t, *J* = 9.5 Hz, 6H, *H*-3), 5.11 (d, *J* = 6.3 Hz, 12H, b), 5.05 (t, *J* = 9.7 Hz, 6H, *H*-4), 4.98 (dd, *J* = 9.6, 8.0 Hz, 6H, *H*-2), 4.60 (dt, *J* = 14.4, 4.0 Hz, 6H, j), 4.53–4.47 (m, 12H, j', *H*-1), 4.24 (dt, *J* = 8.4, 4.5 Hz, 12H, i, *H*-6), 4.13 (dd, *J* = 12.3, 2.2 Hz, 6H, *H*-6'), 3.93 (ddd, *J* = 10.6, 8.8, 3.5 Hz, 6H, i'), 3.70 (ddd, *J* = 10.0, 4.6, 2.4 Hz, 6H, *H*-5), 2.07 (s, 18H, COCH₃), 2.01 (s, 18H, COCH₃), 1.97 (s, 18H, COCH₃), 1.92 (s, 18H, COCH₃). ¹³C-NMR (150 MHz, CDCl₃) δ 169.6 (C=O), 169.1 (C=O), 168.4 (C=O), 168.4 (C=O), 154.2 (CO-aromatic), 143.6 (C-triazole), 142.7 (C_p-aromatic), 123.3 (CH-triazole), 120.9 (C_m-aromatic), 114.3 (C_o-aromatic), 99.5 (C-1), 71.5 (C-2), 70.9 (C-3), 69.9 (C-4), 67.2 (C-5), 66.7 (C_j), 61.2 (C_b), 60.7 (C-6), 48.9 (C_i), 19.7 (COCH₃), 19.7 (COCH₃), 19.6 (COCH₃), 19.5 (COCH₃). ³¹P-NMR (243 MHz, CDCl₃) δ 9.72. MALDI-TOF: [M]⁺ calcd for C₁₅₀H₁₇₉N₂₁O₇₂P₃: 3519.020; found, 3519.489.

Synthesis of 36. Compound **35** (100 mg, 0.03 mmol) and sodium methoxide (16 μL from 1 M solution in MeOH) in 3 mL of methanol were stirred for 4 h and the mixture was treated following the general procedure (III) described above. Deprotected compound **36** (78 mg, quant.) was obtained as a white powder. ¹H-NMR (600 MHz, MeOD) δ 8.05 (s, 6H), 6.70 (dd, *J* = 40.7, 9.1 Hz, 24H), 5.02 (s, 12H), 4.51 (t, *J* = 5.0 Hz, 12H), 4.26 (d, *J* = 7.9 Hz, 6H), 4.17–4.07 (m, 6H), 4.01–3.84 (m, 6H), 3.75 (dd, *J* = 12.1, 1.9 Hz, 6H), 3.55 (dd, *J* = 12.1, 5.8 Hz, 6H), 3.31 (t, *J* = 9.0 Hz, 6H), 3.27–3.22 (m, 6H), 3.18 (d, *J* = 9.6 Hz, 6H), 3.11 (dd, *J* = 9.2, 8.0 Hz, 6H). ¹³C-NMR (150 MHz, MeOD) δ 156.3, 145.2, 144.2, 126.5, 122.7, 116.6, 103.8, 77.3, 77.1, 74.3, 70.9, 68.9, 62.4, 62.1, 51.4, 49.4, 49.0, 24.2. ³¹P-NMR (243 MHz, MeOD) δ 10.25. MALDI-TOF: [M + H]⁺ calcd for C₁₀₂H₁₃₂N₂₁O₄₈P₃: 2512.778; found, 2512.851.

Synthesis of 37. Into a solution of hexapropargylated core (**15**) (25 mg, 0.025 mmol, 1.0 equiv.) in a mixture of THF/H₂O (4 mL, 3:1, *v/v*), was added compound **22** (140 mg, 0.25 mmol, 10 equiv.), Na-ascorbate (10 mg, 0.05 mmol, 2.1 equiv.) and CuSO₄·5H₂O (10.8 mg, 0.04 mmol, 1.8 equiv.). The mixture was stirred at 50 °C for 2 h, then at room temperature for 5 h. Upon completion of the reaction, EtOAc was added to the reaction mixture and further processed as given in general procedure (I) to afford compound **37** as a white powder (101 mg, 96%); *R*_f = 0.22 (with 4% MeOH in CH₂Cl₂ as eluents). ¹H-NMR (600 MHz, CDCl₃) δ 7.85 (s, 6H, *H*-triazole), 6.81 (dd, *J* = 29.7, 9.0 Hz, 24H, aromatic), 5.33 (dd, *J* = 10.0, 3.4 Hz, 6H, *H*-3), 5.28 (t, *J* = 10.0 Hz, 6H, *H*-2), 5.25 (dd, *J* = 3.2,

1.6 Hz, 6H, *H-4*), 5.13 (d, *J* = 7.6 Hz, 12H, b), 4.86 (s, 6H, *H-1*), 4.54 (t, *J* = 5.1 Hz, 12H, c), 4.28 (dd, *J* = 12.2, 4.9 Hz, 6H, *H-6*), 4.08 (dd, *J* = 12.3, 2.2 Hz, 6H, *H-6'*), 4.05 (ddd, *J* = 9.7, 4.8, 2.3 Hz, 6H, *H-5*), 3.88 (t, *J* = 5.2 Hz, 12H, d), 3.81–3.76 (m, 6H, j), 3.67–3.65 (m, 6H, j'), 3.63 (d, *J* = 3.7 Hz, 12H, i), 3.61 (d, *J* = 7.6 Hz, 48H, g, f, e, h), 2.14 (s, 18H, COCH₃), 2.09 (s, 18H, COCH₃), 2.02 (s, 18H, COCH₃), 1.98 (s, 18H, COCH₃). ¹³C-NMR (150 MHz, CDCl₃) δ 170.7 (C=O), 170.0 (C=O), 169.9 (C=O), 169.7 (C=O), 155.3 (CO-aromatic), 144.6 (C-triazole), 143.6 (C_P-aromatic), 124.2 (CH-triazole), 121.8 (C_m-aromatic), 115.3 (C_O-aromatic), 97.7 (C-1), 70.7 (C_d), 70.6 (C_g), 70.5 (C_f), 69.9 (C_e), 69.6 (C_h), 69.5 (C_j), 69.4 (C-2), 69.1 (C-3), 68.4 (C-4), 67.4 (C-5), 66.1 (C_i), 62.4 (C_b), 62.3 (C-6), 50.2 (C_c), 20.9 (COCH₃), 20.8 (COCH₃), 20.7 (COCH₃), 20.7 (COCH₃). ³¹P-NMR (243 MHz, CDCl₃) δ 9.68. ESI⁺-HRMS: [M + 2H]²⁺ calcd for C₁₈₆H₂₅₄N₂₁O₉₀P₃, 2158.2604; found: 2158.2588.

Synthesis of 38. Compound **37** (100 mg, 0.023 mmol) and sodium methoxide (16 µL from 1 M solution in MeOH) in 3 mL of methanol were stirred for 4 h and the mixture was treated following the general procedure (III) described above. Deprotected compound **38** (77 mg, quant.) was obtained as a white solid. ¹H-NMR (300 MHz, D₂O) δ 7.96 (s, 6H, *H*-triazole), 6.71 (s, 24H, aromatic), 4.99 (s, 12H, b), 4.82 (s, 6H, *H-1*), 4.49 (s, 12H, c), 3.93–3.75 (m, 36H, *H-2,3,4,5,6* and 6'), 3.74–3.38 (m, 84H, d, e, f, g, h, i, j). ³¹P-NMR (122 MHz, D₂O) δ 10.11. ESI⁺-HRMS: [M + 2H]²⁺ calcd for C₁₃₈H₂₀₆N₂₁O₆₆P₃, 1653.6321; found: 1653.6342.

Synthesis of 39. Into a solution of hexapropargylated core (**15**) (26 mg, 0.026 mmol, 1.0 equiv.) in a mixture of THF/H₂O (4 mL, 3:1, *v/v*), was added (**26**) (400 mg, 0.24 mmol, 9.6 equiv.), Na-ascorbate (11 mg, 0.06 mmol, 2.1 equiv.) and CuSO₄·5H₂O (12 mg, 0.05 mmol, 1.8 equiv.). The mixture was stirred at 50 °C for 2 h, then at room temperature for 5 h. Upon completion of the reaction, EtOAc was added to the reaction mixture and further processed as given in general procedure (I) to afford compound **39** as a white powder (272 mg, 97%); *R*_f = 0.2 (with 5% MeOH in CH₂Cl₂ as eluents). ¹H-NMR (600 MHz, CDCl₃) δ 7.82 (s, 6H, H_A-triazole), 7.69 (s, 18H, H_B-triazole), 6.82 (dd, *J* = 32.8, 8.8 Hz, 24H, aromatic), 5.22 (t, *J* = 10.0 Hz, 18H, *H-3*), 5.19 (d, *J* = 3.2 Hz, 12H, *H-4*), 5.17 (s, 12H, *H-2*), 5.09 (s, 12H, b), 4.79 (s, 18H, *H-1*), 4.59 (dd, *J* = 10.5, 5.7 Hz, 36H, i), 4.54 (s, 36H, h), 4.49 (t, *J* = 5.0 Hz, 12H, c), 4.19 (dd, *J* = 12.3, 5.0 Hz, 18H, *H-6*), 4.14–4.07 (m, 18H, j'), 4.02 (dd, *J* = 12.3, 1.8 Hz, 18H, *H-6'*), 3.89 (m, 18H, j), 3.86 (t, *J* = 5.2 Hz, 12H, d), 3.62–3.59 (m, 18H, *H-5*), 3.55–3.48 (m, 24H, e, f), 3.46 (s, 36H, g'), 3.40 (s, 36H, g), 2.11 (s, 54H, COCH₃), 2.06 (s, 54H, COCH₃), 2.01 (s, 54H, COCH₃), 1.96 (s, 54H, COCH₃). ¹³C-NMR (150 MHz, CDCl₃) δ 170.6 (C=O), 169.9 (C=O), 169.6 (C=O), 169.1 (C=O), 155.4 (CO-aromatic), 145.5 (C_B-triazole), 144.6 (C_A-triazole), 143.5 (C_P-aromatic), 124.2 (C_{AH}-triazole), 123.7 (C_{BH}-triazole), 121.8 (C_m-aromatic), 115.3 (C_O-aromatic), 97.5 (C-1), 71.0 (C_f), 70.3 (C_e), 69.7 (C_g), 69.4 (C_d), 69.2 (C-2), 69.1 (C-3), 68.9 (C-4), 68.8 (C-5), 66.3 (C_j), 65.7 (C_b), 64.8 (C_h), 62.2 (C-6), 50.3 (C_i), 49.5 (C_c), 45.3 (C_q), 20.8 (COCH₃), 20.7 (COCH₃), 20.7 (COCH₃), 20.7 (COCH₃). ³¹P-NMR (243 MHz, CDCl₃) δ 9.54. MALDI-TOF: [M + H]⁺ calcd for C₄₅₀H₆₀₇N₇₅O₂₂₂P₃: 10705.772; found, 10706.833.

Synthesis of 40. Compound **39** (200 mg, 0.02 mmol) and sodium methoxide (16 µL from 1 M solution in MeOH) in 3 mL of methanol were stirred for 4 h and the mixture was treated following the general procedure (III) described above. Deprotected compound **40** (150 mg, quant.) was obtained as a white solid. ¹H-NMR (600 MHz, D₂O) δ 8.05 (s, 1H), 7.92 (s, 3H), 6.74 (dd, *J* = 42.4, 7.8 Hz, 4H), 5.09 (s, 2H), 4.75 (s, 3H), 4.61–4.51 (m, 6H), 4.45 (s, 6H), 4.02 (s, 3H), 3.83 (s, 6H), 3.71 (d, *J* = 10.8 Hz, 3H), 3.63 (ddd, *J* = 25.4, 15.8, 7.5 Hz, 8H), 3.36 (dd, *J* = 75.3, 44.3 Hz, 12H), 3.11–3.02 (m, 3H). ¹³C-NMR (150 MHz, D₂O) δ 215.7, 154.9, 144.3, 143.8, 142.9, 125.3, 125.1, 121.7, 115.8, 99.5, 72.8, 70.5, 69.9, 69.7, 68.9, 68.7, 68.3, 66.3, 65.4, 63.6, 61.4, 60.6, 50.1, 49.9, 44.8, 30.2, 29.7, 29.6, 29.4, 29.3, 29.2. ³¹P-NMR (243 MHz, D₂O) δ 10.06. MALDI-TOF: [M + H]⁺ calcd for C₃₀₆H₄₆₃N₇₅O₁₅₀P₃: 7681.011; found, 7681.383.

4. Conclusions

The synthesis of a new library of glycodendrimers possessing pegylated sugars in the aglycones with different valences from 2 to 18, has been achieved in satisfying yields provided by the highly efficient click chemistry. The above set of assay is relevant in demonstrating the relative binding abilities of these glycodendrimers for their respective lectins. In DLS measurements, the use of kinetics of mannodendrimers-protein aggregation in presence of the mannose-specific lectin ConA gave useful preliminary results. We noticed that, highly substituted glycodendrimers demonstrated a higher capacity to crosslink ConA by forming insoluble complexes within a short time frame. Hence, the results obtained herein suggest that dendrimers harboring pegylated mannosides provided gradual and functional binding interactions with a model mannose-binding protein such as ConA. Perhaps, more importantly, is the fact that the synthetic strategy that we recently coined “onion peel strategy” offers advantages over classical ones [32,47,54–57]. Indeed, by choosing the cyclotriphosphazene core having six functional groups available (an A₆ core) together with an AB₃ pentaerythritol scaffold at the next generation, provided a dendrimeric architecture from which, a total of 18 surface groups can be achieved by a convergent synthesis in a short synthetic sequence leading to a G1 generation. Ongoing activities, aimed at measuring the inhibition of biofilm formation from uropathogenic *E. coli*, are underway.

Supplementary Materials: Supplementary materials are available online.

Author Contributions: C.S. performed the experiments, analyzed the NMR data and DLS measurements and wrote the paper. T.C.S. and L.M.S. contributed equally to this work. A.A. co-directed the student C.S. and proofread the paper. R.R. conceived the paper, designed the thematic, wrote and finalized the paper.

Funding: This research was funded by Natural Science and Engineering Research Council of Canada (NSERC) and the Fonds du Québec—Nature et Technologies to R.R.

Acknowledgments: This work was supported by grants from the Natural Science and Engineering Research Council of Canada (NSERC) to R.R. including a Canadian Research Chair and the Fonds du Québec—Nature et Technologies to R.R.

Conflicts of Interest: The authors declare no conflict of interest. The founding sponsors had no role in the design of the study; in the collection, analyses, or interpretation of data; in the writing of the manuscript and in the decision to publish the results.

References

1. Firon, N.; Ashkenazi, S.; Mirelman, D.; Ofek, I.; Sharon, N. Aromatic alpha-glycosides of mannose are powerful inhibitors of the adherence of type 1 fimbriated *Escherichia coli* to yeast and intestinal epithelial cells. *Infect. Immun.* **1987**, *55*, 472–476. [[PubMed](#)]
2. Vanwetswinkel, S.; Volkov, A.N.; Sterckx, Y.G.; Garcia-Pino, A.; Buts, L.; Vranken, W.F.; Bouckaert, J.; Roy, R.; Wyns, L.; van Nuland, N.A. Study of the structural and dynamic effects in the FimH adhesin upon alpha-d-heptyl mannose binding. *J. Med. Chem.* **2014**, *57*, 1416–1427. [[CrossRef](#)] [[PubMed](#)]
3. Wellens, A.; Lahmann, M.; Touaibia, M.; Vaucher, J.; Oscarson, S.; Roy, R.; Remaut, H.; Bouckaert, J. The tyrosine gate as a potential entropic lever in the receptor-binding site of the bacterial adhesin FimH. *Biochemistry* **2012**, *51*, 4790–4799. [[CrossRef](#)] [[PubMed](#)]
4. Costerton, J.W.; Stewart, P.S.; Greenberg, E.P. Bacterial biofilms: A common cause of persistent infections. *Science* **1999**, *284*, 1318–1322. [[CrossRef](#)] [[PubMed](#)]
5. Touaibia, M.; Roy, R. Glycodendrimers as anti-adhesion drugs against type 1 fimbriated *E. coli* uropathogenic infections. *Mini Rev. Med. Chem.* **2007**, *7*, 1270–1283. [[CrossRef](#)] [[PubMed](#)]
6. Rabbani, S.; Krammer, E.M.; Roos, G.; Zalewski, A.; Preston, R.; Eid, S.; Zihlmann, P.; Prevost, M.; Lensink, M.F.; Thompson, A.; et al. Mutation of Tyr137 of the universal *Escherichia coli* fimbrial adhesin FimH relaxes the tyrosine gate prior to mannose binding. *IUCr* **2017**, *4*, 7–23. [[CrossRef](#)] [[PubMed](#)]
7. Hung, C.S.; Bouckaert, J.; Hung, D.; Pinkner, J.; Widberg, C.; DeFusco, A.; Auguste, C.G.; Strouse, R.; Langermann, S.; Waksman, G.; et al. Structural basis of tropism of *Escherichia coli* to the bladder during urinary tract infection. *Mol. Microbiol.* **2002**, *44*, 903–915. [[CrossRef](#)] [[PubMed](#)]

8. Touaibia, M.; Krammer, E.M.; Shiao, T.C.; Yamakawa, N.; Wang, Q.; Glinschert, A.; Papadopoulos, A.; Mousavifar, L.; Maes, E.; Oscarson, S.; et al. Sites for Dynamic Protein-Carbohydrate Interactions of O- and C-Linked Mannosides on the *E. coli* FimH Adhesin. *Molecules* **2017**, *22*, 1101. [[CrossRef](#)] [[PubMed](#)]
9. Knight, S.D.; Bouckaert, J. Structure, function and assembly of type 1 fimbriae. *Top. Curr. Chem.* **2009**, *288*, 67–107. [[PubMed](#)]
10. Schaechter, M. *Escherichia coli* and Salmonella 2000: The view from here. *Microbiol. Mol. Biol. Rev.* **2001**, *65*, 119–130. [[CrossRef](#)] [[PubMed](#)]
11. Mulvey, M.A.; Schilling, J.D.; Martinez, J.J.; Hultgren, S.J. Bad bugs and beleaguered bladders: Interplay between uropathogenic *Escherichia coli* and innate host defenses. *Proc. Natl. Acad. Sci. USA* **2000**, *97*, 8829–8835. [[CrossRef](#)] [[PubMed](#)]
12. Aronson, M.; Medalia, O.; Schori, L.; Mirelman, D.; Sharon, N.; Ofek, I. Prevention of colonization of the urinary tract of mice with *Escherichia coli* by blocking of bacterial adherence with methyl α -D-mannopyranoside. *J. Infect. Dis.* **1979**, *139*, 329–332. [[CrossRef](#)] [[PubMed](#)]
13. Papadopoulos, A.; Shiao, T.C.; Roy, R. Diazo transfer and click chemistry in the solid phase syntheses of lysine-based glycodendrimers as antagonists against *Escherichia coli* FimH. *Mol. Pharm.* **2012**, *9*, 394–403. [[CrossRef](#)] [[PubMed](#)]
14. Mammen, M.; Choi, S.-K.; Whitesides, G.M. Polyvalent Interactions in Biological Systems: Implications for Design and Use of Multivalent Ligands and Inhibitors—Mammen—1998—Angewandte Chemie International Edition—Wiley Online Library. *Angew. Chem. Int. Ed.* **1998**, *37*, 2754–2794. [[CrossRef](#)]
15. Lee, R.T.; Lee, Y.C. Affinity enhancement by multivalent lectin—carbohydrate interaction. *Glycoconj. J.* **2000**, *17*, 543–551. [[CrossRef](#)] [[PubMed](#)]
16. Kitov, P.I.; Shimizu, H.; Homans, S.W.; Bundle, D.R. Optimization of tether length in nonglycosidically linked bivalent ligands that target sites 2 and 1 of a Shiga-like toxin. *J. Am. Chem. Soc.* **2003**, *125*, 3284–3294. [[CrossRef](#)] [[PubMed](#)]
17. Kiessling, L.L.; Gestwicki, J.E.; Strong, L.E. Synthetic multivalent ligands as probes of signal transduction. *Angew. Chem. Int. Ed. Engl.* **2006**, *45*, 2348–2368. [[CrossRef](#)] [[PubMed](#)]
18. Roy, R. Syntheses and some applications of chemically defined multivalent glycoconjugates. *Curr. Opin. Struct. Biol.* **1996**, *6*, 692–702. [[CrossRef](#)]
19. Roy, R. A decade of glycodendrimer chemistry. *TIGGS* **2003**, *15*, 291–310. [[CrossRef](#)]
20. Roy, R.; Touaibia, M. 3.36-Application of Multivalent Mannosylated Dendrimers in Glycobiology. In *Comprehensive Glycoscience*; Kamerling, H., Ed.; Elsevier: Oxford, UK, 2007; pp. 821–870.
21. Touaibia, M.; Wellens, A.; Shiao, T.C.; Wang, Q.; Sirois, S.; Bouckaert, J.; Roy, R. Mannosylated G(0) dendrimers with nanomolar affinities to *Escherichia coli* FimH. *Chem. Med. Chem.* **2007**, *2*, 1190–1201. [[CrossRef](#)] [[PubMed](#)]
22. Touaibia, M.; Shiao, T.C.; Papadopoulos, A.; Vaucher, J.; Wang, Q.; Benhamioud, K.; Roy, R. Tri- and hexavalent mannoside clusters as potential inhibitors of type 1 fimbriated bacteria using pentaerythritol and triazole linkages. *Chem. Commun.* **2007**, 380–382. [[CrossRef](#)] [[PubMed](#)]
23. Nagahori, N.; Lee, R.T.; Nishimura, S.; Page, D.; Roy, R.; Lee, Y.C. Inhibition of adhesion of type 1 fimbriated *Escherichia coli* to highly mannosylated ligands. *Chembiochem Eur. J. Chem. Biol.* **2002**, *3*, 836–844. [[CrossRef](#)]
24. Pieters, R.J. Intervention with bacterial adhesion by multivalent carbohydrates. *Med. Res. Rev.* **2007**, *27*, 796–816. [[CrossRef](#)] [[PubMed](#)]
25. Imberty, A.; Chabre, Y.M.; Roy, R. Glycomimetics and glycodendrimers as high affinity microbial anti-adhesins. *Chem. Eur. J.* **2008**, *14*, 7490–7499. [[CrossRef](#)] [[PubMed](#)]
26. Sleiman, M.; Varrot, A.; Raimundo, J.M.; Gingras, M.; Goekjian, P.G. Glycosylated asterisks are among the most potent low valency inducers of Concanavalin A aggregation. *Chem. Commun.* **2008**, 48, 6507–6509. [[CrossRef](#)] [[PubMed](#)]
27. Chabre, Y.M.; Papadopoulos, A.; Arnold, A.A.; Roy, R. Synthesis and solvodynamic diameter measurements of closely related mannodendrimers for the study of multivalent carbohydrate-protein interactions. *Beilstein J. Org. Chem.* **2014**, 1524–1535. [[CrossRef](#)] [[PubMed](#)]
28. Touaibia, M.; Roy, R. First synthesis of “Majoral-Type” glycodendrimers bearing covalently bound alpha-D-mannopyranoside residues onto a hexachlorocyclotriphosphazene core. *J. Org. Chem.* **2008**, *73*, 9292–9302. [[CrossRef](#)] [[PubMed](#)]

29. Pagé, D.; Roy, R. Synthesis of divalent α -D-mannopyranosylated clusters having enhanced binding affinities towards concanavalin A and pea lectins. *Bioorg. Med. Chem. Lett.* **1996**, *6*, 1765–1770. [[CrossRef](#)]
30. Sharon, N.; Ofek, I. Safe as mother's milk: Carbohydrates as future anti-adhesion drugs for bacterial diseases. *Glycoconj. J.* **2000**, *17*, 659–664. [[CrossRef](#)] [[PubMed](#)]
31. Bock, V.D.; Hiemstra, H.; van Maarseveen, J.H. CuI-Catalyzed Alkyne–Azide “Click” Cycloadditions from a Mechanistic and Synthetic Perspective. *Eur. J. Org. Chem.* **2006**, 51–68. [[CrossRef](#)]
32. Bagul, R.S.; Hosseini, M.; Shiao, T.C.; Saadeh, N.K.; Roy, R. Heterolayered hybrid dendrimers with optimized sugar head groups for enhancing carbohydrate–Protein interactions. *Polym. Chem.* **2017**, *8*, 5354–5366. [[CrossRef](#)]
33. Chabre, Y.M.; Roy, R. Design and Creativity in Synthesis of Multivalent Neoglycoconjugates. *Adv. Carbohydr. Chem. Biochem.* **2010**, *63*, 165–393. [[PubMed](#)]
34. Chabre, Y.M.; Roy, R. Multivalent glycoconjugate syntheses and applications using aromatic scaffolds. *Chem. Soc. Rev.* **2013**, *42*, 4657–4708. [[CrossRef](#)] [[PubMed](#)]
35. Chabre, Y.M.; Roy, R. Recent trends in glycodendrimer syntheses and applications. *Curr. Top. Med. Chem.* **2008**, *8*, 1237–1285. [[CrossRef](#)] [[PubMed](#)]
36. Caminade, A.M.; Ouali, A.; Laurent, R.; Turrin, C.O.; Majoral, J.P. The dendritic effect illustrated with phosphorus dendrimers. *Chem. Soc. Rev.* **2015**, *44*, 3890–3899. [[CrossRef](#)] [[PubMed](#)]
37. Caminade, A.-M.; Turrin, C.-O.; Majoral, J.-P. Biological properties of phosphorus dendrimers. *New J. Chem.* **2010**, *34*, 1512–1524. [[CrossRef](#)]
38. Wang, L.; Yang, Y.-X.; Shi, X.; Mignani, S.; Caminade, A.-M.; Majoral, J.-P. Cyclotriphosphazene core-based dendrimers for biomedical applications: An update on recent advances. *J. Mater. Chem. B* **2018**, *6*, 884–895. [[CrossRef](#)]
39. Caminade, A.M.; Turrin, C.O.; Majoral, J.P. Biological properties of water-soluble phosphorhydrazone dendrimers. *Braz. J. Pharm. Sci.* **2013**, *49*, 34–43. [[CrossRef](#)]
40. Caminade, A.M.; Hameau, A.; Majoral, J.P. The specific functionalization of cyclotriphosphazene for the synthesis of smart dendrimers. *Dalton Trans.* **2016**, *45*, 1810–1822. [[CrossRef](#)] [[PubMed](#)]
41. Park, S.; Shin, I. Carbohydrate microarrays for assaying galactosyltransferase activity. *Org. Lett.* **2007**, *9*, 1675–1678. [[CrossRef](#)] [[PubMed](#)]
42. Pratt, J.; Roy, R.; Annabi, B. Concanavalin-A-induced autophagy biomarkers requires membrane type-1 matrix metalloproteinase intracellular signaling in glioblastoma cells. *Glycobiology* **2012**, *22*, 1245–1255. [[CrossRef](#)] [[PubMed](#)]
43. Papp, I.; Dervedde, J.; Enders, S.; Riese, S.B.; Shiao, T.C.; Roy, R.; Haag, R. Multivalent presentation of mannose on hyperbranched polyglycerol and their interaction with concanavalin A lectin. *Chembiochem Eur. J. Chem. Biol.* **2011**, *12*, 1075–1083. [[CrossRef](#)] [[PubMed](#)]
44. Roy, R.; Trono, M.C.; Giguère, D. Effects of Linker Rigidity and Orientation of Mannoside Cluster for Multivalent Interactions with Proteins. *ACS Symp. Ser.* **2005**, *896*, 137–150.
45. Dam, T.K.; Roy, R.; Page, D.; Brewer, C.F. Negative cooperativity associated with binding of multivalent carbohydrates to lectins. Thermodynamic analysis of the “multivalency effect”. *Biochemistry* **2002**, *41*, 1351–1358. [[CrossRef](#)] [[PubMed](#)]
46. Dam, T.K.; Roy, R.; Das, S.K.; Oscarson, S.; Brewer, C.F. Binding of multivalent carbohydrates to concanavalin A and Dioclea grandiflora lectin. Thermodynamic analysis of the “multivalency effect”. *J. Biol. Chem.* **2000**, *275*, 14223–14230. [[CrossRef](#)] [[PubMed](#)]
47. Bagul, R.S.; Hosseini, M.M.; Shiao, T.C.; Roy, R. “Onion peel” glycodendrimer syntheses using mixed triazine and cyclotriphosphazene scaffolds. *Can. J. Chem.* **2017**, *95*, 975–983. [[CrossRef](#)]
48. Wang, G.N.; Andre, S.; Gabius, H.J.; Murphy, P.V. Bi- to tetravalent glycoclusters: Synthesis, structure-activity profiles as lectin inhibitors and impact of combining both valency and headgroup tailoring on selectivity. *Org. Biomol. Chem.* **2012**, *10*, 6893–6907. [[CrossRef](#)] [[PubMed](#)]
49. Zhu, J.; Zhu, X.; Kang, E.T.; Neoh, K.G. Design and synthesis of star polymers with hetero-arms by the combination of controlled radical polymerizations and click chemistry. *Polymer* **2007**, *48*, 6992–6999. [[CrossRef](#)]
50. Caverio, E.; Zablocka, M.; Caminade, A.-M.; Majoral, J.P. Design of Bisphosphonate-Terminated Dendrimers. *Eur. J. Org. Chem.* **2010**, *2010*, 2759–2767. [[CrossRef](#)]

51. Lindhorst, T.K.; Kötter, S.; Krallmann-Wenzel, U.; Ehlers, S. Trivalent α -D-mannoside clusters as inhibitors of type-1 fimbria-mediated adhesion of *Escherichia coli*: structural variation and biotinylation. *J. Chem. Soc. Perkin Trans. 1* **2001**, 823–831. [[CrossRef](#)]
52. Yin, L.; Chen, Y.; Zhang, Z.; Yin, Q.; Zheng, N.; Cheng, J. Biodegradable micelles capable of mannose-mediated targeted drug delivery to cancer cells. *Macromol. Rapid Commun.* **2015**, *36*, 483–489. [[CrossRef](#)] [[PubMed](#)]
53. Zhang, S.; Moussodia, R.-O.; Sun, H.-J.; Leowanawat, P.; Muncan, A.; Nusbaum, C.D.; Chelling, K.M.; Heiney, P.A.; Klein, M.L.; André, S.; Roy, R.; Gabius, H.-J.; Percec, P. Mimicking biological membranes with programmable glycan ligands self-assembled from amphiphilic Janus glycodendrimers. *Angew. Chem. Int. Ed. Engl.* **2014**, *53*, 10899–10903. [[CrossRef](#)] [[PubMed](#)]
54. Abbassi, L.; Chabre, Y.M.; Kottari, N.; Arnold, A.A.; André, S.; Josserand, J.; Gabius, H.-J.; Roy, R. Multifaceted glycodendrimers with programmable bioactivity through convergent, divergent and accelerated approaches using polyfunctional cyclotriphosphazenes. *Polym. Chem.* **2015**, *6*, 7666–7683. [[CrossRef](#)]
55. Sharma, R.; Naresh, K.; Chabre, Y.M.; Rej, R.; Saadeh, N.K.; Roy, R. “Onion peel” dendrimers: A straightforward synthetic approach towards highly diversified architectures. *Polym. Chem.* **2014**, *5*, 4321–4331. [[CrossRef](#)]
56. Sharma, R.; Zhang, I.; Abbassi, L.; Rej, R.; Maysinger, D.; Roy, R. A fast track strategy toward highly functionalized dendrimers with different structural layers: An “onion peel approach”. *Polym. Chem.* **2015**, *6*, 1436–1444. [[CrossRef](#)]
57. Sharma, R.; Kottari, N.; Chabre, Y.M.; Abbassi, L.; Shiao, T.C.; Roy, R. A highly versatile convergent/divergent “onion peel” synthetic strategy toward potent multivalent glycodendrimers. *Chem. Commun.* **2014**, *50*, 13300–13303. [[CrossRef](#)] [[PubMed](#)]

Sample Availability: Samples of the compounds are not available from the authors.



© 2018 by the authors. Licensee MDPI, Basel, Switzerland. This article is an open access article distributed under the terms and conditions of the Creative Commons Attribution (CC BY) license (<http://creativecommons.org/licenses/by/4.0/>).

Article

Evaluation of Amino-Functional Polyester Dendrimers Based on Bis-MPA as Nonviral Vectors for siRNA Delivery

Patrik Stenström ¹, Dario Manzanares ^{2,3}, Yuning Zhang ¹, Valentin Ceña ^{2,3} and Michael Malkoch ^{1,*}

¹ Fiber and Polymer Technology, KTH Royal Institute of Technology, 10044 Stockholm, Sweden; pstens@kth.se (P.S.); yunzha@kth.se (Y.Z.)

² Unidad Asociada Neurodeath, Universidad de Castilla-La Mancha, 02006 Albacete, Spain; dariomanzafarmacia@gmail.com (D.M.); valentin.cena@gmail.com (V.C.)

³ CIBERNED, Instituto de Salud Carlos III, 28029 Madrid, Spain

* Correspondence: malkoch@kth.se; Tel.: +46-8790-8768

Received: 24 July 2018; Accepted: 10 August 2018; Published: 14 August 2018

Abstract: Herein, we present the first evaluation of cationic dendrimers based on 2,2-bis(methylol)propionic acid (bis-MPA) as nonviral vectors for transfection of short interfering RNA (siRNA) in cell cultures. The study encompassed dendrimers of generation one to four (G1–G4), modified to bear 6–48 amino end-groups, where the G2–G4 proved to be capable of siRNA complexation and protection against RNase-mediated degradation. The dendrimers were nontoxic to astrocytes, glioma (C6), and glioblastoma (U87), while G3 and G4 exhibited concentration dependent toxicity towards primary neurons. The G2 showed no toxicity to primary neurons at any of the tested concentrations. Fluorescence microscopy experiments suggested that the dendrimers are highly efficient at endo-lysosomal escape since fluorescently labeled dendrimers were localized specifically in mitochondria, and diffuse cytosolic distribution of fluorescent siRNA complexed by dendrimers was observed. This is a desired feature for intracellular drug delivery, since the endocytic pathway otherwise transfers the drugs into lysosomes where they can be degraded without reaching their intended target. siRNA-transfection was successful in C6 and U87 cell lines using the G3 and G4 dendrimers followed by a decrease of approximately 20% of target protein p42-MAPK expression.

Keywords: dendrimer; siRNA; RNAi; bis-MPA; monodisperse; polycation

1. Introduction

In 1998 researchers found that short sequences of double-stranded RNA could selectively degrade target mRNA through RNA interference (RNAi) and thus prevent the expression of disease-causing proteins [1]. This discovery awarded the authors Andrew Z. Fire and Craig C. Mello the Nobel Prize in 2006. Since nearly any protein-coding gene in the body can theoretically be targeted, the technique is applicable to a much broader array of diseases than those treatable with conventional drugs. These short RNA sequences of 21–23 bases were later termed short interfering RNAs (siRNAs), and are presently being investigated in clinical trials as potential treatments for cancer [2,3] and transthyretin amyloidosis (ATTR) [4,5], a life-threatening disease with cardiac and peripheral nerve symptoms.

However, some major obstacles have to be overcome to attain a successful treatment using siRNA. Free siRNA is rapidly degraded by ribonucleases (RNases) [6], and can be recognized by the immune system to cause inflammatory response [7]. The greatest challenge is perhaps the cellular uptake due to its large size and negative charge. RNAi can only occur through the formation of the RNA-induced silencing complex (RISC) [8], which takes place in cytoplasmic bodies called processing

bodies (P-bodies) that are located throughout the cytoplasm [9]. Thus, it is necessary for the siRNA and its carrier to efficiently escape the endocytic pathway. These obstacles and examples of strategies for overcoming them have been extensively reviewed [10–12].

Viral vectors are generally considered to be the most efficient carriers for nucleic acid delivery. However, these are still struggling to achieve clinical approval due to problems with immune responses and other safety concerns, as well as their complexity of preparation [13–15]. This has led the scientific community towards the development of synthetic alternatives to viral vectors such as liposomes [16], polymers [17], and other nanoparticles [18].

Transfection of neuronal cells can be especially challenging [19,20]. Neurons are generally sensitive to alterations in their environment, and in vivo the brain is separated from the blood stream by the blood–brain barrier (BBB). Successful transfection techniques include the use of liposomes [16], electroporation [21], and viral vectors [22,23]. However, these techniques suffer from drawbacks such as immunological concerns, low transfection rates, or complex methodology.

Dendrimers, being highly branched and compact scaffolds, have been proposed as promising candidates for transporting siRNA inside cells and protecting it from degradation while travelling through the body or staying in the extracellular medium [24]. Cationic dendrimers of e.g., poly(propyleneimine) (PPI) [25], poly(amidoamine) (PAMAM) [26–29], poly(L-Lysine) (PLL) [30] and carbosilane [31,32] types have been shown to form complexes with siRNA through charge interactions, shielding it from RNases and successfully silencing gene expression in cells making them promising nonviral transfection agents. Unfortunately, all the mentioned dendrimers have high solution stability counteracting an important feature for any carrier i.e., the prerequisite of rapid biodegradation into smaller benign compounds that are safely cleared from the body.

Polyester dendrimers based on 2,2-bis(methylol)propionic acid (bis-MPA) are known for their biocompatibility and the biodegradation of their internal esters [33,34]. In a previous publication, a facile route to postfunctionalization of bis-MPA dendrimers with the amino-acid β -alanine was presented [35]. These dendrimers, featuring primary amino groups as ammonium-trifluoroacetate salts, showed lower cytotoxicity in neurons than PAMAM-analogues and exhibited rapid degradation at physiologically relevant pH and temperature.

In this work, we present the first evaluation of dendrimers based on 2,2-bis(methylol)propionic acid (bis-MPA) as nonviral vectors for siRNA delivery. Dendrimers of generation 1–4 with 6–48 ammonium-trifluoroacetate end-groups are evaluated with respect to siRNA complexation, cytotoxicity, and transfection in cell lines and primary neurons in vitro. Knockdown of mitogen-activated protein kinase 1 (p42-MAPK) is monitored to quantify transfection efficiency. The synthesis of a rhodamine-labeled generation four amino-functional dendron is presented, which allows subcellular localization evaluation of these materials using fluorescence microscopy.

2. Results

2.1. Synthesis

The synthesis of amino-functional dendrimers of generation 1–4 has been previously published [35]. Here, the same technique was applied to a previously synthesized generation four dendron [36] equipped with a protected tetraethylene glycol linker at its focal point to enable coupling of e.g., fluorophores with less steric hindrance. The amino end-groups were afforded by attachment of boc protected β -alanines through the fluoride-promoted esterification (FPE) protocol [37]. The hydroxyl at the tetraethylene glycol focal point was activated by catalytic hydrogenation, without affecting the boc protections, and rhodamine B was attached through the FPE route. A hydrophobic byproduct suspected to be the lactone form of rhodamine B [38] was observed. This byproduct was easily removed when the boc-protected crude was deprotected with trifluoroacetic acid by extraction from a water solution. The pure amino-functional dendron was then obtained by lyophilization.

All relevant dendritic structures explored in this study are shown in Figure 1. The synthesis of these sophisticated dendritic scaffolds including their analytical data ($^1\text{H-NMR}$, $^{13}\text{C-NMR}$, MALDI, and fluorescence data for the rhodamine labeled dendron) are presented in detail in the supporting information.

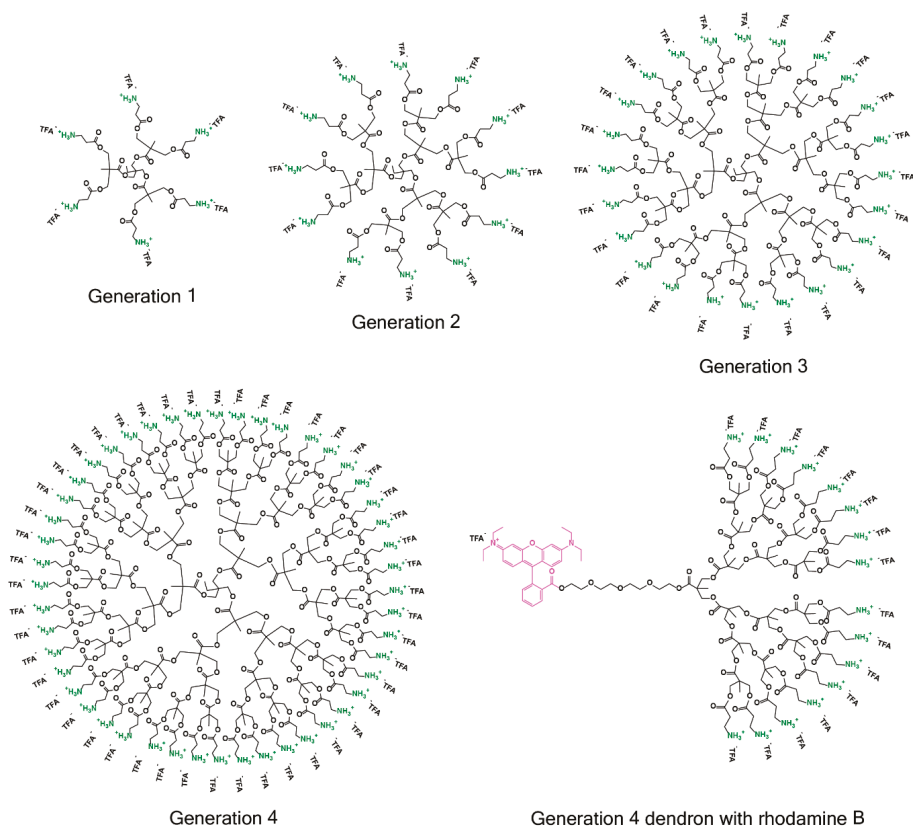


Figure 1. Structures of the generation one to four amino-functional bis-MPA dendrimers that are included in this study, as well as the rhodamine B-labeled generation 4 dendron synthesized to study the subcellular localization of these materials. TFA⁻ is an abbreviation for trifluoroacetate.

2.2. siRNA Complexation and RNase Protection

The complexation ability of the dendrimers to fully complexate all of the siRNA was evaluated by investigating the optimum ratio between the nitrogens on the dendrimer and phosphorous on the siRNA (N/P ratio). This study was performed by agarose gel retardation as specified in the materials & methods section.

All four generations (G1–G4) of TMP-cored amino functional bis-MPA dendrimers were able to complex siRNA, with N/P ratios for complexation ranging from 1.5 to 3 for G2–G4 (data not shown). However, the G1 required a much higher N/P ratio of 19 to fully complex the siRNA. The high N/P ratio found for full complexation may be due to the previously demonstrated autodegradation of these dendrimers [35] in which loss of amino groups reduces the number of charges on the dendrimer over time. To explore the solution storage stability and the effects of the degradation on their ability to complex the siRNA the dendrimers were stored in a stock solution consisting of a pH 5.5 HEPES buffer

at 4 °C and the gel retardations were performed at different time points under the same experimental conditions. Only the G1 showed a significant loss of complexation ability, which is presented in Figure S1 in the supporting information.

Due to these drawbacks, the G1 was excluded from additional studies while the ability of G2–G4 to protect siRNA from RNase-mediated degradation was further explored. As shown in Figure 2, G2–G4 dendrimers were able to protect siRNA from degradation, therefore making them promising candidates as carriers for siRNA transfection.

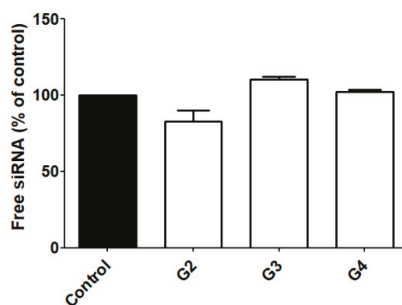


Figure 2. RNase protection. siRNA protection studies for G2–G4 dendrimers were performed at an N/P ratio of 2.5 as indicated in materials & methods. Recovered intact siRNA was measured by densitometric analysis and quantified using Image J. Data represent mean \pm s.e.m. of four independent experiments.

2.3. Cytotoxicity

The cytotoxicity of the amino functional bis-MPA dendrimers (G2–G4) was explored in different cell types by monitoring lactate dehydrogenase (LDH) release to the extracellular medium, which is a marker for late irreversible toxicity that indicates cell death. Neither generation showed any toxicity up to 10 μ M in rat astrocytes, rat glioma (C6), and human glioblastoma (U87) cell lines (data not shown). The G3 and G4 showed dose dependent toxicity in primary neurons, starting between 1 and 5 μ M for G3 and 0.1–1 μ M for G4. The G2 showed no signs of toxicity even at the highest tested concentration (10 μ M). Figure 3 displays the results from the cytotoxicity experiment on neurons.

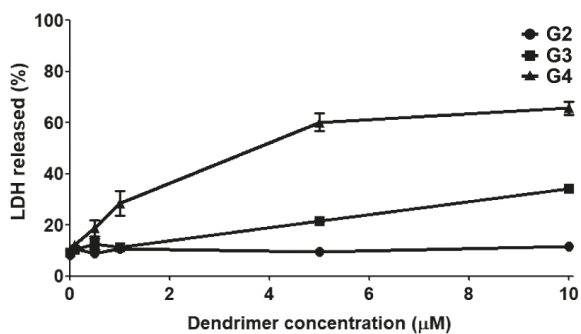


Figure 3. Cytotoxicity in primary neurons. Neurons were exposed to the indicated dendrimer concentration for 72 h. Data are expressed as mean \pm s.e.m. of four independent experiments for G2 and G3 and 12 for G4. Where no error bars are visible, they were smaller than the symbol size.

2.4. Subcellular Localization

In order to study the dendrimers ability to enter cells and their localization, C6 and U87 cells were exposed to the rhodamine-labeled G4 dendron for 4 h and studied in a fluorescence microscope. Figure 4 details a representative example of these images with C6 cells, in which the fluorophore is located in mitochondria.

The stability of the aromatic ester bond between the rhodamine and the dendron was studied using MALDI. No detachment of the rhodamine label was detected for up to 48 h in pH 7.4 and 37 °C even though almost complete loss of β -alanine functional groups and quite extensive loss of internal bis-MPA units were observed. These results are shown in Figures S2–S4.

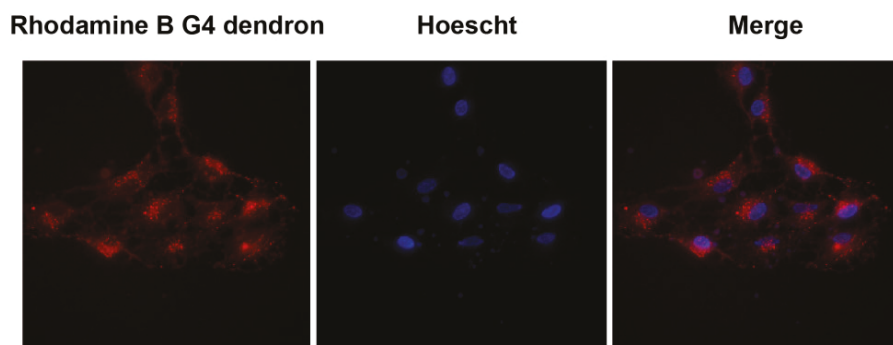


Figure 4. Subcellular tracking of the rhodamine-B labeled G4 dendron. Rat glioma C6 cells were incubated with the G4 dendron (1 μ M) for 4 h. Nuclei were labeled with Hoescht 33342. The subcellular distribution of the signal suggests a mitochondrial localization. The experiment shows a representative image of seven different experiments recorded from three different cell cultures.

2.5. Transfection

The low toxicity noted for these dendrimers and observed complexation with siRNA make them ideal candidates as transfecting agents. Unfortunately, neither transfection nor protein knockdown of significant levels was observed in primary neurons. However, transfection of carboxyfluorescein(FAM)-labeled siRNA into the cytoplasm was observed in C6 and U87 cells using the G3 and G4 dendrimers. An example image of U87 cells transfected with siRNA using the G4 dendrimer is shown in Figure 5A. A 20% decrease in p42-MAPK protein levels could be detected in rat glioma C6 using the G3 and G4 as siRNA carriers. As a comparison, a decrease of around 60% was observed using the commercially available Interferin[®] siRNA transfection reagent. The protein knockdown levels are presented in Figure 5B.

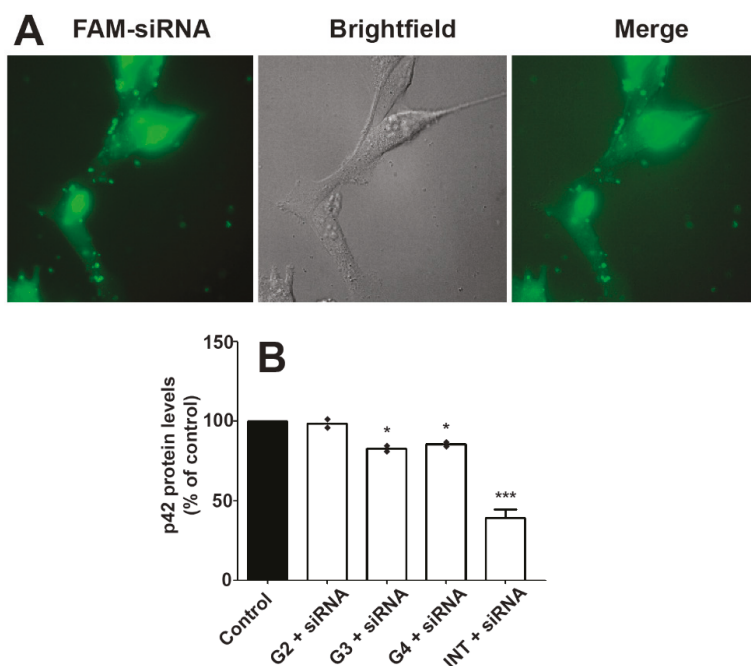


Figure 5. Dendrimer-mediated siRNA transfection. (A) Human glioblastoma U87 cells were incubated for 4 h in the presence of complexes (FAM-labeled siRNA (100 nM)/dendrimer (1 μ M)) and the image was recorded as indicated in materials & methods. The fluorophore distribution indicates that FAM-siRNA reaches cell cytoplasm. The experiment shows a representative image using the G4 dendrimer from five different experiments recorded from two different cell cultures. (B) C6 rat glioma cells were incubated with complexes formed by incubating dendrimers with siRNA (100 nM) designed to degrade p42-MAPK mRNA. Cells were lysed after 72 h and p42-MAPK protein levels were determined. Interferin[®] (INT) was used as a reference transfection agent. Interferin[®]-mediated scramble siRNA transfection did not show any effect on p42-MAPK protein levels and that data have been omitted from the figure for the sake of clarity. Data represent mean \pm s.e.m. of two experiments. * $p < 0.05$; *** $p < 0.001$.

3. Discussion

3.1. siRNA Complexation and RNase Protection

The dendrimer–siRNA complexes are formed by charge interactions, where the cationic ammonium groups on the dendrimers interact with the anionic phosphate groups in the siRNA chain, which is illustrated in Figure 6. The required ratio of amino groups on the dendrimer to phosphate groups on the siRNA (N/P ratio) in order bind all of the siRNA in a solution is a measurement of the complexation efficiency. The G1, having only six amino groups able to carry cationic charges as ammonium ions, was very poor at forming complexes with the siRNA requiring a very high excess of amines, while G2–G4 with 12, 24, and 48 terminal amino groups proved very efficient at siRNA complexation with N/P ratios of 1.5:3. This shows the existence of a minimum number of amino groups per dendrimer and/or a minimum molecular weight for efficient siRNA complexation. Similar N/P values for full complexation have been obtained using Tomalia’s PAMAM dendrimers [27,29].

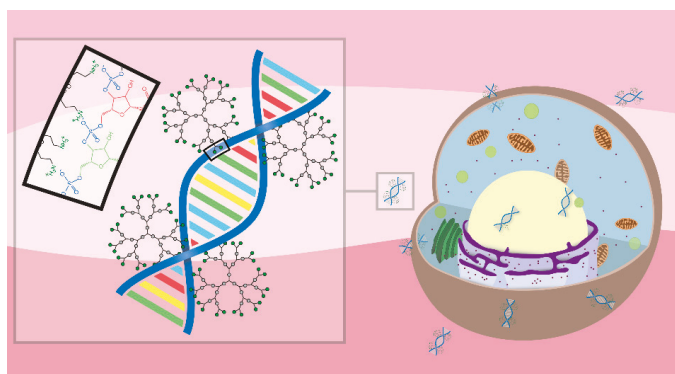


Figure 6. Graphical illustration of the complex formation between amino-functional bis-MPA dendrimers and siRNA, and the transfection of a cell.

A relevant challenge when using nanoparticles as carriers for therapeutic molecules is the fate of those particles once they have delivered their payload [39]. This issue can be tackled by designing nanoparticles that can be degraded into small molecular fragments that are easily cleared by the target cells [40,41]. Nonetheless, a balance should be maintained between the degradation rate and the time needed to perform their biological/therapeutic actions, and the carriers should have reasonable storage stability. This fact is exemplified by the G1 in Figure S1, for which a reduction in siRNA complexing ability can be observed at different times of storage, caused by the reduction of terminal amino-groups as the dendrimer degrades, which has been previously demonstrated on dendrimers [35] and hereby also on a dendron in Figures S2–S4. However, the loss of function was not observed for higher generation dendrimers, which indicates the existence of a plateau of the complexing capability at a molecular weight and charge somewhere between the G1 and G2, since the complexing ability of G2–G4 was not significantly reduced.

The 21 bp double stranded siRNA used in the experiments can be considered as a rigid stick [42]. This will enable several dendrimers to exist around the rod-like siRNA. The remaining amino/ammonium groups on the dendrimer are thus able to sterically limit the accessibility of the RNase to the nucleic acid and so preventing its degradation, as was observed for G2–G4. A slight degradation of the siRNA of around 20% was observed for the G2, while no significant degradation could be observed for G3 and G4. As a result, it can be concluded that complete protection against RNases is obtained by a theoretical dendrimer between the G2 and G3.

3.2. Cytotoxicity

Polycations are known for potential cytotoxicity that is governed by several factors such as the nature of the cationic charge, the structure, and the size/molecular weight [43]. However, PLL based dendrimers, also consisting of amino acids, have shown potential as cationic nanoparticles with low cytotoxicity [44,45]. These dendrimers are composed of amide bonds, which are generally much more stable than the polyester bonds used to build bis-MPA dendrimers. The herein studied dendrimers have similarities to PLL dendrimers, but are more easily degraded into smaller constituents taking advantage of their hydrolytical degradation mechanism. Low cytotoxicity for bis-MPA dendrimers functionalized with lysine, showing the same rapid solution degradation through loss of its terminal lysine groups, has also been reported [46].

None of the studied dendrimers (G1–G4) were cytotoxic in astrocytes, rat glioma (C6), or human glioblastoma (U87) cell lines for up to 10 μM . However, in a previous study [35], the G4 exhibited dose-dependent toxicity at the same concentrations in U87 cells in an MTT assay. The subcellular localization experiments suggested that these materials localize in mitochondria, where the reduction of

3-(4,5-dimethylthiazol-2-yl)-2,5-diphenyltetrazolium bromide (MTT) takes place [47]. One explanation to the discrepancy between the two assays is that the dendrimers, somehow, interfere with the MTT reduction to create false negatives in the assay. Previous studies have shown an increase of reactive oxygen species (ROS) in mitochondria associated with the uptake of cationic polymers [48,49], which has been shown to decrease the activity of MTT reducing enzymes [50]. Moreover, the MTT assay measures early stage reduction in cell viability that eventually leads to cell death, while the LDH assay measures LDH release to the culture medium caused by severe damage to the cellular membrane, which is a generally accepted marker for late stage toxicity. It is possible that the reduction in cell viability, caused by reduction in the mitochondrial functional, is reversible which could be another explanation for this discrepancy.

The G3–G4 showed dose-dependent cytotoxicity on primary rat cortical neurons, while the G2 showed no signs of toxicity towards these cells. This absence of toxicity from the G2 is quite remarkable in itself considering the sensitive nature of primary neurons, and that the G2 possesses twelve primary amino groups per dendrimer. Very similar levels of cell death were previously observed with differentiated neuronal cells cultured with the G4 [35]. In that study, the G2 also proved exceptional biocompatibility in a range of cell lines. The toxicity from the dendrimers most likely arises from the rupture of the cell membranes caused by their cationic exterior. In contrast to G2, the G3 and G4 have a greater number of cationic charges on their exterior, thus making them more efficient at rupturing cell membranes and causing toxicity. The collective results from earlier and current study further cement the influence of the dendritic generation on the cytotoxicity on primary neurons.

3.3. Subcellular Localization

Studying the subcellular localization of drug carriers is highly relevant. The carriers should be able to escape the endocytic pathway into relevant organelles and avoid being trapped and destroyed in lysosomes. As exemplified in Figure 4, the fluorophore distribution resembles mitochondrial rather than endosomal distribution. Ester derivatives of rhodamine B (rhodamine 123, 6G, and 3B) have shown to be highly specific fluorescent probes for mitochondria themselves [51]. The uptake of these rhodamine esters is due to their cationic charge at physiological pH and the potential over the inner mitochondrial membrane, resulting in a net negative charge on the inside of the mitochondria [52,53]. Similar mitochondrial localization for the polyester dendrimers, without the rhodamine label, cannot be entirely concluded in this study. However, it is in accordance with the previous reasoning on the discrepancy between the MTT and LDH assays, and numerous cationic species have been shown to selectively localize in mitochondria [54–58]. As for most nanoparticles, the probable cell entrance of the Bis-MPA dendrimers is by endocytosis. This observation is shown in Figure 5A where the diffuse fluorescent pattern indicates endosomal escape. The punctate structures were observed by the presence of fluorescent FAM siRNA in endosomes. Consequently, if the cellular uptake is presumed to be endocytosis, this selective mitochondrial localization suggests a very efficient endo-lysosomal escape [59] of these dendrimers.

3.4. Transfection

Efficient transfection should result in a very marked decrease in target protein levels. Unfortunately, the amino functional bis-MPA dendrimers did not cause noticeable transfection of the siRNA into primary neurons at the tested conditions. However, neuronal cells are known to be hard to transfect and are generally sensitive to cytotoxicity.

As shown in Figure 5A, transfection was however observed in U87 cell lines with the G3 and G4 dendrimers, since the fluorescent FAM-labeled siRNA could be seen throughout the cytoplasm. Similar transfection was observed in C6 cells. This transfection resulted in a downregulation of the target protein expression by around 20%. For comparison, the commercial transfection reagent Interferin® was included in the study, with which a 60% downregulation was observed.

A probable reason for this relatively low transfection and protein downregulation could be that the interaction between the dendrimers and the siRNA is not strong enough for the complex to remain intact long enough for the transfection process to occur, or that the dendrimers simply degrade too fast inside the cells, leading to premature release of the siRNA. Another plausible explanation is that the charge-interactions are too strong, inhibiting siRNA release and the formation of the RISC. The dilemma of achieving both strong complexation and efficient dissociation of the siRNA/polymer-complex has been discussed in previous publications [60]. More in-depth studies would be required to determine the cause for this specific system and take measures to improve the protein knockdown levels. However, considering that this is a very initial study of the performance of these dendrimers in delivering siRNA, aspects of the results are promising and give insights into how to construct benign and efficient dendrimers for siRNA delivery [61].

4. Materials and Methods

4.1. Synthesis Protocols

Amino-functional bis-MPA dendrimers [35], boc-protected β -alanine [35,62], and the tetraethylene glycol bis-MPA dendron [36] were synthesized according to previously published procedures. Other synthesis protocols are presented in the supporting information.

4.2. MALDI-ToF-MS

Matrix-assisted laser/desorption ionization time-of-flight mass spectrometry (MALDI-ToF-MS) was performed on a Bruker Ultraflex-III (KTH, Stockholm, Sweden) calibrated with Spherical dendritic calibrants (Polymer Factory; Stockholm, Sweden). Samples were prepared using a mass ratio of 1:1:40 of sample, NaTFA and matrix in tetrahydrofuran (THF). 0.5–1.5 μ L of the THF solution was deposited on a stainless steel sample plate using the dried droplet method. *trans*-2-[3-(4-*tert*-Butylphenyl)-2-methyl-2-propenylidene]malononitrile (DCTB) was used as matrix for nonpolar samples while 2,5-dihydroxybenzoic acid (DHB) was used for polar samples. The acquired spectra were analyzed with FlexAnalysis version 2.2 from Bruker Daltonics (KTH, Stockholm, Sweden).

4.3. NMR Spectroscopy

NMR spectroscopy was carried out on a Bruker Avance (KTH, Stockholm, Sweden) III 400 MHz instrument. ^1H -NMR was carried out using 32 scans, a relaxation delay of 1 s, and a spectral window of 20 ppm. ^{13}C -NMR was carried out using 512 scans, a relaxation delay of 2 s, and a spectral window of 240 ppm. Samples were dissolved in chloroform-*d* or methanol-*d* (Cambridge Isotope Laboratories; Tewksbury, MA, USA). The acquired spectra were analyzed with MestreNova version 9.0.0-12821 from Mestrelab Research (Santiago de Compostela, Spain).

4.4. Cell Cultures

Primary cultures of rat cortical neurons were prepared as previously described [63]. The frontolateral cortical lobes were dissected out of Sprague–Dawley embryonic day 17 fetuses, mechanically dissociated and resuspended in serum-free neurobasal medium supplemented with B27 (Invitrogen, Barcelona, Spain) containing 2 mM L-glutamine, penicillin (20 units/mL), and streptomycin (5 μ g/mL). The cortical neurons were seeded on PLL-coated culture plates.

Astrocytes were isolated from one day old rat pups as previously described [64] and cultured in Dulbecco's Modified Eagle's Medium (DMEM) (Thermo Fisher; Waltham, MA, USA) supplemented with 10% heat-inactivated fetal calf serum; 2 mM L-glutamine, 5 μ g/mL streptomycin, and 20 units/mL penicillin at 37 °C. All animal experimental studies were conducted in accordance with the guidelines of the Ethical Committee of Animal Experimentation at University of Castilla-La Mancha (Albacete, Spain). All studies involving animals are reported in accordance with the guidelines of the

European Union (2010/63/EU) for the use of laboratory animals and in accordance with the ARRIVE guidelines for reporting experiments involving animals [65].

C6 rat glioblastoma and U87 human glioblastoma cancer cell lines were obtained from ATCC (Manassas, VA, USA) and were maintained according to the provider instructions. All cell types were maintained at 37 °C in a humidified atmosphere containing 5% CO₂.

4.5. Fluorescence Spectroscopy

Fluorescence spectroscopy of the rhodamine-labeled generation 4 bis-MPA dendron was performed using a Tecan Safire 2 plate reader. Excitation was set to 500 nm and emission was recorded from 280 nm to 800 nm with 5 nm increments.

4.6. Fluorescence Microscopy

Fluorescent signals from C6 and U87 cells were recorded as previously described [61]. Cells were seeded at a concentration of 100,000 cells/mL onto 20 mm diameter glass coverslips (Deckgläser; Baden-Württemberg, Germany) and cultured in 6 well plates (Sardstedt; Nümbrecht, Germany) for 24 h in DMEM supplemented with 10% heat-inactivated fetal calf serum; 2 mM L-glutamine, 5 µg/mL streptomycin, and 20 units/mL penicillin maintained at 37 °C in a humidified atmosphere containing 5% CO₂. Afterwards, cells were treated with the rhodamine-labeled generation 4 bis-MPA dendron (1 µM) in culture medium for 4 h. The cells were then washed three times with Krebs–Henseleit solution with the following ionic composition (in mM): NaCl, 140; CaCl₂, 2.5; MgCl₂, 1; KCl, 5; HEPES, 5, Glucose, 11; (pH: 7.4) and mounted on the stage of a Nikon Eclipse TE2000-E fluorescence microscope (Nikon, Tokyo, Japan). The samples containing the cells were stimulated and recorded at the following wavelengths (excitation/emission): rhodamine B G4 dendron (530 nm/600 nm), FAM-siRNA (488 nm/520 nm), and Hoescht (350 nm/450 nm), and observed through a 40x oil immersion objective. Data was obtained using the NIS Elements AR software (Nikon, Tokyo, Japan).

4.7. Agarose Gel Retardation

Agarose gel electrophoresis was performed as previously described [66]. Nanoparticle/siRNA complexes were prepared using 100 nM siRNA with increasing dendrimer concentrations in order to achieve the indicated N/P ratios. The mixture was incubated for 30 min at room temperature and the samples were loaded onto 1.2% agarose gel containing ethidium bromide (50 µg/mL). Electrophoresis was carried on at 60 mV for 15 min, and the resulting gels were photographed under UV illumination. The fluorescent bands were acquired and digitized using a developer (Vilber; Marne La Vallée, France) and analyzed using Image J [67].

4.8. siRNA Protection against RNases

Dendrimer-mediated siRNA protection from RNase-mediated degradation was studied as previously described [68]. Nanoparticles, at the indicated concentrations, were incubated for 30 min with siRNA (100 nM) followed by addition of RNase (0.25% *w/v*; Sigma, Barcelona; Spain) and incubation for another 30 min at 37 °C. RNase was then inactivated by keeping the samples at 4 °C for 15 min and after which heparin (0.5 USP units) was added. The samples were kept at 4 °C for an additional 20 min to completely release siRNA from the nanoparticles while RNase remained inactivated as previously described [29]. Samples were then loaded onto a 1.2% agarose gel containing ethidium bromide (50 µg/mL), and run under the same experimental conditions as indicated above. Fluorescent bands were acquired and digitized using a developer (Vilber, Marne-la-Vallée, France) and analyzed using the Image J software [67].

4.9. siRNA Transfection & Western Blot Analysis

Cells were incubated either with the dendrimer alone or with the dendrimer/siRNA dendriplexes formed by incubating the corresponding dendrimer (0.5 μ M) with either scramble noncoding siRNA or specific siRNA (100 nM; Sigma, Barcelona, Spain) for rat p42-MAPK (sense: 5'-GUAUAUACAUCAGCUAAUUAU-3', antisense: 5'-AUAUUAGCUGAAUGUAUAUAC-3') for 30 min as previously described [61]. Cells were treated for 72 h, the medium was washed twice and the cells were lysed. Western blots were performed as previously described using 15% SDS-PAGE gels [69]. Polyclonal anti-p42-MAPK antibody (1:1000) (Cell Signaling Technology; Danvers, MA, USA) and polyclonal anti- β -actin antibody (1:4000) (Sigma Chemical Co.; St. Louis, MO, USA) were used to correct for protein loading. Immunocomplexes were visualized using an enhanced chemiluminescence system (Millipore, Burlington, MA, USA). For comparison, the commercial Interferin[®] transfection reagent was included in the study and used according to its specified protocol. Transfection using FAM-labeled siRNA was performed using previously published protocol [61]. Densitometric analysis of immunoreactive bands was performed using Image J [67].

4.10. Cytotoxicity Studies

For viability experiments, LDH release to the incubation medium was used as an index of cellular death as previously described [70]. Cells were cultured in 24-well culture plates at a concentration of 100,000 cells/mL and treated with different dendrimer concentrations ranging from 0.1 to 10 μ M for 72 h in culture medium. The culture medium was collected, the cells were washed with phosphate-buffered saline, and lysed using 0.9% Triton X-100 (*v/v*) in saline. The LDH activity present in the culture media, as well as that present in the lysates, was measured spectrophotometrically at 490 nm on a 96-well plate reader using the Cytotox 96 Kit (Promega; Madrid, Spain). Percentage of toxicity was calculated as the percentage of LDH released in comparison to the LDH present in the cells at the beginning of the experiment as previously described [70].

4.11. Degradation

The generation four rhodamine-labeled amino-functional dendron was dissolved in a McIlvaine buffer of pH 7.4 at a concentration of 0.5 mM. The pH of the solution was reconfirmed after the addition of the dendron. At set time points, 3 μ L aliquots were mixed with 20 μ L of a solution with 1 g/L of NaTFA and 10 g/L of 2,5-DHB. 1 μ L of this solution was deposited on a stainless steel MALDI-plate and analyzed with MALDI-ToF-MS.

5. Conclusions

Amino-functional bis-MPA dendrimers of generation one to four have been investigated as nonviral vectors for siRNA delivery in primary neurons, astrocytes, glioma, and glioblastoma cell lines. The G2–G4 dendrimers were efficient at forming charge-interaction complexes with siRNA at N/P ratios of 1.5:3 for full siRNA complexation, and they were nontoxic to astrocytes, glioma, and glioblastoma cell lines. G3–G4 showed dose-dependent cytotoxicity towards primary neurons, while the G2 showed no signs of toxicity at the tested concentrations. Fluorescence microscopy experiments suggested efficient endo-lysosomal escape by the dendrimers, with distinct mitochondrial subcellular localization. Transfection and protein downregulation was not observed in primary neurons. However, transfection was successful into rat glioma and human glioblastoma cells, followed by a slight reduction in target protein expression of around 20%. This is the first reported evaluation of bis-MPA dendrimers for the intracellular delivery of siRNA, where the benefits and challenges of these materials are outlined.

Supplementary Materials: The following are available online, Figure S1: Solution storage influence on the siRNA complexation of G1. Figures S2–S4: Degradation of the fluorescent G4 dendron. Figure S5: Fluorescence spectrum of the rhodamine B G4 dendron. Synthesis protocols, NMR- and MALDI-spectra.

Author Contributions: For research articles with several authors, a short paragraph specifying their individual contributions must be provided. The following statements should be used “Conceptualization, V.C., M.M, P.S.; Methodology, P.S., Y.Z. and D.M.; Software, P.S. and Y.Z.; Validation, V.C. and M.M.; Formal Analysis, V.C., P.S. and Y.Z.; Investigation, D.M., P.S. and Y.Z.; Resources, M.M. and V.C.; Data Curation, P.S., Y.Z. and V.C.; Writing-Original Draft Preparation, P.S., Y.Z., V.C. and M.M.; Writing-Review & Editing, P.S., Y.Z., V.C. and M.M.; Visualization, P.S. and Y.Z.; Supervision, V.C. and M.M.; Project Administration, M.M.; Funding Acquisition, V.C. and M.M.”, please turn to the CRediT taxonomy for the term explanation. Authorship must be limited to those who have contributed substantially to the work reported.

Funding: The APC was funded by MDPI.

Acknowledgments: This work was supported AB Wilhelm Beckers Jubileumsfond (P.S.), and by the Spanish Ministerio de Economía y Competitividad (grants no. BFU2014-59009-P and SAF2017-89288-R from MINECO/AEI/FEDER/UE). Y.Z. acknowledges the support from Barncancerfonden (Grant number: TJ2017-0009).

Conflicts of Interest: The authors declare no conflicts of interest.

References

1. Fire, A.; Xu, S.Q.; Montgomery, M.K.; Kostas, S.A.; Driver, S.E.; Mello, C.C. Potent and specific genetic interference by double-stranded RNA in *Caenorhabditis elegans*. *Nature* **1998**, *391*, 806–811. [[CrossRef](#)] [[PubMed](#)]
2. Davis, M.E. The first targeted delivery of sirna in humans via a self-assembling, cyclodextrin polymer-based nanoparticle: From concept to clinic. *Mol. Pharm.* **2009**, *6*, 659–668. [[CrossRef](#)] [[PubMed](#)]
3. Zuckerman, J.E.; Gritli, I.; Tolcher, A.; Heidel, J.D.; Lim, D.; Morgan, R.; Chmielowski, B.; Ribas, A.; Davis, M.E.; Yen, Y. Correlating animal and human phase Ia/Ib clinical data with CALAA-01, a targeted, polymer-based nanoparticle containing siRNA. *Proc. Natl. Acad. Sci. USA* **2014**, *111*, 11449–11454. [[CrossRef](#)] [[PubMed](#)]
4. Coelho, T.; Adams, D.; Silva, A.; Lozeron, P.; Hawkins, P.N.; Mant, T.; Perez, J.; Chiesa, J.; Warrington, S.; Tranter, E.; et al. Safety and efficacy of rna therapy for transthyretin amyloidosis. *N. Engl. J. Med.* **2013**, *369*, 819–829. [[CrossRef](#)] [[PubMed](#)]
5. Suhr, O.B.; Coelho, T.; Buades, J.; Pouget, J.; Conceicao, I.; Berk, J.; Schmidt, H.; Waddington-Cruz, M.; Campistol, J.M.; Bettencourt, B.R.; et al. Efficacy and safety of patisiran for familial amyloidotic polyneuropathy: A phase II multi-dose study. *Orphanet J. Rare Dis.* **2015**, *10*, 109. [[CrossRef](#)] [[PubMed](#)]
6. Hickerson, R.P.; Vlassov, A.V.; Wang, Q.; Leake, D.; Ilves, H.; Gonzalez-Gonzalez, E.; Contag, C.H.; Johnston, B.H.; Kaspar, R.L. Stability study of unmodified siRNA and relevance to clinical use. *Oligonucleotides* **2008**, *18*, 345–354. [[CrossRef](#)] [[PubMed](#)]
7. Judge, A.D.; Sood, V.; Shaw, J.R.; Fang, D.; McClintock, K.; MacLachlan, I. Sequence-dependent stimulation of the mammalian innate immune response by synthetic siRNA. *Nat. Biotechnol.* **2005**, *23*, 457–462. [[CrossRef](#)] [[PubMed](#)]
8. Hammond, S.M.; Bernstein, E.; Beach, D.; Hannon, G.J. An RNA-directed nuclease mediates post-transcriptional gene silencing in *Drosophila* cells. *Nature* **2000**, *404*, 293–296. [[CrossRef](#)] [[PubMed](#)]
9. Sen, G.L.; Blau, H.M. Argonaute 2/RISC resides in sites of mammalian mRNA decay known as cytoplasmic bodies. *Nat. Cell Biol.* **2005**, *7*, 633–636. [[CrossRef](#)] [[PubMed](#)]
10. De Fougerolles, A.; Vornlocher, H.P.; Maraganore, J.; Lieberman, J. Interfering with disease: A progress report on siRNA-based therapeutics. *Nat. Rev. Drug Discov.* **2007**, *6*, 443–453. [[CrossRef](#)] [[PubMed](#)]
11. Whitehead, K.A.; Langer, R.; Anderson, D.G. Knocking down barriers: Advances in siRNA delivery. *Nat. Rev. Drug Discov.* **2009**, *8*, 129–138. [[CrossRef](#)] [[PubMed](#)]
12. Wittrup, A.; Lieberman, J. Knocking down disease: A progress report on siRNA therapeutics. *Nat. Rev. Genet.* **2015**, *16*, 543–552. [[CrossRef](#)] [[PubMed](#)]
13. Thomas, C.E.; Ehrhardt, A.; Kay, M.A. Progress and problems with the use of viral vectors for gene therapy. *Nat. Rev. Genet.* **2003**, *4*, 346–358. [[CrossRef](#)] [[PubMed](#)]
14. Kay, M.A. State-of-the-art gene-based therapies: The road ahead. *Nat. Rev. Genet.* **2011**, *12*, 316–328. [[CrossRef](#)] [[PubMed](#)]
15. Stewart, M.P.; Sharei, A.; Ding, X.Y.; Sahay, G.; Langer, R.; Jensen, K.F. In vitro and ex vivo strategies for intracellular delivery. *Nature* **2016**, *538*, 183–192. [[CrossRef](#)] [[PubMed](#)]

16. Dalby, B.; Cates, S.; Harris, A.; Ohki, E.C.; Tilkins, M.L.; Price, P.J.; Ciccarone, V.C. Advanced transfection with Lipofectamine 2000 reagent: Primary neurons, siRNA, and high-throughput applications. *Methods* **2004**, *33*, 95–103. [[CrossRef](#)] [[PubMed](#)]
17. Urban-Klein, B.; Werth, S.; Abuharbeid, S.; Czubayko, F.; Aigner, A. RNAi-mediated gene-targeting through systemic application of polyethylenimine (PEI)-complexed siRNA in vivo. *Gene Ther.* **2005**, *12*, 461–466. [[CrossRef](#)] [[PubMed](#)]
18. Lee, J.S.; Green, J.J.; Love, K.T.; Sunshine, J.; Langer, R.; Anderson, D.G. Gold, poly(beta-amino ester) nanoparticles for small interfering rna delivery. *Nano Lett.* **2009**, *9*, 2402–2406. [[CrossRef](#)] [[PubMed](#)]
19. Karra, D.; Dahm, R. Transfection techniques for neuronal cells. *J. Neurosci.* **2010**, *30*, 6171–6177. [[CrossRef](#)] [[PubMed](#)]
20. Perez-Martinez, F.C.; Guerra, J.; Posadas, I.; Ceña, V. Barriers to nonviral vector-mediated gene delivery in the nervous system. *Pharm. Res.* **2011**, *28*, 1843–1858. [[CrossRef](#)] [[PubMed](#)]
21. Dib-Hajj, S.D.; Choi, J.S.; Macala, L.J.; Tyrrell, L.; Black, J.A.; Cummins, T.R.; Waxman, S.G. Transfection of rat or mouse neurons by biolistics or electroporation. *Nat. Protoc.* **2009**, *4*, 1118–1127. [[CrossRef](#)] [[PubMed](#)]
22. Royo, N.C.; Vandenberghe, L.H.; Ma, J.Y.; Hauspurg, A.; Yu, L.; Maronski, M.; Johnston, J.; Dichter, M.A.; Wilson, J.M.; Watson, D.J. Specific AAV serotypes stably transduce primary hippocampal and cortical cultures with high efficiency and low toxicity. *Brain Res.* **2008**, *1190*, 15–22. [[CrossRef](#)] [[PubMed](#)]
23. Sun, T.; Luo, J.G.; Jia, M.R.; Li, H.; Li, K.Z.; Fu, Z.J. Small interfering RNA-mediated knockdown of NF-kappa Bp65 attenuates neuropathic pain following peripheral nerve injury in rats. *Eur. J. Pharmacol.* **2012**, *682*, 79–85. [[CrossRef](#)] [[PubMed](#)]
24. Jatava, P.; Ceña, V. Use of nanoparticles for glioblastoma treatment: A new approach. *Nanomedicine (Lond.)* **2017**, *12*, 2533–2554. [[CrossRef](#)] [[PubMed](#)]
25. Taratula, O.; Garbuzenko, O.B.; Kirkpatrick, P.; Pandya, I.; Savla, R.; Pozharov, V.P.; He, H.X.; Minko, T. Surface-engineered targeted PPI dendrimer for efficient intracellular and intratumoral siRNA delivery. *J. Control. Release* **2009**, *140*, 284–293. [[CrossRef](#)] [[PubMed](#)]
26. Kang, H.M.; DeLong, R.; Fisher, M.H.; Juliano, R.L. Tat-conjugated PAMAM dendrimers as delivery agents for antisense and siRNA oligonucleotides. *Pharm. Res.* **2005**, *22*, 2099–2106. [[CrossRef](#)] [[PubMed](#)]
27. Zhou, J.H.; Wu, J.Y.; Hafdi, N.; Behr, J.P.; Erbacher, P.; Peng, L. PAMAM dendrimers for efficient siRNA delivery and potent gene silencing. *Chem. Commun.* **2006**, 2362–2364. [[CrossRef](#)] [[PubMed](#)]
28. Nam, H.Y.; Nam, K.; Hahn, H.J.; Kim, B.H.; Lim, H.J.; Kim, H.J.; Choi, J.S.; Park, J.S. Biodegradable PAMAM ester for enhanced transfection efficiency with low cytotoxicity. *Biomaterials* **2009**, *30*, 665–673. [[CrossRef](#)] [[PubMed](#)]
29. Rodrigo, A.C.; Rivilla, I.; Perez-Martinez, F.C.; Monteagudo, S.; Ocana, V.; Guerra, J.; Garcia-Martinez, J.C.; Merino, S.; Sanchez-Verdu, P.; Ceña, V.; et al. Efficient, nontoxic hybrid ppv-pamam dendrimer as a gene carrier for neuronal cells. *Biomacromolecules* **2011**, *12*, 1205–1213. [[CrossRef](#)] [[PubMed](#)]
30. Kaneshiro, T.L.; Lu, Z.R. Targeted intracellular codelivery of chemotherapeutics and nucleic acid with a well-defined dendrimer-based nanoglobular carrier. *Biomaterials* **2009**, *30*, 5660–5666. [[CrossRef](#)] [[PubMed](#)]
31. Weber, N.; Ortega, P.; Clemente, M.I.; Shcharbin, D.; Bryszewska, M.; de la Mata, F.J.; Gomez, R.; Munoz-Fernandez, M.A. Characterization of carbosilane dendrimers as effective carriers of siRNA to HIV-infected lymphocytes. *J. Control. Release* **2008**, *132*, 55–64. [[CrossRef](#)] [[PubMed](#)]
32. Posadas, I.; Lopez-Hernandez, B.; Clemente, M.I.; Jimenez, J.L.; Ortega, P.; de la Mata, J.; Gomez, R.; Munoz-Fernandez, M.A.; Ceña, V. Highly efficient transfection of rat cortical neurons using carbosilane dendrimers unveils a neuroprotective role for HIF-1 α in early chemical hypoxia-mediated neurotoxicity. *Pharm. Res.* **2009**, *26*, 1181–1191. [[CrossRef](#)] [[PubMed](#)]
33. Gillies, E.R.; Dy, E.; Frechet, J.M.J.; Szoka, F.C. Biological evaluation of polyester dendrimer: Poly(ethylene oxide) “Bow-Tie” hybrids with tunable molecular weight and architecture. *Mol. Pharm.* **2005**, *2*, 129–138. [[CrossRef](#)] [[PubMed](#)]
34. Feliu, N.; Walter, M.V.; Montanez, M.I.; Kunzmann, A.; Hult, A.; Nystrom, A.; Malkoch, M.; Fadeel, B. Stability and biocompatibility of a library of polyester dendrimers in comparison to polyamidoamine dendrimers. *Biomaterials* **2012**, *33*, 1970–1981. [[CrossRef](#)] [[PubMed](#)]
35. Stenström, P.; Hjorth, E.; Zhang, Y.N.; Andrén, O.C.J.; Guette-Marquet, S.; Schultzberg, M.; Malkoch, M. Synthesis and in vitro evaluation of monodisperse amino-functional polyester dendrimers with rapid degradability and antibacterial properties. *Biomacromolecules* **2017**, *18*, 4323–4330. [[CrossRef](#)] [[PubMed](#)]

36. Stenström, P.; Andren, O.C.J.; Malkoch, M. Fluoride-promoted esterification (fpe) chemistry: A robust route to bis-mpa dendrons and their postfunctionalization. *Molecules* **2016**, *21*, 366. [[CrossRef](#)] [[PubMed](#)]
37. Garcia-Gallego, S.; Hult, D.; Olsson, J.V.; Malkoch, M. Fluoride-promoted esterification with imidazolide-activated compounds: A modular and sustainable approach to dendrimers. *Angew. Chem. Int. Ed. Engl.* **2015**, *54*, 2416–2419. [[CrossRef](#)] [[PubMed](#)]
38. Rosenthal, I.; Peretz, P.; Muszkat, K.A. Thermochromic and hyperchromic effects in rhodamine-b solutions. *J. Phys. Chem.* **1979**, *83*, 350–353. [[CrossRef](#)]
39. Longmire, M.; Choyke, P.L.; Kobayashi, H. Clearance properties of nano-sized particles and molecules as imaging agents: Considerations and caveats. *Nanomedicine (Lond.)* **2008**, *3*, 703–717. [[CrossRef](#)] [[PubMed](#)]
40. Green, J.J.; Shi, J.; Chiu, E.; Leshchiner, E.S.; Langer, R.; Anderson, D.G. Biodegradable polymeric vectors for gene delivery to human endothelial cells. *Bioconjug. Chem.* **2006**, *17*, 1162–1169. [[CrossRef](#)] [[PubMed](#)]
41. Woodrow, K.A.; Cu, Y.; Booth, C.J.; Saucier-Sawyer, J.K.; Wood, M.J.; Saltzman, W.M. Intravaginal gene silencing using biodegradable polymer nanoparticles densely loaded with small-interfering RNA. *Nat. Mater.* **2009**, *8*, 526–533. [[CrossRef](#)] [[PubMed](#)]
42. Dumitru, A.C.; Herruzo, E.T.; Rausell, E.; Cena, V.; Garcia, R. Unbinding forces and energies between a siRNA molecule and a dendrimer measured by force spectroscopy. *Nanoscale* **2015**, *7*, 20267–20276. [[CrossRef](#)] [[PubMed](#)]
43. Fischer, D.; Li, Y.X.; Ahlemeyer, B.; Kriegelstein, J.; Kissel, T. In vitro cytotoxicity testing of polycations: Influence of polymer structure on cell viability and hemolysis. *Biomaterials* **2003**, *24*, 1121–1131. [[CrossRef](#)]
44. Ohsaki, M.; Okuda, T.; Wada, A.; Hirayama, T.; Niidome, T.; Aoyagi, H. In vitro gene Transfection using dendritic poly(L-lysine). *Bioconjug. Chem.* **2002**, *13*, 510–517. [[CrossRef](#)] [[PubMed](#)]
45. Kaneshiro, T.L.; Wang, X.; Lu, Z.R. Synthesis, characterization, and gene delivery of Poly-L-lysine octa(3-aminopropyl)silsesquioxane dendrimers: Nanoglobular drug carriers with precisely defined molecular Architectures. *Mol. Pharm.* **2007**, *4*, 759–768. [[CrossRef](#)] [[PubMed](#)]
46. Duran-Lara, E.F.; Marple, J.L.; Giesen, J.A.; Fang, Y.L.; Jordan, J.H.; Godbey, W.T.; Marican, A.; Santos, L.S.; Grayson, S.M. Investigation of lysine-functionalized dendrimers as dichlorvos detoxification agents. *Biomacromolecules* **2015**, *16*, 3434–3444. [[CrossRef](#)] [[PubMed](#)]
47. Mosmann, T. Rapid colorimetric assay for cellular growth and survival: Application to proliferation and cytotoxicity assays. *J. Immunol. Methods* **1983**, *65*, 55–63. [[CrossRef](#)]
48. Bexiga, M.G.; Varela, J.A.; Wang, F.J.; Fenaroli, F.; Salvati, A.; Lynch, I.; Simpson, J.C.; Dawson, K.A. Cationic nanoparticles induce caspase 3-, 7- and 9-mediated cytotoxicity in a human astrocytoma cell line. *Nanotoxicology* **2011**, *5*, 557–567. [[CrossRef](#)] [[PubMed](#)]
49. Liu, Y.; Lu, H.R.; Lan, A.P.; Hu, Y.; Li, H.P.; Chen, J. Mitochondria-targeted nanocarriers using hyperbranched polycations wrapped carbon nanotubes for augment photodynamic therapeutic effects. *J. Control. Release* **2017**, *259*, E170–E171. [[CrossRef](#)]
50. Sliwka, L.; Wiktorska, K.; Suchocki, P.; Milczarek, M.; Mielczarek, S.; Lubelska, K.; Cierpial, T.; Lyzwa, P.; Kielbasinski, P.; Jaromin, A.; et al. The comparison of mtt and cvs assays for the assessment of anticancer agent interactions. *PLoS ONE* **2016**, *11*, e0155772. [[CrossRef](#)] [[PubMed](#)]
51. Johnson, L.V.; Walsh, M.L.; Chen, L.B. Localization of mitochondria in living cells with rhodamine-123. *Proc. Natl. Acad. Sci. USA* **1980**, *77*, 990–994. [[CrossRef](#)] [[PubMed](#)]
52. Mitchell, P.; Moyle, J. Estimation of membrane potential and pH difference across the cristae membrane of rat liver mitochondria. *Eur. J. Biochem.* **1969**, *7*, 471–484. [[CrossRef](#)] [[PubMed](#)]
53. Johnson, L.V.; Walsh, M.L.; Bockus, B.J.; Chen, L.B. Monitoring of relative mitochondrial-membrane potential in living cells by fluorescence microscopy. *J. Cell Biol.* **1981**, *88*, 526–535. [[CrossRef](#)] [[PubMed](#)]
54. Yameen, B.; Choi, W.I.; Vilos, C.; Swami, A.; Shi, J.J.; Farokhzad, O.C. Insight into nanoparticle cellular uptake and intracellular targeting. *J. Control. Release* **2014**, *190*, 485–499. [[CrossRef](#)] [[PubMed](#)]
55. Marrache, S.; Dhar, S. Engineering of blended nanoparticle platform for delivery of mitochondria-acting therapeutics. *Proc. Natl. Acad. Sci. USA* **2012**, *109*, 16288–16293. [[CrossRef](#)] [[PubMed](#)]
56. Wang, X.H.; Peng, H.S.; Yang, L.; You, F.T.; Teng, F.; Tang, A.W.; Zhang, F.J.; Li, X.H. Poly-L-lysine assisted synthesis of core-shell nanoparticles and conjugation with triphenylphosphonium to target mitochondria. *J. Mater. Chem. B* **2013**, *1*, 5143–5152. [[CrossRef](#)]

57. Orosz, A.; Bosze, S.; Mezo, G.; Szabo, I.; Herenyi, L.; Csik, G. Oligo- and polypeptide conjugates of cationic porphyrins: Binding, cellular uptake, and cellular localization. *Amino Acids* **2017**, *49*, 1263–1276. [[CrossRef](#)] [[PubMed](#)]
58. Zhang, G.Y.; Liu, G.H.; Zhang, Y.; Yan, M.Q.; Bi, H. TPP-modified protein-polymer bioconjugate as a mitochondria-targeting nanocarrier. *J. Control. Release* **2017**, *259*, E169–E170. [[CrossRef](#)]
59. Boussif, O.; Lezoualc'h, F.; Zanta, M.A.; Mergny, M.D.; Scherman, D.; Demeneix, B.; Behr, J.P. A versatile vector for gene and oligonucleotide transfer into cells in culture and in vivo: Polyethylenimine. *Proc. Natl. Acad. Sci. USA* **1995**, *92*, 7297–7301. [[CrossRef](#)] [[PubMed](#)]
60. Kwon, Y.J. Before and after endosomal escape: Roles of stimuli-converting siRNA/polymer interactions in determining gene silencing efficiency. *Acc. Chem. Res.* **2012**, *45*, 1077–1088. [[CrossRef](#)] [[PubMed](#)]
61. Manzanares, D.; Araya-Duran, I.; Gallego-Yerga, L.; Jativa, P.; Marquez-Miranda, V.; Canan, J.; Blanco, J.L.J.; Mellet, C.O.; Gonzalez-Nilo, F.D.; Fernandez, J.M.G.; et al. Molecular determinants for cyclooligosaccharide-based nanoparticle-mediated effective siRNA transfection. *Nanomedicine (Lond.)* **2017**, *12*, 1607–1621. [[CrossRef](#)] [[PubMed](#)]
62. Salmon-Chemin, L.; Buisine, E.; Yardley, V.; Kohler, S.; Debreu, M.A.; Landry, V.; Sergheraert, C.; Croft, S.L.; Krauth-Siegel, R.L.; Davioud-Charvet, E. 2- and 3-substituted 1,4-naphthoquinone derivatives as subversive substrates of trypanothione reductase and lipoamide dehydrogenase from *Trypanosoma cruzi*: Synthesis and correlation between redox cycling activities and in vitro cytotoxicity. *J. Med. Chem.* **2001**, *44*, 548–565. [[CrossRef](#)] [[PubMed](#)]
63. Posadas, I.; Perez-Martinez, F.C.; Guerra, J.; Sanchez-Verdu, P.; Ceña, V. Cofilin activation mediates Bax translocation to mitochondria during excitotoxic neuronal death. *J. Neurochem.* **2012**, *120*, 515–527. [[CrossRef](#)] [[PubMed](#)]
64. Kipp, M.; Karakaya, S.; Pawlak, J.; Araujo-Wright, G.; Arnold, S.; Beyer, C. Estrogen and the development and protection of nigrostriatal dopaminergic neurons: Concerted action of a multitude of signals, protective molecules, and growth factors. *Front. Neuroendocr.* **2006**, *27*, 376–390. [[CrossRef](#)] [[PubMed](#)]
65. Kilkenny, C.; Browne, W.J.; Cuthill, I.C.; Emerson, M.; Altman, D.G. Improving Bioscience Research Reporting: The ARRIVE Guidelines for Reporting Animal Research. *PLoS Biol.* **2010**, *8*, e1000412. [[CrossRef](#)] [[PubMed](#)]
66. Monteagudo, S.; Perez-Martinez, F.C.; Perez-Carrion, M.D.; Guerra, J.; Merino, S.; Sanchez-Verdu, M.P.; Ceña, V. Inhibition of p42 MAPK using a nonviral vector-delivered siRNA potentiates the anti-tumor effect of metformin in prostate cancer cells. *Nanomedicine (Lond.)* **2012**, *7*, 493–506. [[CrossRef](#)] [[PubMed](#)]
67. Schindelin, J.; Arganda-Carreras, I.; Frise, E.; Kaynig, V.; Longair, M.; Pietzsch, T.; Preibisch, S.; Rueden, C.; Saalfeld, S.; Schmid, B.; et al. Fiji: An open-source platform for biological-image analysis. *Nat. Methods* **2012**, *9*, 676–682. [[CrossRef](#)] [[PubMed](#)]
68. Janiszewska, J.; Posadas, I.; Jativa, P.; Bugaj-Zarebska, M.; Urbanczyk-Lipkowska, Z.; Ceña, V. Second generation amphiphilic poly-lysine dendrons inhibit glioblastoma cell proliferation without toxicity for neurons or astrocytes. *PLoS ONE* **2016**, *11*, e0165704. [[CrossRef](#)] [[PubMed](#)]
69. Perez-Carrion, M.D.; Ceña, V. Knocking down hmgb1 using dendrimer-delivered siRNA unveils its key role in nmda-induced autophagy in rat cortical neurons. *Pharm. Res.* **2013**, *30*, 2584–2595. [[CrossRef](#)] [[PubMed](#)]
70. Posadas, I.; Vellecco, V.; Santos, P.; Prieto-Lloret, J.; Ceña, V. Acetaminophen potentiates staurosporine-induced death in a human neuroblastoma cell line. *Br. J. Pharm.* **2007**, *150*, 577–585. [[CrossRef](#)] [[PubMed](#)]

Sample Availability: Samples of the compounds are not available from the authors.



© 2018 by the authors. Licensee MDPI, Basel, Switzerland. This article is an open access article distributed under the terms and conditions of the Creative Commons Attribution (CC BY) license (<http://creativecommons.org/licenses/by/4.0/>).

Review

New Advances in General Biomedical Applications of PAMAM Dendrimers

Renan Vinicius de Araújo, Soraya da Silva Santos, Elizabeth Igne Ferreira and Jeanine Giarolla *

Laboratory of Design and Synthesis of Chemotherapeutics Potentially Active in Neglected Diseases (LAPEN), Department of Pharmacy, Faculty of Pharmaceutical Sciences, University of São Paulo—USP, 580—Building 13, São Paulo SP 05508-900, Brazil; renan.arajo@usp.br (R.V.d.A.); soraya.ssantos@yahoo.com.br (S.d.S.S.); elizabeth.igne@gmail.com (E.I.F.)

* Correspondence: jeanineg@usp.br; Tel.: +55-11-3091-3793

Received: 4 July 2018; Accepted: 7 September 2018; Published: 2 November 2018

Abstract: Dendrimers are nanoscopic compounds, which are monodispersed, and they are generally considered as homogeneous. PAMAM (polyamidoamine) was introduced in 1985, by Donald A. Tomalia, as a new class of polymers, named ‘starburst polymers’. This important contribution of Professor Tomalia opened a new research field involving nanotechnological approaches. From then on, many groups have been using PAMAM for diverse applications in many areas, including biomedical applications. The possibility of either linking drugs and bioactive compounds, or entrapping them into the dendrimer frame can improve many relevant biological properties, such as bioavailability, solubility, and selectivity. Directing groups to reach selective delivery in a specific organ is one of the advanced applications of PAMAM. In this review, structural and safety aspects of PAMAM and its derivatives are discussed, and some relevant applications are briefly presented. Emphasis has been given to gene delivery and targeting drugs, as advanced delivery systems using PAMAM and an incentive for its use on neglected diseases are briefly mentioned.

Keywords: PAMAM; dendrimers; drug delivery; gene delivery; nanotechnology

1. History

The origin of dendrimers dates back to 1978, when Fritz Vögtle, the then professor of the Kekulé Institut for Organic Chemistry and Biochemistry, reported in his paper “Cascade- and Nonskid-Chain-Like Syntheses of Molecular Cavity Topologie” [1], the newly developed syntheses of many innovative, groundbreaking organic structures. Later on, this led to the development of supramolecular chemistry, including cavitands, cyclophanes, speleands, propeller compounds, and other structures possessing molecular cavity topologies. These iterative-like molecules were the first precursors of poly(propylene imine) dendrimers (PPI) [2].

“A New Class of Polymers: Starburst-Dendritic Macromolecules” described by Prof. Dr. Donald A. Tomalia, in 1985, displays his discussion about the concept, definition, synthesis, and characterization of the “starburst polymers”, a new class of polymers whose building blocks are nowadays referred to as dendrimers. For the first time, polyamidoamine (PAMAM) was presented, as well as its first to seventh synthesized generations [3]. The synthesis from 7 to 11 were also described afterwards, but dendrimers higher than 11, being energetically unstable, cannot be obtained [4].

In a parallel research, Prof. Dr. George R. Newkome reported in his paper “Micelles. Part 1. Cascade Molecules—A New Approach to Micelles”. A (27)-arborol [5], the synthesis and characterization of which he named “unimolecular micelles” or “arborol” (derived from the Latin word *arbor*) possessed the same branching, tree-like architecture of dendrimers. Even though arborols and dendrimers are synonyms, the latter is currently used more often.

2. Introduction

Dendrimers comprise a class of nanoscopic compounds, with a well-defined monodispersed and homogeneous molecular structure. Being considered as the fourth and newest class of polymers [6–8], these dendrimers differ from the classical oligomers/polymers due to their symmetry, high branching, and maximized terminal functional density [3,9].

These kinds of molecules are composed of three main components: (1) an initiator multifunctional core, acting as a ‘germination seed’, an anchor point to dendrimer growth; (2) interior layers and inner branches composing the generations; and (3) an outer layer, the terminal functionalized branch, as schematized in Figure 1 [3,10]. The terminal functionality can be modified by adding small molecules, including ions, drugs, and biomolecules. This process can drastically change the physicochemical, reactivity, dynamics, and biological properties of dendrimers.

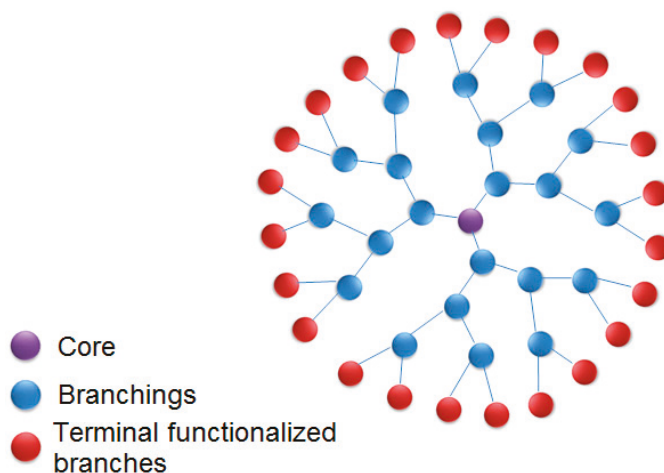


Figure 1. Dendrimers: general structure.

Considering the most diverse fields on dendrimer applications, such as drug delivery, vaccines, antimicrobials, brain ischemia, and dental glue, the main objective of this paper is to discuss the latest PAMAM advances over the past three years (2016, 2017, and 2018).

3. Structure and Synthesis

PAMAM was the first dendrimer that was synthesized and commercialized, and it is the most well-studied and well-characterized class of dendrimers [11]. There are many general approaches for dendrimer synthesis, with convergent [12] and divergent methods [3] being the most commonly used methods. In the last few years, some new methodologies have been developed, such as combined convergent–divergent, click synthesis, hypercores, branched monomers, double exponential, and lego chemistry [7,13–15].

The PAMAM dendrimer core can be composed of linear chain molecules containing primary amines. The most commonly compounds are ethylenediamine (EDA, four core multiplicity, meaning, therefore, up to four branches), ammonia (three core multiplicity), or cystamine (four core multiplicity), as shown in Figure 2 [7].

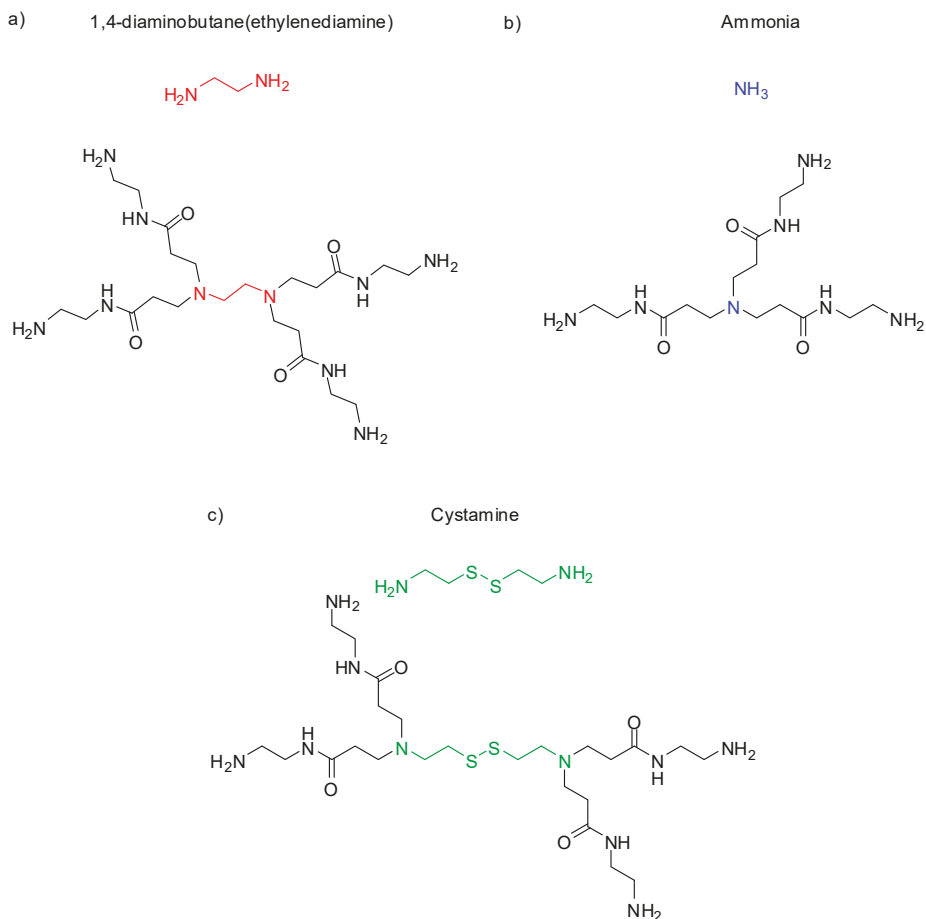


Figure 2. Common cores and G0 polyamidoamine (PAMAM) derivatives of each core.

In order to grow further generations, it is necessary to undergo an exhaustive, repetitive, two-step process consisting of (1) Michael addition reactions with an alkyl acrylate, which creates half-generations (i.e., G0.5, G1.5, etc.), composed of terminal ester groups [16–19]; and (2) in order to obtain full dendrimer generation, ester amidation with an excess of ethylenediamine must be applied. PAMAM-G1, as well as its branching generations, are shown in Figure 3.

The PAMAM molecular weight, the number of atoms, and the terminal primary amine groups increase exponentially for each generation, while the radius increases roughly linearly, by approximately 10 Å per generation [5]. This combination of growth patterns results in a rather interesting property: while low-number generations exhibit almost linear geometries, later generations show more globular-like shapes. The cavities that are intrinsically present in the globular shapes of high PAMAM generations make them suitable agents for encapsulating and adsorbing biomolecules [11,19,20].

The dendritic properties of PAMAM differentiate it from other polymers, since its tree-like architecture enables exponential growth and terminal functionality density [11]. This feature is extensively explored to enhance drug delivery properties, to control release agents [10], and to encapsulate imaging agents [21].

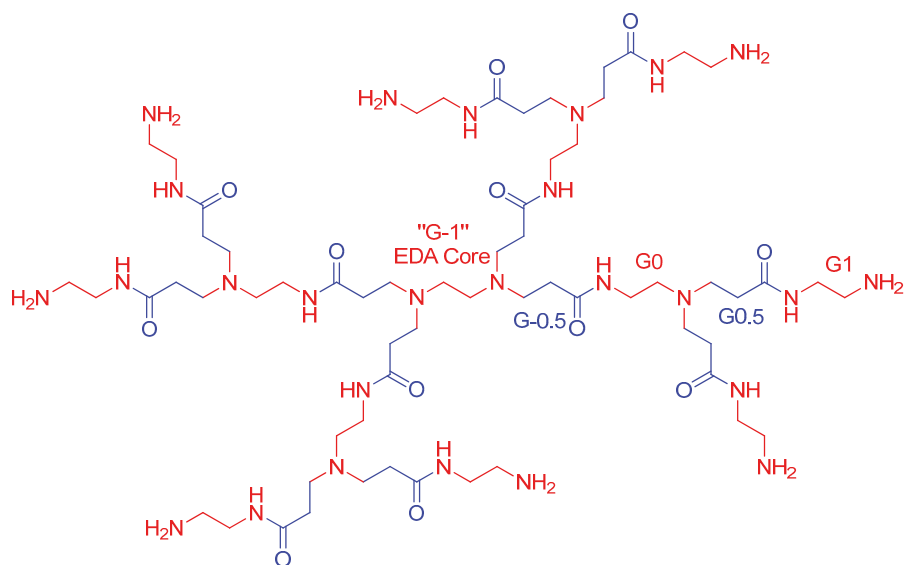


Figure 3. PAMAM generations.

4. Toxicity and Safety Concerns

Toxicity and safety are usually the main concerns regarding PAMAM dendrimers. The cytotoxicity is dependent on their concentration, charge, and generation. Cationic derivatives display significant toxicity compared to their neutrally or negatively-charged counterparts, and the cytotoxicity increases along with generation and concentration [22–27].

PAMAM-G3.5 and PAMAM-G4 dendrimers were evaluated in zebrafish models, an established animal model for a nanoparticle toxicity assay [23,28]. PAMAM-G4 with amine terminal groups showed lethal and sublethal parameters, dose, and exposure time-dependence. PAMAM-G3.5-COOH, on the other hand, was not toxic or deadly at any concentration. Pryor and colleagues employed zebrafish models to analyze the toxicity of PAMAM dendrimers of different generations (G3, G4, G5, and G6) with cationic ($-NH_2$) terminal groups, (G5 and G6) anionic (succinamic acid), and (G6) neutral terminal groups (amidoethanol) [29]. In this study, neutral or anionic dendrimers did not show significant morbidity or mortality at the concentrations tested. On the other hand, positively charged terminal groups induced mortality (lethal effect) and relevant cardiac impacts, as well as pericardial edema (sublethal effect). According to the authors, the terminal group, the number of generations, and the size of the molecules are related to their toxicities in zebrafish models [23,28–32]. For cationic dendrimers, it was verified that more toxicity was present with lower generation and size. These data contrast with findings in cell culture, in which higher-generation dendrimers are more toxic. It is likely that this might have happened because the cationic moieties bind to the cell membrane (negatively charged), and destabilize it, leading to cell lysis [23,33,34].

In Caco-2 models, PAMAM dendrimers showed a decrease in cell viability, with generation-dependent toxicity, while higher generations such as PAMAM-G3 and PAMAM-G4 presented lower cell viability than G0, G1, or G2. However, in a similar study performed with L929 mouse fibroblasts, G3 dendrimers did not exhibit significant cytotoxicity up to 1 mg/mL, and no hemolytic effects up to 10 mg/mL, being less cytotoxic and hemolytic than other polycations [24–26]. Moreover, the functionalization of the dendrimer surface was assessed regarding the toxicity and immune cell activation, suggesting the possible triggering of inflammatory

reactions [35]. Several studies have demonstrated the decrease of PAMAM toxicity through its PEGylation [36] (Figure 4), as reported by Wang et al. (2010) [37].

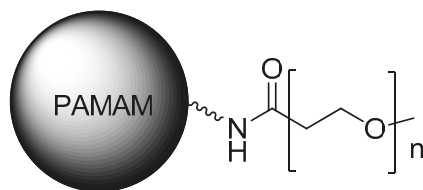


Figure 4. PEGylation of PAMAM is one of the strategies for decreasing its toxicity.

Najlah et al. [38] (2017) described the use of diethylene glycol (DEG) and lauroyl chains as new surface modifiers to functionalize PAMAM-G0 and PAMAM-G3. The main objective of this work was to decrease the cytotoxicity of naproxen, as well as to improve the pharmacokinetics of the drug profile. The study revealed great enhancement in the transport of naproxen conjugates across Caco-2 cell monolayers, for both lauroyl and DEG derivatives, and for PAMAM-G0 and PAMAM-G3, while PAMAM-G0 conjugates also presented low cytotoxicities. Pyrrolidone as a new surface modifier has also been employed [39,40]. Half-generation anionic PAMAM has been proven to possess very low cytotoxicity, lytic, and hemolytic properties in a broad concentration range. Also, it presented no toxicity *in vivo* [26,41], this being noteworthy as a promising dendrimer family for future biomedical applications.

PAMAM dendrimers can activate the immune response [42]. This is considering that the positively charged dendrimers may be employed as vaccine carriers, due to their ability to increase cytokine production [36,43]. Regarding PAMAM immunogenicity, the dendrimer was not immunogenic by itself, as it did not induce production against dendrimer-specific antibodies [44,45]. However, the dendrimer conjugation with a protein carrier (albumin to PAMAM-G0 and interleukin-3 to PAMAM-G5 dendrimers) induced the formation of antibodies for dendrimer surface groups, such as amine and oxyamine [45]. Therefore, these studies have indicated the need to conjugate PAMAM dendrimers to a protein carrier for antigenic effect [46].

5. Biomedical Applications

5.1. Odontology

Wu and coworkers reported the properties of carboxyl-terminated poly(amidoamine) (PAMAM-COOH)-alendronate (ALN) conjugated with (ALN-PAMAM-COOH) on the remineralization of hydroxyapatite on acid-etched enamel, both *in vitro* and *in vivo* [47]. Additionally, Wang and coworkers [48] also presented the remineralization properties of PAMAM-G3 for the treatment of dentinal tubule occlusions, which also exhibited great results. Also, Gao and coworkers [49] studied the biomineralization effects of PAMAM-G4. For comparison, sodium fluoride (NaF), being a desensitizing agent, was used as a positive control. Dentine permeability, morphology, and surface deposits were measured, and both samples were submitted to brushing and an acid challenge. The results showed that both PAMAM and NaF reduced dentine permeabilization to significant levels, at 25.1% and 20.7%, respectively. PAMAM also demonstrated good results with creating precipitates on dentine surfaces; it was initially slower than NaF, but then had similar results after 28 days. Moreover, PAMAM induced biomineralization, not only at a superficial level on dentine surfaces, but also on a deeper level, reaching the dentinal tubules. PAMAM still exhibited a stronger resistance to acid challenge, to a greater degree than NaF, and it proved to be a more reliable and stable dentinal tubule occlusion agent. Liang and coworkers [50] also performed similar studies, using a composite with nanoparticles of amorphous calcium phosphate (NACP) and PAMAM, which provided positive results.

Yang Ge and coworkers [51] reported a novel dental adhesive comprising PAMAM-G3 and dimethylaminododecyl methacrylate (DMADDM), which featured not only remineralization, but also anti-caries, and biofilm-regulating properties. The adhesive showed similar bond strengths compared to the control group, lower lactic acid production, and the metabolic activity of biofilms, inhibiting three-species biofilm growth, EPS production, and improved remineralization on dentin, as observed through scanning electron microscopy. PAMAM is regarded as a promising agent for a wide range of applications in the odontology area [52–57].

5.2. Anti-Atrophics, Analgesics, and Anti-Inflammatories

PAMAM has also been used as an anti-atrophic agent. Márquez-Miranda and colleagues [58] have reported the application of PAMAM-G4-OH conjugated to angiotensin (1-7) (Ang-(1-7)) (Figure 5) in rats to prevent skeletal atrophy associated to disuse by immobilization. The results demonstrated that PAMAM-Ang (1-7) almost fully recovered muscular fiber diameters and regulated proteins, which in an atrophic state, would be differentially regulated. Those compounds were the pioneers for an injectable formulation, improving the stability of Ang-(1-7) in the human body. The potential of PAMAM for drug delivery was evident, allowing for possibilities for other peptides formulations for disuse-induced skeletal muscle atrophy treatment in humans [59–61].

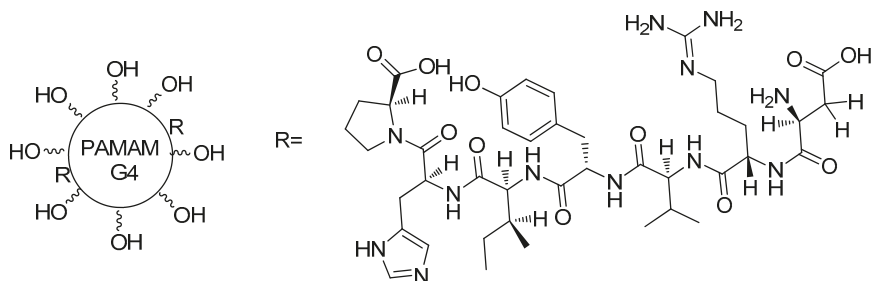


Figure 5. Structure of the PAMAM-G4-OH-Ang-(1-7) compound [58].

Another use for PAMAM is as an anti-inflammatory and anti-thrombotic agent. Its ability as a nucleic acid scavenging agent has been explored by Lee and colleagues [62], evaluating the extent of the capabilities of both PAMAM-G3 and polyethyleneimine (PEI) as a nucleic acid binding-polymers (NABP). For the experiment, the dendrimer was immobilized on microfiber meshes, as an attempt to attenuate the cytotoxicity of the free dendrimers. The study demonstrated that both dendrimers are able to neutralize damage-associated molecular patterns (DAMPs) and pathogen-associated molecular patterns (PAMP), such as cell-free DNA and RNA. These types of molecules can be identified by specific toll-like receptors (TLR), and they are known for triggering the immune system. The capacity of the dendrimer for scavenging these molecules can prevent an exacerbated immune response and blood coagulation, which could lead to a thrombotic state. The NABP-immobilized PSMA/polystyrene microfiber mesh (both PEI and PAMAM) reported no cytotoxicity. Overall, both immobilized dendrimers demonstrated great potential for *ex vivo* treatments, and they can potentially be used in intensive care units, especially on extracorporeal membrane oxygenation, continuous veno-venous hemofiltration (CVVH), and continuous renal replacement therapy, as anti-inflammatory and anti-thrombotic filters for patients with traumas or organ acceptance derived from traumatic injuries. PAMAM-G3 was also applied as a NABP for systemic lupus erythematosus treatment [63]. The findings showed that PAMAM reduced the circulation of soluble autoantibodies, skin inflammation, halted platelet depletion and inflammation-associated organ damage, and generally improved the lupus pathology. This report is believed to be a breakthrough for the application of dendrimers for autoimmune disease therapy.

Dexamethasone conjugated with PAMAM-G4-OH (PAMAM-Dex) was used by Soiberman and colleagues [64] for corneal inflammation treatment, by a cross-linked thiolene click chemistry system and hyaluronic acid. PAMAM-Dex was injected subconjunctivally. The administration of dexamethasone had significant results, such as lower central corneal thickness, better corneal clarity, prevention of high intraocular pressure, and also significant neovascularization reduction, which could be explained by the decrease of macrophage infiltration and pro-inflammatory cytokines. The PAMAM-Dex prodrug depicted a 10-fold effectiveness for the inflammation treatment, when compared to the free drug, and the effects of a single dose remained for two weeks. Therefore, those achievements not only played an important role for steroid-based therapies, but also provided relief and better treatment acceptance by the patient, since the administration was far less frequent, causing much less discomfort.

PAMAM-G4-OH-triamcinolone acetonide (PAMAM-TA) (Figure 6), characterized by selective uptake towards microglia cells, was synthesized and administered intrathecally into the spinal cords of mice by Kim et al. [65] to evaluate its effect as an anti-inflammatory and analgesic [65–67]. When tested upon microglia cells in mice, PAMAM-TA prevented the upregulation of proinflammatory cytokines upon stimulation with lipoteichoic acid at levels as high as 90%. The compound also relieved nerve injury-induced neuropathic pain, due to the activation of spinal cord microglia, lowering Nox2, IL-1 β , TNF- α , and IL-6 upregulation by up to 90%, when compared to the control group. This measurement suggests that PAMAM-TA could also have pain relieving effects, and the hypothesis was addressed through a van Frey test, which confirmed its strong analgesic effects in mice. The effects of a single dose lasted for up to three days and showed no cytotoxicity. The PAMAM-conjugated TA can represent a great improvement to free TA, as it prevents direct injections to the central nervous system (CNS), considering that these are very risky, and it also prevents the high levels of steroids, which could cause neurotoxicity. A previous study by Kambhampati [68] also reported on the use of the same compound for the treatment of retinal epithelial pigment cells, where the PAMAM-TA compound presented a better inhibition of VEGF production on the hypoxic cells, even with a 100-fold lower concentration than free TA. Both neuroinflammation and VEGF production are keys to diseases such as diabetic macular edema, proliferative diabetic retinopathy, and exudative age-related macular degeneration [69,70].

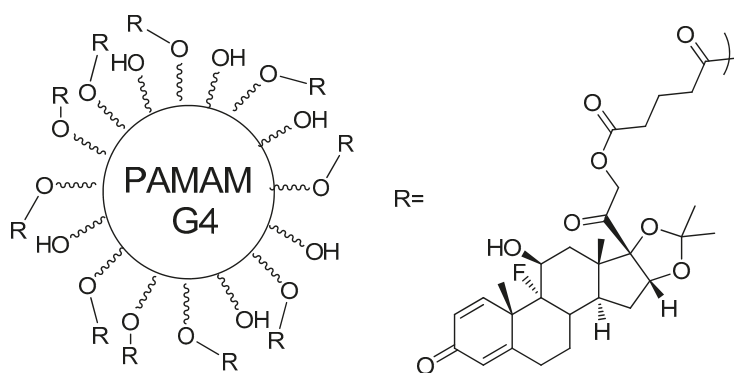


Figure 6. PAMAM-G4 functionalized with 10 molecules of triamcinolone acetonide attached, and glutaric acid as spacer agent [65,68].

5.3. Targeting Dendrimers

Nucleic acid aptamers have received prominence as drug carriers, due to their high affinity to specific ligands, their chemical flexibility, and their tissue permeability. Different aptamer–drug complex or nanoparticles systems were obtained for several applications, such as toxins, peptides,

chemotherapeutics, oligonucleotides, and aptamer-mediated drug delivery, cancer treatment, neurological, and immunological diseases. Aptamer-PAMAM dendrimers were developed for targeting in chemo-immunotherapy using aptamers coupled to PAMAM through CpG-rich oligonucleotides carrying, also, DOX (doxorubicin-chemotherapeutic drug) (Figure 7) [71].

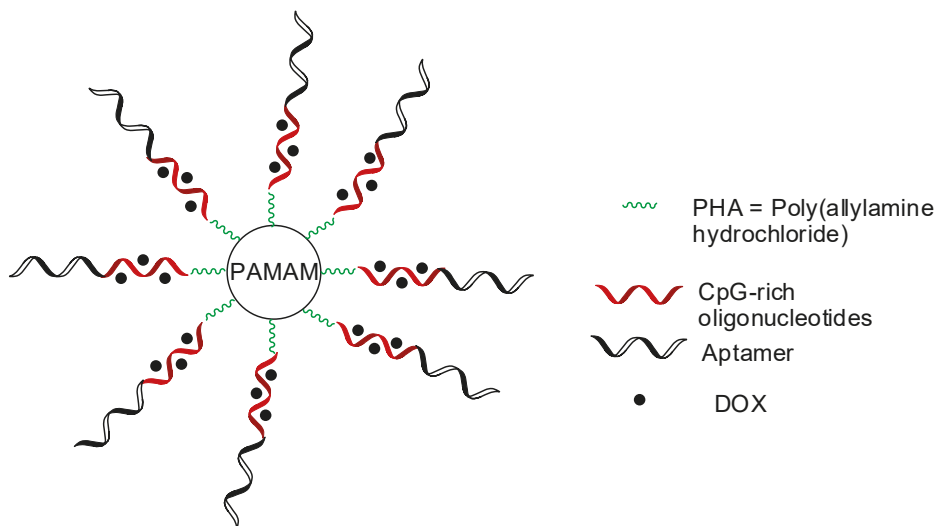


Figure 7. Aptamer-PAMAM dendrimers coupled with CpG-rich oligonucleotides loading doxorubicin-chemotherapeutic drug (DOX) [71].

PAMAM succinamic acid, in another investigation, was conjugated to oligodeoxynucleotides on the surface, resulting in single-stranded oligodeoxynucleotide-conjugated dendrimers (sONT-DENs). Anti-prostate-specific membrane antigen (PSMA) aptamers were functionalized with the sONT-DENs, resulting double-stranded aptamer-sONT-DEN derivatives, and then DOX was encapsulated. This complex displayed antitumor activity and in vivo specificity in prostate tumor models [72]. PEGylated PAMAM has also been hybridized with anti-nucleolin aptamer and 5-fluorouracil (5-FU-anticancer drug), revealing 5-FU-specific accumulation in target tumor cells [73]. Additionally, three different aptamers (MUC-1, AS1411, and ATP) were conjugated to dendrimers for targeting delivery of epirubicin (chemotherapeutic agent). The derivative dendrimers containing AS1411 aptamer is exhibited in Figure 8 [74]. These compounds were internalized into tumor cells, and presented acceptable cytotoxicity in vitro, and inhibition of tumor growth in vivo [73].

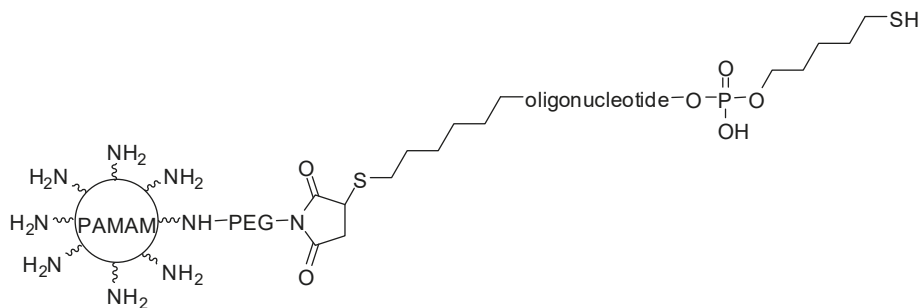


Figure 8. Smart AS1411 aptamer-functionalized/PAMAM dendrimers as nanocarriers for targeting drug delivery for gastric cancer [74].

Folic acid is the directing group of folate receptors, and it is widely used as targeting nanocarriers for anticancer drugs. PAMAM dendrimers were functionalized with folic acid and isothiocyanate (fluorescein agent), and DOX was loaded. This compound was planned to act simultaneously as a drug-targeted and pH-responsive system, therefore carrying DOX into tumor cells. The findings showed high affinity to folate receptors and a therapeutic efficacy for the dendrimers tested [75,76].

The use of stem cells and PAMAM were also investigated. Dendrimer surfaces were coated with adhesion molecules that were selectively expressed on the cellular endothelium, aimed at reaching diseased tissues such as bone marrow cells. In this study, the authors coated the surface of stem cells with PAMAM, which were previously coupled with adhesion moieties. The latter molecules are targeting groups for surgically created cutaneous and corneal wounds. These derivatives showed advantages in relation to ordinary bone marrow cell transplantation in mouse models, especially for wound healing and neovascularization. Also, they observed the specific delivery of coated stem cells to cutaneous wound tissues and injured corneas, without uptake in common organs such as the lung, liver, and spleen. Thus, the planned compounds proved to be specific, and part of a biocompatible strategy that is used to increase the efficiency of drug targeting for regenerative diseases. This cell coating technology can mediate cell–cell interactions and tissue-targeted cell delivery for wound healing, as well as for non-toxicity in vivo (murine models) and in vitro (human cells) [77].

5.4. Gene Delivery

Alternatives to viral-mediated gene delivery for gene therapy have been actively studied recently [78]. There is a growing concern related to the use of virus for this purpose, since it shows a lack of specificity, a low transfection rate, immunogenicity, toxicity, or even oncogenicity [79]. In this context, dendrimers are being largely used as an effective non-viral mediated gene delivery system. The amine functionalities of PAMAM, as well as the surface groups presented in PEI, can bind effectively to nucleic acids in physiological pH, due to polycationic nature of these compounds [80]. They offer advantages over other polymers, such as the control of physicochemical and pharmacokinetic properties, and the possibility of addition of protecting or directing groups. The transfection efficacy of PAMAM dendrimers tends to increase with generation, reaching a stable transfection rate in the eighth generation [81].

Different strategies have been used to improve the properties of PAMAM as a non-viral mediated gene delivery agent. Conjugation of group II chaperonin thermosome (THS) in PAMAM-G4 was tested by the group of Nussbaumer [82]. This compound was considered to be a new architecture for gene delivery, carrying KIF11- and GAPDH-silencing interfering RNAs (siRNAs) to cancer cells with good results, significantly inhibiting the proliferation of those cells.

Carbon nanotubes (CNT) were used as another platform for binding PAMAM and PEI for delivering microRNAs (miRNAs) [83]. Different sizes of CNT were used, including bidimensional

sheets (bucky papers (BP)) and the corresponding molecules, which are effective for transfection in different ways (BP, for example, can act as a ‘nanoneedle’ to pierce the cell). The CNT strategy [83] was then be applied by Masotti and coworkers [84], employing PAMAM and PEI coated with CNT, which was conjugated with miR-503 oligonucleotides, aiming at the regulation of angiogenesis in endothelial cells. On the other hand, miR-503, whose target is named CDC25A, is overexpressed on diabetes mellitus, and also the gene that is responsible for endothelial cells proliferation [85]. The study reported not only 99% of PAMAM-CNT-miR-503 system transfection efficacy, but also highly efficient miRNA release in endothelial cells, being therefore able to regulate the cell proliferation population. The stability of miR-503 towards RNase was also greatly improved. Finally, the number of vessels on a sponge model subcutaneous implant on mice treated with PAMAM-CNT-miR-503 was significantly reduced when compared to both the control and free miR-503 (Figure 9).

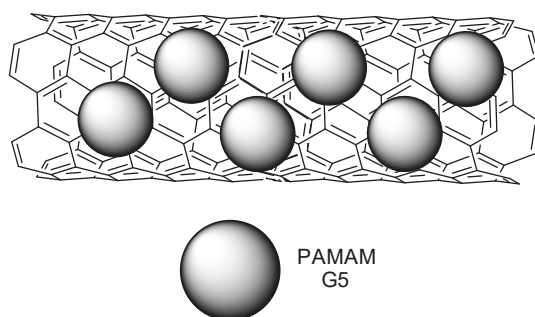


Figure 9. Schematic representation of the proposed binding mode of PAMAM on carbon nanotubes (CNT) [83].

A study regarding new method of delivering the H5-DNA vaccine against avian influenza was performed by Bahadoran [86]. Using a complex system with the H5-Green Fluorescent Protein gene cloned into the expression vector pBud, Bahadoran designed a system composed of pBud-H5-GFP and the interferon-regulatory factor (IRF)3. This pBud-H5-GFP system was then conjugated into a transactivator of transcription (TAT) bound with PAMAM (PAMAM-TAT). The results demonstrated low toxicity and good skin permeation. The cellular uptake of the pBud-H5-GFP-IRF3 was better when conjugated to PAMAM-TAT, compared to the free dendrimer. The introduction of the IRF3 group improved the immune response, a common problem faced with some DNA vaccines [87].

The effects of a double suicide gene, cytosine deaminase (CD) in combination with thymidine kinase (TK)—conjugated with PAMAM-G5, as anti-scarring agents on human Tenon’s capsule fibroblasts—were studied by Yang and colleagues [88]. In therapy, there are simultaneous administrations of ganciclovir (GCV) and 5-fluorocytosine (5-FC), aiming at the prevention of infection in the post-operative period of glaucoma filtering surgery. The TK gene can turn GCV into its phosphorylated form, and the CD gene can transform 5-FC into 5-fluorouracyl. Both transformed compounds are highly cytotoxic to the cells that express these genes, with low or no cytotoxicity to human cells [89,90]. The cell viability was greatly reduced when both 5-FC and GCV were administered to CV- and TK-transfected cells. Although the low transfection efficiency of PAMAM in the assay, the “bystander effect” [91] occurred, killing the non-transfected cell population nearby transfected cell populations, enhancing the efficacy of the treatment.

Kretzmann et al. [92] designed a flexible dendritic polymer to solve the delivery difficulties related to genomic engineering. Linear dendronized polymers are controllable and they represent synthetic platforms, providing an efficient and atoxic agent for delivering precise gene editing tools, such as CRISPR (clustered regularly interspaced short palindromic repeats) systems and TALE (transcription activator-like effectors) proteins. The authors above reported that redesigned dendrimer

architecture may solve the packaging ability and toxicity troubles that are related to higher level of generation (Figure 10).

Gold-PAMAM dendrimers (AuPAMAM) were designed to transfect cells, proving to be quite efficient in this aspect. The respective compound was analyzed in two cell lines: (1) a “hard to transfect” CT26 cell line; and (2) an “easy to transfect” SK-BR3 cell line. Many intracellular transport mechanisms, which affect the gene therapy, unknown, presenting great barriers to the planning of gene delivery carriers. Figueroa et al. [93] investigated the intracellular processes that may explain cell-to-cell variations, as well as vector-to-vector distinctions in the gene transfectability of AuPAMAM. The findings demonstrated higher transfection in the SK-BR3 cell line than in CT26. The latter cells presented greater hindrance, which impairs the internalization DNA/vector complexes in comparison to SK-BR3 cells. This investigation was the first step to identifying and designing more effective application-specific non-viral carriers.

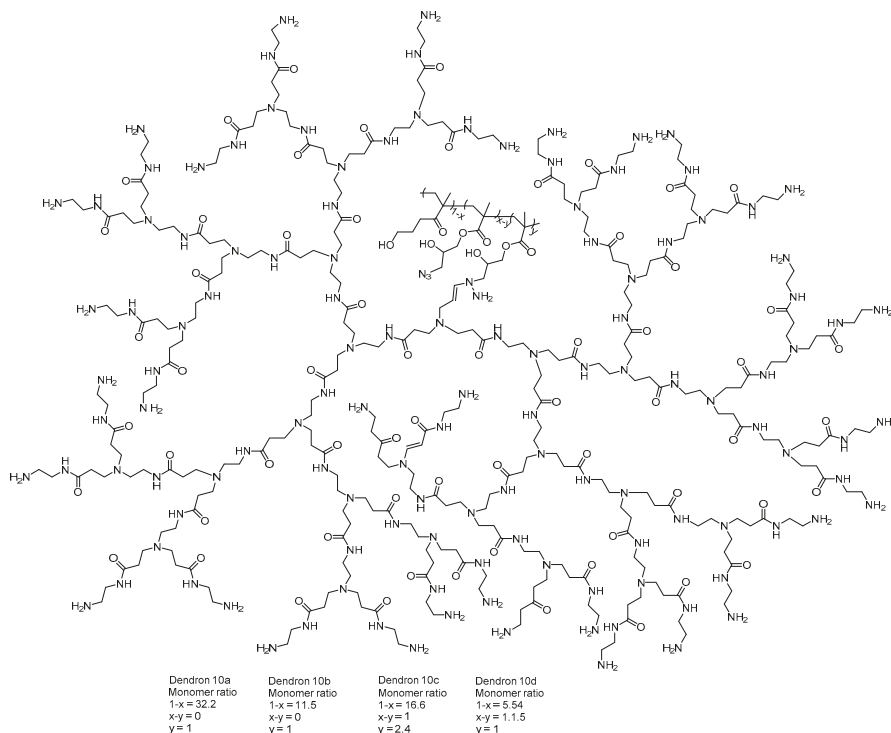


Figure 10. PAMAM-G5 functionalized with linear copolymers for gene delivery as CRISPR (clustered regularly interspaced short palindromic repeats) [92].

In another study, Chen and co-workers [94] developed self-assembling PAMAM dendrimers for small interfering RNA (siRNA) delivery. These compounds consisted of small amphiphilic dendrons in dendrimer micelles, showing a structural definition equivalent to common high dendrimer generations. This research group has been studying PAMAM as nanovectors for siRNA delivery in vitro and in vivo, and currently, one of them is being tested in clinical trials [95–101]. In this investigation, the authors synthesized amphiphilic molecules composed of a hydrophilic PAMAM dendron head, and a hydrophobic portion containing a linear hydrocarbon chain of variable length (Figure 11), and their performance in siRNA delivery was affected by the equilibrium of the hydrophobic and hydrophilic components. In addition, these self-assembling dendrons, which presented no toxicity, reached gene

silencing in highly refractory human hematopoietic CD34 stem cells, which might be explored for future biomedical applications [94].

Liu and colleagues [102] published a library of surface-engineered dendrimers, which can be applied as siRNA carriers. Structure–activity relationship (SAR) studies demonstrated that hydrophobic ligands—such as aliphatic chains, aromatic rings, fluorine, and bromine atoms—are fundamental for polymers, since they may provide high levels of gene silencing efficacy. Among the obtained compounds, the intermediate E9-2 (Figure 12) displayed higher transfection in stem cells than commercial lipid carriers, as Lipo 2000. It is important to highlight that the derivatives were able to deliver several siRNA into different cell lines, with a minimum level of cytotoxicity. Currently, SAR findings provided the development of a second-generation library of dendrimers with high gene transfection activity, contributing to the rational design of further potent siRNA nanocarriers.

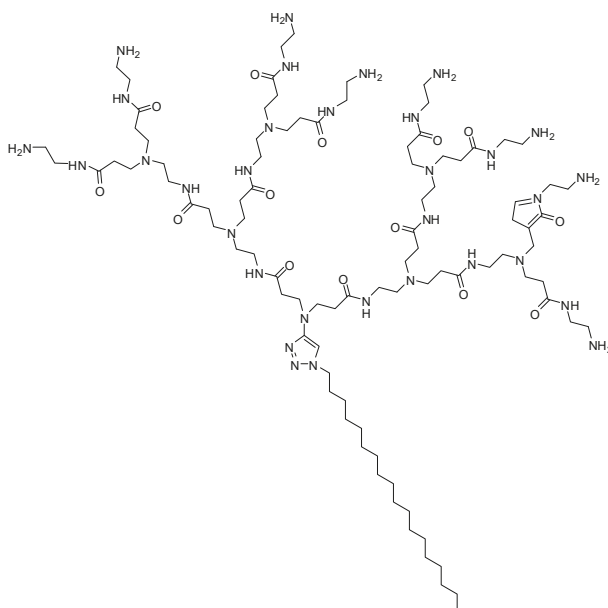


Figure 11. Amphoteric promising dendron for small interfering RNA (siRNA) delivery [94].

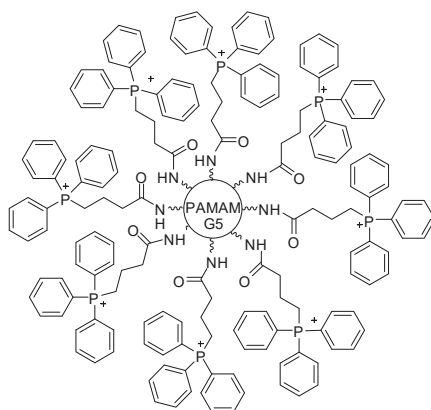


Figure 12. Dendrimer E9-2 with a high ability of gene transfection in a stem cell model [102].

The surfaces of baculoviruses was modified with a PAMAM dendrimer, resulting in a kind of compound that was capable of efficiently loading the *VEGF* transgene in transduced human adipose-derived stem cells (hASCs), which can overexpress pro-angiogenic genes. According to the authors, this derivative presented enhanced transduction efficiency based on dendrimer features. Furthermore, assays with transduced hASCs into a murine myocardial infarction model showed vascularization increase and cardiac function improvement, when compared with control therapy containing unmodified hASCs [103,104]. The same research group developed PAMAM–baculovirus complexes that were microencapsulated in poly(glycolic-co-lactic acid) (PLGA) to overcome plasma inactivation and to extend gene delivery. The stent was coated with the respective microcapsules, and it was implanted in canine femoral arteries. The pro-angiogenic effects of the VEGF-mediated baculovirus treatment were observed with regard to endothelial regeneration in injured regions four months after its application [105].

The PAMAM dendrimer was also coated with recombinant baculovirus to stimulate the overexpression of VEGF (vascular endothelial growth factor—a protein that is responsible for stimulating of the formation of blood vessels). This approach could be employed to repair damage in cardiac tissue [106].

Dendrimers as a non-virus mediated gene delivery system have also been used extensively in the fields of neuroscience [79,107], cancer [108,109], and tissue reparation [110], among others [111].

5.5. Oral Delivery

PAMAM dendrimers have been extensively studied as an oral drug delivery vehicle, since it presents the ability to cross intestinal epithelial barriers. Several investigations have been published, aiming to understand and/or improve pharmacokinetic parameters. The major concern is that PAMAM toxicity and biocompatibility are mainly related to the chemical groups that are present on the surface [112].

Propranolol (a poorly soluble drug) was conjugated to PAMAM-G3 and PAMAM-G3–lauroyl dendrimers, using a chloroacetyl spacer. The respective prodrug increased their drug water solubilities, and also enhanced its apical-to-basolateral transport across Caco-2 cell lines [113]. In vivo oral absorption was similarly analyzed using PAMAM-G3 functionalized with DOX. The findings revealed a 300-fold increase in the oral bioavailability of the prodrug when compared to the free drug [114].

Kolhatkar and co-workers [115] developed PAMAM derivatives complexed to 7-ethyl-10-hydroxycamptothecin (SN-38—an anticancer drug). These compounds presented up to a 10-fold higher permeability, as well as an increase of 100-fold cellular uptake when compared with free SN-38 (Figure 13). Camptothecin was also formulated and co-delivered with cationic PAMAM-G4 and

PAMAM-G3.5-COOH. Both dendrimers exhibited an increase of 2- to 3-fold intestinal absorption of camptothecin in vivo [116]. As a conclusion, PAMAM dendrimers can be applied to enhance the intestinal permeability of drugs with poor oral bioavailability, as well as targeting drug delivery [112].

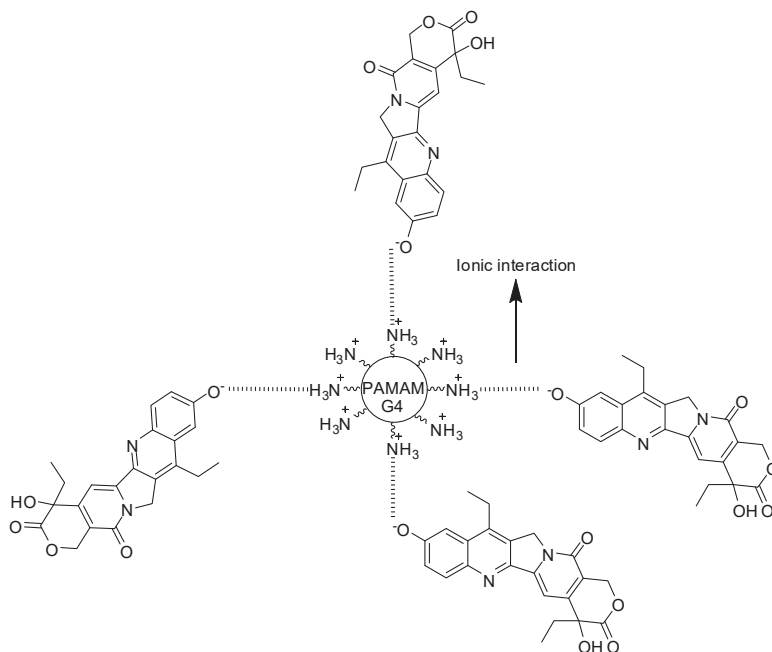


Figure 13. A PAMAM dendrimer complexed to 7-ethyl-10-hydroxy-camptothecin [115].

5.6. Pulmonary Biodistribution

PAMAM dendrimers have been investigated as pulmonary drug delivery agents through oral inhalation. PAMAM-G3 and its PEGylated counterpart were evaluated for lung cellular biodistribution. The compound presents a peak of concentration in systemic circulation within a few hours after pulmonary delivery in the presence or absence of PEG, presenting positive or negative charges, even with different sizes. However, highly PEGylated dendrimers demonstrated the highest peak plasma concentration upon pulmonary delivery. These results can be useful for designing strategies regarding dendrimer-based pulmonary drug delivery [117].

Anionic PAMAM dendrimers and dextran probes, two polymers containing similar molecular sizes, were analyzed by endocytic uptake in lung tissues. Both compounds were passively absorbed in the intact lung. However, the dendrimer compound showed a slower absorption rate when it was compared to dextran. Moreover, anionic PAMAM presented lung biocompatibility and quick uptake into the pulmonary epithelium, and this extended the transportation in the lung. These results therefore support the use of delivery systems of inhaled PAMAM-based drugs for its controlled release to the lung [118].

5.7. Antimicrobial Activity

Carbon nanodots (CND), obtained from starch and other carbon sources, have been used for different biomedical applications, as they present low toxicity, as well as fluorescent features. PAMAM dendrimers (generations greater than three, named as G3) are large polycationic molecules, demonstrating antibacterial properties, while the lower-numbered generations did not show a degree

of antimicrobial efficacy. Studies reported that PAMAM can also damage the integrity of microbial membranes, which possess an overall anionic charge. Moreover, the respective compounds can improve the cell uptake of antibiotics into the bacterium, consequently showing synergistic effects. In this context, CNDs could act as a molecular scaffold for grafting small polycationic amines, since they exhibit high cationic surface density, therefore improving the antimicrobial action. Ngu-Schwemlein and colleagues [119] conjugated PAMAM-G0 and PAMAM-G1 dendrimers (Figure 14) containing CNDs as molecular scaffolds, to increase their aminated cationic concentration, and hence, evaluated their antimicrobial activity. Furthermore, these PAMAM dendrimers conjugated to CNDs were assessed in association with tetracycline or colistin, presenting antibacterial synergic action.

PAMAM-G7 was assayed against Gram-negative and Gram-positive bacteria. The dendrimer was potentially able to inhibit the growth of both kinds of microbia, and their cytotoxicity was dependent on the exposure time and the concentration. Although more studies are required, this investigation suggested that PAMAM-G7 could be a potential antimicrobial agent. According to the authors, the antibacterial property of dendrimers is probably mediated through the disruption of the bacterial membrane by terminal amine groups. These functional groups are taken up onto bacterial cell surfaces, and then diffused through the cell wall. Thus, dendrimers interact with the cytoplasmic membrane, resulting in its disruption and disintegration, which results in the release of electrolytes, such as potassium and phosphate ions—and nucleic acids such as DNA and RNA—from the cell [120].

Similar investigation was developed by Rastegar and co-workers [121]. The authors synthesized PAMAM-G6 and evaluated its antibacterial properties against Gram-negative bacteria (*P. aeruginosa* and *E. coli*, for example) and Gram-positive bacteria (*S. aureus* and *B. subtilis*), which were isolated from different clinical samples, as well as from microorganisms standard strains. The dendrimer exhibited a good response regarding removal of microorganisms in both conditions, being an effective antimicrobial agent. According to the authors, the mechanism of action was the induction of autophagy and the decrease of *P. aeruginosa* infection and growth. Moreover, it displayed mucolytic activities, indicating its potential in recovering *P. aeruginosa* cystic fibrosis lung disease induction.

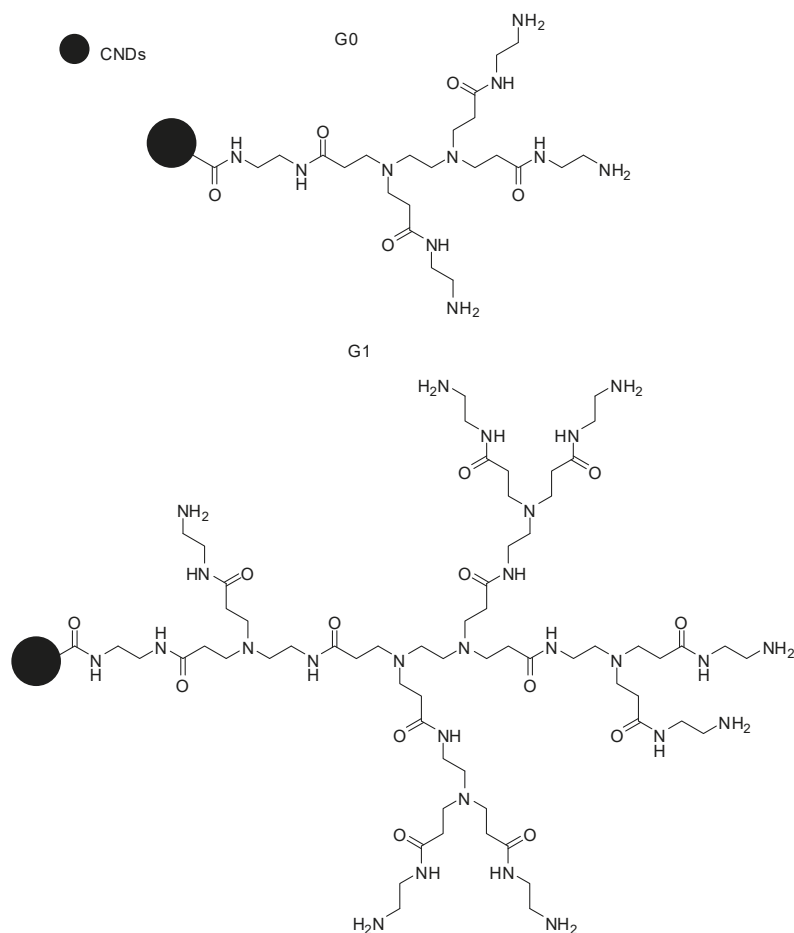


Figure 14. PAMAM dendrimer conjugated to CNDs (carbon nanodots) [119].

Several studies demonstrated the ability of the PAMAM dendrimer to improve antifungal activity as consequence of increased drug solubility in water [122,123]. Winnicka et al. [124] reported the water solubility increase of clotrimazole, which, consequently enhanced its antifungal action against different *Candida* strains. In another investigation, hydrogels of polyacrylic acid-containing clotrimazole, PAMAM-G2 and PAMAM-G3 (–NH₂ or –OH terminated groups) induced bioadhesive features and viscosity [125]. The same research group formulated a mixture containing ketoconazole (hydrophobic drug) and PAMAM-G2 (–NH₂ or –OH terminal groups), which was demonstrated to be 16 times more potent against *Candida* when compared to the free drug [126].

PAMAM dendrimers from different generations (G1–G3) were explored as agents for improving amphotericin B water solubility. The findings showed great water solubility regarding the higher generations and the concentration. Also, the complexed amphotericin–dendrimer showed sustained release in vitro [127].

In another antimicrobial approach, PAMAM-G5 dendrimers were combined to SIRT-1 (an enzyme involved in HIV-1 replication) inhibitor (HR-73) for brain HIV-1 infection. The results showed an increase of SIRT-1 inhibition, which could act in HIV reactivation from latent reservoirs. All findings

therefore suggested the importance of the association between the drug and the dendrimer, since its ability to deliver anti-retroviral drugs could improve the drugs' pharmacokinetics [128].

5.8. Other Applications

Several dendrimers of PAMAM-G2 and PAMAM-G3 containing anionic, neutral, and/or cationic surfaces were studied by Yamini and coworkers [129] to measure their effects on the protective antigen (PA) blockage channel of the anthrax toxin. PA, more specifically in an 83 kDa monomer peptide (PA83) present in the anthrax toxin, which is cleaved to PA63 [130]. The latter peptide can then oligomerize into a ring-shaped heptamer, facilitating the uptake of lethal and edema factors into the host cells. Also, it is present in the anthrax toxin, leading ultimately to cell death [131]. PAMAM can inhibit PA63 activity by blocking the lumen channels that are negatively charged, as illustrated in Figure 15. Cationic PAMAM compounds performed better, with an IC_{50} of 7.2 ± 4.7 nM for the best PAMAM-G2-NH₂ compound (in contrast to 14 mM for the anionic derivative). A dendron of cationic PAMAM-G3 was also able to diminish the toxicity issues, possessing an IC_{50} of 16.4 ± 4.0 nM. PAMAM-G2, containing 12 hydroxyl functionalities and four terminal amino groups (PAMAM-G2, 75% OH, 25% NH₂) presented an IC_{50} of 122 ± 35 nM. All cationic PAMAM compounds also performed well in the kinetics studies, presenting a decent residence time and dissociation constant. The inhibition of PA63 activity can potentially prevent infected cell death, and its efficacy can be evaluated in further investigations.

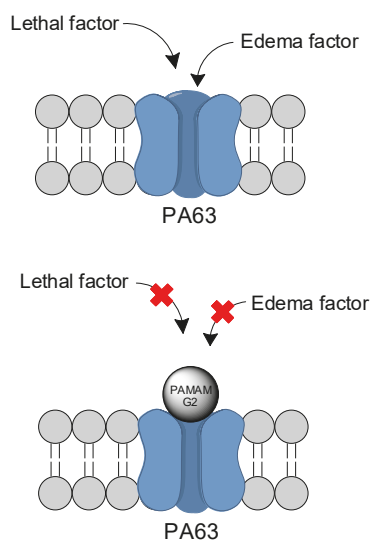


Figure 15. Blockage of the PA63 channel by PAMAM compounds [129].

Zhao and coworker [132] employed PAMAM–polyvalerolactone–poly(ethylene glycol) (PAMAM–PVL–PEG) to design a unimolecular micelle (unimNP), aiming to address the problem of retinal ganglion cell (RGC) loss on glaucoma. This unimNP was conjugated to cholera toxin B (CTB) domain to make the micelles selective towards the RGC. Dehydroepiandrosterone (DHEA) was used as agonist for the Sigma-1 receptor (S1R), a protein receptor that proved to be RGC-protective [133,134]. In vitro studies demonstrated sustained release of DHEA for periods of up to two months. On the other hand, in in vivo studies with mice injected with *N*-methyl-D-aspartate, which can induce RGC death, unimNP with CTB were able to protect RGC from cell death for periods of up to 14 days, and attenuate oxidative stress and the activation of microglia/macrogliia. S1R has shown increasing evidence of playing a major role in a plethora of neurological diseases—such as depression,

anxiety, schizophrenia, Parkinson's disease, Alzheimer's disease, amyotrophic lateral sclerosis, stroke, and others [135,136]—showcasing the importance of a sustained release platform for targeting the respective receptor.

A liver-cell spheroid shaped, aggregated in a human hematopoietic stem cell culture, was achieved by Chen and coworkers [137] using PAMAM conjugated with integrin ligand, arginine-glycine-aspartic acid (RGD), and PEG, resulting in a PAMAM–RGD–PEG compound. PAMAM–RGD–PEG promoted the hepatocytes growth in 3D spheres, as this condition mimics the cell's natural microenvironment. Additionally, it also helped to maintain cells in a healthy and functional state, greatly decreased the presence of ROS, promoted cell proliferation, and led to higher concentrations of albumin and urea. Furthermore, it also leads to a higher expression of urea-dependent enzymes Arg1 and OTC, enhancing the basic functions of the cells. These cells could potentially represent a great advance for bioartificial liver systems, being extracorporeal detoxification systems that are useful for liver failures [138].

PAMAM dendrimers were applied to control diabetes, since it is one of the leading causes of death worldwide [139]. Zhang and co-workers [140] then designed an advanced glucose-sensitive system, consisting of a smart microgel derivative from PAMAM-G1 dendrimers [141,142].

Parkinson's disease (PD) was assessed using a PAMAM-G4 conjugated to glutathione (PAMAM–GSH) (Figure 16), aiming to deliver glutathione into PC12 cells [143]. Glutathione is a tripeptide that plays an important antioxidant and antiapoptotic role in the brain, whose depletion has already been correlated to PD [144,145]. PAMAM–GSH was able to lower intracellular levels of reactive oxygen species, and to reduce the levels of cleaved caspase-3 in the assays, achieving 10% of their original concentrations. Curiously, these antioxidative and antiapoptotic properties were significantly higher when PAMAM–GSH was at low concentrations. PAMAM–GSH also demonstrated a lower cytotoxicity than the PAMAM-G4 itself. Other strategies for the treatment of PD with PAMAM were also explored in the past [146,147]. There are also reports on PAMAM being applied to Alzheimer's disease and other prionic diseases [148–150].

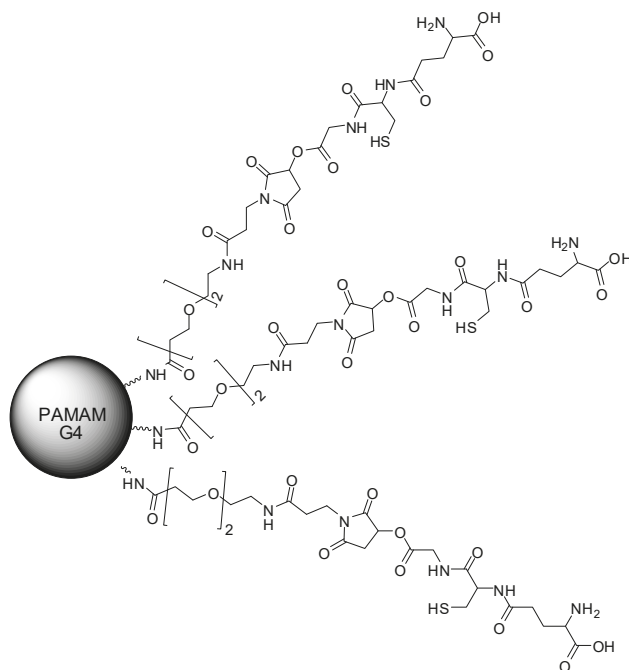


Figure 16. The PAMAM–poly(ethylene glycol) (PEG)–glutathione (GSH) compound [142].

Nitric oxide (NO)—an important free radical gas—exhibits actions such as antimicrobial action, muscle relaxant, vasodilation, and the stimulation of growth factor [151]. However, NO is unstable under different conditions, especially in biological environments. In this context, Stasko et al. [152] designed a modified PAMAM dendrimer as a NO delivery carrier. This vehicle can store up to 2 μmol NO/mg dendrimer, and releases NO when triggered with copper (II) or light. Other examples of PAMAM dendrimers functionalized with NO donors groups (*S*-nitrosothiols, *N*-acetylpenicillamine and *N*-acetylcysteine) have been described [153,154].

In a different approach, estradiol was conjugated to a positively charged PAMAM dendrimer through a hydrolytically stable bond. Also, the dendrimer was coupled to the fluorescent reagent tetramethylrhodamine, which provides a convenient way to improve intracellular visualization (Figure 17). This compound was able to bind to the estrogen receptor with a similar affinity as free estradiol. Even though it cannot be taken up into the nucleus, it can still stimulate gene expression. According to the authors, this derivative can be applied to mimic the protective effects of estradiol on the cardiovascular system in mice [155].

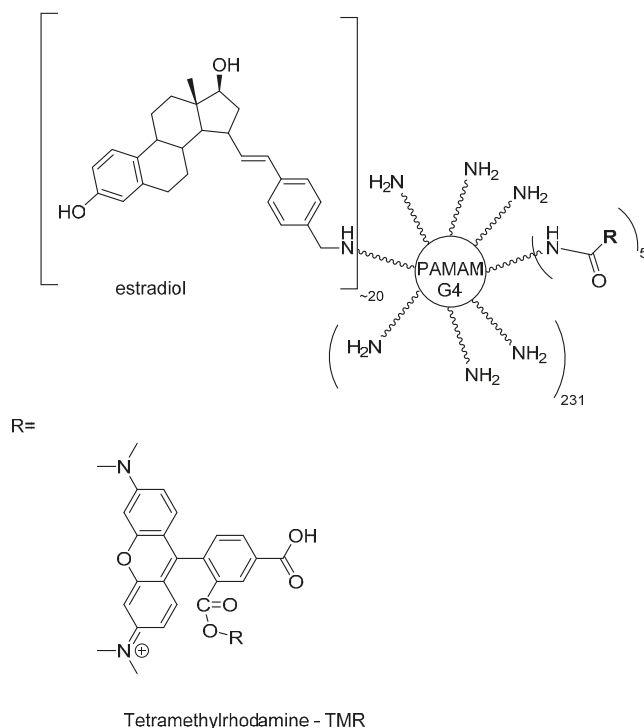


Figure 17. A PAMAM dendrimer conjugated to estradiol [151].

Srinageshwar and colleagues [156] evaluated novel mixed surface PAMAM dendrimers that are able to cross the blood–brain barrier when administered via the carotid artery in mice. In this investigation, there was a comparison between PAMAM dendrimers composed of neutral ($-\text{OH}$) and cationic ($-\text{NH}_2$) groups on the surface, called the mixed cationic surface ($-\text{NH}_2$) (Figure 18). According to the authors, mixed surface compounds were able to cross the blood–brain barrier (BBB) when injected systemically. Thus, they could reach the brain cells, indicating that they are a potential CNS drug delivery system. In addition, these compounds demonstrated reduced toxicities.

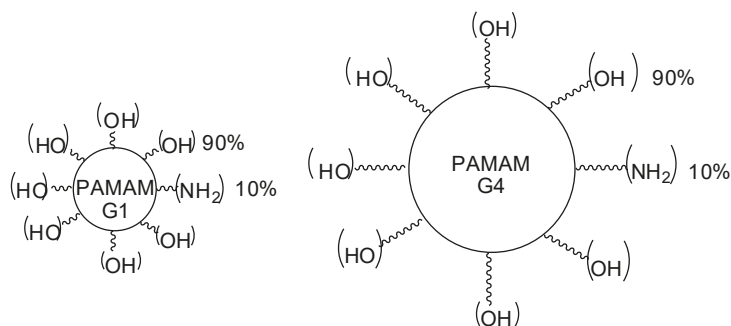


Figure 18. PAMAM-G1 and PAMAM-G4 dendrimers containing mixed surface groups, neutral ($-\text{OH}$ —90%) and cationic ($-\text{NH}_2$ —10%) moieties [152].

6. Concluding Remarks

After more than three decades of dendrimer discovery and the introduction of PAMAM, this area has advanced significantly, and newly-derived molecular architectures have arisen from this starting point. However, PAMAM continues to be the dendrimer basis for many applications, such as those showcased in this review. It is worth noting the versatility of PAMAM as an important carrier for drug delivery and biomedical applications. Studies with many therapeutic classes have been developed over the years. Drugs that are either covalently linked (prodrugs) or adsorbed to PAMAM branches have been assayed, with most of them being chemotherapeutic agents, such as anticancer agents and antimicrobials. In the era of gene therapy, the role of PAMAM as a non-viral mediated gene delivery system must be emphasized. Many examples have been briefly described—such as dendrimers of silencing RNA and precise gene editing tools, such as CRISPR—whose use deserves increasing interest. Notwithstanding, some areas should stimulate interest in using dendrimers as PAMAMs. Neglected diseases, especially those that have been nearly forgotten, need more effort in studies that are purposed towards better chemotherapeutic agents. The therapeutic arsenal against most of them is very scarce or non-existent. Imbued with the spirit of contributing to this field, we have been working on prodrug designs for either drugs or bioactive compounds, using many carriers, including PAMAM. Antichagasic, leishmanicide, tuberculostatic, and antimalarial PAMAM prodrugs have been designed and are being synthesized (data not published), with the purpose of improving either their pharmaceutics and pharmacokinetics, or indirectly improving their pharmacodynamic properties. As has been aforementioned in this review, the targeting of drugs mediated through PAMAM is an area that must be further explored, and we have been trying to reach better selectivity by using directing groups to achieve this. To summarize, the knowledge of all of the properties of PAMAM as a carrier, as we have briefly exposed in this review, could lead to the increase of compounds that have been submitted to clinical trials in order to introduce derivatives with better properties than their drugs/bioactive prototypes. We hope that the examples that herein have been given about PAMAM applications could incite new ideas for researchers who are involved in the fascinating world of dendrimers.

Author Contributions: Conceptualization, J.G. and R.V.d.A.; Software, R.V.d.A. and S.d.S.S.; Writing-Original Draft Preparation, R.V.d.A., S.d.S.S. and E.I.F.; Writing-Review & Editing, R.V.d.A., S.d.S.S., J.G. and E.I.F.; Supervision, J.G.; Project Administration, J.G.; Funding Acquisition, J.G.

Funding: This research was funded by Fundação de Amparo à Pesquisa do Estado de São Paulo (FAPESP) grant number 2015/19438-1 for J.G., and 2017/21154-7 for R.V.d.A., and Conselho Nacional de Desenvolvimento Científico e Tecnológico (CNPq research fellowship) for Ferreira EI's research fellowship, for J.G. for grant number 422928/2016-0 and for S.d.S.S. for their scholarship 153232/2018-8.

Conflicts of Interest: The authors declare no conflict of interest.

References

- Buhleier, E.; Wehner, W.; Vögtle, F. “Cascade”- and “nonskid-chain-like” syntheses of molecular cavity topologies. *Synthesis* **1978**, *1978*, 155–158. [[CrossRef](#)]
- Tomalia, D.A. In memoriam of Prof. Dr. Fritz Vögtle (1939–2017). *Can. J. Chem.* **2017**, *95*, ix–x. [[CrossRef](#)]
- Tomalia, D.A.; Baker, H.; Dewald, J.; Hall, M.; Kallos, G.; Martin, S.; Roeck, J.; Ryder, J.; Smith, P. A new class of polymers: Starburst-dendritic macromolecules. *Polym. J.* **1985**, *17*, 117–132. [[CrossRef](#)]
- Maiti, P.K.; Çağın, T.; Wang, G.; Goddard, W.A. Structure of PAMAM dendrimers: Generations 1 through 11. *Macromolecules* **2004**, *37*, 6236–6254. [[CrossRef](#)]
- Newkome, G.R.; Yao, Z.; Baker, G.R.; Gupta, V.K. Micelles. Part 1. Cascade molecules: A new approach to micelles. A [27]-arborol. *J. Org. Chem.* **1985**, *50*, 2003–2004. [[CrossRef](#)]
- Tomalia, D.A. Birth of a new macromolecular architecture: Dendrimers as quantized building blocks for nanoscale synthetic polymer chemistry. *Prog. Polym. Sci.* **2005**, *30*, 294–324. [[CrossRef](#)]
- Flory, P.J. *Principles of Polymer Chemistry*; Cornell University Press: Ithaca, NJ, USA, 1953; ISBN 9780801401343.
- Roovers, J. *Branched Polymers II*; Springer: Berlin/Heidelberg, Germany, 1999; ISBN 9783540497806.
- Abbasi, E.; Aval, S.F.; Akbarzadeh, A.; Milani, M.; Nasrabadi, H.T.; Joo, S.W.; Hanifehpour, Y.; Nejati-Koshki, K.; Pashaei-Asl, R. Dendrimers: Synthesis, applications, and properties. *Nanoscale Res. Lett.* **2014**, *9*, 247. [[CrossRef](#)] [[PubMed](#)]
- Santos, S.S.; Ferreira, E.I.; Giarolla, J. Dendrimer prodrugs. *Molecules* **2016**, *21*, 686. [[CrossRef](#)] [[PubMed](#)]
- Menjoge, A.R.; Kannan, R.M.; Tomalia, D.A. Dendrimer-based drug and imaging conjugates: Design considerations for nanomedical applications. *Drug Discov. Today* **2010**, *15*, 171–185. [[CrossRef](#)] [[PubMed](#)]
- Hawker, C.J.; Fréchet, J.M.J. Preparation of polymers with controlled molecular architecture. A new convergent approach to dendritic macromolecules. *J. Am. Chem. Soc.* **1990**, *112*, 7638–7647. [[CrossRef](#)]
- Taghavi, N.; Azar, P.; Mutlu, P.; Khodadust, R.; Gunduz, U. Poly(amidoamine) (PAMAM) nanoparticles: Synthesis and biomedical applications. *Hacettepe J. Biol. Chem.* **2013**, *41*, 289–299.
- Tomalia, D.A.; Fréchet, J.M.J. Discovery of dendrimers and dendritic polymers: A brief historical perspective. *J. Polym. Sci. Part A Polym. Chem.* **2002**, *40*, 2719–2728. [[CrossRef](#)]
- Kesharwani, P.; Jain, K.; Jain, N.K. Dendrimer as nanocarrier for drug delivery. *Prog. Polym. Sci.* **2014**, *39*, 268–307. [[CrossRef](#)]
- Gautam, S.P.; Sharma, A.K.G.A.; Madhu, T.G. Synthesis and analytical characterization of ester and amine terminated PAMAM dendrimers. *Glob. J. Med. Res.* **2013**, *13*, 7–15.
- Tomalia, D.A.; Naylor, A.M.; Goddard, W.A. Starburst dendrimers: Molecular-level control of size, shape, surface chemistry, topology, and flexibility from atoms to macroscopic matter. *Angew. Chem. Int. Ed. Engl.* **1990**, *29*, 138–175. [[CrossRef](#)]
- Peterson, J.; Ebber, A.; Allikmaa, V.; Lopp, M. Synthesis and CZE analysis of PAMAM dendrimers with an ethylenediamine core. *Proc. Estonian Acad. Sci. Chem.* **2001**, *50*, 156–166.
- Parsian, M.; Mutlu, P.; Yalcin, S.; Tezcaner, A.; Gunduz, U. Half generations magnetic PAMAM dendrimers as an effective system for targeted gemcitabine delivery. *Int. J. Pharm.* **2016**, *515*, 104–113. [[CrossRef](#)] [[PubMed](#)]
- Svenson, S.; Tomalia, D.A. Dendrimers in biomedical applications-reflections on the field. *Adv. Drug Deliv. Rev.* **2012**, *64*, 102–115. [[CrossRef](#)]
- Tomalia, D.A.; Reyna, L.A.; Svenson, S. Dendrimers as multi-purpose nanodevices for oncology drug delivery and diagnostic imaging. *Biochem. Soc. Trans.* **2007**, *35*, 61–67. [[CrossRef](#)] [[PubMed](#)]
- Jain, K.; Kesharwani, P.; Gupta, U.; Jain, N.K. Dendrimer toxicity: Let’s meet the challenge. *Int. J. Pharm.* **2010**, *394*, 122–142. [[CrossRef](#)] [[PubMed](#)]
- Martinez, C.S.; Igartúa, D.E.; Calienni, M.N.; Feas, D.A.; Siri, M.; Montanari, J.; Chiramoni, N.S.; del Alonso, S.V.; Prieto, M.J. Relation between biophysical properties of nanostructures and their toxicity on zebrafish. *Biophys. Rev.* **2017**, *9*, 775–791. [[CrossRef](#)] [[PubMed](#)]
- El-Sayed, M.; Ginski, M.; Rhodes, C.; Ghandehari, H. Transepithelial transport of poly(amidoamine) dendrimers across Caco-2 cell monolayers. *J. Control. Release* **2002**, *81*, 355–365. [[CrossRef](#)]
- Fischer, D.; Li, Y.; Ahlemeyer, B.; Krieglstein, J.; Kissel, T. In vitro cytotoxicity testing of polycations: Influence of polymer structure on cell viability and hemolysis. *Biomaterials* **2003**, *24*, 1121–1131. [[CrossRef](#)]

26. Malik, N.; Wiwattanapatapee, R.; Klopsch, R.; Lorenz, K.; Frey, H.; Weener, J.W.; Meijer, E.W.; Paulus, W.; Duncan, R. Dendrimers: Relationship between structure and biocompatibility in vitro, and preliminary studies on the biodistribution of 125I-labelled polyamidoamine dendrimers in vivo. *J. Control. Release* **2000**, *65*, 133–148. [[CrossRef](#)]
27. Duncan, R.; Izzo, L. Dendrimer biocompatibility and toxicity. *Adv. Drug Deliv. Rev.* **2005**, *57*, 2215–2237. [[CrossRef](#)] [[PubMed](#)]
28. King Heiden, T.C.; Dengler, E.; Kao, W.J.; Heideman, W.; Peterson, R.E. Developmental toxicity of low generation PAMAM dendrimers in zebrafish. *Toxicol. Appl. Pharmacol.* **2007**, *225*, 70–79. [[CrossRef](#)] [[PubMed](#)]
29. Pryor, J.B.; Harper, B.J.; Harper, S.L. Comparative toxicological assessment of PAMAM and thiophosphoryl dendrimers using embryonic zebrafish. *Int. J. Nanomed.* **2014**, *9*, 1947–1956. [[CrossRef](#)]
30. Jones, C.F.; Campbell, R.A.; Brooks, A.E.; Assemi, S.; Tadjiki, S.; Thiagarajan, G.; Mulcock, C.; Weyrich, A.S.; Brooks, B.D.; Ghandehari, H.; et al. Cationic PAMAM dendrimers aggressively initiate blood clot formation. *ACS Nano* **2012**, *6*, 9900–9910. [[CrossRef](#)] [[PubMed](#)]
31. Oliveira, E.; Casado, M.; Faria, M.; Soares, A.M.V.M.; Navas, J.M.; Barata, C.; Piña, B. Transcriptomic response of zebrafish embryos to polyaminoamine (PAMAM) dendrimers. *Nanotoxicology* **2014**, *8*, 92–99. [[CrossRef](#)] [[PubMed](#)]
32. Bodewein, L.; Schmelter, F.; Di Fiore, S.; Hollert, H.; Fischer, R.; Fenske, M. Differences in toxicity of anionic and cationic PAMAM and PPI dendrimers in zebrafish embryos and cancer cell lines. *Toxicol. Appl. Pharmacol.* **2016**, *305*, 83–92. [[CrossRef](#)] [[PubMed](#)]
33. Lee, H.; Larson, R.G. Coarse-grained molecular dynamics studies of the concentration and size dependence of fifth- and seventh-generation PAMAM dendrimers on pore formation in DMPC bilayer. *J. Phys. Chem. B* **2008**, *112*, 7778–7784. [[CrossRef](#)] [[PubMed](#)]
34. Tajarobi, F.; El-Sayed, M.; Rege, B.D.; Polli, J.E.; Ghandehari, H. Transport of poly amidoamine dendrimers across Madin-Darby canine kidney cells. *Int. J. Pharm.* **2001**, *215*, 263–267. [[CrossRef](#)]
35. Bertero, A.; Boni, A.; Gemmi, M.; Gagliardi, M.; Bifone, A.; Bardi, G. Surface functionalisation regulates polyamidoamine dendrimer toxicity on blood-brain barrier cells and the modulation of key inflammatory receptors on microglia. *Nanotoxicology* **2014**, *8*, 158–168. [[CrossRef](#)] [[PubMed](#)]
36. Huang, M.; Yang, C.S.; Xin, Y.; Jiang, G. Epidermal growth factor receptor-targeted poly(amidoamine)-based dendrimer complexed oncolytic adenovirus: Is it safe totally? *J. Thorac. Dis.* **2017**, *9*, E89–E90. [[CrossRef](#)] [[PubMed](#)]
37. Wang, W.; Xiong, W.; Zhu, Y.; Xu, H.; Yang, X. Protective effect of PEGylation against poly(amidoamine) dendrimer-induced hemolysis of human red blood cells. *J. Biomed. Mater. Res. Part B Appl. Biomater.* **2010**, *93*, 59–64. [[CrossRef](#)] [[PubMed](#)]
38. Najlah, M.; Freeman, S.; Khoder, M.; Attwood, D.; D'Emanuele, A. In vitro evaluation of third generation PAMAM dendrimer conjugates. *Molecules* **2017**, *22*, 1661. [[CrossRef](#)] [[PubMed](#)]
39. Janaszewska, A.; Studzian, M.; Petersen, J.F.; Ficker, M.; Paolucci, V.; Christensen, J.B.; Tomalia, D.A.; Klajnert-Maculewicz, B. Modified PAMAM dendrimer with 4-carbomethoxypyrrolidone surface groups-its uptake, efflux, and location in a cell. *Colloids Surf. B Biointerfaces* **2017**, *159*, 211–216. [[CrossRef](#)] [[PubMed](#)]
40. Janaszewska, A.; Gorzkiewicz, M.; Ficker, M.; Petersen, J.F.; Paolucci, V.; Christensen, J.B.; Klajnert-Maculewicz, B. Pyrrolidone modification prevents PAMAM dendrimers from activation of pro-inflammatory signaling pathways in human monocytes. *Mol. Pharm.* **2018**, *15*, 12–30. [[CrossRef](#)] [[PubMed](#)]
41. Jesús, P.D.O.L.; Ihre, H.R.; Gagne, L.; Fréchet, J.M.J.; Szoka, F.C. Polyester dendritic systems for drug delivery applications: In vitro and in vivo evaluation. *Bioconjug. Chem.* **2002**, *13*, 453–461. [[CrossRef](#)]
42. Qiu, X. Effect of poly(amidoamine) dendrimers on the structure and activity of immune molecules. *Biochim. Biophys. Acta* **2015**, *1850*, 419–425. [[CrossRef](#)]
43. Naha, P.C.; Davoren, M.; Lyng, F.M.; Byrne, H.J. Reactive oxygen species (ROS) induced cytokine production and cytotoxicity of PAMAM dendrimers in J774A.1 cells. *Toxicol. Appl. Pharmacol.* **2010**, *246*, 91–99. [[CrossRef](#)] [[PubMed](#)]
44. Roberts, J.C.; Bhalgat, M.K.; Zera, R.T. Preliminary biological evaluation of polyamidoamine (PAMAM) starburst dendrimers. *J. Biomed. Mater. Res.* **1996**, *30*, 53–65. [[CrossRef](#)]

45. Lee, S.C.; Parthasarathy, R.; Duffin, T.D.; Botwin, K.; Zobel, J.; Beck, T.; Lange, G.; Kunneman, D.; Janssen, R.; Rowold, E.; et al. Recognition properties of antibodies to PAMAM dendrimers and their use in immune detection of dendrimers. *Biomed. Microdevices* **2001**, *3*, 53–59. [[CrossRef](#)]
46. Ilinskaya, A.N.; Dobrovolskaia, M.A. Understanding the immunogenicity and antigenicity of nanomaterials: Past, present and future. *Toxicol. Appl. Pharmacol.* **2016**, *299*, 70–77. [[CrossRef](#)] [[PubMed](#)]
47. Wu, D.; Yang, J.; Li, J.; Chen, L.; Tang, B.; Chen, X.; Wu, W.; Li, J. Hydroxyapatite-anchored dendrimer for in situ remineralization of human tooth enamel. *Biomaterials* **2013**, *34*, 5036–5047. [[CrossRef](#)] [[PubMed](#)]
48. Wang, T.; Yang, S.; Wang, L.; Feng, H. Use of poly (Amidoamine) dendrimer for dentinal tubule occlusion: A preliminary study. *PLoS ONE* **2015**, *10*, e0124735. [[CrossRef](#)] [[PubMed](#)]
49. Gao, Y.; Liang, K.; Li, J.; Yuan, H.; Liu, H.; Duan, X.; Li, J. Effect and stability of poly(amido amine)-induced biomaterialization on dentinal tubule occlusion. *Materials* **2017**, *10*, 384. [[CrossRef](#)] [[PubMed](#)]
50. Liang, K.; Weir, M.D.; Xie, X.; Wang, L.; Reynolds, M.A.; Li, J.; Xu, H.H.K. Dentin remineralization in acid challenge environment via PAMAM and calcium phosphate composite. *Dent. Mater.* **2016**, *32*, 1429–1440. [[CrossRef](#)] [[PubMed](#)]
51. Ge, Y.; Ren, B.; Zhou, X.; Xu, H.H.K.; Wang, S.; Li, M.; Weir, M.D.; Feng, M.; Cheng, L. Novel dental adhesive with biofilm-regulating and remineralization capabilities. *Materials* **2017**, *10*, 26. [[CrossRef](#)] [[PubMed](#)]
52. Liang, K.; Xiao, S.; Wu, J.; Li, J.; Weir, M.D.; Cheng, L.; Reynolds, M.A.; Zhou, X.; Xu, H.H.K. Long-term dentin remineralization by poly(amido amine) and rechargeable calcium phosphate nanocomposite after fluid challenges. *Dent. Mater.* **2018**, *34*, 607–618. [[CrossRef](#)] [[PubMed](#)]
53. Liang, K.; Xiao, S.; Weir, M.D.; Bao, C.; Liu, H.; Cheng, L.; Zhou, X.; Li, J.; Xu, H.H.K. Poly (amido amine) dendrimer and dental adhesive with calcium phosphate nanoparticles remineralized dentin in lactic acid. *J. Biomed. Mater. Res. Part B Appl. Biomater.* **2017**, *106*, 2414–2424. [[CrossRef](#)] [[PubMed](#)]
54. Xiao, S.; Liang, K.; Weir, M.D.; Cheng, L.; Liu, H.; Zhou, X.; Ding, Y.; Xu, H.H.K. Combining bioactive multifunctional dental composite with PAMAM for root dentin remineralization. *Materials* **2017**, *10*, 89. [[CrossRef](#)] [[PubMed](#)]
55. Liang, K.; Zhou, H.; Weir, M.D.; Bao, C.; Reynolds, M.A.; Zhou, X.; Li, J.; Xu, H.H.K. Poly(amido amine) and calcium phosphate nanocomposite remineralization of dentin in acidic solution without calcium phosphate ions. *Dent. Mater.* **2017**, *33*, 818–829. [[CrossRef](#)] [[PubMed](#)]
56. Liang, K.; Weir, M.D.; Reynolds, M.A.; Zhou, X.; Li, J.; Xu, H.H.K. Poly (amido amine) and nano-calcium phosphate bonding agent to remineralize tooth dentin in cyclic artificial saliva/lactic acid. *Mater. Sci. Eng. C* **2017**, *72*, 7–17. [[CrossRef](#)] [[PubMed](#)]
57. Chen, L.; Yuan, H.; Tang, B.; Liang, K.; Li, J. Biomimetic remineralization of human enamel in the presence of polyamidoamine dendrimers in vitro. *Caries Res.* **2015**, *49*, 282–290. [[CrossRef](#)] [[PubMed](#)]
58. Márquez-Miranda, V.; Abrigo, J.; Rivera, J.C.; Araya-Duran, I.; Aravena, J.; Simon, F.; Pacheco, N.; Gonzalez-Nilo, F.D.; Cabello-Verrugio, C. The complex of PAMAM-OH dendrimer with angiotensin (1–7) prevented the disuse-induced skeletal muscle atrophy in mice. *Int. J. Nanomed.* **2017**, *12*, 1985–1999. [[CrossRef](#)] [[PubMed](#)]
59. Qi, R.; Gao, Y.; Tang, Y.; He, R.; Liu, T.; He, Y.; Sun, S.; Li, B.; Li, Y.; Liu, G. PEG-conjugated PAMAM dendrimers mediate efficient intramuscular gene expression. *AAPS J.* **2009**, *11*, 395–405. [[CrossRef](#)] [[PubMed](#)]
60. Narsireddy, A.; Vijayashree, K.; Adimoolam, M.G.; Manorama, S.V.; Rao, N.M. Photosensitizer and peptide-conjugated PAMAM dendrimer for targeted in vivo photodynamic therapy. *Int. J. Nanomed.* **2015**, *10*, 6865–6878. [[CrossRef](#)]
61. Santos, S.S.; Gonzaga, R.V.; Silva, J.V.; Savino, D.F.; Prieto, D.; Shikay, J.M.; Silva, R.S.; Paulo, L.H.A.; Ferreira, E.I.; Giarolla, J. Peptide dendrimers: Drug/gene delivery and other approaches. *Can. J. Chem.* **2017**, *95*, 907–916. [[CrossRef](#)]
62. Lee, J.; Jackman, J.G.; Kwun, J.; Manook, M.; Moreno, A.; Elster, E.A.; Kirk, A.D.; Leong, K.W.; Sullenger, B.A. Nucleic acid scavenging microfiber mesh inhibits trauma-induced inflammation and thrombosis. *Biomaterials* **2017**, *120*, 94–102. [[CrossRef](#)] [[PubMed](#)]
63. Holl, E.K.; Shumansky, K.L.; Borst, L.B.; Burnette, A.D.; Sample, C.J.; Ramsburg, E.A.; Sullenger, B.A. Scavenging nucleic acid debris to combat autoimmunity and infectious disease. *Proc. Natl. Acad. Sci. USA* **2016**, *113*, 9728–9733. [[CrossRef](#)] [[PubMed](#)]

64. Soiberman, U.; Kambhampati, S.P.; Wu, T.; Mishra, M.K.; Oh, Y.; Sharma, R.; Wang, J.; Al Towerki, A.E.; Yiu, S.; Stark, W.J.; et al. Subconjunctival injectable dendrimer-dexamethasone gel for the treatment of corneal inflammation. *Biomaterials* **2017**, *125*, 38–53. [[CrossRef](#)] [[PubMed](#)]
65. Kim, H.; Choi, B.; Lim, H.; Min, H.; Oh, J.H.; Choi, S.; Cho, J.G.; Park, J.S.; Lee, S.J. Polyamidoamine dendrimer-conjugated triamcinolone acetonide attenuates nerve injury-induced spinal cord microglia activation and mechanical allodynia. *Mol. Pain* **2017**, *13*, 1–11. [[CrossRef](#)] [[PubMed](#)]
66. Nance, E.; Zhang, F.; Mishra, M.K.; Zhang, Z.; Kambhampati, S.P.; Kannan, R.M.; Kannan, S. Nanoscale effects in dendrimer-mediated targeting of neuroinflammation. *Biomaterials* **2016**, *101*, 96–107. [[CrossRef](#)] [[PubMed](#)]
67. Zhang, F.; Nance, E.; Alnasser, Y.; Kannan, R.; Kannan, S. Microglial migration and interactions with dendrimer nanoparticles are altered in the presence of neuroinflammation. *J. Neuroinflamm.* **2016**, *13*, 65. [[CrossRef](#)] [[PubMed](#)]
68. Kambhampati, S.P.; Mishra, M.K.; Mastorakos, P.; Oh, Y.; Luty, G.A.; Kannan, R.M. Intracellular delivery of dendrimer triamcinolone acetonide conjugates into microglial and human retinal pigment epithelial cells. *Eur. J. Pharm. Biopharm.* **2015**, *95*, 239–249. [[CrossRef](#)] [[PubMed](#)]
69. Buschini, E.; Piras, A.; Nuzzi, R.; Vercelli, A. Age related macular degeneration and drusen: Neuroinflammation in the retina. *Prog. Neurobiol.* **2011**, *95*, 14–25. [[CrossRef](#)] [[PubMed](#)]
70. Simó, R.; Hernández, C. Intravitreal anti-VEGF for diabetic retinopathy: Hopes and fears for a new therapeutic strategy. *Diabetologia* **2008**, *51*, 1574–1580. [[CrossRef](#)] [[PubMed](#)]
71. Catuogno, S.; Esposito, C.L.; de Franciscis, V. Aptamer-mediated targeted delivery of therapeutics: An update. *Pharmaceuticals* **2016**, *9*, 69. [[CrossRef](#)] [[PubMed](#)]
72. Lee, I.H.; An, S.; Yu, M.K.; Kwon, H.K.; Im, S.H.; Jon, S. Targeted chemoimmunotherapy using drug-loaded aptamer-dendrimer bioconjugates. *J. Control. Release* **2011**, *155*, 435–441. [[CrossRef](#)] [[PubMed](#)]
73. Barzegar Behrooz, A.B.; Nabavizadeh, F.; Adiban, J.; Shafiee Ardestani, M.; Vahabpour, R.; Aghasadeghi, M.R.; Sohanaki, H. Smart bomb AS1411 aptamer-functionalized/PAMAM dendrimer nanocarriers for targeted drug delivery in the treatment of gastric cancer. *Clin. Exp. Pharmacol. Physiol.* **2017**, *44*, 41–51. [[CrossRef](#)] [[PubMed](#)]
74. Taghdisi, S.M.; Danesh, N.M.; Ramezani, M.; Lavaee, P.; Jalalian, S.H.; Robati, R.Y.; Abnous, K. Double targeting and aptamer-assisted controlled release delivery of epirubicin to cancer cells by aptamers-based dendrimer in vitro and in vivo. *Eur. J. Pharm. Biopharm.* **2016**, *102*, 152–158. [[CrossRef](#)] [[PubMed](#)]
75. Wen, S.; Liu, H.; Cai, H.; Shen, M.; Shi, X. Targeted and pH-responsive delivery of doxorubicin to cancer cells using multifunctional dendrimer-modified multi-walled carbon nanotubes. *Adv. Healthc. Mater.* **2013**, *2*, 1267–1276. [[CrossRef](#)] [[PubMed](#)]
76. Sifaka, P.I.; Üstündağ Okur, N.; Karavas, E.; Bikiaris, D.N. Surface modified multifunctional and stimuli responsive nanoparticles for drug targeting: Current status and uses. *Int. J. Mol. Sci.* **2016**, *17*, 1440. [[CrossRef](#)] [[PubMed](#)]
77. Liu, Z.J.; Daftarian, P.; Kovalski, L.; Wang, B.; Tian, R.; Castilla, D.M.; Dikici, E.; Perez, V.L.; Deo, S.; Daunert, S.; et al. Directing and potentiating stem cell-mediated angiogenesis and tissue repair by cell surface e-selectin coating. *PLoS ONE* **2016**, *11*, e0154053. [[CrossRef](#)] [[PubMed](#)]
78. Wu, J.; Huang, W.; He, Z. Dendrimers as carriers for siRNA delivery and gene silencing: A review. *Sci. World J.* **2013**, *2013*, 630654. [[CrossRef](#)] [[PubMed](#)]
79. Jayant, R.D.; Sosa, D.; Kaushik, A.; Atluri, V.; Vashist, A.; Tomitaka, A.; Nair, M. Current status of non-viral gene therapy for CNS disorders. *Expert Opin. Drug Deliv.* **2016**, *13*, 1433–1445. [[CrossRef](#)] [[PubMed](#)]
80. Ramamoorth, M.; Narvekar, A. Non viral vectors in gene therapy—An overview. *J. Clin. Diagn. Res.* **2015**, *9*, GE01–GE06. [[CrossRef](#)] [[PubMed](#)]
81. Kukowska-Latallo, J.F.; Bielinska, A.U.; Johnson, J.; Spindler, R.; Tomalia, D.A.; Baker, J.R. Efficient transfer of genetic material into mammalian cells using Starburst polyamidoamine dendrimers. *Proc. Natl. Acad. Sci. USA* **1996**, *93*, 4897–4902. [[CrossRef](#)] [[PubMed](#)]
82. Nussbaumer, M.G.; Duskey, J.T.; Rother, M.; Renggli, K.; Chami, M.; Bruns, N. Chaperonin-dendrimer conjugates for siRNA delivery. *Adv. Sci.* **2016**, *3*, 1600046. [[CrossRef](#)] [[PubMed](#)]

83. Celluzzi, A.; Paolini, A.; D’Oria, V.; Risoluti, R.; Materazzi, S.; Pezzullo, M.; Casciardi, S.; Sennato, S.; Bordi, F.; Masotti, A. Biophysical and biological contributions of polyamine-coated carbon nanotubes and bidimensional buckypapers in the delivery of mirnas to human cells. *Int. J. Nanomed.* **2017**, *13*, 1–18. [[CrossRef](#)] [[PubMed](#)]
84. Masotti, A.; Miller, M.R.; Celluzzi, A.; Rose, L.; Micciulla, F.; Hadoke, P.W.F.; Bellucci, S.; Caporali, A. Regulation of angiogenesis through the efficient delivery of microRNAs into endothelial cells using polyamine-coated carbon nanotubes. *Nanomed. Nanotechnol. Biol. Med.* **2016**, *12*, 1511–1522. [[CrossRef](#)] [[PubMed](#)]
85. Caporali, A.; Meloni, M.; Völlenkle, C.; Bonci, D.; Sala-Newby, G.B.; Addis, R.; Spinetti, G.; Losa, S.; Masson, R.; Baker, A.H.; et al. Deregulation of microRNA-503 contributes to diabetes mellitus-induced impairment of endothelial function and reparative angiogenesis after Limb Ischemia. *Circulation* **2011**, *123*, 282–291. [[CrossRef](#)] [[PubMed](#)]
86. Bahadoran, A.; Ebrahimi, M.; Yeap, S.K.; Safi, N.; Moeini, H.; Hair-Bejo, M.; Hussein, M.Z.; Omar, A.R. Induction of a robust immune response against avian influenza virus following transdermal inoculation with H5-DNA vaccine formulated in modified dendrimer-based delivery system in mouse model. *Int. J. Nanomed.* **2017**, *12*, 8573–8585. [[CrossRef](#)] [[PubMed](#)]
87. Pereira, V.B.; Zurita-Turk, M.; Saraiva, T.D.L.; De Castro, C.P.; Souza, B.M.; Mancha Agresti, P.; Lima, F.A.; Pfeiffer, V.N.; Azevedo, M.S.P.; Rocha, C.S.; et al. DNA vaccines approach: From concepts to applications. *World J. Vaccines* **2014**, *4*, 50–71. [[CrossRef](#)]
88. Yang, J.; Shi, L.K.; Sun, H.M.; Wang, Y.M. Antiproliferative effect of double suicide gene delivery mediated by polyamidoamine dendrimers in human tenon’s capsule fibroblasts. *Exp. Ther. Med.* **2017**, *14*, 5473–5479. [[CrossRef](#)] [[PubMed](#)]
89. Candice, L.W.; Django, S.; Margaret, E.B. The role of herpes simplex virus-1 thymidine kinase alanine 168 in substrate specificity. *Open Biochem. J.* **2008**, *2*, 60–66. [[CrossRef](#)]
90. Chaszczewska-Markowska, M.; Stebelska, K.; Sikorski, A.; Madej, J.; Opolski, A.; Ugorski, M. Liposomal formulation of 5-fluorocytosine in suicide gene therapy with cytosine deaminase—For colorectal cancer. *Cancer Lett.* **2008**, *262*, 164–172. [[CrossRef](#)] [[PubMed](#)]
91. Xiao, J.; Zhang, G.; Li, B.; Wu, Y.; Liu, X.; Tan, Y.; Du, B. Dioscin augments HSV-tk-mediated suicide gene therapy for melanoma by promoting connexin-based intercellular communication. *Oncotarget* **2017**, *8*, 798–807. [[CrossRef](#)] [[PubMed](#)]
92. Kretzmann, J.A.; Ho, D.; Evans, C.W.; Plani-Lam, J.H.C.; Garcia-Bloj, B.; Mohamed, A.E.; O’Mara, M.L.; Ford, E.; Tan, D.E.K.; Lister, S.; et al. Synthetically controlling dendrimer flexibility improves delivery of large plasmid DNA. *Chem. Sci.* **2017**, *8*, 2923–2930. [[CrossRef](#)] [[PubMed](#)]
93. Figueroa, E.; Bugga, P.; Asthana, V.; Chen, A.L.; Stephen Yan, J.; Evans, E.R.; Drezek, R.A. A mechanistic investigation exploring the differential transfection efficiencies between the easy-to-transfect SK-BR3 and difficult-to-transfect CT26 cell lines. *J. Nanobiotechnol.* **2017**, *15*, 36–51. [[CrossRef](#)] [[PubMed](#)]
94. Chen, C.; Posocco, P.; Liu, X.; Cheng, Q.; Laurini, E.; Zhou, J.; Liu, C.; Wang, Y.; Tang, J.; Col, V.D.; et al. Mastering dendrimer self-assembly for efficient siRNA delivery: From conceptual design to in vivo efficient gene silencing. *Small* **2016**, *12*, 3667–3676. [[CrossRef](#)] [[PubMed](#)]
95. Zhou, J.; Wu, J.; Hafdi, N.; Behr, J.P.; Erbacher, P.; Peng, L. PAMAM dendrimers for efficient siRNA delivery and potent gene silencing. *Chem. Commun.* **2006**, *14*, 2362–2364. [[CrossRef](#)] [[PubMed](#)]
96. Liu, X.; Wu, J.; Yammine, M.; Zhou, J.; Posocco, P.; Viel, S.; Liu, C.; Ziarelli, F.; Fermeglia, M.; Pricl, S.; et al. Structurally flexible triethanolamine core pamam dendrimers are effective nanovectors for DNA transfection in vitro and in vivo to the mouse thymus. *Bioconjug. Chem.* **2011**, *22*, 2461–2473. [[CrossRef](#)] [[PubMed](#)]
97. Liu, X.; Liu, C.; Catapano, C.V.; Peng, L.; Zhou, J.; Rocchi, P. Structurally flexible triethanolamine-core poly(amidoamine) dendrimers as effective nanovectors to deliver RNAi-based therapeutics. *Biotechnol. Adv.* **2014**, *32*, 844–852. [[CrossRef](#)] [[PubMed](#)]
98. Zhou, J.; Neff, C.P.; Liu, X.; Zhang, J.; Li, H.; Smith, D.D.; Swiderski, P.; Aboellail, T.; Huang, Y.; Du, Q.; et al. Systemic administration of combinatorial dsRNAs via nanoparticles efficiently suppresses HIV-1 infection in humanized mice. *Mol. Ther.* **2011**, *19*, 2228–2238. [[CrossRef](#)] [[PubMed](#)]
99. Reebye, V.; Sætrom, P.; Mintz, P.J.; Huang, K.W.; Swiderski, P.; Peng, L.; Liu, C.; Liu, X.; Lindkær-Jensen, S.; Zacharoulis, D.; et al. Novel RNA oligonucleotide improves liver function and inhibits liver carcinogenesis in vivo. *Hepatology* **2014**, *59*, 216–227. [[CrossRef](#)] [[PubMed](#)]

100. Kala, S.; Mak, A.S.C.; Liu, X.; Posocco, P.; Pricl, S.; Peng, L.; Wong, A.S.T. Combination of dendrimer-nanovector-mediated small interfering RNA delivery to target Akt with the clinical anticancer drug paclitaxel for effective and potent anticancer activity in treating ovarian cancer. *J. Med. Chem.* **2014**, *57*, 2634–2642. [[CrossRef](#)] [[PubMed](#)]
101. Cui, Q.; Yang, S.; Ye, P.; Tian, E.; Sun, G.; Zhou, J.; Sun, G.; Liu, X.; Chen, C.; Murai, K.; et al. Downregulation of TLX induces TET3 expression and inhibits glioblastoma stem cell self-renewal and tumorigenesis. *Nat. Commun.* **2016**, *7*, 10637. [[CrossRef](#)] [[PubMed](#)]
102. Liu, H.; Chang, H.; Lv, J.; Jiang, C.; Li, Z.; Wang, F.; Wang, H.; Wang, M.; Liu, C.; Wang, X.; et al. Screening of efficient siRNA carriers in a library of surface-engineered dendrimers. *Sci. Rep.* **2016**, *6*, 25069. [[CrossRef](#)] [[PubMed](#)]
103. Paul, A.; Shao, W.; Abbasi, S.; Shum-Tim, D.; Prakash, S. PAMAM dendrimer-baculovirus nanocomplex for microencapsulated adipose stem cell-gene therapy: In vitro and in vivo functional assessment. *Mol. Pharm.* **2012**, *9*, 2479–2488. [[CrossRef](#)] [[PubMed](#)]
104. Whitlow, J.; Pacelli, S.; Paul, A. Polymeric nanohybrids as a new class of therapeutic biotransporters. *Macromol. Chem. Phys.* **2016**, *217*, 1245–1259. [[CrossRef](#)] [[PubMed](#)]
105. Paul, A.; Elias, C.B.; Shum-Tim, D.; Prakash, S. Bioactive baculovirus nanohybrids for stent based rapid vascular re-endothelialization. *Sci. Rep.* **2013**, *3*, 2366. [[CrossRef](#)] [[PubMed](#)]
106. Hasan, A.; Waters, R.; Roula, B.; Dana, R.; Yara, S.; Alexandre, T.; Paul, A. Engineered biomaterials to enhance stem cell-based cardiac tissue engineering and therapy. *Macromol. Biosci.* **2016**, *16*, 958–977. [[CrossRef](#)] [[PubMed](#)]
107. Joshi, C.R.; Labhasetwar, V.; Ghorpade, A. Destination brain: The past, present, and future of therapeutic gene delivery. *J. Neuroimmune Pharmacol.* **2017**, *12*, 51–83. [[CrossRef](#)] [[PubMed](#)]
108. Xin, Y.; Huang, M.; Guo, W.W.; Huang, Q.; Zhang, L.Z.; Jiang, G. Nano-based delivery of RNAi in cancer therapy. *Mol. Cancer* **2017**, *16*, 134–143. [[CrossRef](#)] [[PubMed](#)]
109. Xiao, B.; Ma, L.; Merlin, D. Nanoparticle-mediated co-delivery of chemotherapeutic agent and siRNA for combination cancer therapy. *Expert Opin. Drug Deliv.* **2017**, *14*, 65–73. [[CrossRef](#)] [[PubMed](#)]
110. Wu, P.; Chen, H.; Jin, R.; Weng, T.; Ho, J.K.; You, C.; Zhang, L.; Wang, X.; Han, C. Non-viral gene delivery systems for tissue repair and regeneration. *J. Transl. Med.* **2018**, *16*, 29–49. [[CrossRef](#)] [[PubMed](#)]
111. Palmerston Mendes, L.; Pan, J.; Torchilin, V. Dendrimers as nanocarriers for nucleic acid and drug delivery in cancer therapy. *Molecules* **2017**, *22*, 1401. [[CrossRef](#)] [[PubMed](#)]
112. Yellepeddi, V.K.; Ghandehari, H. Poly(amido amine) dendrimers in oral delivery. *Tissue Barriers* **2016**, *4*, e1173773. [[CrossRef](#)] [[PubMed](#)]
113. D’Emanuele, A.; Jeyprasesphant, R.; Penny, J.; Attwood, D. The use of a dendrimer-propranolol prodrug to bypass efflux transporters and enhance oral bioavailability. *J. Control. Release* **2004**, *95*, 447–453. [[CrossRef](#)] [[PubMed](#)]
114. Ke, W.; Zhao, Y.; Huang, R.; Jiang, C.; Pei, Y. Enhanced oral bioavailability of doxorubicin in a dendrimer drug delivery system. *J. Pharm. Sci.* **2008**, *97*, 2208–2216. [[CrossRef](#)] [[PubMed](#)]
115. Kolhatkar, R.B.; Swaan, P.; Ghandehari, H. Potential oral delivery of 7-ethyl-10-hydroxy-camptothecin (SN-38) using poly(amidoamine) dendrimers. *Pharm. Res.* **2008**, *25*, 1723–1729. [[CrossRef](#)] [[PubMed](#)]
116. Sadekar, S.; Thiagarajan, G.; Bartlett, K.; Hubbard, D.; Ray, A.; McGill, L.D.; Ghandehari, H. Poly(amido amine) dendrimers as absorption enhancers for oral delivery of camptothecin. *Int. J. Pharm.* **2013**, *456*, 175–185. [[CrossRef](#)] [[PubMed](#)]
117. Zhong, Q.; Merkel, O.M.; Reineke, J.J.; Da Rocha, S.R.P. Effect of the route of administration and PEGylation of poly(amidoamine) dendrimers on their systemic and lung cellular biodistribution. *Mol. Pharm.* **2016**, *13*, 1866–1878. [[CrossRef](#)] [[PubMed](#)]
118. Morris, C.J.; Aljayyousi, G.; Mansour, O.; Griffiths, P.; Gumbleton, M. Endocytic uptake, transport and macromolecular interactions of anionic PAMAM dendrimers within lung tissue. *Pharm. Res.* **2017**, *34*, 2517–2531. [[CrossRef](#)] [[PubMed](#)]
119. Ngu-Schwemlein, M.; Chin, S.F.; Hileman, R.; Drozdowski, C.; Upchurch, C.; Hargrove, A. Carbon nanodots as molecular scaffolds for development of antimicrobial agents. *Bioorg. Med. Chem. Lett.* **2016**, *26*, 1745–1749. [[CrossRef](#)] [[PubMed](#)]

120. Gholami, M.; Mohammadi, R.; Arzanlou, M.; Akbari Dourbash, F.; Kouhsari, E.; Majidi, G.; Mohseni, S.M.; Nazari, S. In vitro antibacterial activity of poly (amidoamine)-G7 dendrimer. *BMC Infect. Dis.* **2017**, *17*, 395. [[CrossRef](#)] [[PubMed](#)]
121. Rastegar, A.; Nazari, S.; Allahabadi, A.; Falanji, F.; Akbari Dourbash, F.; Rezai, Z.; Alizadeh Matboo, S.; Hekmat-Shoar, R.; Mohseni, S.M.; Majidi, G. Antibacterial activity of amino- and amido-terminated poly (amidoamine)-G6 dendrimer on isolated bacteria from clinical specimens and standard strains. *Med. J. Islam. Repub. Iran* **2017**, *31*, 368–376. [[CrossRef](#)] [[PubMed](#)]
122. Voltan, A.; Quindós, G.; Alarcón, K.; Fusco-Almeida, A.M.; Mendes-Giannini, M.J.; Chorilli, M. Fungal diseases: Could nanostructured drug delivery systems be a novel paradigm for therapy? *Int. J. Nanomed.* **2016**, *11*, 3715–3730. [[CrossRef](#)] [[PubMed](#)]
123. Bondaryk, M.; Staniszewska, M.; Zielińska, P.; Urbańczyk-Lipkowska, Z. Natural antimicrobial peptides as inspiration for design of a new generation antifungal compounds. *J. Fungi* **2017**, *3*, 46. [[CrossRef](#)] [[PubMed](#)]
124. Winnicka, K.; Sosnowska, K.; Wieczorek, P.; Sacha, P.T.; Tryniszewska, E. Poly(amidoamine) dendrimers increase antifungal activity of clotrimazole. *Biol. Pharm. Bull.* **2011**, *34*, 1129–1133. [[CrossRef](#)] [[PubMed](#)]
125. Sosnowska, K.; Szekalska, M.; Winnicka, K. The effect of PAMAM dendrimers with amine or hydroxyl terminal groups on the bioadhesive properties of hydrogels with clotrimazole. *Polimery/Polymers* **2016**, *61*, 322–326. [[CrossRef](#)]
126. Winnicka, K.; Wroblewska, M.; Wieczorek, P.; Sacha, P.T.; Tryniszewska, E. Hydrogel of ketoconazole and PAMAM dendrimers: Formulation and antifungal activity. *Molecules* **2012**, *17*, 4612–4624. [[CrossRef](#)] [[PubMed](#)]
127. Jose, J.; Charyulu, R.N. Prolonged drug delivery system of an antifungal drug by association with polyamidoamine dendrimers. *Int. J. Pharm. Investig.* **2016**, *6*, 123–127. [[CrossRef](#)] [[PubMed](#)]
128. The 23 rd scientific conference of the Society on Neuroimmune Pharmacology: Program and Abstracts. *J. Neuroimmune Pharmacol.* **2017**, *12*, 3–77. [[CrossRef](#)] [[PubMed](#)]
129. Yamini, G.; Kalu, N.; Nestorovich, E.M. Impact of dendrimer terminal group chemistry on blockage of the anthrax toxin channel: A single molecule study. *Toxins* **2016**, *8*, 337. [[CrossRef](#)] [[PubMed](#)]
130. Chekanov, A.V.; Remacle, A.G.; Golubkov, V.S.; Akatov, V.S.; Sikora, S.; Savinov, A.Y.; Fugere, M.; Day, R.; Rozanov, D.V.; Strongin, A.Y. Both PA63 and PA83 are endocytosed within an anthrax protective antigen mixed heptamer: A putative mechanism to overcome a furin deficiency. *Arch. Biochem. Biophys.* **2006**, *446*, 52–59. [[CrossRef](#)] [[PubMed](#)]
131. Nassi, S.; Collier, R.J.; Finkelstein, A. PA63 channel of anthrax toxin: An extended β -barrel. *Biochemistry* **2002**, *41*, 1445–1450. [[CrossRef](#)] [[PubMed](#)]
132. Zhao, L.; Chen, G.; Li, J.; Fu, Y.; Mavlyutov, T.A.; Yao, A.; Nickells, R.W.; Gong, S.; Guo, L.W. An intraocular drug delivery system using targeted nanocarriers attenuates retinal ganglion cell degeneration. *J. Control. Release* **2017**, *247*, 153–166. [[CrossRef](#)] [[PubMed](#)]
133. Smith, S.B.; Duplantier, J.; Dun, Y.; Mysona, B.; Roon, P.; Martin, P.M.; Ganapathy, V. In vivo protection against retinal neurodegeneration by sigma receptor 1 ligand (+)-pentazocine. *Investig. Ophthalmol. Vis. Sci.* **2008**, *49*, 4154–4161. [[CrossRef](#)] [[PubMed](#)]
134. Mavlyutov, T.A.; Nickells, R.W.; Guo, L.-W. Accelerated retinal ganglion cell death in mice deficient in the Sigma-1 receptor. *Mol. Vis.* **2011**, *17*, 1034–1043. [[PubMed](#)]
135. Cobos, E.; Entrena, J.; Nieto, F.; Cendan, C.; Pozo, E. Pharmacology and therapeutic potential of sigma1 receptor ligands. *Curr. Neuropharmacol.* **2008**, *6*, 344–366. [[CrossRef](#)] [[PubMed](#)]
136. Nguyen, L.; Lucke-Wold, B.P.; Mookerjee, S.; Kaushal, N.; Matsumoto, R.R. Sigma-1 receptors and neurodegenerative diseases: Towards a hypothesis of sigma-1 receptors as amplifiers of neurodegeneration and neuroprotection. *Adv. Exp. Med. Biol.* **2017**, *964*, 133–152. [[CrossRef](#)] [[PubMed](#)]
137. Chen, Z.; Lian, F.; Wang, X.; Chen, Y.; Tang, N. Arginine–glycine–aspartic acid–polyethylene glycol–polyamidoamine dendrimer conjugate improves liver-cell aggregation and function in 3-d spheroid culture. *Int. J. Nanomed.* **2016**, *11*, 4247–4259. [[CrossRef](#)]
138. Pless, G. Artificial and bioartificial liver support. *Organogenesis* **2007**, *3*, 20–24. [[CrossRef](#)] [[PubMed](#)]
139. Chen, C.; Zhao, X.-L.; Li, Z.-H.; Zhu, Z.-G.; Qian, S.-H.; Flewitt, A. Current and emerging technology for continuous glucose monitoring. *Sensors* **2017**, *17*, 182. [[CrossRef](#)] [[PubMed](#)]

140. Zhang, X.; Gao, C.; Lü, S.; Duan, H.; Jing, N.; Dong, D.; Shi, C.; Liu, M. Anti-photobleaching flower-like microgels as optical nanobiosensors with high selectivity at physiological conditions for continuous glucose monitoring. *J. Mater. Chem. B* **2014**, *2*, 5452–5461. [[CrossRef](#)]
141. Mereuta, L.; Schiopu, I.; Asandei, A.; Park, Y.; Hahm, K.S.; Luchian, T. Protein nanopore-based, single-molecule exploration of copper binding to an antimicrobial-derived, histidine-containing chimera peptide. *Langmuir* **2012**, *28*, 17079–17091. [[CrossRef](#)] [[PubMed](#)]
142. Castagnola, M.; Zuppi, C.; Rossetti, D.V.; Vincenzoni, F.; Lupi, A.; Vitali, A.; Meucci, E.; Messina, I. Characterization of dendrimer properties by capillary electrophoresis and their use as pseudostationary phases. *Electrophoresis* **2002**, *23*, 1769–1778. [[CrossRef](#)]
143. Sun, H.J.; Wang, Y.; Hao, T.; Wang, C.Y.; Wang, Q.Y.; Jiang, X.X. Efficient GSH delivery using PAMAM-GSH into MPP-induced PC12 cellular model for Parkinson's disease. *Regen. Biomater* **2016**, *3*, 299–307. [[CrossRef](#)] [[PubMed](#)]
144. Dringen, R. Metabolism and functions of glutathione in brain. *Prog. Neurobiol.* **2000**, *62*, 649–671. [[CrossRef](#)]
145. Zeevalk, G.D.; Razmpour, R.; Bernard, L.P. Glutathione and Parkinson's disease: Is this the elephant in the room? *Biomed. Pharmacother.* **2008**, *62*, 236–249. [[CrossRef](#)] [[PubMed](#)]
146. Fülöp, L.; Mándity, I.M.; Juhász, G.; Szegedi, V.; Hetényi, A.; Weber, E.; Bozsó, Z.; Simon, D.; Benko, M.; Király, Z.; et al. A foldamer-dendrimer conjugate neutralizes synaptotoxic β -amyloid oligomers. *PLoS ONE* **2012**, *7*, e39485. [[CrossRef](#)] [[PubMed](#)]
147. Rekas, A.; Lo, V.; Gadd, G.E.; Cappai, R.; Yun, S.I. PAMAM Dendrimers as potential agents against fibrillation of α -Synuclein, a Parkinson's Disease-related protein. *Macromol. Biosci.* **2009**, *9*, 230–238. [[CrossRef](#)] [[PubMed](#)]
148. Lim, Y.; Mays, C.E.; Kim, Y.; Titlow, W.B.; Ryou, C. The inhibition of prions through blocking prion conversion by permanently charged branched polyamines of low cytotoxicity. *Biomaterials* **2010**, *31*, 2025–2033. [[CrossRef](#)] [[PubMed](#)]
149. Klajnert, B.; Cangiotti, M.; Calici, S.; Majoral, J.P.; Caminade, A.M.; Cladera, J.; Bryszewska, M.; Ottaviani, M.F. EPR Study of the interactions between dendrimers and peptides involved in Alzheimer's and Prion Diseases. *Macromol. Biosci.* **2007**, *7*, 1065–1074. [[CrossRef](#)] [[PubMed](#)]
150. Klajnert, B.; Cortijo-Arellano, M.; Cladera, J.; Bryszewska, M. Influence of dendrimer's structure on its activity against amyloid fibril formation. *Biochem. Biophys. Res. Commun.* **2006**, *345*, 21–28. [[CrossRef](#)] [[PubMed](#)]
151. Lautner, G.; Meyerhoff, M.E.; Schwendeman, S.P. Biodegradable poly(lactic-co-glycolic acid) microspheres loaded with *S*-nitroso-*N*-acetyl-D-penicillamine for controlled nitric oxide delivery. *J. Control. Release* **2016**, *225*, 133–139. [[CrossRef](#)] [[PubMed](#)]
152. Stasko, N.A.; Fischer, T.H.; Schoenfish, M.H. *S*-Nitrosothiol-modified dendrimers as nitric oxide delivery vehicles. *Biomacromolecules* **2008**, *9*, 834–841. [[CrossRef](#)] [[PubMed](#)]
153. Kou, Y.; Wan, A. Synthesis of novel *N*-diazoniumdiolates based on hyperbranched polyethers. *Bioorg. Med. Chem. Lett.* **2008**, *18*, 2337–2341. [[CrossRef](#)] [[PubMed](#)]
154. Wo, Y.; Brisbois, E.J.; Bartlett, R.H.; Meyerhoff, M.E. Recent advances in thromboresistant and antimicrobial polymers for biomedical applications: Just say yes to nitric oxide (NO). *Biomater. Sci.* **2016**, *4*, 1161–1183. [[CrossRef](#)] [[PubMed](#)]
155. Harrington, W.R.; Kim, S.H.; Funk, C.C.; Madak-Erdogan, Z.; Schiff, R.; Katzenellenbogen, J.A.; Katzenellenbogen, B.S. Estrogen dendrimer conjugates that preferentially activate extranuclear, nongenomic versus genomic pathways of estrogen action. *Mol. Endocrinol.* **2006**, *20*, 491–502. [[CrossRef](#)] [[PubMed](#)]
156. Srinageshwar, B.; Peruzzaro, S.; Andrews, M.; Johnson, K.; Hietpas, A.; Clark, B.; McGuire, C.; Petersen, E.; Kippe, J.; Stewart, A.; et al. PAMAM dendrimers cross the blood–brain barrier when administered through the carotid artery in C57BL/6j mice. *Int. J. Mol. Sci.* **2017**, *18*, 628. [[CrossRef](#)] [[PubMed](#)]



MDPI
St. Alban-Anlage 66
4052 Basel
Switzerland
Tel. +41 61 683 77 34
Fax +41 61 302 89 18
www.mdpi.com

Molecules Editorial Office
E-mail: molecules@mdpi.com
www.mdpi.com/journal/molecules



MDPI
St. Alban-Anlage 66
4052 Basel
Switzerland

Tel: +41 61 683 77 34
Fax: +41 61 302 89 18

www.mdpi.com



ISBN 978-3-03897-379-9